



# **SPRAY DRYING OF DETERGENTS IN COUNTER CURRENT TOWERS:**

**A STUDY OF TURBULENT SWIRLING FLOWS, FOULING  
AND AGGLOMERATION**

by

Victor Francia García

A thesis submitted to the University of Birmingham  
for the degree of Doctor of Engineering, EngD

School of Chemical Engineering  
College of Engineering and Physical Sciences  
University of Birmingham, Birmingham, UK  
September 2014

UNIVERSITY OF  
BIRMINGHAM

**University of Birmingham Research Archive**

**e-theses repository**

This unpublished thesis/dissertation is copyright of the author and/or third parties. The intellectual property rights of the author or third parties in respect of this work are as defined by The Copyright Designs and Patents Act 1988 or as modified by any successor legislation.

Any use made of information contained in this thesis/dissertation must be in accordance with that legislation and must be properly acknowledged. Further distribution or reproduction in any format is prohibited without the permission of the copyright holder.

## **Abstract**

This thesis is concerned with the manufacture of granular laundry detergents in counter-current swirl spray dryers. The global demand of powdered detergents is expected to increase into the next decade despite the increasing use of liquids, but the production in large swirl dryers such as those used by the sponsoring company, Procter & Gamble, is still poorly understood. The agglomeration of droplets and particles is at the heart of the process. It limits the capacity of the spray dryers and determines the main product properties. In order to control it, manufacturers have to rely heavily on experience and semi-empirical models because the access to comprehensive studies is extremely rare. The technology is only available at full scale because it makes use of swirling flows that are very difficult to replicate otherwise. Considerable costs are committed to large-scale experimentation to ensure manufacturability and product quality, particularly for new formulations. The optimization of the process requires agglomeration to be treated on a theoretical basis, which constitutes the main objective of this work.

This thesis outlines a complete framework to construct a numerical model of a swirl dryer. It examines the sources of agglomeration, identifies the steps to be followed and the limitations of the current approaches. It studies in detail the air fluid dynamics and reveals that friction has a major effect in the operation of these dryers. Friction is ignored in current models and yet, it gives rise to a drastic decay of the swirling motion and the formation of large recirculation zones. This work identifies three flow regimes across units of different scale and design, and sets up new rules to scale and control the vortex structure. The results explain the origin of the errors in current models and stress the need for a better understanding of how swirling flows develop in a confinement with rough walls. The thesis then moves into studying the interaction between the wall deposits and the solid phase. Using a tracer it documents for the first time how fouling takes place at the walls of swirl dryers. Deposition of droplets and semi-dried particles forms a clustered structure at the wall that continuously builds up and breaks down releasing fragments back into the air. This equilibrium is disregarded in all previous attempts to describe the process, and yet this work demonstrates it is an essential part of it, which plays a major role in the growth and the residence time of the solids. Finally, this thesis proposes the compartmentalization of the unit to simplify numerical models. It studies the agglomeration a function of rate, the configuration of nozzles and the heat transferred at different sections of the dryer. Special attention is paid to quantify the interaction between sprays, set up the basis for the construction of a multi-zone growth model and propose new ways to control growth based upon the wall dynamics.

## **Acknowledgements**

The people that are there no matter what, friends, family.

At times, this project has been a challenge in many aspects. I want to thank Dr. Hong Sing Tan, and Professor Mike Hounslow for their honest advice. Also a word for Adrien Serout and few others in Newcastle with whom I shared many laughs away from the politics of things. The crew in Newcastle put up with very unconventional experiments and never shied away from giving it a go.

Dr. Luis Martin de Juan in P&G has made a large contribution to this work. It is well beyond what one expects from an industrial supervisor and I thank him for that and for his help to tackle this work from an academic perspective. All in all, we were in it together and we did get it done. A word also for Professor Andrew Bayly and the many discussions we have shared. Not all of them were easy, but I want to thank him for his recognition and his ability to shoot comments in the right direction. Finally, many thanks also to Professor Mark Simmons for his availability and his patience with my writing which have really helped all the way through.

## List of Contents

### Introduction

<b>1</b>	<b>Introduction</b>	<b>1</b>
<b>2</b>	<b>A general frame for the study of counter-current swirl dryers</b>	<b>4</b>
2.1	Continuous phase fluid dynamics	6
2.2	Particle dispersion in isothermal conditions	6
2.3	Heat and mass exchange transfer processes in the absence of agglomeration	6
2.4	Wall fouling. Deposition, Sintering and Re-entrainment	7
2.5	Particle agglomeration in an air-borne condition	8
2.6	Experimental independent validation	8
<b>3</b>	<b>Thesis objectives</b>	<b>9</b>
<b>4</b>	<b>Thesis structure</b>	<b>10</b>
<b>5</b>	<b>Thesis outline</b>	<b>11</b>

### PART A. AIR SWIRLING FLUID DYNAMICS

#### Chapter I The continuous phase: Tower design, operation and measurement

	<b>Summary</b>	<b>12</b>
<b>1</b>	<b>Design and generation of the air flow in a counter-current spray dryer.</b>	<b>13</b>
1.1	Swirl generation mechanism.	13
1.2	Plenum.	13
1.3	Angular momentum flux. Swirl intensity.	13
1.4	Scale up.	15
1.5	Operation ranges.	15
<b>2</b>	<b>Methodology and Instrumentation for the characterization of the fluid dynamics.</b>	<b>17</b>

#### Chapter II Characterization of the air swirling flow in an industrial scale

	<b>Summary</b>	<b>21</b>
<b>1</b>	<b>Introduction</b>	<b>19</b>
<b>2</b>	<b>Analysis</b>	<b>23</b>
2.1	Fluid dynamics parameters.	23
2.2	Swirl intensity.	24
<b>3</b>	<b>Results and discussion.</b>	<b>27</b>
3.1	Time averaged velocity field.	27

3.1.1	Downstream effects.	27
3.1.2	Self similarity.	33
3.1.3	Asymmetry.	35
3.1.4	The decay of the swirl.	35
3.2	Turbulence statistics and periodicity.	39
3.2.1	Turbulent kinetic energy and intensity.	39
3.2.2	Reynolds stresses.	41
3.2.3	Eddy viscosity and anisotropy.	44
3.2.4	Precession of the vortex core.	44
	<b>Conclusions</b>	<b>51</b>

### **Chapter III Scaling criteria. Instabilities, recirculation and the role of friction**

	<b>Summary</b>	<b>52</b>
<b>1</b>	<b>Introduction</b>	<b>53</b>
<b>2</b>	<b>Characterization of particulate wall deposits and roughness height.</b>	<b>53</b>
<b>3</b>	<b>Results and discussion.</b>	<b>57</b>
3.1	Time averaged velocity field.	58
3.1.1	Wall friction	53
3.1.2	Vortex breakdown and recirculation zones	61
3.1.3	Symmetry and distribution to the inlet nozzles.	69
3.1.4	Self similarity.	70
3.1.5	The swirl decay.	73
3.1.6	A note on the scale up of the fluid dynamics.	77
3.2	Turbulence statistics.	78
3.2.1	Turbulent kinetic energy and normal stresses.	78
3.2.1.1	Production of turbulence owed to friction.	78
3.2.1.2	Relation to $Re$ and $\Omega$ range.	79
3.2.2	Reynolds stresses.	85
3.2.3	Periodical phenomena	91
	<b>Conclusions</b>	<b>97</b>

## **PART B. PARTICLE DYNAMICS**

### **Chapter IV The discrete phase: Agglomeration, tower subdivision and measurement**

	<b>Summary</b>	<b>99</b>
--	----------------	-----------

<b>1 Particle growth in swirl counter-current spray dryers.</b>	<b>100</b>
1.1 Wall-borne growth processes	101
1.2 Air-borne growth processes	102
1.2.1 Eulerian-Lagrangian approaches	103
1.2.2 Eulerian-Eulerian approaches	103
1.2.3 Contact and adhesion forces	105
<b>2 Operation of the detergent slurry lines</b>	<b>107</b>
<b>3 Particle dynamics</b>	<b>108</b>
3.1 Dispersion of the sprays	108
3.2 Tower subdivision	109
<b>4 Methodology and measurement.</b>	<b>114</b>
4.1 Slurry properties and atomization..	114
4.2 Product properties.	115
4.3 The drying chamber.	116
4.3.1 Wall deposition.	116
4.3.2 Temperatures.	116
4.3.3 Start up and operation.	118

## **PART B1.FOULING DYNAMICS**

### **Chapter V A tracer analysis: A dynamic equilibrium of deposition and wear**

<b>Summary</b>	<b>120</b>
<b>1 Introduction</b>	<b>121</b>
<b>2 Experimental set up and measurement</b>	<b>124</b>
<b>3 The renewal of particulate multi-layers</b>	<b>126</b>
3.1 Description of air-borne and wall-borne states	126
3.2 Outline of the tracer experiments	127
3.3 Generation and tracking of a set of active wall deposits. Sequence for a wash out experiment.	128
3.4 A note in the solid hold up and the correct conditioning of the deposits during changeovers	131
<b>4 Results and Discussion</b>	<b>133</b>
4.1 Transient production	133
4.2 Steady state production	133
4.3 Deposition and re-entrainment equilibrium	135
4.4 Quantification of the re-entrainment rate	137
4.5 Granule structure and morphology	140
4.5.1 Small and average size particles, < 850 $\mu$ m	140

4.5.2	Large particles, > 850 $\mu$ m	140
4.6	Residence time of the re-entrained material	147
4.7	Time scales in the re-entrainment mechanics	148
4.8	Exit size of air and wall-borne material	153
<b>5</b>	<b>A wall dynamics framework for swirl assisted dryers</b>	<b>153</b>
5.1	Deposition and contact mechanics	154
5.2	Ageing	157
5.3	Origin of the disruptive stresses	159
5.4	Mechanisms of re-entrainment	159
5.4.1	Dry mechanisms of erosion	159
5.4.2	Wet mechanisms of erosion	161
5.4.3	Shedding and breakage	162
	<b>Conclusions</b>	<b>162</b>

## PART B2.AGGLOMERATION KINETICS

### Chapter VI Operation of single nozzles and interaction between multiple spraying levels

	<b>Summary</b>	<b>165</b>
<b>1</b>	<b>Investigation of the growth in the operation of single nozzles.</b>	<b>166</b>
1.1	Unit design and operation	166
1.2	Experimental design and operation conditions	166
1.3	Results and Discussion	168
1.3.1	Temperature field	168
1.3.2	Wall deposits	170
1.3.3	Atomization, aging and solid-liquid separation	172
1.3.4	Product Analysis	174
1.3.4.1	Aggregation patterns in the use of single nozzle	174
1.3.4.2	Composition heterogeneity in the use of single nozzles	176
1.3.4.2.1	Water content, $X_w$ .	176
1.3.4.2.2	Activity, $X_s$	179
<b>2</b>	<b>Investigation of the interaction between multiple sprays.</b>	<b>181</b>
2.1	Agglomeration sources in a multi-level system.	181
2.2	Unit design and operation	184
2.3	Experimental design and operation conditions	184
2.4	Results and Discussion	189

2.4.1	Mass and energy balances across the chamber.	189
2.4.2	Wall deposits	196
2.4.3	Product Analysis	197
2.4.3.1	Aggregation patterns in multi-level systems.	197
2.4.3.2	Composition heterogeneity in multi-level systems	203
2.4.3.2.1	Water content, $X_w$ .	203
2.4.3.2.2	Activity, $X_s$	203
	<b>Conclusions</b>	<b>207</b>
	<b>Final Summary, Next Steps</b>	<b>209</b>

## APPENDIXES

### Appendix I The use of sonic anemometry for the study of a large confined turbulent swirling flows

	<b>Summary</b>	<b>A I - 213</b>
<b>1</b>	<b>Introduction</b>	<b>A I - 214</b>
1.1	Applicability of laser-based techniques	A I - 214
1.2	Use of sonic anemometry	A I - 215
<b>2</b>	<b>Application to a large confined vortex</b>	<b>A I - 216</b>
2.1	Operation of the units	A I - 216
2.2	Instrumentation and Methodology	A I - 217
2.2.1	Sonic anemometer	A I - 217
2.2.2	Location and orientation of the sonic path	A I - 218
2.2.3	Corrections and transformations	A I - 220
<b>3</b>	<b>Error analysis</b>	<b>A I - 222</b>
3.1	Sources of uncertainty	A I - 222
3.2	Large time scale variability	A I - 223
3.3	Aerodynamic disruption	A I - 223
3.3.1	Local aerodynamic disruption	A I - 223

3.3.1.1	Revolution of the anemometer head	A I - 225
3.3.1.2	Correlation to the shadow of the transducers	A I - 229
3.3.2	Disruption of the vortex development	A I - 246
3.4	Use of internal correction functions	A I - 254
3.5	Shift in the sonic pulse	A I - 254
	<b>Conclusions</b>	<b>A I - 257</b>
<b>Appendix II    Analysis of particle structure and the generation of porosity</b>		
	<b>Summary</b>	<b>A II - 259</b>
<b>1</b>	<b>Analysis of particle morphology</b>	<b>A II - 260</b>
1.1	Shape	A II - 260
1.2	Contacts and aggregates	A II - 260
1.3	Drying and breakage	A II - 261
<b>2</b>	<b>Particle density</b>	<b>A II - 262</b>
<b>3</b>	<b>Pore size distributions</b>	<b>A II - 263</b>
	<b>Conclusions</b>	<b>A II - 269</b>
<b>Appendix III    Control of the growth and wear mechanisms</b>		
	<b>Summary</b>	<b>A III - 290</b>
<b>1</b>	<b>Introduction</b>	<b>A III - 291</b>
<b>2</b>	<b>Experimental methodology</b>	<b>A III - 291</b>
2.1	Unit design and operation	A III - 291
2.2	Air operation. Temperature vs Momentum	A III - 291
<b>3</b>	<b>Results and Discussion</b>	<b>A III - 294</b>
3.1	Axial distribution of the heat exchanged	A III - 294
3.2	Decay of the vortex momentum	A III - 303
3.2.1	Air-borne contacts	A III - 305
3.2.2	Wall contacts	A III - 305
3.3	Wall deposits	A III - 307
3.4	Product Analysis	A III - 308
3.4.1	Aggregation patterns under different air inlet conditions.	A III - 308
3.4.2	Composition heterogeneity under different air inlet conditions.	A III - 316
	<b>Conclusions</b>	<b>A III - 319</b>
	<b>REFERENCES</b>	<b>R - 320</b>

## List of Tables

### PART A. AIR SWIRLING FLUID DYNAMICS

#### Chapter I

<b>Table 1</b>	Tower design parameters for all the scales considered.	15
<b>Table 2</b>	Range of superficial air velocity and Reynolds numbers considered.	15

#### Chapter II

<b>Table 1</b>	Swirl decay rates as a function of Reynolds number.	37
----------------	---	----

#### Chapter III

<b>Table 1</b>	Axial distribution of deposits in the dryers	54
<b>Table 2</b>	Swirl decay rate as a wall conditions function of the wall conditions.	75

### PART B1. FOULING DYNAMICS

#### Chapter V

<b>Table 1</b>	Comparison of the main operation variables to a reference production in Chapter VI.	126
<b>Table 2</b>	A summary of the statistics of the exit age distribution of the re-entrained material.	149

### PART B2. AGGLOMERATION KINETICS

#### Chapter VI

<b>Table 1</b>	Main process variables as a function of the nozzle operation level.	167
<b>Table 2</b>	Initial net wall deposition rate as a function of the nozzle location.	172
<b>Table 3</b>	Summary of operation conditions for the multi-level system and the related experiments studying the contribution of each nozzle to the product.	190
<b>Table 4</b>	Summary of the energy balance and the heat exchange rates in the chamber for a multi-level system.	194
<b>Table 5</b>	Summary of the energy balance and the heat exchange rates in the chamber for the experiments studying the contribution of each nozzle to the product	194
<b>Table 6</b>	Axial variation of the air superficial velocity in the chamber	195
<b>Table 7</b>	Summary of the initial deposition rates across the chamber	196
<b>Table 8</b>	Statistics of the mass based product size distributions.	200

## APPENDIXES

### Appendix I

<b>Table 1</b>	Uncertainty of the velocity measurements in steady state at a fixed location and under a calibrated mode.	A I - 224
<b>Table 2</b>	Uncertainty of the velocity measurements as a function of the orientation of the instrument for the low and moderate turbulent kinetic energy in the outer annular section of the vortex.	A I - 247
<b>Table 3</b>	Uncertainty of the velocity measurements as a function of the orientation of the instrument for high variability in the transition to the inner central jet of the vortex.	A I - 247

### Appendix II

<b>Table 1</b>	Particle density and porosity for the product obtained in a single nozzle production and a multi-level system as a function of particle size.	A II - 264
----------------	---	------------

### Appendix III

<b>Table 1</b>	Process conditions for the operation of different nozzles at high or low inlet air temperatures.	A III - 295
<b>Table 2</b>	Process conditions for the operation of different nozzles or a multi-level system at high or low inlet air temperatures.	A III - 296
<b>Table 3</b>	Summary of the energy balance and the drying rates in the chamber for operation of all configurations considered under high or low inlet air temperatures.	A III - 302
<b>Table 4</b>	Axial variation of the air superficial velocity in the chamber	A III - 304
<b>Table 5</b>	Axial variation of the axial momentum flux in the chamber.	A III - 304
<b>Table 6</b>	Summary of the initial deposition rates across the chamber for different nozzle positions.	A III - 307
<b>Table 7</b>	Summary of the initial deposition rates across the chamber for different nozzle positions and configurations.	A III - 308
<b>Table 8</b>	Statistics of the mass based exit product size distribution for all cases considered.	A III - 310

## List of Figures

### PART A. AIR SWIRLING FLUID DYNAMICS

#### Introduction

- |                 |  |   |
|-----------------|--|---|
| <b>Figure 1</b> | Visualization of the near wall region through Particle Image Velocimetry , PIV, experiments Hassall (2011). Reproduction with permission from the authors. | 2 |
| <b>Figure 2</b> | General numerical framework for the description of swirl counter-current spray dryers.   | 5 |

#### Chapter I

- |                 |   |    |
|-----------------|---|----|
| <b>Figure 1</b> | Nomenclature and general outline of the air line and the inlet ports for three counter-current spray drying towers. | 14 |
| <b>Figure 2</b> | Depiction the anemometer ensemble and connexions and all the modifications introduced                               | 18 |

#### Chapter II

- |                  |   |    |
|------------------|---|----|
| <b>Figure 1</b>  | Air velocity magnitude in all levels across the cylindrical chamber of the dryer.                                       | 28 |
| <b>Figure 2</b>  | Air axial velocity in all levels across the cylindrical chamber of the dryer.   | 30 |
| <b>Figure 3</b>  | Air tangential velocity in all levels across the cylindrical chamber of the dryer.                                      | 32 |
| <b>Figure 4</b>  | Air radial velocity in all levels across the cylindrical chamber of the dryer.  | 34 |
| <b>Figure 5</b>  | The axial decay of the swirl intensity across the cylindrical chamber of a tall-form dryer.                             | 36 |
| <b>Figure 6</b>  | The effect of the bulk Reynolds in the axial decay of the swirl intensity.  | 36 |
| <b>Figure 7</b>  | Turbulent kinetic energy in all levels across the cylindrical chamber of the dryer.                                     | 40 |
| <b>Figure 8</b>  | The axial variation of all normal stresses.   | 42 |
| <b>Figure 9</b>  | The impact of Reynolds in all normal stresses.  | 43 |
| <b>Figure 10</b> | Development of the Reynolds stresses across the cylindrical chamber   | 45 |
| <b>Figure 11</b> | The impact of Reynolds in the Reynolds stresses.  | 46 |
| <b>Figure 12</b> | The field anisotropy, and eddy viscosities.   | 47 |
| <b>Figure 13</b> | Example of the times series for the instantaneous tangential velocity at different locations in the unit.               | 49 |
| <b>Figure 14</b> | Analysis of periodical flow structures in the vortex. Periodogram of the velocity at different locations in the vortex. | 50 |

#### Chapter III

- |                 |   |    |
|-----------------|---|----|
| <b>Figure 1</b> | Visual inspection of the wall deposits for different initial conditions.                      | 55 |
| <b>Figure 2</b> | Detail of the deposits morphology and the roughness height for different cases and scales.    | 56 |
| <b>Figure 3</b> | A transversal cut of the deposits at the wall of largest scale.                               | 57 |
| <b>Figure 4</b> | Air velocity magnitude in all levels of one dryer for cases showing different wall deposits.  | 59 |
| <b>Figure 5</b> | Tangential air velocity in all levels of one dryer for cases showing different wall deposits. | 60 |

<b>Figure 6</b>	Axial air velocity in all levels of one dryer for cases showing different wall deposits.	62
<b>Figure 7</b>	Vortex breakdown and operation regimes in counter-current tall-form dryers.	64-66
<b>Figure 8</b>	Comparison of the velocity field in different scales. Scalability of the velocity field.	67
<b>Figure 9</b>	Comparison of the velocity field in different scales. The impact of the swirl intensity in the vortex development	68
<b>Figure 10</b>	Comparison of the velocity field in different scales. Impact of the air distributor in the vortex symmetry	70
<b>Figure 11</b>	Loss of self similarity in the velocity field under a strong friction	71-72
<b>Figure 12</b>	The impact of different wall deposits in the decay of the swirl intensity across one tower	74
<b>Figure 13</b>	Comparison of the decay of the swirl intensity for different towers according to the length given in diameters	77
<b>Figure 14</b>	Comparison of the decay of the swirl intensity for different towers according to the relative distance to the low pressure points generated at the bottom and top of the cylinder.	77
<b>Figure 15</b>	The impact of friction in the production of turbulent kinetic energy in one tower.	80
<b>Figure 16</b>	The impact of friction in the axial normal stress in one tower	81
<b>Figure 17</b>	The impact of friction in the radial normal stress in one tower.	82
<b>Figure 18</b>	The impact of friction in the tangential normal stress in one tower.	83
<b>Figure 19</b>	The evolution of the turbulent kinetic energy and all normal stresses with Reynolds in a scenario of strong friction.	84
<b>Figure 20</b>	Comparison of the turbulent kinetic energy and normal stresses in different towers showing a similar swirl intensity and flow structure.	86
<b>Figure 21</b>	The turbulent kinetic energy and normal stresses in a tower showing a higher swirl intensity and recirculation.	87
<b>Figure 22</b>	The impact of friction in the axial tangential Reynolds stress.	88
<b>Figure 23</b>	The impact of friction in the radial tangential Reynolds stress.	89
<b>Figure 24</b>	The impact of friction in the radial axial Reynolds stress.	90
<b>Figure 25</b>	Comparison of the development of Reynolds stresses in different towers showing a similar swirl intensity and flow structure.	92
<b>Figure 26</b>	The development of Reynolds stresses in a tower showing a higher swirl intensity and recirculation.	93
<b>Figure 27</b>	Analysis of the impact of friction in the periodical flow structures in the vortex. Periodogram of the velocity at different levels of a tower with different wall conditions.	94
<b>Figure 28</b>	Times series of the tangential velocity at different locations of towers of a larger scale	95
<b>Figure 29</b>	Analysis of the impact of the operation regime in the periodical flow structures in the vortex. Periodogram of the velocity at different levels of the largest towers.	96

## **PART B. PARTICLE DYNAMICS**

### **Chapter IV**

<b>Figure 1</b>	PIV visualization of the wall deposits and the near wall region (reproduced with permission from Hassall 2011) and illustration of the different types of wall impacts.	101
-----------------	---	-----

<b>Figure 2</b>	Typical morphology for spray dried detergent granules.	105
<b>Figure 3</b>	General outline of operation of a counter-current spray drying tower.	108
<b>Figure 4</b>	Compartmentalization and illustration of the spray dispersion in a counter-current spray drying tower	110
<b>Figure 5</b>	Illustration of the coalescence near the nozzle due the pick-up effect of different sized droplets.	113
<b>Figure 6</b>	PIV visualization of the concentrated annulus in the near wall region. (reproduced with permission from Hassall (2011) and Illustration of the interaction between the high velocity droplets and the high concentration region near the wall.	113
<b>Figure 7</b>	Measurements in the dryer: location of inspection areas of the walls, air temperature sensors in the cylinder and exhaust line, at the inlet line and the bottom section, and the sensors at the dryer walls	117
<b>Figure 8</b>	Detail of the arrangement of the thermocouples in a metallic hollow bar for the measurement of air temperature inside some areas of the dryer.	118

## **PART B1.FOULING DYNAMICS**

### **Chapter V**

<b>Figure 1</b>	Operation of the dryer described in Chapter IV. Modifications for the conduction of the tracer analysis.	125
<b>Figure 2</b>	Location of the wall inspection areas and the spray projection area monitored separately.	127
<b>Figure 3</b>	Air axial temperature distribution for a similar production ( $S_2$ in Chapter VI) and wall deposits axial distribution, and initial net deposition rate.	127
<b>Figure 4</b>	Description of particle history as a combination of two parallel reactors associated to the air and wall borne states.	128
<b>Figure 5</b>	Description of the tracer sequence. Initial stages, changeover and production with and without the tracer.	130
<b>Figure 6</b>	Description of the tracer sequence. Final stages, changeover and production with and without the tracer.	132
<b>Figure 7</b>	Time evolution of the tower exit rate and the product weight based size probability density function.	134
<b>Figure 8</b>	Averaged size probability density function for the spray and the product during the entire sequence.	135
<b>Figure 9</b>	Evolution of the deposits observed at the inspection level exposed to the spray projection.	136
<b>Figure 10</b>	Evolution of the normalized weight of the extractable plate present at the surface of the photographs in figure 9.	137
<b>Figure 11</b>	The ratio of material of wall-borne origin in samples taken during the wash out experiment.	139
<b>Figure 12</b>	Wall borne material. Micrographs for the initial sample and the mode of the age distribution.	141
<b>Figure 13</b>	Wall-borne material. Micrographs for the initial sample and for large particle sizes.	143
<b>Figure 14</b>	Structure of mixtures of air-borne and wall-borne material	144
<b>Figure 15</b>	Distribution of wall-borne material within the structure of large granules.	145
<b>Figure 16</b>	Examples of the distribution of wall-borne material in the interior of large granules.	145
<b>Figure 17</b>	Examples of granule morphology.	145
<b>Figure 18</b>	Heterogeneity of the structure of large granules showing show both sides of the same granule.	146
<b>Figure 19</b>	Detail of the age distribution of the re-entrained material. Comparison between the mass averaged	150

values and all size classes.

<b>Figure 20</b>	Age distribution of the re-entrained material. Comparison between the mass averaged value and small and average sized particles.	151
<b>Figure 21</b>	Age distribution of the re-entrained material. Comparison between the mass averaged value and the large sized particles.	152
<b>Figure 22</b>	Volume and mass bases size probability density functions of the atomization and the air and wall borne material.	154
<b>Figure 23</b>	Wall dynamics in counter-current spray drying. Cycle of deposition, ageing and wear at the wall.	156
<b>Figure 24</b>	Examples of the presence of ligaments in the elutriated powder and coiled structures in the product.	157
<b>Figure 25</b>	Examples of the solid bridges that bound primary particles together within large and average size granules.	158
<b>Figure 26</b>	Examples of the contacts between the air-borne and wall-borne material in the product.	160

## **PART B2.AGGLOMERATION KINETICS**

### **Chapter VI**

<b>Figure 1</b>	General outline of the sections of a counter-current spray drying tower, the air inlets and the swirl generation system.	166
<b>Figure 2</b>	Axial distribution of the air temperature as a function of nozzle position.	169
<b>Figure 3</b>	Axial distribution of wall deposits during a period of 10 to 15 min under steady state operation.	171
<b>Figure 4</b>	Comparison of the initial droplet size distribution and the product. Analysis of the variation due to ageing and the effects of solid-liquid separation.	173
<b>Figure 5</b>	Mass based product size distributions as a function of the axial location of the nozzle and different wall conditions.	175
<b>Figure 6</b>	Variation of the product water content across the product for different nozzle positions.	177
<b>Figure 7</b>	Comparison of product water content and the powder equilibrium relative humidity.	178
<b>Figure 8</b>	Variation of the content in surfactant/s across the product for different nozzle positions.	180
<b>Figure 9</b>	Subdivision of a swirl counter-current drying tower using various spraying levels.	182
<b>Figure 10</b>	Interaction fluxes between different spray levels.	184
<b>Figure 11</b>	Description of product and slurry lines in the dryer, including the nozzles used in the work described in section 2, their projection area, and the accessory water dual nozzles placed across the cylindrical chamber.	185
<b>Figure 12</b>	Location of the wall inspection areas; description of the air line and location and nomenclature of the temperature sensors used in the work described in section 2.	186
<b>Figure 13</b>	Description of the different experiments including the production in a multi-nozzle system and the isolation of contribution of each of the nozzles.	187
<b>Figure 14</b>	Air temperature field for all cases considered.	191
<b>Figure 15</b>	Axial variation of the cross sectional average temperature of the air.	193
<b>Figure 16</b>	Wall deposits at the top sections, and within the area of the spray projection of the top nozzle.	196
<b>Figure 17</b>	Wall deposits immediately above the spray projection from the bottom nozzle	196

<b>Figure 18</b>	Comparison of the mass based size distributions associated to the atomization and the product in a multi-nozzle system.	198
<b>Figure 19</b>	Comparison of the mass based product size distribution in a multi-level system and the contribution of either spray independently.	199
<b>Figure 20</b>	Comparison of the production for each spray in a multi-level system to the conditions of a single level operation.	201
<b>Figure 21</b>	Comparison of the contribution of the bottom nozzle #3 and the expectation if there were no interactions between the sprays.	202
<b>Figure 22</b>	Variation of the product water content for independent operation of the bottom nozzle in a multi-level production.	204
<b>Figure 23</b>	Variation of the product water content for the multi-level production and the top nozzle versus their replicates under different wall conditions.	205
<b>Figure 24</b>	Variation of the content in surfactant/s for the multi-level production and the contribution of each nozzle.	206

## APPENDIXES

### Appendix I

<b>Figure 1</b>	General outline of the air line in a tall-form swirl dryer. Illustration corresponds to Scale I (Chapter I)	A I - 218
<b>Figure 2</b>	Anemometer nomenclature. Spar measurement axis, the frames of reference; and attack angles.	A I - 218
<b>Figure 3</b>	Depiction the anemometer and door ensemble; the use of a back extension and definition of the frame of reference of the cylinder, the anemometer measurement axes, and the alignments.	A I - 219
<b>Figure 4</b>	Description of the position and misalignment of the ensemble in the horizontal plane and the transformations between the anemometer reference frame to the true polar coordinates.	A I - 222
<b>Figure 5</b>	Illustration of the anemometer rotation twisting the frame in a tangential flow (left to right).	A I - 225
<b>Figure 6</b>	Head revolution in a tangential flow. Position and anemometer frame of reference for different rotation angles.	A I - 227
<b>Figure 7</b>	Depiction of the drag area and the volume disrupted during the revolution described in figure 6.	A I - 228
<b>Figure 8</b>	Evolution of measurement of velocity in the anemometer frame of reference during the revolution. Low turbulence kinetic energy in the annular section of the vortex.	A I - 230
<b>Figure 9</b>	Evolution of measurement of velocity in the anemometer frame of reference during the revolution. Moderate turbulence kinetic energy in the annular section of the vortex	A I - 231
<b>Figure 10</b>	Evolution of measurement of velocity in the anemometer frame of reference during the revolution. High turbulence kinetic energy in the transition to the central jet of the vortex.	A I - 232
<b>Figure 11</b>	Evolution of the measurement of turbulence in the anemometer frame of reference during the revolution. Low turbulence kinetic energy in the annular section of the vortex.	A I - 233
<b>Figure 12</b>	Evolution of the measurement of turbulence in the anemometer frame of reference during the revolution. Moderate turbulence kinetic energy in the annular section of the vortex.	A I - 234
<b>Figure 13</b>	Evolution of the measurement of turbulence in the anemometer frame of reference during the	A I - 235

	revolution. High turbulence kinetic energy in the transition to the central jet of the vortex.	
<b>Figure 14</b>	Evolution of the measurement of turbulence in the polar frame of reference of the cylinder, during the revolution. Low turbulence kinetic energy in the annular section of the vortex.	A I - 236
<b>Figure 15</b>	Evolution of the measurement of turbulence in the polar frame of reference of the cylinder, during the revolution. Moderate turbulence kinetic energy in the annular section of the vortex.	A I - 237
<b>Figure 16</b>	Evolution of the measurement of turbulence in the polar frame of reference of the cylinder. High turbulence kinetic energy in the transition to the central jet of the vortex.	A I - 238
<b>Figure 17</b>	Correlation of the errors in velocity magnitude and direction with the path shadow for both independent half revolutions. Low turbulence kinetic energy in the annular section of the vortex.	A I - 240
<b>Figure 18</b>	Correlation of the errors in velocity magnitude and direction with the path shadow for both independent half revolutions. Moderate turbulence kinetic energy in the annular section of the vortex.	A I - 241
<b>Figure 19</b>	Correlation of the errors in velocity magnitude and direction with the path shadow for both independent half revolutions. High turbulence kinetic energy in the transition to the central jet of the vortex.	A I - 242
<b>Figure 20</b>	Correlation of the errors in variability with the path shadow for both independent half revolutions. Low turbulence kinetic energy in the annular section of the vortex.	A I - 243
<b>Figure 21</b>	Correlation of the errors in variability with the path shadow for both independent half revolutions. Moderate turbulence kinetic energy in the annular section of the vortex.	A I - 244
<b>Figure 22</b>	Correlation of the errors in variability with the path shadow for both independent half revolutions. High turbulence kinetic energy in the transition to the central jet of the vortex.	A I - 245
<b>Figure 23</b>	Correlation between errors in velocity magnitude and direction and the attack angle. Low turbulence kinetic energy in the annular section of the vortex.	A I - 248
<b>Figure 24</b>	Correlation between errors in velocity magnitude and direction and the attack angle. Moderate turbulence kinetic energy in the annular section of the vortex.	A I - 249
<b>Figure 25</b>	Correlation between errors in velocity magnitude and direction and the attack angle. High turbulence kinetic energy in the transition to the central jet of the vortex.	A I - 250
<b>Figure 26</b>	Correlation between errors in variability and the attack angle. Low turbulence kinetic energy in the annular section of the vortex.	A I - 251
<b>Figure 27</b>	Correlation between errors in variability and the attack angle. Moderate turbulence kinetic energy in the annular section of the vortex.	A I - 252
<b>Figure 28</b>	Correlation between errors in variability and the attack angle. High turbulence kinetic energy in the transition to the central jet of the vortex.	A I - 253
<b>Figure 29</b>	Illustration of the disruption to the transport of turbulence by the arrangement crossing the vortex core.	A I - 255
<b>Figure 30</b>	Example of the population of instantaneous attack angles obtained with and without the use of the calibration.	A I - 256

## Appendix II

<b>Figure 1</b>	Variation of particle density and porosity in a single nozzle operation	A II - 265
<b>Figure 2</b>	Variation of particle density and porosity in a multi-level operation.	A II - 265
<b>Figure 3</b>	Intrusion curves of Hg for the product in a single nozzle operation.	A II - 266

<b>Figure 4</b>	Intrusion curves of Hg for the product in a multi-level nozzle operation.	A II - 267
<b>Figure 5</b>	Comparison of the intrusion curves of Hg for the product of a single or a multi-level operation.	A II - 268
<b>Figure 6</b>	Typical morphology of detergent granules under optical microscopy.	A II - 270
<b>Figure 7</b>	Examples of morphology. Single nozzle operation. Elutriates.	A II - 271
<b>Figure 8</b>	Examples of morphology. Multi-level operation. Elutriates.	A II - 272
<b>Figure 9</b>	Examples of morphology. Single nozzle operation. $x_p < 150 \mu m$ .	A II - 273
<b>Figure 10</b>	Examples of morphology. Multi-level operation. $x_p < 150 \mu m$ .	A II - 274
<b>Figure 11</b>	Examples of morphology. Single nozzle operation. $150 < x_p < 250 \mu m$ .	A II - 275
<b>Figure 12</b>	Examples of morphology. Multi-level operation. $150 < x_p < 250 \mu m$ .	A II - 276
<b>Figure 13</b>	Examples of morphology. Single nozzle operation. $250 < x_p < 355 \mu m$ .	A II - 277
<b>Figure 14</b>	Examples of morphology. Multi-level operation. $250 < x_p < 355 \mu m$ .	A II - 278
<b>Figure 15</b>	Examples of morphology. Single nozzle operation. $355 < x_p < 450 \mu m$ .	A II - 279
<b>Figure 16</b>	Examples of morphology. Multi-level operation. $355 < x_p < 450 \mu m$ .	A II - 280
<b>Figure 17</b>	Examples of morphology. Single nozzle operation. $450 < x_p < 600 \mu m$ .	A II - 281
<b>Figure 18</b>	Examples of morphology. Multi-level operation. $450 < x_p < 600 \mu m$ .	A II - 282
<b>Figure 19</b>	Examples of morphology. Single nozzle operation. $600 < x_p < 850 \mu m$ .	A II - 283
<b>Figure 20</b>	Examples of morphology. Multi-level operation. $600 < x_p < 850 \mu m$ .	A II - 284
<b>Figure 21</b>	Examples of morphology. Single nozzle operation. $850 < x_p < 1180 \mu m$ .	A II - 285
<b>Figure 22</b>	Examples of morphology. Multi-level operation. $850 < x_p < 1180 \mu m$ .	A II - 286
<b>Figure 23</b>	Examples of morphology. Multi-level operation. $850 < x_p < 1180 \mu m$ .	A II - 287
<b>Figure 24</b>	Examples of morphology. Single nozzle operation. $1180 < x_p < 1800 \mu m$ .	A II - 288
<b>Figure 25</b>	Examples of morphology. Multi-level operation. $1180 < x_p < 1800 \mu m$ .	A II - 289

### Appendix III

<b>Figure 1</b>	General outline of operation of a counter-current spray drying tower.	A III - 292
<b>Figure 2</b>	Measurements in the dryer: location of inspection areas of the walls, air temperature sensors in the cylinder and exhaust line, at the inlet line and the bottom section, and the sensors at the dryer walls.	A III - 293
<b>Figure 3</b>	Air temperature field for all the cases considered under different inlet air conditions.	A III - 297
<b>Figure 4</b>	Variation of the cross-sectional average air temperature for all the cases considered under different inlet air conditions.	A III - 298
<b>Figure 5</b>	Summary of the energy balance across different sections of the chamber for all cases considered under different inlet air conditions.	A III - 300
<b>Figure 6</b>	Description of concentration, dispersion and the rate of wall impacts associated to the transition of the swirling air flow from high to low velocities by increasing the drying temperature.	A III - 306
<b>Figure 7</b>	Inspection of the wall deposits associated to top levels in a single nozzle operation under different inlet air conditions.	A III - 307

<b>Figure 8</b>	Inspection of the wall deposits associated to top levels in a multi-level operation under different inlet air conditions	A III - 307
<b>Figure 9</b>	Comparison of the droplet size to the reference growth patterns from Chapter VI.	A III - 309
<b>Figure 10</b>	Variation of the product size distribution from the top nozzle under different inlet air conditions.	A III - 311
<b>Figure 11</b>	Variation of the product size distribution from the middle nozzle under different inlet air conditions.	A III - 312
<b>Figure 12</b>	Variation of the product size distribution from the bottom nozzle under different inlet air conditions.	A III - 313
<b>Figure 13</b>	Visualization of the near wall region through Particle Image Velocimetry , PIV, experiments, reported by Hassall (2011). Reproduction with permission from the authors.	A III - 314
<b>Figure 14</b>	Variation of the product mass based particle size distribution in a multi-level system under different inlet air conditions.	A III - 315
<b>Figure 15</b>	Variation of the product water content for a single nozzle operation under different inlet air conditions.	A III - 317
<b>Figure 16</b>	Variation of the product water content for a single nozzle operation or a multi-level system under different inlet air conditions.	A III - 318

## Publications

The following journal publications arise from this work, are submitted or ready for submission:

Francia V., Martin L., Bayly A.E. and Simmons M.J.H. (2014). The role of wall deposition and re-entrainment in swirl spray dryers. Submitted to AICHE J.

Francia V., Martin L., Bayly A.E. and Simmons M.J.H. (2014). Use of sonic anemometry for the study of turbulent swirling flows in large confined industrial units. Submitted to Measurement Science and Technology.

Francia V., Martin L., Bayly A.E. and Simmons M.J.H. (2014). An experimental investigation of the swirling flow in a tall-form counter-current spray dryer. Submitted to Experimental Thermal and Fluid Science.

Ali M., Mahmud T., Heggs P.J., Ghadiri M., Bayly A.E., Francia V., Djurdjevic D., Ahmadian H., Martin L. (2014). CFD Modelling of swirling flow in a counter-current pilot-plant spray drying tower. Submitted to Chemical Engineering Science.

Francia V., Martin L., Bayly A.E. and Simmons M.J.H. (2014). The influence of wall friction on flow regimes and scale up of swirl spray dryers. Submitted to Chemical Engineering Science.

Francia V., Martin L., Bayly A.E. and Simmons M.J.H. (2015). Agglomeration in swirl tall-form spray dryers I: Operation of single atomizers. To be submitted to Chemical Engineering Science.

Francia V., Martin L., Bayly A.E. and Simmons M.J.H. (2015). Agglomeration in swirl tall-form spray dryers II: Interaction between multiple spraying levels. To be submitted to Chemical Engineering Science.

Francia V., Martin L., Bayly A.E. and Simmons M.J.H. (2015). Agglomeration in swirl tall-form spray dryers III: Control of growth and wear mechanisms. To be submitted to Chemical Engineering Science.

The following publications are accepted in the proceedings of peer-reviewed international conferences as a first author:

Francia, V., Martin, L., Bayly, A.E. and Simmons, M.J.H., 2011. Origin of particle aggregation mechanisms in a pilot scale counter-current spray drying tower. Oral Presentation. Full paper accepted. 5th International Granulation Workshop. Lausanne, Switzerland.

Francia, V., Martin, L., Bayly, A.E. and Simmons, M.J.H., 2013. The role of wall friction in the development, decay and breakage of an air vortex turbulent confined vortex. Oral Presentation. Full paper accepted. 8th International Congress in multi phase flow, ICMF, Jeju, South Korea.

Francia, V., Martin, L., Bayly, A.E. and Simmons, M.J.H., 2014. Deposition and wear of deposits in swirl spray driers: The equilibrium exchange rate and the wall-borne residence time. Oral Presentation. Full paper accepted. Procedia Engineering. The 7th World Congress in particle Technology. Beijing, R.P. China.

Francia, V., Martin, L., Bayly, A.E. and Simmons, M.J.H., 2014. Particle aggregation in large counter-current spray drying towers: Nozzle configuration, vortex momentum and temperature. Oral Presentation. Full paper accepted. Procedia Engineering. The 7th World Congress in particle Technology. Beijing, R.P. China.

or as a contributor:

Ali M., Mahmud T., Heggs P.J., Ghadiri M., Francia V., Bayly A.E., Djurdjevic D., Ahmadian H. and Martin L. (2013). CFD modeling of a counter-current spray drying tower. Oral Presentation. 8th International Congress in multi phase flow, ICMF, Jeju, South Korea.

In addition to talks in Procter & Gamble R&D, the following invited talks have been given in academia:

Francia, V. 2011. Relevance of particle aggregation in a counter-current spray drying tower. Invited talk, Institute of Particle Science and Engineering. The University of Leeds. June 2011, Leeds. United Kingdom.

## Nomenclature

$A$	Swirl decay rate in equation (11), Chapter II. or Absorbance, Chapter V.
$A_c$	Cross sectional area in the cylinder, $m^2$
$A_i$	Combined area of all the air inlet ports, $m^2$
$B$	Swirl decay constant in equation (11), Chapter II.
$C$	Collision rate kernel, Chapter IV, $m^3 s^{-1}$
$D$	Diameter of the cylinder, $m$
$E$	Age probability density function, $s^{-1}$ .
$G$	Storage or loss module of the slurry, $Pa$
$G_\theta$	Axial angular momentum flux, $kg m^{-1} s^{-2}$
$G_z$	Axial momentum flux, $kg s^{-2}$
$G_{z,av}$	Axial momentum flux based on the bulk/superficial velocity $U_{av}$ , $kg s^{-2}$
$H$	Length of the cylindrical chamber of the dryer, above the air inlet ports, $m$
$H_{A,IN}$	Inlet air enthalpy rate taking ambient air as a reference, $J s^{-1}$
$\Delta H$	Rate of enthalpy variation, $J s^{-1}$
$\Delta H_{Lat}$	Latent enthalpy rate of the vapour generated, $J s^{-1}$
$\Delta H_{DA,Sn}$	Enthalpy variation between the outlet and inlet dry air, $J s^{-1}$
$\Delta H_{P,Sn}$	Enthalpy variation between the outlet streams of product, elutriates and water vapour and the inlet stream of slurry, $J s^{-1}$
$M$	Total mass, $kg$ or Mass rate, $kg s^{-1}$
$M_A$	Air inlet mass rate, $kg s^{-1}$
$M_{DA}$	Dry air mass rate through the cylinder, $kg s^{-1}$
$M_c$	Air mass rate through the cylinder, $kg s^{-1}$
$M_i$	Combined air mass rate through the inlet ports, $kg s^{-1}$
$Oh^2$	Ohnesorge number, $Oh^2 = 2 \mu_p^2 / x_p \rho_p \sigma_p$
$P$	Static air pressure, $kg m^{-1} s^{-2}$
$Pe$	Peclet number. Ratio of convective to diffusive mass transfer, defined as $Pe =$

$\frac{x_p \partial x_p}{4d_w \partial t}$  for a receding surface at constant evaporation rate Vehring *et al.* (2007)

$P_S$	Combined shadow of all sonic paths, $P_S = \sum_{i=1}^{i=3} s_i$ , Appendix I.
$Q_{Loss}$	Rate of heat lost in the dryer, Js <sup>-1</sup>
$Q_{Ex}$	Rate of heat ex-changed in the dryer, Js <sup>-1</sup>
$Q_{Lat}$	Rate of heat utilised in vaporization, Js <sup>-1</sup>
$Q_S$	Rate of heat transferred to the solids, Js <sup>-1</sup>
$R$	Radius of the cylinder, m
$R_i$	Radius of the tower cross-section at the level of the air inlet ports, m
$Re$	Reynolds number $Re = DU_{av}/\nu$
$S$	Swirl number in equation (5), Chapter II or Dilution factor in equation (1), Chapter V
$St$	Strouhal number, $St = f \cdot D / \bar{U}_{av}$
$T$	Time averaged temperature, °C
$T_A$	Time averaged air temperature, °C
$\tilde{T}_A$	Air mass averaged temperature, $\tilde{T}_A = \int \bar{\rho}_A \bar{U}_A \bar{T}_A dA / \int \bar{\rho}_A \bar{U}_{A,z} dA$ , where $U_A$ is taken from the values at isothermal conditions in Chapter II, °C
$T_{amb}$	Ambient air temperature, °C
$T_{Boil}$	Boiling temperature, °C
$T_P$	Temperature of the product in the tower belt, °C
$T_S$	Temperature of the slurry at the nozzle, °C
$U$	Time averaged velocity / velocity component, m s <sup>-1</sup>
$U_A$	Air velocity, m s <sup>-1</sup>
$U_{av}$	Bulk or superficial air velocity. $U_{av} = M_C / \rho A_C$ , m s <sup>-1</sup>
$U_i$	Velocity component in <i>i</i> -th-axis, m s <sup>-1</sup> or Air velocity at the inlet ports, $U_i = M_i / \rho A_i$ , m s <sup>-1</sup>
$U_p$	Particle velocity, m s <sup>-1</sup>
$U_{p,i}$	Initial droplet velocity from the nozzle, m s <sup>-1</sup>
$U_{p,Sd}$	Particle sedimentation or free falling velocity, m s <sup>-1</sup>

$U_{p,t}$	Particle terminal velocity, $\text{m s}^{-1}$
$U_{p,x}$	Axial component of the particle velocity, $\text{m s}^{-1}$
$U_{p,\theta}$	Tangential component of the particle velocity, $\text{m s}^{-1}$
$W$	Mass exited in a given time and size range, Chapter V, $\text{kg}$
$X$	Spatial coordinates in equation (2), Chapter IV. or Ratio of wall-borne material in equation (1), Chapter V.
$X_w$	Water mass fraction
$X_s$	Surfactant/s mass fraction in a dry basis
$a$	Revolution angle, Appendix I, $^\circ$
$a_1, a_2, a_3$	Frame of reference of the anemometer in Figure 2, Appendix I
$d$	Diameter of the vortex finder, $\text{m}$
$d_w$	Water diffusivity, $\text{m}^2 \text{s}^{-1}$
$erH$	Powder equilibrium relative humidity, $\%$
$f$	Oscillation frequency, $\text{Hz}$ or Particle size density function, $\log(\mu\text{m})^{-1}$ or Number density field in Chapter IV, $\text{m}^{-6}$
$g$	Head revolution angle, Appendix I, $^\circ$
$h$	Convective heat transfer coefficient, $\text{J m}^{-2} \text{s}^{-1} \text{K}^{-1}$
$n$	Particle number concentration, $\text{m}^{-3}$
$r$	Coordinate in the radial direction, $\text{m}$ or Rate, $\text{kg s}^{-1}$ or Heat transfer rate per m and kg of dry slurry, $\text{J m}^{-1} \text{g}^{-1} \text{kg}^{-1}$
$r_{d,o}$	Initial wall deposition rate, $\text{g m}^{-2} \text{min}^{-1}$
$r_c$	Collision rate per unit volume, $\text{m}^{-3} \text{s}^{-1}$
$r_a$	Aggregation rate per unit volume, $\text{m}^{-3} \text{s}^{-1}$
$rH$	Relative humidity, $\%$
$s_i$	Shadow of the $i$ -th path x 1/3, Appendix I
$u_i$	Air velocity fluctuation in the $i$ -axis, $\text{m s}^{-1}$

$u_p$	Particle velocity field, $\text{m s}^{-1}$
$w$	Exit rate of dyed or wall-borne material, Chapter V, $\text{kg s}^{-1}$
$x_p$	Particle diameter, $\mu\text{m}$
$x$	Distance from the centreline in along a diameter, $\text{m}$ or Distance from the inner wall along $D$ , Appendix I, $\text{m}$
$y$	Cartesian axis in figure 4, Appendix I, $\text{m}$
$z$	Axial coordinate in the tower, above the air inlet ports, $\text{m}$

*Greek letters and symbols*

$\Delta$	Variation, or error after the subtraction of the reference, Appendix I
$\phi$	Probability of particle collision
$\Omega$	Swirl intensity.
$\alpha$	Gyration angle or misalignment over $\alpha_2$ in Figure 3, Appendix I, $^\circ$
$\beta$	Aggregation rate kernel, Chapter IV, $\text{m}^3 \text{s}^{-1}$ or Gyration angle or misalignment over $\alpha_3$ in Figure 3, Appendix I, $^\circ$
$\gamma$	Anemometer misalignment in the horizontal plane, Figure 4, Appendix I, $^\circ$
$\delta$	Attack angle to the horizontal plane in equation (1), Appendix I, $^\circ$
$\varepsilon$	Roughness wall height, $\text{m}$ or Intra-particle porosity, %
$\varepsilon_{abs}$	Intra-particle porosity in pores below the envelope threshold, Appendix II, %
$\varepsilon_{ske}$	Intra-particle porosity, Appendix II, in pores between the envelope and skeletal thresholds, Appendix II, %
$\eta_t$	Thermal efficiency in the dryer, $\eta_t = (T_{A,IN} - T_{A,EX}) / (T_{A,IN} - T_{amb})$
$\eta_h$	Heat transfer efficiency in the dryer, $\eta_h = Q_s / H_{A,IN}$
$\kappa$	Specific turbulent kinetic energy, $\text{m}^2 \text{s}^{-2}$
$\lambda$	Swirl decay rate in equation (9), Chapter II or Attack angle to the frame axis $\alpha_2$ in equation (2), Appendix I, $^\circ$
$\mu$	Slurry viscosity, $\text{kg s}^{-1}\text{m}^{-1}$
$\nu$	Kinematic viscosity, $\text{m}^2 \text{s}^{-1}$

$\xi$	Axial alignment of the air inlet ports, Chapter I, °
$\rho$	Density, kg m <sup>-3</sup>
$\rho_{abs}$	Absolute particle density including no pores in Appendix II, kg m <sup>-3</sup>
$\rho_{bulk}$	Bulk particle density in Appendix II, including cavities $< 353\mu m$ , kg m <sup>-3</sup>
$\rho_{env}$	Envelope particle density, including pores smaller than the threshold in Table 1 in Appendix II in Appendix II, kg m <sup>-3</sup>
$\rho_{ske}$	Skeletal particle density in Appendix II, including pores $< 6 nm$ , kg m <sup>-3</sup>
$\sigma$	Surface tension, kg s <sup>-2</sup>
$\sigma_{ij}$	Variance / Covariance of velocity fluctuations $u_i u_j$ , m <sup>2</sup> s <sup>-2</sup>
$\theta$	Tangential coordinate in the tower, °
$\tau_w$	Wall shear stress, kg m <sup>-1</sup> s <sup>-2</sup>
$\tau_p$	Particle residence time, s <sup>-1</sup>
$\varphi$	Radial alignment of the air inlet nozzles, °
$\epsilon$	Collision efficiency (probability of growth)

*Subscripts, superscripts and caps*

$A$	For the air.
$C, O$	With and without the use of the calibration function, Appendix I
$E$	For the elutriated fraction, or Value of the best estimate taken as reference, Appendix I
$EP$	For the full powder exiting the tower (elutriates + product from the bottom)
$P$	For the particle. or For the product exiting the tower from the bottom,
$IN$	Inlet conditions.
$DA$	Dry air.
$EX$	Exhaust conditions
$T, B$	Related to the top or bottom set of sonic transducers, Appendix I
$W', U', V'$	Spar measurement axis of the H50 Solent Anemometer in Figure 2, Appendix I.
$a_i$	Along the $i$ -th spar axis of the anemometer.

<i>d</i>	Deposition.
<i>e</i>	Erosion.
<i>ith</i>	For the <i>i</i> -th section or the <i>i</i> -th percentile in Appendix I.
<i>n</i>	Time range, Chapter V
<i>o</i>	Initial or at the initial sample, Chapter V
<i>p</i>	For the particles, or the product from the tower bottom end
<i>r</i>	Radial direction or Reference point in equations (9) and (11), Chapter II
<i>r, z, <math>\theta</math></i>	Polar coordinates, along radial, vertical and tangential direction.
<i>s</i>	For the <i>s</i> -th size fraction, Chapter V
<i>t</i>	At time <i>t</i> , or in sample at time <i>t</i> , Chapter V.
<i>w</i>	For the water or at the wall.
<i>z</i>	Axial position in the tower measured from the air inlets.
<i>abs</i>	Absolute.
<i>env</i>	Envelope.
<i>final</i>	At the average of the steady state period.
<i>Lat</i>	Latent
<i>log</i>	Based in the logarithm of time <i>t</i> .
<i>max</i>	Upper side of an interval
<i>ref</i>	For the reference obtained in $P - 2$ in Chapter V
<i>wall</i>	At the wall
*	For the door-anemometer ensemble.
—	Indicates time average.
°, —, +	Best estimate, under and over estimations of $\Omega$ , Chapter III
+ , ~, —	Operation at different $T_A$ and $U_A$ ranges, Appendix III
1,2,3	Auxiliary axis in Figure 4, Appendix I or Sonic path numbers, Appendix I

*Abbreviations*

<i>AD</i>	Age distribution.
<i>CDC</i>	Characteristic Drying Curve.
<i>CFD</i>	Computational Fluid Dynamics.
<i>CRZ</i>	Central recirculation region.
<i>DSC</i>	Differential Scanning Calorimetry.
<i>FFT</i>	Fast Fourier Transform.
<i>LDA</i>	Laser Doppler Anemometry.
<i>LES</i>	Large Eddy Simulations.
<i>PID</i>	Proportional, Integral and Derivative controller.
<i>PIV</i>	Particle Image Velocimetry.
<i>PVC</i>	Precession of the vortex core.
<i>REA</i>	Reaction Engineering Approach.
<i>RMS</i>	Reaction Engineering Approach.
<i>VBD</i>	Vortex breakdown.



# INTRODUCTION

## 1. Introduction

The work in this thesis is concerned with the manufacture of granular laundry detergents, and has been carried out under the sponsorship and supervision of Procter & Gamble (P&G), a global manufacturer. The detergents are comprised of a granular mixture of which 30 – 90 % of the material is produced in large counter-current spray dryers. Huntington (2004) explains the evolution of use of swirl designs in P&G, from the initial comprehensive works in the 70's to the current need for a better standardization. One of the main obstacles is the lack of knowledge of how particles interact in the dryer and of which agglomeration mechanisms control the structure of the final granules. This is poorly understood in a swirl counter-current unit because the data is scarce and rarely public. Huntington (2004) stresses the need to combine the growing knowledge of agglomeration and spray drying processes in academia with the experience of manufacturers in design and operation. This work pursues the construction of an overall working frame and addresses the main issues to investigate experimentally particle interactions.

Agglomeration is used to control the size of many particulate products, but usually involves simple processes where material properties do not change (e.g. addition of a liquid binder in a solid matrix, wet granulation). Spray drying differs and it is the main operation used by industry for the production of powders from slurry with a high solvent content (e.g. water). These are atomized into a drying chamber, where the volatile phases are removed by contact with a dry gas (e.g. hot air) to generate a particulate product. In these cases, agglomeration shows a far more complex physics because the morphology of the droplets or particles changes. Co-current flow between the solids and air is preferred for manufacture of degradable products such as pharmaceuticals, enzymes and food. Here, the spray and the air come into contact at the top of a chamber where most of the heat and mass is exchanged (Masters 1972). The dry product is not exposed to high temperatures because flowing down, the solids lose their water content and the air temperature drops rapidly. Conversely, counter-current designs are used for the production of thermally stable powders such as detergents or ceramic materials where the hot air is introduced at the bottom end of the chamber. This causes an increase in the residence time of droplets and particles and improved energy efficiency by establishing a higher overall  $\Delta T$  between the phases. P&G makes use of a strong turbulent swirling flow to further optimise the heat and mass transfer by increasing the relative velocity between the air and the solids.

Most published data refers to co-current spray dryers, particularly used by the food industry. Large swirl

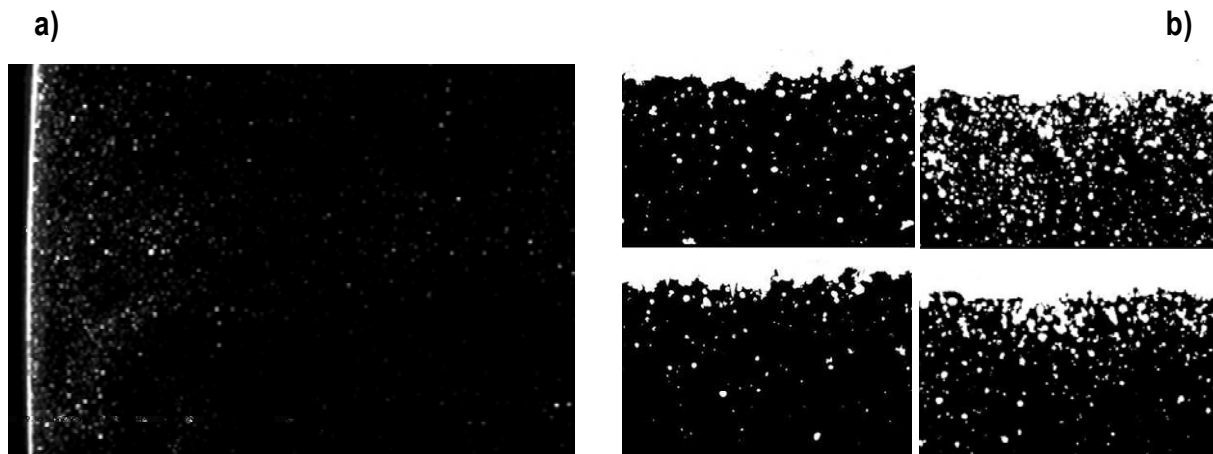


**Figure 1.** Visualization of the near wall region through Particle Image Velocimetry , *PIV*, experiments, reported by Hassall (2011) a) near wall particle concentration (cross section, wall on the left) and b) wall multi-layered deposits (cross section, wall on the top). Reproduction with permission from the authors.

counter-current towers possess a) more complex fluid dynamics due to the recirculation and instabilities generated by the centrifugal force and a higher particle concentration,  $n$ ; b) a more complex particle dynamics, intimately related to the interaction with the wall where most of the product appears to concentrate and flow down (see Figure 1a, Hassall 2011) and c) the promotion of particle-particle and particle-wall contacts, which lead to coalescence, agglomeration, breakage and substantial wall deposition (see Figure 1b, Hassall 2011).

A lack of precise understanding of the growth mechanisms is a major drawback of current numerical models (e.g. Langrish and Fletcher 2003; Fletcher et al 2006; Zbiciński and Xuanyou 2006; Langrish 2009; Palzer 2011). Huntington (2004) explains some of the implications for the detergent industry. Full scale dryers tend to maximise the production rate whilst maintaining certain quality thresholds, in particular the product size and density. As the rate increases agglomeration grows significantly and the product becomes too coarse and too wet, limiting capacity and energy efficiency. P&G patented designs (Davies *et al.* 1971) reduce the agglomeration by placing several atomizers in multiple levels and can operate at higher particle loadings than nil swirl towers or co-current dryers (Huntington 2004).

However, significant particle growth occurs in all cases and the increase in size governs the overall drying efficiency in the unit, and most of final product properties. This is neither well understood nor has been optimised. There is a clear dearth of data as pointed by Zbiciński and Piatkowski (2009). Some of the reasons behind are, 1- the large costs involved in experimentation, 2- the complexity of generating reliable and comprehensive data at full scale (e.g. unit volumes are  $> 100 - 1000 m^3$ ) 3- multiple

design standards, listed by Huntington (2004), 4- restricted access to actual production units, 5- difficulty of sampling or installing any type of probe inside a drying chamber, and as a result of this 6- difficulties in characterising experimentally drying kinetics, agglomeration or fouling in an independent manner.

The stability of the swirling flow has been studied in laboratory and pilot scale facilities by Sharma (1990), Fieg *et al.* (1998) or later Bayly *et al.* (2004) and described numerically by Harvie *et al.* (2001) or more recently Ali (2014). However, moving into large units, experiments are rarely reported. Residence time analysis has been carried out by Place *et al.* (1959) and Paris *et al.* (1972), and limited measurements of air velocities are given by Wawrzyniak *et al.* (2012). Visualization of the near wall region is reported by Hassall (2011). The description of the solid phase and drying kinetics in pilot scale towers was also included in the study of Fieg *et al.* (1998) and in the extensive work of the Professor Ireneusz Zbiciński's group at Lodz Technical University, Poland. They report experimental data in Zbiciński (1995), Zbiciński *et al.* (2002a, 2002b) and Zbiciński and Piatkowski (2007, 2009) and numerical work in Zbiciński and Zietara (2004) and Zbiciński and Xuanyou (2006).

Oakley (1994), Masters (1995) and Kemp and Oakley (2002) describe further how scale up still relies heavily on experience and the operation of pilot scale units. In part, this owes to the challenges faced by mathematical modelling. Particle dynamics is driven by the complexity of the interactions between the solids and the air, which involve large heat and mass transfer rates (Oakley 2004). Langrish and Fletcher (2003) or the recent review by Kuriakose and Anandharamakrishnan (2010) highlight the many benefits of using Computational Fluid Dynamics (CFD) models, for the optimization of co-current units. Many authors provide examples of coupled Eulerian-Lagrangian models (e.g. Zbicinski 1995, Harvie *et al.* 2002, Huang *et al.* 2006; Mezhericher *et al.* 2010a). In many cases, describing the continuous phase presents no major issues in a co-current mode, but it remains a challenge in counter-current towers due the instability of the swirl, similar to other cyclonic flows in separators or in swirl combustors.

The solids are usually treated in a Lagrangian manner using the method given by Crowe (1980, 1983) to describe the interaction term between the phases. Integrating numerically these processes in a large volume remains a major computational challenge, particularly when attempting to track particle-particle contacts. Heat and mass exchange terms can be computed by the application of a Characteristic Drying Curve (Langrish and Kocke 2001) or the more recent Reaction Engineering Approach (e.g. Chen and Lin 2005), but often include solving a complex single droplet drying model to describe how droplets transform into porous particles. Mezhericher *et al.* (2010b) reviews the many efforts made in this regard

(e.g. Kadja and Bergeles 2003, Dalmaz *et al.*, 2007, Mezhericher *et al.*, 2007, 2008). In the case of detergents and slurries containing solids, droplet drying entails a transition from an initial viscoelastic drop to the formation of an outer hard porous crust, which then thickens, followed ultimately by the generation of cavities when vapour forms inside and either bursts out or expands the structure (e.g. Hetch and King 2000, Handscomb *et al.* 2009, Handscomb and Kraft 2010).

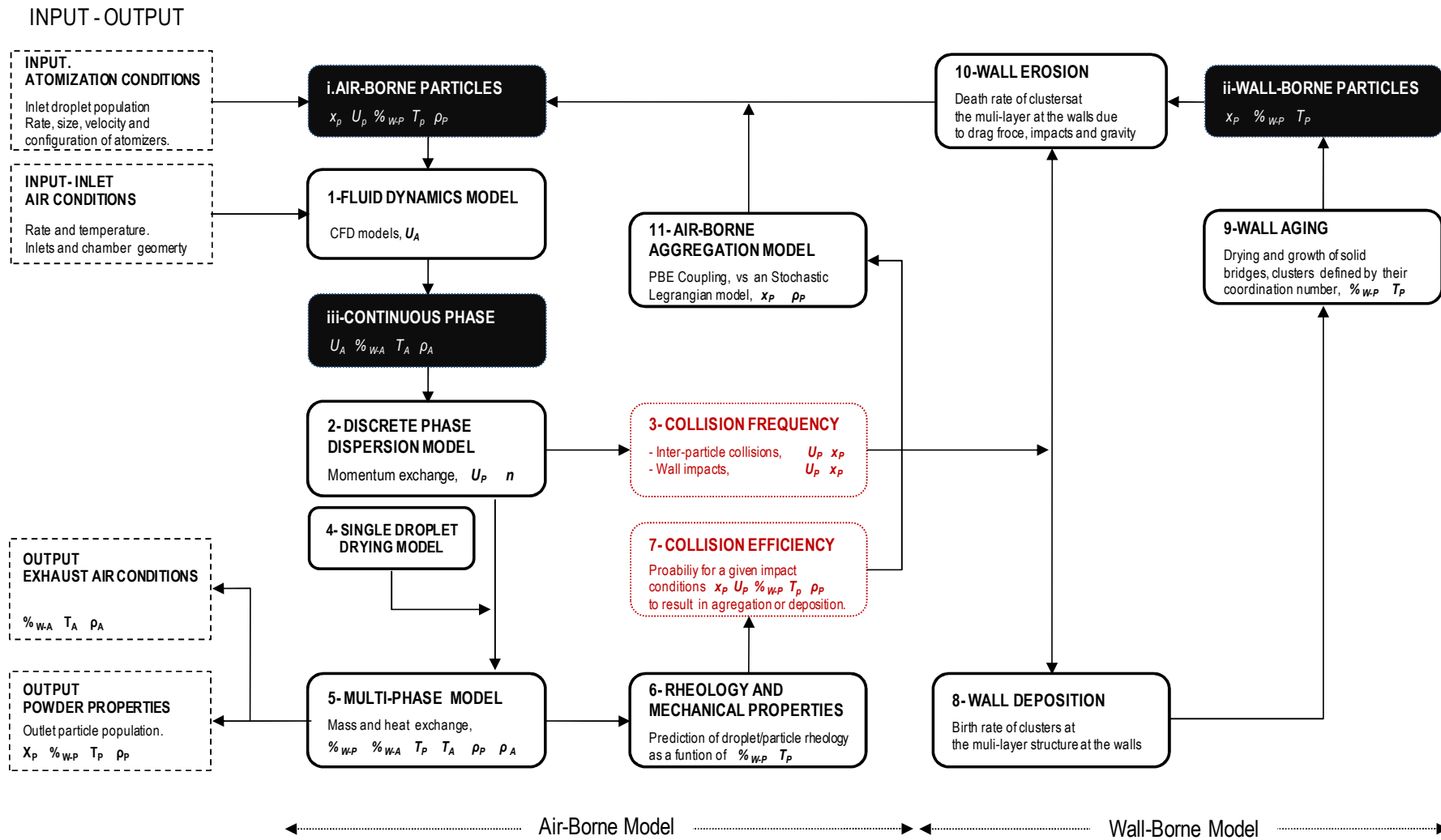
The use of Euler-Lagrange multi-phase models has been recently reviewed by Subramaniam (2013). These models suit spray dryers because in general, co-current units show a low  $n$  and can be considered dilute systems (i.e. particle loading does not affect the air significantly) with the exception of areas where the spray/s cause a significant disruption to the air. Counter-current units cannot be *a priori* be considered comparable. In the context of swirl, accumulation occurs in an annular region near the wall (see Figure 1a), and it is unclear what impact this has on the air flow. Furthermore, complexities arise from a) the flow stability affected by the swirl intensity, the particle loading and wall friction (Moshkin *et al.* 2007) and b) the effects of fouling and the interaction between the particles that concentrate near the wall and those that are deposited, see Figures 1a and 1b.

Particle interactions and aggregation have been studied far less. Coalescence or growth models have been mainly developed on the basis of sprays (e.g. Ruger *et al.*, 2000 or Nijdam *et al.*, 2006) and were only applied to co-current dryers. Sommerfeld (2001) first provided a stochastic collision model that was implemented into a CFD framework for prediction of agglomeration (Verdurmen *et al.*, 2004; Guo *et al.*, 2004). However, a better description of the contacts is still needed. This drives most recent efforts (e.g. Hoeven 2010, Kuschel and Sommerfeld 2013, Focke *et al.*, 2013). The contact mechanics, numerical and experimental work and their relation to detergent manufacture are discussed in Chapter IV.

## **2. A general frame for the study of counter-current swirl dryers.**

This thesis describes a systematic study of a swirl counter-current spray drying tower. With the purpose of linking all aspects of the process and their inter-dependency, Figure 2 outlines the architecture of a full numerical model. The properties of the exit powder, i.e. an output, are connected to the properties of the powder 1- in the flowing air, i.e. in an air-borne state denoted [ i ] in Figure 2; the particles that form the deposits, i.e. wall-borne, [ ii ]; and the continuous phase, [ iii ]. The initial conditions are the properties of inlet air flow, and those of atomized droplets which can be measured.

**Figure 2.** General numerical framework for the description of swirl counter-current spray dryers connecting the properties of *i-* the particles in the air, *ii-* the particles forming the deposits, and *iii-* the air continuous phase. Input and output data are given to an air-borne and wall-borne model, and sub-models for the description of all transport phenomena and particle interactions.  $n$ ,  $x_p$ ,  $U$ ,  $\%_{w}$ ,  $T$  and  $\rho$  denote respectively concentration, size, velocity, water content, temperature and density,  $A$  or  $P$  denote for the air or the particles.



## 2.1. Continuous phase fluid dynamics

A CFD model, denoted [1] in Figure 2, makes use of inlet air conditions to predict the pressure and air velocity field,  $U_A$  in any geometry. One of the main contributions of this thesis is in providing full scale validation data. The use of production units has to be stressed, not only due to the complexity in obtaining the data, which explains why they were not previously available, but also due to their impact. The validation of air flow patterns in swirl detergent dryers was achieved at laboratory dryers using clean walls (Bayly *et al.* 2004). Hassall (2011) then provided velocity data for a restricted section near the wall and reported large differences, but the reason for these remained unexplained and inconclusive. Part A of this thesis demonstrates that the discrepancy observed in velocity (i.e.  $> 30\%$ ) is owed to the friction at the walls, inherent in production units due the presence of deposits, but very difficult to replicate in laboratory or pilot scales. In addition, deposits also have a drastic effect upon the flow structure and turbulence. It is clear that errors in [1], for instance in the strength of the swirl, propagate into the use of any of the other sub-models, which cause unreliability in existing coupled models.

## 2.2. Particle dispersion in isothermal conditions.

The description of particle motion in [2] determines velocity,  $U_p$ , and  $n$  profiles in the dryer. At this stage it is unknown which is a) the impact of loading (i.e. evaluation of a dilute system assumption) and b) how the rebound angles and restitution coefficients respond to the collision of non-spherical granules and how these can get trapped at the deposits becoming locked in the structure (see Figure 1b). Both can be fundamental in describing particle flow. It is important to be able to assess any sub-model independently from the other processes. Ideally, this should be done with concentrations or alternatively residence time data obtained with the use of dry detergent powder in isothermal conditions. This has been attempted during this work by measuring the residence time of powder pulses at dilute conditions. A full experimental plan has designed but it is still on hold.

## 2.3. Heat and mass ex-change transfer processes in the absence of agglomeration.

Only once particle dispersion can be described precisely, can the use of a single droplet drying model in [4] allow prediction of the water content,  $\%_w$ , the temperature,  $T$  and density  $\rho$ , of both phases in [5]. Single droplet drying models are relatively well advanced and can be related to each formulation using small scale experiments. Coupling between the models in [1] and [5] is also well established in co-current units. However, the effects of a density change in the swirl stability can be important in this

case. Having validated [1] and [2] independently is key to be able to ensure that [5] is actually capable of replicating the flow in non-isothermal conditions. At this stage, validation data need to be obtained with a formulation and operation conditions that ensure agglomeration is as limited as possible. This implies the use of water or water soluble polymers, and a narrow droplet size. During this work, dispersion and drying [2,4,5] have been studied numerically by the development of a Lagrangian model in collaboration with Imperial College London. It makes use of the velocity field given in Part A. It is not included here since it is still work in progress beyond the scope of this thesis.

Two key numbers need to be computed before one can study particle interactions: a) collision rate [3] and b) collision efficiency [7] that is: the probability of a given collision to result in aggregation. Particle dispersion in [12] determines how particles collide between each other and can be used to define a certain collision rate or frequency in different sections of the chamber. The outcome of the collisions is determined by the size and velocity of the droplets, but also their stickiness and mechanical properties. A different working block, [6] needs to link the different drying states from the multi-phase flow model [1,4,5] to magnitudes such as the yield stress, the surface viscosity and the work of adhesion. Since the Ohnesorge number  $Oh^2 \gg 1$  i.e. the relative strength of surface tension to viscous forces, one expects little effect of the surface tension in the interaction force. Only when it is possible to predict with a reasonable accuracy the properties of the solids when they do not grow, is one in a position to start studying how they may interact.

#### **2.4. Wall fouling. Deposition, Sintering and Re-entrainment.**

A major contribution of this work is the characterization of fouling and how this is a central to the manufacture of detergents under swirl (Chapter V). This view opposes the traditional description that regards deposits as an operational draw back in co-current (Ozmen and Langrish 2003) and counter-current units (Huntington 2004). In addition, it is important to start accounting for the changes particles undergo when they deposit, during the time they spend at the walls and how they re-incorporate with the bulk. The collision rate with the wall in [3] and the contact models in [7] determine which impacts result in deposition in [8]. This builds up a set of particles borne at the walls of the dryer [ ii ]. They keep on drying and may sinter while they are part of the deposits [9] until other impacts, drag and gravity make them detach in [10] back into an air-borne state [ i ] (Figure 1b provides the visualization of clusters detaching). Indeed, they detach with a different set of properties from the deposited particles.

## **2.5. Particle agglomeration in an air-borne condition.**

At a point in the dryer, knowledge of the collision frequency and efficiency enables the implementation of an air-borne growth model in [11] and computation of aggregation rates. Of course when particles increase in size, trajectories in [2] and drying kinetics in [4] are affected, and all properties need to be recomputed. Chapter IV discusses the use of stochastic Lagrangian or Eulerian models for this purpose. It suffices to say that all the input data required is given by a working air-borne model [1 2 4 5 6].

The state-of-the-art in swirl large towers is certainly far from being at this position. This makes the numerical work inconclusive and constrains the conduction of experiments. Experimental data is very restricted and often limited only to inlet and outlet product properties, with no data within the drying chamber. In these conditions it is very difficult to identify which is the root of the changes in the product properties when for instance one operates at different air conditions or atomizer configurations (i.e. changing [1 2 3]) or when the properties of the slurry change (i.e. affecting [4 5 6 7]).

## **2.6. Experimental independent validation.**

In this context, industry needs to assess new designs based upon unknown growth processes. This forces manufacturers to commit to large experimental costs and make use of available numerical tools. This enforces the tendency to use all sub-models in Figure 2. Note that in practice they are available in the libraries of commercial packages, with the exception of the wall. They could be used but without experimental validation. Of course, assumptions can be made based upon the manufacturer's experience, but it is often impossible for designers to differentiate between the effects of the different sub-models because they do not possess validation data. This occurs because it is very complex to isolate experimentally the study of the wall cycle in [8 9 10] from the contacts in the flow in [3 7 10] or the performance of [1], [2] or [4]. As a consequence, one easily falls in the speculation on numerical solutions of a large model, based upon the parameters used in each section. Huntington (2004) is right in arguing that this sort of numerical tools facilitates decision making and trouble-shooting. However, it also carries a risk in using sub-models out of the space where they were validated. This needs to be stressed: experimental validation of each sub-model in the relevant range is the only way for a larger frame to retain physical meaning, instead of constituting a valuable but complex fitting exercise.

The description of the swirling fluid dynamics in Part A is a good example. A drastic decay of the swirl strength has been linked in isothermal conditions to wall friction (i.e. this excludes the effects of heat,

mass and momentum transfer). This was unsuspected in the field. Wall boundary conditions and wall functions used in CFD packages in [2] now need to account for a large roughness, but probably will be modified in more depth. However, models had been validated in the past also at isothermal conditions, but in clean laboratory dryers (Bayly *et al.* 2004) and pilot scale facilities (Sharma 1990). The swirl decay was not observed and that prevented the acknowledgement of the role of deposits. When one proceeded to use of the rest of the sub-models, then error was propagated and led to the belief that the swirl decay observed during the production of powder (Hassall 2011) could be owed to an attenuation caused by the solid phase. This stressed the need for more accurate drag laws in the dispersion model [3]. This indeed looks as a reasonable assumption, yet it leads to a severe misinterpretation because it is rooted in the use of a model (i.e. wall function in CFD models [2]) that is not validated in swirling flows over rough walls, despite its wide use in this context in industry and academia (e.g. Harvie *et al.* 2001).

### 3. Thesis objectives

This work pursues a better knowledge of the origin, rate and outcome of interactions in detergent spray drying. Huntington (2004) underscores the need to control the effect that agglomeration has in:

- a) Energy consumption.
- b) Product properties.
  - a. **Size.** Production of excessively coarse or fine product increases the fraction of the powder that needs to be discarded, and reduces plant capacity. Not only the mean size is an important feature but the entire exit size distribution needs to be tailored carefully.
  - b. **Composition.** This determines the stability of the product in storage and its flow ability.
  - c. **Structure.** It is the main attribute of spray dried granules and it is linked to performance.

At this time a complete numerical description of growth is far from feasible. It requires a detailed knowledge of the multi-phase flow, not currently available either experimentally or supported through numerical models. In this scenario it is important to first 1- address the issues moving in Figure 2 towards a position where it is possible to compute particle collision frequency and efficiency in a tower, and then 2- identify by which governing mechanism the particle interactions occur and where they do in the unit so that 3- a growth model could be eventually built and validated. Three major issues are listed.

- a) Failure to predict quantitatively the swirling flow of the continuous phase at isothermal conditions.
- b) Inability to predict the exit powder water content and temperature. This is believed to result from models ignoring growth and the residence time that a part of the product spends at the walls.
- c) Insufficient computational capacity or available contact models to describe all possible types of contacts. However, the lack of data makes impossible to discriminate between them.

#### **4. Thesis Structure**

This thesis is constructed as a collection of self contained investigations that address the pitfalls in the process listed above. The general working framework given in section 2 serves to link these all together and is used as the route map to for this thesis and the future work. The conclusions arising from each independent investigation are given at the end of each relevant chapter and a few remarks on the general impact on the future work in counter-current spray drying community and the industrial sponsor are given at the end of the thesis under Final Remarks, and Industrial Impact.

The thesis is subdivided in Part A and B, according to the study of the fluid or particle dynamics:

Part A. It provides the characterization of the continuous fluid dynamics across different dryer designs and scales. It reports time-averaged velocity fields, the swirl decay, analysis of the turbulence, flow stability and periodical structures (Chapter II) and how these relate to deposition and scale up (Chapter III). Appendix I includes a supporting analysis on the use and error of the technique: sonic anemometry.

Part B. Chapter IV describes the unit and the process, proposing the compartmentalization of the tower to simplify the description of the system and account only for the governing contacts in key areas. Chapter V provides the first experimental evidence of the wall cycle. It quantifies the re-entrainment rate from the deposits and the residence time distribution of the product at the walls. It serves as validation for a wall model or the fit of a user-defined function at the boundaries of CFD commercial packages. Then, Chapter VI quantifies the different growth sources during the operation of a single atomizer, those originated by a different drying kinetics and the growth associated to particle recirculation when multiple nozzles are used. Appendix II provides data in relation to particle structure and the contribution of aggregation to the formation of high porosities and Appendix III provides a supporting study describing how the growth patterns respond to the modification of the inlet air temperature and momentum.

## 5. Thesis Outline

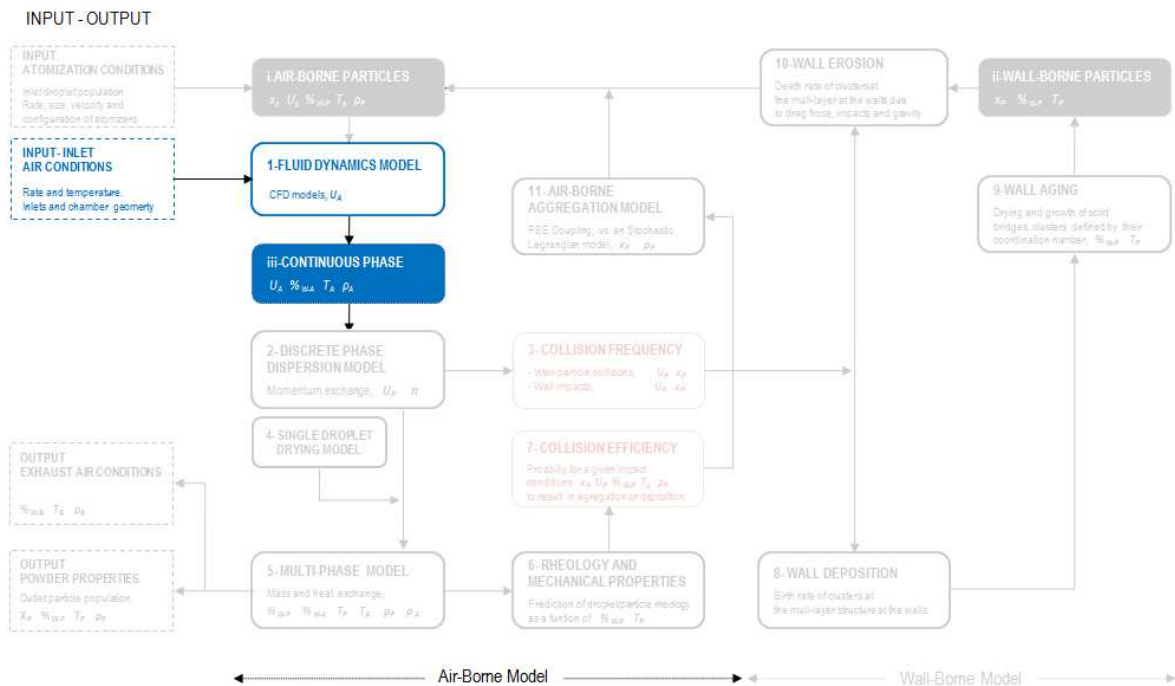
<b>Introduction</b>		<b>1</b>
<b>PART A</b>	<b>Air swirling fluid dynamics.</b>	<b>12</b>
Chapter I	The continuous phase: Tower design, operation and measurement	12
Chapter II	Characterization of the air swirling flow in an industrial scale	21
Chapter III	Scaling criteria. Instabilities, recirculation and the role of friction	52
<b>PART B</b>	<b>Particle dynamics</b>	<b>99</b>
Chapter IV	The discrete phase: Agglomeration, tower subdivision and measurement	99
<b>B1</b>	<b>Fouling dynamics</b>	<b>120</b>
Chapter V	A tracer analysis: A dynamic equilibrium of deposition and wear	120
<b>B2</b>	<b>Agglomeration kinetics</b>	<b>165</b>
Chapter VI	Operation of single nozzles and interaction between multiple spraying levels	165
<b>Final Remarks, Next Steps</b>		<b>209</b>
<b>APPENDIXES</b>		<b>213</b>
Appendix I	The use of sonic anemometry for the study of a large confined turbulent swirling flows	213
Appendix II	Analysis of particle structure and the generation of porosity	259
Appendix II	Control of the growth and wear mechanisms	290
<b>REFERENCES</b>		<b>320</b>



# PART A

## CHAPTER I

# THE CONTINUOUS PHASE TOWER DESIGN, OPERATION AND MESUREMENT



**Summary**

This chapter describes the general design of the air flow delivery system in counter-current spray swirl dryers. It outlines the tower geometry and the operation conditions investigated in the Part A of this thesis at three industrial units. It discusses the rationale for maintaining geometrical similarity in the design of the exhaust and inlet ports of the dryer, and how the modification of the scale, the aspect ratio of the cylindrical chamber and the inlet velocity at different scales serve to study the fluid dynamics at the relevant Reynolds numbers and angular momentum fluxes in detergent manufacture.

## 1. Design and generation of the swirling flow in a counter-current spray dryer.

Three detergent industrial counter-current spray drying towers, property of Procter & Gamble, have been used for the investigation of the air fluid dynamics. Figure 1 illustrates their general design, the nomenclature, the location of the accesses into the cylindrical chamber and the design of the air inlets.

### 1.1. Swirl generation mechanism.

The means to produce a vortex in open pipes include the use of vanes, rotating cylinders or tangential inlets (e.g. Steenbergen and Voskamp, 1998). In a tall-form dryer the generation of the swirl is slightly more complex. It responds to the orientation of the inlet ports but also the design of the hip and the cone at the bottom part of the dryer. A distributor, denoted plenum, feeds the inlet air into a series of ports that are arranged symmetrically at the bottom of the cylindrical chamber. They inject the flow towards a conical section with a certain angular momentum (i.e. alignment angles,  $\varphi$  and  $\xi$ , are defined in Figure 1c). The pressure balance generated at the cone causes the formation of a vortex that rises into the cylinder, where it converges inwards and exits through a central conduit inserted at the top, denoted vortex finder. It presents a series of internal channels named straighteners, which break the swirl before the air is directed into the cyclones. The unit operates below the atmospheric pressure, leading to some entrainment from the bottom end (i.e.  $< 5\%$  of the air mass rate in the absence of particles).

### 1.2. Plenum.

The design of the air distributor can have an important effect in the symmetry of the flow field. Huntington (2004) describes the use of an open bustle ring that surrounds the body of the tower at the bottom of the cylinder. The ring is connected the air inlet line and feed a series of nozzles into the conical section, which are arranged symmetrically in order to balanced the momentum flow into the cone. This design is based upon the manufacturer experience and the recommendation of numerical simulations. Chapter III provides further experimental supported studying different modifications.

### 1.3. Inlet angular momentum flux. Swirl intensity.

The strength of the swirling motion across the unit has been quantified by the use of a circulation parameter, or swirl intensity  $\Omega$ . Chapter III discusses the usual practise and proposes the definition of  $\Omega$  as the non-dimensional flux of angular momentum,  $G_\theta$ , across the cylinder, normalized by the axial momentum,  $G_{z,av}$ , based upon the superficial air velocity,  $\bar{U}_{av}$ . On the same basis an initial value,  $\Omega_i$

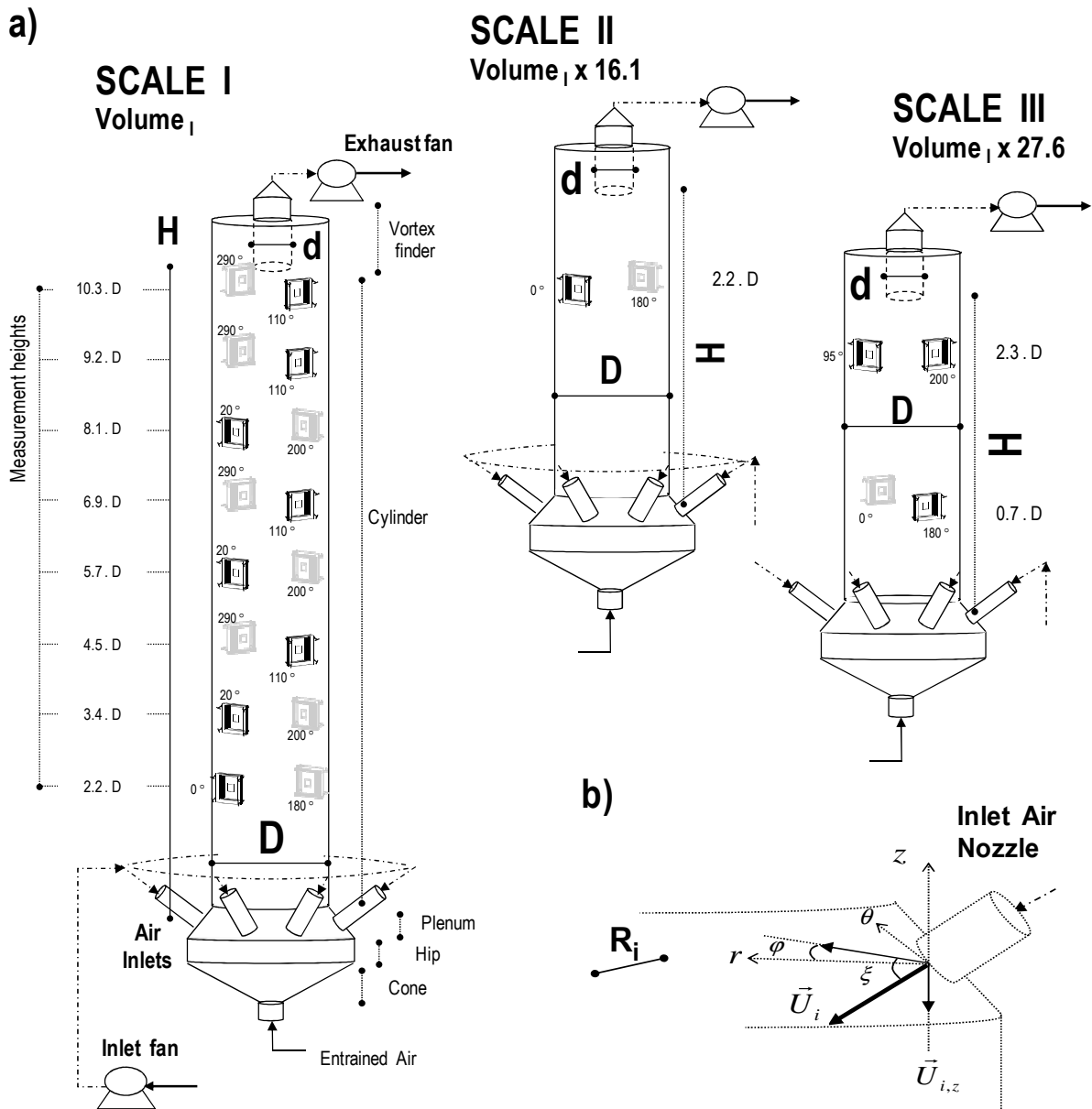


**Figure 1.** a) Nomenclature and general outline of the air delivery system in the three counter-current spray drying towers, including the different sections of the dryer, the scale relative to the volume of Scale I, and the location of accesses into the dryer. b) Detail of the air inlet nozzle/s: direction of the inlet velocity  $\bar{U}_i$ , and the port alignments,  $\varphi$  and  $\xi$ .

can be computed making of the inlet conditions. In isothermal operation, it reads

$$\Omega_i = \frac{G_{\theta,i}}{R \cdot G_{z,av}} = \frac{\bar{M}_i \bar{U}_i \theta R_i / \pi R^2}{\bar{M}_C \bar{U}_{av} R / \pi R^2} = \frac{\bar{M}_i^2}{\bar{M}_C^2} \frac{A_C}{A_i} \frac{R_i}{R} \cdot \sin \varphi \cos \xi \quad (1)$$

$\Omega_i$  is an exclusive function of the geometry and it is proposed as a characteristic design parameter, in the same manner that the geometric swirl number is a characteristic of cyclones (Gupta *et al.* 1984). It

responds to a) the alignment of inlets, b) the ratio between the mass rate through the inlets  $\bar{M}_i$  and the cylinder  $\bar{M}_C$  and c) two contraction ratios specific to the tower design, between the radius at the cylinder  $R_C$  and the inlet  $R_i$  ring, and the combined area of all inlets,  $A_i$  and the cylinder,  $A_C$ .

#### 1.4 Scale up.

Oakley (1994), Masters (1995) and more recently Kemp and Oakley (2002) discuss some of the issues in scaling up spray dryers and count them among the most complex unit operations. Huntington (2004) lists the implications in a counter-current swirl unit, including a) the lack dynamic similarity, b) the deviation between the air flow and particle swirl patterns, c) the large influence of the temperature history in particle kinetics, and c) the complexity in conducting kinetic tests with small droplet sizes. Fouling and growth are found fundamental in this thesis, and thus we may add d) the difficulty in isolating experimentally the effects of drying kinetics, dispersion or agglomeration, and e) a complex experimental characterization, pointed by Zbicinski and Piatkowski (2009), that leads to limited data under production and very restricted access to validation. These limitations are discussed in Chapter IV.

Huntington (2004) describes the design criteria in P&G and argues that the standardization of the air flow field is an ongoing challenge because multiple tower geometries and configurations are still used across the industry. Zbicinski and Piatkowski (2009) or Wawrzyniak *et al.* (2012) stress this is a complex matter in swirl towers due to the lack of a reliable and comprehensive air velocity data sets in a full scale. Part A of this thesis aims to address this issue. Chapter II characterizes a single tower, which is taken as a reference. It studies the flow structure, the stability and the friction associated to the relevant range of Reynolds numbers,  $Re$ , expected in industry. Chapter III then discusses the scalability of the flow field, and proposes control strategies to replicate the structure across different designs, conditions and scales. This is done by manipulating  $\Omega_i$  and accounting for the effect of the friction at the walls. Scaling up the particle dynamics is a more complex issue because it requires studying the effects in particle residence time and the kinetics of agglomeration. These are investigated further in Part B and Appendix III.

#### 1.5. Operation ranges.

Table 1 summarizes the geometry of units. It provides the main aspect ratios and the resulting inlet flux of angular momentum,  $\Omega_i$ . Table 2 includes the range of superficial velocities and  $Re$  considered.

Note the mean particle size of the detergent is not scaled for it is a desired product property. Larger towers tend to maintain a similar range of superficial and sedimentation velocities in the dryer and

**Table 1.** Aspect and contraction ratio, total volume,  $V$ , and initial swirl intensity,  $\Omega_i$  for all the scales.

Design	Scale I	Scale II	Scale III
$H/D$	10.58	2.97	2.87
$d/D$	0.29	0.28	0.31
$R_i/R$	$r_{c,1}$	$r_{c,2} < r_{c,1}$	$r_{c,2} < r_{c,1}$
$\Omega_i$	5.1 - 5.4	3.4 - 3.6	7.7 - 8.2
$V/V_{Scale I}$	1.0	16.1	27.6

**Table 2.** Superficial air velocity estimated as  $\bar{U}_{av} = \bar{M}_C / \bar{\rho}_A A_C$  and Reynolds number  $Re = \bar{\rho}_A \cdot D \cdot \bar{U}_{av} / \mu_A$

Operation		$Re \cdot 10^{-5}$	$\bar{U}_{av} / \bar{U}_{av, Re_1}$
Scale I	$Re_1$	1.04 - 1.09	0.98 - 1.02
	$Re_2$	1.47 - 1.50	1.39 - 1.44
	$Re_3$	2.21 - 2.24	2.09 - 2.17
Scale II	$Re_4$	6.74 - 6.91	1.81 - 1.85
Scale III	$Re_5$	4.79 - 5.12	1.04 - 1.10

control the particle residence time  $\tau_p$  by adjusting the length of the cylinder (i.e.  $H/D$ ) and the position of the atomizers. This means that while  $Re$  increases with increasing the scale ( $\propto D$ ), the particle centrifugal inertia diminishes ( $\propto D^{-1}$ ); hence, the lack of dynamic similarity. This represents a challenge when scaling the effects owed to gravity (i.e. particle accumulation, drying and agglomeration) and centrifugal forces (i.e. a preferential concentration near the wall and fouling). The contribution of both of these effects to the generation of particle growth will be studied in Part B and Appendix III.

In relation to the air fluid dynamics, one needs to acknowledge the effects of changes in the geometry:

- **Vortex finder:** Chapters II and III detail how the contraction has a large impact in the flow stability. For this reason geometrical similarity is maintained by keeping a constant  $d/D$  in all units.
- **Inlet alignment,  $\varphi, \xi$  :** Sharma (1990) compares different ranges in a pilot counter-current dryer, and shows these have a severe effect in the shape, stability and symmetry of the vortex generated. This was later supported by the numerical work of Harvie *et al.* (2001) and led to the usual ranges observed in the manufacture of detergents, listed by Huntington (2004). In this case the values are kept constant across the scales. In addition, in order to produce stable patterns in the cylinder, the geometry of the bottom section of the dryer needs to be optimised. Any modifications from the standard geometries of the hip and cone seen in the P&G designs have been left out of this work.
- **Inlet angular velocity.** Chapter III described the operation at a different  $\Omega_i$ . This has been obtained by modifying the radius of the plenum and the inlet ports, i.e.  $R_i/R$  and  $A_C/A_i$  in equation (1). A wider plenum or a reduction of the area of the inlet ports,  $A_i$ , increases the inlet angular velocity and thus  $G_{\theta,i}$ , by increasing respectively  $R_i$  or the inlet tangential velocity,  $\bar{U}_{\theta,i}$ . Scale II and III

operate respectively at a lower and higher  $\Omega_i$  than Scale I. This was obtained by reducing  $R_i/R$  to a constant value and modifying the area of the inlet ports (i.e.  $A_C/A_i$ ). Chapters II and III discuss the effects in the flow structure. Notice also that  $H/D$  reduces from Scale I to Scales II and III. In essence this shortens the length of the cylinder and thus decreases the wall surface area and the effect of friction. Chapter III discusses which is the role of friction in stability, and identifies how under these conditions, different operation regimes arise from the ranges of  $\Omega$  observed in the cylinder.

## 2. Methodology and Instrumentation for the characterization of the fluid dynamics.

The work presented in Part A describes the air fluid dynamics in the relevant ranges of  $\bar{U}_{av}$  and  $Re$  and under a selection of representative designs in industry. During these investigations only the air flow was operated. All measurements were taken in ambient conditions and in the absence of particles in the dryer to exclude any other effects than design in the stability of the swirl. All the systems were handled manually to avoid spurious variations in the rate. The relative head of the inlet and exhaust air fans in Figure 1 was adjusted to maintain a target mass rate and exit pressure, set in all cases to  $-6 \pm 1$  mbar, and measured at the exit of the vortex finder, before the exhaust fan in Figure 1.

A Horizontal Symmetry 50 Sonic Solent Anemometer (Gill Instruments Ltd.) served to acquire velocity measurements. It makes use of three independent pairs of ultrasonic transducers that alternate to emit and receive a sonic pulse. Analysis of its propagation velocity allows the derivation of the velocity of the medium along three independent directions. Measurements were taken during 60 s at a reporting frequency of 50 Hz, with the exception of Case A, Scale I (Chapter III) taken at 20 Hz. A door was engineered *ad hoc* to assemble around the anemometer frame. Figure 2 illustrates this ensemble and defines the frames of reference for the anemometer and the cylinder. Once it is fixed in the accesses shown in Figure 1, the door aligns with the inner wall and the anemometer frame with perpendicular into the cylinder. Air velocity is measured at a large range of radial tangential and axial coordinates by positioning in the anemometer frame inwards in all the accesses depicted in Figure 1. In all cases, the axis  $a_1$  is aligned with the tower axial direction,  $z$ , to minimize all the sources of error.

The application of sonic anemometry to an industrial context is a novel contribution of this work. It provides a major improvement in the quality and level of detail of the data at full scale units. Consider that the use of Pitot tubes and flow visualization techniques are still the most commonly used. It is however an intrusive method and requires a careful evaluation of the uncertainty. Errors arise mainly

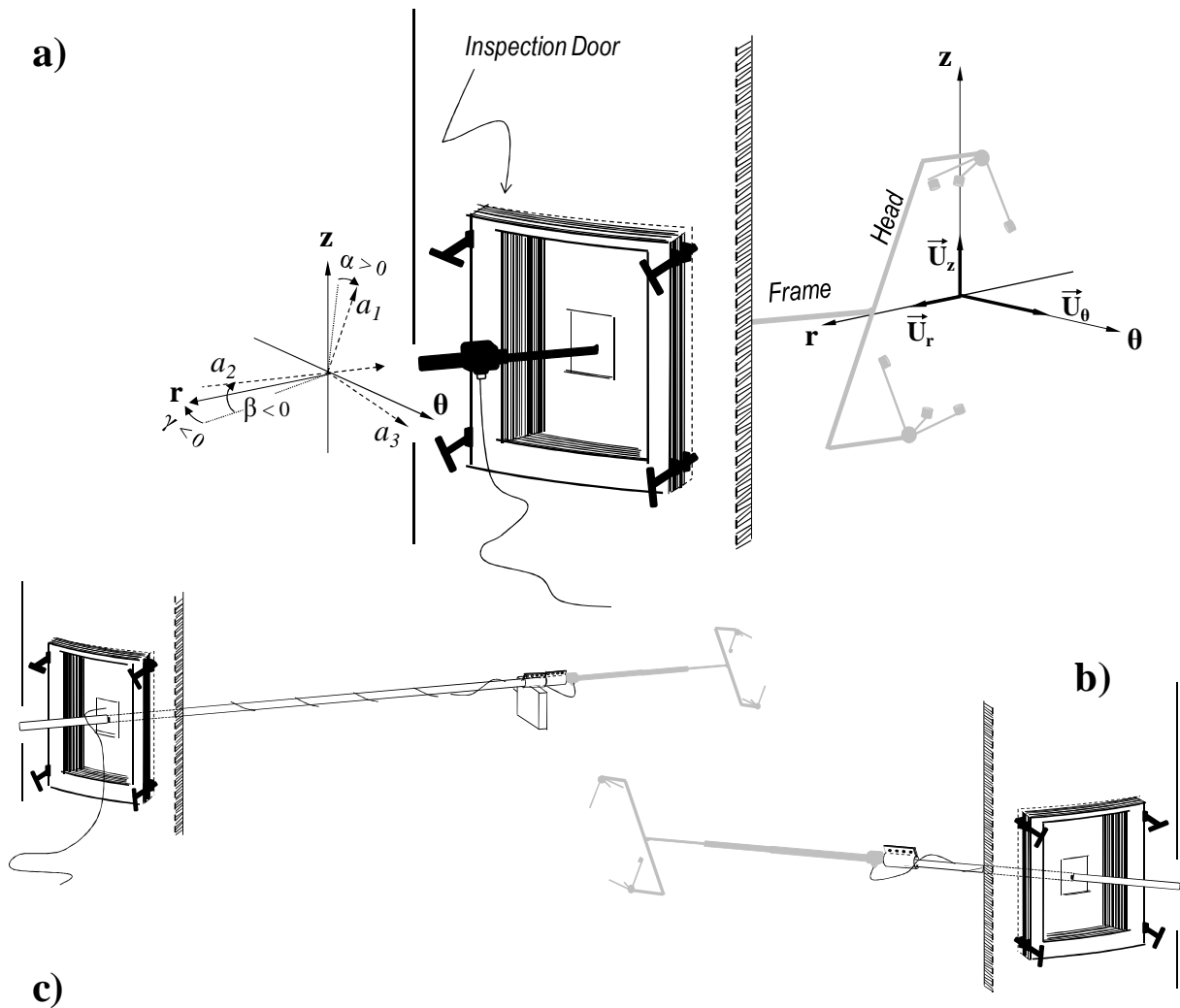


**Figure 2.** a) Depiction of the ensemble and connexions, and definition of the frame of reference of the cylinder,  $(rk\theta)$ , the anemometer measurement axes,  $(a_1a_2a_3)$ , and the alignments,  $\alpha, \beta, \gamma$ . (b) and (c) Illustration of the use of a back extension (b) and (c). Drawings not to scale.

from the disruption caused to the flow, but include others related to the methodology, the correction algorithms and short-comings assumptions in commercial instruments. Appendix I studies these particularities and describes the application of anemometry to large confined swirling flows. It reports:

- 1- Detailed description of the method.
- 2- Corrections to express the raw data in a polar frame of reference.
- 3- Evaluation of the uncertainty arising from:
  - a. Time averaging.
  - b. Local aerodynamic disruption.
  - c. Distortion of the flow stability.

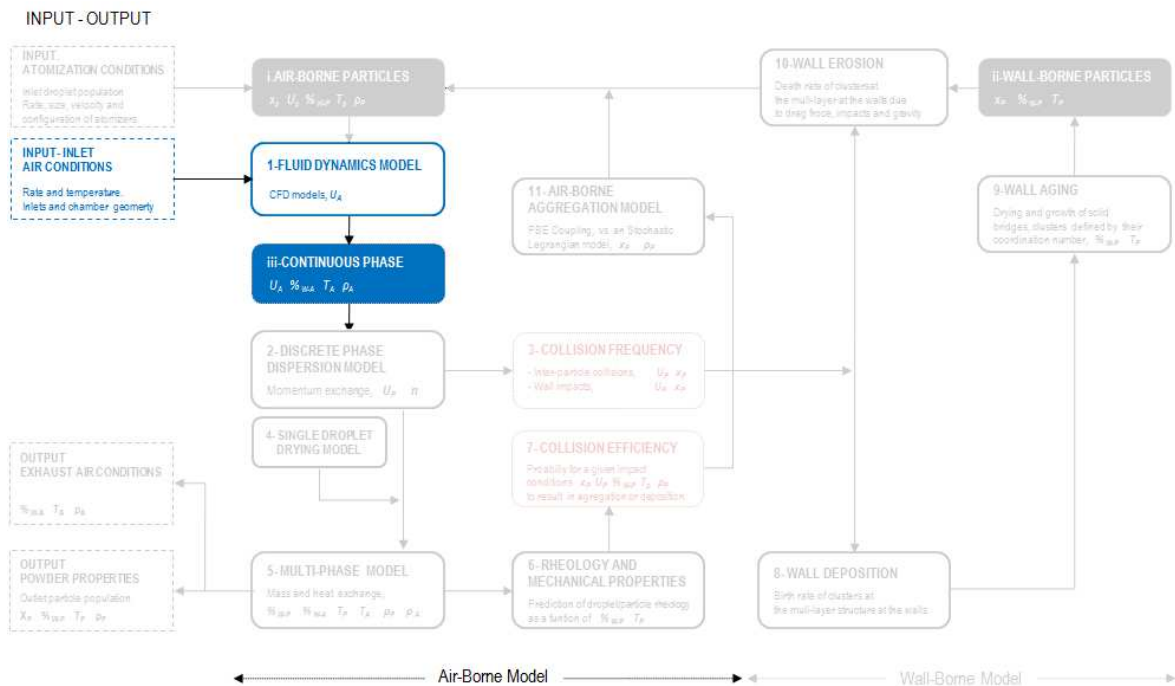
- a. Use of the calibration functions.
- b. Non-linearity of the sonic pulse.

The maximum uncertainty limits associated to the use of this arrangement for the measurement of speed, direction and turbulence statistics are kept  $< 1 - 4 \%$  in speed,  $\pm 3^\circ$  in direction and  $\pm 7 - 31 \%$  in turbulent kinetic energy, considered sufficient for design and engineering purposes.

# PART A

## CHAPTER II

# CHARACTERIZATION OF THE SWIRLING FLOW IN AN INDUSTRIAL SCALE



## Summary

This chapter studies experimentally the swirling flow established in Scale I (Chapter I) working at isothermal conditions and in the absence of particles. The flow structure is compared to that in similar confinements such as combustors or cyclones and the decay of the swirling motion in the cylindrical chamber is compared to the expectations in open pipes.

The data reported here serves to a) discuss how the influence of the vortex finder governs the development of the flow, causes a central jet and is responsible of suppression of recirculation in the dryer; b) provide the first evidence of substantial wall friction in spray dryers, leading to a stronger decay of the angular momentum flux than anticipated in literature, c) identify asymmetric flow structures owed to the design of the inlet and exhaust lines, and d) characterize the turbulent field, including periodical flow oscillations, their frequency and their contribution to mixing.

## 1. Introduction.

Amongst the main advantages of spray drying processes are the generation of low density granules with an open structure that allows industry to tailor consumer preferences and the performance of detergents (Appel 2000). Product properties, particularly the morphology of the final granules, depend on the temperature history and the level of agglomeration undergone throughout the dryer. Studying the air fluid dynamics is fundamental to predict how particles are brought together, and understand the way in which particle size and porosity are generated. Counter-current units are used for the manufacture of thermally stable powders, such as detergents, applying strongly turbulent swirling flows to enhance the heat and mass transfer and optimize the contact between the phases (Huntington, 2004).

The development of strong turbulent swirling flows under confinement has been studied in detail for free developing or non-recirculating systems (i.e. also referred to as once through swirling flows, such as open pipes, tubes or concentric cylinders) and in systems where the confinement restricts the vortex development (i.e. combustors, burners or cyclones). The study of large scale units such as swirl drying towers is however far more limited. In a long confinement the swirling motion decays due the development of the boundary layer and the action of the wall shear stress (frictional losses). This is described by the work of Kitoh (1991) or Steenbergen and Voskamp (1998) in open pipes and was extended by Chang and Dhir (1994 or 1995) to a higher swirl intensity ranges and the use of tangentially injected flows. By contrast, the structure of the boundary layer in a production dryer is intimately related to the presence and disposition of deposits. The swirl causes most of the product to concentrate near the wall and generates thick multi-layered deposits (see Hassall 2011 and Chapter V). This chapter is focussed on the assessment of the effect that the modification of the wall roughness has on the development of the air flow patterns. Deposits are generally ignored in the experimentation and numerical description of dryers. However, in production units they are unavoidable and exhibit a large roughness height. This is expected to disrupt significantly the boundary layer and the structure of the turbulence close to the wall, according to the discussion given by Jimenez (2004) or Volino *et al.* (2007) in unidirectional flow over rough walls.

Recirculation patterns and the stability in vortices are often studied in terms of the Reynolds number  $Re$  and the ratio between the centrifugal and axial momentum, characterised by circulation parameter, swirl number or intensity,  $\Omega$ . When the swirl develops in an open cylinder, at a sufficiently high intensity the adverse pressure gradient generated by the centrifugal forces causes the reversion of the flow. This

originates a central recirculation zone, denoted *CRZ*, in the region upstream. As the swirl decays along the cylinder, the centrifugal force decreases and a stagnation point forms downstream, where the flow reverses back. This is referred to as a vortex breakdown, *VBD*, and often carries some associated oscillations. These effects are complicated by the interaction with the design in cases where the confinement is more restrictive, such as in combustors, cyclones or dryers. In these units, an increase in  $\Omega$  or *Re* interacts in a more complex manner with the exit boundaries, referred to as downstream effects. Escudier *et al.* (1980), Escudier and Keller (1985) and Derksen (2005) provide detailed studies in a combustor, describing the stabilizing effect that an exit contraction can have in the flow upstream.

The origin of periodic oscillations associated with the *VBD* as the precession of the vortex core, *PVC*, is discussed amongst others by Syred (2006) in the case of combustors or O'Doherty *et al.* (1999) and Derksen and Van den Akker (2004) in cyclones. While these are beneficial in combustors, for they increase mixing and stabilize the flame, they are considered detrimental to the collection efficiency in cyclones. Usui *et al.* (1985), Langrish *et al.* (1993) and Kieviet *et al.* (1997) were the first to report similar aerodynamic instabilities in co-current spray dryers, followed by the work of Southwell and Langrish (2001) and Langrish *et al.* (2004), but no work in this regard is available in counter-current swirl units.

It is very important to provide turbulence data in dryers because large models often lack any means to evaluate how the closure models actually perform. This is particularly important for counter-current swirl units in a) determining the elutriation of fines; this concerns with the description of a high angular velocity core, first identified by the work of Sharma (1990); Harvie *et al.* (2001) points to the need of applying a Reynolds-Stress Transport Model, *RSTM*, to be able to describe this region, which has been reported by Ali *et al.* (2013) and Ali (2014), b) the flow near the wall, to assess how semi-empirical wall functions for a rough walls could apply to strong swirling flows, c) an adequate replication of the anisotropy for which there is ample experimental evidence, and d) the description of the aerodynamic instabilities observed experimentally, which increase the level of mixing and affect primarily the inner jet.

In spite of the complexities above, experimental data on the air flow patterns in counter-current tall form dryers are very rare and restricted in nature. The studies in pilot scale facilities include flow visualization techniques and some related *RTD* analysis, first reported by Paris (1971), Keey and Pham (1976), or later Sharma (1990). Fieg *et al.* (1994) report data obtained with vane anemometers but only in the last decade have authors such as Bayly *et al.* (2004) or Zbicinski and Piatkowski (2009) provided a higher

level of detail by taking advantage of laser-based flow diagnostic techniques in laboratory or pilot plant units respectively. Data at actual production scales is even more restricted (Wawrzyniak *et al.*, 2012) and a similar level of detail is not yet available. Detailed studies are of small scope and limited to particle image velocimetry, *PIV*, analysis near the wall (Hassall, 2011).

This chapter addresses the lack of data at a production scale providing the characterization of the flow in a counter-current spray drying tower at isothermal conditions, Scale I (Chapter II). Time average velocity and the turbulence field are reported at the cylindrical chamber of the dryer. The more common features described in swirling flows in pipes, combustors or cyclones are discussed, including (a) the effects linked to the design of an exit contraction, section 3.1.1; (b) the impact of  $Re$ , section 3.1.2; (c) the asymmetry, section 3.1.3; d) the effect of wall roughness and the decay of the swirl intensity, section 3.1.4; e) the description of turbulence, sections 3.2.1 to 3.2.3 and f) periodic structures, section 3.2.4

## 2. Analysis.

### 2.1. Fluid dynamics parameters.

At each condition, velocity fluctuations, turbulent kinetic energy and the stress tensor are obtained from the Reynolds decomposition of the velocity and the statistics of instantaneous measurements. The time averaged profiles of the axial and tangential velocities,  $\bar{U}_z$  and  $\bar{U}_\theta$  are available at a higher accuracy (Appendix I). Under the assumption of an axi-symmetrical system the azimuthal average of  $\bar{U}_z$  and  $\bar{U}_\theta$  permits one to estimate the average radial velocity profile  $\bar{U}_r$ , that satisfies the continuity equation below. The Mach numbers across the cylinder allow compressibility effects to be neglected.

$$\nabla \cdot (\rho U) = \frac{\partial \rho}{\partial t} \quad (1)$$

Velocity gradients are then computed making use of the spatial grid generated with all the measurements and eddy viscosities are estimated with the Boussinesq equations (2) to (4) (Kitoh 1991) assuming an axi-symmetrical system and away from the contraction where  $\partial \bar{U}_r / \partial z$  can be neglected.

$$v_{r,z} = -\frac{\overline{u_r u_z}}{\partial \bar{U}_z / \partial r} \quad (2) \quad v_{r,\theta} = -\frac{\overline{u_r u_\theta}}{r \cdot \partial \left( \frac{\bar{U}_\theta}{r} \right) / \partial r} \quad (3) \quad v_{z,\theta} = -\frac{\overline{u_z u_\theta}}{\partial \bar{U}_\theta / \partial z} \quad (4)$$

Sources other than turbulence may contribute to the variability of the velocity measurement. These are known to be associated to the presence of instabilities in the structure of the vortex and their characteristic time scales are identified by applying a fast Fourier transform, *FFT*, to the velocity signal.

## 2.2. Swirl intensity.

A circulation parameter, denoted swirl number or swirl intensity, is often used to provide a general description of swirling flows. It defines at a cross section the ratio between the angular momentum flux,  $G_\theta$ , to the axial momentum flux,  $G_z$ , given below (i.e. Webber and Dugué 1992):

$$S = \frac{G_\theta}{G_z \cdot R} \quad (5)$$

Strict integral definitions for  $G_\theta$  and  $G_z$  derive from the conservation of momentum and angular momentum and require knowledge of static pressure and the turbulent terms (Sloan *et al.* 1986). Often they are too convoluted for many practical applications, which has generalised the use of simplified swirl numbers where momentum fluxes are estimated only on the basis of the convective flow, either excluding turbulence and/or static pressures, or estimating the latter through the tangential velocity profiles. Considering that in the unit investigated here the top exit constitutes a 90% contraction of the flow area; this causes the acceleration of the flow in its vicinity and substantial changes in the pressure field upstream. For that reason, an estimate of  $G_x$  neither accounting for the pressure term nor including accurate velocity measurements within the core, is not likely to be axially preserved, at least at the upper part of the cylinder. This complicates the interpretation of  $S$  in this particular unit.

The main focus of this work is not concerned with aerodynamic instabilities highly dependent on  $S$ , but rather examines the preservation of the swirl, which is especially relevant for the dynamics of the solid phase. On this basis, this work will follow the more usual practice in the study of decaying swirling flows in open cylinders by normalizing  $G_\theta$  in equation (5) by a constant mean axial momentum flux  $G_{z,av}$  (Yajnik *et al.*, 1973). The resulting swirl intensity,  $\Omega$ , is then defined as the non-dimensional flux of angular momentum normalized by the axial momentum flux  $G_{z,av}$  based on the superficial air velocity  $\bar{U}_{av}$ . This has been simplified to the expression below given by Kitoh (1991).

$$\Omega = 2\pi\rho \int_0^R \frac{\bar{U}_z \bar{U}_\theta}{\rho\pi\bar{U}_{av}^2 R^3} r^2 \cdot dr \quad (6)$$

Other popular definitions, perhaps of a more difficult physical interpretation include the work of Chang and Dhir (1994), who studied the decay in open tubes with tangential inlets but with no contraction. They defined intensity in terms of a “*tangential momentum*” term. In this case, the use of  $\Omega$  is preferred in the benefit of a straight forward interpretation as the axial decay of  $G_\theta$ . In a confinement with smooth

walls, this owes to the action of the tangential wall shear stress  $\tau_{w,\theta}$  in the velocity field. This is given below from the Reynolds averaged equation of the angular momentum in cylindrical coordinates, for an incompressible, stationary and axi-symmetric vortex (Steenbergen and Voskamp 1998).

$$\tau_{w,\theta} = \frac{\rho}{R^2} \int_0^R r^2 \frac{\partial}{\partial z} \left( \bar{U}_\theta \bar{U}_z + \overline{u_\theta u_z} - v \frac{\partial \bar{U}_z}{\partial z} \right) dr \quad (7)$$

Equation (7) illustrates that the change in the angular momentum flux contained in the convective flow  $\bar{U}_\theta \bar{U}_z$  between two sections owes to the moments exerted on the fluid by three shear stresses: that at the wall, and those coming from the turbulent and viscous terms. A very common assumption in pipes consists of considering the wall as the main contributor, and neglect the stresses originated by  $\overline{u_\theta u_z}$  and the axial development  $v \partial(\bar{U}_z)/\partial z$ . This permits one to describe the rate of change of  $\Omega$  as the non-dimensional tangential wall shear stress, combining (6) and (7) to the expression given in (8) for where velocities have been normalised by  $\bar{U}_{av}$  and the axial distance  $z$  by the cylinder diameter,  $D$ .

$$\frac{2\tau_{w,\theta}}{\frac{1}{2}\rho\bar{U}_{av}^2} = \frac{d\Omega}{d(z/D)} \quad (8) \quad \Omega = \Omega_r \cdot e^{-\lambda\left(\frac{z-z_r}{D}\right)} \quad (9)$$

In this way an axial decay of  $\Omega$  can be directly obtained in (9), providing a certain background to the many experimental evidence of an exponential swirl decay in open pipes. However, this is only a realistic approximation at very small values of  $\Omega$  (common in pipe flow), where  $\tau_{w,\theta}$  and  $\Omega$  have been found to be proportional (Kitoh 1991 or Steenbergen and Voskamp 1998). According to the measurements of Kitoh (1991), strictly speaking this occurs only for  $\Omega < 0.04$  in an open pipe. At a higher  $\Omega$  range the relation between  $\tau_{w,\theta}$  and  $\Omega$  requires either experimental measurement or the estimation from numerical studies (e.g. Najafi *et al.*, 2011). The work of Kitoh's (1991) provides data up to  $\Omega = 0.9$  and defines the ranges where the piecewise linear relation given in (10) can be assumed. This leads to a slightly more complex decay function in (11), similar to that of Seno and Nagata (1972) where  $\Omega_r$  and  $z_r$  define an initial reference point.

$$\frac{2\tau_{w,\theta}}{\frac{1}{2}\rho\bar{U}_{av}^2} = A \cdot \Omega + B \quad (10) \quad \Omega = \left( \Omega_r + \frac{B}{A} \right) \cdot e^{2 \cdot A \cdot \left( \frac{z-z_r}{D} \right)} - \frac{B}{A} \quad (11)$$

The study of swirl decay focuses in open pipes where  $\Omega$  seldom exceeds 1 (Steenbergen and Voskamp 1998). This is far below the values in swirl spray dryers, better represented by the studies of

Chang and Dhir (1994, 1995). They worked at a comparable  $\Omega$  range and a similar swirl generation mechanism than the dryer investigated here, in order to promote turbulence and enhance the heat and mass transfer in an open tube. Although carried out at lower  $Re$  and in the absence of deposits the results are still useful to compare to the cylindrical chamber of the units described in this thesis. They proposed a non-linear dependency to  $(z/D)^{0.7}$  and a decay rate strongly correlated to the ratio of the inlet tangential and axial rates, which in a sense remains a measure of geometry and the initial value of  $\Omega$ , defined here by  $\Omega_i$  (Chapter I). This correlation was later modified by Erdal (2001) or Gomez *et al.* (2004) to include the effect of  $Re$  and the number of tangential injectors.

The decay rate,  $\lambda$  or  $A$ , is known to be a function of  $\Omega$  in open pipes and it is expected to decrease for higher  $Re$  in a similar manner that the friction factor does in fully developed pipe flow over smooth walls. Steenbergen and Voskamp (1998) summarize the data in this regard and attribute a considerable scatter to the swirl generation mechanisms and the  $\Omega$  range. Few data however are available for the swirl decay over rough walls or in a more restrictive confinement. Contrary to an open system, in the cylindrical section of combustors, cyclones or dryers, the confinement has a more dominant role. The response of the pressure field to an increase in  $\Omega$  or  $Re$  in these cases is conditioned by the upstream flow and the specific design of the exit duct. A purely geometric swirl number, similar to  $\Omega_i$ , is usually defined according to the design of the inlets, body and outlets (Gupta *et al.* 1984).

Finally, the wall roughness of the dryers merits further comment. Deposits occur on the walls of any production unit. They modify the inner surface and establish roughness elements over a wide range of length scales. This is seldom accounted for but one expects it to determine friction and the turbulence in the boundary layer. Wall friction in similar confinements such as cyclones has an important effect in pressure drop and collection efficiency (Cortes and Gil 2007) what makes important to have an accurate descriptions of roughness in numerical models (e.g. Kim and Lee 2000 or Kaya *et al.* 2011). In the operation of counter-current towers the deposits grow considerably and distribute heterogeneously. This work maintains homogeneous roughness with a twofold purpose: a) ensure an easier numerical reproduction, and b) replicate the best scenario in industry given by recently “cleaned” walls. Chapter III details the characteristics of the deposits left at the wall and compares this reference to the flow field established under a different thickness and coverage. In this case, reproducible conditions were obtained by cleaning the inner surface with an automatic ring designed to ensure the layer of deposits is thinner than  $0.006 D$ . A perfectly homogeneous layer cannot be obtained, but rather a coarse

definition is given whereby the roughness height  $\varepsilon$  ranges between  $0 - 0.006 D$ . These values lie well above the experiments of Seno and Nagata (1972) who report values between  $0.0018 - 0.0025$  and most of the work reviewed in Steenbergen and Voskamp (1998), which nonetheless shows some data obtained at pipes for values as high as  $0.015$ .

### 3. Results and discussion.

This section discusses the development of the vortex in the Scale I, defined in Chapter I. It describes in detail the effects associated to the exit contraction in section 3.1.1, the self similarity and asymmetries in sections 3.1.2 and 3.1.3, and the decay of the swirl in section 3.1.4. The turbulence field is given in section 3.2, presenting the development of the turbulent kinetic energy,  $\kappa$ , and normal,  $\overline{u_i u_i}$ , and Reynolds stresses,  $\overline{u_i u_j}$ , along with the estimates of eddy viscosities,  $\nu_{i,j}$ , and periodic flow structures.

#### 3.1. Time averaged velocity field.

##### 3.1.1. Downstream effects.

Figures 1 to 4 present the time averaged velocity profile,  $\overline{U}$ , and its decomposition in vertical, tangential and radial direction,  $\overline{U}_z$ ,  $\overline{U}_\theta$  and  $\overline{U}_r$ , normalized by the superficial air velocity  $\overline{U}_{av}$ , and for all profiles for all the  $Re$  given in Chapter I. It includes the radial profiles at different heights in the cylinder, denoted with  $z$ , from Figures a) to h). The error bars in all subsequent figures represent the maximum error limits. The measurements denoted by crosses represent data carrying unknown uncertainty. A detailed analysis of the derivation of the measurement error is available in Appendix I.

The large centrifugal inertia shifts the point of maximum velocity,  $\overline{U}_{Max}$  in Figure 1 and maximum tangential velocity,  $\overline{U}_{\theta,Max}$ , in Figure 3 towards the wall, approximately at  $r = 0.70 R$  at the bottom end of the cylinder. As the vortex rises it converges inwards and the location of  $\overline{U}_{Max}$  moves closer the centre and towards the exit, increasing from  $3.3 \overline{U}_{av}$  to  $7 \overline{U}_{av}$  from the bottom to the top ends.

The flow faces a contraction at the vortex finder. With no swirl this would cause the acceleration of the flow in the vicinity of the exit and a global increase in pressure upstream. In the presence of the swirl, the centrifugal force term in the momentum equation complicates these effects and the entire flow field upstream may be affected. This is particularly well known in combustors or swirl injectors where authors such as Escudier *et al.* (1980), Escudier and Keller (1985) or Chao *et al.* (1991) have demonstrated that the presence of an exit contraction has severe effects in the stability of the vortex upstream. It modifies

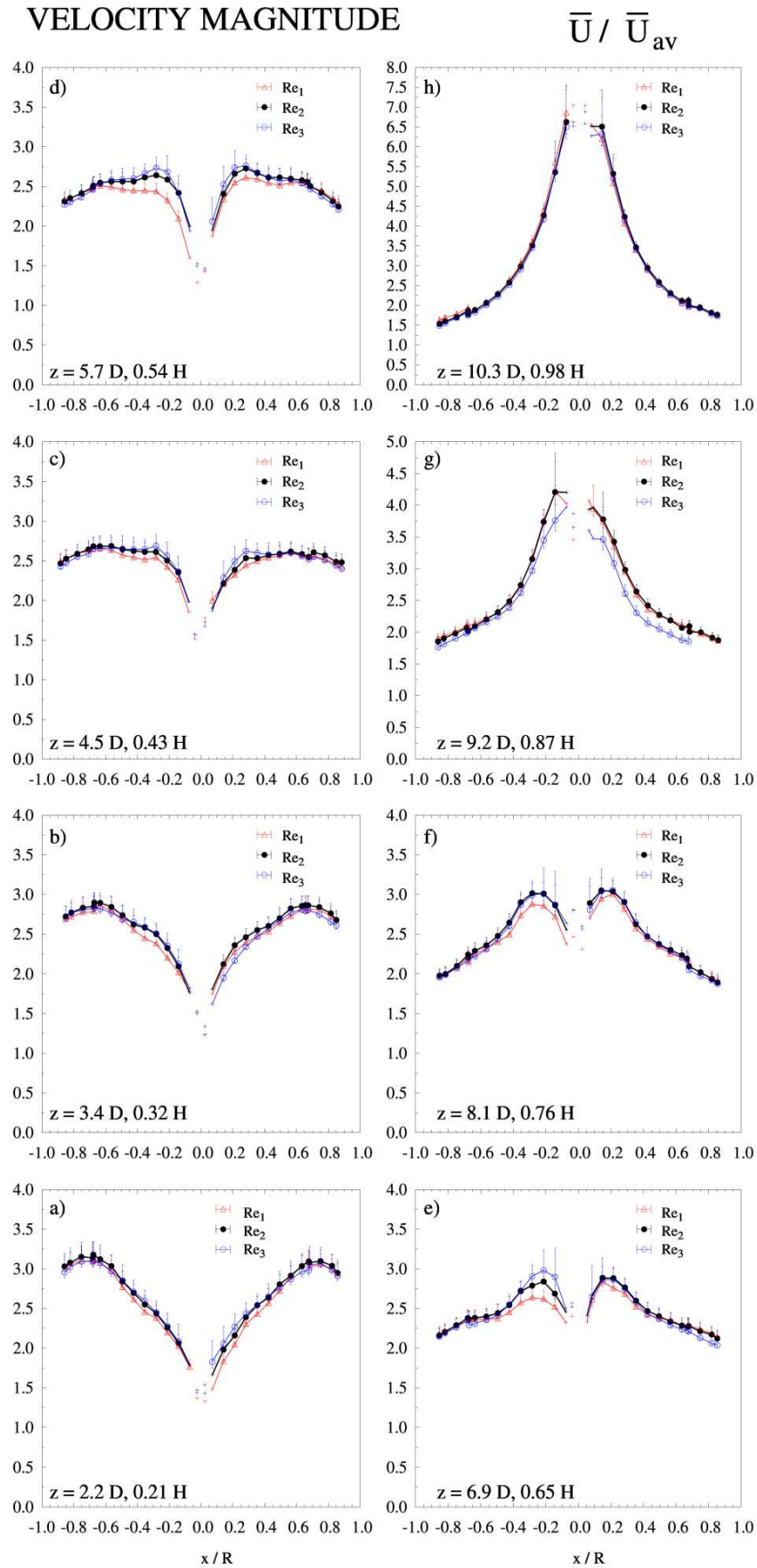


**Figure 1.** Velocity magnitude along the cylinder,  $\bar{U}$  ( $x = -r$  for  $\theta < \pi$  and  $x = r$  for  $\theta > \pi$ ).

the extension of the central recirculation zone and in occasions produces the transition to a jet like axial velocity profile. In this case, the air in the dead volume above the vortex finder may be considered to present a symmetrical and unidirectional flow, and thus radial pressure gradients  $\partial P/\partial r$  balance the centrifugal force term  $\rho U_\theta^2/r$  in the momentum equation. In the sections below the vortex finder, a negative radial pressure gradient must cause a certain flow inwards that facilitates the formation of the central jet from which the bulk mass rate exits the unit (in a similar fashion to the operation of cyclones, being the inner and outer vortices counter-current in a cyclone or co-current in a swirl drying tower).

Chang and Dhir (1994) describe a similar vortex with no exit contraction. A comparable  $\Omega$  causes the reversion of the axial flow at the centre of their open cylinder, owing to an adverse pressure gradient originated by high centrifugal forces. The fact that this does not occur here is related to the influence of the top boundary. Figure 2 shows that  $\bar{U}_z$  in all cases show two maxima: a central jet associated to the diameter of the vortex finder and one nearby the wall, related to the centrifugal inertia. On the one hand, the contraction causes acceleration in its vicinity due to a reduced cross-sectional area. On the other, it causes a rise in the pressure at some point downstream which can be transmitted down the cylinder as a shock wave, such as described by Escudier and Keller (1985) in their investigation of the effect of an increasing swirl number in the recirculation caused upstream of a contraction.

Describing the way in which the fans deliver the targets may illustrate this effect. Consider a tower that operates at a target exit static pressure, and an inlet fan that controls the inlet flow. Consider now a perturbation that increases  $\Omega_i$  and how the velocity field responds. As the vortex reaches the top at higher  $\Omega$ , the radial pressure gradient does not suffice to overcome the centrifugal force term and subsequently causes no inwards flow. The vortex feeds the dead regions above the exit and the accumulation results in an increase in pressure. This is transmitted to lower levels as an inertial wave causing a rise in the energy required from the inlet fan to maintain the same bulk flow, in a similar manner to an increase in the pressure drop. The exhaust line maintains the same exit pressure, and thus higher gradients develop that increase velocities throughout the unit. The steady state flow field is established when the radial static pressure gradient causes the generation of an upwards inner jet that contains the target mass flow. As described by Escudier and Keller (1985) this effect greatly depends upon the swirl number, for the adverse pressure gradient caused by the swirl opposes the flow inwards.

In this case the higher  $\Omega$  is, the larger are the gradients towards the exit that form the jet, or in other

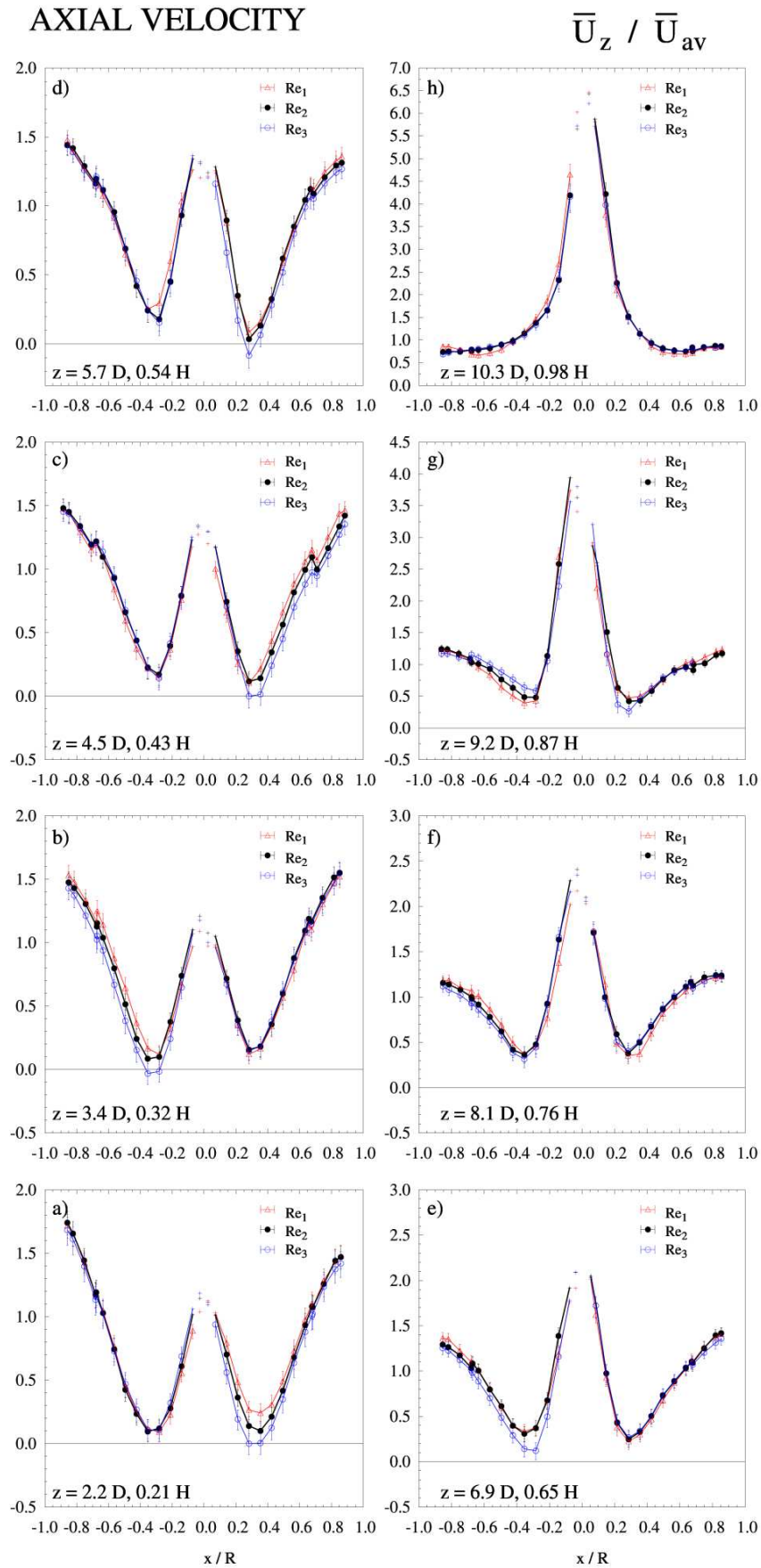


**Figure 2.** Axial velocity  $\bar{U}_z$  associated to the vortex in Figure 1.

words, the further down the cylinder the influence of the exit has to be transmitted in order to originate sufficient flow inwards. As gradients towards the exit duct increase, they overcome the influence of the centrifugal force and suppress the reversion at sections sufficiently close to it. Figure 2 shows that in this case they are sufficient to suppress recirculation in the entire cylinder, where  $\bar{U}_z$  shows a central jet. This feature confirms the observations of Sharma (1990) or Bayly *et al.* (2004) at smaller dryers, or the expectation from numerical works (e.g. Harvie *et al.* 2001; Ali 2014), and contrasts the reports under the operation of the slurry nozzles, where the central jet is lost (Zbicinski and Piatkowski 2009).

In accordance with Escudier and Keller (1985), a rise or a reduction in  $\Omega$  at the contraction level may disrupt the stabilizing effect of the contraction. This has been confirmed in Chapter III by the identification of different operation regimes in counter-current dryers, and its correlation to the  $\Omega$  prevailing in the chamber. In the case of “cleaned” walls treated here, as the flow rises it converges inwards and the  $\bar{U}_{z,Max}$  close to the wall diminishes from  $1.5 - 1.8 \bar{U}_{av}$  at the bottom to  $< 1 \bar{U}_{av}$  at the top. In parallel the values at the jet increases from  $1.1 - 1.4 \bar{U}_{av}$  for  $z \leq 5.7 D$  to values  $> 5 - 6 \bar{U}_{av}$  close to the top. For most of the cylinder the radius of the jet (i.e. location of  $\bar{U}_{z,Min}$ ) responds to the diameter of the exit, extending slightly above  $r = 0.30 R$  only at the bottom. At the outer axial flow reduces and the minimum is lost, showing a very similar profile to the data given by Escudier *et al.* (1980) or Derksen (2005).

In regards to the swirl, comparison to ideal patterns defined by  $\bar{U}_\theta = C \cdot r^n$  aids in the analysis of complex systems (Sloan *et al.* 1986). A forced vortex (i.e. solid body rotation) is defined by  $n = 1$  while a free-like structure (i.e. potential vortex) shows an inverse relation between  $\bar{U}_\theta$  and  $r$  defined by  $n = -1$ , descriptive of irrotational flows such in tornados or whirlpools. Making use of these, the comparison to the Burgers solution or a Rankine ideal pattern serves to study the features of confined vortices of the so called “concentrated” type. These comprise of an inner forced vortex and an outer free-like structure. Actual experimental profiles need also including a transition region nearby the location of  $\bar{U}_{\theta,Max}$ , where the gradient diminishes and blends both structures. According to these definitions, the flow may be divided into four regions: 1- the inner forced vortex 2- the annular or transition region 3- the outer free-like vortex, and 4- the boundary layer.

Figure 3 shows large transition regions being generated at the bottom, between  $r \sim 0.10 R$  and  $0.79 R$ . As the vortex rises the location of  $\bar{U}_{\theta,Max}$  moves inwards from  $r \sim 0.70 R$  to  $0.20 R$  and

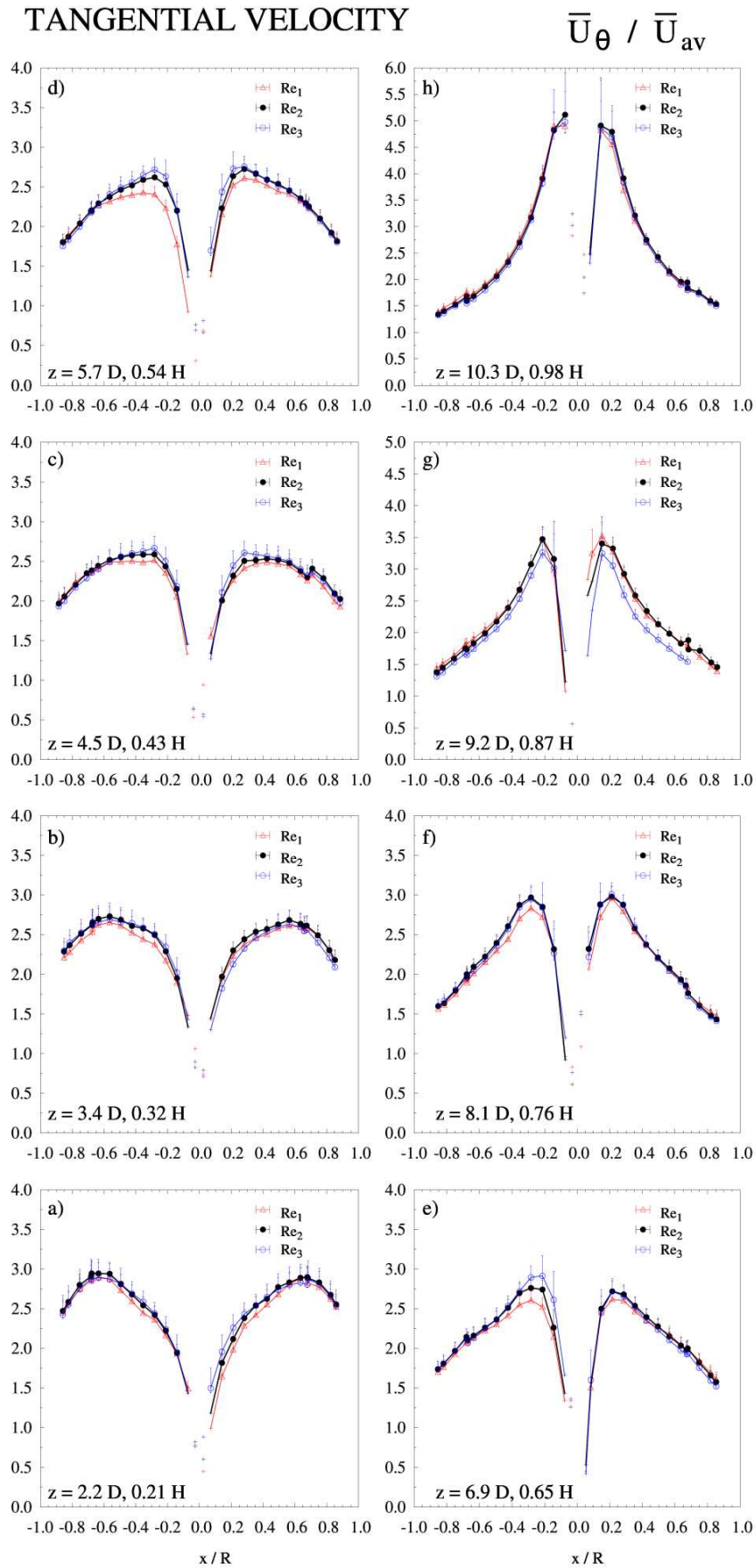


**Figure 3.** Tangential velocity  $\bar{U}_\theta$  associated to the vortex in Figure 1.

the transition region narrows substantially, particularly between the levels  $z = 3.4 D$  and  $5.7 D$ . After this point, the outer region shows a linear decrease of  $\bar{U}_\theta$  with  $r$  between  $z = 6.9 D$  and  $8.1 D$ , that develops into an inverse relation at the top  $z = 10.3 D$ . At this point the transition region is restricted to between  $r \sim 0.15 R$  and  $0.20 R$  and the vortex follows closely a Rankine pattern. In all levels the radius of the forced vortex is contained within the jet, and relatively constant  $r \sim 0.15 R$ .

The transfer of the angular momentum inwards causes the value of  $\bar{U}_{\theta,Max}$  to increase axially, and shifts its location to the central region where a clear forced core of high  $\bar{U}_\theta$  appears for  $z \geq 5.7 D$ . In parallel,  $\bar{U}_\theta$  decreases in the outer region from around  $3.0 \bar{U}_{av}$  at  $z = 2.2 D, r = 0.70 R$  to values below  $2.0 \bar{U}_{av}$  and  $1.5 \bar{U}_{av}$  moving from  $z = 6.9 D$  to  $10.3 D$ . The shapes of the profiles agree well with the mentioned experimental and numerical studies and confirm the observations of Sharma (1990). However it shows a much larger decrease in  $\bar{U}_\theta$ . Comparison against the data in a scaled down clean tower (Bayly *et al.* 2004) show a decrease here from 27 – 37% in  $\bar{U}_\theta$  at  $r = 0.70 R$  and levels  $z = 0.30 H$  and  $0.90 H$  respectively. This owes to the effect of deposits in the friction and is discussed further in section 3.1.4. These data confirm the observations of Hassall (2011) working in the same dryer. Hassall (2011) compared *PIV* data to that of Bayly *et al.* (2004) and reported similar differences in  $\bar{U}_\theta$  from 30 – 40% for the same heights, and  $r = 0.91 R$ .

Radial velocities are given in Figure 4. Despite a higher uncertainty, certain levels show significantly higher values than expected from continuity in equation (1) (see Figure 4c or 4e) what suggests the presence of a consistent transversal flow, and an asymmetrical flow structure, discussed in section 3.1.3.

### 3.1.2. Self similarity.

Comparison across the range of  $Re$  is included in Figures 1 to 4. All the velocities collapse into a characteristic profile when they are normalized by  $\bar{U}_{av}$ , thus establishing the self-similar nature of the flow. This is expected in the context of swirling flows at a sufficiently large  $Re$  number (e.g. Litvinov *et al.* 2013). It implies that an increase in rate and thus  $\bar{U}_{av}$  and  $Re$  simply causes an increase in  $\bar{U}$  at any point in the vortex structure, but no changes to its direction. In this way, no differences should be expected in the friction factor (see section 3.1.4) not in the effects caused by the contraction. The exception is the behaviour of three dimensional asymmetries described below, and the slight deviations observed for  $\bar{U}_\theta$  at the lowest range at  $Re_1$  in Figures 3d and 3e.

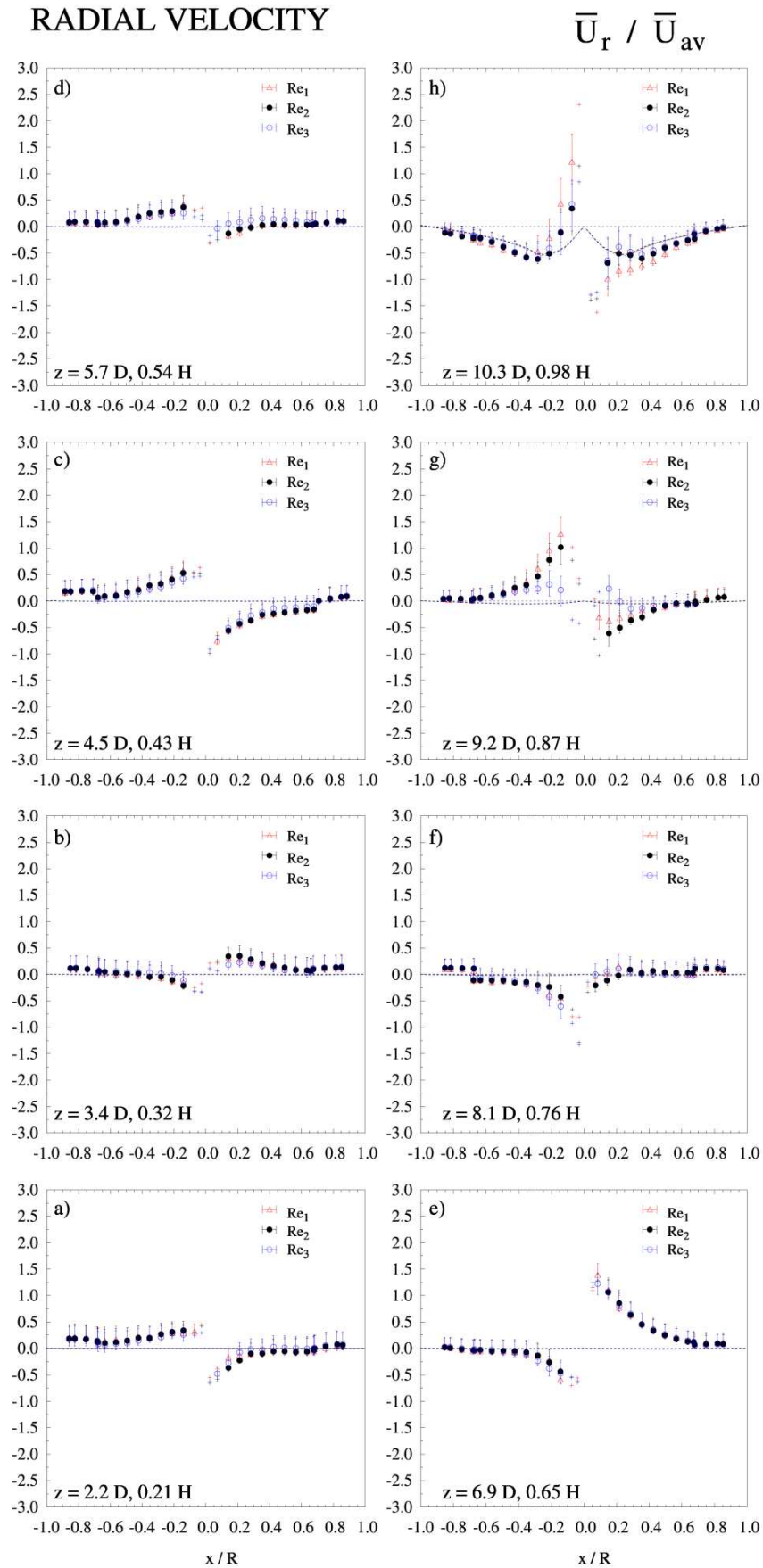


**Figure 4.** Radial velocity  $\bar{U}_r$ , associated to Figure 1. Lines provide the estimation based on equation (1).

### 3.1.3. Asymmetry.

The asymmetries in Figures 1 to 4 are likely related to the design of the exit and the swirl generation mechanism. The use of tangential inlets is known to develop asymmetric structures (e.g. Hreiz et al. 2011). This can be avoided by placing a sufficient number of inlets in pairs orientated symmetrically as described in Chapter I. In counter-current dryers, the generation of the vortex gains in complexity, because it does not derive directly from a tangential injection but occurs at the bottom end. Huntington (2004) lists the usual designs in large swirl towers and Sharma (1990) or Harvie *et al.* (2001) describe the sensitivity of the vortex shape to the orientation of inlets, discussing the difficulties to obtain stable patterns. Ensuring an adequate balance in the pressure, or mass rate, between all inlets is fundamental.

Most of data are not fully axi-symmetric. Differences are particularly visible in Figure 2 for  $\bar{U}_z$ , at both the values of  $\bar{U}_{z,Max}$  close to the wall and  $\bar{U}_{z,Min}$ . At the bottom end of the cylinder,  $\bar{U}_{z,Max}$  varies from  $1.8 \bar{U}_{av}$  to  $1.5 \bar{U}_{av}$  between both sides, while  $\bar{U}_{z,Min}$  ranges between  $0.1 \bar{U}_{av}$  to  $0.3 \bar{U}_{av}$  for  $Re_1$ . As the flow rises, the asymmetry in the outer region stabilizes, but it persists within the transition to the central jet. The correlation with  $Re$  is of interest: whilst one side remains self-similar, the opposite varies significantly. The location where  $\bar{U}_z$  varies appears to spiral upwards in the cylinder from  $z = 2.2 D$  to  $6.9 D$  (see Figure 2 and the tangential position of the accesses in Chapter I). This points to a coherent asymmetric structure, a consequence perhaps of different mass rates at some of the inlets. As  $Re$  increases  $\bar{U}_{z,Min}$  drops in all these locations, which could be explained by a better equilibration when the pressure drop at the distributor decreases for higher  $Re$ . At the top of the unit, asymmetries occur in both  $\bar{U}_z$  and  $\bar{U}_r$ , indicating a strong transversal flow (i.e. from one side to another in the cylinder). At  $z = 9.2 D$ , lower  $Re$  results in an improved symmetry, attributed to preferential paths to the exit. These often owe to the design of the exhaust line and the partial blockage of the inner channels inside the exit duct, unavoidable in production.

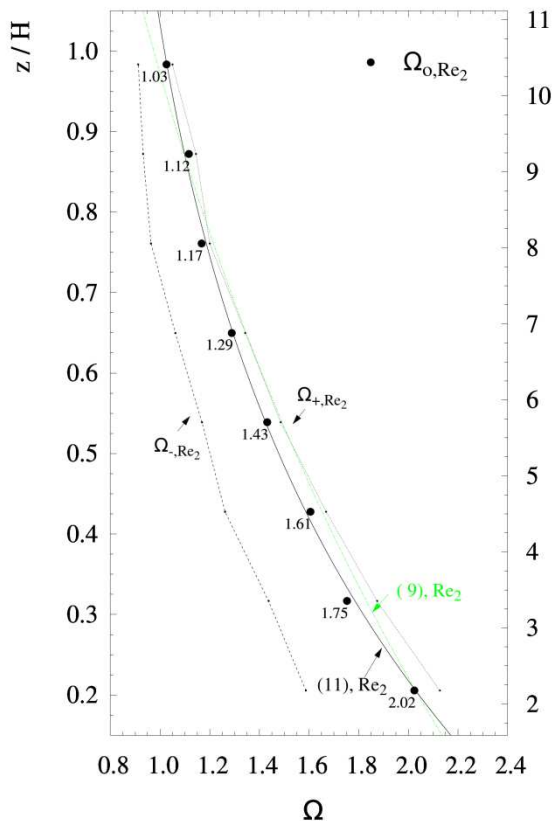
### 3.1.4. The decay of the swirl.

Figure 5 shows the decay of the swirl intensity  $\Omega$  as a function of the height in the cylinder. It does not follow the exponential decay given by (9) what suggests the wall shear stress  $\tau_{w,\theta}$  is not proportional to  $\Omega$ . This is expected at such high values,  $1 < \Omega < 2$ . In this range the axial decay is well approximated by a piecewise linear relation as proposed by Kitch (1991), and given in equation (11).

It should be noted that the method does permit the measurement of velocity close to the wall. This

range is extrapolated in Figures 1 to 4, and used in equation (6) for the calculation of  $\Omega$ . Three estimates are given according to the way in which  $\bar{U}_z$  and  $\bar{U}_\theta$  are reconstructed. The best estimate,  $\Omega_o$ , is obtained by a linear extrapolation from the last measurement to an intermediate point after which the velocity follows the logarithmic law of the wall. The thickness of the logarithmic region is set according to the condition of the volume rate complying with the integration of the axial velocity profile. In order to give perspective on the absolute maximum errors, the following estimates are computed according to, a) a linear decrease of the velocity from the last measurement to zero at the wall, which causes under prediction of  $\Omega$  and the air flow rate, denoted  $\Omega_-$  b) a constant value, causing over prediction of both, denoted  $\Omega_+$ .

The data provided by Bayly *et al.* (2004) or Hassall (2011) indicate velocities do not start decaying sharply close to the wall up to  $r > 0.98 R$  for at least  $\bar{U}_\theta$ . As a result,  $\Omega_-$  yields far greater errors in the integration of the mass rate, in particular for the cases described in Chapter III. Errors in the mass



**Figure 5.** The axial decay of  $\Omega$  across the cylindrical chamber of a tall-form dryer.  $\Omega_o$ ,  $\Omega_+$  and  $\Omega_-$  provide respectively the best estimate and over and under predictions; lines provide the fit to equations (9) and (11).

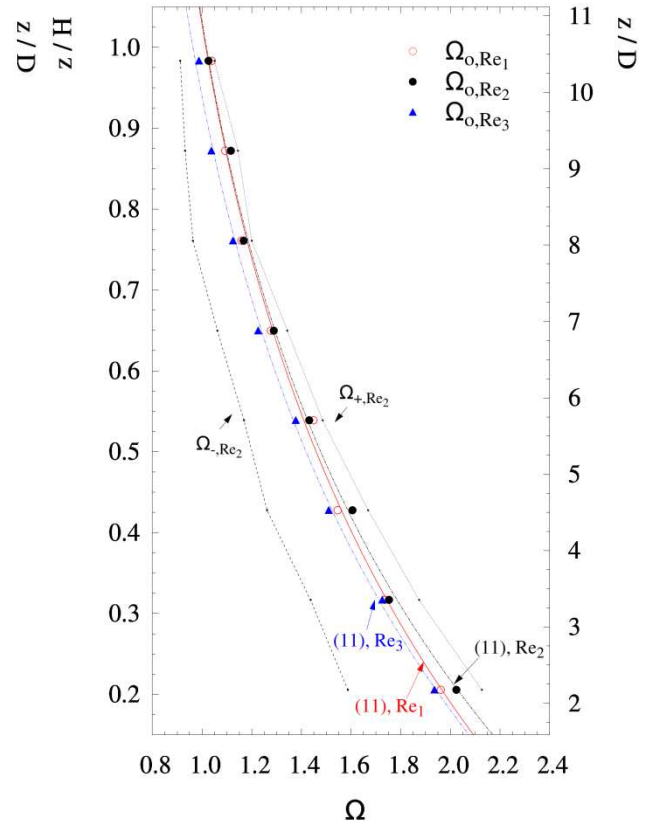


**Figure 6.** The effect of the bulkRe in the decay of  $\Omega$ .  $\Omega_o$ ,  $\Omega_+$  and  $\Omega_-$  represent respectively the best estimate and over and under predictions of  $\Omega$ ; lines provide the fit to equation (11)

**Table 1.** Swirl decay rates as a function of  $Re$ . Fit to a proportional or linear relation between  $\tau_{w,\theta}$  and  $\Omega$  in (9) and (11).

Case	$Re \cdot 10^{-5}$	$\Omega_r$	$A$	$B$	$\lambda$
$Re_1$	$1.06 \pm 0.03$	1.96	-0.080	0.054	0.085
$Re_2$	$1.49 \pm 0.02$	2.02	-0.086	0.061	0.089
$Re_3$	$2.22 \pm 0.02$	1.93	-0.081	0.051	0.090

rate for  $\Omega_o$  are however kept  $< 0.1\%$  in all the profiles shown here and in Chapter III with the exception of strongly asymmetrical sections where errors can reach up to  $4\%$  (cases B and C in Scale I, or Scale II, Chapter III) and up to  $13\%$  at the top of Scale III (Chapter III).

Figure 6 shows the decay of  $\Omega$  for all the  $Re$  studied. The data demonstrates that the swirl decay is independent of  $Re$  in the ranged studied. The decay rates from the fit to equations (9) and (11) are summarized in Table 1. The values are between  $0.08 - 0.09$ , significantly above the usual in open pipes, which range between  $0.019 - 0.032$  for  $5 \cdot 10^4 < Re < 3 \cdot 10^5$  (Steenbergen and Voskamp 1998) or between  $0.02 - 0.06$  for  $10^4 < Re < 10^5$  in the work of Najafi *et al.* (2011). Higher values are reported by Chang and Dhir (1994), who work at comparable swirl intensity to this work. Once the flow develops in their tube, for  $z \geq 6D$ , their decay rates may be rewritten in terms of  $\Omega$  and  $\lambda$  using the velocity data. Taking as a reference  $z_r = 6D$  they show that  $\lambda$  varies from  $0.06$  to  $0.11$  for  $\Omega_r = 1.6$  and  $\Omega_r = 3.9$ . These constitute higher values than usual in open pipes, which can be explained by the fact of working at higher  $\Omega$  values and at lower  $Re = 1.2 \cdot 10^4$ .

The data in Table 1 shows a comparable decay rate  $\lambda$  in a counter-current dryer at a similar  $\Omega$  but at much higher  $Re > 10^5$  that the experiments of Chang and Dhir (1994). Several considerations follow. Firstly, a higher  $\lambda$  is likely related to an increase in the roughness caused by a thin layer of particulate deposits at the walls. Interestingly, the decay rate  $\lambda$  is observed within the same order of magnitude of the friction factor expected for coarse roughness in a fully developed pipe flow,  $0.08$  or  $0.02$  for the Darcy and Fanning friction factors at  $\varepsilon/D = 0.05$  (Moody *et al.* 1944). This withstands the assertion of Steenbergen and Voskamp (1998) who discuss a general relation between  $\lambda$  and the friction factor for smooth open pipe flow, and whose correlation for clean walls however does not hold here.

Secondly, the lack of correlation between  $\lambda$  and  $Re$  is also due to a higher roughness. The traditional view of pressure drop in a rough pipe states that as the height of the roughness  $\varepsilon$  increases, most of the elements stand above the extension of the viscous sub-layer and the drag originated in the friction

starts to depend exclusively on  $\varepsilon/D$ . For the range used here,  $\varepsilon/D \sim 0.006$ , the friction factor in rough pipes becomes independent of Reynolds numbers for  $Re > 10^5$  (Moody *et al.* 1944). Chapter III discusses the effect that an increase in  $\varepsilon/D$  and the coverage of the deposits has in modifying  $\lambda$ . In addition, for the geometry presented here the sensitivity of  $\lambda$  to  $Re$  is likely reduced at the operation at sufficiently high  $\Omega$  numbers, where the vortex shape, and thus the velocity profile close to the wall is dominated by the influence of the contraction. Consider an open pipe operating at similar  $\Omega_i$ ; when  $\lambda$  decreases at high  $Re$ ,  $\Omega_i$  is simply allowed to penetrate further in the pipe. In a short confinement, the penetration length is restricted by the dimensions of the cylinder, as in the “natural length” or “vortex length” effect in a cyclone (Cortes and Gil 2007). In this case when the flow faces the exit at a sufficiently high  $\Omega$  the contraction has a substantial influence in the flow upstream. Thus, the velocity profile near the wall and the relation between  $\tau_{w,\theta}$  and  $\Omega$  becomes a stronger function of  $\Omega$  and less sensitive to the effect of  $Re$  in the development of the boundary layer (Maddahian *et al.* 2011). These data are the first of their type for a large scale dryer. They stress the importance of roughness in real systems and suggest this type of dryers operate under a high level of friction. It is then important to find ways to characterize deposits and account for their effect in the fluid dynamics. The implications for numerical modelling should not be ignored. Large scale computational fluid dynamics, *CFD*, models using smooth wall assumptions over-predict  $\bar{U}_\theta$  at the top of the tower by 30 – 40%. The use of wall functions in a swirling system remains a challenging task (Jakirlic *et al.* 2002), and inclusion of these effects entails operating out of the limits of the standard functions for an unidirectional flow in rough walls (e.g. Jimenez, 2004). In these circumstances, it is unclear how boundary conditions may be treated if roughness elements in the order of *mm* or *cm* govern the friction. Perhaps more importantly, it is unclear which impact this would bring to the generation of turbulence and the structure of the boundary layer, both fundamental aspects in particle flow and wall deposition.

The reason for these effects having remained unnoticed lies in the challenge in obtaining full scale data (Huntington 2004 or Zbicinski and Piatkowski 2009) and consequent lack of any reported studies. Numerical works rarely benefit from data obtained in production units but gain validation from works in laboratory or pilot-scale facilities. This often serves as a valid guide for design purposes but cannot easily replicate characteristics inherent to a full scale, where a final validation should always be pursued. This has potentially caused fully coupled models of large dryers to contain a severe bias error in the

prediction of the particle centrifugal inertia. This is critical in a counter-current unit for the interaction with the wall plays a major part in the process (Chapter V).

## 3.2. Turbulence statistics and periodicity.

### 3.2.1. Turbulent kinetic energy and intensity.

The axial variation of the turbulent kinetic energy,  $\kappa$ , is given in Figure 7 for all heights and  $Re$ . Figures 8 and 9 shows the decomposition in normal stresses for the annular outer region. At all heights, a large maximum in  $\kappa$  is observed at the centre of the tower, varying from  $0.2 - 0.3 \bar{U}_{av}^2$  at the bottom,  $> 0.7 \bar{U}_{av}^2$  at  $9.2 D$  and down to  $0.3 - 0.5 \bar{U}_{av}^2$  at the top. The extension of the region of higher variability agrees well with that of the central jet, and is likely to result from an unstable jet, commonly reported in similar cyclonic flows (Hoekstra *et al.* 1999, Lui *et al.* 2006 or Hreiz *et al.* 2011).

Vortices start to present aerodynamic instabilities when the strength of the swirl increases. For low  $Re$ , local recirculation starts for swirl numbers  $> 0.6$  in a straight exit type of device, leading to the stagnation of the flow (O'Doherty *et al.* 1999). This can occur in different ways and leads to various types of  $VBD$  depending on the flow characteristics and the geometry of the system (Luca-Negro and O'Doherty 2001). This is the subject of ample research in aeronautics or combustion. For sufficiently large  $Re$  the instability manifests by formation of periodical structures. The breakdown then results in a coherent oscillation whereby the core of the vortex precesses around its symmetry axis, referred to as the  $PVC$ . The conditions for its occurrence, its characteristics and its transmission are highly dependent on  $Re$ ,  $\Omega$ , the confinement, and the condition of the flow between the  $CRZ$ , the  $VBD$  and the exit, that is: being subcritical or supercritical according to its ability to withstand or not inertial waves (Escudier *et al.* 1985). These are well known in the operation of combustors (Syred 2006) or cyclones where authors such as O'Doherty *et al.* (1999), Derksen and Van den Akker (2004) or Cortes and Gil (2007) pay attention to describe how the  $PVC$  originates at the exit tube. Similar processes are documented at the inlet of co-current dryers by Langrish *et al.* (2004).

Put simply, the  $PVC$  responds to the instability of the core causing it to acquire a spiral shape around which axis fluctuates in a helical orbit. It becomes identifiable by its effect on velocity variability. The velocity variance at a fixed point in the region affected by  $PVC$  comprises of a turbulent term and a periodic signal owed to the fluctuation of the relative position between the observer and the core. This sort of phenomenon is responsible for the large central maximum observed in Figure 7 associated with

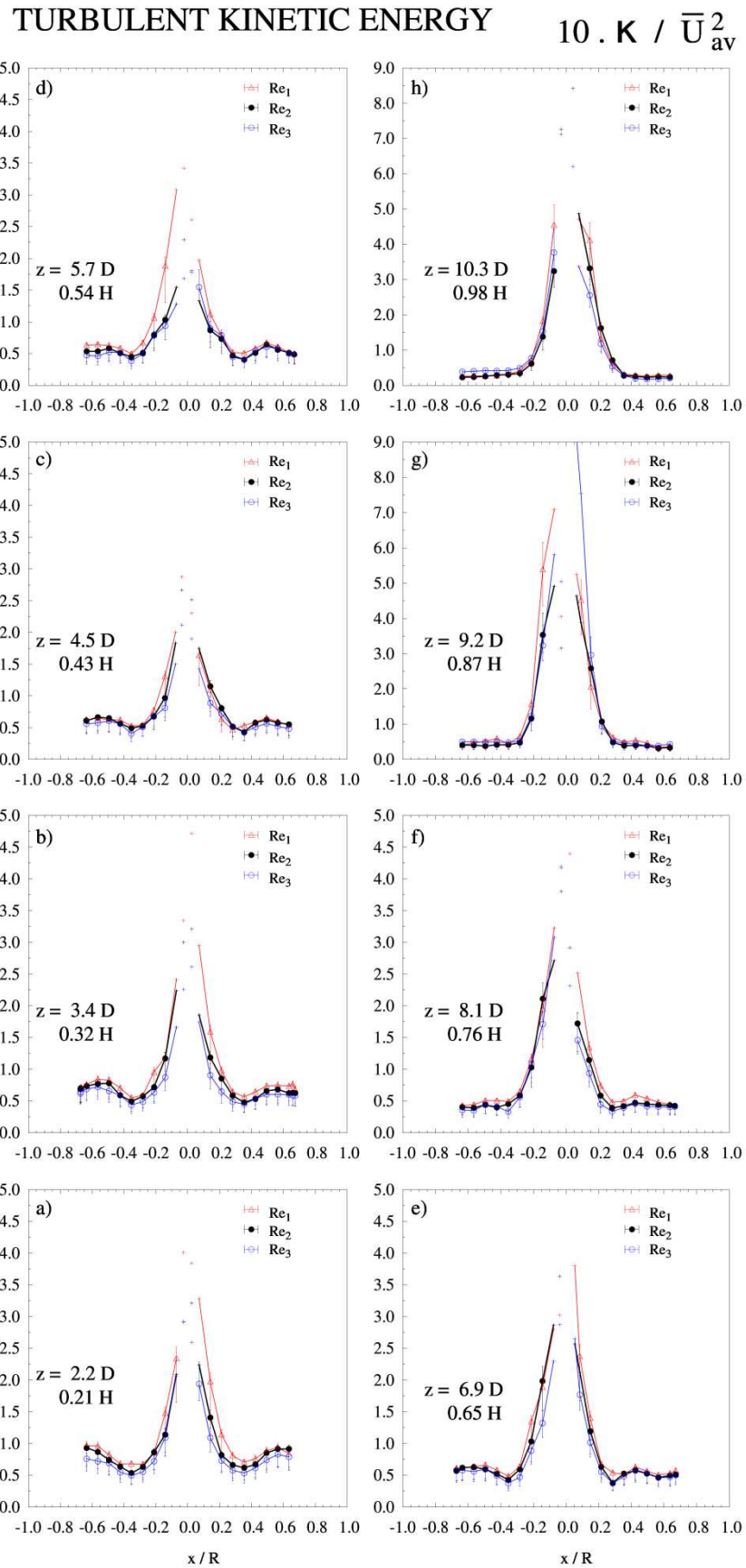


**Figure 7.** Turbulent kinetic energy,  $\kappa$ , associated to Figure 1 at values of  $Re$  shown in Table 1.

no turbulent energy but indicative of the unstable nature of the core, as discussed in section 3.2.4.

Figure 8a details the radial and axial development of  $\kappa$ . As the vortex rises the location of  $\kappa_{Max}$  in the outer region shifts inwards from  $r = 0.60R$ . This region shows comparable  $\kappa$  values and evolution to the reports in open tubes at a similar  $\Omega$  (Chang and Dhir 1994).  $\kappa$  also appears to decrease axially from  $0.06 - 0.09 \bar{U}_{av}^2$  to  $0.02 - 0.03 \bar{U}_{av}^2$  at the top in a linear relation to the decay of  $\Omega$ .

The normal stresses  $\overline{u_z u_z}$  and  $\overline{u_r u_r}$  show the same transition between the inner jet and the outer region, where they range between  $0.02 - 0.07 \bar{U}_{av}^2$  at the bottom, and decrease axially below  $0.02 - 0.03 U_{av}^2$  close to the exit (see Figures 8b and 8d). Both present the same outer maximum that progressively converges inwards. In contrast to an open pipe (Chang and Dhir 1994) clear differences appear between  $\overline{u_r u_r}$  and  $\overline{u_z u_z}$  and the turbulent mixing in the azimuthal direction given by  $\overline{u_\theta u_\theta}$  (Figure 8c), which is 30 – 40% lower and shows no outer maximum. This discrepancy can be explained by the effect the contraction according to the Large Eddy Simulations, *LES*, of Derksen (2005). They describe the disruption caused upstream by an exit contraction, showing the evolution from an open system to a cylinder with a high contraction ratio. The open tube initially shows an inner stabilizing forced vortex and a highly turbulent outer free vortex. Moving into a narrow contraction, the core is distorted and Taylor-Görtler vortices appear in the outer region, which suppress mixing in the azimuthal direction. In addition, detachment from the *PVC* structure of coherent eddies in the axial-radial plane has also been reported in cyclones (Cortes and Gil 2007).

In Figure 9 all measurements show the same trend, reducing  $\kappa$  and normal stresses with increasing  $Re$ . This is an indication of the suppression of turbulence, but the large uncertainty on the measurement makes the differences at the upper part to be no statistically significant at the upper part of the cylinder.

### 3.2.2. Reynolds stresses.

The development of Reynolds stresses is given in Figures 10 and 11.  $\overline{u_z u_\theta}$  is associated to the transfer of angular momentum downstream due to the turbulence, and thus is predominantly positive (see Figure 10a). It shows a maximum at  $r = 0.58 R$  for the bottom of the tower, which then shifts inwards as the influence of the exit transfers most of the angular momentum flux to the central jet. In accordance with the data in open tubes (Chang and Dhir 1994), the decay in  $\Omega$  leads to  $\overline{u_z u_\theta}$  also decreasing axially. Two zones of negative values appear in this case: 1- at the inner region also noticed by Chang and Dhir (1994) who in general report higher values and 2- at the vicinity of the top exit,

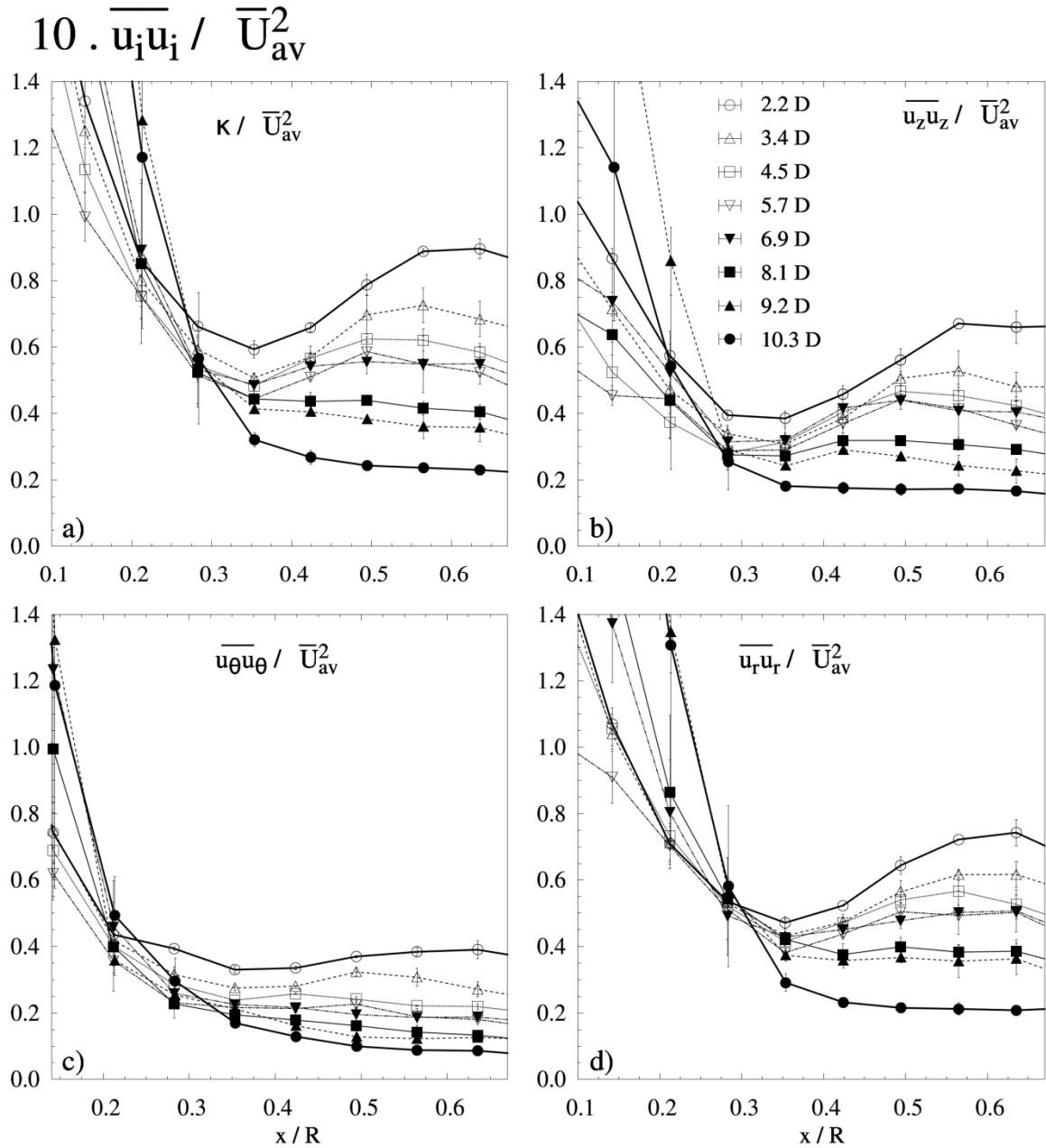


**Figure 8.** Axial variation of all normal stresses at  $Re_2$  shown in Table 1. a)  $\kappa$  b)  $\overline{u_z u_z}$  c)  $\overline{u_\theta u_\theta}$  d)  $\overline{u_r u_r}$ . Data normalized by  $\bar{U}_{av}^2$ . Error bars indicate the variation across tangential locations. Maximum uncertainty ranges in  $\kappa$ ,  $-31, +7\%$ ,  $\overline{u_z u_z}$ ,  $-41, +19\%$ ,  $\overline{u_\theta u_\theta}$ ,  $-23, +19\%$ ,  $\overline{u_r u_r}$ ,  $-35, +22\%$  (Appendix I).

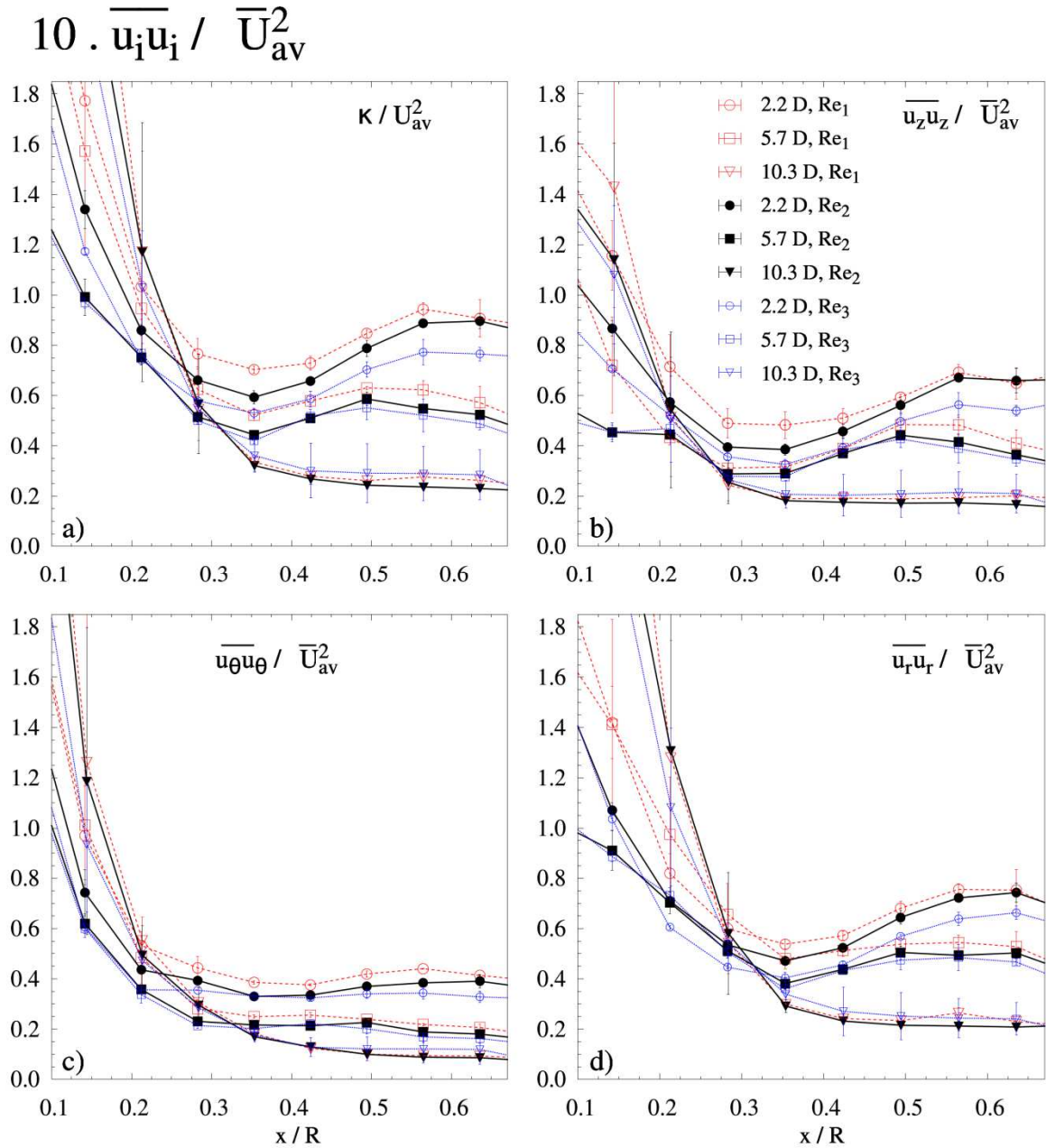


**Figure 9.** Impact of  $Re$  (values in Table 1) upon all normal stresses. a)  $\kappa$  b)  $\overline{u_z u_z}$  c)  $\overline{u_\theta u_\theta}$  d)  $\overline{u_r u_r}$ . Data normalized by  $\overline{U_{av}^2}$ . Error bars indicate the variation across tangential locations. Maximum uncertainty ranges in  $\kappa$ ,  $-31, +7\%$ ,  $\overline{u_z u_z}$ ,  $-41, +19\%$ ,  $\overline{u_\theta u_\theta}$ ,  $-23, +19\%$ ,  $\overline{u_r u_r}$ ,  $-35, +22\%$  (Appendix I).

$z = 10.3 D$  indicative in this case of the recirculation originated at the dead regions above.

$\overline{u_r u_\theta}$  increases as the vortex rises, showing positive values in the outer region, decreasing to a similar transition point at the central jet between  $r = 0.25 R$  and  $0.30 R$ , where they take predominantly positive values in Figure 10b. To the contrary, Figure 10c shows how  $\overline{u_r u_z}$  takes large negative values in the outer region in a similar range and evolution to an open tube (Chang and Dhir, 1994). The values diminish in magnitude with axial position, and acquire a positive sense only close to the exit. A similar transition occurs at the inner region, where they change direction between  $z = 6.9 D$  and  $10.3 D$ .

In contrast to the behaviour of normal stresses, no changes can be observed in the development of the Reynolds stresses during the operation at different  $Re$  in Figure 11.

### 3.2.3. Eddy viscosity and anisotropy.

Eddy viscosities are summarized in Figure 12.  $\nu_{z,\theta}$  shows in Figure 12a a transition at  $0.35 < r < 0.40 R$  where  $\partial \overline{U}_\theta / \partial z$  achieves its locus. This defines the regions where the axial change of  $\overline{U}_\theta$  is dominated by wall friction (i.e. at a higher radius  $r$ ) or by the transfer of angular momentum inwards caused by the influence of the exit (i.e. at a lower radius  $r$ ). The same transition appears as a minimum in  $\nu_{r,\theta}$  which shows in all cases positive values. On the other hand,  $\nu_{r,z}$  is predominantly positive, although it alternates between large positive values in the outer part that diminish towards the centre where it can take small negative values (indicative of negative turbulence energy production).

Comparison of the values of  $\nu_{z,\theta}$  to those of  $\nu_{r,\theta}$  and  $\nu_{r,z}$ , show a substantial difference, in the same order of magnitude that the reports of Kioth (1991) or Chang and Dhir (1994). This confirms ample evidence of the mixing length theory not being able to describe anisotropy in swirling flows. An anisotropy factor  $\alpha_f$  is estimated as the ratio of the shear stress to  $2 \cdot \kappa$  in the same manner as Kioth (1991).  $\alpha_v$  varies significantly in the radial direction. In agreement with Kioth's (1991) observations  $\alpha_v$  also tends to 0.15 in the outer region and diminishes substantially in the transition inwards, taking values between 0.01 – 0.04. However in this case, it rises again at the central jet. As the flow develops axially, the value of  $\alpha_v$  in the outer region and that at which rises at the centre, both increase.

### 3.2.4. Precession of the vortex core.

This work focuses in studying the structure of the flow at large scale. In this context, the use of sonic anemometry results beneficial despite it entails working with lower accuracy than the common laser

$$10^2 \cdot \overline{u_i u_j} / \overline{U_{av}^2}$$

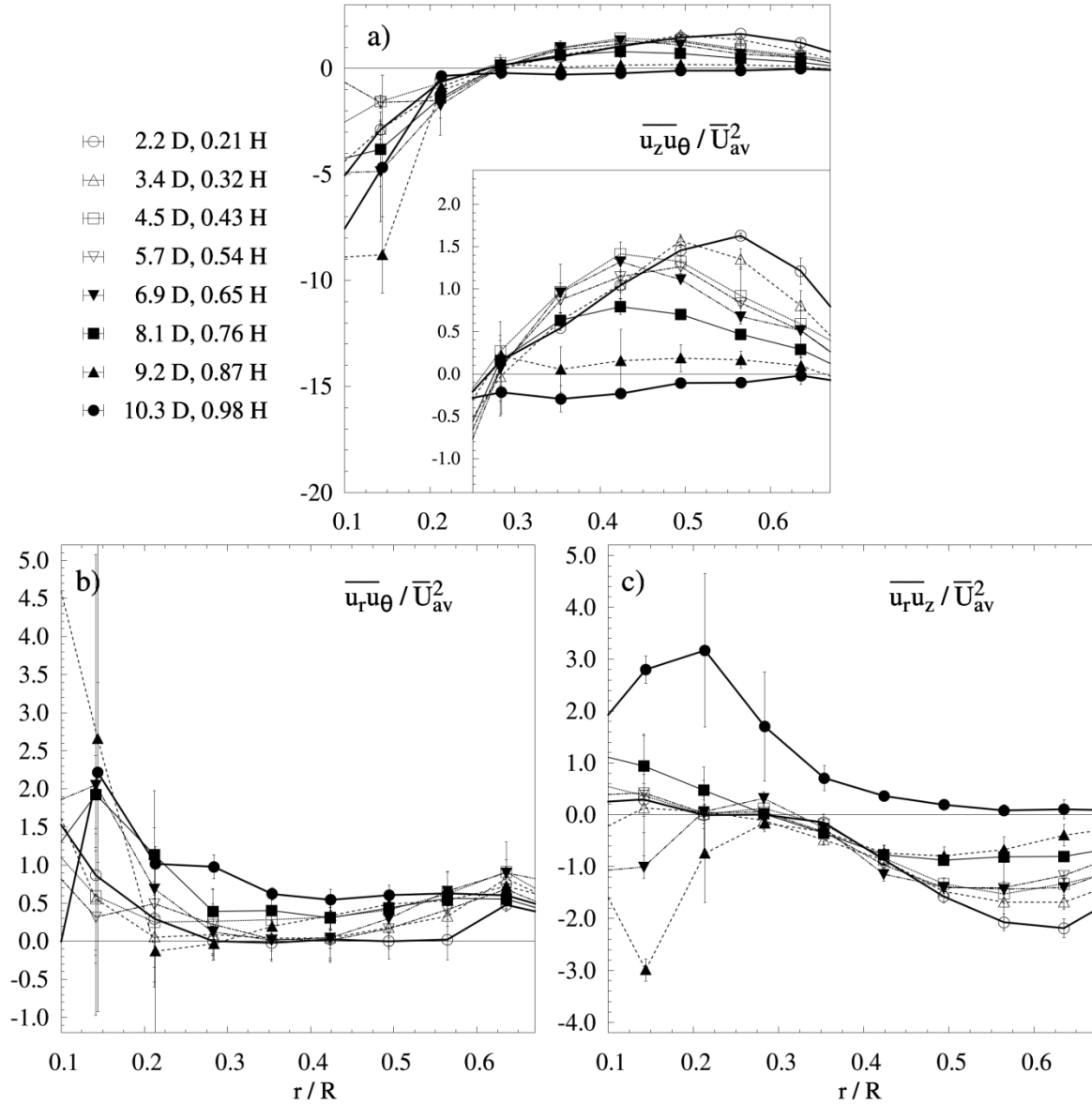


**Figure 10.** Development of the Reynolds stresses at  $Re_2$  (Table 1) .a)  $\overline{u_z u_\theta}$ , b)  $\overline{u_r u_\theta}$ , c)  $\overline{u_r u_z}$ . Data is normalized by  $\overline{U_{av}^2}$ . Error bars indicate the variation across tangential locations. Maximum uncertainty ranges in  $\overline{u_z u_\theta}$ ,  $-23, +19\%$ ,  $\overline{u_r u_\theta} \pm 100\%$ ,  $\overline{u_r u_z}$ ,  $\pm 200 - 400\%$  (Appendix I).

$$10^2 \cdot \overline{u_i u_j} / \overline{U}_{av}^2$$

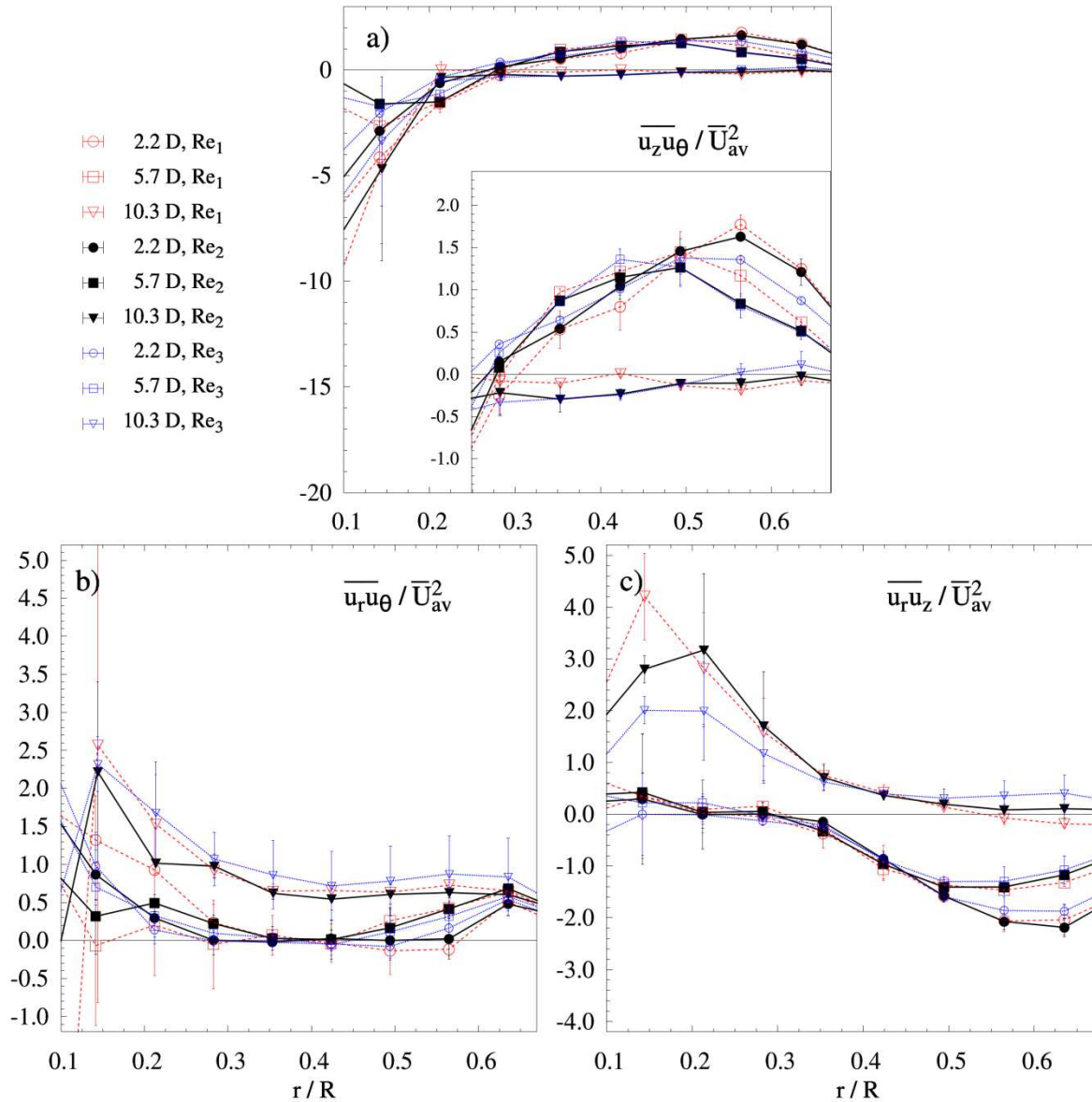


**Figure 11.** Impact of  $Re$  (values in Table 1) in the development of Reynolds stresses. a)  $\overline{u_z u_\theta}$  b)  $\overline{u_r u_\theta}$  c)  $\overline{u_r u_z}$ . Data is normalized by  $\overline{U}_{av}^2$ . Error bars indicate the variation across tangential locations. Maximum uncertainty ranges in  $\overline{u_z u_\theta}$ ,  $-23, +19\%$ ,  $\overline{u_r u_\theta} \pm 100\%$ ,  $\overline{u_r u_z}$ ,  $\pm 200 - 400\%$  (Appendix I).

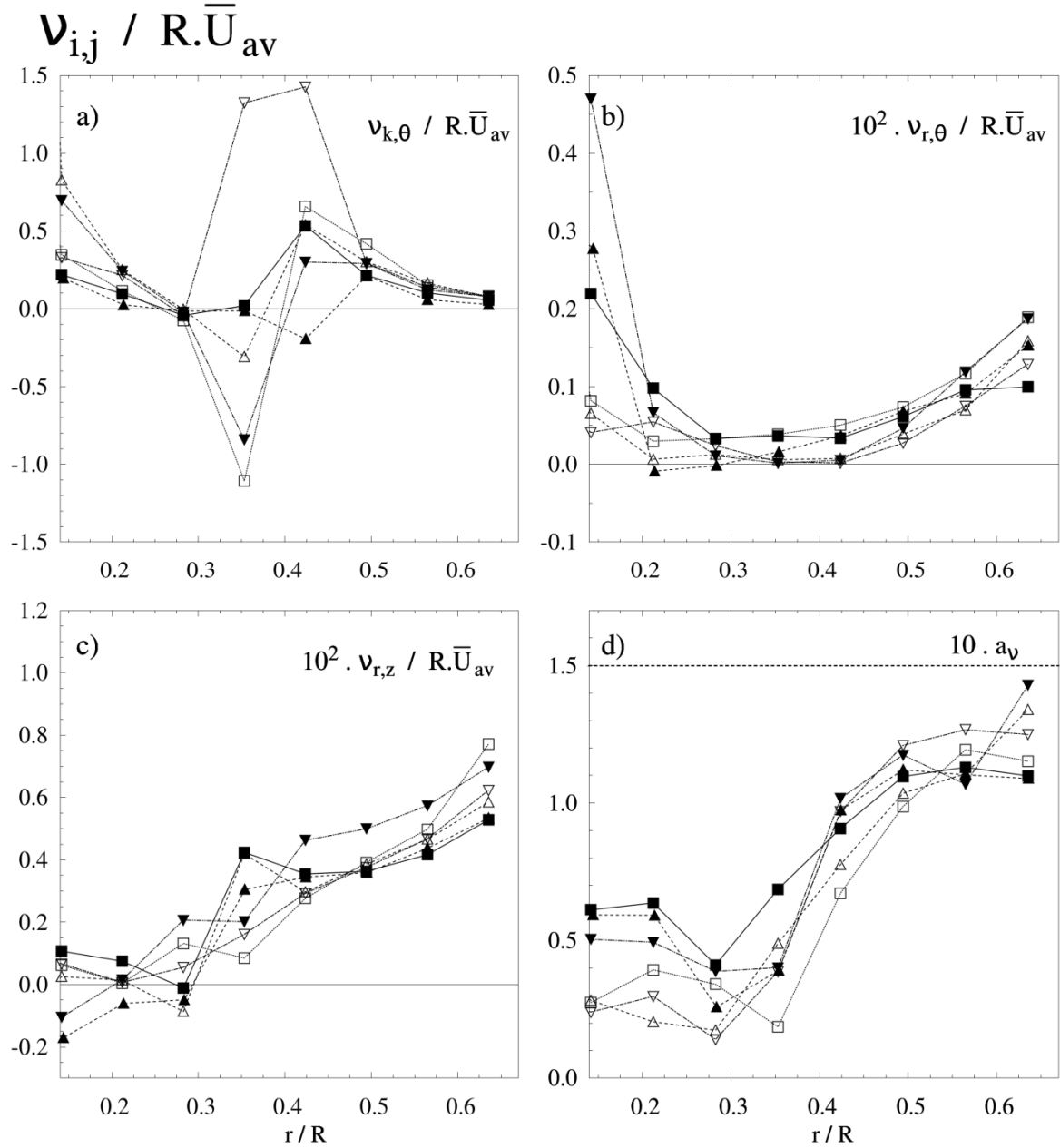


**Figure 12.** Anisotropy, and eddy viscosities for all levels and  $Re_2$ . For nomenclature see Figure 10. a)  $v_{z,\theta}$  b)  $v_{r,\theta}$  c)  $v_{r,z}$  and d)  $a_v = (\overline{u_r u_z^2} + \overline{u_r u_\theta^2})/2\kappa$ . Viscosity data is normalized by  $R \cdot \bar{U}_{av}$ .

based techniques used for the study of turbulence. Nonetheless, analysis of the time scales contained in the velocity signal produce reasonable results and reveals periodicity at various time scales.

This is not surprising for high-amplitude oscillations and long history effects are a common feature of the inner vortex in cyclones and co-current spray dryers where it was first acknowledged by Usui *et al.* (1985) or Kieviet *et al.* (1997). Southwell and Langrish (2001) and Langrish *et al.* (2004) have more recently related them to the precession of the vortex core. A similar behaviour is observed in a counter-current unit. Figure 13 shows an example of the velocity signal at series of positions in the dryer. At the top part of the core, an oscillation in the order of seconds appears superimposed upon faster fluctuations owed to the turbulence. The analysis of the different time scales is given in Figure 14 by the application of a *FFT*. It illustrates the correlation of periodicity, position and *Re* by superimposing the periodograms obtained for *U* at the inner and outer vortices, and the transition between both systems. Several periodic signals are observed, a) in agreement with Figure 13, a large time scale oscillation appears in the core, restricted to  $9.2 D \leq z \leq 10.3 D$ , and b) an oscillation at a higher frequency occurs in transition towards the inner vortex; this is only identifiable between  $r = 0.20 R$  to  $0.35 R$  and extends upstream in the cylinder from  $z = 9.2 D$  to levels below up to  $5.7 D$ ,  $3.4 D$  and  $2.2 D$  according to the increase in *Re*.

Periodical structures such as the *PVC* often originate by the *VBD* within the exit and inlet ducts in confined units, (e.g. the exit of cyclones or inlet air duct in co-current dryers. They are often characterized by the Strouhal number, *St* ( $St = f \cdot D / \bar{U}_{av}$  where *f* is the oscillation frequency). At large *Re*, the *PVC* maintains at constant *St* (Syred 2006) what means that when ones increases the bulk velocity in the same unit, the fluctuation occurs faster. This is a common observation in cyclones (O'Doherty *et al.* 1999 or Derksen and Van den Akker 2004), and also reported by Litvinov *et al.* (2013) in tangential swirlers. Figure 14 shows a similar behaviour in this counter-current swirl dryer. The oscillation frequency, *f*, in the transition region increases linearly with the  $\bar{U}_{av}$  (from 0.8 to 1.1 and 1.6 *Hz* for  $Re_1$ ,  $Re_2$  and  $Re_3$ ) what means it occurs at a constant  $St \approx 1.4 - 1.5$ . In this case no similar correlation with *Re* can be appreciated at top core, perhaps due to the low resolution.

These observations suggest that counter-current swirl dryers present similar preceding core to that observed in cyclones where the entire inner jet can adopt a sort of helical movement, described in the review of Cortes and Gil (2007). At some point before or within the exit, perhaps between levels

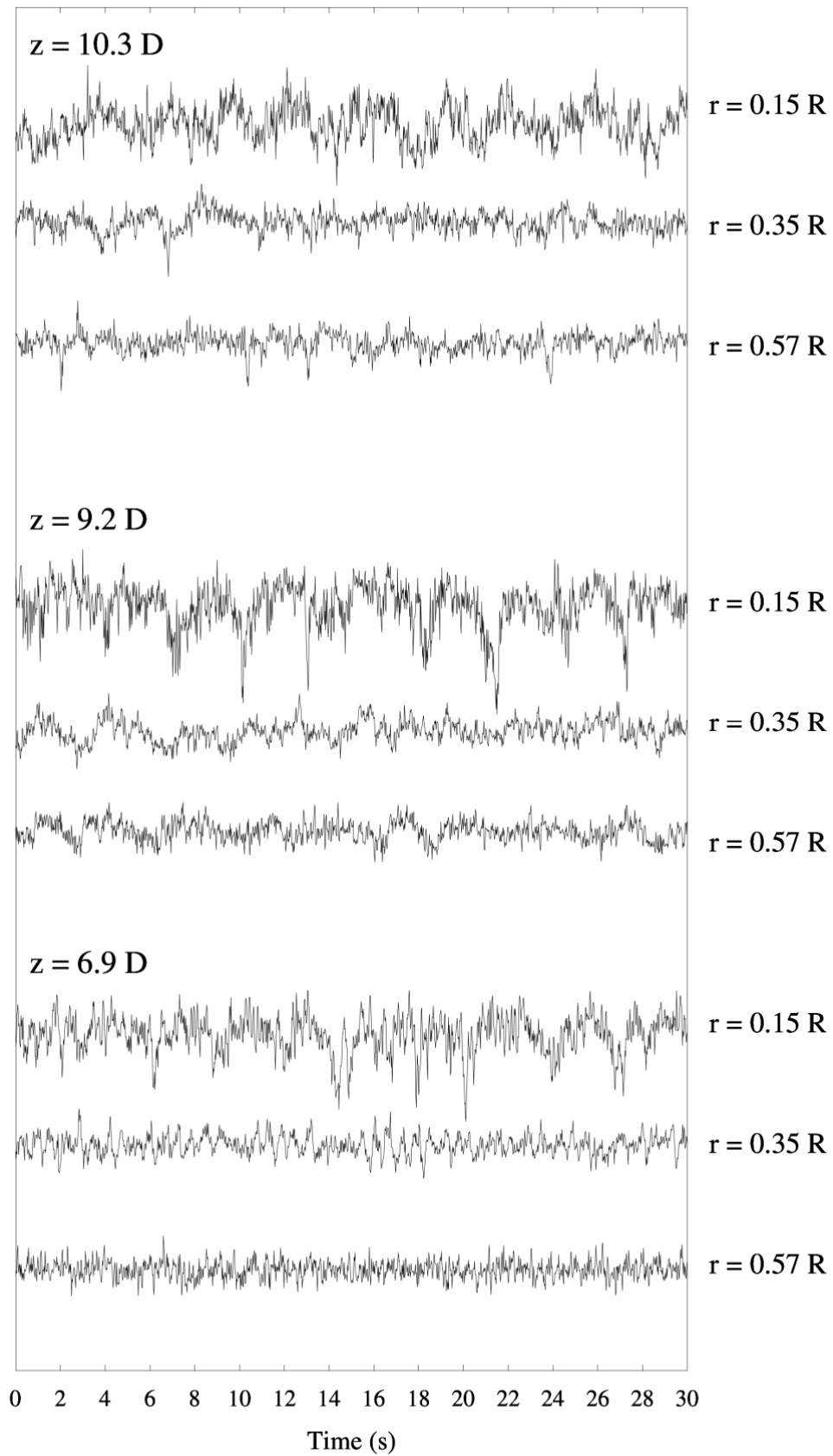


**Figure 13.** Times series for  $U_\theta$  at different locations in the unit.

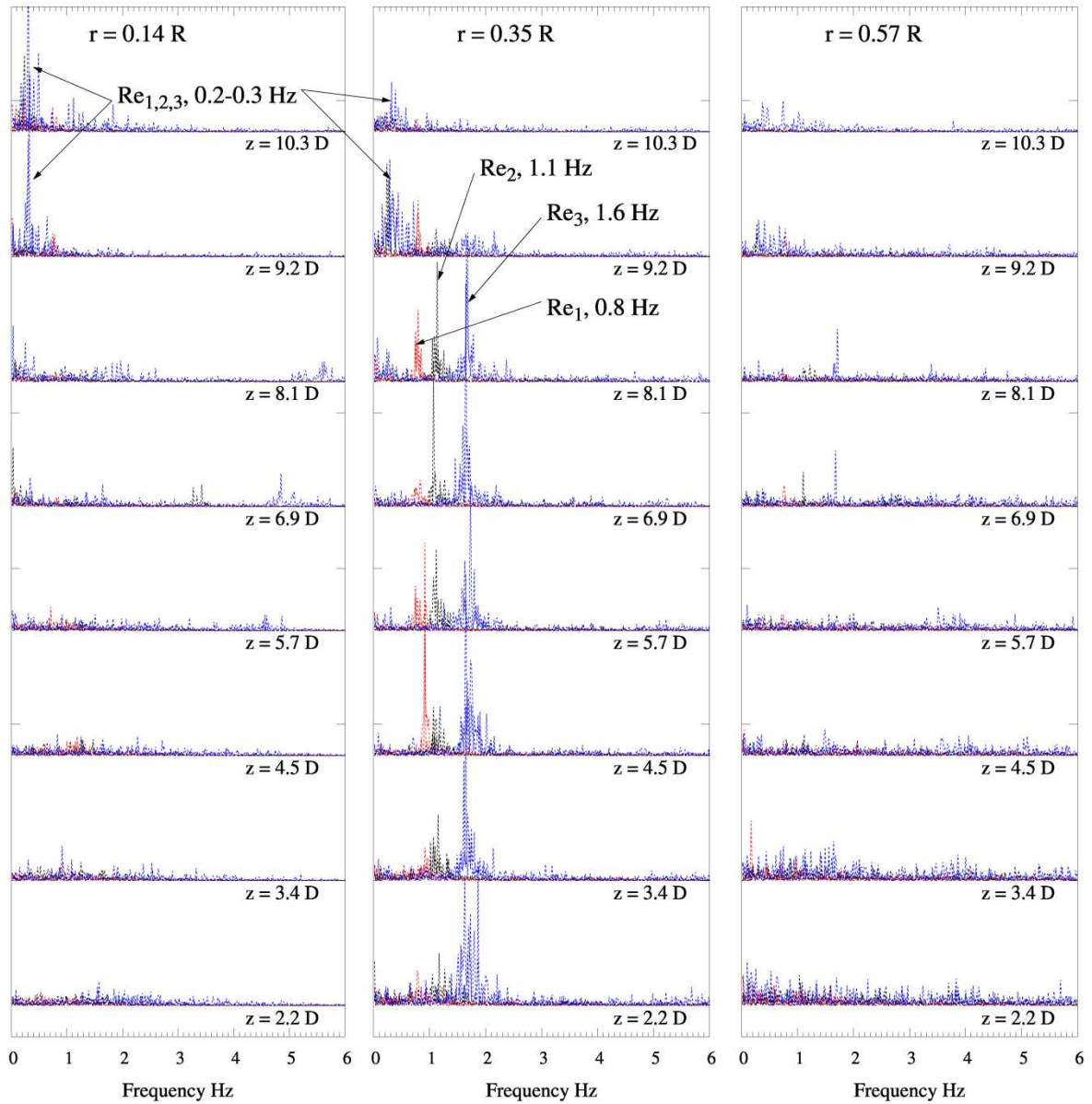


**Figure 14.** Analysis of periodical flow structures in the vortex. Periodogram of  $U$  for all heights at the inner region  $r = 0.14 R$ . (left), transition,  $r = 0.35 R$  (centre) and outer region,  $r = 0.57 R$  (right). Arbitrary y unit; scaling changes from 1 on  $r = 0.35R$  or  $0.57R$  to 0.5 on  $r = 0.14R$ .

$5.7 D \leq z \leq 6.9 D$ , the high centrifugal force in the forced vortex may cause stagnation, the reversion of the flow at the centre line (not measureable here due to a low resolution) and originate an oscillation that extends both downstream and upstream, in the same manner as it does in reverse flow cyclones.

## Conclusions

The swirling fluid dynamics of the continuous phase in an industrial scale tall-form spray dryer has been described at isothermal conditions, making use of an economic and time-efficient experimental arrangement. It has been possible to identify:

- The role of the downstream effects in the development of the vortex.
- Consistent field asymmetries.
- The development of a self-similar vortex structure, invariant within the  $Re$  operating range.
- Strong swirl decay owing to the confinement and presence of particulate deposits at the walls.
- The characteristic turbulence structure, including its anisotropy through the description of normal stresses, and rough estimates of Reynolds stresses and the eddy viscosity ranges
- Periodical structures that oscillate at constant  $St$ , likely related to the precession of the vortex core.

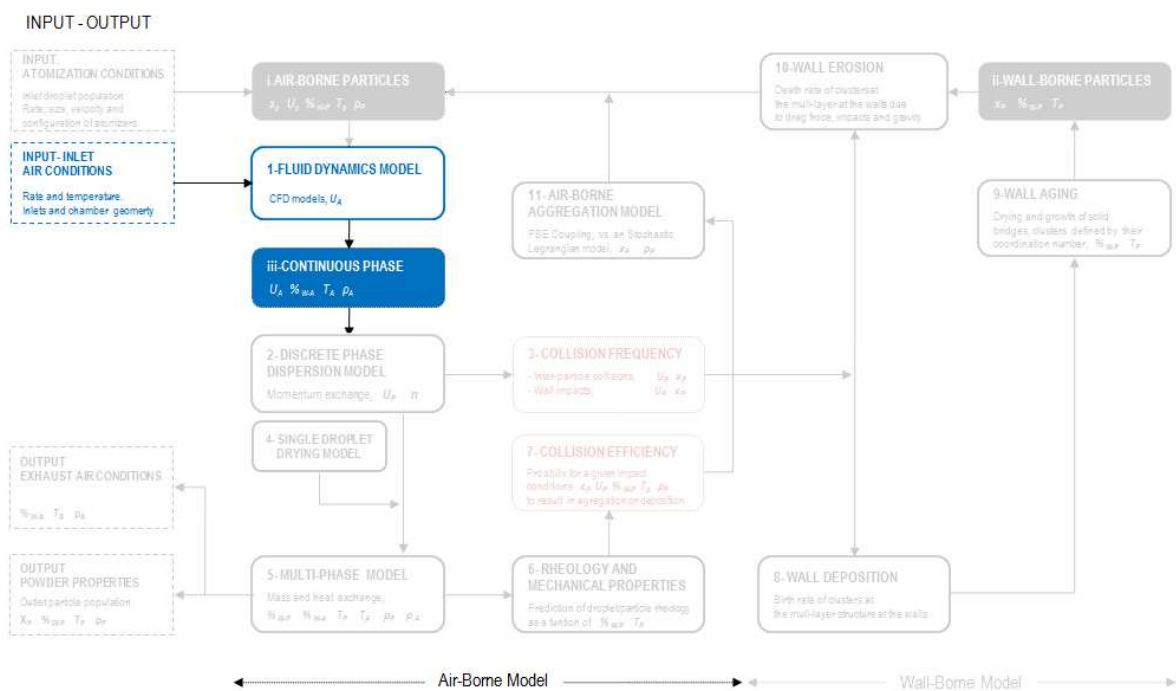
The suppression of the recirculation owed to the vortex finder, the mixing owing to the  $PVC$ , or most importantly the role that the friction at the walls has in the swirl decay represent relevant changes in the usual assumptions in counter-current swirl dryers relying in a smooth wall. The omission of the swirl decay has been responsible of an over prediction of  $\bar{U}_\theta > 30 - 40\%$  in numerical models that use smooth walls as a boundary conditions. The study of semi-empirical wall functions for rough walls over pipes and how to apply a similar approach to strong swirling flows must become an area of focus to describe the vortex in large swirl dryers and similar particulate systems prone to deposition. Notice that the effects observed here in the continuous phase gain relevance in the prediction of particle dispersion, drying and aggregation. In any tower, all of these are intimately related with the centrifugal inertia that solids gain from the air. In essence, the swirl establishes the concentration of particles near the wall and the rates of deposition and erosion, crucial in the process (Chapter V). In addition, the description of the turbulence and the recirculation is crucial to estimate particle residence time, and particularly the elutriation of fine powder.

Clearly, being able to replicate numerically the swirl decay observed in production units becomes of paramount importance to advance in the prediction any of the features of particle dynamics.

# PART A

## CHAPTER III

### SCALING CRITERIA: INSTABILITIES, RECIRCULATION AND THE ROLE OF FRICTION



## Summary

This work investigates the scalability of the air flow field in swirl tall-form dryers under isothermal conditions and in the absence of particles, making use of three industrial units described in Chapter I. It discusses the response of the velocity field to changes in the unit aspect ratio, and the operation at different ranges of Reynolds numbers,  $Re$ , and swirl intensities,  $\Omega$ . Special attention has been paid to quantify the impact of friction in the flow. The decay of the swirl in one of the dryers has been studied operating under deposits at the walls of different coverage and thickness. As friction becomes more relevant a) a substantial production of turbulence is observed and b) the reduction in centrifugal force diminishes the influence of the vortex finder, leading to instabilities and recirculation in the dryer.

A transition between different operation regimes has been identified and correlated to the swirl intensity that prevails in the cylindrical chamber, so that the non-dimensional velocity field could be predicted with an adequate knowledge of how  $\Omega$  evolves in a given tower. This work provides the means for an estimation of the decay based on the unit geometry and the decay rates reported. The wall friction has a remarkable effect in the structure of the vortex, which may shed some light over many of the unresolved scale-up issues observed in swirl spray dryers and similar confinements prone to deposition.

## 1. Introduction.

Chapter II provides the first evidence of a strong decay of the angular momentum flux across tall-form dryers. This is attributed to a large roughness even after having cleaned the walls, and is only detected when accessing full scale units. Laboratory or pilot plant facilities face a serious challenge in replicating some characteristics inherent to production. In addition to the issues in reproducing a comparable roughness, they struggle to cover a) the range of different designs of the cone, the air distributor to the inlets or the exhaust lines seen in industry, and b) the operation at the same ranges of  $Re$ . The lack of data in production units has made the role of friction unnoticed for a long time. However, large discrepancies, 30 – 40 %, are detected between the measurements of the air tangential velocity in large dryers (Chapter II or Hassall 2011) and laboratory units (Bayly *et al.* 2004). The origin is now understood, but it remains unclear to which extent a different tower design or the actual configuration of deposits in industry can impact the swirl decay. This is important because according to Escudier and Keller (1985) the stabilizing effect of the contraction is likely function of the  $\Omega$  that prevails near the vortex finder, which depends on its initial value  $\Omega_i$  (i.e. a geometrical design parameter), but also the evolution (i.e. the decay rate and the aspect ratio). Obtaining a better understanding of how the wall friction correlates to design and wall conditions becomes a pressing issue. Consider that the “cleaned” walls used in Chapter II are not representative of actual production conditions. In any tower, the deposits invariably develop further in the shape of bands and patches, which lead to larger roughness elements.

The design of these units can change substantially across different production plants, which include units acquired over decades and coming from different industries (Huntington 2004). In order to establish a general standardization and scale up criteria, it is necessary to extend the work in Chapter II and evaluate how the wall shear stress and flow stability responds to the common operation ranges for  $\Omega$  and  $Re$ , and the actual wall roughness observed in industry. This has been addressed by:

- a) Investigation of the swirl decay rates associated to the representative range of deposits coverage, distribution and thickness, obtained after the operation of an industrial unit, Scale I (Chapter I).
- b) Characterization of the different operation regimes associated to the design values of three industrial units described in Chapter I, where the aspect ratio and the range of  $\Omega$  and  $Re$  have been modified.

## 2. Characterization of particulate wall deposits and roughness height.

Deposits occur at the walls of any counter-current spray drying tower, not in homogeneous manner, but

developing as bands at the inner wall. Their characteristics vary according to the position of slurry atomizers and the drying conditions. Bottom sections show a highly compacted structure, being subject to faster drying and stronger aerodynamic stresses. In contrast, at the upper part the deposits show lower densities and a high moisture because they are comprised of elutriated particles, face weaker stresses and do not dry, being subject to cool local air conditions. The thicker bands are located in region of the slurry atomizer/s. In these areas, a fraction of the atomized droplets projects onto the wall at a high momentum and builds up thick multi-layered structures (see Part B). Three different deposits configurations have been investigated in Scale I (Chapter I), namely case A, B and C:

- **A, Cleaned walls.** Conditions associated to unit start up, before production begins.
- **B, Standard operation.** Conditions associated to a short term production (i.e. a single cycle in steady state) where the walls are previously cleaned. These correspond to the conditions given in Part B, Chapter V, and the reference operation of a single atomizer,  $S_2$ , in Chapter VI.
- **C, Heavy deposition.** Conditions associated to a series of long term productions (i.e. multiple start-up and production cycles) with either partial or no intermediate automatic cleaning.

Figure 1 shows the resulting distribution of deposits at the wall, and Figures 2 and 3 provide details to illustrate their typical structure. Measurement of the coverage and the thickness are given in Table 1. These constitute rough estimates obtained respectively from analysis of photographs in Figure 1 and measurements at the inspection areas (Chapter I). Nonetheless, they allow one to define the sections

**Table 1.** Estimation of the distribution of deposits in axial sections. The range of coverage of the wall is given in each section as the range covered either by patches (< 100%) or a full bands (100%) by analysis of photographs. A range in thickness is provided by punctual measurements. The section including the atomizer or spray projection is given in bold.

	Section		Coverage		Thickness	
	$z/D$		% in $\theta$		$10^2 \cdot \delta/D$	
	From	to	from	to	From	to
Case A	Cone		100		< 0.6	
	0.0	7.1				
	7.1	10.6	0	40	0	< 0.6
Case B	Cone		100		< 0.6	
	0.0	1.8	15	30	0	< 0.6
	1.8	2.4	100		< 0.6	
	2.4	5.7	40	70	0	< 0.6
	<b>5.7</b>	<b>7.1</b>	<b>100</b>		<b>0.6</b>	<b>1.2</b>
	7.1	8.1			0	0.6
	8.2	10.6	Metal			
Case C	Cone				Metal	
	0.0	2.4	5	10	0	< 1.2
	<b>2.4</b>	<b>5.7</b>	<b>50</b>	<b>75</b>	<b>0.6 - 1.2</b>	<b>1.8 - 3.0</b>
	5.7	7.1	10	15	0	< 1.2
	7.1	8.1	100			
	8.1	10.6				



**Figure 1.** Visual inspection of the wall deposits for case A, B and C. Each photograph includes the section of the cylinder shown. Nozzle/s and/or internal instrumentation have been artificially removed to protect intellectual property.

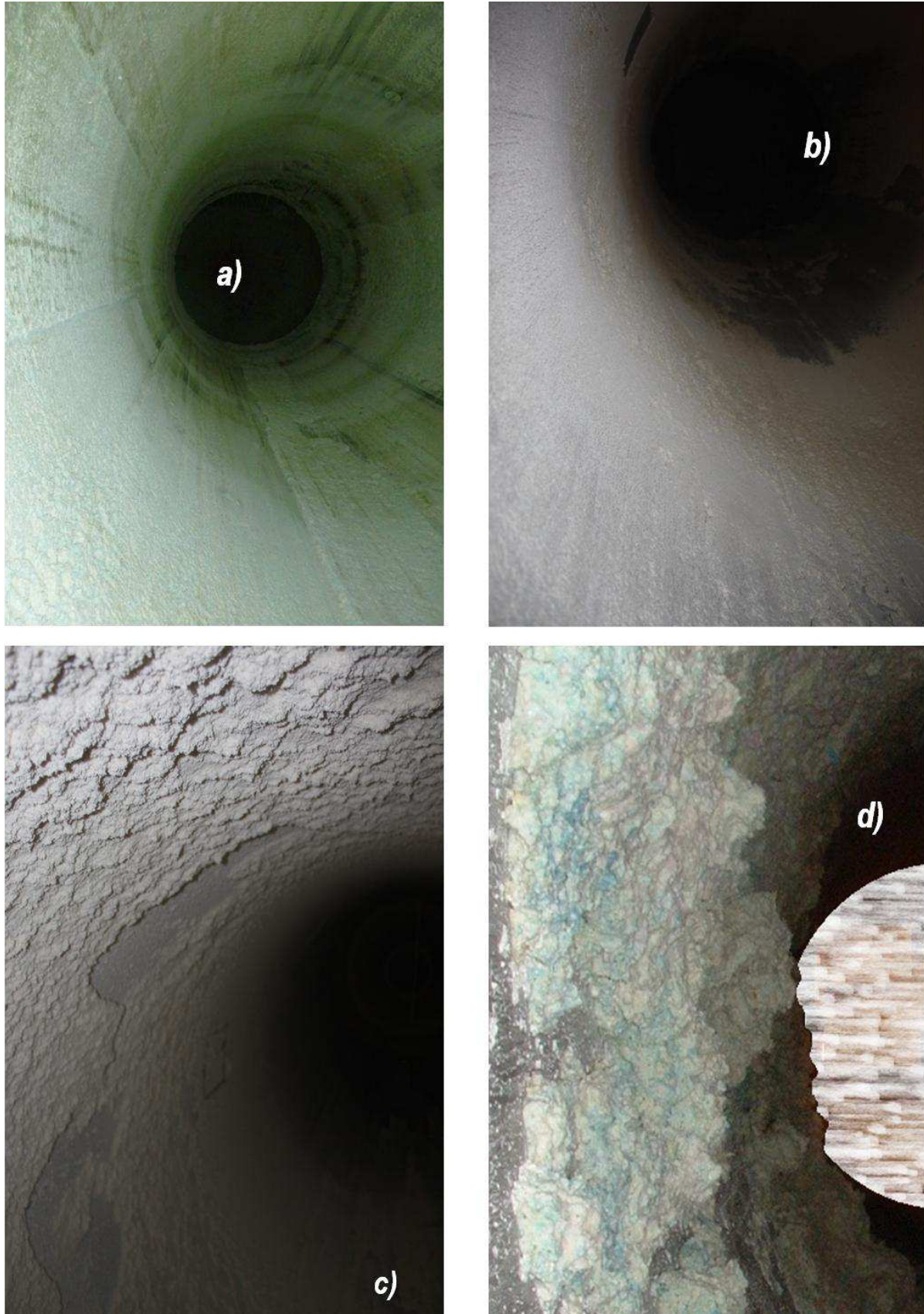


**Figure 2.** Detail of the morphology and the roughness height associated to the deposits. a) and b) show the bottom sections of the cylinder for cases A and B, c) and d) show the obstruction to the flow associated to the spray region in cases B and C.



**Figure 3.** A transversal cut of the deposits at the wall of Scale III. It illustrates how showing a substantial thickness, deposits are homogeneously distributed and the roughness height remains constant, similar to that observed in Scale I, cases A or B.

where the bands acquire a large length scale and compare those with the development of the flow field.

The thickness,  $\delta/D$ , in Table 1 is above the maximum non-dimensional roughness height,  $\varepsilon/D$ , reported in pipes. Only in case A the entire wall can be considered homogeneous and the range of variation of  $\delta/D$  may related to  $\varepsilon/D$  and thus, comparable to a fully rough flow regime. In cases B and C,  $\varepsilon/D$  within a single band or patch of deposits is much lower than its thickness  $\delta/D$ , but in turn it presents a complex two dimensional nature. The multi-layer structure of the deposits shows roughness elements of a wide range of sizes. These result from the voids left behind by the erosion of small particles (i.e.  $100 - 1000 \mu m$ ) up to the detachment of large pieces of several centimetres, which leave cavities of a similar length but with a depth limited by  $\delta/D$  (see Chapter V). This occurs in sections where the multi-layer extends homogeneously (i.e. within the bands given in Table 1, and across the entire surface in Scales II and III). In contrast, at the edges of bands or between the “patches” an abrupt change in the thickness constitutes an obstacle to the flow (see Figures 1 and 2). In these areas, the variation in  $\delta/D$  given in Table 1 is perhaps a better indication of the drag originated at the wall.

### 3. Results and discussion.

The operation with “cleaned” walls has been described in Chapter II (i.e. Scale I case A) and is taken as a reference. Section 3.1.1 describes the effects of an increase in friction owed to the deposits. Section 3.1.2 describes the instabilities associated to the range of  $\Omega$  and which is the role of the contraction. Sections 3.1.3 and 3.1.4 discuss the inlet design and the effect of  $Re$ . Sections 3.1.5 and 3.1.6 report the swirl decay rates and discuss scale up strategies. The production of turbulence owed to friction and

the relation to  $\Omega$  and  $Re$  are described in section 3.2.1. Finally, the changes in the profile of the Reynolds stresses and the behaviour of periodical structures are reported in sections 3.2.2 and 3.2.3.

### 3.1. Time averaged velocity field.

#### 3.1.1. Wall friction.

Figure 4 shows the evolution of the velocity magnitude  $\bar{U}$  across the cylinder for the same bulk flow ( $Re_2$  in Chapter I) and different wall conditions. A clear reduction of  $\bar{U}$  is observed at all positions in the upper part of the unit, comparing case A to case B and case C. This drop translates in a reduction of the tangential velocities,  $\bar{U}_\theta$ , shown in Figure 5. The lower centrifugal force generated then affects the pressure field, which causes a different development of the axial velocities,  $\bar{U}_z$ , given in Figure 6.

Chapter II describes how swirling flows are often characterised by the extension of a) the boundary layer close to the wall, b) the inner and outer regions associated respectively to a forced-like vortex (i.e. a linear increase in  $\bar{U}_\theta$  with  $r$ ) and an outer free-like vortex (i.e. an inverse relation between  $\bar{U}_\theta$  and  $r$ ) and finally, c) the transition or annular region that blends both structures.

Figure 5 shows that all the cases present a similar maximum  $\bar{U}_\theta$  value, at the bottom of the unit in the outer region at  $r = 0.70 R$ . At the inner region however, a tower with “cleaned” walls in case A develops a narrow forced vortex. It extends up to  $r = 0.10 - 0.15 R$  and it is maintained through the entire cylindrical chamber. This originates a wide transition region at the bottom, that narrows progressively as the vortex rises and the location of  $\bar{U}_{\theta,Max}$  shifts to the centre. Above  $z \geq 9.2 D$ , the transition region is reduced drastically and the core and annular regions resemble a forced and a free vortex (i.e. a Rankine pattern). In contrast, at the bottom the cases B and C develop a much wider forced vortex with a radius beyond  $r > 0.40 - 0.50 R$ . As the flow rises, the transfer of angular momentum to the exit shifts  $\bar{U}_{\theta,Max}$  towards the centre, and the transition region shows an abrupt change. In case B, the forced vortex retains a radius up to  $r = 0.20 - 0.30 R$  in the levels below  $z \leq 4.5 D$ , after which it narrows rapidly to  $r < 0.10 - 0.15 R$  in  $z = 6.9 D$ . As a result, the transition also narrows to  $0.15 R < r < 0.30 R$  and keeps decreasing further to  $0.10 R < r < 0.15 R$  at the top  $z > 9.2 D$ . In case C, a similar change occurs but at a lower section. The radius of the inner forced vortex narrows from  $r > 0.30 - 0.40 R$  at  $z = 2.2 D$  to  $r < 0.10 - 0.15 R$  at  $z = 5.7 D$ . After this point, all cases, A, B and C, develop a very similar free vortex in the outer part where  $\bar{U}_\theta$  decreases linearly with  $r$ , which then turns into an inverse relation at the top,  $z = 10.3 D$ .

## WALL DEPOSITS, CASE A, B, C

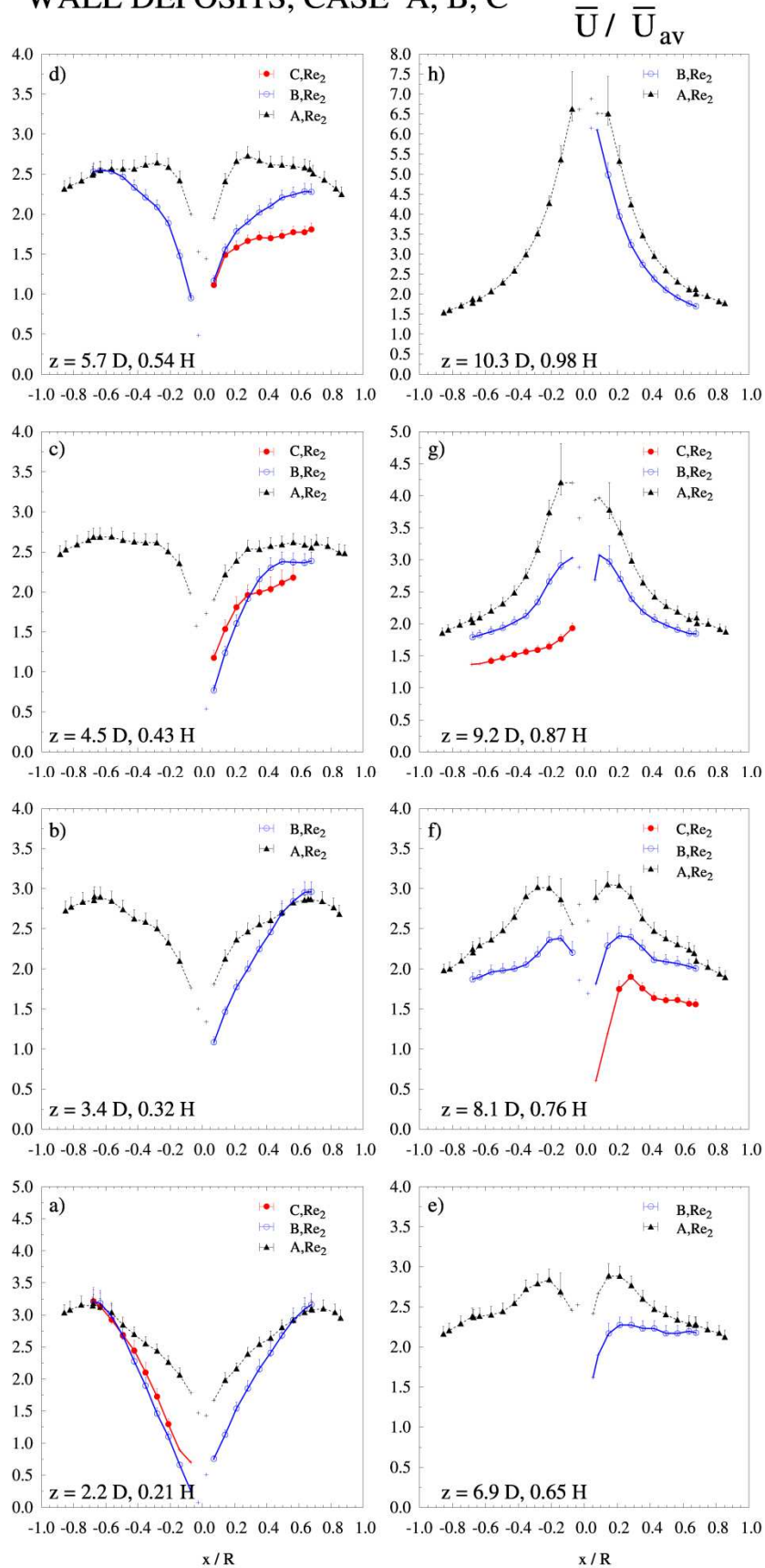


Figure 4. Velocity magnitude  $\bar{U}$  in all levels, Scale I, cases A, B, C. ( $x = -r$  for  $\theta < \pi$  and  $x = r$  for  $\theta < \pi$ ).

## WALL DEPOSITS, CASE A, B, C

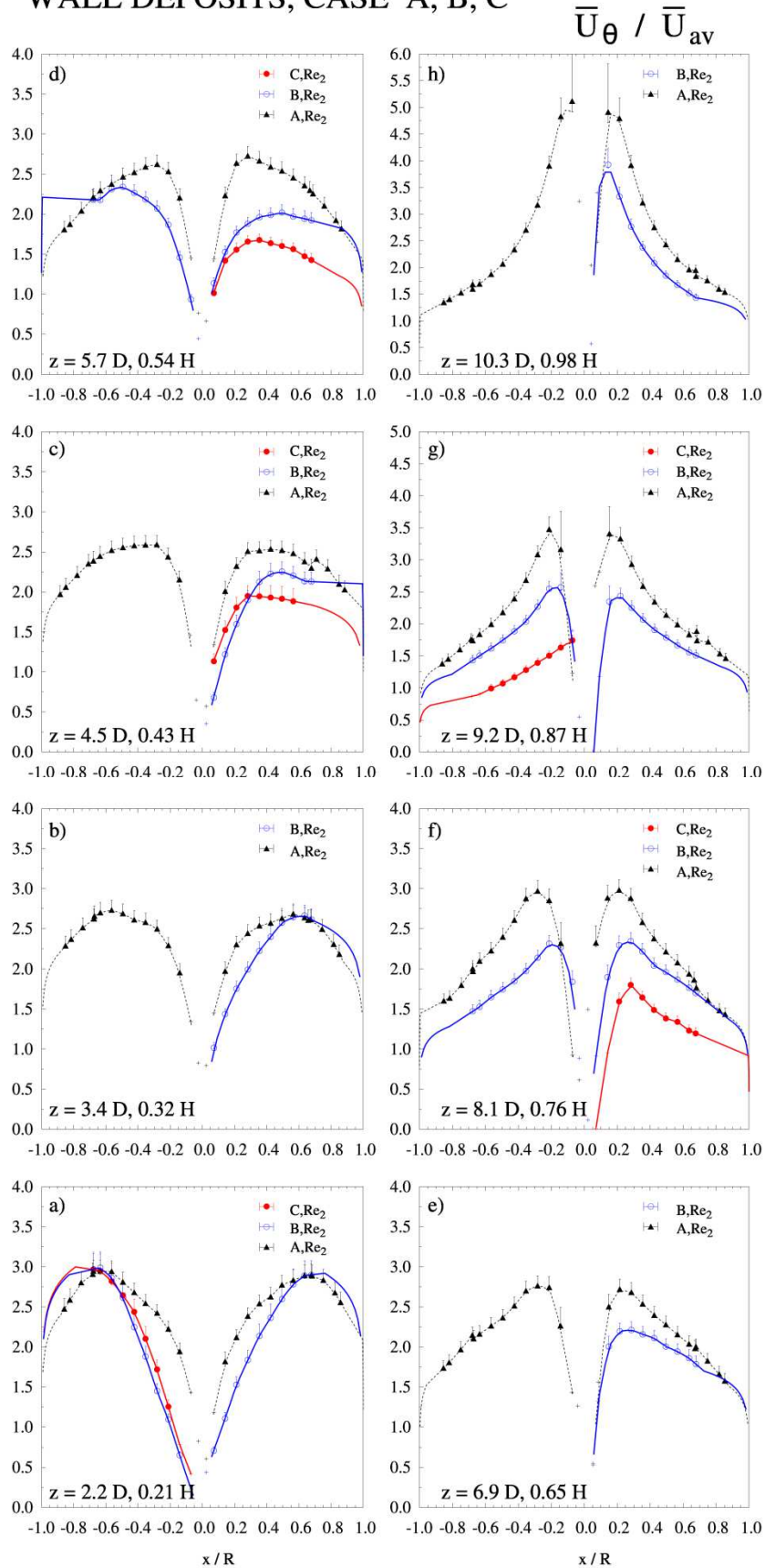


Figure 5. Tangential velocity  $\bar{U}_\theta$  associated to the operation of Scale I, cases A, B and C, shown in Figure 4.

Large differences appear in the magnitude of  $\bar{U}_\theta$ . All the cases show similar values for the levels below  $z \leq 3.4 D$ , but for all the sections above the cases B and C present clearly lower values (see Figure 5). The deficit versus case A is as high as 15 – 30% in case B, and rises up to 40 – 50% in case C. This confirms that a higher friction is being exerted upon the flow. The subsequent reduction in the centrifugal force has a remarkable effect in the vortex structure, discussed below and in section 3.1.2.

In contrast to the behaviour of case A, Figure 6 shows that in cases B and C a central recirculation zone, *CRZ*, has formed at the bottom half of the cylinder,  $z \leq 5.7 D$ , where the axial velocity shows negative values. It presents a conical shape: the diameter decreasing axially until the flow reverts back up between  $5.7 D < z < 6.9 D$  in case B. This leads to the stagnation of the flow and an abrupt change in direction referred to as a vortex breakdown, *VBD*. Beyond the breakdown, case B shows a central jet that increases in magnitude as the flow approaches the exit duct, bringing the position of the minimum axial velocity,  $\bar{U}_{z,Min}$  slightly outwards from  $z = 6.9 D$  to  $9.2 D$ . In relation to a standard operation given by case B, the lack of cleaning and longer productions in case C lead to thicker deposits. This widens the *CRZ* at the bottom of the tower, causing a stronger reverse flow and values of  $\bar{U}_{z,Min} < -1 \bar{U}_{av}$  at  $z = 2.2 D$ . Once the flow reverts back upwards between  $5.7 < z < 8.1 D$  the maximum is not generated at the centre, but now it is displaced outwards at  $r = 0.15 - 0.20 R$ . It aligns with the centre only as the flow approaches the exit duct at the top of the unit,  $z = 9.2 D$ . The magnitude of  $\bar{U}_z$  at the central jet decreases significantly from case A to case B and to case C.

The reversion at the centre is not surprising. It responds to the adverse pressure gradient generated at the core by the high centrifugal forces present at the bottom of the tower. Chang and Dhir (1994) describe it for tangentially injected flows in open tubes. At the same swirl intensity range they observed very similar  $\bar{U}_\theta$  profiles to cases B and C, characterised by the formation of a wide forced vortex at the bottom. This is inhibited in case A by the influence the contraction (Chapter I), but in cases B and C the friction makes the centrifugal force to decay further. This reduces the back pressure generated at the top and allows aerodynamic instabilities to arise within the cylinder, similarly to the case in an open tube.

### 3.1.2. Vortex breakdown and recirculation zones.

The effect of a contraction is similar to that in non-swirling flows, in the sense that it causes acceleration in the vicinity of the exit and an increase in pressure upstream. Under a strong swirl, these effects are complicated because the centrifugal force term in the momentum equation opposes the formation of

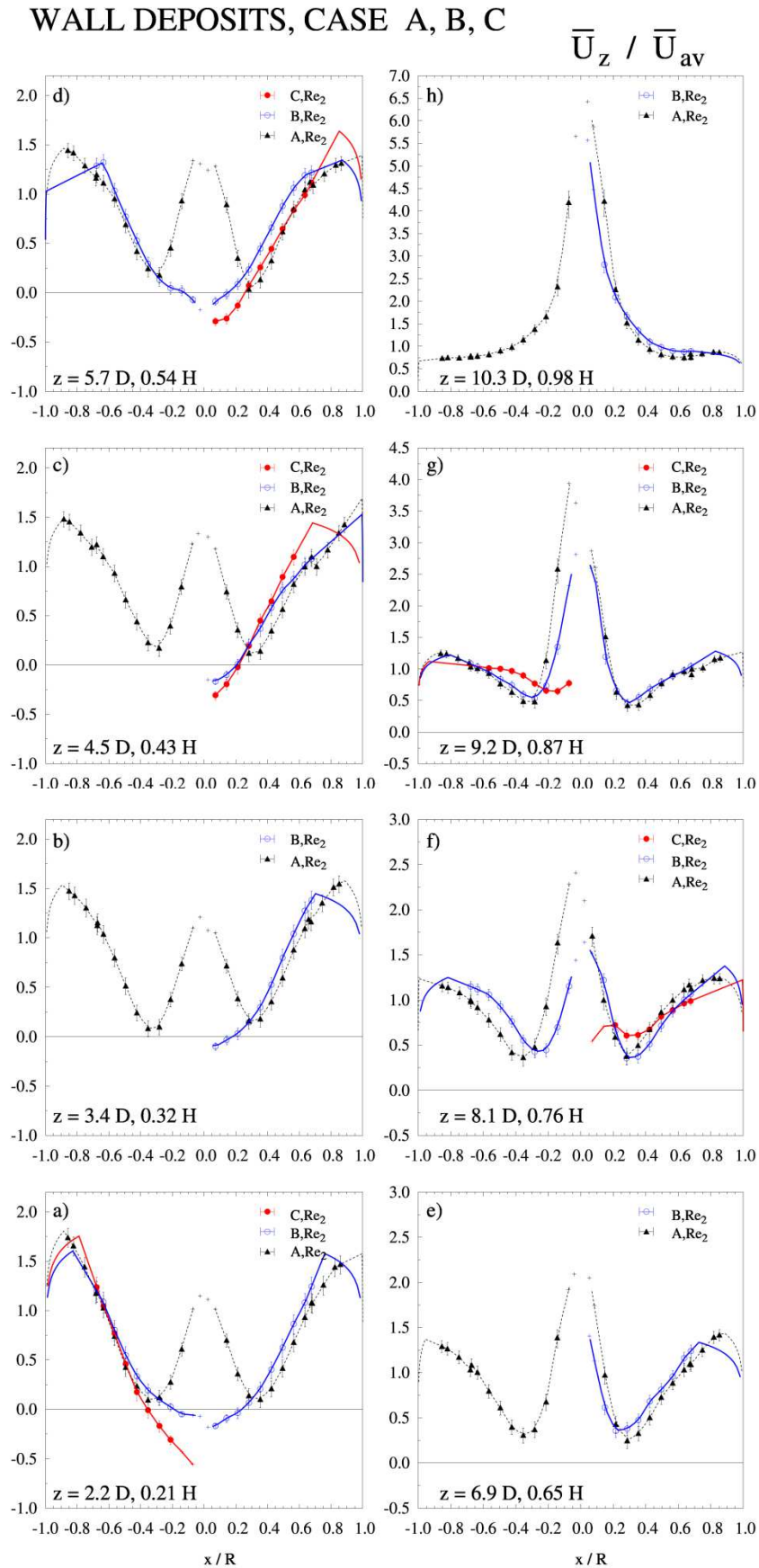


**Figure 6.** Axial velocity  $\bar{U}_z$  associated to the operation of Scale I, cases A, B and C, shown in Figure 4.

negative radial pressures gradients and thus, the flow inwards. Consider for instance the flow in a cyclone: in this case a central upwards jet is formed by a radial flow coming from a downwards outer vortex. In a similar way, one can distinguish two different regions in a swirl spray drying tower, see case A in Figure 6: a) an inner jet-like vortex which is dominated by the pull towards the low pressure at the top exit duct, and b) an outer vortex that flows towards the dead regions above, which is dominated by the interaction with the wall. The leakage from the outer to inner vortices is driven by radial pressure gradients that overcome the centrifugal force term in the momentum equation, owed to  $\bar{U}_\theta^2/r$ . When the flow reaches the top at higher swirl intensity, the pressure gradients required to restrain the flow inwards increase accordingly. Figure 7 shows the transition between different regimes in a counter-current dryer. It provides the comparison of the velocity field and highlights the extension of the jet and the recirculation areas. A clear evolution can be appreciated according to the operating  $\Omega$ :

**a) Dominated by the contraction. No recirculation,  $\Omega_e \geq \sim 1$**

Scale I, case A,  $\Omega_{0.21-0.98H} = 2.02 - 1.03$ .

Scale II,  $\Omega_{0.76H} = 1.29$ .

No CRZ appears under “cleaned” walls. The influence of the contraction is transmitted down the cylinder and suppresses the formation of a wide forced vortex, responsible of recirculation. The overall increase in the pressure gradients explains the higher velocities shown in Figure 4 and why the axial central jet prevails throughout the entire unit. Scale II presents a different aspect ratio and a narrower plenum. However, it operates at a lower  $\Omega_i$  and this allows it to maintain very similar  $\Omega$  values at the top of the tower, see section 3.1.5. Figure 8 shows how this translates into a very similar velocity field at the same relative distance to the exit (i.e.  $z/H$ ), with the exception of higher velocities at the core.

**b) Dominated by the wall. Central Recirculation.  $\Omega_e < \sim 1$**

Scale I, case B,  $\Omega_{0.21-0.98H} = 2.11 - 0.91$

The presence of bands of deposits in case B increments the friction and reduces  $\bar{U}_\theta$  in the upper part. This diminishes the pressure gradient required to overcome the centrifugal force and causes the flow inwards. As lower pressure gradients are generated, lower  $\bar{U}$  follow in Figure 4. The influence of the contraction does not extent as far down the cylinder and this allows a large forced vortex to form at the bottom. In this case the adverse pressure gradient generates a CRZ of conical shape, in a very similar

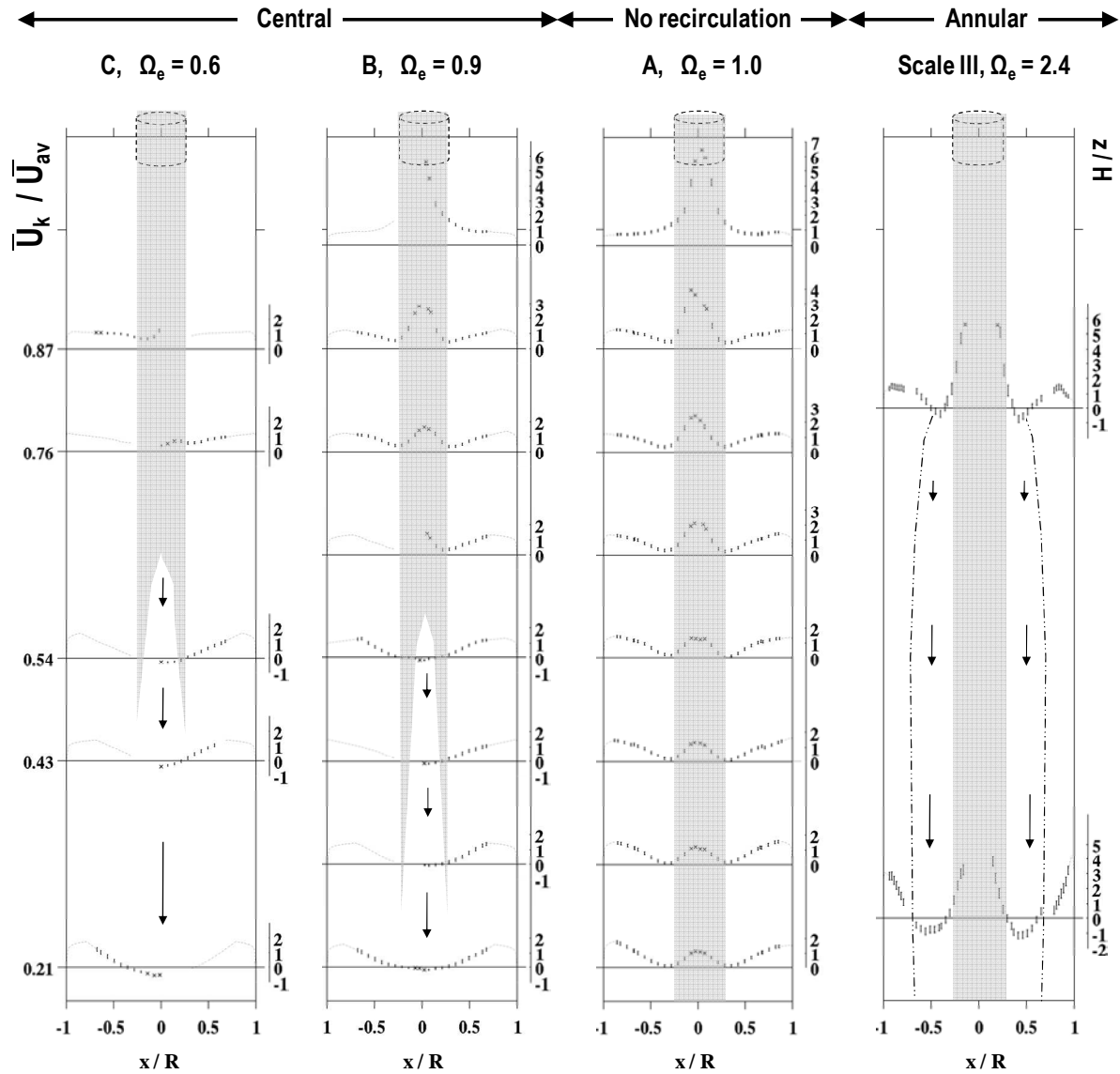


**Figure 7.** Vortex breakdown and operation regimes in counter-current tall-form dryers. Contraction ratio of  $d/D \sim 0.30$ . The shadowed areas delimit the upwards jet; arrows the reverse flow. From left to right, increasing  $\Omega$ , centrifugal forces and the influence of the exit. From bottom to top: plots to scale are given for the radial profiles of the axial velocity  $\bar{U}_z$  for all levels.  $\Omega_e$  denotes the value of  $\Omega$  at the level of the exit contraction.

fashion to the observations in an open tube (Chang and Dhir 1994). The diameter of the *CRZ* decreases with axial position, vanishing at a stagnation point and causing the vortex breakdown, *VBD*. This splits the cylinder in two clearly differentiable sections, governed respectively by the low pressure generated at the core of the vortex at the bottom of cylinder (i.e. due to the high centrifugal force) and at the top vortex finder. In this case, the jet is only generated at regions sufficiently close to the exit duct.

Scale I, case C,  $\Omega_{0.21-0.98H} = 2.26 - 0.58$

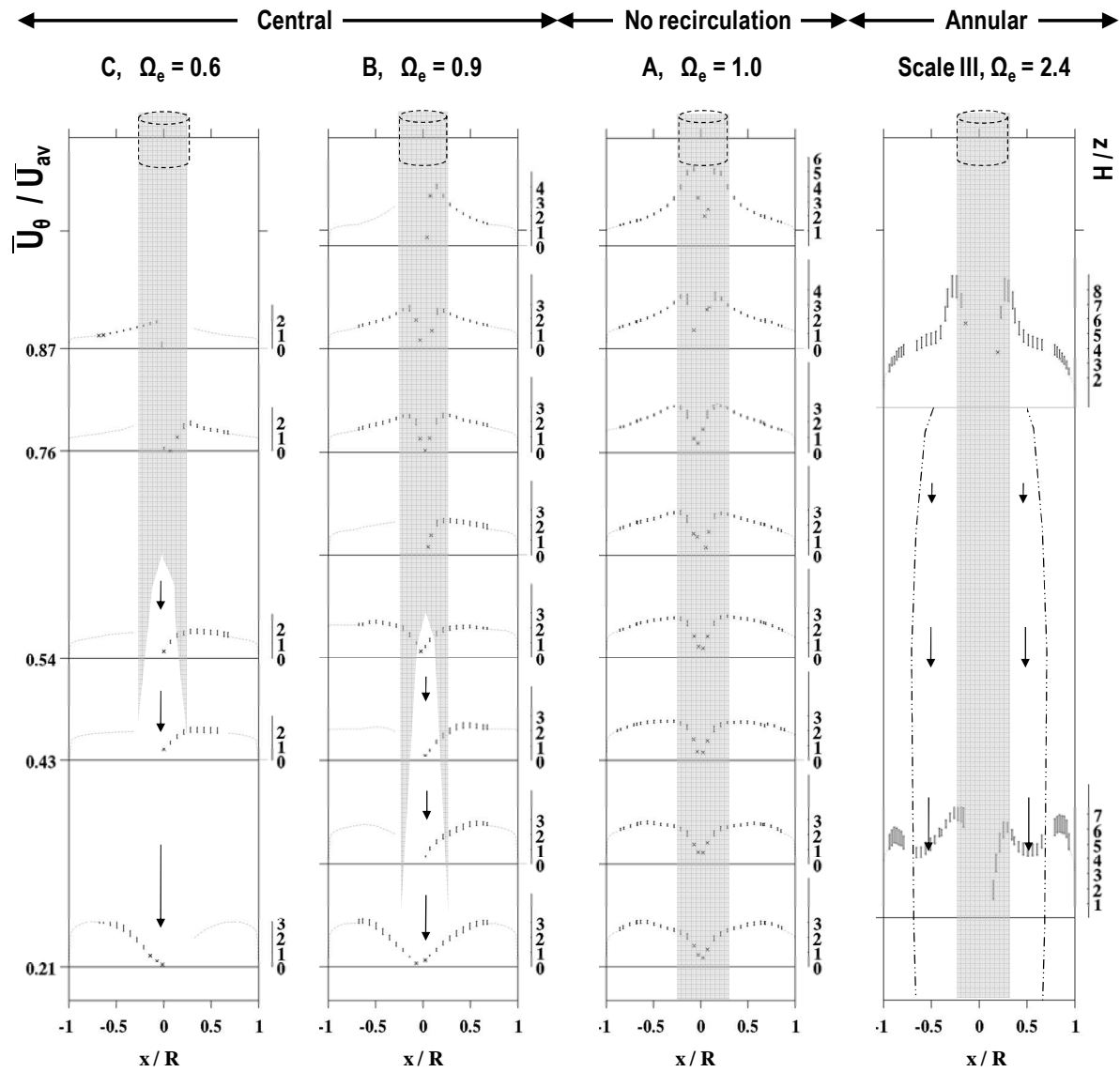
More heterogeneous and thicker deposits in case C cause a stronger drag at the walls. The vortex then faces the contraction at lower  $\Omega$  values and it is easily pulled inwards by a lower pressure gradient. The influence upstream of the contraction diminishes explaining why in case C the *CRZ* widens and extends further up in the cylinder. In this case, lower pressure gradients are established to the exit, which results in lower  $\bar{U}$  in Figure 4 and the loss of the jet-like axial profile for the most part of the cylinder in Figure 6.

**c) Dominated by the contraction. Annular recirculation,  $\Omega_e \geq \sim 2.4$**

Scale III,  $\Omega_{0.26-0.81H} = 4.10 - 2.37$

Scale III shows the opposite behaviour. It presents the same aspect and contraction ratios than Scale II, but a lower  $A_i$  that causes it to operate at a higher  $\Omega_i$ . In contrast to Scales I and II, when the flow reaches the top in Scale III it presents larger centrifugal forces. Accordingly, the pressure gradients required in forming the inner vortex increase, and develop much higher velocities, shown in Figure 9.

A qualitative change can now be observed in the profiles. On the one hand,  $\bar{U}_z$  shows a similar jet-like profile at the centre but achieves a larger maximum. In the other, the higher centrifugal forces at the bottom extend the region of solid body rotation beyond the area of influence of the contraction (i.e. delimited by the diameter of the vortex finder  $r \sim 0.30 R$ ), and this causes again the reversion. A recirculation zone is generated that acquires an annular shape between  $0.30 R < r < 0.65 R$ , which then envelops the central upwards jet. At the top end, the recirculation zone has narrowed significantly but it is maintained in the proximity of the jet. The outer free-like vortex starts immediately after the influence of the vortex finder at  $r = 0.30 R$ , but in contrast to the observations in Scales I and II, it ceases at  $r = 0.78 R$  where  $\bar{U}_\theta$  starts a rapid decrease towards the wall, observed also in  $\bar{U}_z$ .



continuous from Figure 7. From bottom to top: plots to scale for the radial profiles of the tangential velocity  $\bar{U}_\theta$  for all levels.

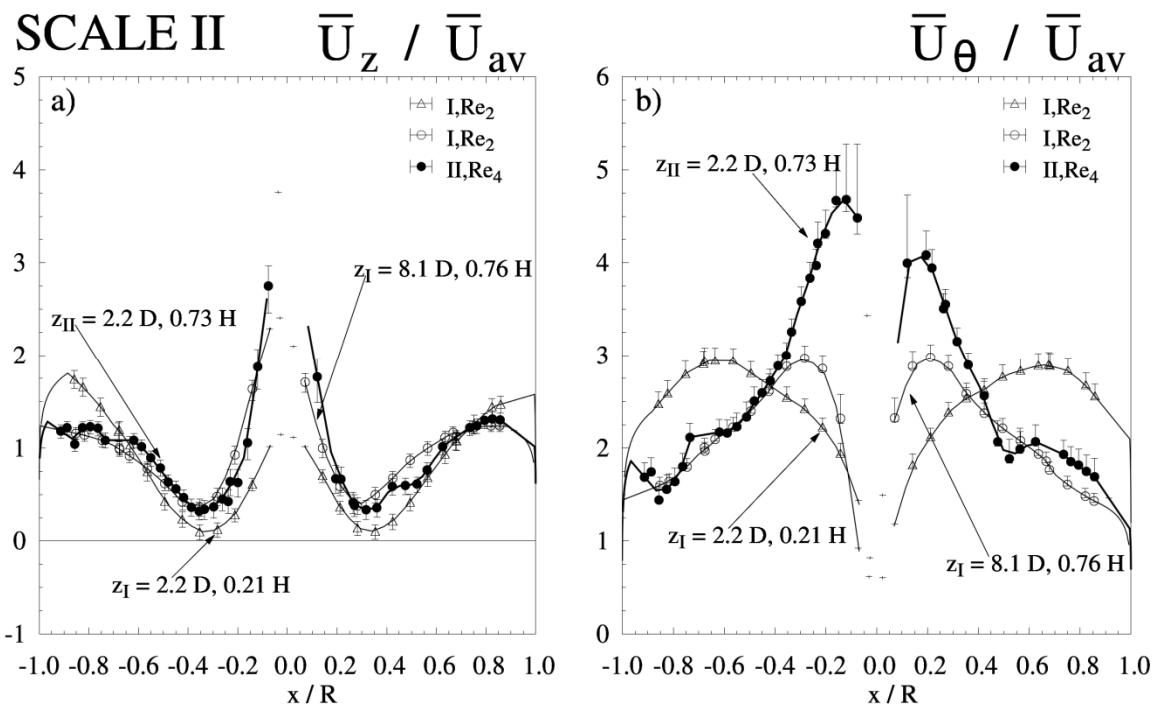


**Figure 8.** The impact of  $\Omega$  in the vortex development. Comparison of the velocity field of Scale I and II. Operating  $Re$  are given in Chapter I. Axial velocity  $\bar{U}_z$  in (a) and tangential  $\bar{U}_\theta$  in (b). The velocity components are given for the same axial levels in terms of  $z/D$  and  $z/H$ .

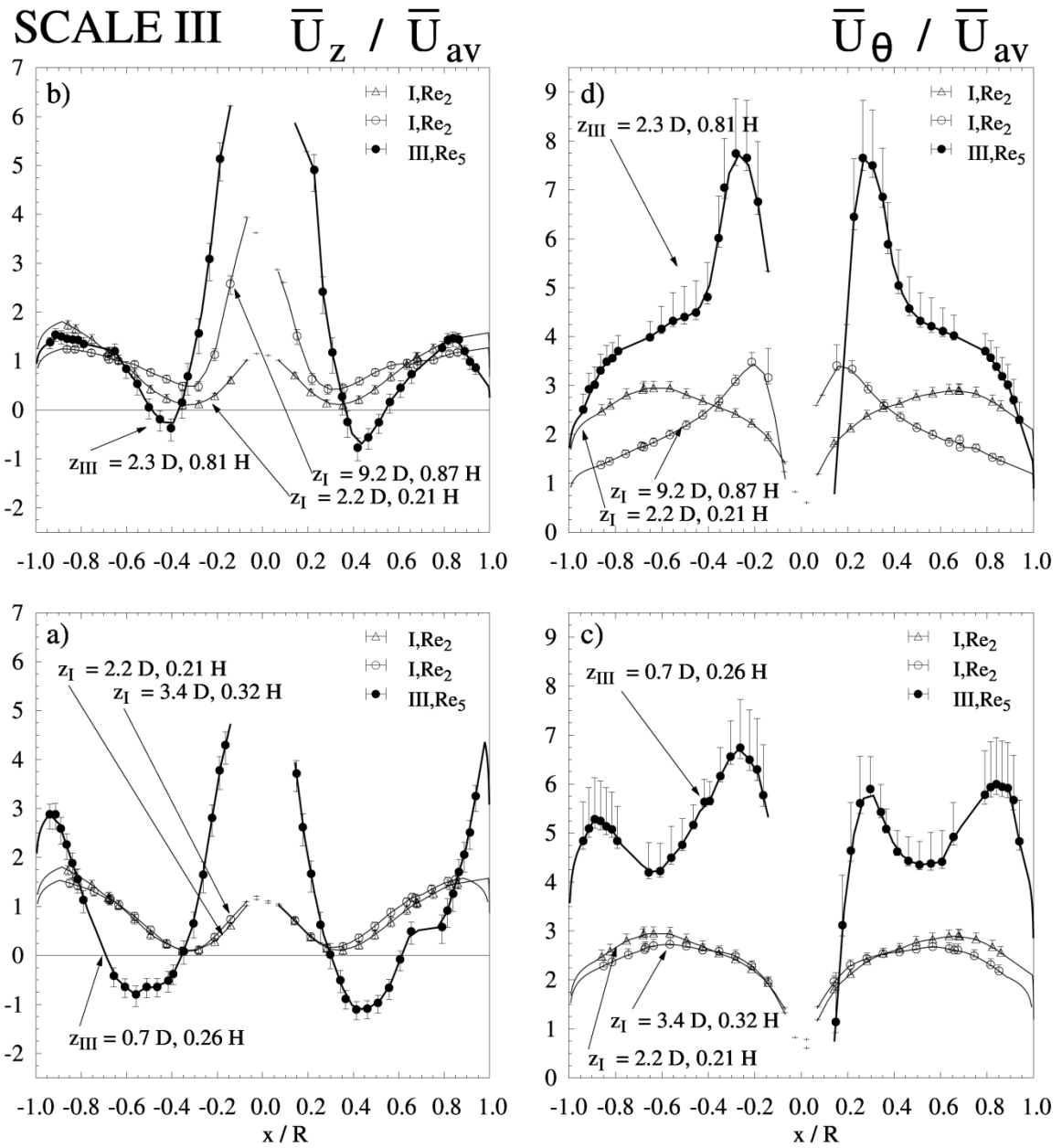


**Figure 9.** The impact of  $\Omega$  in the vortex development. Comparison of the velocity field of Scale I and III. Operating  $Re$  are given in Chapter I. Axial velocity  $\bar{U}_z$  in (a),(b) and tangential  $\bar{U}_\theta$  in (c),(d). The velocity components are given for the same axial levels in terms of  $z/D$  and  $z/H$ .

### 3.1.3. Symmetry and distribution to the inlet nozzles.

Chapter II discusses briefly transversal flow and asymmetries in case A, Scale I. The design of the ring distributor and the feed from the inlet air duct to the plenum can originate preferential paths to the inlet ports. Similarly, blockage of exit channels in the vortex finder (i.e. straiteners), as well as the design of the exhaust air duct in terms of its diameter and the distance to a bend can also be responsible of creating preferential paths to the exit.

With the objective of illustrating these effects, the data in Scale III was obtained using two different types of distributor to the inlets. Design 1 uses two separate branches in a ring disposition, both fed by the same inlet. Each of them feeds consecutive inlet ports at each side of the tower, starting from the same location. The first pair that is fed constitutes neighbouring nozzles, and being those closest to the inlet line, they present lower pressure drop. This is then reduced for subsequent ports. The last pair, again neighbouring ports, is the furthest from the inlet, and presenting the largest pressure drop is expected to give rise to lower air mass rates according to the numerical simulation of the flow in the ring distributor. In contrast, Design 2 uses an open bustle ring, which is expected to aid balancing the pressure drop across the ring and provide a better symmetry between the inlet velocities seen for opposite ports.

The asymmetry resulting from the use of both designs is summarised in Figure 10. The use of the Design 1 results in much larger differences in  $\bar{U}_z$  and  $\bar{U}_\theta$ , particularly in the recirculation zone, up to 50% and 20% respectively. In contrast, the use of Design 2 balances both sides of the vortex and improves the symmetry reducing differences below  $< 10\%$ . This example confirms the expectation of a ring distributor as an optimal configuration, and serves to illustrate the relevance of maintaining constant inlet velocities at all ports to preserve a symmetrical vortex.

### 3.1.4. Self similarity.

Figure 11 compares the velocity field obtained for different  $Re$  in the range  $10^5 - 2 \cdot 10^5$  for Scale I and case C. In case A, all velocities collapse into a characteristic profile with the exception of the asymmetries described in Chapter II. The independence of velocity direction with  $Re$  was attributed a) the large  $Re$  numbers where viscous forces become less significant, b) a fully rough regime where roughness elements are larger than the viscous sub-layer and originate a drag mainly dependent on  $\varepsilon/D$ , and c) high  $\Omega$  values where the influence of the contraction upstream diminishes the effect of  $Re$  in the development of a turbulent boundary layer. The last point remains questionable in cases B

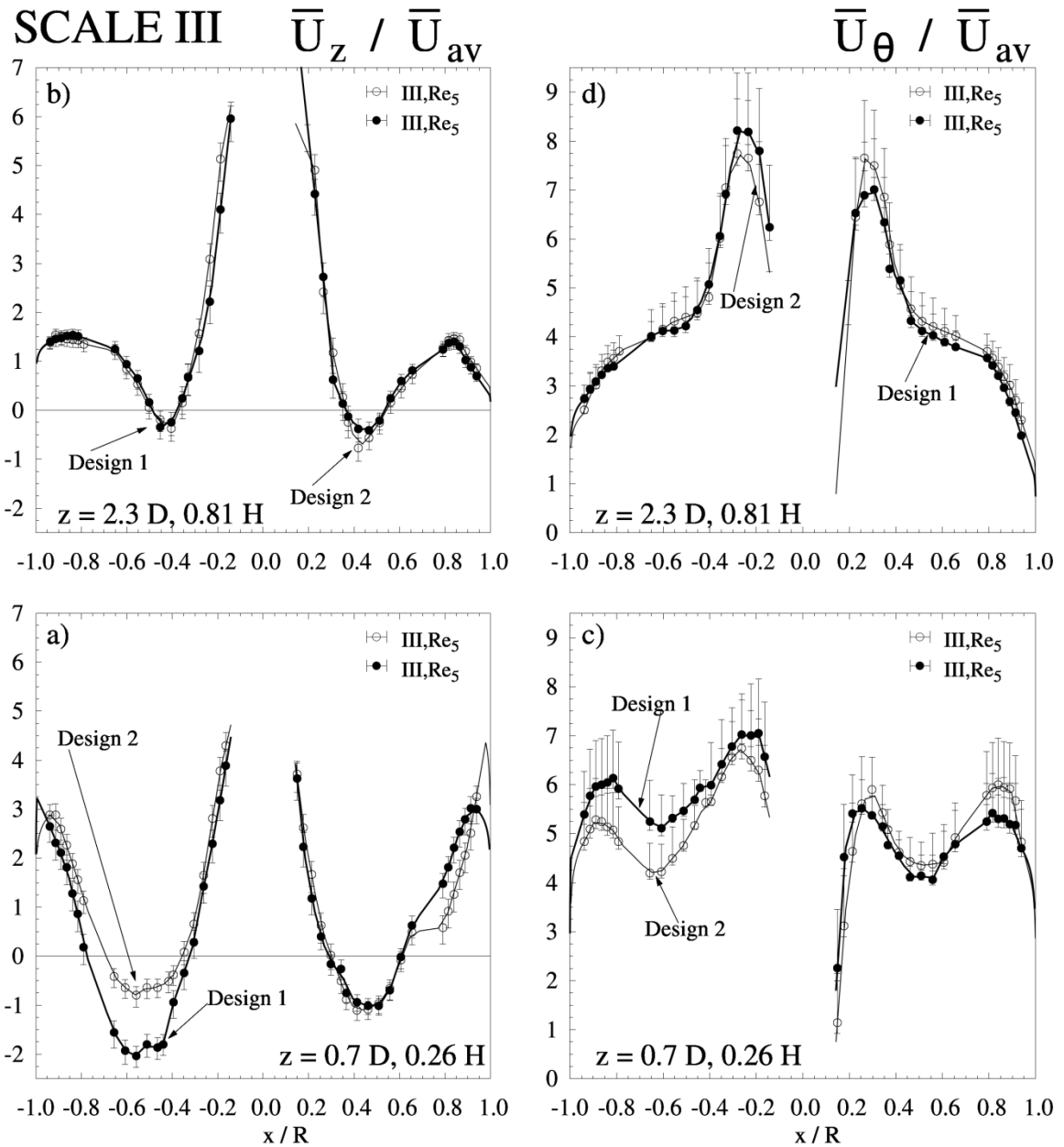


**Figure 10.** Impact of the air distributor in the vortex symmetry in Scale III. Comparison of the use of different distributor designs, Design 1 (two branches) or Design 2 (an open bustle ring). Axial velocity  $\bar{U}_z$  in (a),(b) and tangential  $\bar{U}_\theta$  in (c),(d)

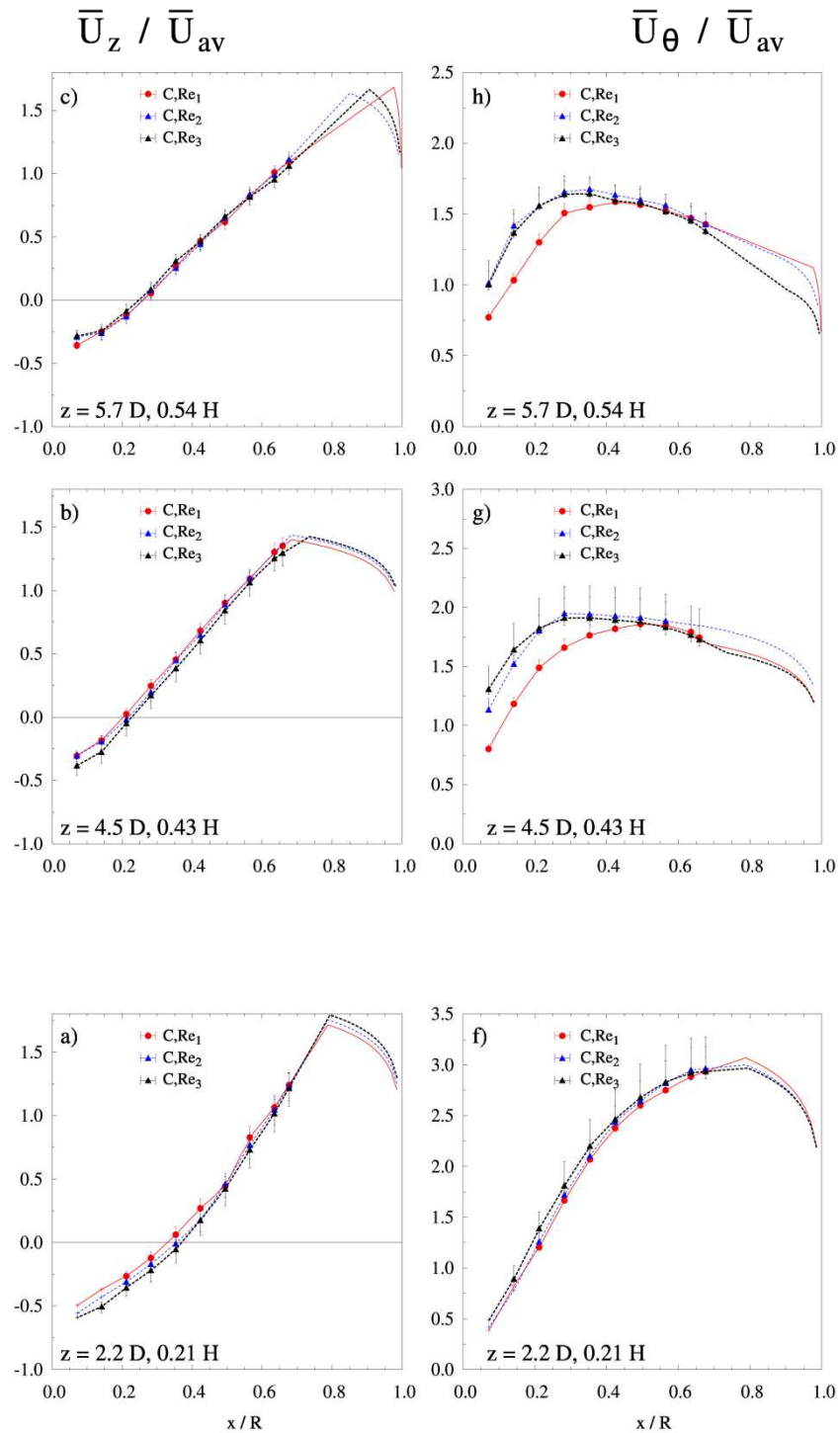
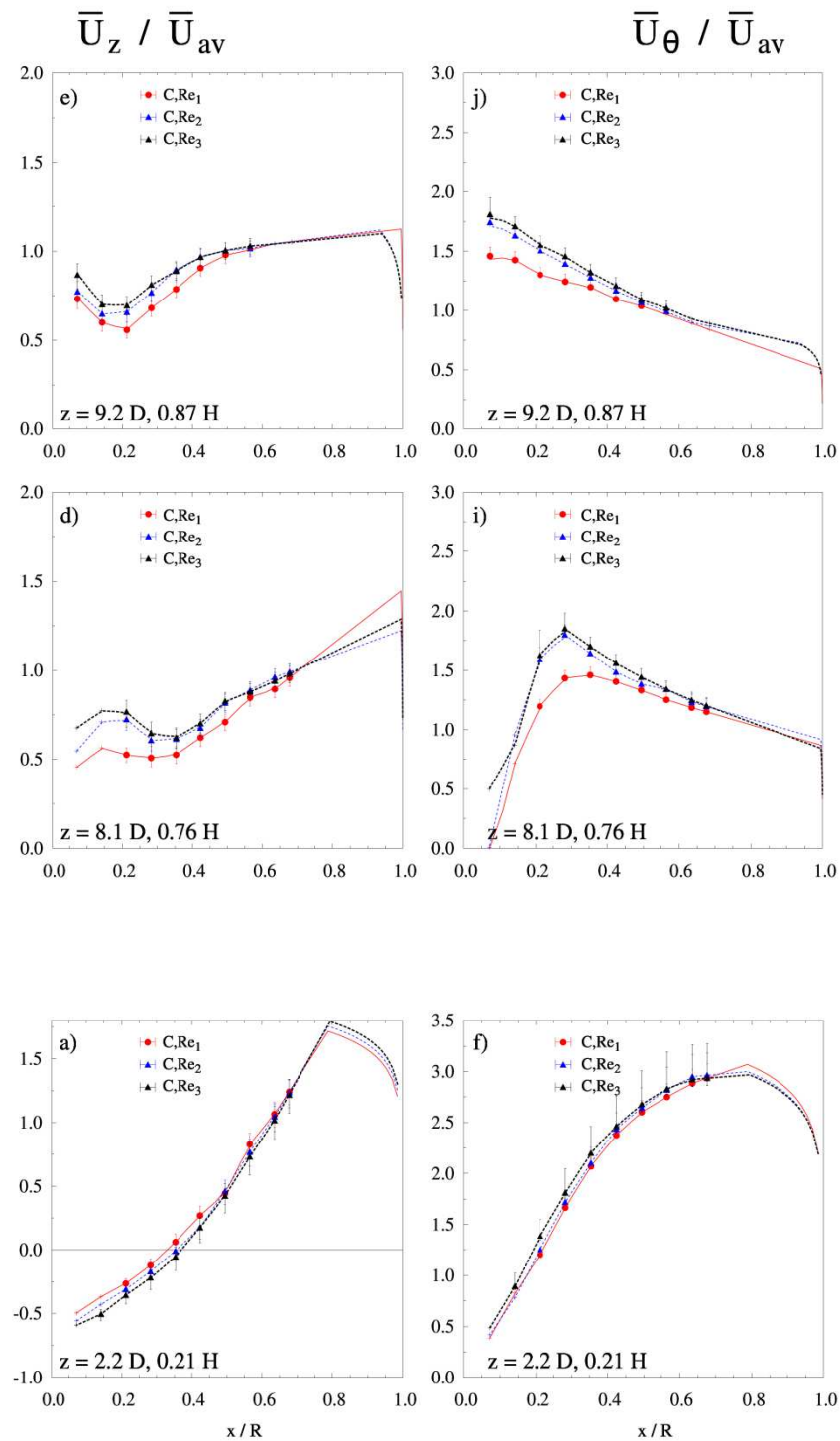


**Figure 11.** Loss of self similarity in the velocity field in  $Re$  range considered under a strong friction, case C, Scale I. Axial  $\bar{U}_z$ , left (a), (b) and (c), and tangential  $\bar{U}_\theta$ , right (f), (g) (h) velocity components. Operating  $Re$  are given in Table 2. Comparison of the velocity field for the bottom section of the unit  $z \leq 5.7 D$ ,  $z \leq 0.54 H$



**continuous from Figure 11.** Axial  $\bar{U}_z$ , left (a), (d) and (e), and tangential  $\bar{U}_\theta$ , right (f), (i) (j) velocity components. Operating  $Re$  are given in Table 2. Comparison of the velocity field at the bottom of the cylinder  $z = 2.2 D = 0.21 H$  in (a), (f) to the levels close to the exit  $z > 5.7 D$ ,  $z > 0.54 H$  in (d), (e) and (i), (j).

and C where a decrease in  $\Omega$  causes the *VBD*. However, Figure 11 shows that a self similar vortex still prevails for high *Re* numbers with independence of the *VBD*. In case C no differences can be appreciated for  $\bar{U}_\theta$  at  $Re_2$  and  $Re_3$ , which has been confirmed further up to  $Re = 1.27 \cdot 10^5$ . However, as *Re* keeps on decreasing to  $Re_1$ ,  $\bar{U}_\theta$  becomes significantly lower in Figure 11. This leads to  $\bar{U}_z$  diminishing at the top of the unit, see the transition from the outer to inner regions at  $z = 8.1 D$ . This is indicative of a displacement in the position of the stagnation point and suggests that the vortex loses the self similarity at a *Re* between  $10^5 < Re < 1.27 \cdot 10^5$ . A further discussion in relation to the role of friction and  $\Omega$  in explaining this behaviour is given in the next section.

### 3.1.5. The swirl decay.

The evolution of  $\Omega_o$  for cases A, B and C in Scale I is summarised in Figure 12 and Table 2. The decay shown in Figure 12a for case A follows the expression of Kitoh (1991), and can be characterised by *Re* independent decay rates 0.08 – 0.09 (Chapter II). Realistically, such conditions occur only during the start up of a spray dryer. The most relevant question is determining the impact of the actual production conditions. The presence of bands and patches of deposits in cases B and C accelerates the decay. In spite of the uncertainty owed to the extrapolation, the axial rate of change of  $\Omega_o$  in Figures 12b and 12c (i.e. the effective shear stress exerted upon the flow) shows a clear relation to the location deposits bands given in Table 1. Abrupt changes in  $\Omega_o$  correlate with the location of the thickest bands within the spray regions, and with the transitions between areas of patches to clean walls.

At the bottom end of the tower the thickness is similar between cases A and B, and Figure 12b shows how  $\Omega_o$  in both follows a similar profile,  $\lambda$  rising up to 0.11 in case B. However, during the spray region, in addition to the  $\varepsilon/D$  characteristic of the band, the flow is forced to overcome the step between patches of deposits onto homogeneous bands. This becomes clear when comparing cases A and B in Figure 12b. In case B a thick band appears throughout the spray region located between  $5.7D < z < 7.1 D$ , and this causes a clear drop in  $\Omega_o$ . This is an unavoidable, for it is consequence the operation of slurry nozzle/s. A similar observation can be made in case C in Figure 12c. It commences with a higher initial value at  $z = 2.2 D$ , perhaps as a result of a reduced friction at the cone since in this case it was perfectly clean, see Table 1. However, at the spray region,  $3.3 D < z < 7.1 D$ , the obstruction becomes much wider, see Figures 1 and 2, and as a result  $\lambda$  rises  $> 0.200$ . In both cases B and C,  $\Omega_o$  remains at stable values at the top end which shows no deposits.

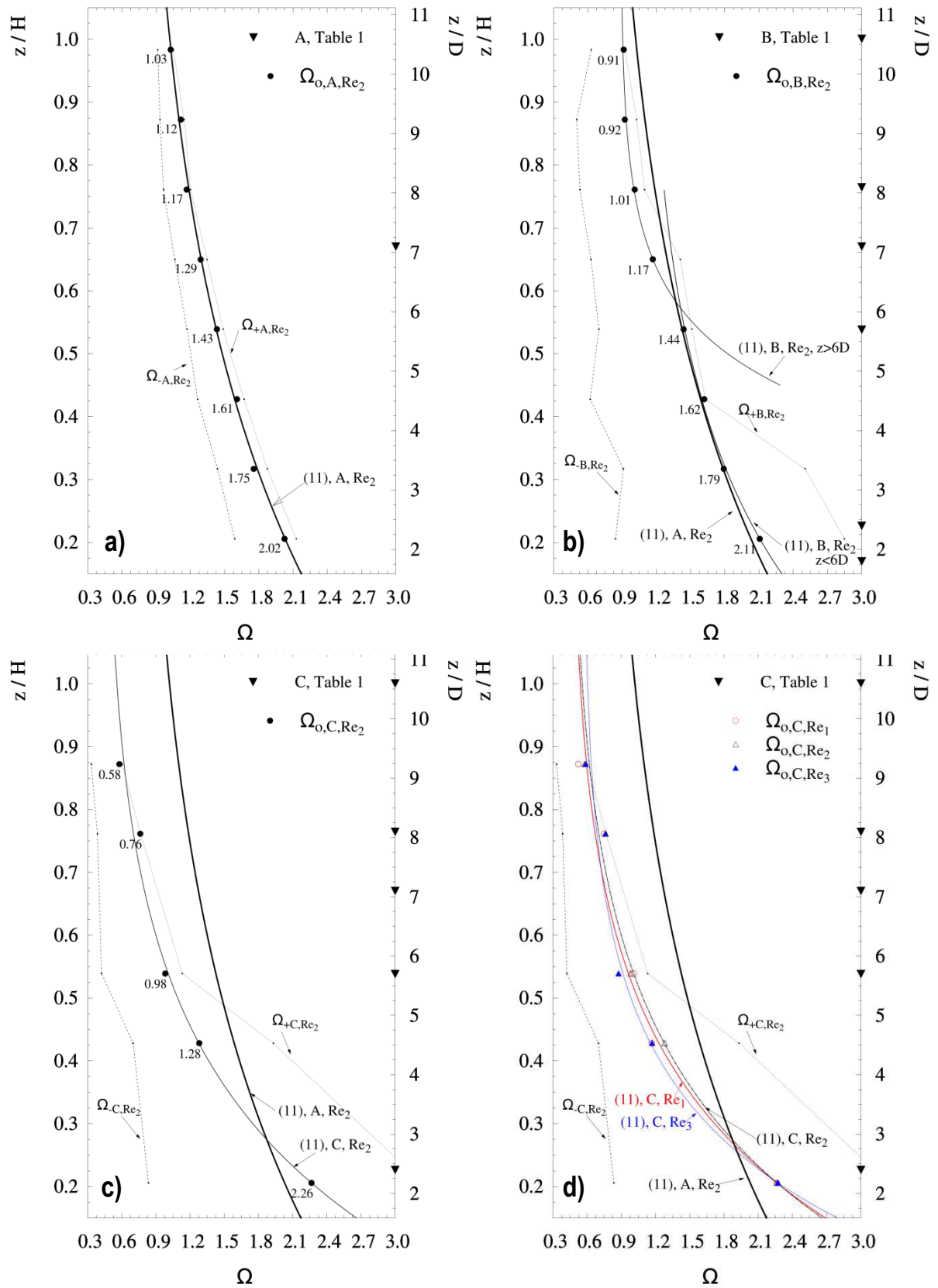


**Figure 12.** Axial decay of  $\Omega$  in the cylindrical chamber of Scale I for cases a) A, b) B, c) C, d) C,  $Re$  dependency. Operating  $Re$  are given in Table 2. The deposit sections in Table 1 are given in the right hand axes.  $\Omega_0$ ,  $\Omega_+$  and  $\Omega_-$  show respectively the best estimate and over and under predictions of  $\Omega$ ; lines provide the fit to equation (11) in Chapter III.

**Table 2.** Swirl decay rate as a function of the wall conditions in Scale I, and the  $Re$ . Fit to a proportional or linear relation between  $\tau_{w,\theta}$  and  $\Omega$  in (9) and (11) (Chapter II).

Case	$Re$	$Re \cdot 10^{-5}$	$\Omega_r$	$A$	$B$	$\lambda$
A	$Re_1$	$1.06 \pm 0.03$	1.96	-0.080	0.054	0.085
A	$Re_2$	$1.49 \pm 0.02$	2.02	-0.086	0.061	0.089
A	$Re_3$	$2.22 \pm 0.02$	1.93	-0.081	0.051	0.090
B	$Re_2$	$1.44 \pm 0.01$	2.11	-0.075	0.026	0.114
B $z < 6D$	$Re_2$	$1.44 \pm 0.01$	2.11	-0.139	0.148	0.111
B $z > 6D$	$Re_2$	$1.44 \pm 0.01$	1.17	-0.379	0.336	0.085
C	$Re_1$	$1.00 \pm 0.01$	2.26	-0.181	0.082	0.221
C	$Re_2$	$1.55 \pm 0.01$	2.26	-0.165	0.073	0.211
C	$Re_3$	$2.29 \pm 0.02$	2.27	-0.224	0.126	0.228

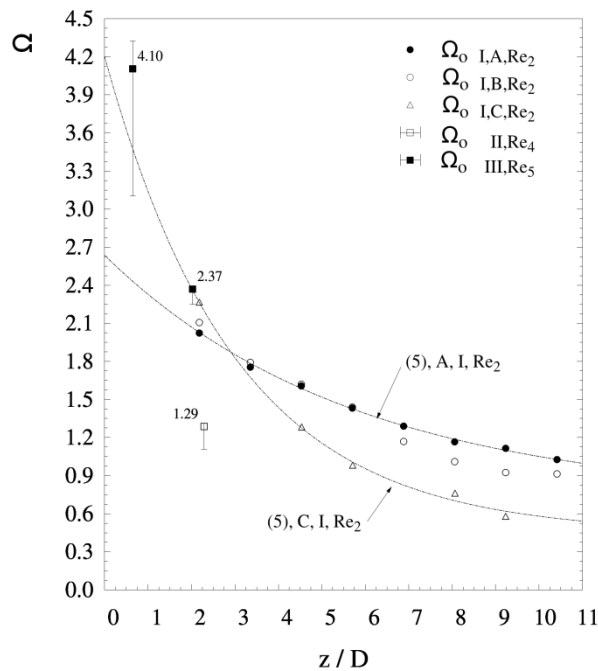
The observation of a correlation between the reduction of the angular momentum flux and the deposits coverage is very relevant. It is not only responsible of the operation under a much weaker swirl than anticipated, but crucially it is the origin of the recirculation and aerodynamic instabilities described earlier. This means that the thickness and distribution of deposits, which are largely ignored in spray drying models, has a drastic effect in the mean flow. A numerical description remains an interesting challenge because it is uncertain how obstructions such as those shown in Figures 1 and 2 could be related to the roughness height  $\varepsilon/D$  used in available wall functions for a rough wall (e.g. Jimenez 2004 or Volino *et al.* 2007). Yet, reality dictates that deposits in dryers will be spatially distributed, shifting from regions of clean walls to uneven patches and stepping into bands of homogeneous thickness, and possibly  $\varepsilon/D$ . In some cases they do not only disturb partially or totally the boundary layer but are large enough to represent an obstruction to the convective flow, which potentially requires the use of very fine meshing nearby the wall. This is the case of the initial drop in  $\Omega_o$  at the bottom of case C, believed to result from a large recirculation owed to the thick patch of deposit shown in Figure 1 ( $z < 3 - 4D$ ). These effects will become clearer in the production of turbulence described in section 3.2.1 where it is shown how drag transfers the kinetic energy dissipated from the convective flow into turbulent kinetic energy. In spite of this complexity, it is undeniable that deposits introduce major changes in the velocity and that their distribution is related to  $\lambda$  and thus  $\tau_{w,\theta}$ .

Figure 12 and Table 2 shows no significant change of  $\lambda$  with  $Re$  for case C. However, analysis of the velocity profiles in section 3.1.4 shows a statistically significant difference in Figure 11. This is lost in the

computation of  $\lambda$  due to the propagation of errors, the extrapolation close to the wall and the fit to equation (11) (Chapter II). According to Figure 11, one must expect that moving into the operation at  $\Omega < 1$  and  $Re < 10^5$  is likely to cause different velocity profiles and increase  $\lambda$ . This behaviour appears only in case C because the influence of the contraction has decreased sufficiently at the bottom of the tower. In these circumstances, the flow shows the  $Re$  dependency expected in the free developing systems studied by Kitoh (1991) or Steenbergen and Voskamp (1998). It still withstands the comparison of  $\lambda$  to the friction factor in a fully rough regime flow in unidirectional flows, since in that case the friction factors start to increase with decreasing  $Re$  at  $Re < 10^5$  (Moody 1944).

Figures 13 and 14 present the evolution across different scales. Figure 13 plots the swirl decay for Scales I, II, and III according to the exponential relation expected in open tubes between  $z/D$  and  $\Omega$ . In contrast, in Figure 14 the axial position  $z$  is normalized by the length of the cylinder,  $H$ , in order to compare the positions in the tower relative to the two low pressure points identified at the top and the bottom of the cylinder (i.e. the exit duct and the bottom core of the vortex). Scale II makes use a lower  $\Omega_i$  but it also presents a shorter aspect ratio,  $H/D$ , which reduces the inner surface area and thus the decay of the swirl. This allows Scale II to develop the same  $\Omega$  values than Scale I at the same relative distance to the exit in Figure 14. In combination with a similar contraction ratio,  $d/D$ , this means that when the vortex faces the exit, the acceleration caused by the vortex finder extends down the cylinder in a comparable way and causes the formation of the central jet. As a result, Scale I and II in Figure 8 show similar velocity profiles in respect to  $z/H$ , but not in respect to  $z/D$ .

This is in contrast to the behaviour at higher  $\Omega_i$  in Scale III. In this case, higher  $\Omega$  values prevail across the entire cylinder. This leads to large differences in the velocity profiles and the generation of an annular recirculation region. The operation at higher  $\Omega$  values causes the decay rate,  $\lambda$ , to increase up to  $\sim 0.200$ , comparable only to case C in Scale I. This cannot be explained by the morphology of the deposits, which in the largest scales II and III are evenly distributed and show a  $\delta/D$  close to the values of case A, see Figure 3. In this case, the high values of  $\Omega$  are responsible of the changes in the velocity direction near the wall because the flow is dominated by the influence of the contraction. In this case, the flow is no longer comparable to free systems where the structure owes to the development of the boundary layer (Kitoh 1991, Najafi *et al.* 2011). In dryers, the wall friction becomes a strong function strong function of  $\Omega$  due the contraction, but  $Re$  independent at sufficiently large numbers.



**Figure 13.** Comparison of the  $\Omega_o$  and the decay rate  $\lambda$  across Scales I, II and III. Error bars indicate variation given by  $\Omega_-$  and  $\Omega_+$ , excluded in Scale I for clarity. Operating  $Re$  are given in Chapter I.

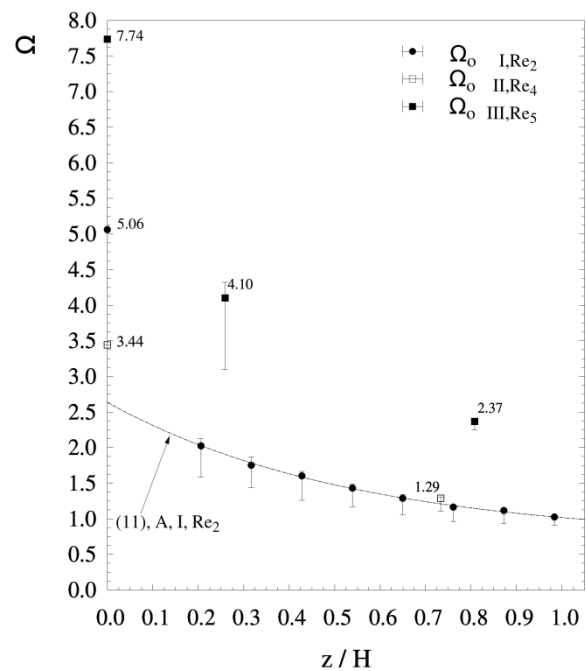


**Figure 14.** Comparison of operation ranges in  $\Omega_o$  across Scales I, II and III. The error bars indicate variation given by  $\Omega_-$  and  $\Omega_+$ . The value of  $\Omega_i$  is plotted at  $z = 0$ . Operating  $Re$  are given in Chapter I.

### 3.1.6. A note on the scale up of the fluid dynamics.

According to Oakley (1994, 2004), one expects the operation at the same  $Re$  numbers (or sufficiently high) to render the same velocity field in different dryers, as long as one maintains geometrical similarity and scaled inlet conditions. In the case of the cylinder of a tall-form swirl dryer, the geometry may be defined by  $H/D$  and  $d/D$ , and the inlet conditions as the velocity profile that enters the cylinder.

This type of scale-up analysis however omits the potential variation of the wall shear stress at the walls. The effect of modifying  $\Omega_i$  has become obvious in this work, but the successful transition from Scale I to Scale II demonstrates that one can obtain a comparable vortex structure if is capable of reproducing a similar evolution of  $\Omega$  in the cylinder. The scale up analysis given by authors such as Masters (1995) or Kemp and Oakley (2002) needs to be reconsidered in the context of swirl dryers to account for the friction. In any given tower the expected swirl decay can be estimated making use of  $H/D$  and the decay rates reported in this thesis as function of the deposits and the  $\Omega$  range.

This procedure can be first used for design purposes and to determine which the optimum tower  $R$  or  $R_i$  are in new units, given that the length of the cylinder is likely limited by the desired particle residence time. Secondly, one can consider modifying  $\Omega_i$  as a control tool. In a given tower  $R$  and

$R_i$  are unlikely to change, but one can in principle modify  $\Omega_i$  simply by constraining the combined area of the inlets  $A_i$  (this requires sufficiently powerful inlet fans). In this manner one can target a desired  $\Omega$  range in the cylinder to drive or suppress the recirculation. This can prove a very useful tool to accommodate changes in the process. For instance, currently it is impossible to control the attenuation of the swirl caused when the deposits growth in changeover periods (i.e. different formulations in industry) or when the particle concentration rises at higher production rates. All could be accounted for by increasing  $\Omega_i$  just in the adequate proportion to maintain a comparable  $\Omega$  value at the top. Thirdly, manipulating the recirculation regions and the strength of the central jet could be extremely useful to control the elutriation rate and the particle residence time. In this sense, the use of computational fluid dynamics models can prove very useful in optimising the location and alignment of nozzles, should they gain the ability of predicting the decay of the swirl and the associated instabilities.

### 3.2. Turbulence statistics.

#### 3.2.1. Turbulent kinetic energy and normal stresses.

##### 3.2.1.1 Production of turbulence owed to friction.

Figures 15 to 18 show the impact of friction in the production of turbulence. They compare the axial development of the turbulent kinetic energy  $\kappa$  and all the normal stresses in cases A, B and C.

$\kappa$  decreases axially in a cleaned tower, case A in Figure 15, and shows a maximum in the outer region that shifts inwards as the flow approaches the exit. In the inner region,  $\kappa$  shows higher values, unrelated to turbulent energy but indicative of the instability of the core. In spite of the uncertainty, it is obvious that deposits in cases B and C modify both, the values and the profile of  $\kappa$ . Standard bands in case B make  $\kappa$  to rise increase  $\sim 67\%$  from a maximum value in the outer region of  $0.09 \bar{U}_{av}^2$  to  $0.15 \bar{U}_{av}^2$ . In this case  $\kappa$  does not show a clear maximum but remains constant across the inner and outer regions. It decreases axially until reaching the *VBD* position between  $z = 5.7 D$  and  $6.9 D$  where it rises again. After this point, the values in the outer region approximate that of case A. The rise in  $\kappa$  at the inner region begins at lower levels but is particularly relevant above the *VBD*, coinciding with the formation of the jet. Case C follows a similar pattern. The deposits are much wider and the higher friction factor at the bottom makes  $\kappa$  to increase to  $0.17 \bar{U}_{av}^2$  at the outer part. It shows the same axial evolution than in case B: a sustained decrease towards the top, in this case to lower values,  $0.01 \bar{U}_{av}^2$  in place of  $0.02 \bar{U}_{av}^2$  in cases A and B.

For the most part, the axial decrease of  $\kappa$  in case A can be explained by the relation between  $\kappa$  and  $\Omega$ , instrumental to many heat and mass transfer processes (Chang and Dhir 1994,1995). However, the presence of deposits enhances the recirculation and this originates a substantial transfer of kinetic energy from the convective flow (i.e. observed as a stronger decay in  $\Omega$ ) into the turbulence. On the one hand this is originated by drag against larger roughness elements, and in the other due to the *VBD*. A clear example is given by case C. Here the friction is mainly originated by the large deposits in the spray region (i.e. notice the distribution of patches at the bottom part in Figure 1,  $z < 3 - 4 D$ ). Despite the large decrease in  $\Omega$ , the generation of turbulence in this region maintains the value of  $\kappa$  constant below  $z \leq 5.7 D$ . After this point, the deposits are reduced,  $\Omega_o$  drops from 0.98 to 0.58 and  $\kappa$  decays. As a passing note, this suggests to the potential of applying similar rough surfaces with the objective of generating turbulence at the cost of swirl intensity in systems where deposition may not be an issue, as for instance the improvement of local mixing in a reactive swirling flow.

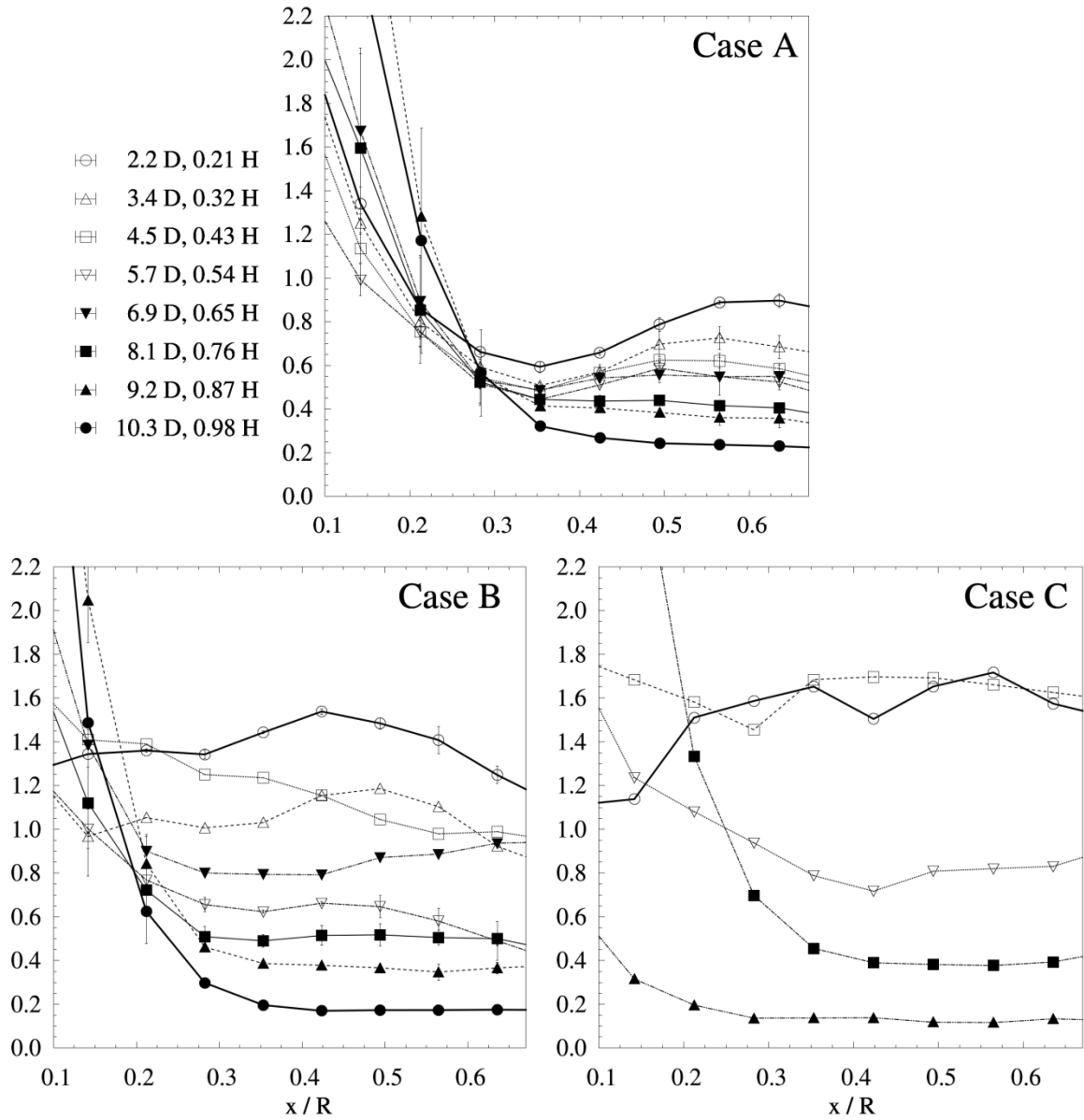
Under a strong friction in cases B and C,  $\overline{u_z u_z}$  begins to show a flat radial profile and as oppose to Case A, it losses both inner and outer maxima in Figure 16. In turn,  $\overline{u_r u_r}$  remains constant at the bottom of the dryer for case B in Figure 17, and decreases only at the bottom core for case C. In both cases B and C, the normal stresses show a similar axial development: they decrease until the breakdown location, showing a subsequent increase and then a final decay close the exit.

In the case of cleaned walls, case A, the normal stress  $\overline{u_\theta u_\theta}$  in Figure 18 shows lower values that  $\overline{u_z u_z}$  and  $\overline{u_r u_r}$  in Figures 16 and 17 and presents no outer maximum. In contrast, in cases B and C  $\overline{u_\theta u_\theta}$  shows comparable values and profiles to  $\overline{u_r u_r}$  and  $\overline{u_z u_z}$  in all the levels below the *VBD*. This is in agreement with the assertion in Chapter II, which on the basis of the studies of Derksen (2005) attributes the suppression of the mixing in the azimuthal direction to the influence of the contraction, limited under a stronger friction. It can be appreciated how in case B the maxima at the outer region of  $\overline{u_z u_z}$  and  $\overline{u_r u_r}$  are disrupted near the breakdown,  $5.7D < z < 6.9D$  and then recover after it.

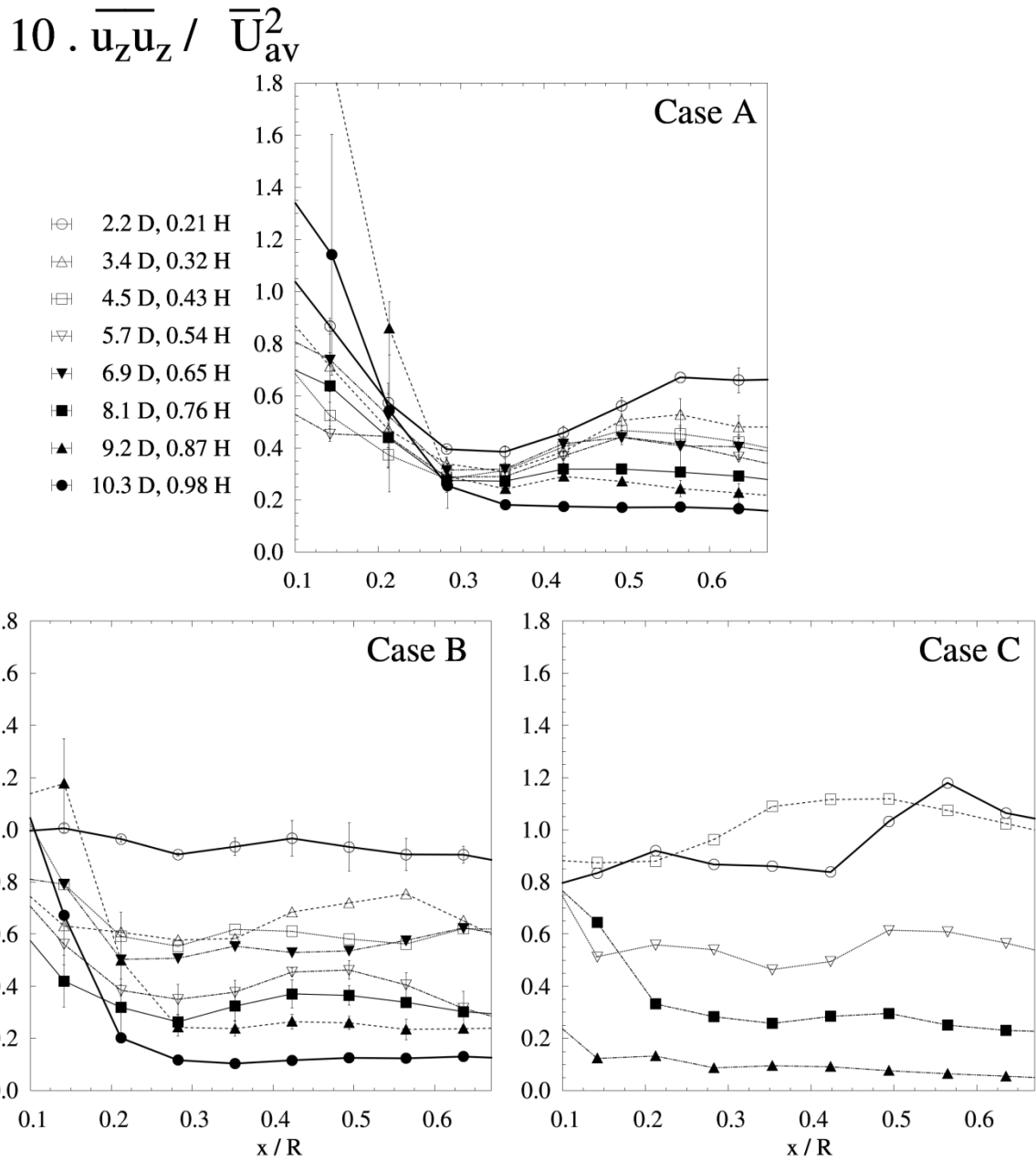
### 3.2.1.2 Relation to $Re$ and $\Omega$ range.

Chapter II shows that in case A, higher  $Re$  are likely to reduce  $\kappa/\overline{U}_{av}^2$ . This appears to be also the case for all normal stresses in case C, shown in Figure 19. In both cases however the large uncertainty does not permit to draw significant statistical differences.

Figures 20 and 21 summarize the impact of scale. Both large scale towers show higher  $\kappa/\overline{U}_{av}^2$ .

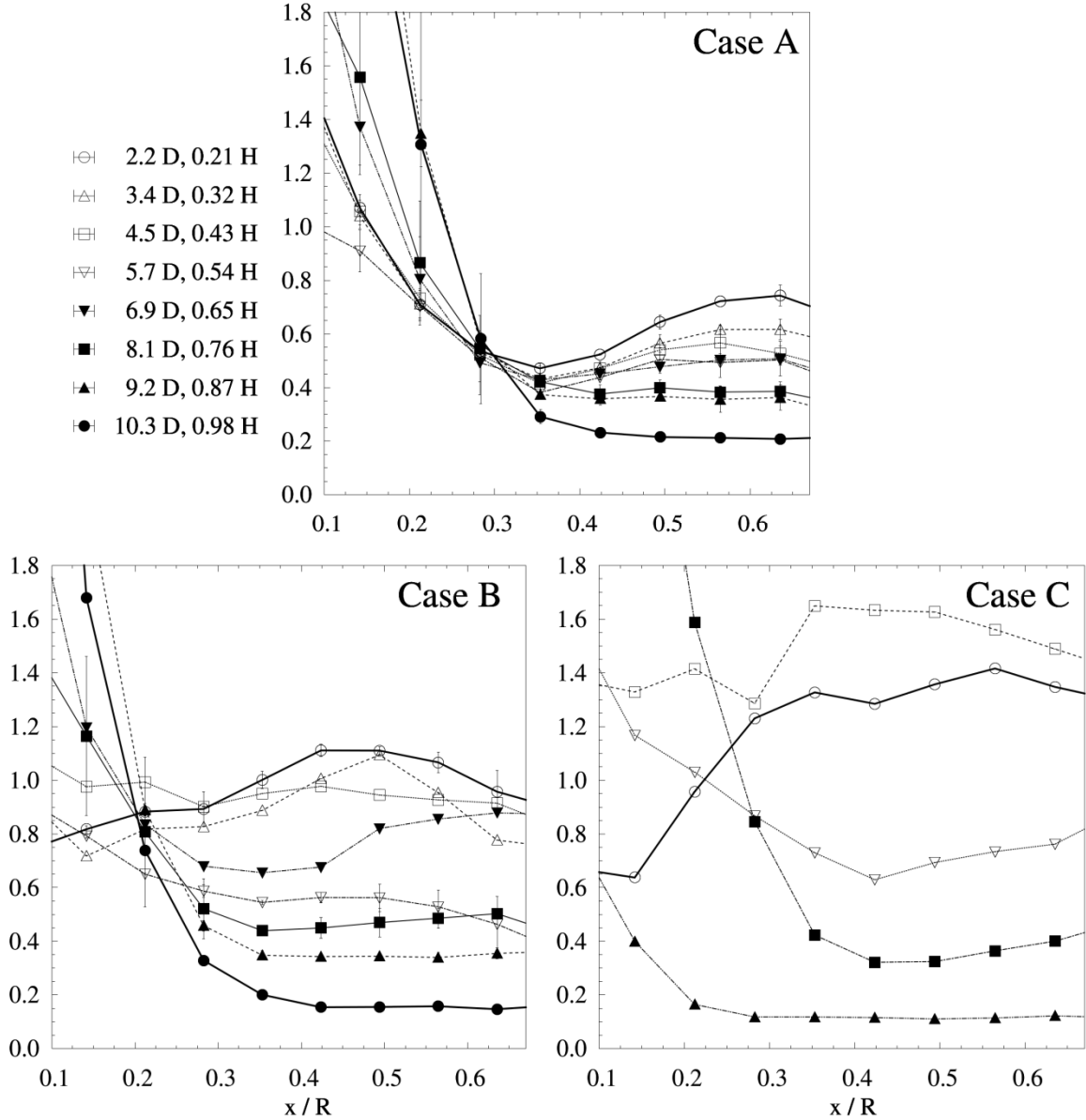
$$10 \cdot \kappa / \bar{U}_{av}^2$$


**Figure 15.** The impact of friction in the turbulent kinetic energy  $\kappa$  in Scale I. Operating  $Re_2 = 1.5 \cdot 10^5$ , see Table 2. Data are normalized by  $\bar{U}_{av}^2$ . Error bars indicate the variation across tangential locations. Maximum uncertainty ranges in  $\kappa$ ,  $-31, +7\%$  (Appendix I).

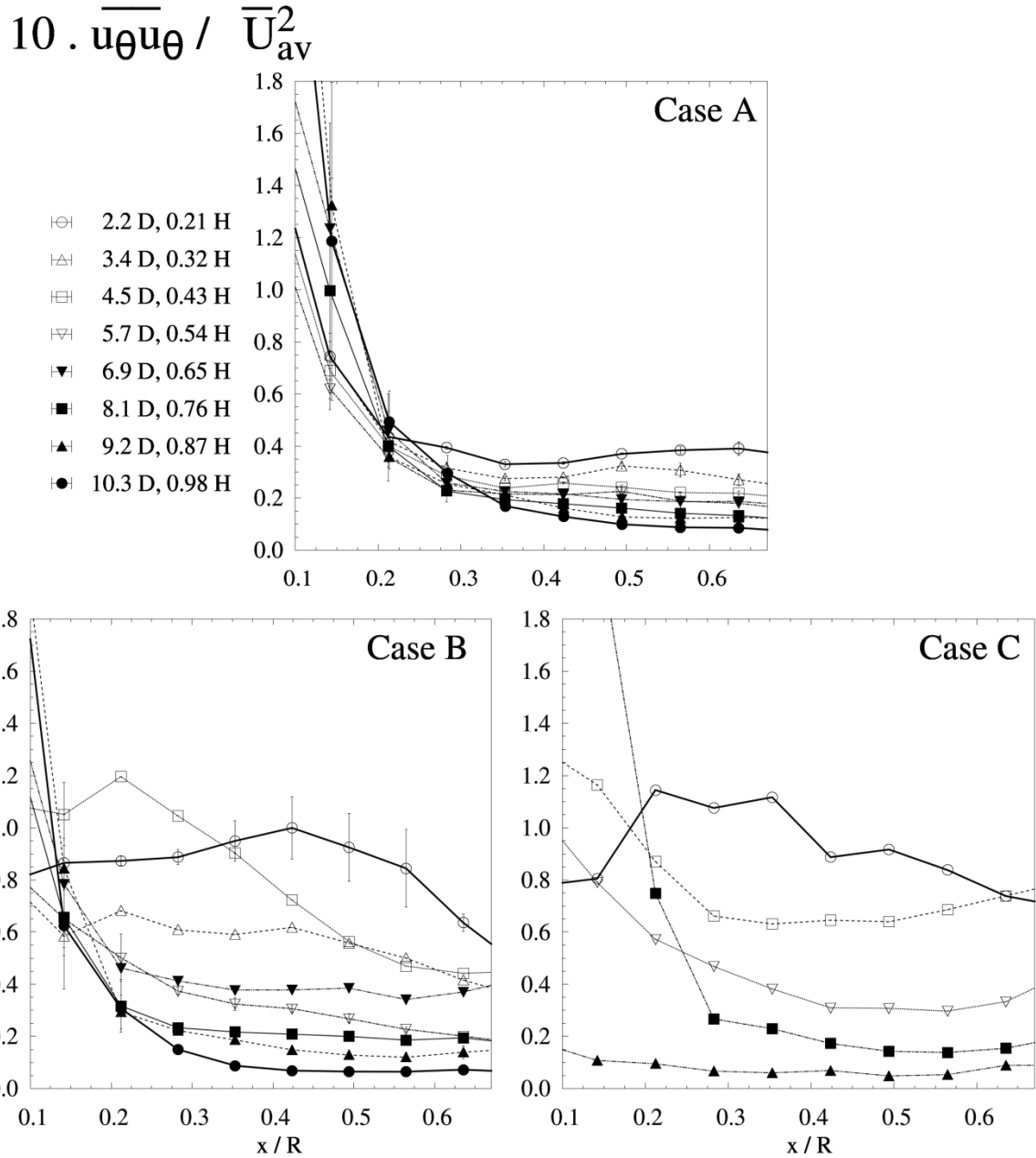


**Figure 16.** The impact of friction in  $\overline{u_z u_z}$  in Scale I. Operating  $Re_2 = 1.5 \cdot 10^5$ , see Table 2. Data are normalized by  $\overline{U_{av}^2}$ . Error bars indicate the variation across tangential locations. Maximum uncertainty ranges in  $\overline{u_z u_z}$ ,  $-41, +19\%$ , (Appendix I).

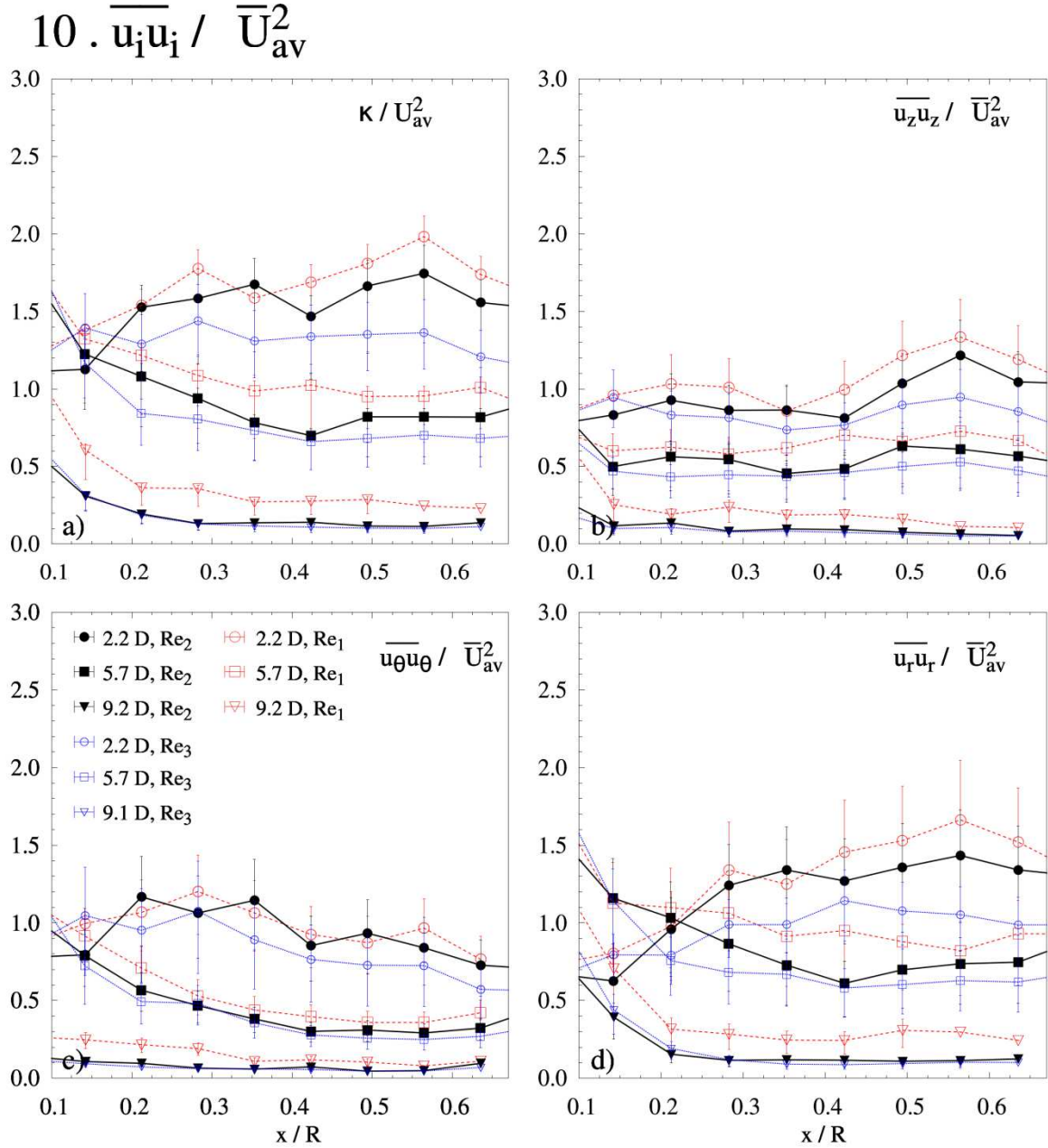
$$10 \cdot \overline{u_r u_r} / \overline{U_{av}^2}$$



**Figure 17.** The impact of friction in  $\overline{u_r u_r}$  in Scale I. Operating  $Re_2 = 1.5 \cdot 10^5$ , see Table 2. Data are normalized by  $\overline{U_{av}^2}$ . Error bars indicate the variation across tangential locations. Maximum uncertainty ranges in,  $\overline{u_r u_r}$ ,  $-35, +22\%$  (Appendix).



**Figure 18.** The impact of friction in  $\overline{u_\theta u_\theta}$  in Scale I. Operating  $Re_2 = 1.5 \cdot 10^5$ , see Table 2. Data are normalized by  $\overline{U}_{av}^2$ . Error bars indicate the variation across tangential locations. Maximum uncertainty ranges in  $\overline{u_\theta u_\theta}$ ,  $-23, +19\%$ , (Appendix I).



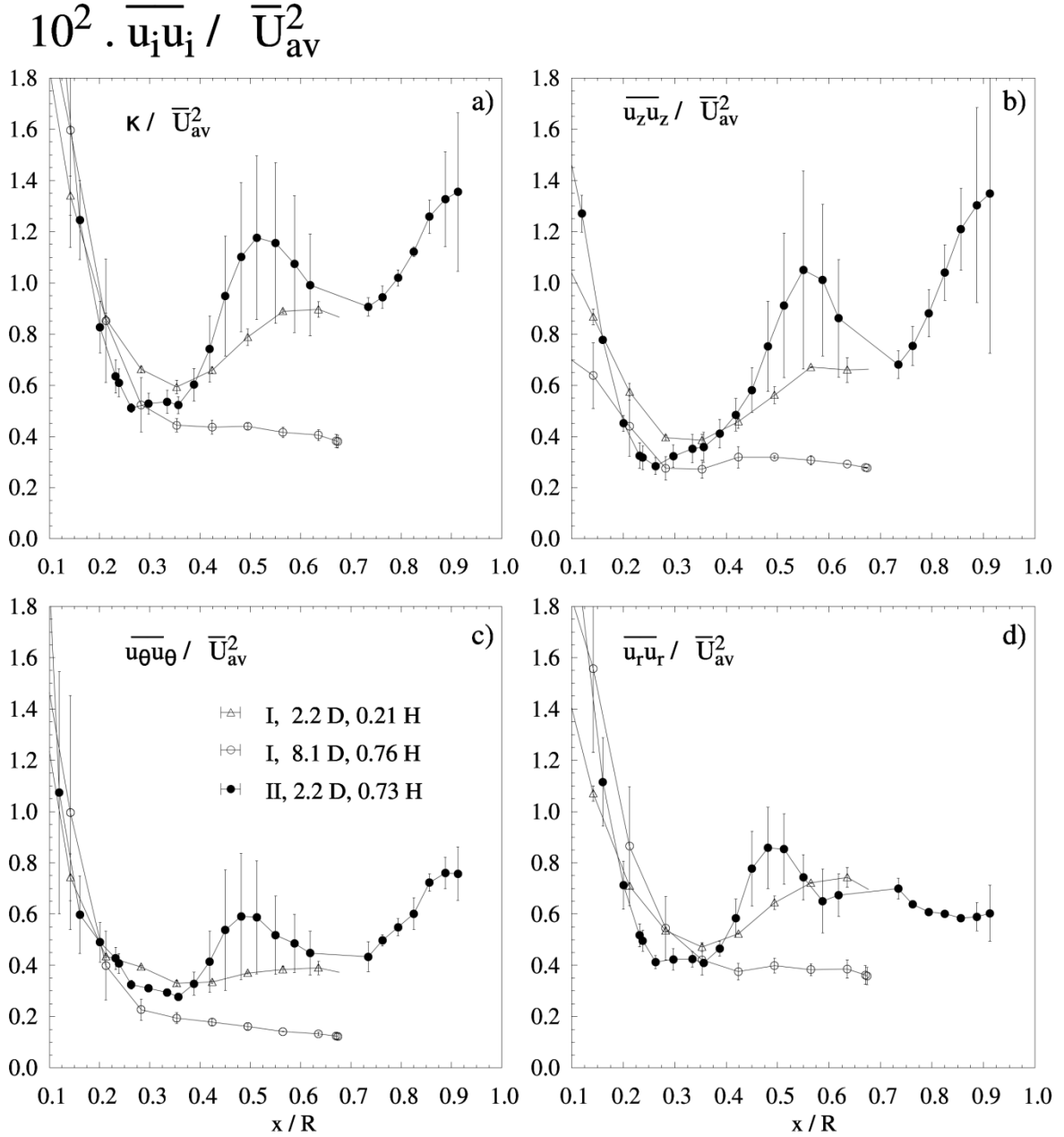
**Figure 19.** The evolution of the turbulent kinetic energy  $\kappa$  and normal stresses with Reynolds in a scenario of strong friction, Scale I. Case C. Operating  $Re$  are given in Table 2. Data are normalized by  $\bar{U}_{av}^2$ . Error bars indicate the variation across tangential locations. Maximum uncertainty ranges in  $\kappa$ ,  $-31, +7\%$ ,  $\overline{u_z u_z}$ ,  $-41, +19\%$ ,  $\overline{u_\theta u_\theta}$ ,  $-23, +19\%$ ,  $\overline{u_r u_r}$ ,  $-35, +22\%$  (Appendix I).

Figure 20 shows that in general Scales I and II present a similar  $\kappa$  range despite Scale II shows a larger maximum in the annular region. The comparable profile between Scales I and II may be associated to the same recirculation patterns described earlier. It can also be appreciated that in Scale II  $\overline{u_\theta u_\theta}$  and  $\overline{u_z u_z}$  rise towards the section near wall, where measurements are not available in Scale I. The increase in  $\kappa$  is emphasised moving to Scale III in Figure 21, which shows values up to ten times higher and a different radial profile. This can be explained due to the higher  $\Omega$  range. At the bottom end of the unit a similar central maximum is associated to the axial jet and contained within the diameter of the vortex finder. In the annular part,  $\kappa$  increases towards the wall, and interestingly this also occurs for all normal stresses, including  $\overline{u_\theta u_\theta}$  which in Scale I shows no outer maximum. At the top of the unit  $\overline{u_r u_r}$  and  $\overline{u_z u_z}$  show respective maxima beyond  $r > 0.30 R$ , likely associated to the abrupt decay in  $\overline{U_\theta}$  shown in Figure 9 and linked to the outer free vortex. Similarly to the behaviour of Scale II, at the top end of the chamber all the normal stresses show a final increase nearby the wall.

### 3.2.2. Reynolds stresses.

Figures 22 to 24 provide comparison of Reynolds stresses as a consequence of modifying the wall conditions.  $\overline{u_z u_\theta}$  is associated to the axial transfer of angular momentum owed to turbulence and thus is predominately positive in Figure 22. In case A, it shows maximum values at the outer region that shift inwards as the flow move close to the top, in an indication of the proximity to the dead regions that suppress the axial transport of momentum. Negative values appear at the top end and within the jet. Cases B and C present a similar evolution: in both the outer maximum shifts inwards until the flow reaches the *VBD*. After this point it moves outwards again and decreases substantially in value. Despite the large increase associated to the friction in  $\kappa$  and all normal stresses, only at the bottom a significant increase in  $\overline{u_z u_\theta}$  follows. Similarly to case A,  $\overline{u_z u_\theta}$  in case B takes predominately negative values at the core and at the top level. In case C however the influence of the contraction is minimal and positive values can also occur at the centre.

$\overline{u_r u_\theta}$  shows a different development in Figure 23 for case A or cases B and C. In case A only positive values occur, but in cases B and C,  $\overline{u_r u_\theta}$  turns negative at the bottom and then undergoes a rapid change in direction between  $2.2 D < z < 3.4 D$  and a transition again to negative values at the core for  $z > 3.4 D$ . Figure 24 shows that  $\overline{u_r u_z}$  takes negative values in for the outer part of the vortex in case A. They decrease axially until shifting to a positive sense only at the top end of the cylinder. In turn



**Figure 20.** Comparison of the turbulent kinetic energy  $\kappa$  and normal stresses in Scales I and II. Operating  $Re$ ,  $Re_2 = 1.5 \cdot 10^5$  for Scale I and  $Re_4 = 6.8 \cdot 10^5$  for Scale II (Chapter I). a)  $\kappa$  b)  $\overline{u_z u_z}$  c)  $\overline{u_\theta u_\theta}$  d)  $\overline{u_r u_r}$ . Data are given for the same axial levels in terms of  $z/D$  and  $z/H$  and normalized by  $\overline{U_{av}^2}$ . Error bars indicate the variation across tangential locations. Maximum uncertainty ranges in  $\kappa$ ,  $-31, +7\%$ ,  $\overline{u_z u_z}$ ,  $-41, +19\%$ ,  $\overline{u_\theta u_\theta}$ ,  $-23, +19\%$ ,  $\overline{u_r u_r}$ ,  $-35, +22\%$  (Appendix I).

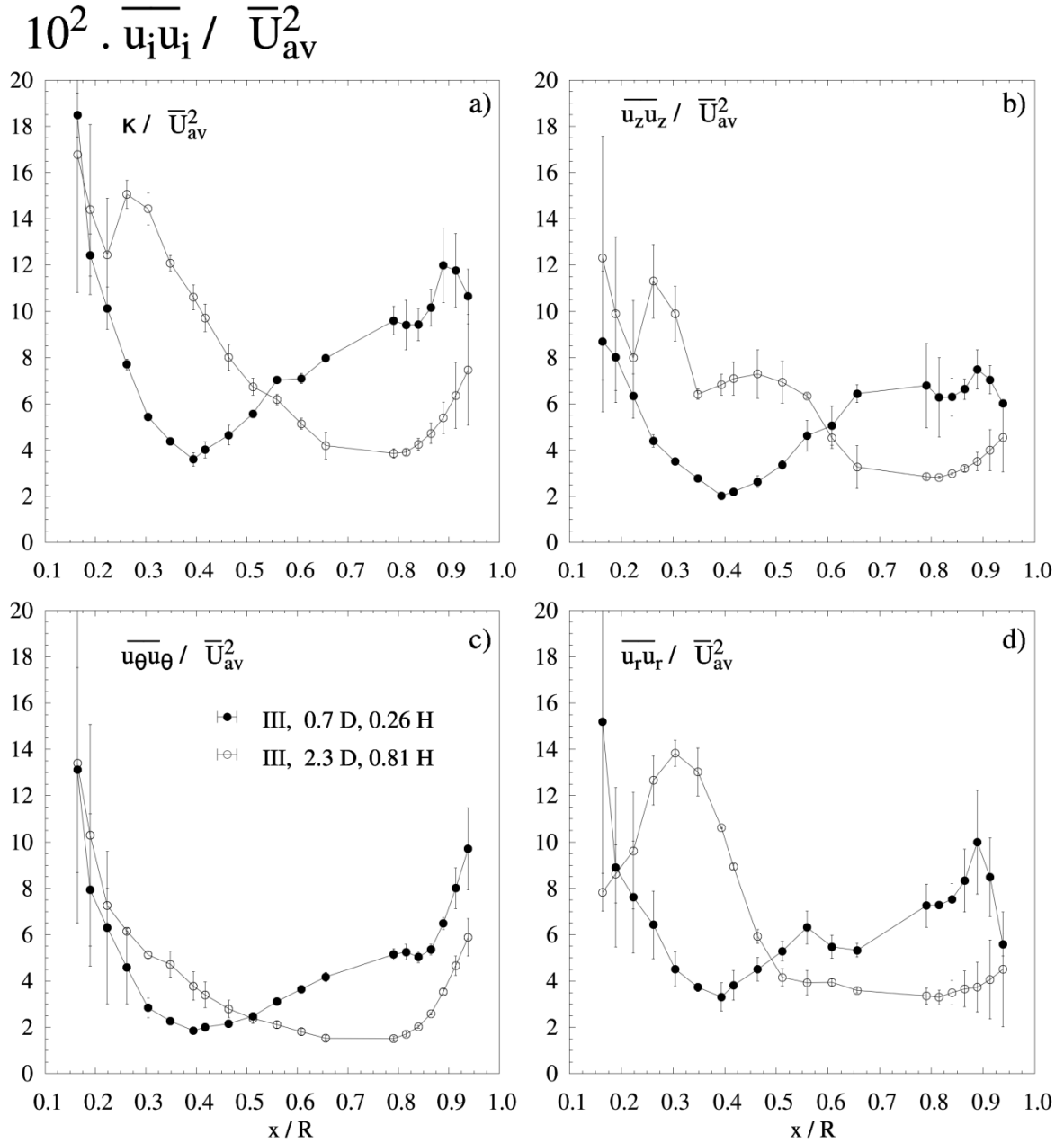


**Figure 21.** The turbulent kinetic energy  $\kappa$  and normal stresses in Scale III a)  $\kappa$  b)  $\overline{u_z u_z}$  c)  $\overline{u_\theta u_\theta}$  d)  $\overline{u_r u_r}$ . Operating  $Re$ ,  $Re_2 = 1.5 \cdot 10^5$  for Scale I and  $Re_4 = 4.9 \cdot 10^5$  for Scale III (Chapter I). Data are normalized by  $\bar{U}_{av}^2$ . Error bars indicate the variation across tangential locations. Maximum uncertainty ranges in  $\kappa$ ,  $-31, +7\%$ ,  $\overline{u_z u_z}$ ,  $-41, +19\%$ ,  $\overline{u_\theta u_\theta}$ ,  $-23, +19\%$ ,  $\overline{u_r u_r}$ ,  $-35, +22\%$  (Appendix I).

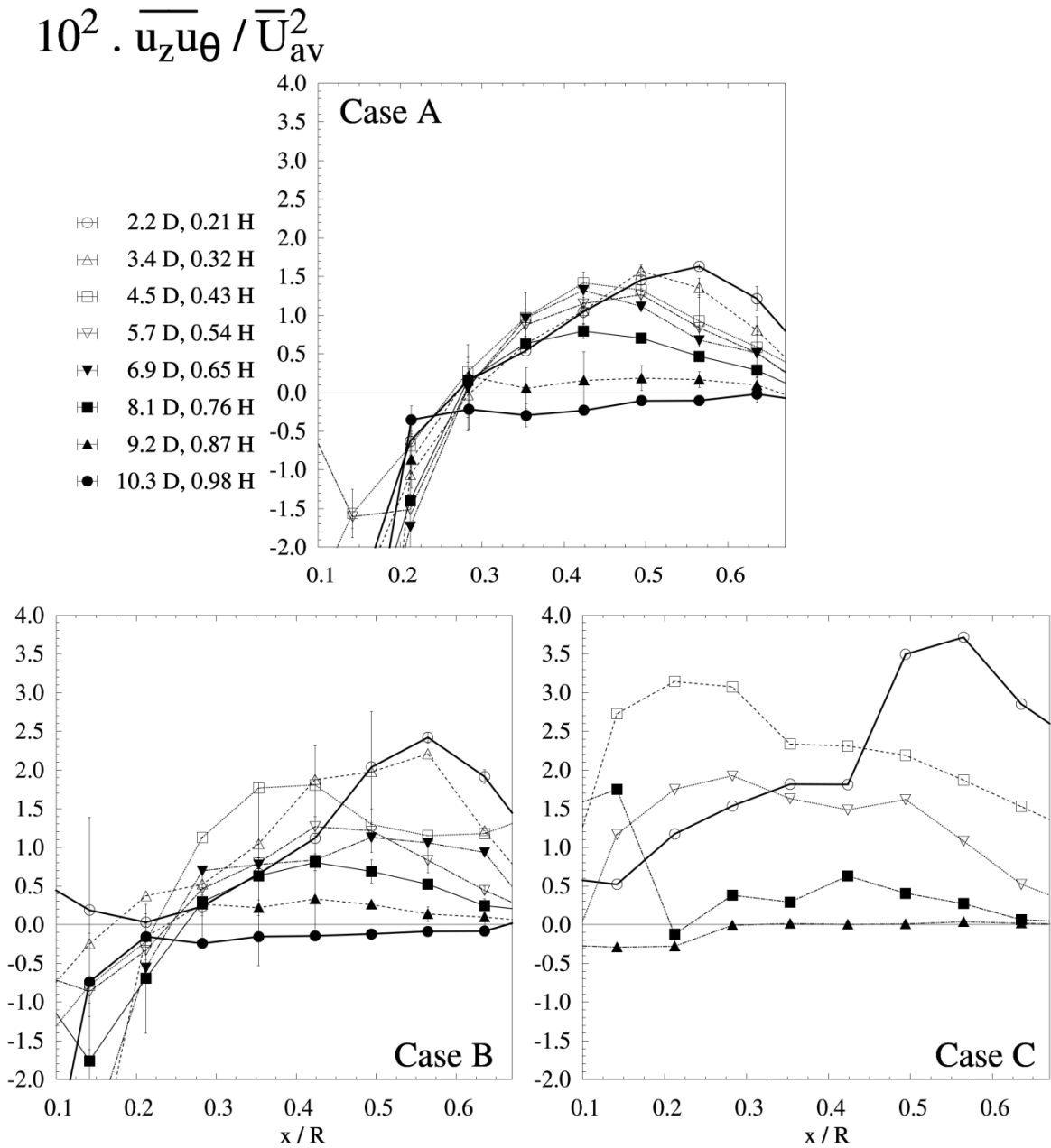


**Figure 22.** The impact of friction in the Reynolds stress  $\overline{u_z u_\theta}$  in Scale I. Operating  $Re_2 = 1.5 \cdot 10^5$ , see Table 2. Data are normalized by  $\overline{U_{av}^2}$ . Error bars indicate the variation across tangential locations. Maximum uncertainty ranges in  $\overline{u_z u_\theta}$ ,  $-33, +19\%$ , (Appendix I).

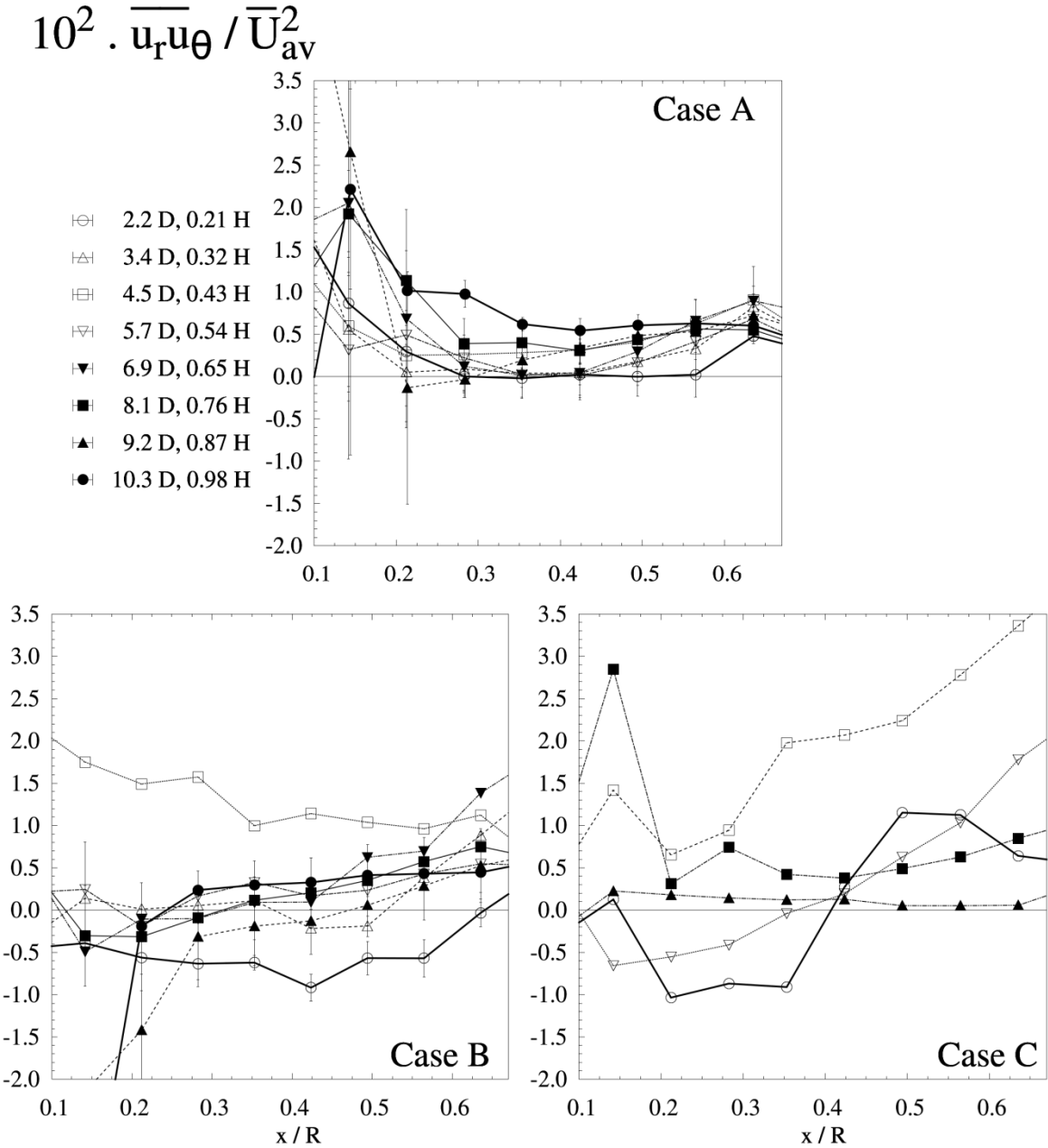


**Figure 23.** The impact of friction in the Reynolds stress  $\overline{u_r u_\theta}$  in Scale I. Operating  $Re_2 = 1.5 \cdot 10^5$ , see Table 2. Data are normalized by  $\overline{U_{av}^2}$ . Error bars indicate the variation across tangential locations. Maximum uncertainty ranges in  $\overline{u_r u_\theta}$ ,  $\pm 100\%$  (Appendix I).

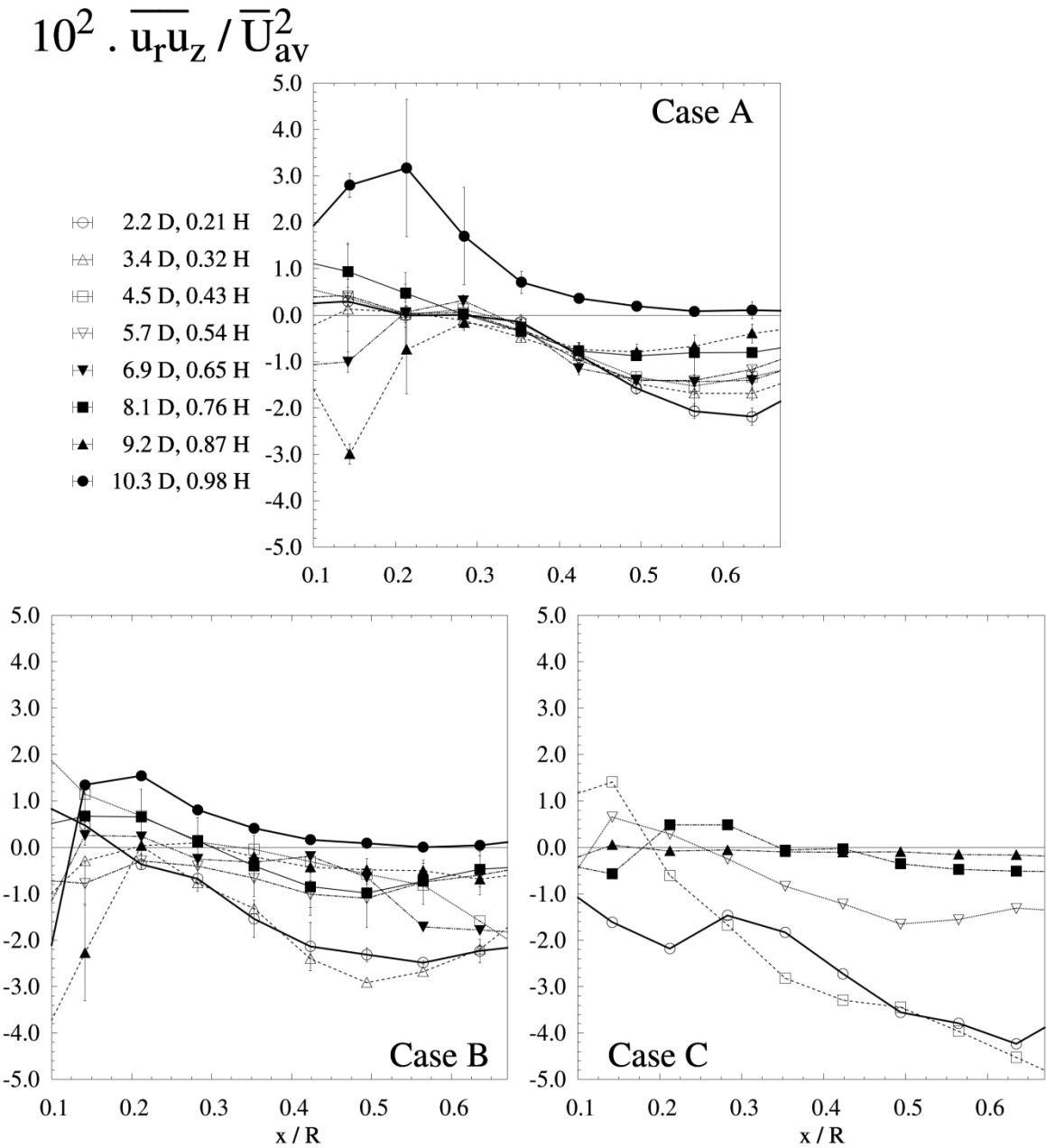


**Figure 24.** The impact of friction in the Reynolds stress  $\overline{u_r u_z}$  in Scale I. Operating  $Re_2 = 1.5 \cdot 10^5$ , see Table 2. Data are normalized by  $\overline{U}_{av}^2$ . Error bars indicate the variation across tangential locations. Maximum uncertainty ranges in  $\overline{u_r u_z}$ ,  $\pm 200 - 400\%$  (Appendix I).

they take predominately positive values at the inner vortex. Under the presence of deposits the negative values in the outer region increase substantially, particularly in case C, and those at the centre drop from cases A to B and C. Figure 25 presents a comparable range and evolution in the Reynolds stresses observed in Scales I and II. In this case,  $\overline{u_r u_\theta}$  shows a distinct maximum in the outer part, beyond the minimum axial velocity ( $r \sim 0.45R$  in Figure 25b), which is absent in Scale I. Similarly to the normal stress, in Scale II all the Reynolds stresses increase approaching the near wall region.

Figure 26 shows that Scale III presents Reynolds stresses ten times higher than those in Scale II. All show a comparable increase in the near wall region and despite the large measurement uncertainty, a similar  $\overline{u_r u_z}$  and  $\overline{u_r u_\theta}$  radial evolution.  $\overline{u_z u_\theta}$  also presents a similar development characterised by maximum positive values in the outer region and a transition to negative within the jet, Figure 26 a, but in this case they turn positive again within the core, which is perhaps linked to forced vortex.

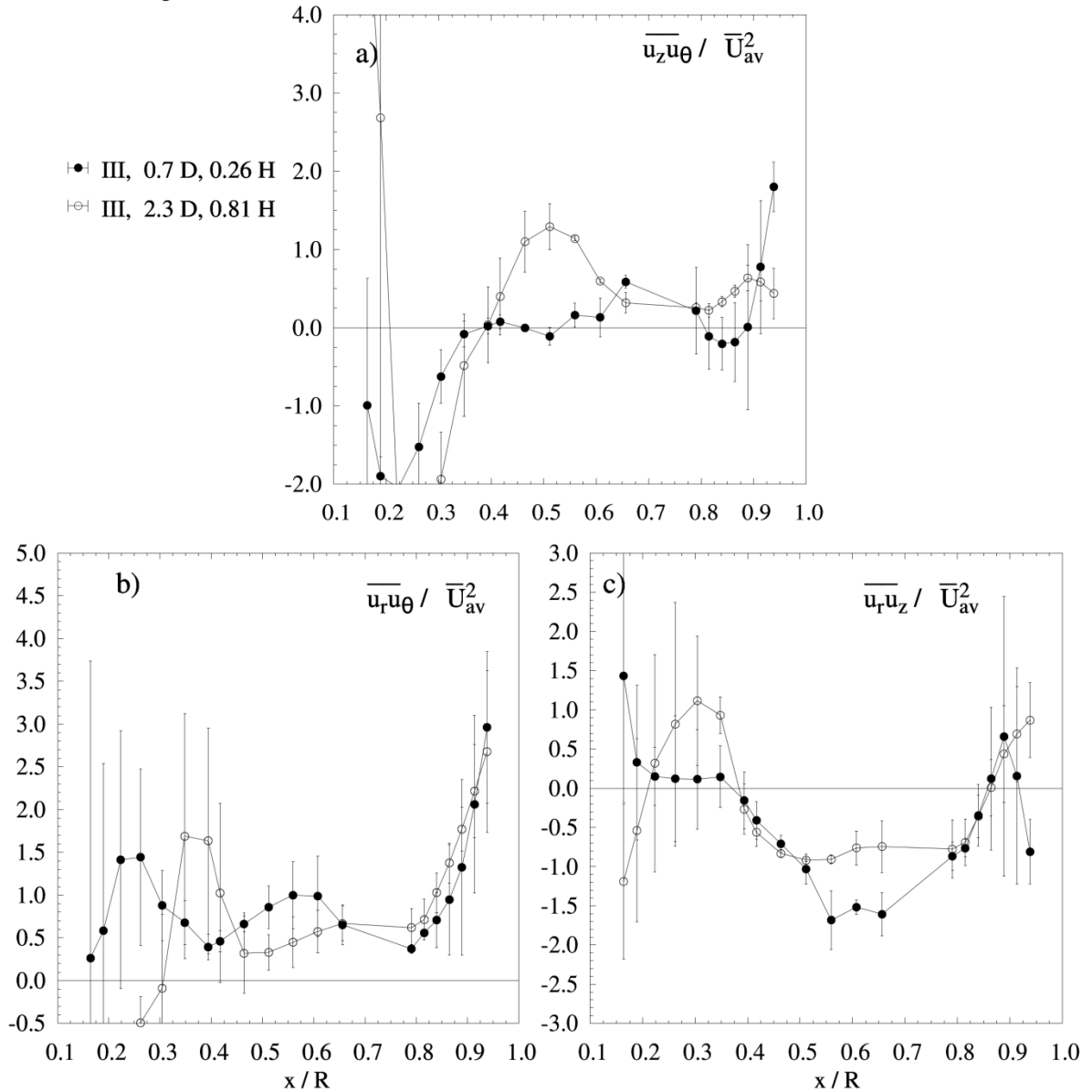
### 3.2.3. Periodical phenomena.

The use of sonic anemometry responds to the requirements of a large scale, and it does not focus in obtaining a large time resolution to characterise fast fluctuations. However, analysis of velocity signal allows one to detect periodicity at different time scales. In the case of cleaned walls, these included a periodical flow structure at constant  $St \approx 1.4 - 1.5$  within the cylinder (Chapter II) and large amplitude oscillations at the top jet, in the order of  $0.2 - 0.3 \text{ Hz}$ . The presence of a similar oscillation in Scales II and III is shown in Figure 28 by the time series of the tangential velocity observed at the jet.

Figures 27 and 29 describe the time scales contained in the signal for cases B and C by superimposing the periodogram obtained from a Fast Fourier Transform (*FFT*) of the velocity signal at all radial profiles. Figure 25 shows a similar large amplitude oscillation at the top centre for all cases in Scale I. This behaviour is well documented in spray dryers and cyclones, and detailed by authors such as by Usui *et al.* (1985) or Kieviet *et al.* (1997) or Southwell and Langrish (2001). The exception is case C in Scale I, where despite the presence of the *VBD* the oscillation is lost, perhaps due to a lower time resolution.

In addition, the higher frequency oscillation observed in case A at the cylinder, prevails in cases B and C for all levels below the *VBD*. In case C, the comparison at different *Re* shows a similar linear variation between  $f$  and  $\overline{U_{av}}$  than in case A. This is interesting, for the flow conserves the operation at the same *St* number despite the large differences in the velocity profiles and the turbulence field. No significant oscillations of this type can be appreciated at any position of Scales II and III.



10.  $\overline{u_i u_j} / \overline{U_{av}^2}$ 

**Figure 26.** The development of Reynolds stresses in Scale III. Operating  $Re$  Operating  $Re$ ,  $Re_2 = 1.5 \cdot 10^5$  for Scale I and  $Re_4 = 4.9 \cdot 10^5$  for Scale III (Chapter I). a)  $\overline{u_z u_\theta}$  b)  $\overline{u_r u_\theta}$  c)  $\overline{u_r u_z}$ . Data are normalized by  $\overline{U_{av}^2}$ . Error bars indicate the variation across tangential locations. Maximum uncertainty ranges in  $\overline{u_z u_\theta} - 23, +19\%$ ,  $\overline{u_r u_\theta} \pm 100\%$ ,  $\overline{u_r u_z} \pm 200 - 400\%$  (Appendix I).

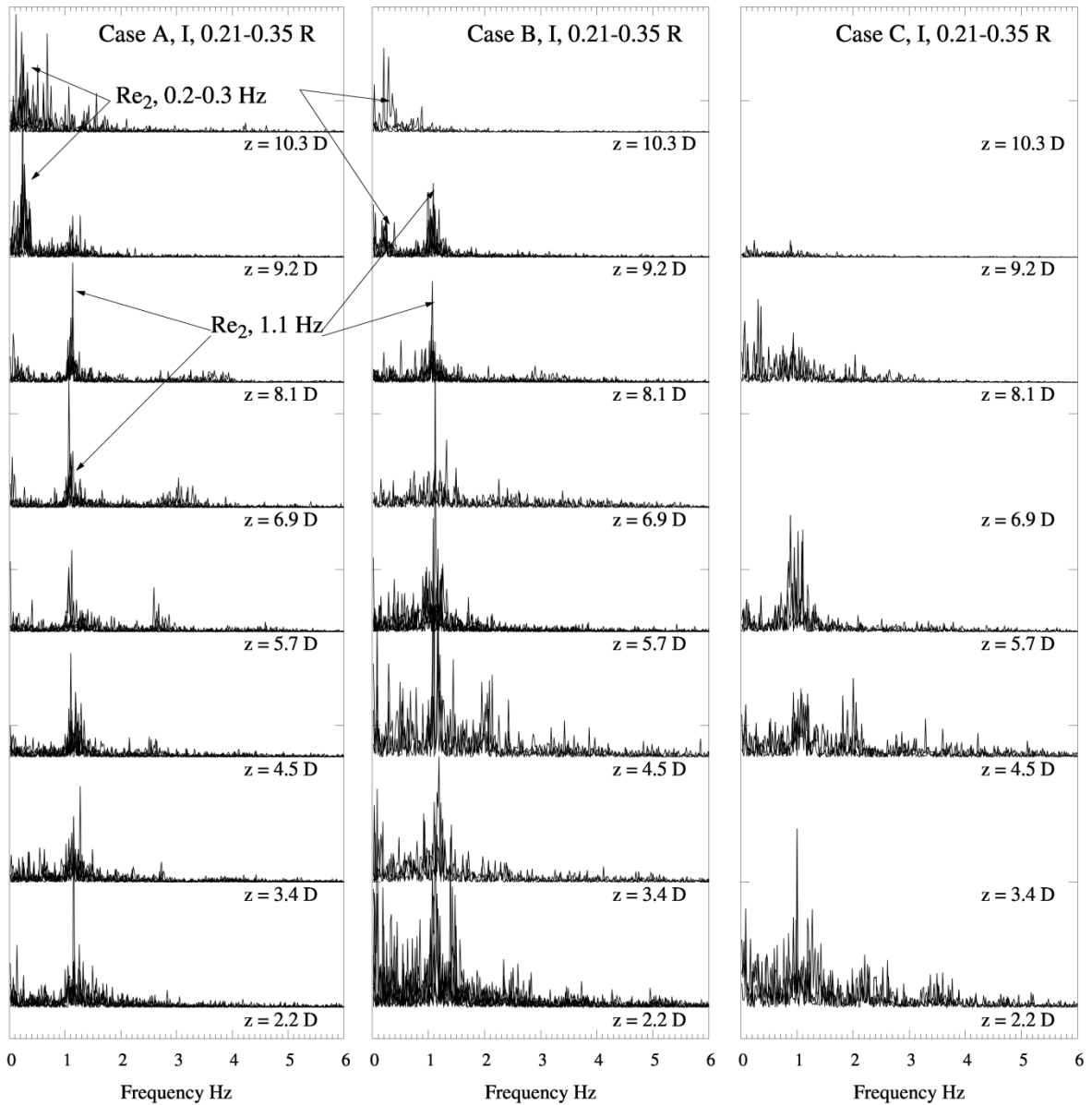


**Figure 27.** Analysis of the impact of friction in the periodical flow structures in the vortex. Periodogram of  $U$  for all the levels at the transition region between the outer and inner vortices.  $0.10 R < r < 0.35 R$ . Arbitrary y units in a linear scale. From left to right, cases A, B and C, at  $Re_2 = 1.5 \cdot 10^5$  in Table 2.

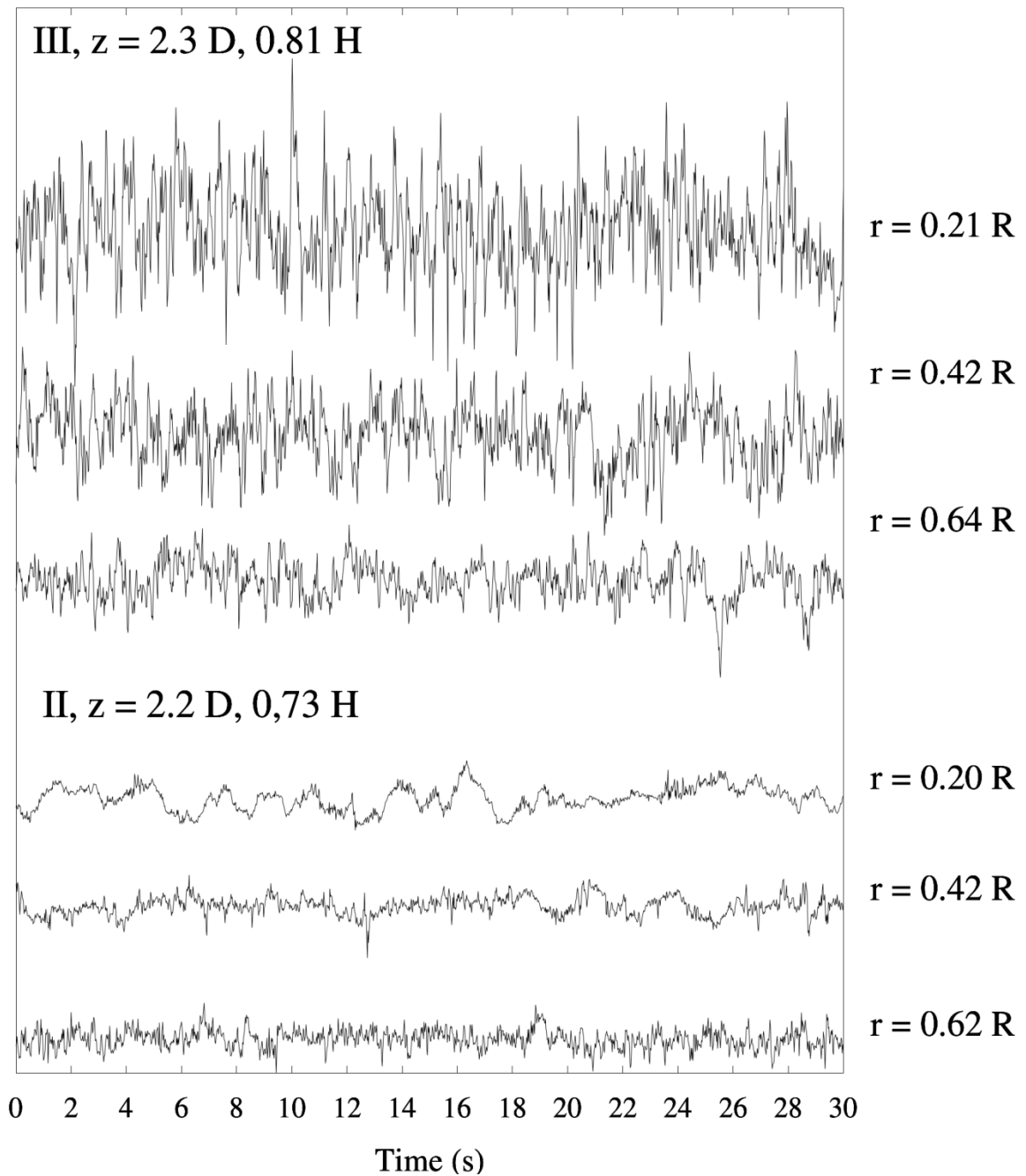


**Figure 28.** Times series for  $U_\theta$  at different locations in Scales II and III (Chapter I);  $y$  units in a common linear scale.

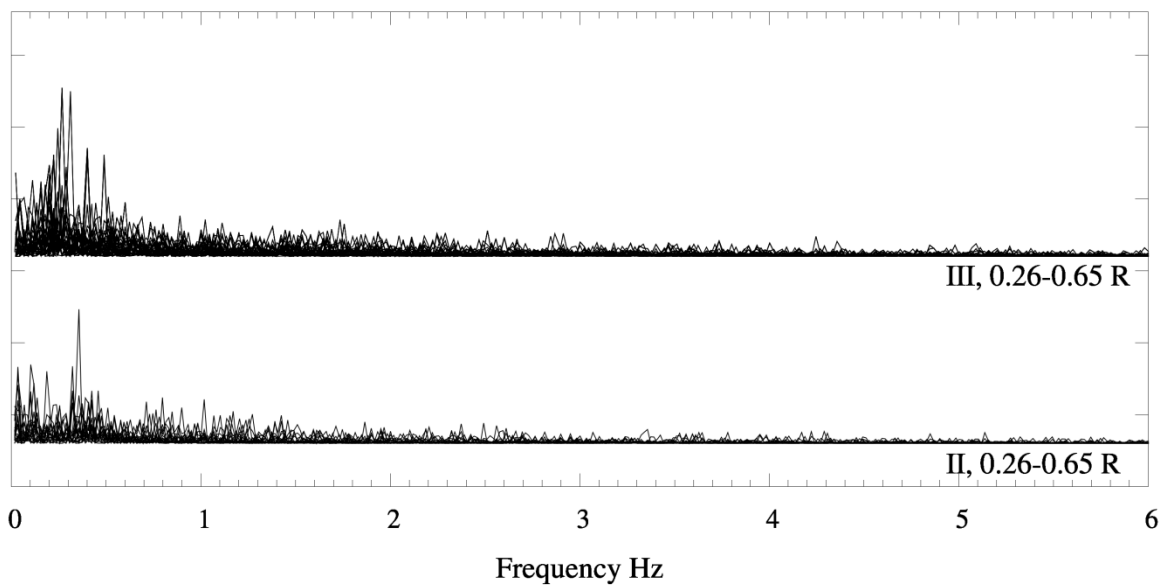


**Figure 29.** Analysis of the impact of the operation regime in the periodical flow structures in the vortex Periodogram of  $U$  for all heights at the transition region. Arbitrary  $y$  units in a linear scale. Top to bottom, Scales II and III for  $Re_4 = 6.8 \cdot 10^5$  and  $Re_5 = 4.9 \cdot 10^5$  respectively, see Table 2

## Conclusions

This work reports the response of the air fluid dynamics in counter-current spray dryers to the relevant operation ranges of  $Re$ ,  $\Omega$  and conditions of the walls observed during the manufacture of detergent powders. The following general conclusions may be summarized:

**a) Wall friction:** It has been studied for (a) a thin particulate layer present on the walls, (b) standard conditions showing uniform bands or (c) heavily built up walls with thick patches. Deposits cause an obvious increase in friction. This modifies the rate of decay of the air swirl intensity  $\Omega$ , from 0.08 in reasonably clean walls to 0.20 as a function of the wall coverage and the deposits thickness, and causes a substantial transfer of energy from the convective flow to the turbulence kinetic energy,  $\kappa$ , which rises up to 67 – 88% in the presence of deposits. The decay rates and the vortex shape is independent of  $Re$  for  $Re > 1.27 \cdot 10^5$ , believed an indication of operation in a fully rough regime.

**b) Recirculation:** Instability arises as a result of the  $\Omega$  that prevails in the cylinder. This responds to the influence of the wall and the design in the pressure field. A transition between different operation regimes has been identified for a single unit, and across scales for a constant exit contraction ratio of  $d/D \sim 0.30$ . In systems where a low  $\Omega$  prevails at the top,  $\Omega_e < \sim 1$  a) the vortex breakdown,  $VBD$ , occurs within the cylindrical chamber and this forms a central recirculation zone,  $CRZ$ , at the bottom of a larger extension and strength for decreasing  $\Omega_e$  and b) a central jet is formed at levels sufficiently close to the exit. When the swirl intensity rises to  $\Omega_e > \sim 1$ , the acceleration caused by the contraction increases the velocities in the chamber, which a) suppresses the  $VBD$  and the  $CRZ$  and b) extends the central jet across the entire unit. A further increase to  $\Omega_e > \sim 2.4$  causes another substantial rise in velocities, so that a stronger jet cohabits with higher centrifugal forces. In these circumstances, the recirculation region formed at the bottom extends beyond the influence of the vortex finder and takes an annular shape that envelops the jet. This transition illustrates the relevance of  $\Omega$  as scaling criteria. It is not possible to predict the flow field in a counter-current dryer on the basis of geometry alone: one needs to consider the swirl decay across the chamber. This can be done by the usage of the inlet parameters defined in this thesis and the correlations given for the relevant  $Re$  and as a function of the actual coverage and thickness  $\delta/D$  of deposits in industry.

**c) Turbulence:** The turbulent kinetic energy,  $\kappa$ , and all normal stresses are in the one hand correlated  $\Omega$ , and in the other respond to the friction. Wall deposits modify both, the values and the evolution

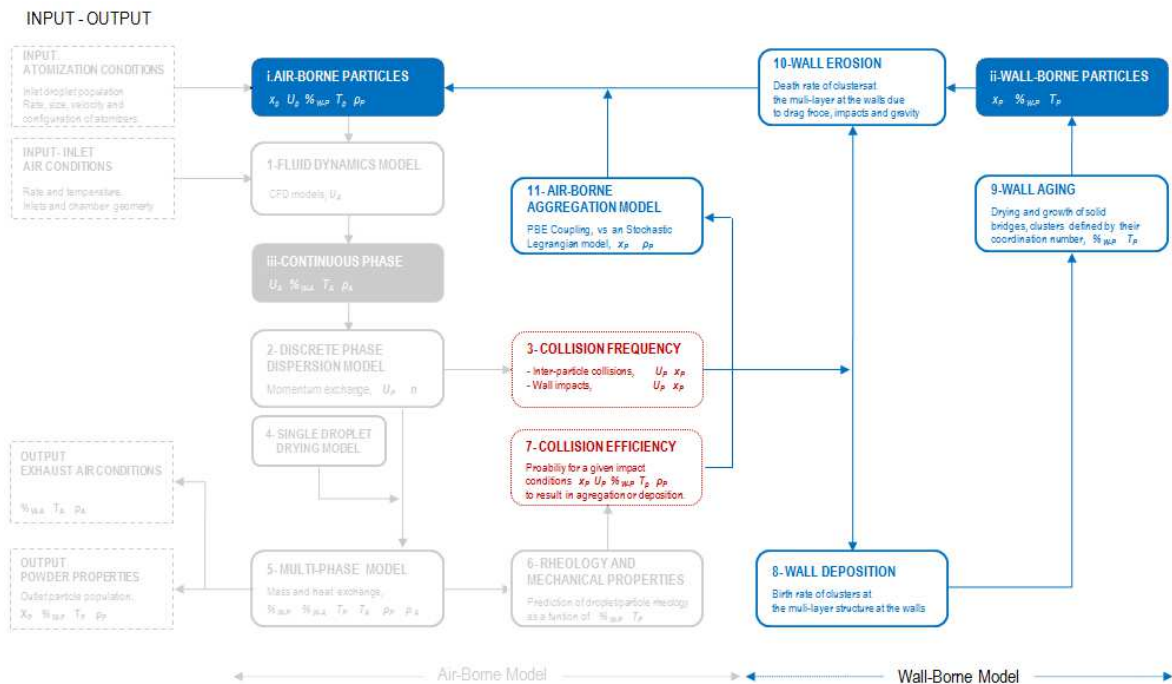
across the chamber. Typical deposits thickness and coverage increases  $\kappa$  up to 67 – 88 % versus the use of cleaned walls. The distribution of Reynolds stresses follows the different flow structures, what may serve as a guide to assess the performance of common closure models. A low frequency oscillation prevails at the top of the dryer for all scales, perhaps as an indication of the precession of the vortex core, *PVC*. Interestingly, the higher frequencies oscillations at a constant *St* number appear only in Scale I, independently on  $\Omega$  and the vortex breakdown, but are lost at the largest units of shorted aspect ratio.



# PART B

## CHAPTER IV

### THE DISCRETE PHASE: AGGLOMERATION TOWER SUBDIVISION AND MEASUREMENT



## Summary

Part B of this thesis is concerned with particle dynamics in swirl counter current spray dryers, in particular the identification of growth mechanisms. This chapter provides a general outline of the interactions expected. Section 1 discusses briefly some of the work in literature, for the most part focused on sprays, co-current dryers and agglomeration devices. The different numerical and experimental approaches used to describe interactions are explained and the current issues and how to apply the knowledge from other fields to swirl counter-current detergent dryers are discussed. Section 2 describes the operation and design of the dryer used for the experiments. Section 3 describes how particles are dispersed in these units and accordingly, proposes a subdivision of the chamber into regions where different types of interactions can be anticipated. Section 4 provides a general outline of the measurement methodology and the set of reference techniques used to characterise the operation and the product in each experiment.

## 1. Particle growth in swirl counter-current spray dryers.

In a dryer droplets come into contact at different drying stages, and upon collision they form aggregates, which determine many of the product properties, from size to porosity or density. Huntington (2004) lays down a detailed description of the manufacture of detergent in P&G towers, and stresses that agglomeration is a key area of work to optimise production. Growth results from the action of different interactions forces as aggregates are formed within the spray or by collision of semi-dried droplets in the air or at the walls. Accordingly, Huntington (2004) lists four types of possible contacts in a swirl tower:

**H1-** Droplet/droplet contacts near a slurry nozzle.

**H2-** Droplet/droplet or droplet-particle contacts when the jets of several sprays overlap.

**H3-** Droplet/particle contacts resulting from different free falling velocities and drying rates of different sized particles. They occur close to the wall and near the spray due to the elutriation of fines.

**H4-** Semi-dried particle / semi-dried particle contacts. These also respond to the differences in the free falling velocities but involve larger and drier particles at the bottom sections of the unit.

The contacts of type **H2** are likely to occur in the largest units, which place multiple nozzles at the same level. This is left out of the scope of this work, focused in a tower with a single nozzle per level. The contacts **H1**, **H3** and **H4** are reviewed in section 1.2 as air-borne growth sources, they are delimited in section 3.2 to given regions of the tower and quantified in Chapter VI as function of a) nozzle position b) production rate and drying environment, and linked to the c) air operation conditions in the Appendix III. The contacts denoted **H3** also respond to the recirculation of particles up and down the chamber when atomizers are placed at various levels. This is studied in detail in Chapter VI.

The wall is ignored in most agglomeration processes. It is not included in the analysis of contact forces for the chemical, food and detergent industries (e.g. Palzer 2011) nor has been mentioned as a growth source in detergent swirl spray dryers. Huntington (2004) links growth to particle contacts in the air: *"...the majority of the agglomeration still occurs in the flowing air patterns rather than onto and off the tower walls..."*. For decades, it was the belief that the material worn off the wall included only very large pieces and that the wall had no significant effect in the process overall. Huntington (2004) acknowledges deposition, but suggests that, *"If gross agglomeration does occur on the tower walls then this product will generally be removed in the post-tower processing, and not affect the product quality"*.

The work reported in Chapter V demonstrates this is not the case and leads to a change in the view of the process, where wall fouling has a central role. To the analysis of contacts given earlier one must include the history of deposits and distinguish between wall-borne and air-borne growth sources.

### 1.1. Wall-borne growth processes.

Deposition is very significant in swirl detergent spray dryers. It is localised mainly near the sprays where wet and large deformable droplets collide with the wall at high momentum. These contacts have been visualized recently in the experiments of Hassall (2011) using Particle Image Velocimetry, *PIV*. They show how clusters form a multi-layer at the wall where particles lock, roll, break-up and occasionally become re-entrained (see Figure 1a, Hassall 2011). Impacts include high velocity wet droplets coming from the spray and collisions of different sized particles at a lower inertia (see Figure 1b).

Chapter V reports the first experimental evidence of fouling having a major impact in the overall dynamics of a dryer. It describes how wall impacts cause a dynamic equilibrium between deposition and re-entrainment by use of a tracer to track the material that is worn off. Quantification of the rate and time scale of these processes demonstrates that deposits renew continuously. A large proportion of the product comprises of re-entrained material which has experienced a higher residence time as a result of having dried at the walls. It is thus incontrovertible that fouling modifies particle drying kinetics and growth. Different wear mechanics have been identified and characterised by their time scale. This is

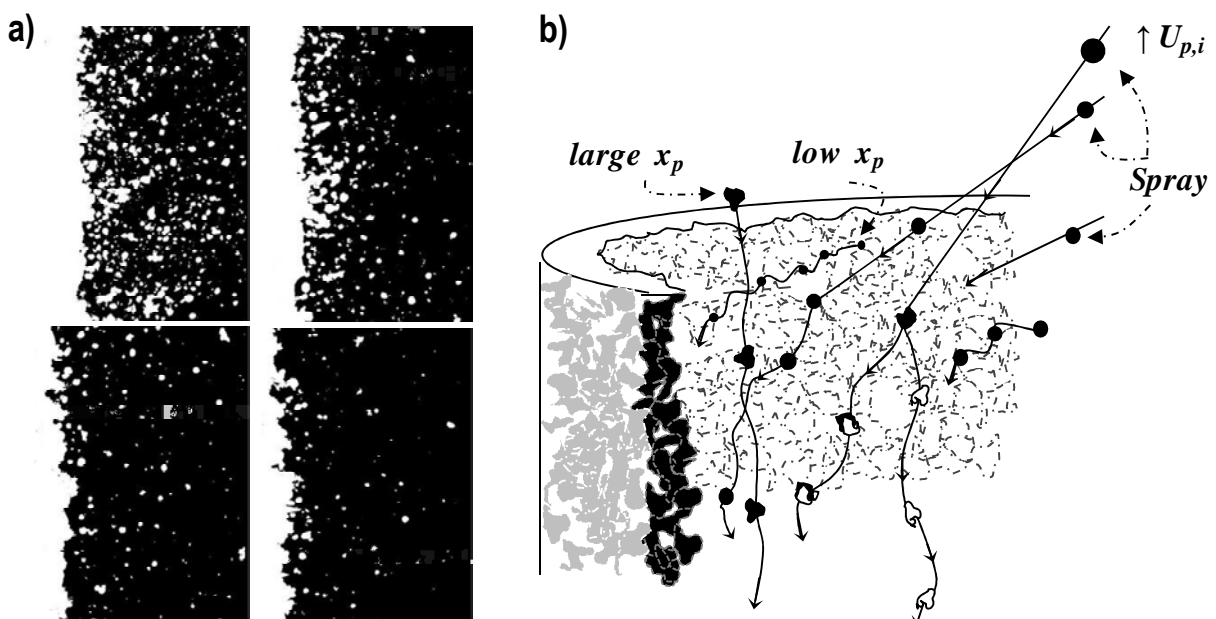


**Figure 1.** a) PIV visualization of the wall deposits (cross section, wall in the left, reproduced from Hassall 2011) b) Illustration of wall impacts from different sized particles  $x_p$  at high velocity  $U_{p,i}$  from the spray or free falling at  $U_{p,t}$

explained in detail in Chapter V. In essence, the difference between the size of the droplets that are deposited and the clusters that are re-entrained causes a net growth rate at the wall. This process is driven by the microstructure of multi-layers such as those in Figure 1a: how the forces evolve as the particles dry and sinter, and how drag, gravity and impacts break the deposits into fragments.

## **1.2. Air-borne growth processes.**

The available work usually targets contact of particles in the flowing air. Growth is a desired feature of many processes and adhesion forces must be incremented to promote it. This is done in granulation, fluid bed agglomeration and most other devices by the addition of some sort of binder to a solid substrate that causes the formation of liquid bridges between particles. Many different interactions can take place depending upon the industrial application. Palzer (2011) provides a general study, distinguishing between hydrophobic / hydrophilic and amorphous / crystalline materials. He describes how temperature determines the viscosity of amorphous hydrophilic substances and how their microstructure is affected when they become plasticised by the absorption of a binder. This is also a typical case in the spray drying of foods that undergo transition through a glassy state. In this context, a certain amount of growth is desired to control the final product size. As described by Williams *et al.* (2009) the fine fractions are in fact injected back to promote the growth in different patented designs.

In counter-current units, agglomeration is often considered as undesirable because it limits capacity by producing too coarse a product. But in fact, a lack of it can generate large elutriation rates and have a similar effect. According to Huntington (2004) growth has rather to be controlled. Due to the large experimental costs, numerical models are crucial to optimize the process. A general description of the architecture is given in the Introduction of this thesis. In relation to growth, a numerical model first needs to predict 1- how particles come together, 2- which are their properties at contact and 3- which is the outcome. The following sections 1.2.1, 1.2.2 and 1.2.3 present the numerical alternatives used to describe them across different processes and how the knowledge obtained from studies on sprays, co-current dryers etc. could be reapplied for detergent manufacture.

### **1.2.1. Eulerian-Lagrangian approaches.**

These are widely applied to the context of sprays. They treat the air flow field as a continuum, i.e. Eulerian, and the particle phase in a discrete manner, i.e. as Lagrangian. Subramaniam (2013) provides a recent review in the case of combustors. Describing how the droplets interact requires first the

prediction of dispersion and from there, using a mathematical model to compute the rate of collisions  $r_c$ . Sommerfeld (2001) introduced the use of a collision frequency or probability. He describes a stochastic model to account for collisions in a turbulent flow. It is derived from the kinetic theory (Rüger *et al.* 2000) and given in (1) as the collision frequency,  $\phi$ , for particle of a size class  $i$ , with all others,  $m$ .

$$\phi^i = \sum_{j=1}^{j=m} \frac{\pi}{4} (x_{p,i} - x_{p,j})^2 |U_{p,i} - U_{p,j}| n_j \quad (1)$$

where  $x_p$ ,  $U_p$ , and  $n$  denote respectively particle size, velocity and concentration. Authors such as Nidjam *et al.* (2006) have used similar frequencies to the description of coalescence in a spray, comparing them to an Eulerian-Eulerian approach, described later. These type of models lead to implementation of a stochastic aggregation rate in a larger fluid dynamics framework. To date, this has been made in co-current (e.g. Verdurmen *et al.* 2004, Guo *et al.* 2004 or Mezhericher *et al.* 2012) or counter-current units (e.g. Zbiciński and Zietara 2004), but with little application. Among the issues, one can identify particle contact mechanics. They require detailed knowledge of the material properties because the outcome of each collision has to be retrieved from a contact model as a function of the impact velocity and the droplet mechanical properties. This remains a very complex subject because the material deformation and the forces established between semi-dried drops are extremely difficult to replicate experimentally at a lab scale. In a swirl counter current tower, one should add the large computational expense. First, it is difficult to track dispersion in such a large volume where anisotropy and vortex instabilities have an important contribution to the mixing. Secondly, it is a challenge to have sufficient resolution (i.e. parcels and number of size bins) to predict how particles accumulate near the wall, with sufficient detail and with mesh independence.

### 1.2.2. Eulerian-Eulerian approaches.

In an Eulerian-Eulerian model the generalised transport equation of the solid phase describes how the particle size distribution function, denoted  $f$ , evolves across the chamber. It is given in (2) with the assumption of steady state and no breakage terms for simplicity (taken from Silva *et al.* 2008). The term in the left hand side describes the dispersion of the solids and the term in the right the birth and death terms in different particle sizes (i.e. the change in the particle size distribution field,  $f$ , due to growth).

$$\nabla_{\mathbf{x}} \cdot [\mathbf{u}_p f(v, \mathbf{x})] = \frac{1}{2} \int_0^v \beta_{(v-\xi, \xi, \mathbf{x})} f(\xi, \mathbf{x}) f(v-\xi, \mathbf{x}) d\xi - \int_0^\infty \beta_{(v, \xi, \mathbf{x})} f(v, \mathbf{x}) f(\xi, \mathbf{x}) d\xi \quad (2)$$

where  $\mathbf{X}$  are the spatial coordinates,  $f_{(v,x)}$  the size distribution field of particles of volume  $v$ ,  $\mathbf{u}_p$  the particle velocity field, and  $\beta$  the aggregation rate kernel, or aggregation frequency.

In most cases all the collisions can be assumed to result in growth, or at least the particle properties do not vary in time or in space (e.g. the binder properties in a granulator) what makes all collisions between partners of the same size to have the same probability to result in growth, denoted collision efficiency  $\epsilon$ . In these cases, the kernels reported,  $\beta$ , includes the effect of both the collision rate,  $r_c$ , dependent on dispersion, and the efficiency,  $\epsilon$ , dependent also on particle properties.

In other units the solid phase changes drastically, such in the case of drying droplets. Here it is useful to express the aggregation rate,  $r_a$ , as a function of  $r_c$  and  $\epsilon$ . Let us use as an example the well-known work of Tan (2004) in fluidised bed melt granulation. The use of population balance equation *PBE* such as (2) assumes particle interactions are a second order process. Tan *et al.* (2004, 2006) use this condition to define  $r_a$  and  $r_c$  in (3) and (4).  $\epsilon$  is then derived in (5) as a function of time to predict how the properties of the binder, and thus the aggregation kinetics changes. Tan *et al.* (2004, 2006) could derive a full expression for  $C_{i,j}$  in (6) on the basis of the kinetic theory of granular flow and separate the effects from dispersion and the material properties in the kernel.

$$r_{a,i,j} = \beta_{i,j} n_i n_j \quad (3) \qquad r_{c,i,j} = C_{i,j} n_i n_j \quad (4)$$

$$\epsilon_{(x,v)} = \frac{r_{a(x,v,\dots)}}{r_{c(x,v,\dots)}} \quad (5) \qquad \beta_{(i,j)} = C_{(i,j)} \epsilon_{(i,j)} \quad (6)$$

This type of theoretical model is very useful because it reveals the link between the growth kinetics and measurable physical magnitudes. However they require a simplified system, and are rarely applicable in real processes. In industry, growth models can be derived semi-empirically using experimental data to fit the parameters in specific cases. This helps reducing the experimentation costs, but loses ability to move between different designs and formulas.

The approach taken by Tan (2004) may also serve to study spray dryers. The birth and death terms in (2) could be rewritten as a function of the frequency and efficiency of the collisions. Unfortunately, the functional forms of  $C$  and  $\epsilon$  are not a constant in the dryer and they vary spatially. The discrimination between different types of contacts made by Huntington (2004) and other authors corresponds to the shape that these functions take at different sections. In a tower,  $r_c$  changes because the relation

between particle velocity,  $U_p$ , and size,  $x_p$ , varies from the spray zone, dominated by the initial inertia, to regions where the particles are free falling. In addition,  $\epsilon$  also changes from one to another location depending on droplet water content,  $X_w$  and mechanical properties such as viscosity  $\mu_p$ . Both decrease as particles dry, impacts become elastic and aggregation ceases.

Indeed, this makes a full resolution of (2) very complicated, but instead opens the opportunity to solve very large systems looking only at the birth and death terms in relevant regions (see section 3.2). Experimental data can allow one to determine the growth kinetics associated to each type of contact at a given zone of the dryer, so that one can connect several, for instance sprays, to predict the behaviour of very large units. These are currently impossible to be dealt with by an Eulerian-Lagrangian model.

### 1.2.3. Contact and adhesion forces

The adhesion forces generated in many agglomeration processes have a capillary (liquid bridges) or a viscous origin (solid bridges). Palzer (2011) links the adhesion of sticky particles to the surface viscosity; the contact angle of the liquid-solid system; the surface tension of the liquid at the surface and the impact contact time and kinetic energy. He mentions that in a spray dryer aggregates can form by an initially large viscoelastic deformation and then the rapid sintering of amorphous substances, which can later evolve to form solid bridges as the particles dry. The general morphologies observed throughout this work support this description. Figure 2 shows a couple of examples and Appendix II provides a more detailed analysis of structure. Palzer (2011) notices how the bridges develop only for a given range of viscosities. As drying progresses the decrease in the droplet viscosity and contact time reduces the diameter of the viscous bridge formed in the impact, and more contacts result in rebound.

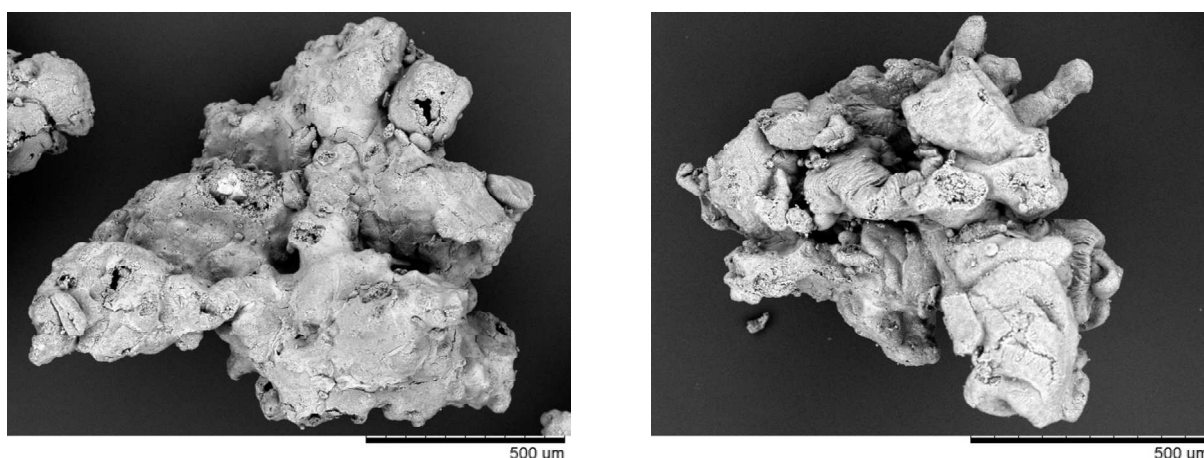


**Figure 2.** Typical morphology for spray dried detergent granules, under the formulation used in this work and the operation conditions described in Part B of this thesis. Photographs show images under Scanning Electron Microscopy.

Measurement of the relevant properties is an issue. Contact models make use single droplet physical magnitudes, available for the characterization of the slurry or the dry powder, but very difficult to obtain in a semi-dried states. Bhandar *et al.* (1997) discusses the issues in measurement of “stickiness” and the characterization of adhesion in spray drying of sugars. Boonyai *et al.* (2004) review the many attempts to describe it experimentally. For instance Adhikari *et al.* (2003) or Werner *et al.* (2007) worked with drying droplets and describe how stickiness evolves, defined as a pull up force in a tack probe.

Surface viscosity is usually used as a threshold for aggregation. Palzer (2009) or Palzer (2011) suggest that in general, values  $< 10^8 Pa.s$  cause spray dried water soluble substances to become “sticky” and cause growth. Most of the work at real scales is focused on co-current dryers, particularly in foods. Palzer (2005) and Palzer (2009) link material properties such as shear viscosity, complex viscosity or the glass transition temperature of amorphous substances to the effects in agglomeration, and Palzer *et al.* (2012) studied the relation to the formation of particle structure and density. Adhikari *et al.* (2004) or Gianfrancesco *et al.* 2009 provide some examples of using the glass transition temperature as a way to establish growth criteria and give thresholds for particles in certain parts of a dryer to become “sticky”.

Detergents are a particularly complex case. The slurries contain surfactant/s, polymers, inorganic salts and water soluble substances, so that both hydrophilic and hydrophobic interactions are present. In this case, the rapid dehydration results in both amorphous and crystalline structures to be present in the product. In this case only some of the components show a transition through a glass state; this could not could not identified in the analysis of the final product. The complexity of these slurries does not permit to use a similar treatment to the examples mentioned above where the glass transition temperature serves as a clear indicator of the tendency of the droplets to aggregate. In a detergent context, the mechanical properties of the droplets owe to a large extent to their content in un-dissolved solids and the evolution of the surfactant/s microstructure during drying, which remains a complex area of study.

Fully coupled numerical spray drying models usually simplify these contacts and consider the impact of viscoelastic drops. Verdumen *et al.* (2004) first discriminated between different drying stages by the Ohnesorge number,  $Oh^2$ , i.e. the relative strength of surface tension to viscous forces. A numerical description of the inter-penetration of two viscous spheres was given by Hoeven (2010), but this type of impacts only begin to be studied experimental by the collision maps built with single drops by Kuschel and Sommerfeld (2013), and the subsequent improved model of Focke *et al.* (2013).

To sum up, available contact models are either prepared for the stochastic or kinetic description, and could apply to certain regions of the tower: as a few examples one can list 1- coalescence of wet droplets, dependent on surface tension and momentum, described by Qian and Law (1997), Post and Abraham (2002) and recently reviewed by Liao and Lucas (2010), 2- formation of liquid bridges (e.g. Simmons 1995) 3- inter-penetration when both partners are considered viscous drops (e.g. Hoeven 2008 or Focke *et al.*, 2013) or 4- sintering in case of sufficient contact time, for instance at the wall (e.g. Seville *et al.*, 1998 or Palzer 2005); one can also implement 5- the use of a capture probability (e.g. Podvysotsky and Shraiber 1984, Dubrovskiy *et al.*, 1992), or a similar Eulerian treatment to the spray zone in wet granulation: 6- nucleation regimes (e.g. Iveson *et al.* 2001; Hapgood *et al.*, 2003) 7- coverage ratios (i.e. Kariuki *et al.*, 2013), or 8- collisions of coated deformable granules (Liu *et al.*, 2000). The last provided a kinetic description of liquid bridges and the widely used Stokes viscous and deformation numbers. In a detergent dryer, these are only applicable to describe contacts of coated dry particles. It is very important to notice that the semi-dried drops develop the opposite structure: a soft wet core encapsulated by a porous hard crust (Hecht and King 2000 or Handscomb *et al.*, 2009). In this case, the effect of the viscoelasticity in particle deformation and sintering is more complex.

## 2. Operation of the detergent slurry lines.

The experimentation to study the operation and particle dynamics in the dryer was conducted in a single industrial counter current tower, property of Procter & Gamble, Scale I (Part A, Chapter I). Figure 3 provides a general outline including the slurry line and the position of all the slurry nozzles.

In all cases the same standard detergent formulation was used, containing a solid phase and aqueous and organic liquid phases, obtained by the addition of surfactant/s, polymer/s and inorganic salts resulting in solids overall content between 30 – 60 % in mass. The slurry is prepared in a batch mixer [2] in Figure 3, denoted crutcher. A larger mixer or homogenizer, denoted drop tank in [3], serves for the transition to a continuous operation. The slurry is pumped at a low pressure in [5] from the drop tank into a hammer mill [6] to break the lumps and avoid damage and blockages downstream. In [7] the slurry is brought to a high pressure and directed in [8] to the atomizers inside the unit. Atomization is performed via a swirl pressure nozzle that provides a hollow cone pattern, located at the centre of the dryer at different axial levels and facing downwards. The reader is referred to Huntington (2004) for a detailed description of the nozzle designs. The same nozzle has been used in all cases, i.e. the same type and size of the tip, chamber and number of swirl injectors into the nozzle chamber.

### 3. Particle dynamics.

#### 3.1. Dispersion of the sprays.

Figure 4 illustrates initial trajectories for droplets of different sizes. These are based on the wall deposition rates reported in Part B and a numerical model that makes use of the experimental velocities in Part A, developed in collaboration with Imperial College London. Both agree with the well-established experience in the company in relation to the flow visualization, and numerical modelling of the sprays. The spray/s and the hot air come into contact in the cylindrical chamber. After atomization, fine droplets are elutriated upwards. Depending on their response time, they can either 1- exit the unit with the exhaust air and be collected in the cyclones, or 2- if sufficiently large, acquire enough centrifugal inertia to migrate to the wall and enter the boundary layer. At the reference conditions of Chapter V the elutriates possess a median mass size of  $x_{p,50} \sim 155 \mu\text{m}$  and a wide range ( $x_{p,90} \approx 310 \mu\text{m}$ ).

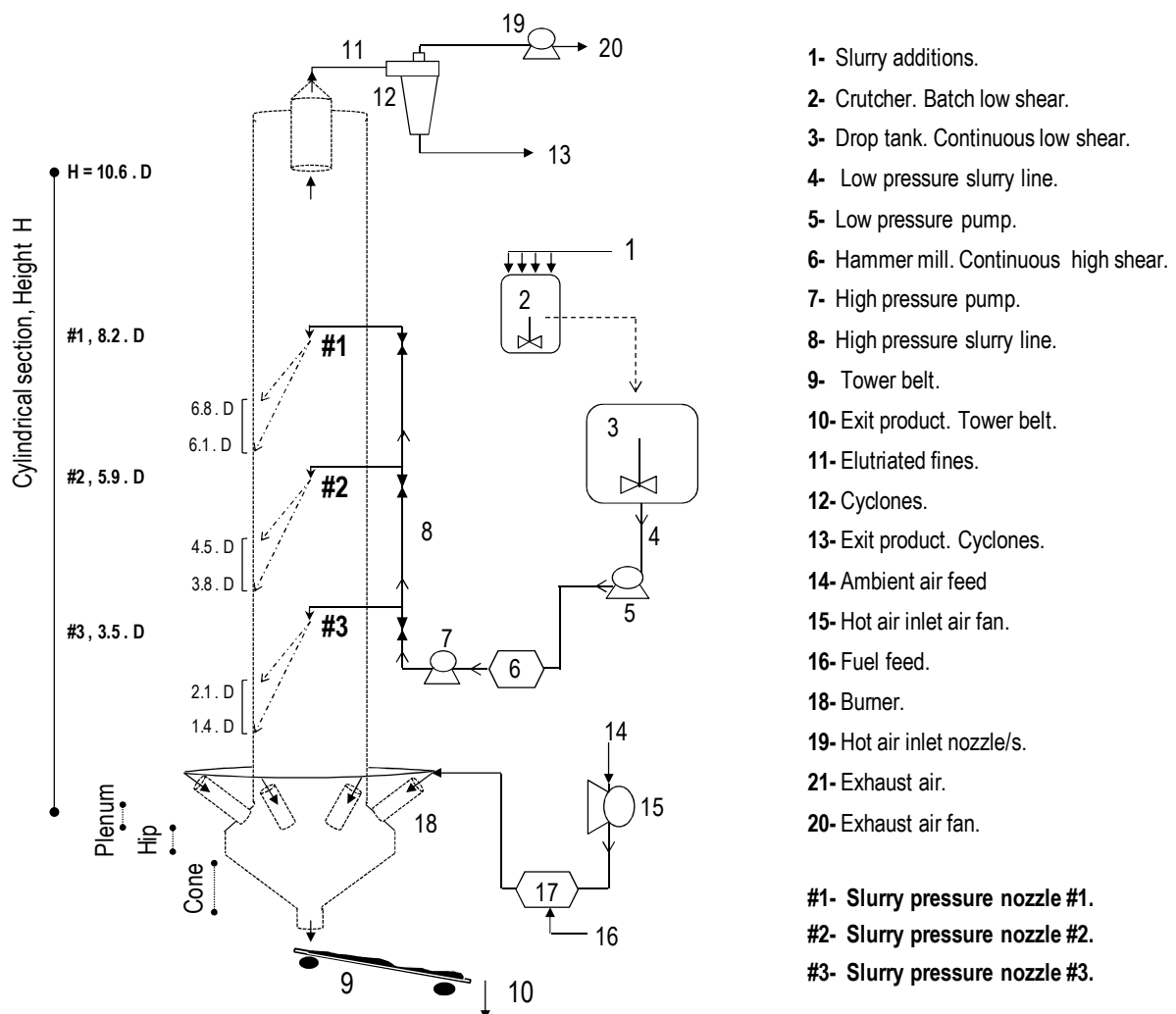


**Figure 3.** General outline of operation of a counter-current spray drying tower. Nomenclature, hot air generation, slurry preparation and atomization lines, including the location of nozzles and the projection area of the sprays at the walls.

In general terms most of the powder flows down as a bulk. As it dries it undergoes multiple wall impacts in similar way to the patterns observed in a cyclone. The spray initially disperse the drops outwards, and as they become entrained in the swirl they approach their terminal velocity, denoted  $U_{p,t}$  (i.e. the free falling or sedimentation velocity is the axial component of  $U_{p,t}$ , denoted  $U_{p,SD}$ ). Due to the swirl, most of the product concentrates near the wall where it causes deposition, and flows down to exit from the bottom end into the tower belt [9] in Figure 3.

The largest drops maintain a high momentum from atomization and barely modify their initial trajectory before colliding to the wall for the first time. One can depict in Figure 3 the area of projection upon the wall according to the spray angle and its hollow cone pattern. Intermediate sizes are more sensitive to drag and become partially entrained before reaching the wall at positions above this projection. A part of the elutriated powder, typically the fractions  $> 80 - 150 \mu m$  can reach the wall above the nozzle.

### 3.2. Tower subdivision

Due to the complexities described, growth is poorly understood and often treated as a “black box”. In order to obtain a workable description one needs to simplify the process and identify the governing contacts. One can find useful to partition the unit in regions where a dominant type of impact can be anticipated so that one can design experiments to isolate their contribution to the process. At first this is done on theoretical bases, and once data are available, numerical models could provide further support. The framework described in the initial introduction needs to be built up from bottom to top, increasing in complexity. The different sub-models given need to be validated independently. A couple of examples: 1- Single droplet drying models must be validated with single droplet experimentation (i.e. drying curves or levitators) or in systems where deposition or aggregation are absent, or 2- A sub-model describing the wall dynamics should not be fitted indirectly to overall product properties, but gain validation from experimental re-entrainment rates, such as those in Chapter V. It should be stressed that an independent validation of each block is the only way for large numerical models to be meaningful. Figure 4 subdivides a spray drying tower into:

- 1- Wall Region-**WR**.
- 2- Nozzle Region-**NR**, comprised of:
  - Nozzle Inertial Region-**NIR**.
  - Nozzle Terminal Region-**NTR**.

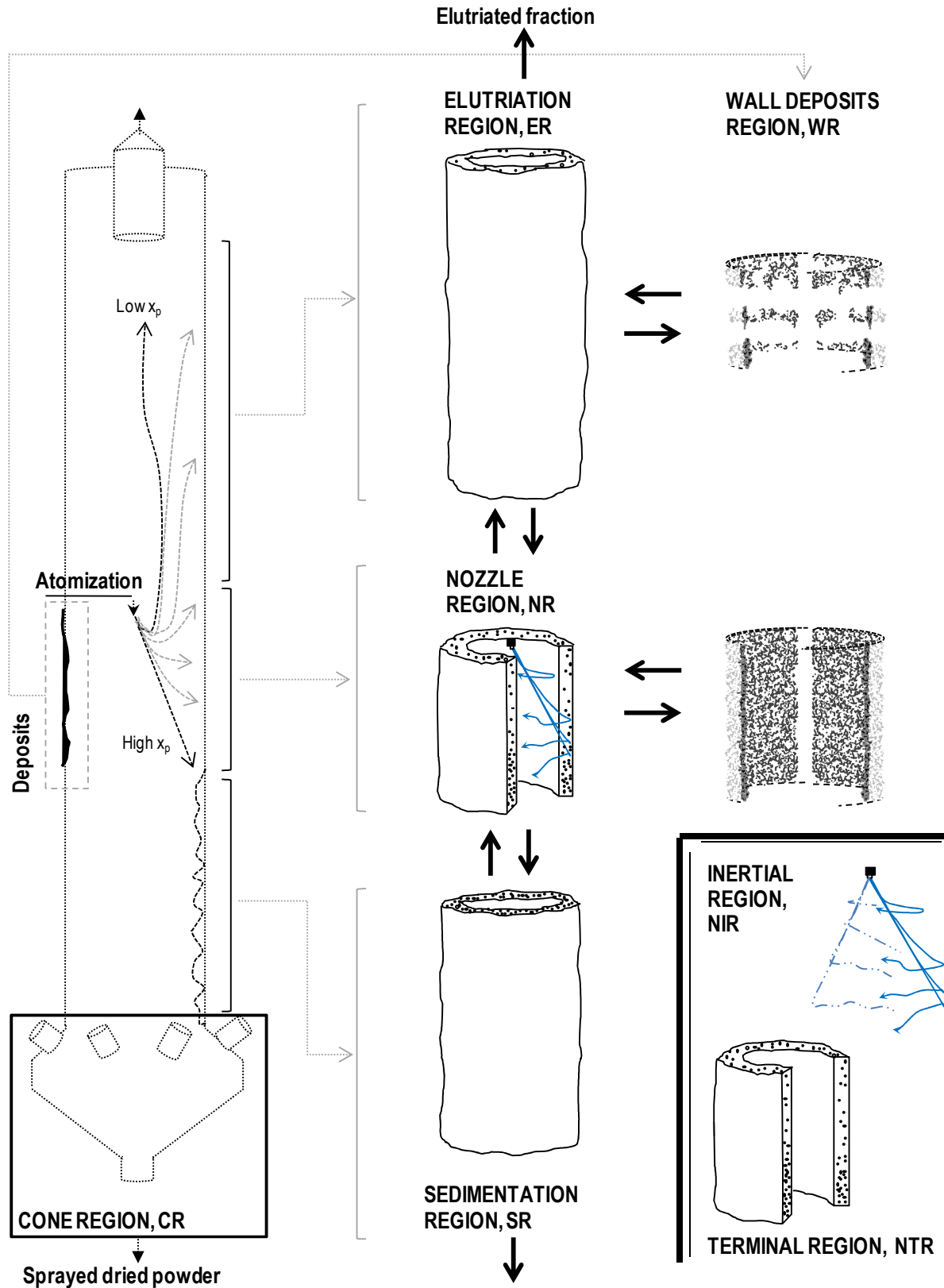


**Figure 4.** Illustration of the spray dispersion in a counter-current spray drying tower. Left : trajectories as a function of droplet size  $x_p$  from smallest to largest values. Right : subdivision of the cylindrical chamber into 1- the wall deposits region-WR, 2- the high velocity spray, Nozzle Inertial Region- NIR, and a concentrated annular region above it: Elutriation Region - ER, across it: Nozzle Terminal Region- NTR, or below it: Sedimentation Region- SR, and 3- the exit section: Cone Region- CR.

3- Sedimentation region/s **-SR**.

4- Elutriation region/s **-ER**.

4- Cone region **-CR**.

The experiments of Hassall (2011) identified that the tower can be split into two zones, the majority of the cross section has a sparse concentration of particles apart from an annular region close to the tower wall where most of the product accumulates and flows down, see later Figure 6a.

Axially, one can define *ER* and *SR* above and below the nozzle. Here particle motion responds to the drag and the turbulence and may be treated as a Markov process (i.e. terminal velocity,  $U_{p,t}$  owing exclusively to size,  $x_p$ , and density,  $\rho_p$ , with no history effect). This condition is key to simplify a kinetic description: when particles grow their velocity is a size / density function. This is not the case in sprays: when new droplets are formed the origin needs to be tracked in a momentum balance between different size classes (e.g. Nidjam *et al.* 2006).

Aggregation in *ER* is due to the stagnation of fines product near the wall. The collisions involve low relative impact velocities, driven by the different size of the particle ( $< 1 \text{ m/s}$ ) and a moderate water content,  $X_w$ , because the fine drops dry rapidly nearby the nozzle (see Chapter VI). Below it, in *SR*,  $n$  increases drastically and the contacts happen at higher velocities owing to the larger differences in size ( $< 2 \text{ m/s}$ ). The contact between semi-dried particles might lead to certain growth in the part closer to the nozzle. However, as the solids move down the unit, they enter regions of higher air temperature,  $T_A$ , and velocity,  $U_A$ . This increases  $n$  further but inhibits growth because  $X_w$  reduces rapidly. Below the cylinder, in *CR*, the particle growth is expected to be negligible because the product is dry and in occasions at its boiling temperature  $T_{Boil}$ .

As oppose to co-current units, in a counter-current tower it is very important to recognise the effect of accumulation. Particles of a given range of size,  $x_p$ , and density,  $\rho_p$ , tend to stagnation (i.e. axial drag balanced by weight). This occurs nearby the wall and generates regions of increasing  $n$ . The solids eventually flow down forming a similar annular concentrated region to that reported by positron emission particle tracking in CBF cyclones (Chan *et al.* 2009). Four related processes prevent the accumulation and explain how the solids hold up near the wall are carried to the bottom exit: 1- the decrease in the air velocity  $U_A$  as particles enter the turbulent boundary layer, 2- as the solid concentrate, they grow and the sedimentation velocity,  $U_{p,sd}$ , increases, 3- the local high  $n$  disrupts

the air flow near the wall and causes the product to flow down as a bulk (i.e. this is often reported as drop in the effective drag coefficient), and 4- turbophoresis ejects particles from the stagnation region and causes recirculation. The accumulation occurs in the entire chamber but involves solids of different size according to the different air velocity  $U_A$  faced at different levels.

Clearly, whenever the stagnation is significant within the nozzle region,  $NR$ , it must have a major impact on the aggregation rate. The nozzle region,  $NR$  has been defined as the volume of the projection of the spray cone, see Figure 4. Within it, two droplet/particle populations are distinguished:

***NIR***: The inertial spray region extends from the nozzle to the wall and contains the recently sprayed droplets whose motion is strongly dependent on history. Drag makes them to be entrained in the swirl and approach the wall, showing a different deceleration depending on their size. In this case (i.e. one central nozzle aligned down) the region of high velocity extends all the way up to the wall, where most droplets collide before having reached their terminal state. The initial wall impact velocity can be estimated for a single  $400 \mu m$  droplet approximately  $\approx 10 m/s$ .

***NTR***: The non-inertial population, free falling particles, concentrates only near the wall. It comprises of droplets that flow up or down, and includes an influx from  $SR$  and  $ER$ . Figure 4 and Chapter V describe a single nozzle, where the recirculation from  $SR$  is very restricted. Chapter VI shows how if multiple sprays are used the elutriation from low sprays has a much more significant effect.

The most relevant sources of growth must be originated in both of these areas because the contacts occur at the highest relative velocities and droplet deformability. Three sources can be distinguished:

- **Aggregation in *NTR***. Similar in all concepts to the interactions in the upper part of  $SR$ .
- **Coalescence in *NIR***. Drag is a function of the droplet size and this results in high relative velocities generated in the spray ( $< 20 m/s$ ). They are responsible of a “scrubbing effect”. Figure 5 illustrates how large droplets, less affected by drag pick up smaller sizes that tend to concentrate. This represents the origin of the coalescence near the spray (e.g. Post and Abraham 2002 or Rürger *et al.* 2000) and the contact H1 described by Huntington (2004). It occurs only nearby the atomizer because the spray dilutes rapidly as it moves towards the wall.
- **Interaction between *NIR* – *NTR***. Drops at high velocity  $U_p$  from the spray do not coalesce far from the nozzle because they are too dilute, but when reaching the wall they cruise across an annular region of high  $n$ , illustrated in Figure 6. The high relative velocity originated, the high  $X_w$

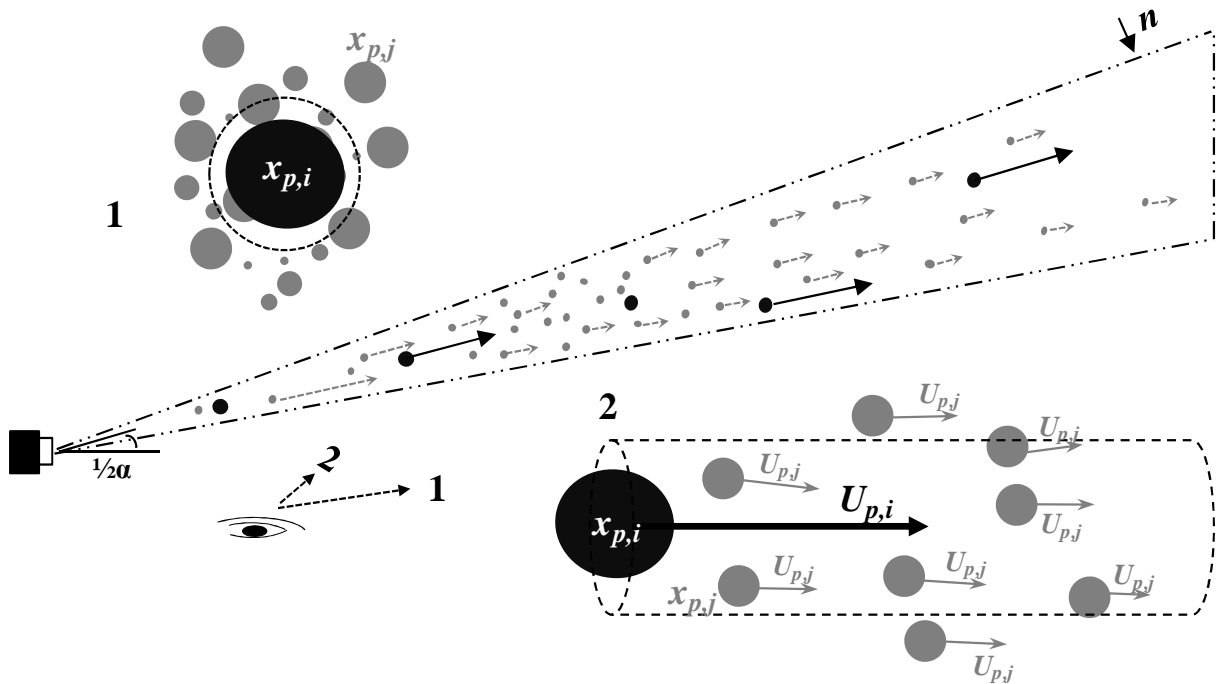


**Figure 5.** Coalescence near the nozzle in *NIR* due the pick-up effect of different sized droplets. Views show particle size classes  $x_{p,i}$  and  $x_{p,j}$ . Views 1 and 2 show respectively the projection along the droplet velocity,  $U_{p,i}$  and the perpendicular. Dotted line shows the collision area used in (1) for the calculation of a collision frequency between two sizes.

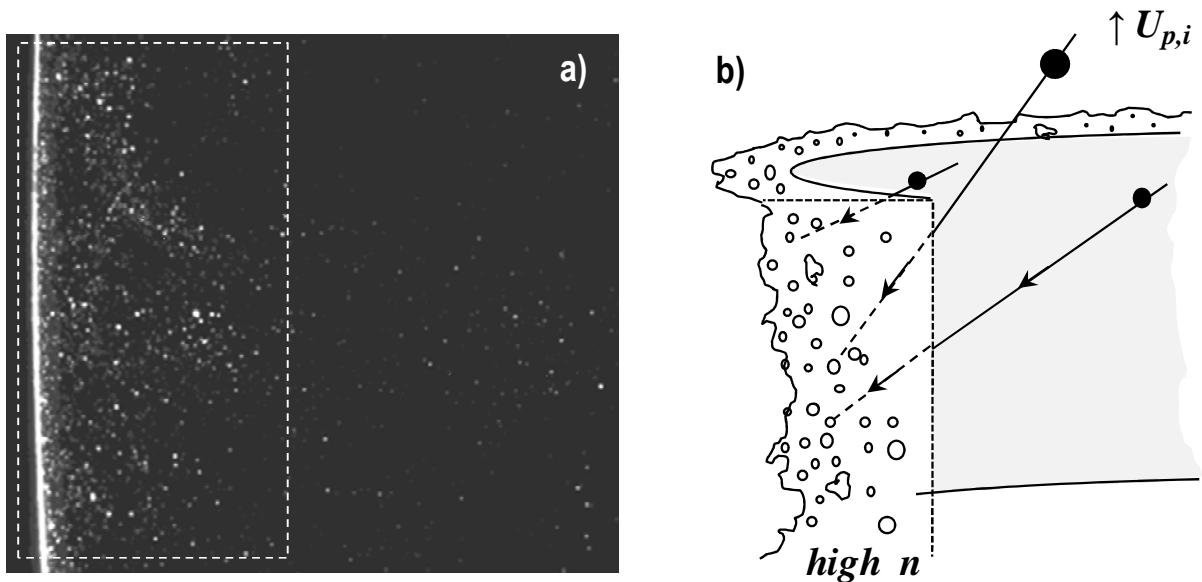


**Figure 6.** a) PIV visualization of the concentrated annulus in the near wall region. (reproduced with permission from Hassall (2011); b) Illustration of the interaction between the high velocity droplets,  $\uparrow U_{p,i}$ , coming from the atomizer, *NIR*, moving across the high concentration region near the wall, *NTR*.

of one partner and the high  $n$  of the other ensure that these are very likely to be the main source of aggregation in the air. They correspond to the contact H3 in Huntington (2004) and brings into contact the spray with drier product close to the wall. This contains material recently sprayed but also the re-entrainment from the deposits and the product that was dispersed upwards and then recirculated back down. Clearly, the  $n$  driven in  $NTR$  by an adequate selection of the nozzle position (Chapter VI) and the air inlet conditions (Appendix III) must be key to control the growth.

As a passing note, it could be argued that high velocity droplets that pick up small particles in Figure 6b, would in essence end up impacting the wall, causing deposition, wear or both. In this way, the size and structure of the aggregates that may be re-entrained later must be ultimately governed by the interaction with the multi-layer, and be less sensitive to any previous contacts in the air. If this argument was validated experimentally, it could simplify the unit description and allow combining the outer annulus in Figure 4 with  $WR$ . Similarly to a boundary layer approach to cyclones (e.g. Kim and Lee 2001), one may be able to describe a large dryer using a 3D numerical flow model only to determine how the spray disperses particles into the near wall region, where a separate 1D kinetic model can take over.

When various sprays are used the flux between the different  $NR$  becomes important. The study of a multi-level system and the contribution of recirculation is given in Chapter VI. This is extremely relevant because it enables the description of very large towers and different nozzle configurations in a modular manner (i.e. connecting sub-models for each region in Figure 4 and accounting for an interaction term).

#### **4. Methodology and Measurement.**

##### **4.1. Slurry properties and atomization.**

The initial slurry properties were characterised by measurement of the shear viscosity and the storage and loss moduli in an oscillatory test with a cup and bowl rheometer (TA Instruments Ltd. AR2000 ex). The impact of the rheology and the slurry microstructure in atomization is discussed in Chapter VI.

The droplet size from the nozzle was obtained using an external rig which replicates the atomization conditions in the unit, using the same nozzle at controlled temperature and mass rate. Several sprays from 1 – 2 s in duration serve to measure the spray angle and the pattern by image analysis. The averaged droplet size distributions are obtained using laser diffraction (Malvern Spraytec Particle Sizer, RTSizer 5.6). The data are averaged over the period when the atomization develops and constant angle and pressures are achieved. Measurements are taken at a sufficient distant from the nozzle to ensure

primary atomization is completed.

#### 4.2. Product properties.

Samples were taken when steady state operation is achieved (see section 4.3.3).

The elutriation rate was measured collecting the entire stream exiting the cyclones in [13] in Figure 3. Given the smaller range, particle size was measured in selected cases with laser diffraction method (Sympatec GmbH HELOS/BR – Rodox, Lenses R2, R4 R7). The product was sampled at the exit of the tower belt [10] in Figure 3. At least ten consecutive  $> 1 \text{ kg}$  samples were taken in  $30 \text{ min}$  collecting the full stream. They were sealed, sampled down and used for the analysis of particle size by sieving with the Taylor series. Comparison with image analysis sizing tools discounted breakage effects (Retsch Technology, Camsizer P4). During the same period a bulk powder sample,  $> 15 - 20 \text{ kg}$  was obtained by blending consecutive samples from [10]. It was sealed and within the next  $< 4 \text{ h}$  sieved manually into 11 classes with the use of large screens (Russell Finex Model 17240). Each fraction was then sealed and later used for the analysis of particle structure, porosity, and composition.

Water and surfactant/s contents,  $X_w$  and  $X_s$ , were analysed with a Toledo Mettler Moisture Balance, and analytical titrations, ensuring respectively errors  $< 10 \%$  and  $3 \%$  for the target values. The equilibrium relative humidity,  $erH$ , was measured with Rotronic HygroLab 3 (probes AW-DIO).

Morphology was studied under optical microscopy (Leica MZ16 A) and Scanning Electron Microscopy (Hitachi TM1000). The reconstruction of porosity in the product was obtained by measurement of the absolute,  $\rho_{abs}$ , and envelope particle densities,  $\rho_{env}$ , of the size classes. This was done making use of He pycnometry (Micromeritics, AccuPyc II 1340) and Hg porosimetry (Micromeritics, Autopore IV) respectively. Appendix II discusses the structure of aggregates. Other methods such as compaction or  $N_2$  adsorption have been used for similar detergent granules to provide values of  $\rho_{abs}$  and  $\rho_{env}$ . However, compaction at  $636 \text{ MPa}$  did not appear to be able to reduce the porosity of a tablet to zero, and gave an unreliable estimate of  $\rho_{abs}$ . Due the large range of pore sizes observed in the aggregates one needs to move into using Hg porosimetry. The use of narrow size classes samples facilitates the separation of inter-particle voids from intra-particle porosity,  $\varepsilon$ , in the intrusion of Hg. The estimation of  $\varepsilon$  is defined below upon the particle  $\rho_{abs}$  and the estimate of  $\rho_{env}$  for a given pore size threshold.

$$\varepsilon(\%) = \left(1 - \frac{\rho_{env}}{\rho_{abs}}\right) \cdot 100 \quad (7)$$

### 4.3. The drying chamber.

Huntington (2004) recognises that measurement of any of the properties of the solids, such as  $n$ ,  $x_p$  or  $U_p$ , inside a dryer is a challenge. The application of optical diagnostics suffers from high  $T_A$  and the tendency for deposition makes very difficult to install any probe inside the unit. In addition, sampling of a representative set of droplets or semi-dried particles is also extremely difficult, particularly because this type of dryers present diameters and height are in the order of meters and tens of meters.

Zbicinski *et al.* (2002a, 2002b) discuss these issues and proposes a sampling arrangement where the measurement of  $T_A$  and air humidity,  $rH_A$ , is obtained by the suction of the air outside of the chamber and the separation of the solids. Measurements with a similar probe have been conducted in this unit but they are found time consuming and difficult to interpret due to a) an obscure definition of the measurement region 2) different particle response times to the suction and c) cooling within the probe.

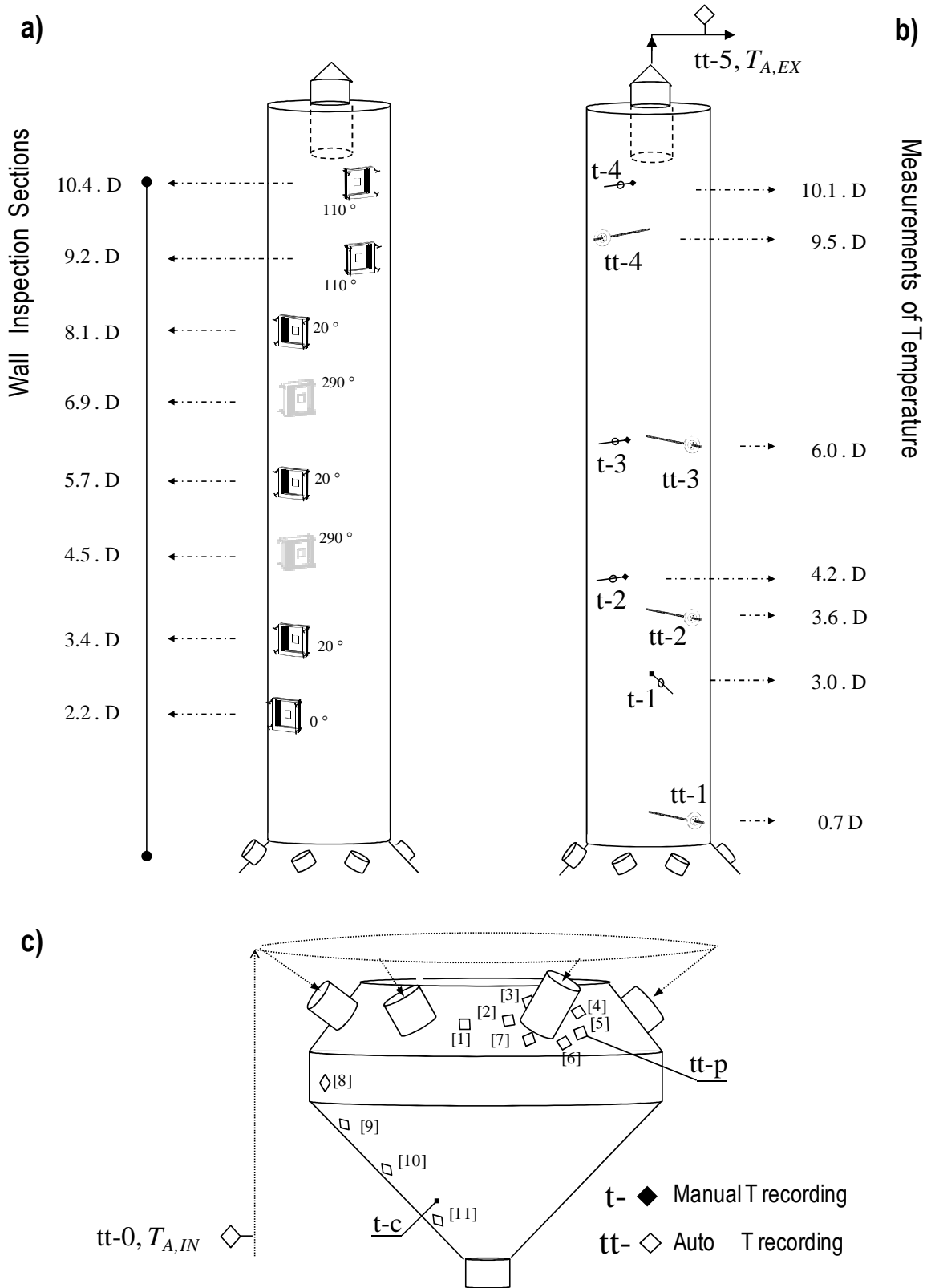
One needs also considering that experiments in large dryers are very expensive; they need to minimise the raw material costs and be fitted in the schedule of production units. Consider that a comprehensive data set implies long experimental plans and in many occasions this is the reason for them to be dropped in benefit of empirical studies. In part, this explains why data in relation to drying profiles or particle dispersion are very rare. Any indication in large towers is extremely helpful, but need to be gathered with a minimum production time. With this in mind, this thesis limits measurements inside the chamber to deposition rates at the walls, indicative of dispersion, and the air temperature field. Figure 7 depicts the location of the inspection areas and the temperature sensors at the walls and inside the unit.

#### 4.3.1. Wall deposition.

The initial net deposition rate,  $r_{d,o}$ , is indicative of the rate of impacts at the wall. It has been measured at the accesses depicted in Figure 7. In similar fashion to the procedures described in co-current units (e.g. Ozmen and Langrish 2003 or Kota and Langrish 2006). These areas are cleaned, and the deposits generated over periods of 10 – 15 *min* are photographed and collected to be weighted. Chapter V describes the used of an extractable plate flushed with the wall to study how the deposition rate evolves.

#### 4.3.2. Temperatures.

Air temperature,  $T_A$ , was monitored automatically by calibrated instruments at the inlet,  $tt - 0$ , and exhaust air lines,  $tt - 5$ . Inside the chamber  $T_A$  was tracked simultaneously by placing K-type



[1]-to[7] measure  $T_w$  and  $T_A$  near inlet, averaged as tt-p.

[8] to [11] measure  $T_w$  only.

**Figure 7.** Measurements in the dryer: location of a) Inspection areas of the walls, and b) Air temperature,  $T_A$  sensors in the cylinder and exhaust line, and c)  $T_A$  sensors at the inlet line and the bottom section, and sensors at the dryer walls,  $T_w$ .

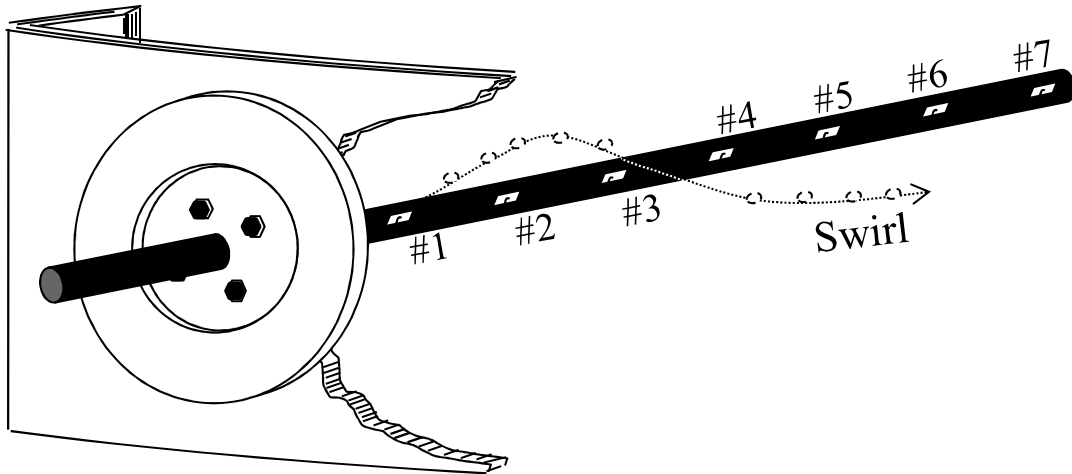


**Figure 8.** Detail of the arrangement of the thermocouples in a metallic hollow bar for the measurement of air temperature inside some areas of the dryer.

thermocouples at the positions depicted. Four hollow metallic bars are aligned with the radius at different levels. Figure 8 illustrates the device used. The bars expose thermocouples in their interior to the air at seven small rectangular openings. In agreement with the assertion of Huntington (2004), deposition in the sensors could be avoided by aligning the openings in the shadow of the swirl and sufficiently far from the projection of the sprays where  $U_p$  drops and particles are sufficiently dry (i.e.  $> 2 - 3 D$  below the atomizer in this case). In positions closer to the nozzle, deposition and condensation was observed on the bars, causing readings to become unreliable. The data obtained in this way have been compared to the exhaust temperature,  $T_{A,Ex}$  ( $tt - 5$ ) in the absence of particles, and working at the relevant range of  $T_A$  and humidity  $rH_A$ . They showed good agreement ( $< 2^\circ\text{C}$ ).

An extra series of measurements is obtained manually using single thermocouples at the locations depicted; and recording the range of variation of  $T_A$  along the radius.

#### 4.3.3. Start up and operation.

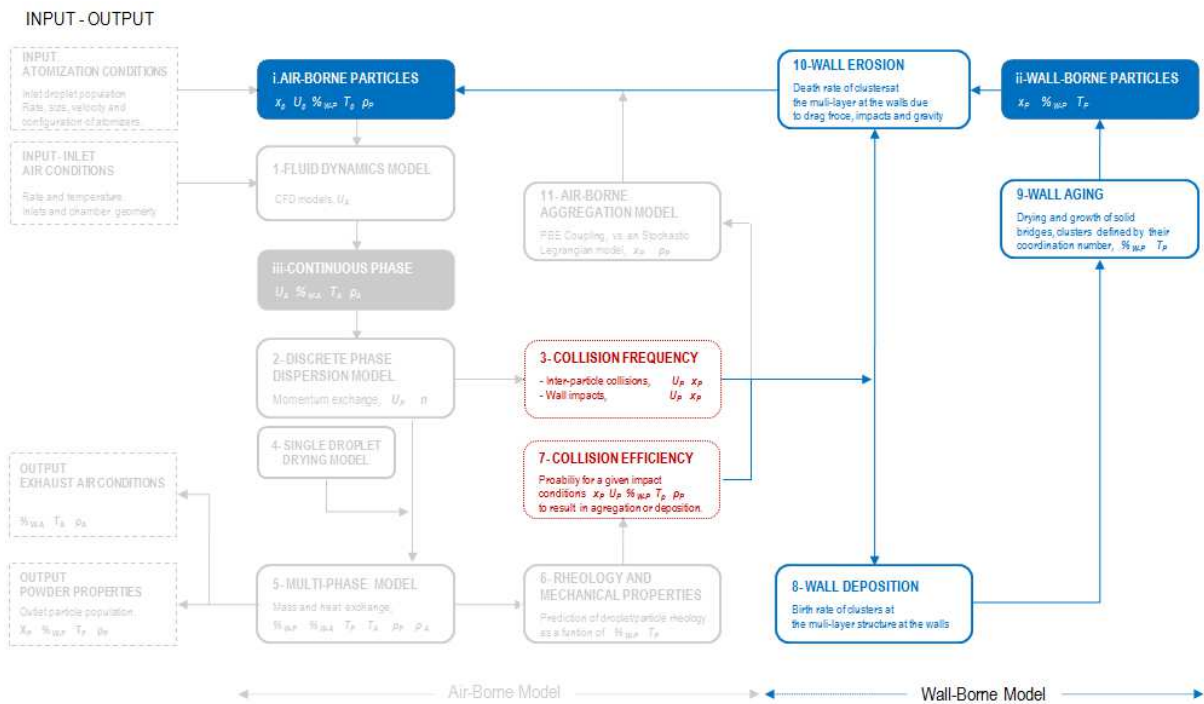
Before the production of powder commences, the burner and inlet air fan in Figure 3 are started and hot air is blown into the dryer. The inlet air rate and temperature,  $M_A$  and  $T_{A,IN}$ , are increased to heat up the unit and then the atomization of slurry begins. At a first stage this leads to insufficient drying and wet powder exits at the tower belt [10] in Figure 3.  $M_A$  and  $T_{A,IN}$  are progressively increased either to the target value, or until the product shows a given water content,  $X_w$ . These are defined according to product stability and flow ability, and discussed further in the data given in Chapter VI and Appendix III.

One cannot afford to operate these units for many hours to assess when the product properties have reached a constant. The start-up period needs to be shortened by using the wall temperature,  $T_{Wall}$ , as a control tool. At steady state one must observe a constant heat loss rate out of the dryer, or in other words, a constant dryer temperature. As  $T_{A,IN}$  is stepwise increased,  $T_{Wall}$  in all positions shown in Figure 7 shows an initial rise and asymptotic behaviour thereafter. This is associated with the energy required to heat up the unit. At full scale this can be fairly slow but failing to recognise it leads to a large error when performing energy balances. Sampling and all averaged measurements were conducted after  $T_{Wall}$  shows a reasonably constant value ( $< 0.5 \text{ }^\circ\text{C}/\text{min}$ ). This ensured that  $X_W$  remains constant and does not decrease with production time as it would if the dryer was being heated.

# PART B1

## CHAPTER V

### A TRACER ANALYSIS : DYNAMIC EQUILIBIRUM OF DEPOSITION AND WEAR



## Summary

This chapter studies the kinetics of deposition and re-entrainment of material from the walls of swirl detergent counter-current spray dryers, making use of Scale I, described in Chapters I and IV.

Identification of the aggregates that are originated from re-suspension of deposits at the walls shows that remarkably,  $> 12 - 20\%$  by mass of the full production is in fact re-entrained material. As a result of going through the wall particle residence times are 10 to 100 times higher than the reports in literature for the trajectories in the flowing air. This constitutes an unexpected and important result and has a major impact in the description of the process. Furthermore, the role of re-entrainment is particularly important in growth and the formation of the largest particles which are aggregates of atomized droplets and re-entrained material. This work shows that wall-borne processes are critical in defining the product attributes and must be addressed in numerical models of these systems.

A description of the micro-mechanics of the deposition, aging and re-entrainment processes has been proposed including shedding and breakage events and dry and wet mechanisms of erosion caused by particle impacts, which according to the data are the main responsible of causing the re-entrainment.

## 1. Introduction.

Fouling remains a fundamental issue in many industries and involves the mechanisms by which discrete particles, clusters, floccules or colloidal structures deposit at the walls of contained units. It is a dynamic process where the deposits are often re-suspended by the action of disruptive stresses such as aerodynamic forces, gravity or the inertia of impacting particles. Colloidal, biological or particulate fouling represents a formidable technical challenge in many applications across the petrochemical industry, aerosols and engines, membrane processes, medical applications and within many processes in the particle technology industry, from packaging to granulation or spray drying.

The underpinning physics which dominates particulate fouling is intimately related to the particle turbulence interaction (Papavergos and Hedley 1984). As particle size and inertia (or relaxation time) increase deposition and re-entrainment become governed by inertial effects and less influenced by turbulent flow. Several studies thus focus on the interactions between particles and near-wall boundary layers for example Ziskind *et al.* (1995) or Soldati and Marchioli (2009) describe how the action of aerodynamic forces and coherent turbulent structures near the wall are responsible for unbalanced rates of particle deposition and ejection events. These systems usually deal with single particles and mono-layers, disregarding particle-particle forces and focusing on describing the particle-surface forces. Henry *et al.* (2012) discuss in detail the concept of colloidal particulate fouling, where a number of authors have extended this treatment to a multi-layer description including the interaction force between the wall-borne clusters. A different approach to re-suspension has also been proposed by Reeks *et al.* (1988) and Reeks and Hall (2001) based on the description of a potential, or energy well, this was extended to a multi-layer kinetic description by Zhang *et al.* (2013). Other important effects include the impact of swirling flows (Zonta *et al.* 2013), wall roughness (Guingo and Minier 2008) or the formation of aggregates near the wall (Marshall 2007).

The study of lower ranges of inertia focuses on short range adhesive and cohesive forces such as Van der Waals or electrostatics, and often associates the cause of re-entrainment to an aerodynamic origin. However, gravity driven mechanisms such as the detachment of large sections, or shedding are also a common subject of study in fields such as combustion. Ash deposition, aging and shedding are recognized phenomena in the comprehensive descriptions given by Wang and Harb (1997) or Zbogor *et al.* (2009) and in the experiments from Bashir *et al.* (2012). Impacts at higher particle inertia can lead to re-suspension, which has received little attention, not the least due to the difficulties in describing their

microstructure (Kota and Langrish 2006).

Particulate multi-layers in industrial processes comprise of a wide range of different materials, which leads to many types of interactions; the nature of cohesive forces varies and different aging processes take place. Unfortunately, reproducing these experimentally is extremely challenging, thus the usual lack of data leads to, at best, semi-empirical models for design purposes (e.g. Epstein 1983). Regimes covering high particle inertias occur in the spray drying of products such as milk, instant coffee, pharmaceutical powders or detergents. Here, particles and droplets with a wide range of size, momentum and composition coexist in the dryer. Inter-particle impacts lead to significant aggregation during the process (Palzer 2011) and wall impacts result in the generation and breakage of a particulate multi-layer at the walls of the dryer. The layer is retained by high cohesive forces, which evolve from a capillary origin to the formation of solid bridges (Farber *et al.* 2003). Their investigation remains a challenging task because it deals with very complex contact mechanics when deformable droplets or semi-dried particles impact a fixed substrate, comprised itself of a network of particles.

In the context of spray drying, the study of deposition and re-entrainment has mostly focused on co-current units and has been associated with three main issues: 1- product degradation and safety and quality concerns, 2- a detriment in the yield and the process efficiency and 3- costs associated to maintenance (Ozmen and Langrish 2003). The research undertaken in the context of the food industry reports ample evidence in this regard (e.g. Kota and Langrish 2006), and provides the most relevant efforts in optimizing the yield (e.g. Langrish and Zbiciński 1994; Hanus and Langrish 2007a; Kota and Langrish 2007) for which the role of the re-suspension has been recently emphasized (Hanus and Langrish 2007b). Counter-current spray dryers operate differently, and benefit from a strong turbulent swirling flow to increase particle residence time and obtain better energy efficiencies (Huntington 2004). On the one hand, the counter flow leads to increased particle concentrations, promoting particle-particle contacts and agglomeration whilst on the other, the action of a strong centrifugal inertia generates a preferential concentration of particles in the near wall region, where certain size fractions tend to stagnation. This causes multiple wall impacts, high deposition rates and the generation of multi-layered deposits at the walls. Very few works pay attention to the wall processes in these units and are limited to the study of the near wall fluid dynamics in restricted sections. Nonetheless, they permit visualization of the particulate multi-layer and highlight the detachment and breakage of clusters (Hassall 2011).

In co-current dryers a given yield decrease responds to the material that accumulates at the wall

(Ozmen and Langrish 2003; Hanus and Langrish 2007b). However, it must be noted that counter-current towers operate constantly for long periods of time without the need for cleaning. Only during the start up and for certain formulations is the accumulation of material observed. It follows that in average terms wall deposition and re-entrainment must be balanced. But, perhaps a more revealing question would be the time scale over which this equilibrium is reached.

In general, a rate or frequency of re-entrainment events is owed to a balance between disruptive stresses and cohesive forces in any given structure. If the stresses are low, large groups of clusters are re-entrained, few events occur and their time scale is high, potentially larger than the process time scale. In this case, re-entrainment is observed as a series of intermittent events despite its average mass rate remaining in balance with the deposition. Re-entrained particles are identifiable by a large size and a different structure from the particles with an air-borne origin. This is for instance the case of many shedding processes in burners (Zbogar *et al.* 2009). On the contrary, if disruptive stresses are much higher than any bonds between particles or particles to the wall the re-entrainment events are much more frequent and particles spend no significant time in contact to the wall.

The work presented in later sections confirms that the particulate multi-layers seen in counter current detergent spray dryers are intermediate scenarios. Disruptive stresses are comparable to the structural forces binding the clusters together and re-entrainment events become more frequent than in a shedding process. The wall-borne time scale now approaches that of the process and the sizes at which clusters are eroded becomes comparable to the size range of the product. In these cases, the processes undergone at the wall can no longer be observed as a series of intermittent events. For that reason, despite having been acknowledged for decades in spray dryers, the re-entrained aggregates simply blend in with the rest of particles in the product, and have been seldom studied.

Current numerical approaches assume that wall-borne processes have a minor contribution to the overall behaviour of the process. The rates of deposition, aging and re-entrainment are largely ignored and related to operational issues for which there is ample evidence, rather than to any significant impact in particle drying, growth or density, which have not yet been studied in detail. This is the purpose of this work. Wall deposition and re-entrainment have been investigated in an industrial scale counter-current spray drying tower. The following sections provide details on a tracer experiment that has permitted quantification of the re-entrainment rates, their impact in particle growth and morphology, and the residence time distributions that are associated to the deposition and re-entrainment cycle.

The data underscore the errors associated with the omission of wall cycle in current models, failing to account a strong effect in the particle drying kinetics, growth and the generation of the final structure of a large part of the exit powder, including the majority of the product of size  $> 850 \mu m$ .

## 2. Experimental set up and measurement.

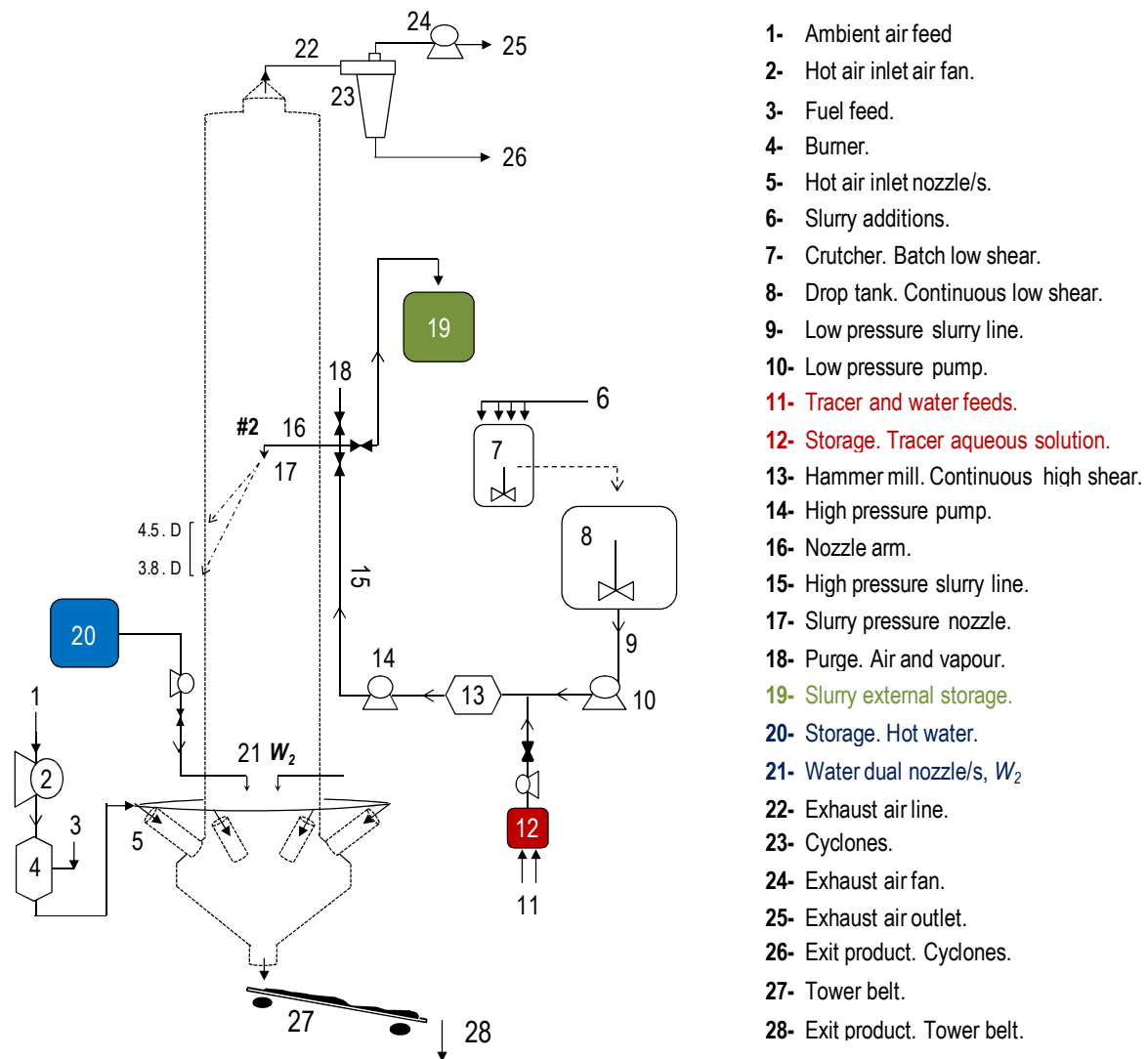
The general operation and measurement methodology is described in Chapter IV. In these experiments atomization is performed from a single nozzle at position #2, at  $5.9 D$ . A detailed characterization of the product in the same conditions is given in the case  $S_2$  (Chapter VI) and the impact of different air conditions is reported in the Appendix III. This work reproduces the same experiment but focuses in the study of the wall. For comparison purposes, Table 1 provides a comparison of the operation conditions during the different production stages defined in the next section.

Figure 1 includes an outline of the tower operation. The following modifications have been made for the conduction of tracer experiments described in this chapter:

1. An injection system for an aqueous solution of dye, [11,12] in Figure 1, is installed at the low pressure line, before the hammer mill, to ensure homogeneous mixing thereafter.
2. A set of water dual nozzles are installed at the bottom end of the tower, [21] in Figure 1, feeding from a water storage tank at  $60^\circ C$  [20].
- 3- A diversion of the high pressure line the end of the nozzle arm discharging into a separate storage tank open to the atmosphere [19].

A fluorescent dye, Sanolin Rhodamine B02, is used as a tracer. It is injected as a concentrated aqueous solution into the slurry low pressure line to provide  $100 ppm$  in the final particulate product. The selection of the dye was made due to its ability to sustain the operating temperatures while providing a relatively high accuracy in visible spectrophotometry. During the tracer experiment, the dye content is determined by the use of a UV/Visible spectrophotometer (Shimadzu UV-2401PC); the absorbance is measured at the maximum absorbance wavelength  $565 nm$  with reference to a blank control solution. The morphology of each size class is analyzed using Scanning Electron Microscopy (Hitachi TM1000) and the distribution of the tracer within the granule is studied under optical microscopy (Leica MZ16 A).

The walls were inspected at the locations shown in Figure 2. Not all show a similar deposition rate, or the same type of deposits. The deposits above the nozzle (i.e.  $> 5.9 D$ ) contains high moisture levels



**Figure 1.** Operation of the dryer described in Chapter IV. Modifications for the conduction of the tracer analysis.

but the initial net deposition rate,  $r_{d,o}$  is small and the deposits are thin. Moving down the chamber, they become drier and more brittle, until the bottom end where no significant deposition occurs. The sections nearby the spray show the highest levels. These are the areas where the hollow spray cone projects onto the wall and the impact of wet droplets at high inertia build up thick deposits (e.g. Figure 1 shows the projection of one side of the hollow cone, the spray is axi-symmetric). Here the outer layers interact with colliding particles and larger pieces often detach from the deposits to flow down close to the wall (Hassall, 2001). In this experiment, this particular location has been monitored separately. A dismantable plate has been designed to be flushed with the inner wall of the cylinder in the inspection area at  $4.5.D$  in Figures 2 and 3. In this manner, a wall section can be, in effect, extracted, weighed and placed back in position at different times during the operation to assess how the deposits evolve.

**Table 1.** Comparison of the main operation variables to the reference production from nozzle #2. This is denoted  $S_2$  and is characterised in detail in Chapter VI and Appendix III.

Scenario	$P - 1$	$CH - 1$	$P - 2$	$CH - 2$	$P - 3$
Slurry line, S, Water lines, W, Product in the tower belt, P, elutriated fines, E, and full exiting power, EP.					
Nozzle	#2	$W_2$	#2	$W_2$	#2
$\bar{M}_{\#2} / \bar{M}_{\#2, S_2}$	$0.93 \pm 0.02$	0	$0.93 \pm 0.03$	0	$0.94 \pm 0.03$
$\bar{M}_{W_2} / \Delta \bar{M}_{Eq}$	0	0.88	0	0.88	0
$\bar{M}_E$ (% $\bar{M}_{EP}$ )	2.8	n / a	n / a	n / a	n / a
$\bar{T}_P - \bar{T}_S$ (°C)	$-3.5 \pm 3.6$	-	$-2.5 \pm 3.9$	-	$-5.3 \pm 4.0$
$X_w - X_{w, S_2}$ (%)	1.4	-	*	-	*
Air, A, rate inlet, IN, and exhaust, EX, conditions.					
$\bar{M}_A / \bar{M}_{A, S_2}$	$1.02 \pm 0.02$	0	$0.99 \pm 0.03$	0	$0.99 \pm 0.02$
$tt - 0, \bar{T}_{A, IN}$ (°C)	$264.9 \pm 2.6$	$264.4 \pm 1.5$	$264.4 \pm 2.7$	$267.5 \pm 4.0$	$264.4 \pm 4.3$
$tt - 5, \bar{T}_{A, EX}$ (°C)	$88.3 \pm 0.5$	$108.2 \pm 8.1$	$89.6 \pm 0.4$	$107.2 \pm 7.6$	$91.2 \pm 1.9$
$t - c$ (°C)	195-206	191-199	195-198	176-186	194-198
$rH_{EX}$ (%)	15	6	14	7	14
Overall Energy Balance					
$Q_{Loss}$ (% $Q_{Ex}$ )	$37.9 \pm 0.6$	-	*	-	*
$Q_{Lat}$ (% $Q_{Ex}$ )	$63.8 \pm 0.6$	-	*	-	*

$T$ : temperature, for location of the sensors see Chapter IV;  $M$ : mass rate;  $rH$ : relative humidity;  $\Delta \bar{M}_{Eq}$ : equivalent rate of water contained in the slurry. For details in the energy balance see Chapter VI.  $Q_{Ex}$ : rate of heat exchanged in the dryer,  $Q_{Ex} = \Delta H_{A, Lat} + Q_{Loss} = -(\Delta H_{DA, Sn} + \Delta H_{P, Sn})$ ;  $Q_{Loss}$ : rate of heat losses;  $Q_{Lat}$ : rate of heat of vaporization.

\* The exit water content  $X_w$  was monitored as constant throughout the experiment. Detailed averaged were taken at  $P - 1$  only.

### 3. The renewal of particulate multi-layers.

#### 3.1. Description of air-borne and wall-borne states.

Wall deposits within a dryer may be regarded as a continuous porous structure that is different from the particles contained in the continuous phase. The material within the exit product can therefore possess a wall or air-borne origin according to whether it has been at any point part of the structure deposited at the wall. On these bases, the tower may be defined by the two different parallel regions depicted in Figure 4a: a) the air-borne region comprised by the air vortex that contains a population of air-borne particles, and b) the wall-borne region, which is comprised by the structure of deposits that remains fixed. Both can be described as spatially distributed reactors where the particles undergo different transformations in Figure 4b. In the air-borne reactor they dry, aggregate and flow, and in the wall-borne reactor, particles dry and may sinter but remain fixed. Both regions interact by a mass flow rate of particles that moves from an air to wall-borne state and vice versa by deposition  $r_d$ , and re-entrainment  $r_e$ . In reality, these rates are distributed through the height of the tower and vary according to the local drying conditions, the deposit properties and the local rate of impacts onto the wall.

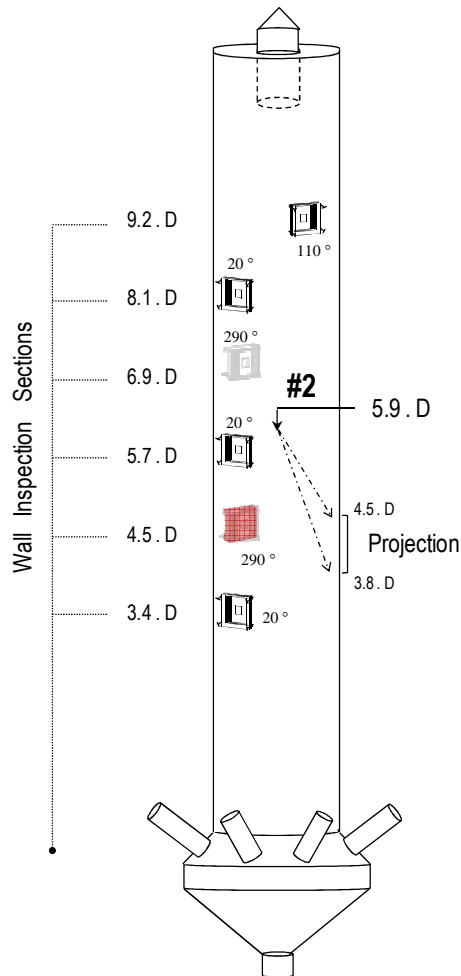


**Figure 2.** Wall inspection areas. The section highlighted lays within the spray projection area and is monitored with an extractable plate

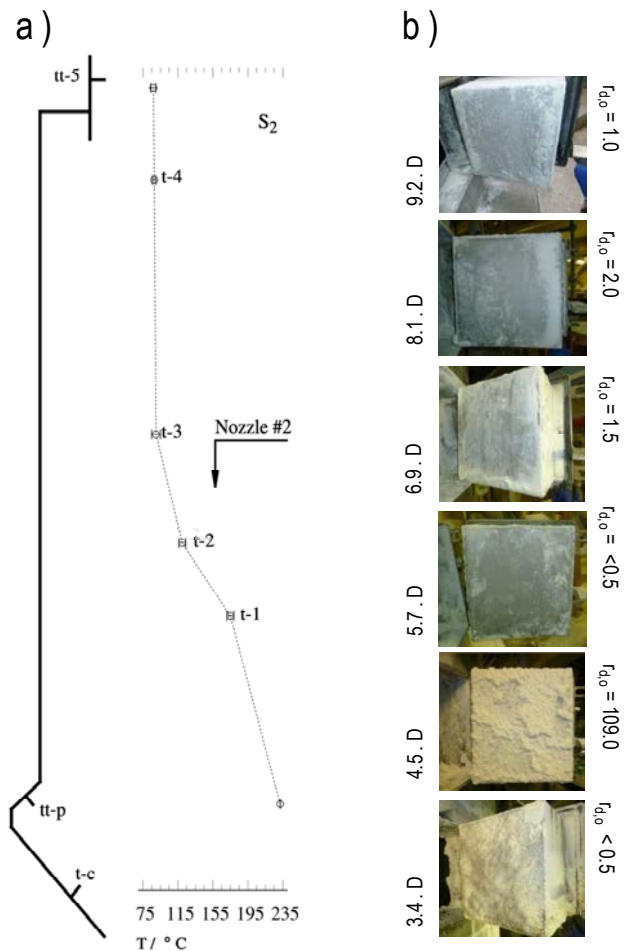


**Figure 3.** a) Air temperature axial distribution for a similar production,  $S_2$  in Chapter VI, error bars denote radial range b) Wall deposits axial distribution, and initial net deposition rate  $r_{d,o}$  in  $g \text{ min}^{-1} \text{ m}^2$

### 3. 2. Outline of the tracer experiments.

Decoupling experimentally the wall and air-borne processes entails determining the exchange rate between both regions in Figure 4 and their particle residence time distributions. The purpose of this chapter is to characterize the wall-borne region only, and evaluate its overall impact. With this objective in mind, it is important to quantify the magnitude of the average re-entrainment rate  $r_e$  and the time the particles spend resident in the wall deposit. This data has been generated by tracking the release of the material contained in the wall-borne region in Figure 4 during a full renewal cycle.

In the real unit, the requirement is to ensure at a given point in time that the material borne at the wall contains a known tracer concentration while that in air-borne state contains none. Several stages will be followed to achieve this. Initially, the unit will be brought to a standard production rate in order to

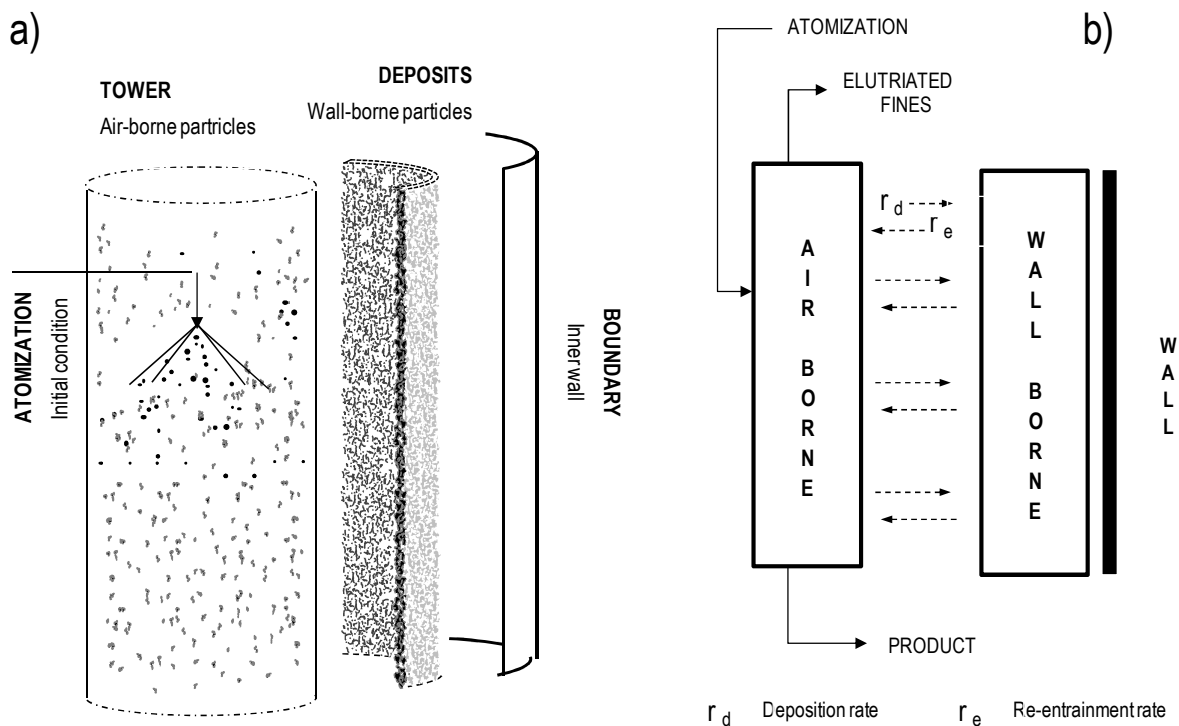


**Figure 4.** Description of particle history as a combination of two parallel reactors associated to the air and wall borne states.

generate a stable layer of deposits, at this point untraceable. Then, the dye solution will be injected such that atomised droplets have certain dye content and deposition and re-entrainment at the wall produces layers of traceable material. The unit will then be emptied of air-borne particles leaving behind a set of traceable deposits. At this point, atomization will be restarted with all droplets containing no tracer. The rate of release of the dyed material from the walls is then quantified by measuring the amount of tracer exiting in the product. In this way, the origin of aggregates can be determined, differentiating those that are generated from re-entrainment of material at the wall from those with a pure air-borne history.

The experimental sequence is illustrated in Figures 5 and 6, and detailed below. The steps are designed to preserve at all times the operating conditions in the tower and maintain the properties of the deposits.

### 3.3. Generation and tracking of a set of active wall deposits. Sequence of a wash out experiment.

- ***P* – 0. Start up. Standard:** The rates of slurry and hot air until ramp up to heat the unit and develop an initial layer of deposit, associated with particle-wall contacts.
- ***P* – 1. Production. Standard:** Steady state production carries out. The product is characterised and a first set of untraceable material generates the particulate deposits at the walls.
- ***CH* – 1. Changeover. Dye injection:** An auxiliary stage prepares the system for the injection.

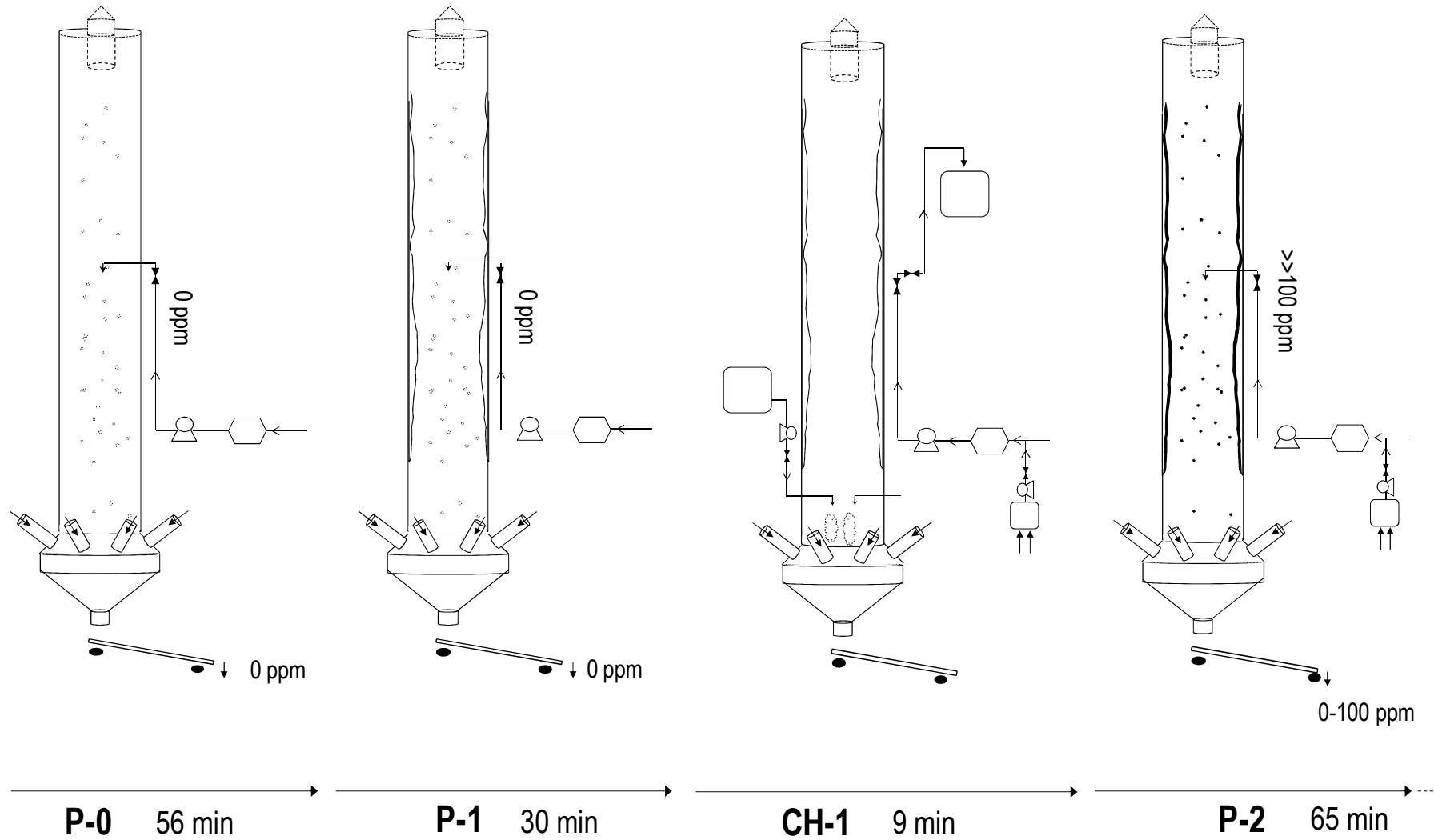
Homogeneous mixing of the slurry and the dye is ensured by the hammer mill in Figure 1, but the long residence time causes axial mixing of the dye in the line [13,14,15]. Two requirements need careful consideration, 1- Deposits traceability: a sharp step change in dye content at the nozzle is necessary to ensure only droplets of known concentration, either the target or zero are produced, and 2- Deposits mechanical properties: the mechanics of deposition and erosion is the aim of the experiment, and thus the properties of the deposits should be maintained. In steady state, most areas are close to the equilibrium with local air conditions which should be kept constant at all times. Under these constraints, the following sequence is executed at the end of the stage  $P - 1$

- The dye injection starts and two following changes are executed simultaneously.
- The slurry line is diverted to an external loop connected to the atmosphere, where it discharges into a container for visual inspection [19] in Figure 1. After this, the nozzle arm itself is purged in [18] with water vapour to avoid solidification and blockage.
- Hot water is diverted into a pair of dual nozzles in [21]. Both spray a fine water mist which flows down into the conical region, with a combined rate set to match the water mass rate that dries when the slurry nozzle is in operation.

In operation most of drying occurs at the bottom of the chamber. As the evaporation rate is kept constant, the operating conditions can be left unchanged and in this way, the deposits in the cylinder are subject to similar air temperature, humidity and velocity. Nonetheless, deposits near the spray region are likely not in equilibrium with the local air, but continuously drying, so to avoid changes in their properties, the length of  $CH - 1$  was minimized as much as possible. Visual inspection and analytical measurements in [19] confirm the point at which the tracer achieved a target constant concentration. At this point, the slurry line is ready to be diverted back into the tower.

- **$P - 2$ . Production. Generation of traceable deposits:** The water flow is stopped in [21] and simultaneously, the slurry flow containing the target tracer concentration is diverted back from the external loop in [19] to the nozzle inside the tower. All settings in the process, including the burner, mixers, pumps and temperature control to remain unchanged. As a result, when the slurry reaches nozzle #2, atomization pressure and subsequently droplet size, returns almost instantaneously to the steady state values observed in  $P - 1$ . Production resumes and the exit powder starts showing the colour derived from the dye. This continues for  $\sim 1h$ , what will be proven sufficient to ensure that active layers in the deposits have been renewed and are

Figure 5. Description of the tracer sequence. Initial stages, changeover and production P – 0, P – 1, CH – 1 and P – 2



comprised of the traceable material. In the last 5 *min*, product sampling is performed.

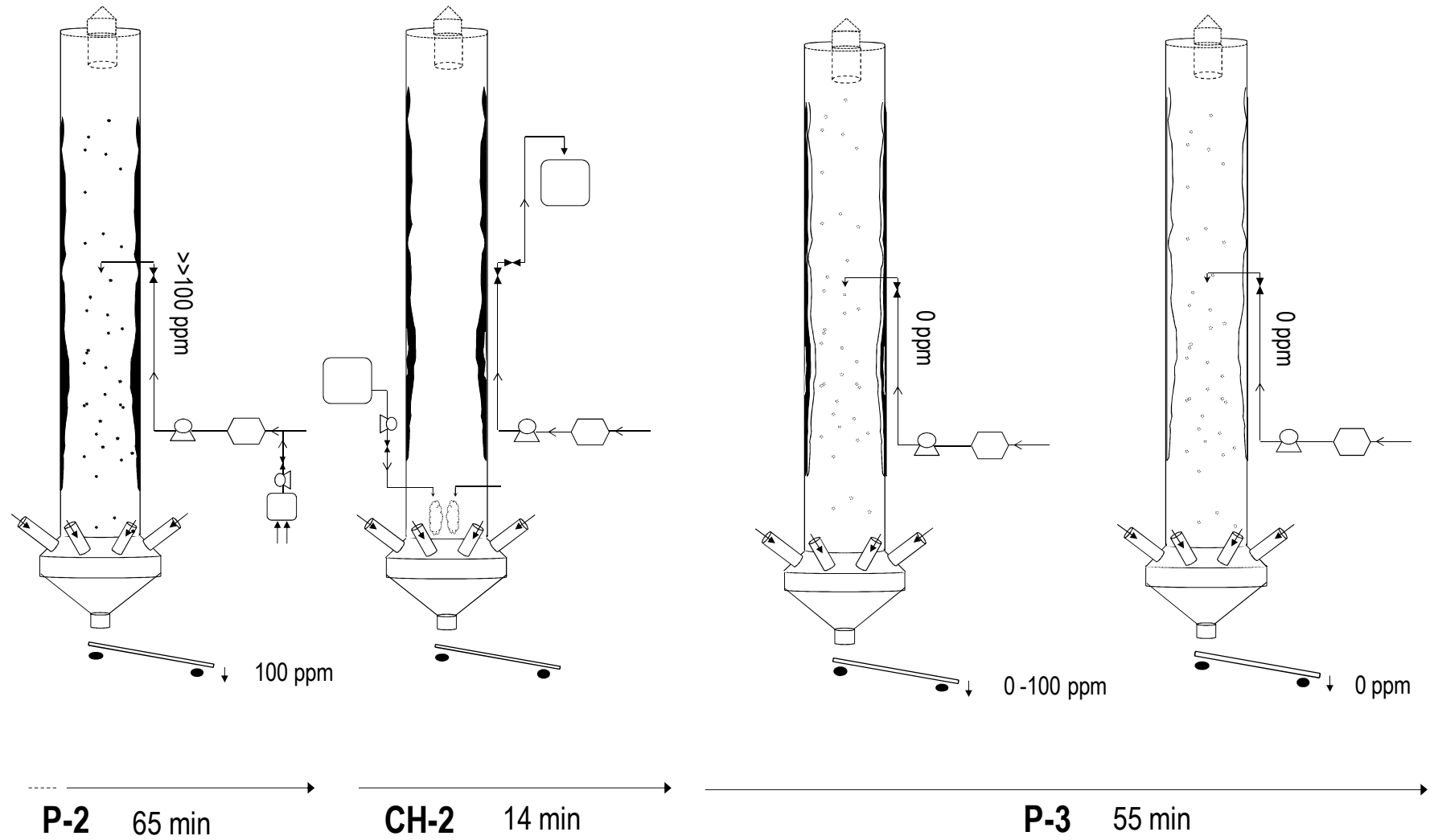
- **CH – 2. Changeover. Disconnection of the injection:** At this point the air-borne and wall-borne reactors in Figure 4b are both full of particles with the tracer. To quantify the exit rate from the wall-borne reactor one needs first to empty the air-borne reactor and then ensuring that the new population of incoming droplets contains no dye. In order to do this, the same changeover is executed, but in this case proceeding to the disconnection of the dye. The slurry is diverted out of the chamber to external container [19] and instead the water is connected. The slurry flow loses the colour until it becomes indistinguishable from the standard white system. Analytical measurements of slurry samples confirm the final dye concentration is below 1 % of the target. At this point the reverse changes are made.
- **P – 3. Production. Renewal of the wall deposits:** The water flow is stopped and simultaneously the slurry which now contains no tracer is diverted back to the nozzle. At this precise point in time, the tower is empty, the entire mass of deposits contains a given concentration of tracer and the entire population of air-borne droplets contains none. This situation is equivalent to setting a target concentration of dye in the material at the wall-borne reactor in Figure 4b, whilst the air-borne reactor is empty. When atomization restarts, the tower fills up and samples are taken for a period of  $\sim 1h$ .

#### 3.4. A note in the solid hold up and the correct conditioning of the deposits during changeovers.

The possible disruption of the deposits during the changeovers could be recognized by three signals: 1- visible changes in their morphology, 2- product exiting the tower belt or the cyclones or 3- stagnation of solids hold up in the air. During CH – 2 the inspection of the wall, discussed in section 4.3, shows no significant changes. In addition, no powder was seen to exit the tower belt, indicating that detachment of large pieces due to gravity is not significant. At the cyclone exit, a negligible flow was observed.

At the end of CH – 1 the tower is assumed to be empty, but it might have contained solid stagnated due the counter flow. Evaluation of this is essential to keep the traceability of the deposits (i.e. ensuring that when the atomization restarts in P – 3 the only particles in the unit that contain the dye are borne at the wall). This has been confirmed in a set of separate experiment. The initial stage of this sequence was repeated but in this case, at the end of CH – 1 the water nozzles and the air system were both

Figure 6. Description of the tracer sequence. Final stages, changeover and production P – 2, CH – 2 and P – 3



shutdown simultaneously. The solids hold up exited through the tower belt and were collected. The amount represents less than 0.4 % of the weight of the deposits and a negligible concentration in the cylinder. It is noticeable however that after 25 *min* of the shutdown, a large section of the deposits detached (4.5 % of the full weight). This highlights the impact that air conditions have in the structure of the deposits and the success of this sequence in preserving it.

## 4. Results and Discussion.

### 4.1. Transient production.

The mass rate of powder exiting the bottom of the tower,  $M_p$ , varies as the unit fills up before reaching the steady state value,  $M_{p,St}$ . To help with interpretation of the data a separate experiment was conducted to determine its evolution. The same sequence is replicated. When the atomization restarts in  $P - 3$ , the exit rate is measured manually during 10 *min*, collecting the entire exit stream. Figure 7 presents the evolution of the rate and the particle size distribution of the samples in  $P - 3$ . It is clear from both that it takes  $\sim 100$  *s* for the unit to fill and achieve the steady state concentration. This is in agreement with the air-borne residence times  $< 30 - 45$  *s* reported for similar units by Harvie *et al.* (2002), Huntington (2004) and more recently Ali *et al.* (2013) or Ali (2014).

The initial distribution in Figure 7 is very narrow and contains primarily the size fractions that later become the mean product size between 300 – 600  $\mu m$ . As time progresses, the distributions span and start containing a larger proportion of small and large sizes, stabilizing close to the steady state average at times  $> 100$  *s*. It is a noticeable fact that both, larger and smaller size fractions take longer to exit, since one expects the large granules to sediment faster and have shorter residence times. This could be a consequence of the fill up, if they are produced only when concentration rises sufficiently. However, it is most likely related to the high level of interaction with the walls, discussed in detail later.

### 4.2. Steady state production.

Figure 8 compares the droplet size distribution obtained at the atomization and time averaged size distributions of the product in stages  $P - 1$ ,  $P - 2$  and  $P - 3$ . The atomization covers a range from 20 – 1000  $\mu m$  and is skewed over the large sizes, having a mode from 350 – 450  $\mu m$ , a median volume droplet size of  $x_{p,50} = 292$   $\mu m$ , and 10<sup>th</sup> and 90<sup>th</sup> percentiles,  $x_{p,10}$  and  $x_{p,90}$  of 85  $\mu m$  and 530  $\mu m$  respectively.

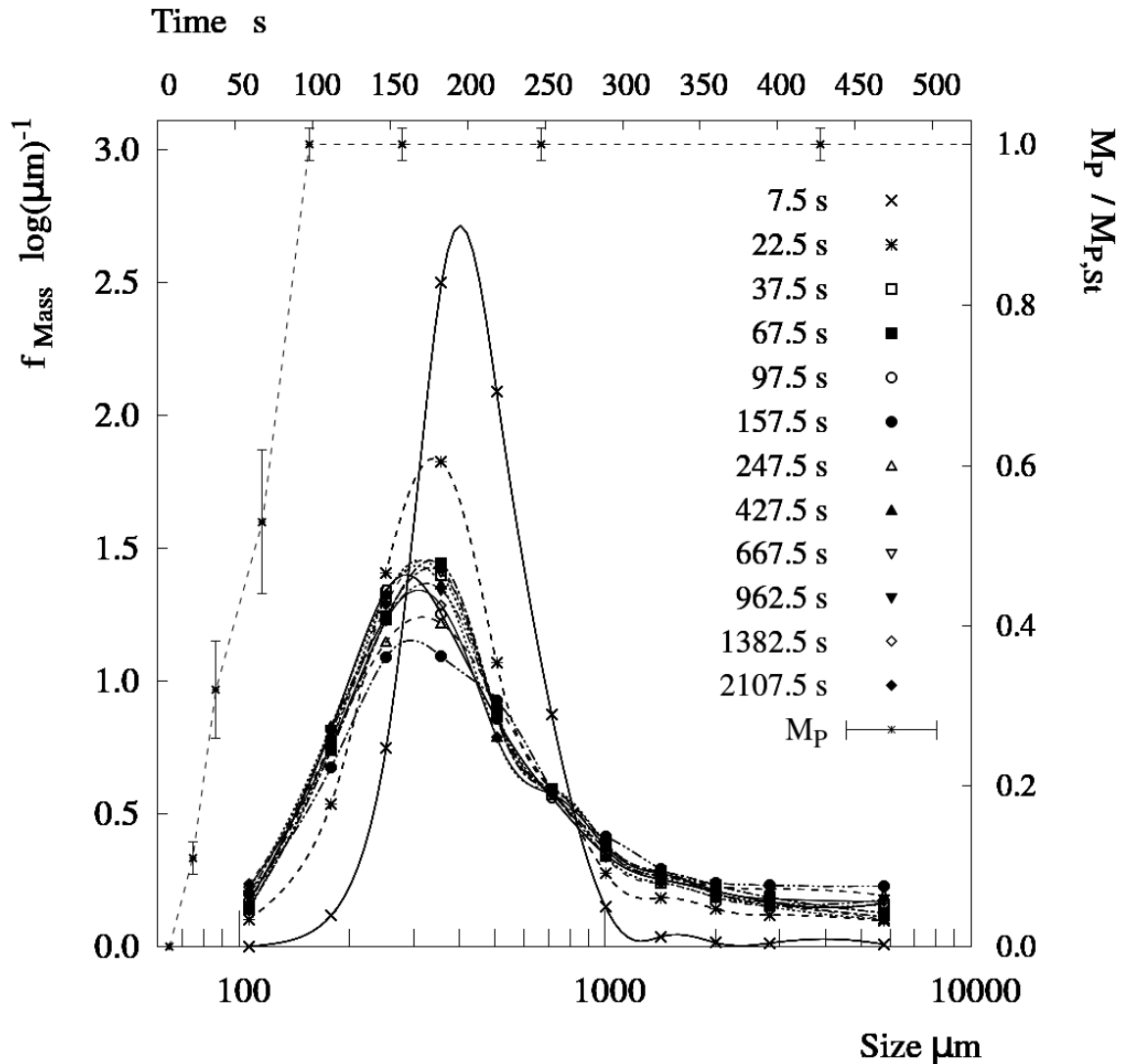


**Figure 7.** Time evolution of the tower exit rate,  $M$  and the product weight based size probability density function in  $P-3$

The product undergoes a significant particle growth, the distributions covering a range from 70 – 10000  $\mu\text{m}$ . They all present a mode between 300 – 400  $\mu\text{m}$ , a median average size  $x_{p,50}$  ranging from 360 – 430  $\mu\text{m}$  and  $x_{p,10}$  from 160 – 180  $\mu\text{m}$ . They also present long tails towards the largest granules  $> 1000 \mu\text{m}$ . However, the later product, obtained during  $P-2$  and  $P-3$  shows a significant difference as to that obtained at early stages in  $P-1$ . At the beginning of the experiment, the product contains less of the largest granules in Figure 8. As the time progresses, the tails become more significant and  $x_{p,90}$  varies from 1350  $\mu\text{m}$  in  $P-1$  to 2450  $\mu\text{m}$  in  $P-3$ .

Stable operating conditions are reached in all,  $P-1$ ,  $P-2$  and  $P-3$ , including constant heat losses. However, the size appears to evolve towards larger granules as production continues for  $\sim 2-3 h$  much higher times than the residence times involved in particle flow. This indicates that

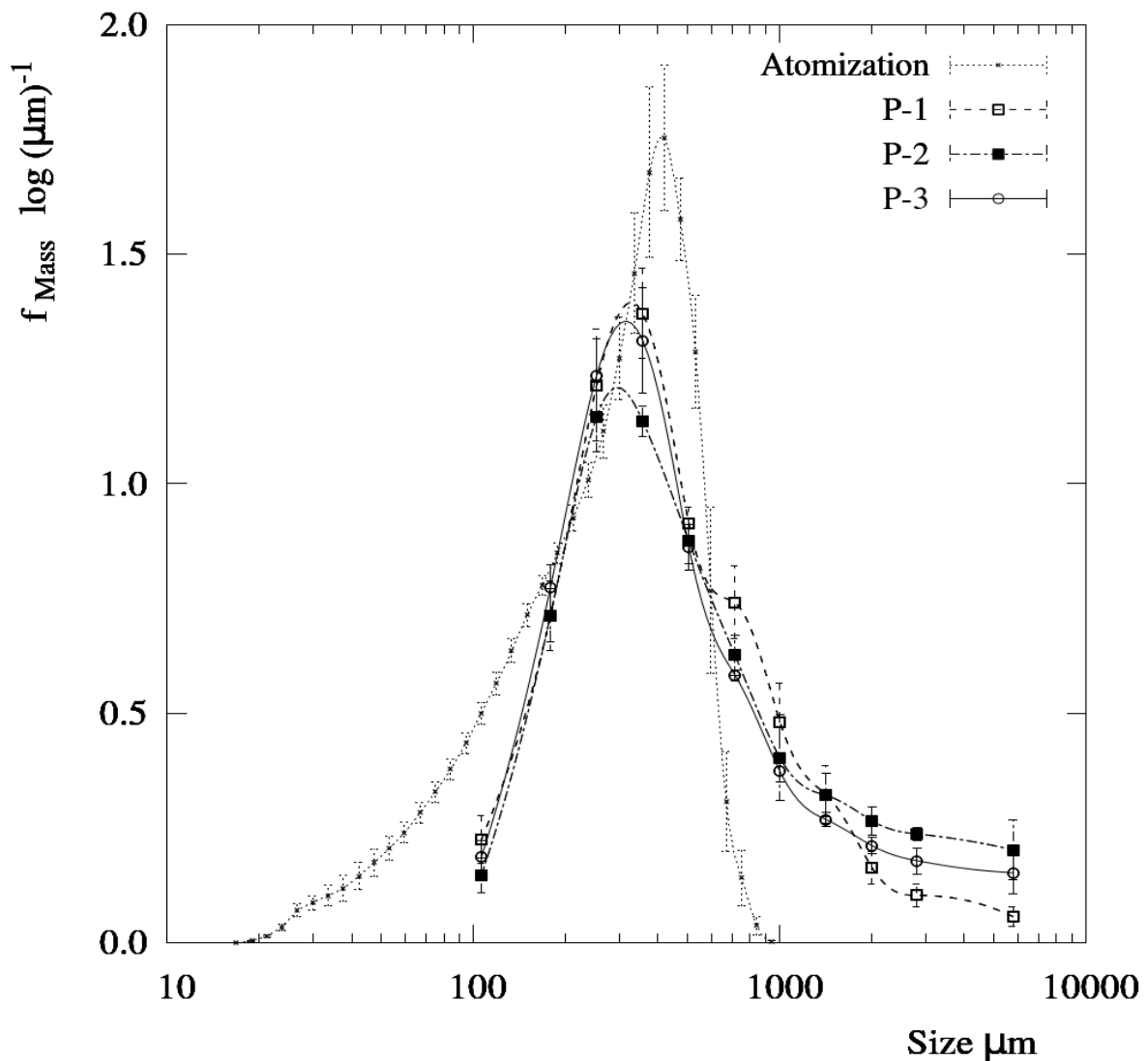


**Figure 8.** Averaged size probability density function for the spray and the product during  $P - 1$ ,  $P - 2$  and  $P - 3$ .

during the initial stages, processes other than fluid dynamics must still be in a transient state. The next section associates this effect with the stabilization of deposition and re-entrainment rates.

#### 4.3. Deposition and re-entrainment equilibrium.

Figure 9 presents a series of photographs of the section of the wall that contains the extractable plate during the entire experiment (level  $4.5 D$  in Figure 2). In parallel, Figure 10 provides the evolution of the weight of the ensemble (plate plus deposits) associated to the images in Figure 9. In the start-up,  $P - 0$ , deposition increases until the product covers the entire surface. During this period, the weight of the deposits rises linearly in Figure 9, at constant net initial deposition rate,  $r_{d,o} = 111 \text{ g min}^{-1} \text{ m}^{-2}$ . After this stage, the weight on the plate stabilizes. No significant variations can be related to either of the

changeovers, what indicates that the mechanical properties of the deposits have been kept within reasonable margins. The tendency to achieve a maximum weight or thickness, where the net deposition rate falls close to zero is a common observation in particulate fouling known as the 'blocking effect' (Henry *et al.* 2012). In cases of low inertia and cohesive forces it is in part related to re-entrainment and in part to the suppression of deposition. A similar evolution was reported by Hassall (2011) in swirl spray dryers at higher cohesive forces and larger inertias, but until now its root cause remained unclear.

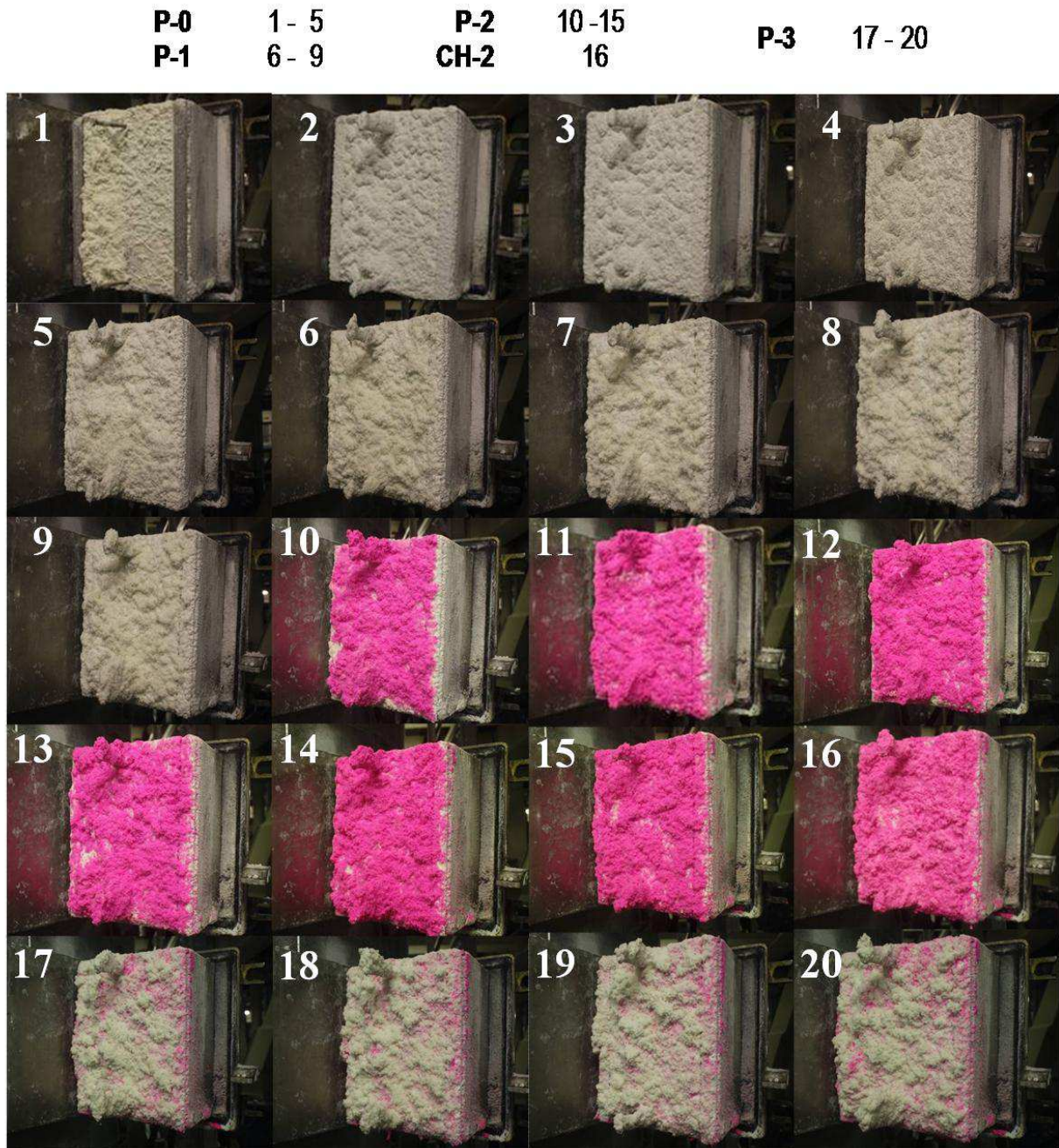


**Figure 9.** Evolution of the deposits observed at the inspection level 4.5xD containing the extractable wall plate.

Figure 9 shows that when the spray varies from white to dyed to white again, from  $P - 1$ ,  $P - 2$  and  $P - 3$ , a change follows in the colour of the deposits. This confirms there is deposition of atomized droplets. But further on, as the colour change occurs, the weight of the ensemble given in Figure 10 remains constant. This is a major and important result as the combination of both observations provides the first experimental evidence of significant wall dynamics in these units. It demonstrates that the rates of deposition  $r_d$  and re-entrainment,  $r_e$  are in equilibrium in this section, and that such a renewal process is responsible for suppressing the growth of the deposits. Notice that they change sharply in colour, not gradually and thus the structure must be renewed quickly. New sets of clusters must be brought from the air into the structure to be re-entrained back into an air-borne state a given time later.

#### 4.4. Quantification of the re-entrainment rate.

The detergent slurry contains three different phases, and it is noted that the dye used in this work distributes preferentially within the organic phase and therefore, dye and surfactant contents are correlated. The surfactant level in the product varies across particles of different sizes as a consequence of a heterogeneous distribution of the solids in the atomization (Mulhem *et al.* 2006) and

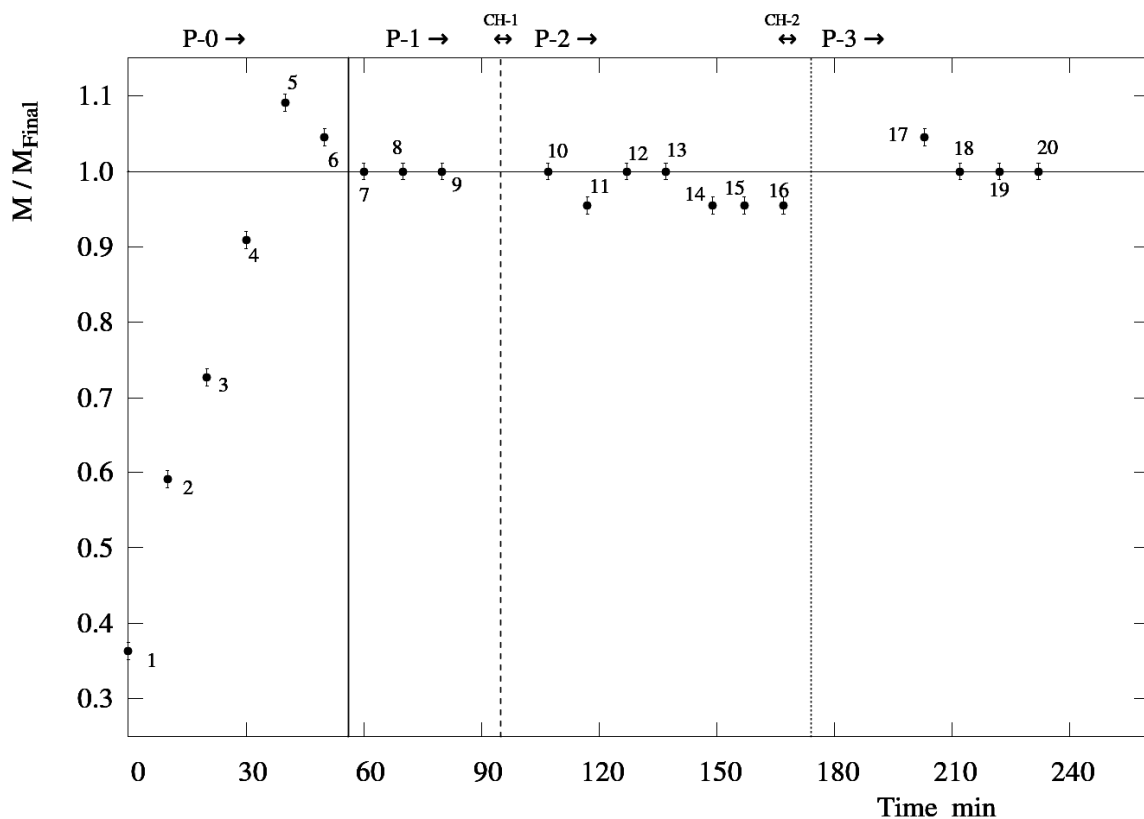


**Figure 10.** Evolution of the normalized weight of the extractable plate present at the surface of the photographs in Figure 9.

the particle growth history. This is discussed in more detail in Chapter VI.

Accordingly, the pure dyed particles also present a similar variation, primarily within the size fraction  $< 212 \mu m$ . The reference dye content has been obtained for each size class from the analysis of pure dyed samples at the end of  $P - 2$ .  $X$  is defined in (1) as the ratio between the dye content of a mixture and that of the pure dyed powder of the same size range, for a given sampling time  $t$ . Thus,  $X$  can be considered equivalent to the ratio of dyed material present in the mixture.

$$X_{s,t} = \frac{S_{s,t} \cdot A_{s,t}}{S_{s,ref} \cdot A_{s,ref}} \quad (1)$$

Notice that during  $P - 3$ , the dyed material has a single possible origin: the wall deposits. Then,  $X$  is equivalent to the ratio of material that in fact, has a wall-borne origin. That is, the material that was part of the deposits and became re-entrained after the atomization starts in  $P - 3$ . The use of (1) carries a certain error when the deposits have a different content in surfactant/s / tracer than the product. All data reported include a largely conservative estimate of the uncertainty based in the actual measurements.

Figure 11 presents the content of wall-borne material for all size fractions of the samples taken during  $P - 3$ . Within the initial  $100 s$  the mass averaged value of  $X$  decreases from an initial value,  $X_o$  of  $20 \pm 1 \%$  to  $12 \pm 1 \%$  of the full production rate when the tower is already filled. This range increases to values between  $31 \pm 1 \%$  to  $15 \pm 1 \%$  for the mass fraction  $< 212 \mu m$  and up to a range between  $37 \pm 3 \%$  to  $10 \pm 1 \%$  the mass fraction  $> 850 \mu m$ .

At the initial time,  $t_0 = 0 s$ , the entire mass of deposits is dyed and the entire population of air-borne droplets is white. At that point, the exit rate of dyed material represented by  $X_o$  can be considered an estimate of the instantaneous re-entrainment rate  $r_e$ . The first re-entrained material will be simply delayed a given time before exiting due to the air-borne flight between the re-entrainment position and the exit. However, at longer times  $t$ , the deposits and the re-entrained granules start containing white material, deposited between  $t_0$  and  $t$  what makes the dyed content in the product diminishes.

The initial decay in  $X$  is however likely to be related to fast time scales in the renewal process. Notice that any deposition and re-entrainment cycles that occur faster than the first sampling time  $\sim 15 s$ , would blend in with the air-borne material, appearing as white in the product. On this basis, the ranges given for  $X$  are minimum estimates of the removal, because the fastest interactions are not included.

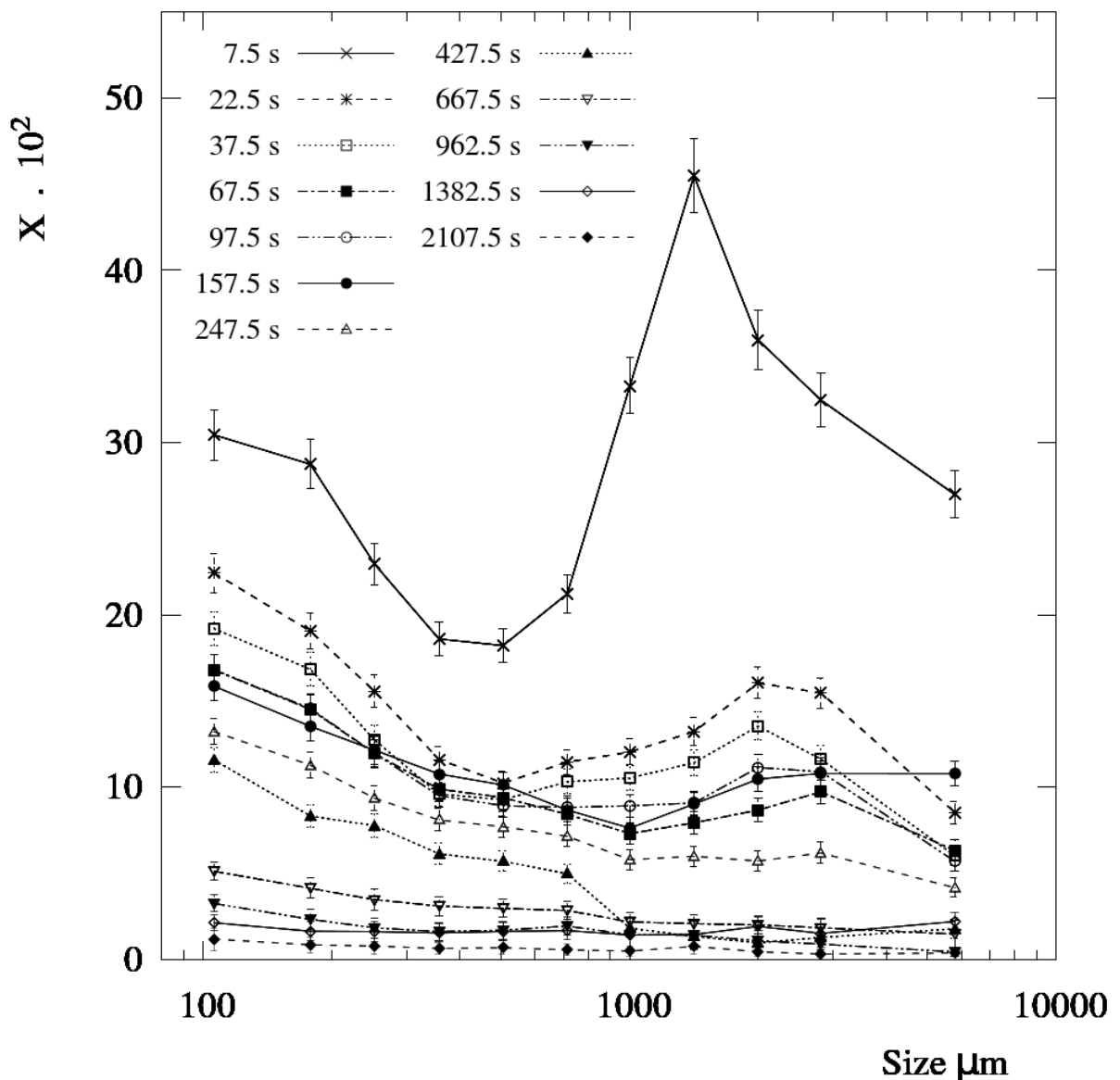


**Figure 11.** The ratio of material of wall-borne origin,  $X$ , in samples taken during P-3. Conservative error limits are given including the measurement and any potential preferential distribution of dye in the wall-borne material.

These observations have major implications in the general view of the behaviour of counter-current spray drying towers. They indicate that a significant fraction of the product,  $> 12\%$  and most likely  $> 20\%$ , is not material originated at the nozzle but is material generated from the wall deposits and its size, structure and drying history is related to the physics governing deposition, ageing and erosion of a network of clusters. These values become even more relevant for smaller and larger aggregates, known to contain a higher moisture level and have a significant impact in the energy balance (Chapter VI).

The following sections describe the influence of the mentioned deposition re-entrainment cycle in particle growth, structure and the overall product residence time.

#### 4.5. Granule structure and morphology.

Figures 12 and 13 show respectively several micrographs of the material that exits the unit within the mode age determined later as  $t \sim 157.5$  s and at the initial sample  $t \sim 7.5$  s. The Figures 14 to 16 provide details on the structure of the mixtures between air-borne droplets and wall-borne clusters. Finally, Figures 17 and 18 include morphology examples observed under SEM analysis.

##### 4.5.1. Small and average size particles, < 850 $\mu$ m.

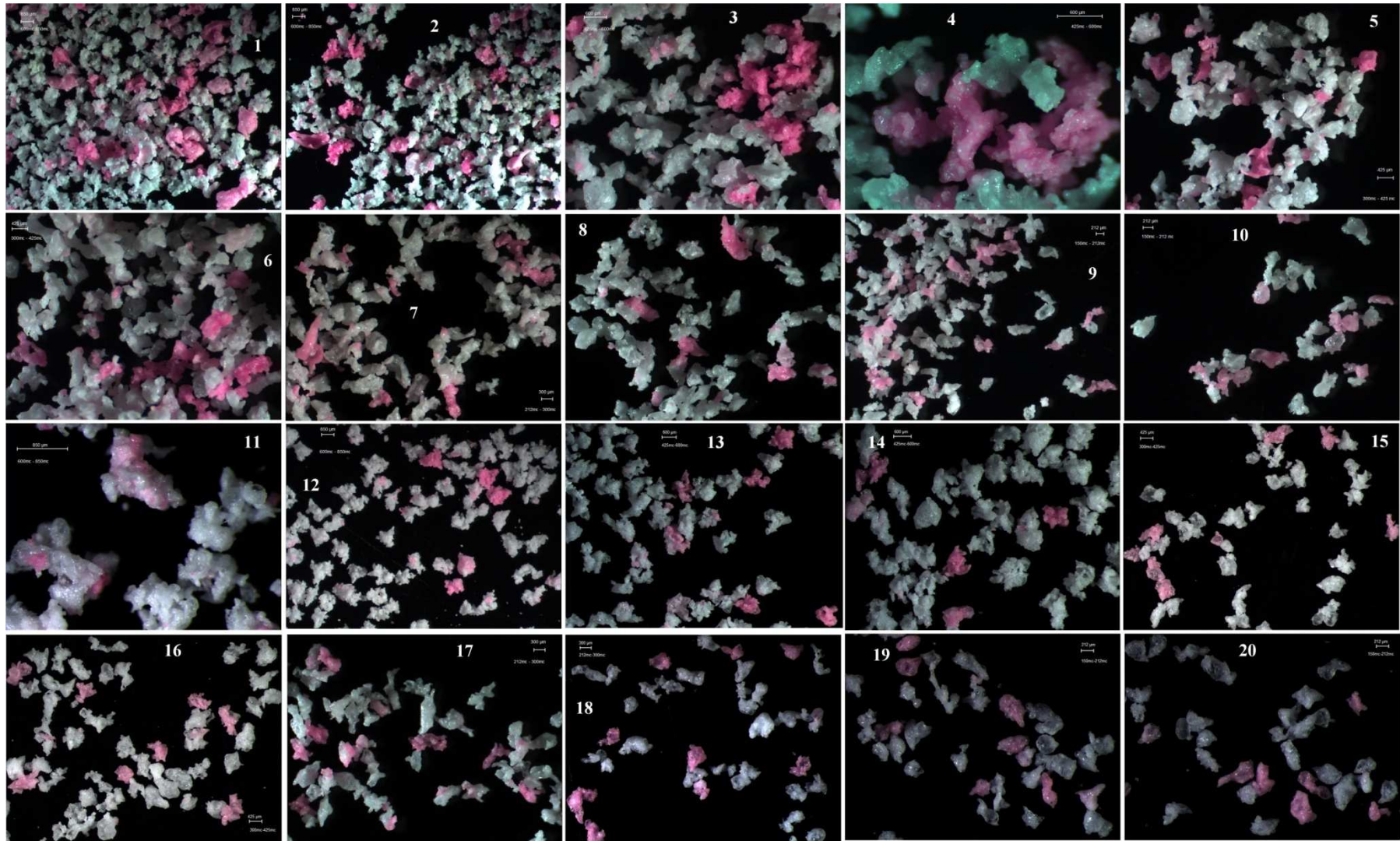
Lower size fractions are comprised, in general terms, of pure particles, either completely white or dyed. Several observations follow. Firstly, the particle history of dyed particles must involve no aggregation with any air-borne droplet. This includes 1- the time they had remained wall-borne, potentially sintering with newly deposited droplets or subject to air-borne impacts, 2- the contact with other particles during the re-entrainment mechanics itself, and 3- the air-borne history from re-entrainment to exit. Secondly, despite the fact that no aggregation occurs, the detachment has been triggered by impacts of air-borne particles. No particles exit during the changeovers nor are they hold up in the air, when tower is empty but the deposits are subject to gravity and the same stresses of aerodynamic origin.

The re-entrainment must follow two potential mechanisms. First, the impacts of dry particles causing a direct detachment: In this case, both, particles and deposits are dry enough not to develop sufficient cohesive forces and cause deposition or capture, but the impacts contain a large enough inertia to break the bonds between the clusters. Second, the detachment of large pieces: being typically of a low density and heterogeneous shape, large clusters are unlikely to sustain the stresses derived from collisions to the wall, and would break down into smaller particles. This detachment can be triggered by the action of gravity alone or combined with the impact of dry particles or wet droplets; this is discussed in more detail in section 5. Note that the impact inertia in combination with gravity may only break individual bonds in the multi-layer structure but eventually lead to detachment of a large section.

##### 4.5.2. Large particles, > 850 $\mu$ m.

In large granules the wall-borne material is distributed in a different manner. It is also comprised of identifiable pure dyed particles, which indicates the presence of a similar production mechanism as for the smaller particles. However, the remaining particles are not purely white but, as illustrated in Figure 13 they are in general mixtures of air-borne and wall-borne material to a different degree. Figure 14 provides examples of the mixtures generated.

**Figure 12.** Wall borne material. Micrographs (1) to (10) show the sample at  $t \sim 7.5$  s; (11) to (20) the sample  $t \sim 157.5$  s. In decreasing size and increasing magnification: (1,2, 11,12)  $600 < x_p < 850 \mu\text{m}$ ; (3,4,13,14)  $425 < x_p < 600 \mu\text{m}$ ; (5,6,15,16)  $300 < x_p < 425 \mu\text{m}$ ; (7,8,17,18)  $212 < x_p < 300 \mu\text{m}$ ; (9,10,19,20)  $150 < x_p < 212 \mu\text{m}$ .



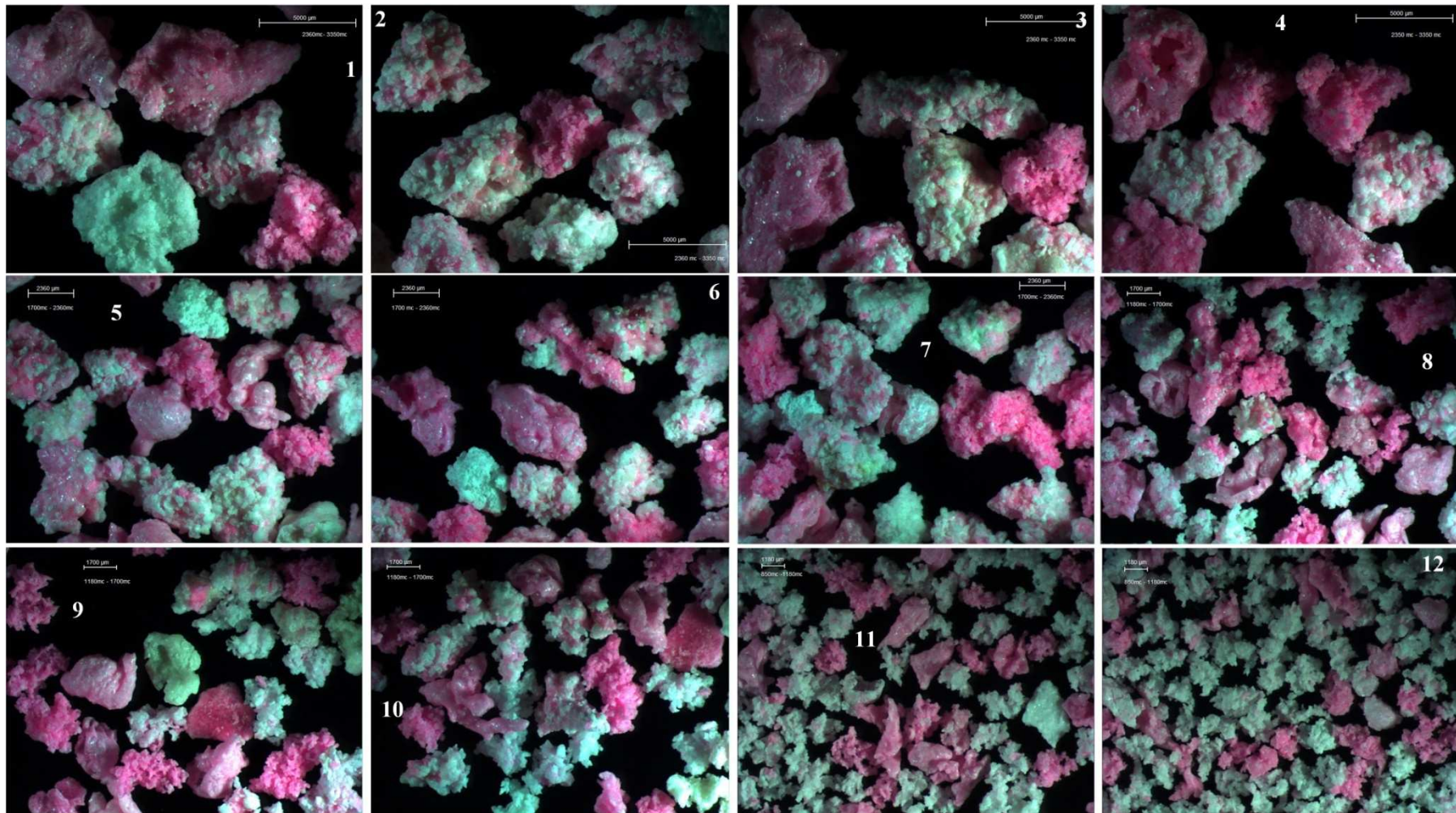
The distribution of dye in large granules is very heterogeneous. Figures 14 and 15 provide examples of the external distribution of dye, where the graduation in the colour intensity at the surface results from an outer layer of white material, varying in thickness. Aggregates range from pure dyed particles to white granules with coloured sections, where dyed primary particles are embedded in the granule. As the time progresses the deposits turn white and mixed granules containing only small sections of coloured material become common. However, the content of dyed material of the largest granules remains  $> 10\%$  after the tower fills up, indicating it is still present in the inner structure of the granule. They vary from homogeneous mixtures containing multitudes of white and dyed primary particles, to granules where a dyed wall-borne nucleus is captured by white air-borne material, see Figure 16.

This analysis demonstrates that a significant proportion of large wall-borne clusters undergo aggregation with atomized material. This is a revealing fact. It suggests that the production of most large aggregates is driven by the dynamics established at the wall. In this sense, the re-entrainment rates given earlier should be taken as an indication of the mass that is re-entrained from the deposits and exits within large individual granules, but noticing that in fact, most if not all of these particles have been involved in the cycle of deposition and re-entrainment.

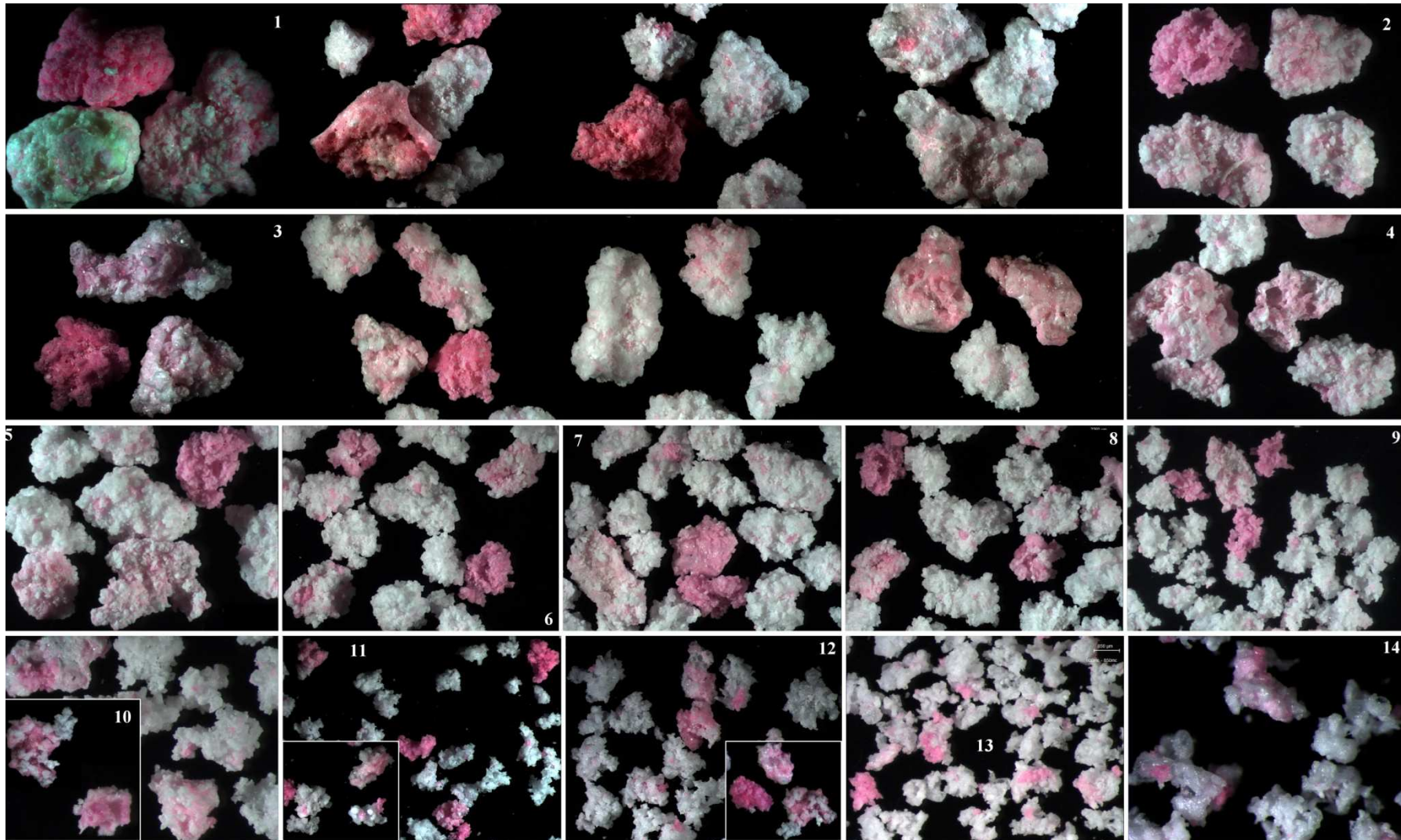
The morphology of the large granules is itself heterogeneous, Figures 17 and 18 provide a few examples and Appendix II discusses in more detail the particle structure obtained. In general, they present a variety of non-spherical structures with large aspect ratios. Primary particles appear to be fused together in a larger matrix what agrees well with the description of fast sintering during spray drying given by Palzer (2011). Low density granules result from having wide collections of cavities, comparable in size to the primary particles that they contain. When particles collide between each other or to the wall, such surface features surely lead to a very different behaviour from spheres, especially with regard to interlocking and the rotation moments. In general, granules could be better described by two dimensional models but in many cases they do not show any real symmetry axes. In addition, Figure 17 includes several examples that present a clear heterogeneity in having smooth and aggregated sides. This feature could be explained by the effect of the wall. In a two dimensional multi-layer, sides can be exposed or not to sintering, and subject or covered from air-borne collisions.

In conclusion, the manner in which the wall-borne material distributes is correlated with the exit size of the re-entrained granules. Small and average sizes are in general terms re-entrained as pure aggregates. Large size classes can also be re-entrained directly but in the majority of cases the process

**Figure 13.** Wall-borne material. Initial sample  $t \sim 7.5$  s in  $P - 3$ . From top to bottom in decreasing size and increasing magnification: (1 to 4)  $2360 < x_p < 3350 \mu\text{m}$ ; (5 to 7)  $1700 < x_p < 2360 \mu\text{m}$ ; (8 to 10)  $1180 < x_p < 1700 \mu\text{m}$ ; (11-12)  $850 < x_p < 1180 \mu\text{m}$ .



**Figure 14.** Structure of mixtures of air-borne and wall-borne material. From top to bottom in decreasing size and increasing magnification: (1)  $x_p > 3350 \mu\text{m}$  ; (2 to 5)  $2360 < x_p < 3350 \mu\text{m}$ ; (6 to 8)  $1700 < x_p < 2360 \mu\text{m}$  ; (9-10)  $1180 < x_p < 1700 \mu\text{m}$ ; (11-12)  $850 < x_p < 1180 \mu\text{m}$ ; (13-14)  $600 < x_p < 850 \mu\text{m}$ .



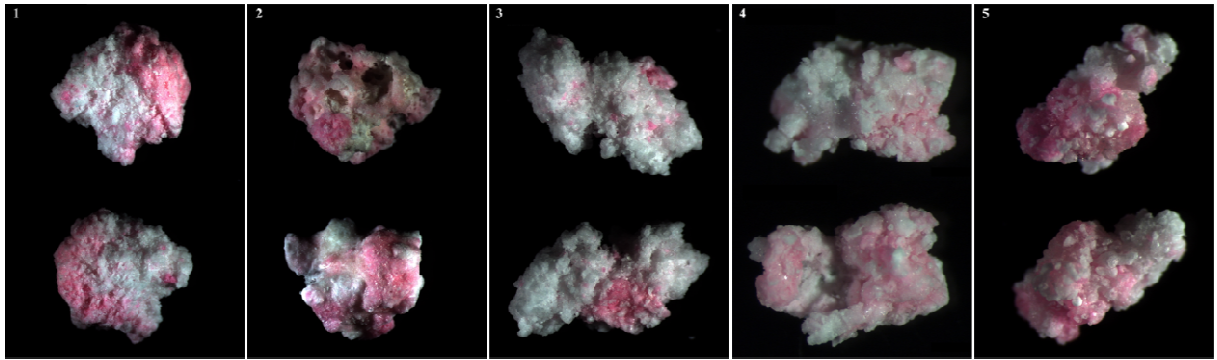


**Figure 15.** Distribution of wall-borne material within the structure of large granules. a) Top and bottom photographs show sides of the same granule. From left to right in decreasing size: (1,2)  $x_p > 3350 \mu\text{m}$ ; (3)  $2360 < x_p < 3350 \mu\text{m}$ ; (4)  $1700 < x_p < 2360 \mu\text{m}$ ; (5)  $1180 < x_p < 1700 \mu\text{m}$ .

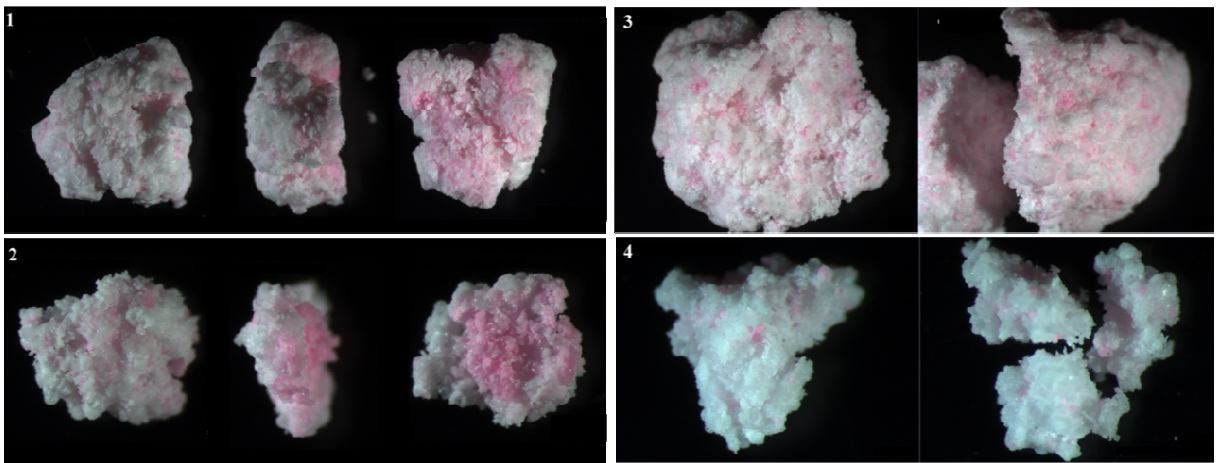


**Figure 16.** Examples of the distribution of wall-borne material in the interior of large granules. (1-2) show left to right, the outer surface, the cut side, the inner side. (3-4) show pairs of whole and cut granules. Micrographs (1,3) correspond to the fraction  $x_p > 3350 \mu\text{m}$ ; (2) to  $2360 \mu\text{m} < x_p < 3350 \mu\text{m}$  (4) to  $1800 \mu\text{m} < x_p < 2360 \mu\text{m}$

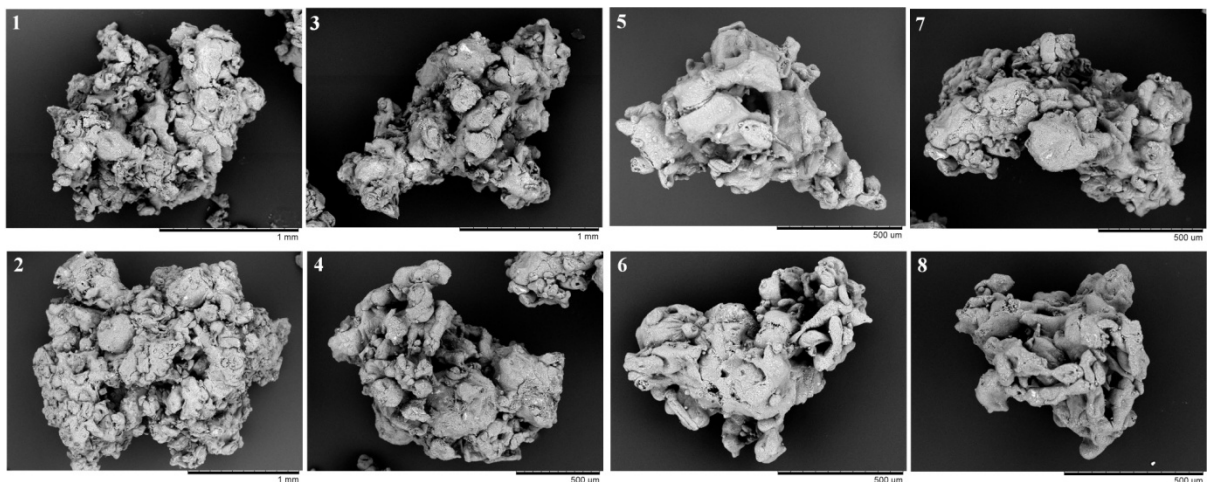


**Figure 17.** Examples of granule morphology. From top to bottom and left to right in decreasing size, (1-2)  $850 < x_p < 1180 \mu\text{m}$ ; (3-4)  $600 < x_p < 850 \mu\text{m}$ ; (5-8)  $425 < x_p < 600 \mu\text{m}$ .

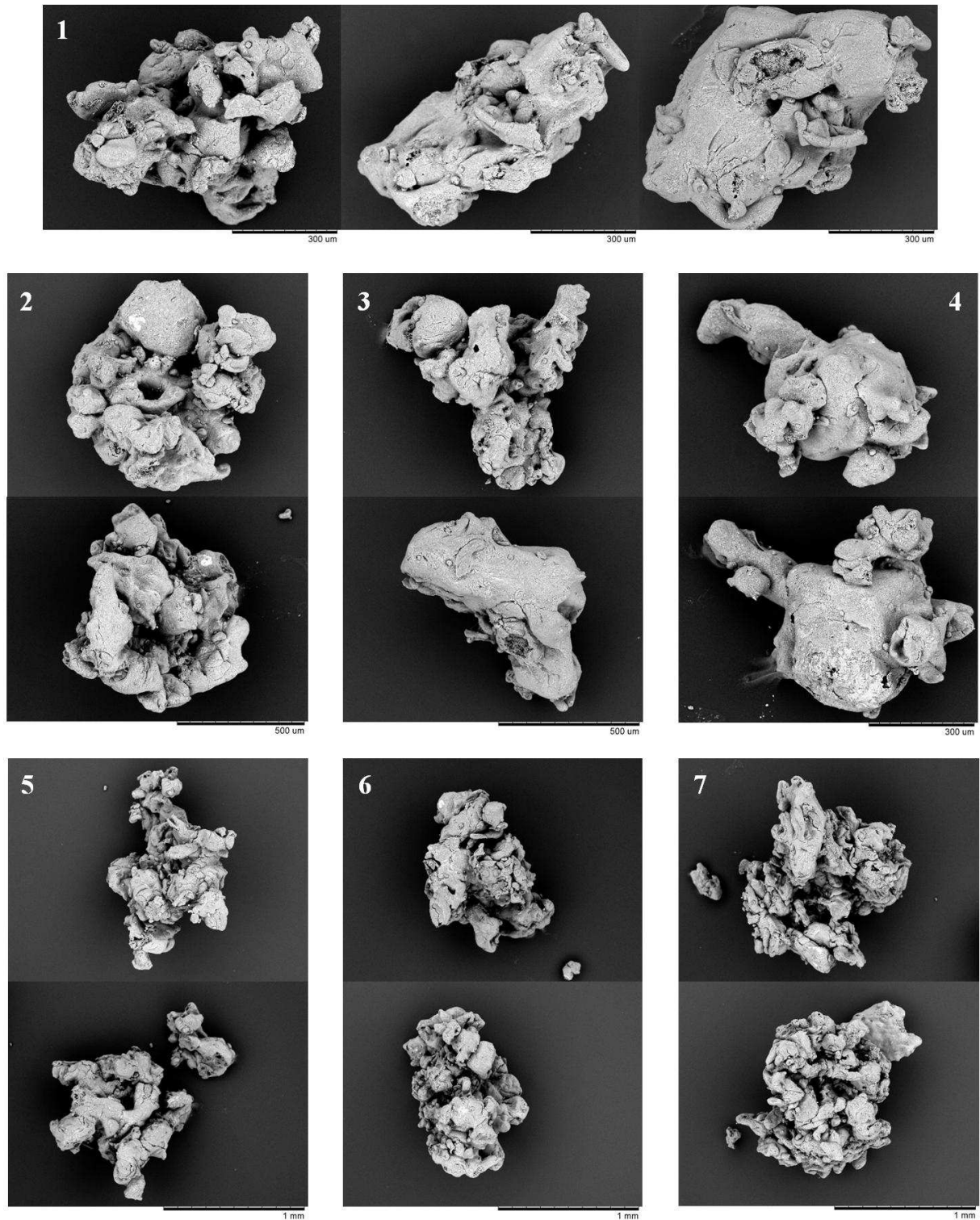


**Figure 18.** Heterogeneity of the structure of large granules. Top and bottom parts of each pair show both sides of the same granule. From top to bottom left to right in increasing size, (1) shows one side, the thickness and the backside, size  $425 < x_p < 600 \mu\text{m}$ ; (2-4)  $600 < x_p < 850 \mu\text{m}$ ; (5-7)  $850 < x_p < 1180 \mu\text{m}$ .

involves the aggregation between wall clusters and air-borne droplets, occurring at some point after deposition, and before their exit from the unit.

#### 4.6. Residence time of the re-entrained material.

The age distribution,  $AD$ , of the re-entrained material can be quantified by measuring the exit rate of dyed material in  $P - 3$  at the intervals defined by the sampling times, as done in a wash out experiment in chemical reactors (Levenspiel 2004). Samples cover the full renewal cycle of the deposits in  $\sim 1h$ , after which the dyed material in the exit product falls  $< 1\%$ . The average exit rate of wall-borne material is denoted  $w$  and given in (2) for the size class  $s$  and time interval  $i$  between the  $i^{th}$  and  $i^{th-1}$  samples. It is function of the exit mass rate,  $M_P$ , and the ratio of material of wall-borne origin,  $X$ , given in Figures 7 and 11. A standard age probability density function,  $E$ , is estimated in (3) normalizing  $w$  by the total re-entrained mass,  $W$ . The latter is obtained in (4) for each size class  $s$  by the integration of  $w$  during the entire renewal process comprised of  $n$  samples.

$$w_{s,i} = \frac{1}{2} (M_{P,s,i-1} X_{s,i-1} + M_{P,s,i} X_{s,i}) \quad (2)$$

$$E_{s,t} = \frac{w_{s,t}}{W_s} \quad (3)$$

$$W_s = \sum_{i=1}^n w_{s,i} \cdot (t_i - t_{i-1}) \quad (4)$$

Note that  $E$  is not in strict terms the product residence time distribution,  $RTD$ . It is the exit age distribution,  $AD$ , of the material borne at the wall after atomization restarts. It includes the residence time that it takes for a granule at the wall to be re-entrained, plus its air-borne residence time to the exit. In order to facilitate the comparisons across the different size ranges,  $E$  are normalized in (3) by the mass re-entrained within each fraction,  $W_s$ . The whole set of functions provided can be interpreted directly as the probability of the material that is re-entrained within a given size range  $s$  to exit at a given time  $t$ . Logarithmic plots allow a better visualization when the distributions present very long tails. For this reason, a density function,  $E_{log}$ , based on a logarithmic time is also calculated in (5).

$$1 = \int_0^{\infty} E_s(t) \cdot dt = \int_0^{\infty} E_{log,s}(t) \cdot d(\log t) \quad (5)$$

The mean or average residence time  $\bar{t}$  is given as the first moment of  $E$  is provided in (6).

$$\bar{t}_s = \int_0^{\infty} t \cdot E_s(t) dt \quad (6)$$

Table 2 summarizes the statistics of  $E$ . A characteristic mode occurs between the samples at 157.5 s and 247.5 s, while  $t_{84}$  ranges from 1350 to 1720 s depending on the size of aggregates. The median age  $t_{50}$  and the mean  $\bar{t}$  range between 310 – 510 s and 710 – 870 s respectively. These values are, in average, from ten to a hundred times higher than the residence time expected from the trajectories of the air-borne particles in similar units, according to Huntington (2004) below 30 s. Harvie *et al.* (2002) or more recently Ali *et al.* (2013) or Ali *et al.* (2014) provide numerical support and report much lower values for the largest particles. The large time they spend at the wall may be behind why models, which simply assumed partially elastic collisions to the wall, struggle to explain how they dry in the chamber in such short air-borne residence times.

As time progresses the relative error in  $E$  becomes higher due to the smaller concentrations of dye. The tail of the distributions prolongs for a long time and at the final part, a large section is defined by fewer samples. This lead to a higher uncertainty in  $w$  and the integration in (4), what explains why the confidence intervals in  $t_{50}$  and  $t_{84}$  are larger. This is particularly relevant for the largest granules which show a secondary mode at larger times.

#### 4.7. Time scales in the re-entrainment mechanics.

The origin of the correlation between the aggregate size and how the re-entrained material distributes in the structure becomes clear under the analysis of the age associated to the different sizes. The  $AD$  of the whole re-entrained material is compared with those of each size fraction in Figure 19. Two distinct sets of distributions can be distinguished: one is related to smaller fractions than the average product, another to large granules  $> 850 \mu m$ . These are split in Figures 20 and 21.

The smaller fractions result of the re-entrainment of pure particles in the product and present a wide span in Figure 20. In particular, the fractions  $< 300 \mu m$  present a secondary mode between 300 – 600  $\mu m$  and a prolonged exponential decay. As expected, larger particles, closer to the mean sizes, drive the overall size distributions given in Figure 7 and follow closely the average  $AD$ .

$E$  for the large classes is shown in Figure 21. As the size rises  $> 850 \mu m$ , particle history starts to include the aggregation of air and wall-borne material, the function changes, narrowing significantly the exponential decay. The set of functions obtained for large sizes is clearly different from the mass

**Table 2.** A summary of the statistics of the exit age distribution  $E$  of the re-entrained material, given in Figures 19 and 20.

<b>Size Class</b>	$t_{16}$	$t_{50}$	$t_{84}$	$\bar{t}$	$X_{o,s}$
$\mu\text{m}$	$\times 10^2 \text{ s}$	$\times 10^2 \text{ s}$	$\times 10^2 \text{ s}$	$\times 10^2 \text{ s}$	$\times 10^2$
<b>&lt; 150</b>	$1.6 \pm 0.1$	$5.0 \pm 0.3$	$15.6 \pm 2.1$	$7.9 \pm 0.4$	$30 \pm 2$
<b>150 - 212</b>	$1.4 \pm 0.1$	$4.5 \pm 0.5$	$13.5 \pm 2.7$	$7.4 \pm 0.6$	$29 \pm 2$
<b>212 - 300</b>	$1.4 \pm 0.1$	$4.6 \pm 0.6$	$14.6 \pm 3.3$	$7.6 \pm 0.7$	$23 \pm 2$
<b>300 - 425</b>	$1.5 \pm 0.1$	$4.9 \pm 0.7$	$15.0 \pm 3.4$	$7.8 \pm 0.8$	$19 \pm 1$
<b>425 - 600</b>	$1.4 \pm 0.1$	$4.7 \pm 0.7$	$15.1 \pm 3.2$	$7.8 \pm 0.7$	$18 \pm 1$
<b>600 - 850</b>	$1.5 \pm 0.1$	$5.1 \pm 0.8$	$15.2 \pm 3.0$	$8.1 \pm 0.8$	$21 \pm 2$
<b>850 - 1180</b>	$1.3 \pm 0.1$	$5.0 \pm 1.4$	$16.0 \pm 3.4$	$8.2 \pm 1.0$	$33 \pm 3$
<b>1180 - 1700</b>	$1.3 \pm 0.1$	$5.1 \pm 1.6$	$17.2 \pm 3.4$	$8.4 \pm 0.9$	$46 \pm 3$
<b>1700 - 2360</b>	$1.2 \pm 0.1$	$4.1 \pm 1.5$	$16.2 \pm 3.1$	$8.1 \pm 0.9$	$34 \pm 3$
<b>2360 - 3350</b>	$1.1 \pm 0.1$	$3.1 \pm 0.7$	$14.5 \pm 3.5$	$7.1 \pm 1.0$	$31 \pm 3$
<b>&gt; 3350</b>	$1.4 \pm 0.1$	$4.0 \pm 1.6$	$16.8 \pm 2.0$	$8.7 \pm 0.9$	$27 \pm 2$
<b>Total</b>	<b><math>1.4 \pm 0.1</math></b>	<b><math>4.7 \pm 0.3</math></b>	<b><math>15.1 \pm 1.3</math></b>	<b><math>7.8 \pm 0.3</math></b>	<b><math>20 \pm 1</math></b>

averaged distribution, and progressively narrows around the mode with increasing particle size.

In addition, a secondary mode appears in all sizes around  $1100 - 1700 \mu\text{m}$ . As illustrated by the logarithmic plots, it gains relevance in the largest classes. The span of this mode cannot be estimated accurately however, it is worth observing that it is the presence of this feature which modifies the average statistics of large sizes, moving them towards larger means, comparable in Table 2 to smaller classes. The  $AD$  functions however have a clearly different nature. In Figure 21,  $AD_s$  tend to be closer to an ideal plug flow reactor,  $PFR$  with axial dispersion, than they are to continuous stirred tank reactor,  $CSTR$ . This indicates that despite being mixtures, large granules do not come from a well-mixed structure that renews gradually. This would result in the exponential decay of  $E$ , where the mixtures would be generated gradually. The re-entrainment however seems to occur at a faster time scale that produces mixtures from the first moment that then exit with a narrow age range.

The decrease with  $t$  seen in Figure 20 for the smaller fractions is better approximated by an exponential decay. However, these sizes exit as pure particles, which again discards the possibility of release from a well-mixed layer. The slow decrease here rather than mixing indicates the kinetics of the renewal. Notice that the probability of the particle impacts to re-entrain dyed old clusters decreases with

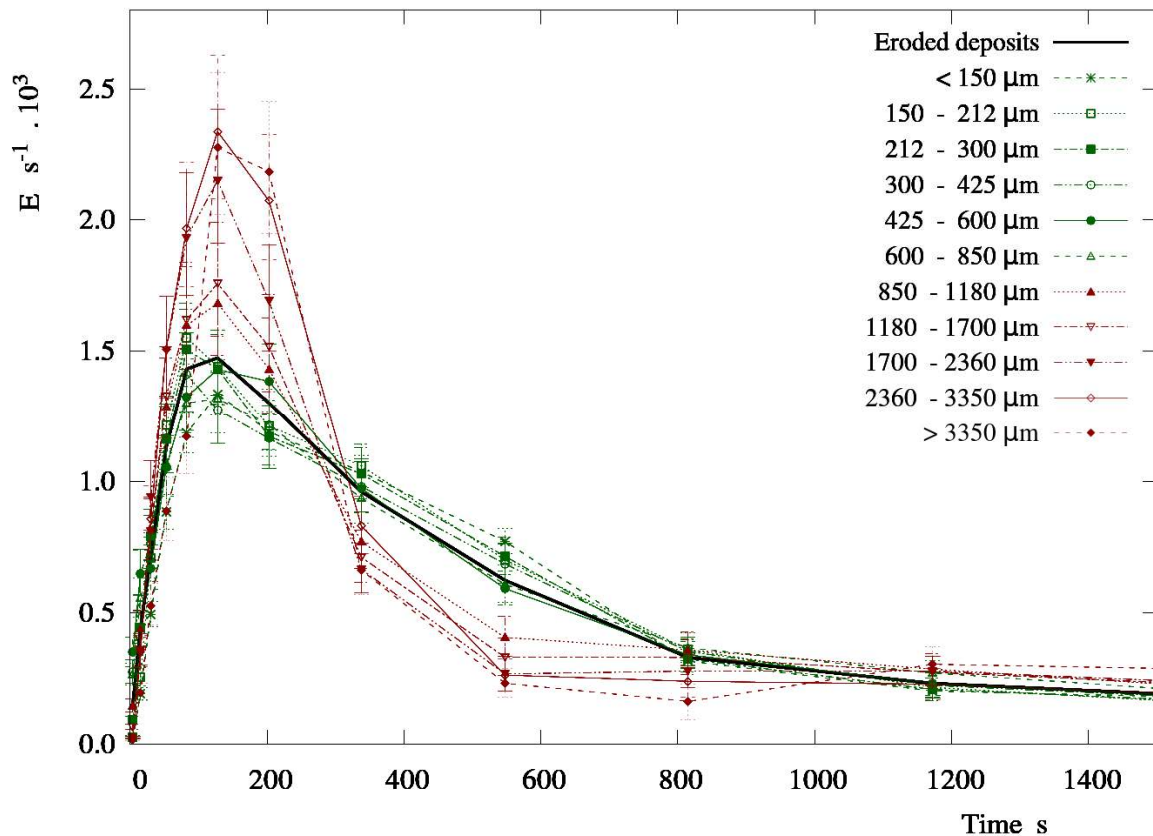


**Figure 19.** Detail of  $E$ . Comparison between the mass averaged values and the functions for all size classes.

$t$ , as the structure renews and the surface exposing dyed clusters -of age above  $t$  - decreases.

All the distributions shown may be fitted to a system of ideal reactors. In particular, the inflexion point in the average profile fits well with the summation of two exponentials resulting from two *CSTRs* in parallel (Levenspiel 2004). In each branch, one *CSTR* followed by one *PFR* could be used to represent the time in the wall-borne and air-borne regions. And either a large or a small *CSTR* in each branch could approximate respectively the long or short time scales observed in the re-entrainment.

However, it is important to note the limitations of such approaches. Note that the values of  $E$  reported here are in effect an average over the entire deposits' surface, which is itself very heterogeneous, see Figures 3 and 9. Deposits are not a well mixed structures, but layers that grow in thickness and then break up. This very likely happens at different time scales in different sections of the wall because the properties of the deposits (e.g. water content) and the stresses they are subject to (e.g. drag or particle impacts) change substantially. This type of spatial effects cannot be described accurately by a *CSTR* approximation. An example may be found in the secondary mode in Figure 21. This feature does not comply with a gradual renewal of outer layers, for it suggests a sharp increase in the re-entrainment

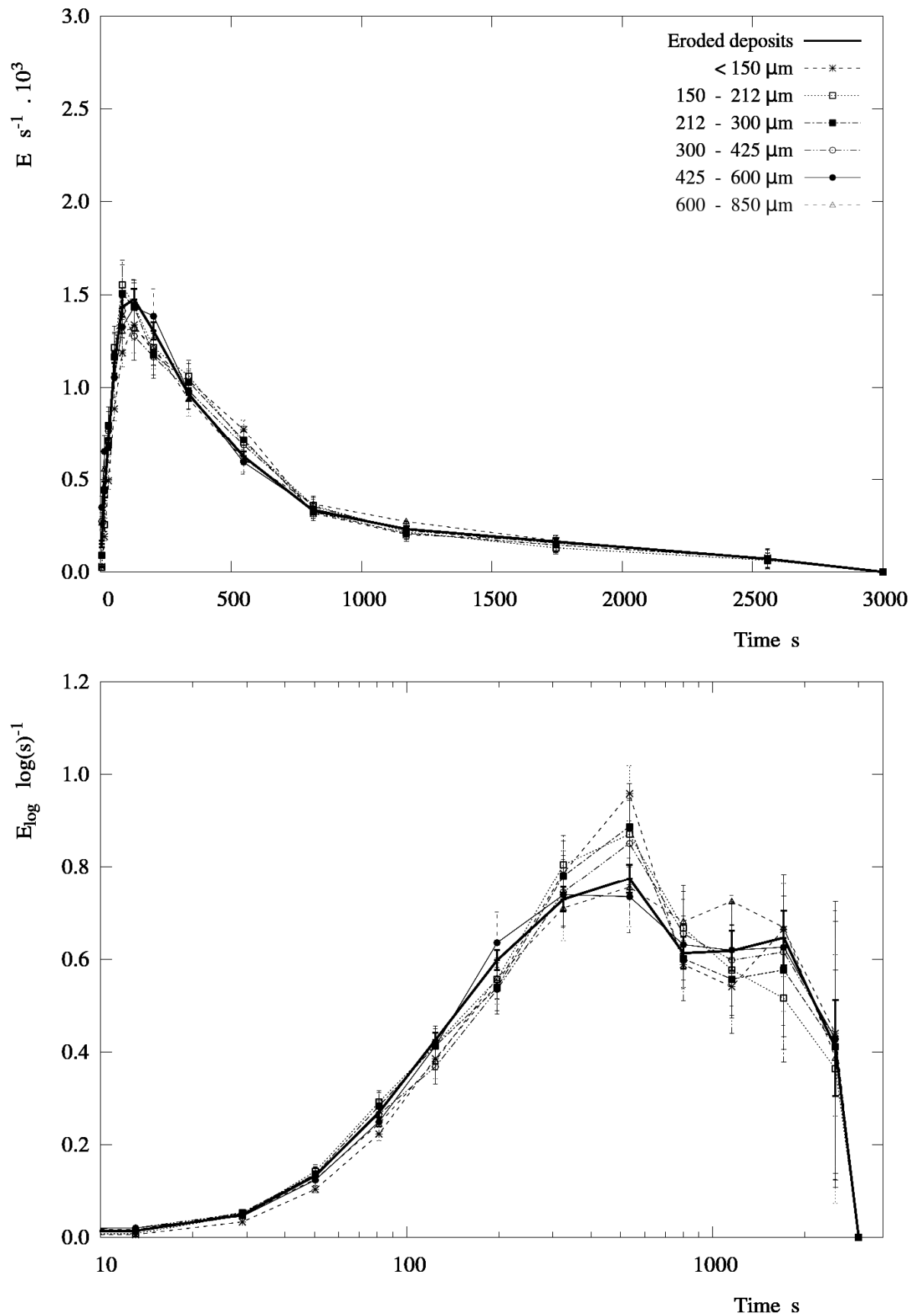


Figure 20.  $E$ ,  $E_{\log}$ . Comparison between the mass averaged value and functions for small and average size  $d$  particles.

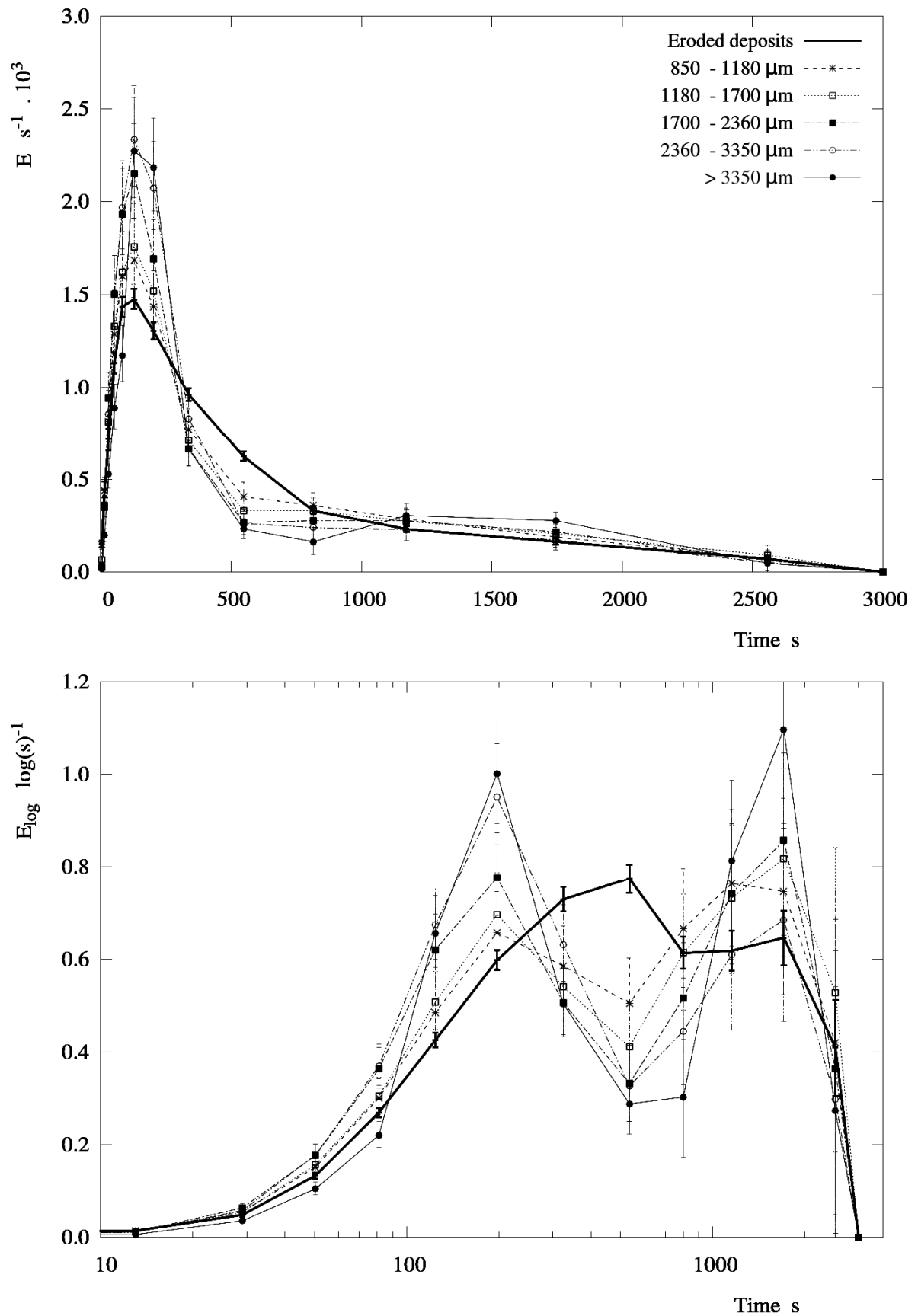


Figure 21.  $E$ ,  $E_{\log}$ . Comparison between the mass averaged value and functions for the large sized particles.

rate. A significant part of the re-entrained mass, see  $t_{50}$  for large sizes, exits the unit at a time scale one order of magnitude higher than the mode, and twice higher than the mean in Figure 21. Such a sudden change in the re-entrainment might be linked with certain sections of the wall where deposits are allowed to grow thicker and shedding events dominate the re-entrainment. Notice that these phenomena are a common observation in dryers (see section 3.4 or Hassall 2011) and can release a considerable mass (see section 3.4). Such type of intermittency may explain the secondary mode seen in Figure 21 and the corresponding shoulder in all smaller classes in Figure 19.

To sum up, Figures 19 to 21 demonstrate that various time scales are involved in the re-entrainment process, and correlated with the final size of granules. In combination with the analysis of the morphology, it appears that fast and slow time scales are associated respectively to re-entrainment of granules with and without the aggregation with air-borne material.

#### **4.8. Exit size of air and wall-borne material.**

The size distributions of air-borne and wall-borne material are compared with the initial droplet size in Figure 22. A clear growth pattern is seen in both cases. The material with air or wall-borne origin shows a very similar size range. The population of eroded aggregates has a higher proportion of the smaller fragments but both show a similar tail towards the large granules and similar distributions. Bearing in mind that there are no particular differences in the structure of pure granules -air-borne or wall-borne-, there are no clear evidences to suggest that both populations are generated in a different manner.

The question remains on whether the aggregation observed for pure particles in the product occurred 1- before they were deposited, i.e. coalescence, 2- upon the deposition itself, 3- during a long time in wall-borne state or 4- after re-entrainment. Note that the population of pure white particles may have also interacted with the deposits but at faster time scales than the measurement. The same origins can be thought for the mixtures, with the obvious exception of aggregation before deposition. The likelihood of the different hypothesis will be analyzed in the next section.

#### **5. A wall dynamics framework for swirl assisted dryers.**

The observations given in previous sections are used here to discuss the most likely dynamics of deposition and re-entrainment within counter current swirl dryers, and highlight specific areas for research. An outline is provided in Figure 23, which depicts the ageing process and different contact

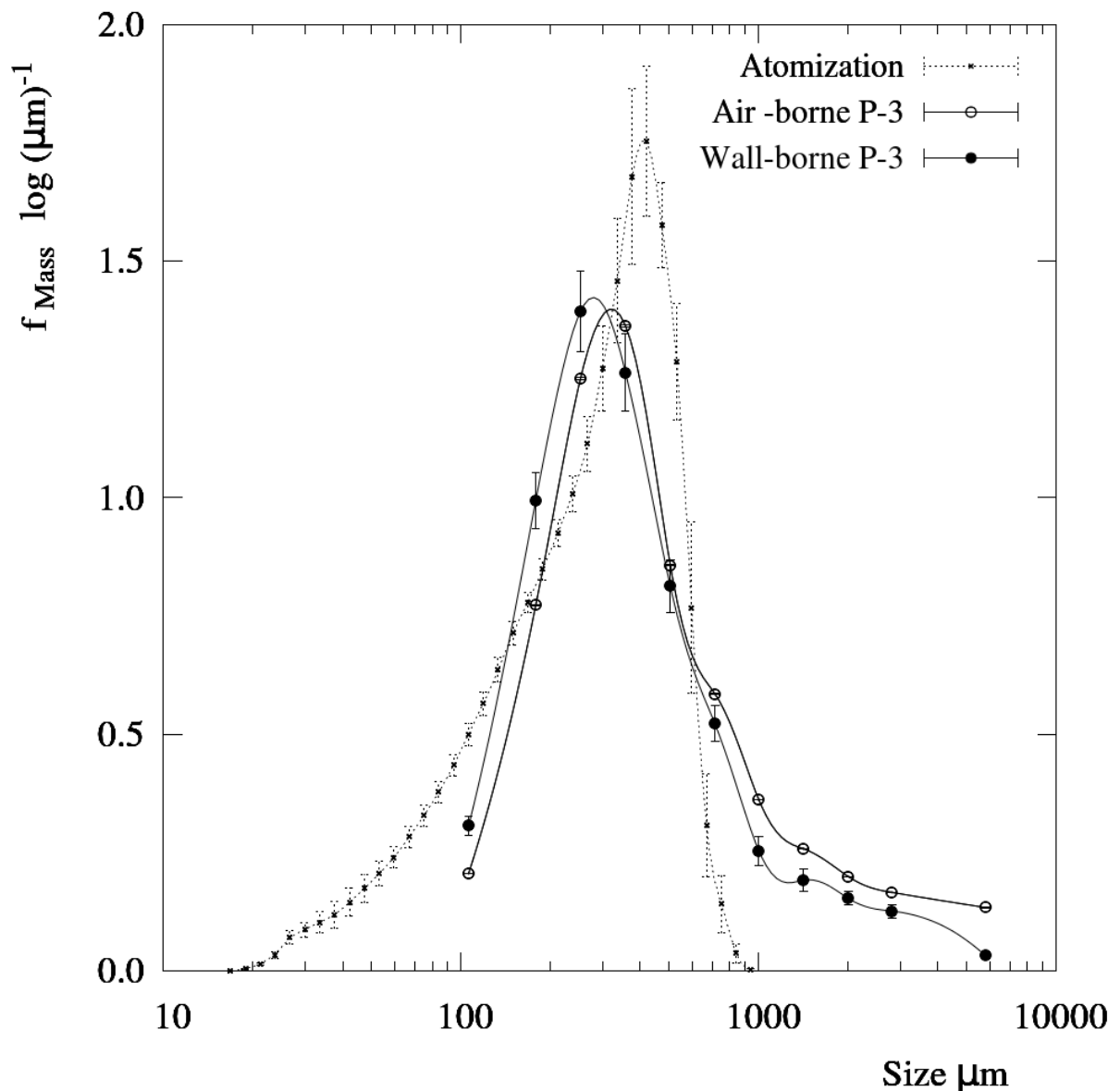


**Figure 22.** Volume and mass bases size probability density functions of the atomization and the air and wall borne material.

mechanics by which the air-borne product may interact with the multi-layer structure.

Figure 23 considers the sources of re-entrainment associated to the action of aerodynamic forces, gravity and the impact of wet droplets and dry particles. These lead to dry and wet mechanisms of erosion, and cause the detachment and breakage of large clusters.

### 5.1. Deposition and contact mechanics.

Chapter IV reviews briefly the different type of contacts established in the flowing air of spray dryers and the interaction forces involved. The impacts to a fix substrate can be thought in very similar terms, but need to recognise the role of the microstructure, that is, how the cohesive forces drive the behaviour of

the wall-borne partners. The contact between a semi-dried droplet and the substrate occurs at a time scale and a contact area that depend on their drying state and the impact inertia. Deposition occurs only if the area is large enough so that the adhesive force overcome the aerodynamic disruptive stresses of a similar time scale, plus those from an inertial source: a)- the shear stress caused by gravity and the centrifugal inertia -which both tend to generate rotation- and b)- the elastic recovery which causes a normal detaching force.

Impacts between sufficiently dry partners in stage [11] in Figure 23 result in rebound due to developing low adhesive forces, [14]. The bonds between wall-borne clusters, however, need sustaining the stresses derived from the impact what may or may not cause the breakage of the microstructure and re-entrainment in [11,12,13] or [11,12,5,6]. This sort of erosion is detailed in sections 5.4.1 and 5.4.3.

Impacts develop a higher contact area when droplets are more deformable in stage [1]. Two possibilities may be considered. One, deposition at low inertias in [2], where both adhesive (droplet-cluster) and cohesive forces (between clusters) can sustain the stresses from the impact. Another, at high inertias in [8] owed to the impact of the largest droplets from the spray. Here the contact area and the shear stress generated by the impact are increased. Capture occurs when the shear stress breaks the bridges between neighbouring clusters but the adhesive forces between the droplet and the cluster can sustain it, see stages [1,8,9] or [1,8,5,6,7] in Figure 23. This sort of erosion is detailed in section 5.4.2 and 5.4.3.

Other factors such as wall roughness, particle shape and interlocking play an important role. The balance of forces at the contact depends greatly on the disposition of the roughness (Guingo and Minier 2008) and the sole action of the heterogeneities owed to the deposits can have an important effect in particle flow and residence time (e.g. Sommerfeld 1992; Sommerfeld and Qui 1993). Consider that in this case the surface features of the clusters at the wall are very large, comparable to the cavities of impacting particles, if not the particles themselves, see Figure 17. This can make particles to get trapped at the wall by simply locking or rotating in the cavities of the outer layers in the deposits. This would increase significantly the residence time and may explain the difference between the mode residence time given in section 4.7 (157.5 – 247.5 s) and the air-borne residence time in numerical simulations, ten times lower

To sum up, the non-spherical nature of particles remains an issue in regards to the description of rotation and rolling at the wall. Morphologies such as those in Figures 12 to 18 ensure very different

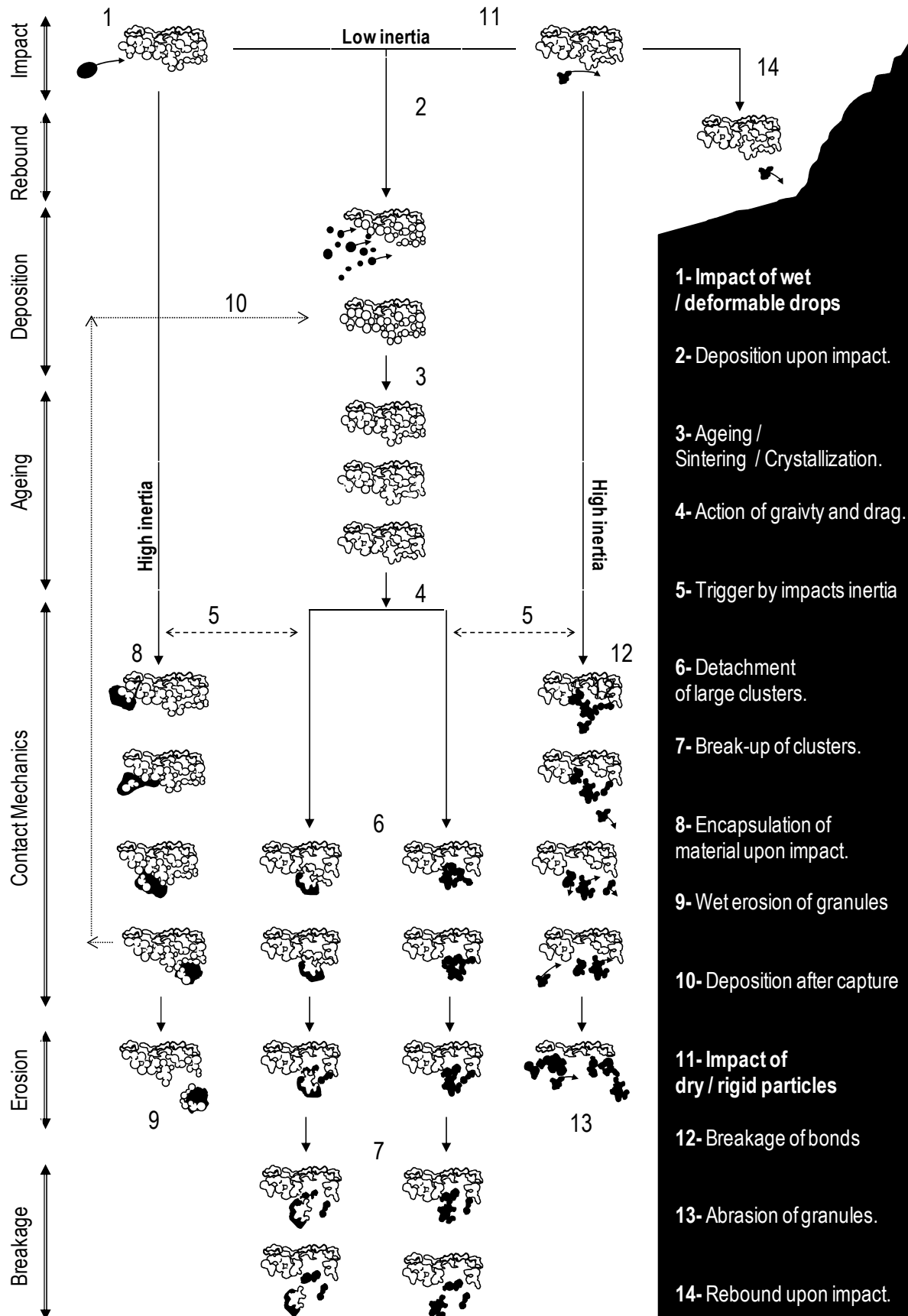


**Figure 23.** Wall dynamics in counter-current spray drying. Cycle of deposition, ageing and wear at the wall.

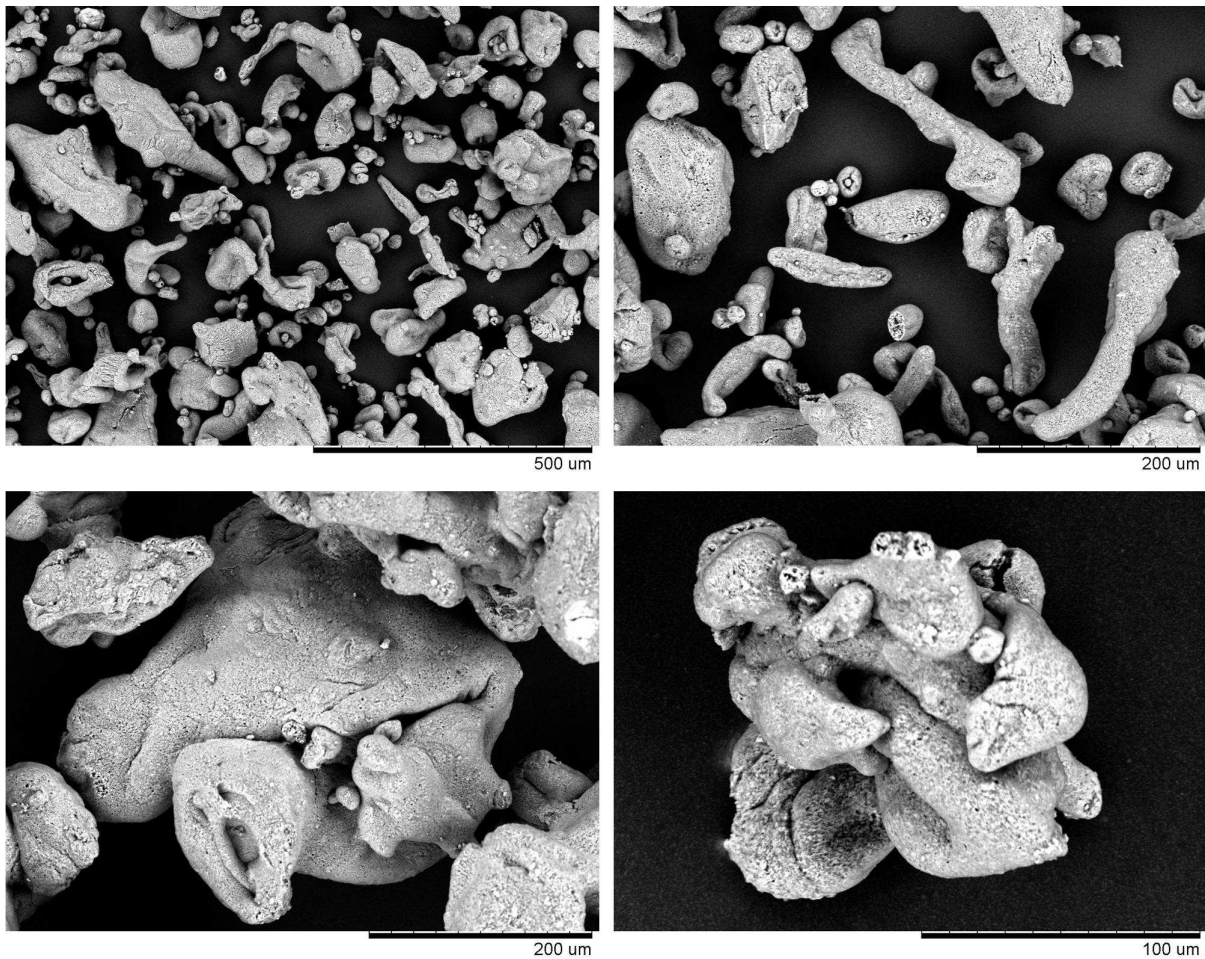


**Figure 24.** Examples of the presence of ligaments in the elutriated fines -top- and the coiled structures in the product.

contacts to those of spherical models. An example of the droplet morphology can be provided by the analysis of the elutriated fines. These contain many ligaments produced during atomization, illustrated in Figure 24. Upon the impact to the wall, this shape causes a higher rotational moment, lead to multiple contacts and appear as coiled structures in the product (for a more detailed description see Appendix II).

## 5.2. Ageing.

The particle-particle forces in the structure evolve as time progresses in stage [3]. The cohesive strength is modified when new bridges are formed by the impact of droplets in [2] and [10] and the existing bridges solidify in [3] (e.g. Tardos and Gupta 1996; Bikaa *et al.* 2005). As this occurs, the clusters start containing higher numbers of primary particles but are sustained by a lower specific contact area, what facilitates their removal. The size of the re-entrained cluster would depend on the spatial distribution of the bridges, in terms of their contact area and their strength.

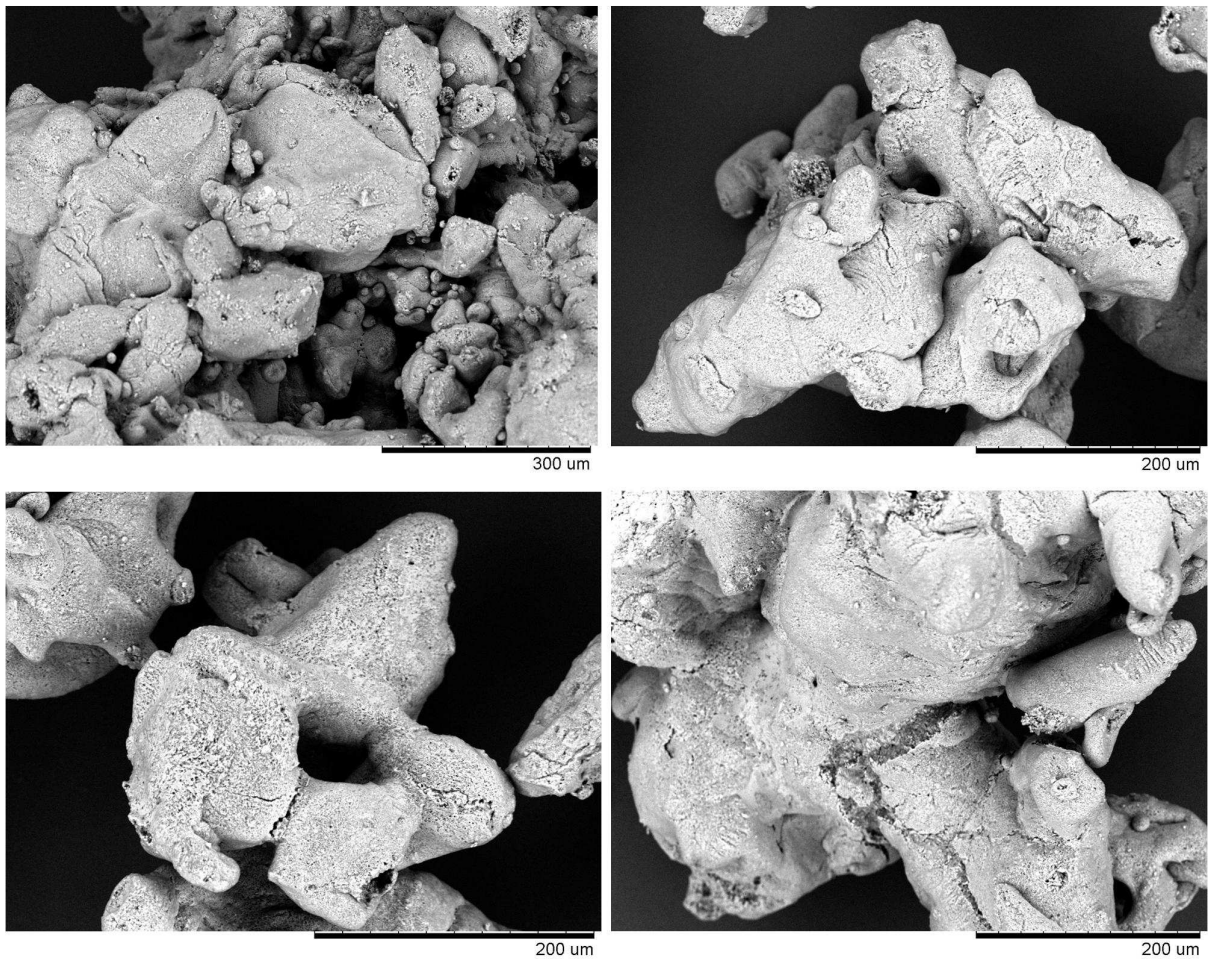


**Figure 25.** Examples of the solid bridges that bound primary particles together within large and average size granules.

The evolution of solid bridges such as those shown in Figures 25 and 26, would respond to the rates of different transport phenomena, some of which are described in detail by Wang and Harb (1997) for the erosion of ash deposits. On one hand, external heat and mass transfer rates dry the structure, increase its porosity and accelerate the crystallization of salts, but on the other hand, contacts between particles with different water contents drive the migration of species and modify properties such as the surface viscosity. These are long time scale processes, which occur along with the momentum transfer driven by impacts, and the action of the Laplace pressure and gravity, ultimately determining the sintering rate. To describe the strength of the clusters it is important to evaluate the relative time scales of these phenomena. As drying progresses, material properties such as viscosity or diffusion coefficients vary across several orders of magnitude. Thus, the effective rates at which liquid and solid bridges thin or sinter are constrained by the time it takes for the viscous-like material deposited to turn into a deformable solid. This occurs at a certain drying stage, increasing drastically viscous forces, reducing the mobility of species and making the momentum transfer negligible.

### 5.3. Origin of the disruptive stresses.

As the layer grows, large clusters cannot sustain the stresses caused by the inertia of the impacts gravity and drag and lift forces due to the air flow near the wall. This leads to the breakage of bonds and the re-entrainment of material. However, it is interesting to note that when particles are not present in the tower, re-entrainment stops: thus particle impacts are necessary to cause re-entrainment.

The trigger mechanism may be simply related to the growth of the clusters, or to the breakage of the bridges between them. Re-entrainment would occur at different time scales in each case: 1- A long one occurs after deposition, aging and shedding in [2,3,4,5,6] in Figure 23, where the size of the re-entrained cluster is rather related to the microstructure of the multi-layer, and 2- A short one occurs after the impact of dry particles in [11,12,13] or wet droplets in [1,8,9], where the size of the re-entrained cluster is also related to the characteristics of the impact.

In stage [6], gravity or aerodynamic driven forces suffice to induce the removal of clusters when they grow sufficiently. Now, growing implies that there is aggregation between new droplets and the wall-borne clusters, and as such, we should expect the granules in the product to be mixtures of wall-borne material (dyed) and air-borne material (white). Indeed, this occurs for the large granules but it does not for most of the product. The next section discusses the mechanisms given in Figure 23 by which wall-borne clusters can be re-entrained either as pure dyed particles or as mixtures.

### 5.4. Mechanisms of re-entrainment.

The material bounded at the multi-layer exits the unit in two different populations: 1- A set of granules that cover the entire size range is re-entrained directly with no aggregation and at a long time scale, and 2- Another set of granules  $> 850 \mu m$  is comprised of aggregates of wall-bore clusters and air-borne droplets and exits the unit at much shorter time scale. Both show intermittencies at a large time scale.

#### 5.4.1. Dry mechanisms of erosion.

They result from multiple impacts of dry particles with sufficient inertia to break bonds within the structure. This causes the direct re-entrainment of aggregates without any further aggregation, as depicted in [11,12,13] in Figure 23. In combination with gravity it may be also be responsible of triggering the detachment of larger clusters and their subsequent breakage in stages [11,12,5,6,7].

These types of contact are associated with both, drier particles (small and average size fractions) and

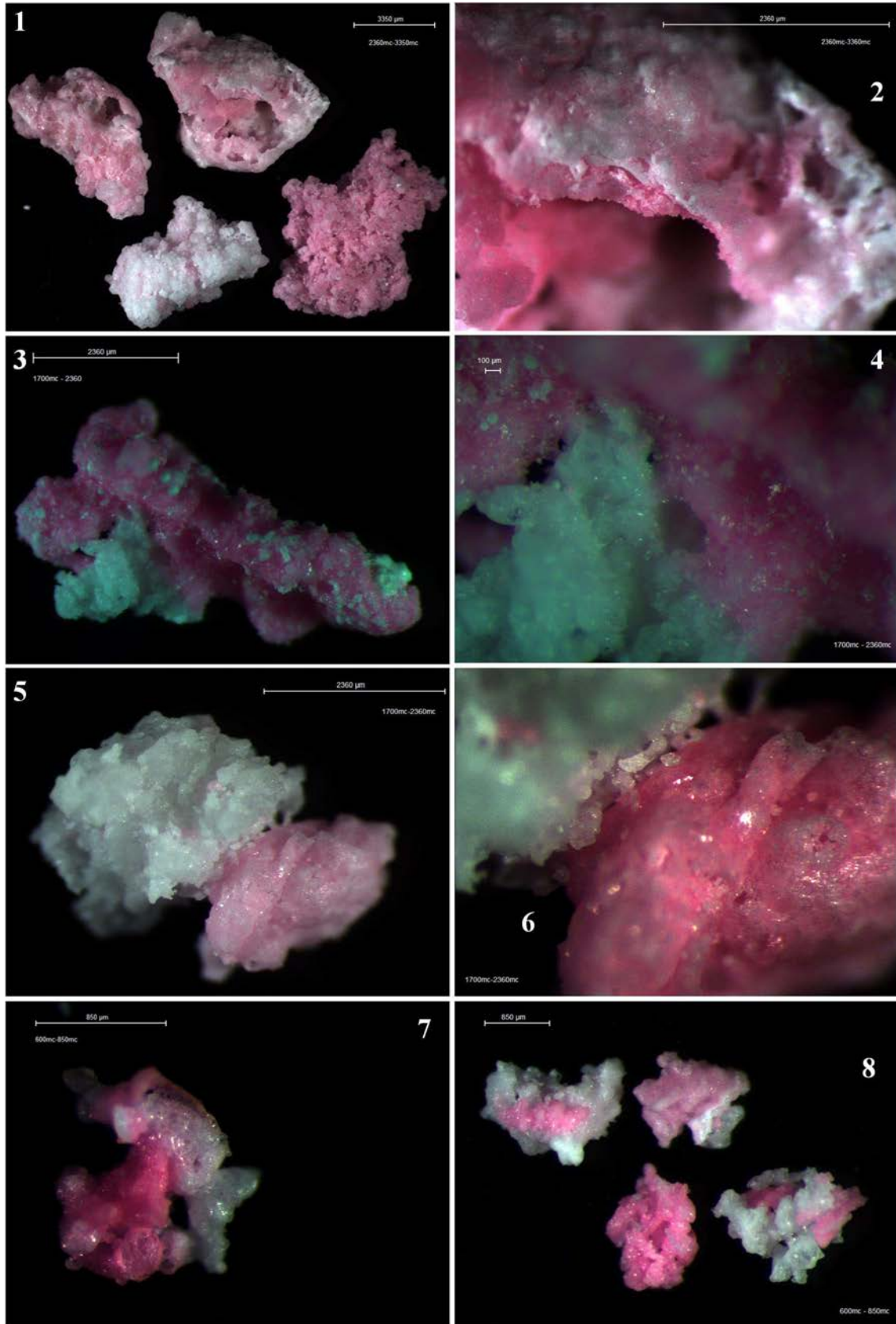


**Figure 26.** Examples of the contacts between the air-borne and wall-borne material in the product. Layering in (1-2) to solid bridges of different contact area in (3-4)(5-6) and (7) and primary particles embedded in the structure in (8).

drier sections of the multi-layer above and below the projection of the nozzle in Figure 2. The small inertia associated to the flight of these particles causes the re-entrained clusters to be of small and medium sizes. Notice that this type of re-entrainment occurs as a single event. For this reason, one may associate the long decay in  $E$  in Figure 20 to the time that particles remain fixed at the wall rather than to the time of flight between the wall and the exit.

The lack of mixtures is noticeable. Most coloured average sized clusters do not appear to sinter with the material deposited thereafter, which has two possible explanations. One is that the time at which drying fixes the size after deposition is much faster than the sintering rate. This suggests that growth occurred before the time at the wall, e.g. during coalescence, or at the deposition impact itself. Another explanation comes from the production of pure particles by breakage in stage [7]. In this case, the largest granules are more likely to survive containing the mixed regions, leaving smaller particles pure.

#### **5.4.2. Wet mechanisms of erosion.**

A part of the re-entrained product has a different history, involving aggregation with air-borne material. It becomes identifiable by large granules having a characteristic residence time and morphology. Mixed large granules may be produced by 1- aggregation upon the deposition of new droplets, 2- sintering during the wall-borne state or 3- contacts after the erosion. The latter implies coating after numerous impacts with small droplets or the capture by large ones. Both are very unlikely given the low concentrations away from the wall (Hassall 2011). In regards to the second, sintering, it may be responsible of the solid bridges in Figures 25 or 26, but it is not the main mechanism responsible of generating the mixtures, because they do not exit only at larger times but from the first moment.

The most likely origin for mixtures is direct growth upon the impact of wet droplets in [8]. These impacts have the largest inertia and are common in the areas close to the nozzle projection. Here droplets  $> 200 \mu m$  still have high water contents and momentum when they impact the wall, what occurs at tangential angles  $< 10^\circ$ . Upon colliding, they deform, lose energy due to viscous dissipation and capture aggregates, either in close proximity to the wall or already bounded at the structure. Stages [1,8, 9] in Figure 23 describe a rolling mechanism whereby wall-borne clusters act as initial rigid nuclei that becomes encapsulated. This appears as a likely contact mechanics in agreement with the morphology of large granules and similar "Rock'n Roll" mechanisms proposed for re-suspension of single particles (e.g. Vatisstas 1992; Reeks and Hall 2001 or Zhang *et al.* 2013). Newly formed

encapsulates may deposit in [10], roll or saltate along the surface, or become detached in [9]. If rolling or saltation occurs, the surface may keep picking up clusters, developing new contacts in a snowball effect. Its ability to grow then decreases as the surface dries and the inertia dissipates.

As opposed to dry erosion, re-entrainment now is comprised of multitude events occurring at fast time scales. Thus, the mode in Figure 21 can be thought to be related not to the time in a wall-borne state, but rather to the air-borne history which is obviously affected by the high level of interaction with the wall. The values may be related to the saltation of granules, documented before in counter-current spray dryers (Hassall 2011). They may indicate the time it takes for wet large granules, initially formed close to the nozzle projection, to saltate down the surface in contact with the deposits. In a very similar manner to rolling over a tilted plane, the centrifugal inertia and the lift force act as normal forces to the wall, and the combination of gravity and the drag acts as the shear force moving granules to the exit.

#### **5.4.3. Shedding and breakage.**

Deposits in Figure 9 do not show a perfect multi-layer distribution. They show large variations in thickness, and identifiable groups of clusters at the surface. This is the result of a shadow effect, where the heterogeneity of the outer layer makes particles to pile onto the same area rather than homogeneously across the surface. This is emphasized in swirl dryers by the non-spherical shapes and by the low impact angles to the wall. As the clusters formed grow, they become destabilized and detach.

The shedding process is illustrated in step [6], Figure 23. As described before, it may be triggered directly by the growth of the layer or by the impact of particles / droplets at high inertia. Once large clusters are detached, they are not likely to sustain the stresses in an air-borne state and break down into smaller fragments which contain both, pure particles or mixtures depending on whether the initial impact involved wet droplets or dry particles in [8,5,6,7] or [12,5,6,7] or both if the detachment was purely the consequence of growth in [4,5,6,7]. The presence of these intermittent events may explain the largest time scale features observed for all size classes  $> 1100 \text{ s}$ .

#### **Conclusions.**

This work demonstrates that the wall dynamics have a remarkable impact in swirl counter-current spray dryers. The influence of the re-entrainment kinetics goes beyond prior considerations, dominating the drying kinetics, the particle growth and the structure of a significant proportion of the product generated, at least under similar conditions with regards to fluid dynamics stresses and formulation.

**a) Rate.** The case studied focuses on standard detergent formulations. In this case, deposition and re-entrainment are found to be in equilibrium for the most relevant sections in the unit. The re-entrainment rate comprises  $> 12 - 20 \%$  in mass of the full production, becoming higher for both smaller size fractions and particularly aggregates  $> 850 \mu m$  in diameter.

**b) Time scale.** The mechanics of re-entrainment varies for aggregates of different size. Small and average size particles are directly re-entrained with no aggregation with air-borne material. In contrast, aggregates  $> 850 \mu m$  appear as mixtures of both and thus are almost entirely involved in cycle of deposition and re-entrainment. In general terms, the granules are asymmetric, have high aspect ratios, numerous asperities and large cavities, perhaps as a consequence of being sections of a low density network. However, no differences can be seen between pure re-entrained particles and the rest. Bearing in mind that the re-entrainment rates given are under predictions, the level of interaction with the multi-layer may be much higher. The time scale of the equilibrium at the wall has also an important effect in the residence time of the product, thus affecting its drying. The material undergoing this cycle has a residence time one to two orders of magnitude higher than the values expected from their air-borne trajectories. Such a large deviation should have serious implications in the performance of numerical models. Note that by ignoring the wall cycle they neglect the largest proportion of the time that an important part of the product and of most large granules remain exposed to heat and mass transfer rates. This represents a serious handicap in the ability to predict final product properties.

**c) Growth and Structure:** Considering that the main advantage of spray dryers comes from the porosity and structure generated, understanding of the mechanisms by which the multilayer develops and breaks down becomes critically important. Along this line, different re-entrainment time scales have been identified as the responsible of producing re-suspension either with or without the aggregation with air-borne material. These have been correlated respectively with the origin of larger and smaller aggregate sizes. Accordingly, a series of mechanisms has been proposed to describe the process. These include the re-entrainment caused by the impact of dry particles, capture and aggregation caused by the impact of wet droplets, and their combination with gravity to cause the detachment of large clusters and their breakage.

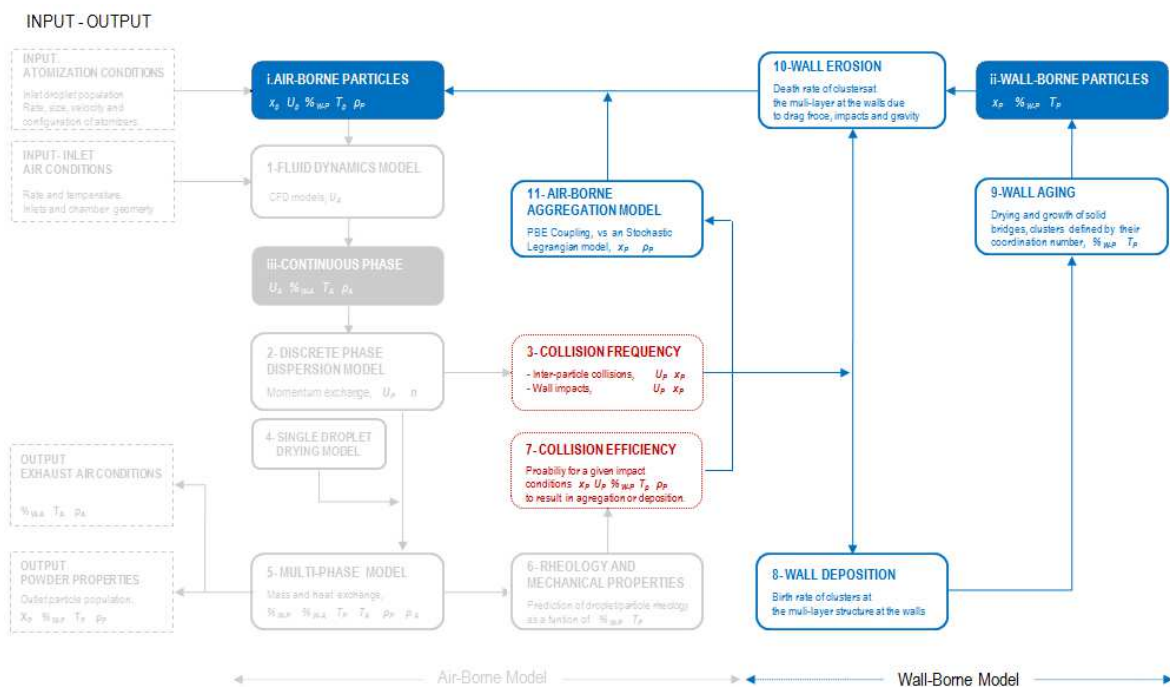
In summary, this work highlights the relevance of deposition, ageing and re-entrainment processes in the overall kinetics of spray dryers. Numerical models based exclusively in the description of the fluid

dynamics are not sufficient to replicate the overall process, which is intimately related to evolution of the deposits. For that reason, addressing these current limitations implies obtaining a set of constitutive equations capable of describing the multi-layer structure and the mechanics governing its renewal. This could lead to a better control of re-entrainment rate by changing operating conditions such as swirl intensity, kinetic energy or the slurry formulation. This is discussed further in the experiments reported in the Appendix III, describing the effect of different air inlet conditions in particle growth.

# PART B2

## CHAPTER VI

### AGGLOMERATION IN THE OPERATION OF SINGLE NOZZLES AND MULTIPLE NOZZLE LEVELS



## Summary

This chapter investigates particle growth in the operation of a swirl counter-current spray dryer under various production rates and configuration of nozzles. Section 1 studies the use of a single central nozzle at different positions to modify how the solids disperse in the unit. The data show that 1- a substantial particle growth occurs from any nozzle location, 2- the breakage of large granules contributes to formation of the finest fractions in the powder, and 3- the product shows a large heterogeneity in composition due the separation of solids and liquids during the atomization. Bringing the spray to a lower position increases the temperature faced by the droplets but reduces their residence time. This narrows the mode in the size distributions, but instead promotes the formation of granules  $> 850 \mu m$ . Appendix III provides a supporting investigation that relates this behaviour to the promotion and suppression of the re-entrainment from the walls.

Section 2 studies a higher production rate and the use of multiple nozzles. This increases the particle / drop concentration in the dryer, and modifies the temperature and velocity fields. In this case the product presents a clear bi-modal size distribution and it is more heterogeneous in its composition and porosity (see Appendix II). A series of experiments has been outlined to evaluate the contribution to growth of each individual nozzle and of their interaction. In a two level system, aggregation is inhibited at the bottom spray and promoted at the top where most of the largest granules are formed. The top spray is accountable for  $\sim 60 \%$  of the product generated with a size  $> 600 \mu m$ . Both levels interact by the capture of fines elutriated towards the top spray and this is responsible of at least  $\sim 10 \%$  of the mass in the same size fractions. The data provides allow correlating the product size to the heat exchanged in each nozzle region and quantifying their interaction. This constitutes the first experimental grounds for the compartmentalization of these towers and the simplification of future numerical models.

## 1. Investigation of the growth in the operation of single nozzles.

### 1.1. Unit design and operation.

The unit design is described in Chapter I (Scale I) and operation and standard measurements in Chapter IV. Figure 1 includes an outline of the unit and the location of the sensors referred to later.

### 1.2. Experimental design and operation conditions.

Production was studied varying the nozzle height in the cylinder, from position #1 to #2 and #3 (Figure 1). Relative rates, atomization conditions and inlet and exhaust conditions are summarised in Table 1. The target inlet air temperature and mass rate are maintained constant. They are selected to dry the powder to a final average water content,  $X_w$ , comparable to the target observed in industry.

This section studies how the exhaust conditions and the product properties are modified when the

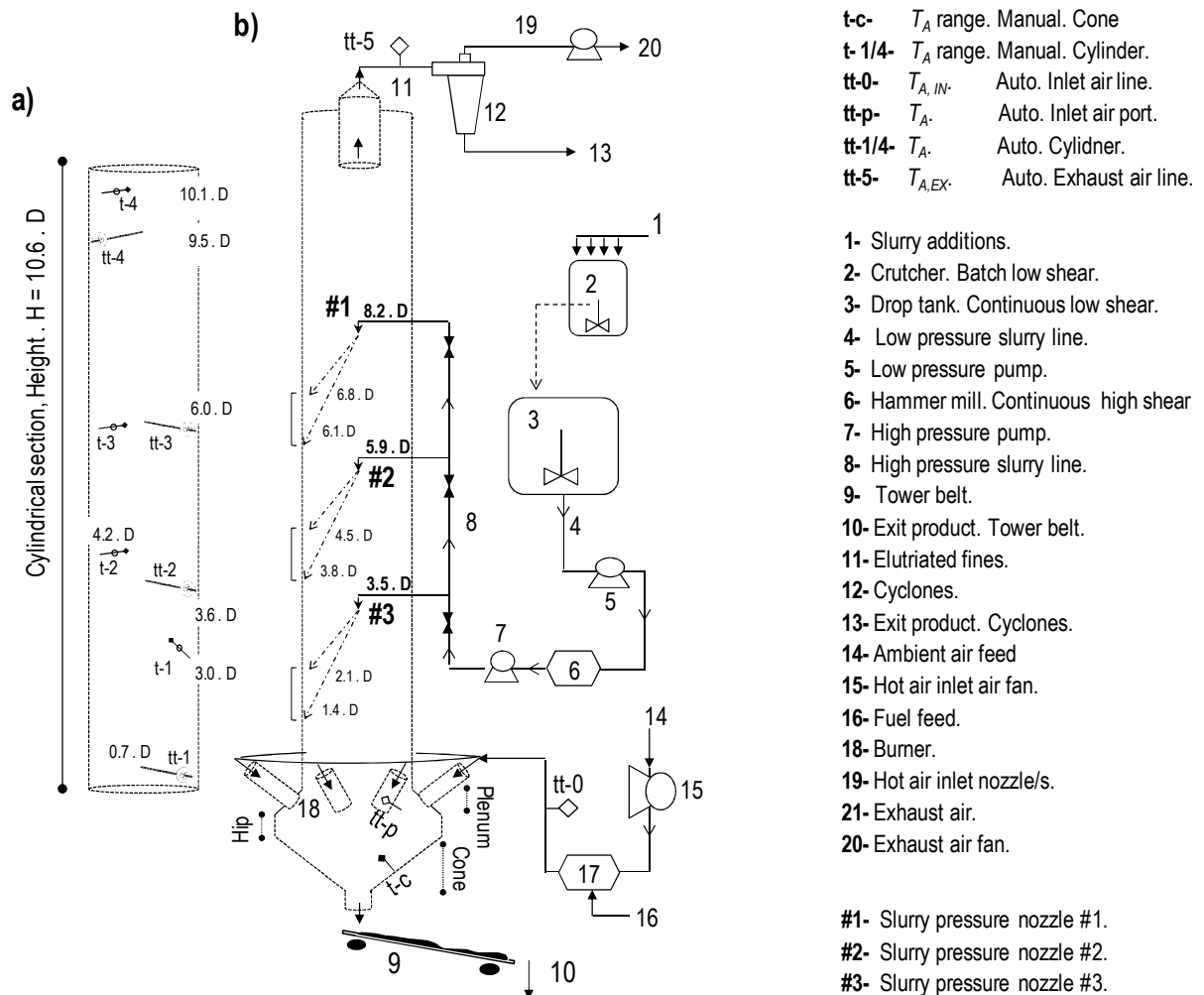


**Figure 1.** General outline of the sections of a counter-current spray drying tower, the air inlets and the swirl generation system. a) Location of the temperature sensors (Chapter IV). b) Location of the sprays and their projection upon the wall; operation of the air and slurry lines and location of the inlet and outlet air temperature sensors.

**Table 1.** Main process variables as a function of the nozzle operation level. Inlet and outlet air, slurry and product streams.

Scenario	$S_1$	$S_{1-r}$	$S_2$	$S_3$
Slurry line, S, Water lines, W, Product in the tower belt, P, elutriated fines, E, and full exiting power, EP.				
Nozzle	#1	#1	#2	#3
$\bar{M}_S / \bar{M}_{S,S_1}$	$1.00 \pm 0.02$	$1.02 \pm 0.04$	$1.00 \pm 0.03$	$0.99 \pm 0.01$
$\bar{M}_E$ (% $\bar{M}_{EP}$ )	4.0	5.6	2.7	2.0
$\bar{T}_P - \bar{T}_S$ (°C)	$-4.7 \pm 3.4$	$-6.9 \pm 5.2$	$-1.4 \pm 4.6$	$-2.5 \pm 4.3$
$X_W - X_{W,S_1}$ (%)	0	-0.01	-0.69	4.5
Air, A, rate inlet, IN, and exhaust, EX, conditions.				
$\bar{M}_A / \bar{M}_{A,S_1}$	$1.00 \pm 0.01$	$1.00 \pm 0.05$	$1.00 \pm 0.01$	$0.99 \pm 0.01$
$tt - 0, \bar{T}_{A,IN}$ (°C)	$272.2 \pm 2.1$	$272.9 \pm 8.4$	$273.0 \pm 1.7$	$269.3 \pm 2.3$
$tt - 5, \bar{T}_{A,EX}$ (°C)	$81.7 \pm 0.5$	$87.9 \pm 1.7$	$86.8 \pm 0.5$	$89.8 \pm 1.7$
$rH_{EX}$ (%)	20	17	17	14
Overall Energy Balance				
$Q_{Loss}$ (% $Q_{EX}$ )	$34.8 \pm 1.3$	$31.0 \pm 1.4$	$31.3 \pm 1.1$	$40.6 \pm 0.5$
$Q_{Lat}$ (% $Q_{EX}$ )	$65.2 \pm 1.3$	$69.0 \pm 1.4$	$68.7 \pm 1.1$	$59.4 \pm 0.5$
$\Delta H_{p,Sn}$ (% $Q_{EX}$ )	$0.7 \pm 2.0$	$0.6 \pm 2.0$	$1.0 \pm 1.6$	$-1.5 \pm 0.9$
$\eta_t$	$0.76 \pm 0.01$	$0.73 \pm 0.04$	$0.74 \pm 0.01$	$0.72 \pm 0.02$
$\eta_h$	$0.50 \pm 0.02$	$0.50 \pm 0.03$	$0.51 \pm 0.02$	$0.43 \pm 0.01$

\*  $T$ : temperature;  $M$ : mass rate;  $rH$ : relative humidity; For details in the energy balance see section 2.4.1.  $Q_{EX}$ : rate of heat exchanged in the dryer,  $Q_{EX} = \Delta H_{A,Lat} + Q_{loss} = -(\Delta H_{DA,Sn} + \Delta H_{P,Sn})$ ;  $Q_{Loss}$ : rate of heat losses;  $Q_{Lat}$ : rate of heat of vaporization;  $Q_S$ : rate of heat transferred to the solids,  $Q_S = -(\Delta H_{DA,Sn} + Q_{loss}) = \Delta H_{A,Lat} + \Delta H_{P,Sn}$ . Thermal efficiency  $\eta_t = (T_{A,IN} - T_{A,EX}) / (T_{A,IN} - T_{amb})$ . Heat transfer efficiency  $\eta_h = Q_S / H_{A,IN}$  where  $H_{A,IN}$  is the inlet air enthalpy taking ambient air as the reference.

nozzle changes location. Inlet air conditions are maintained in all cases to keep the same range of air superficial velocities,  $\bar{U}_{av}$  in the dryer. In this way, one can associate the changes in particle residence time, drying kinetics and impacts to the wall to the effect that the nozzle position has in the local dispersion of the spray. All experiments use the same nozzle, slurry formulation and atomization conditions to render a constant droplet size. This is confirmed by the variations in pressure and temperature,  $\pm 0.05$  bar and  $\pm 2$  °C, which result in a constant slurry mass rate,  $\bar{M}_S$ , in Table 1.

Chapter III demonstrates that deposits can disrupt severely the flow structure, for instance deposits originated in a previous production or in a formula changeover. To consider how they can impact particle dynamics,  $S_1$  has been replicated under initially heavily built up walls in  $S_{1-r}$  (Case C in Chapter III).

Elutriation rate in Table 1 decreases with nozzle height, varying from 4.0 – 5.6 % in  $S_1$  to 2.7 % and 2.0 % spraying from lower levels in  $S_2$  and  $S_3$ . As the nozzle is brought downwards fine particles have a longer time to migrate to the wall as they rise in the cylinder, concentrate and flow down. This explains why they are more likely to escape the influence of the top contraction.

### 1.3. Results and Discussion

#### 1.3.1. Temperature field.

Figure 2 shows the axial gradient of the air temperature,  $\tilde{T}_A$ . It decreases gradually up the tower as the air rises and approaches the spray region, after which it decreases drastically to values close to the exhaust,  $\bar{T}_{A,EX}$ . This is explained by the rapid drying of fines and confirms that no significant heat and mass transfer occurs above the nozzle. The evaporation rate can be estimated from an overall water mass balance. This allows an overall energy balance to be conducted as shown in Table 1. It presents the fraction of the overall heat exchanged  $Q_{EX}$  that is utilised either in the heat loss out of the dryer or in the latent heat of water. In all cases treated, large heat losses occur, for the most part owing to the large  $\Delta T$  at the bottom part of the dryer. This is clearly visible in the drop observed between the temperature at the inlet air distributor,  $tt - 0$  ( $\bar{T}_{A,IN}$  in Table 1) and the plenum,  $t - p$  in Figure 2.

When the nozzle is brought down in  $S_3$  the product presents a substantially higher water content,  $X_w$ , which can be explained by the solids having a shorter residence time  $\tau_p$  and containing a high proportion of largest granules (see section 1.3.4.1). The thermal efficiency,  $\eta_t$  (Masters 1972) measures the amount of energy transferred from the air. It decreases slightly from  $S_1$  to  $S_2$  and  $S_3$ . However,  $\eta_t$  cannot distinguish whether the energy is actually transferred to the solids or loss. It is important noticing that  $Q_{LOSS}$  increases significantly in  $S_3$ . As the residence time of the solids decreases, the energy transferred to the particles is lower and therefore the tower reaches higher temperatures, particularly at the bottom, thus leading to higher heat losses. This is better accounted for by using the heat transfer efficiency  $\eta_h$  defined in Table 1 as the ratio of the inlet air enthalpy utilised in drying and heating the solids. It remains constant in  $S_1$  and  $S_2$ , but clearly drops in  $S_3$ , which means that in that case one requires from a higher energy input to dry the product to the same level.

Particle drying rates depend largely on structure, and evolve as the droplet turns into a porous particle. Drops initially show a shrinkage period, where drying is dominated by external heat and mass transfer. It is widely accepted that droplets containing solids develop an outer shell or crust after a critical solids concentration. At this point the droplet size is locked; drying thickens the porous crust and becomes limited by the internal diffusion of water. The droplets then heat up and in the process eventually may reach their boiling temperature,  $T_{Boil}$ , causing a sudden formation of vapour (e.g. Hecht and King 2000 or Handscomb *et al.* 2009) which can either burst out or expand the structure in a process referred to

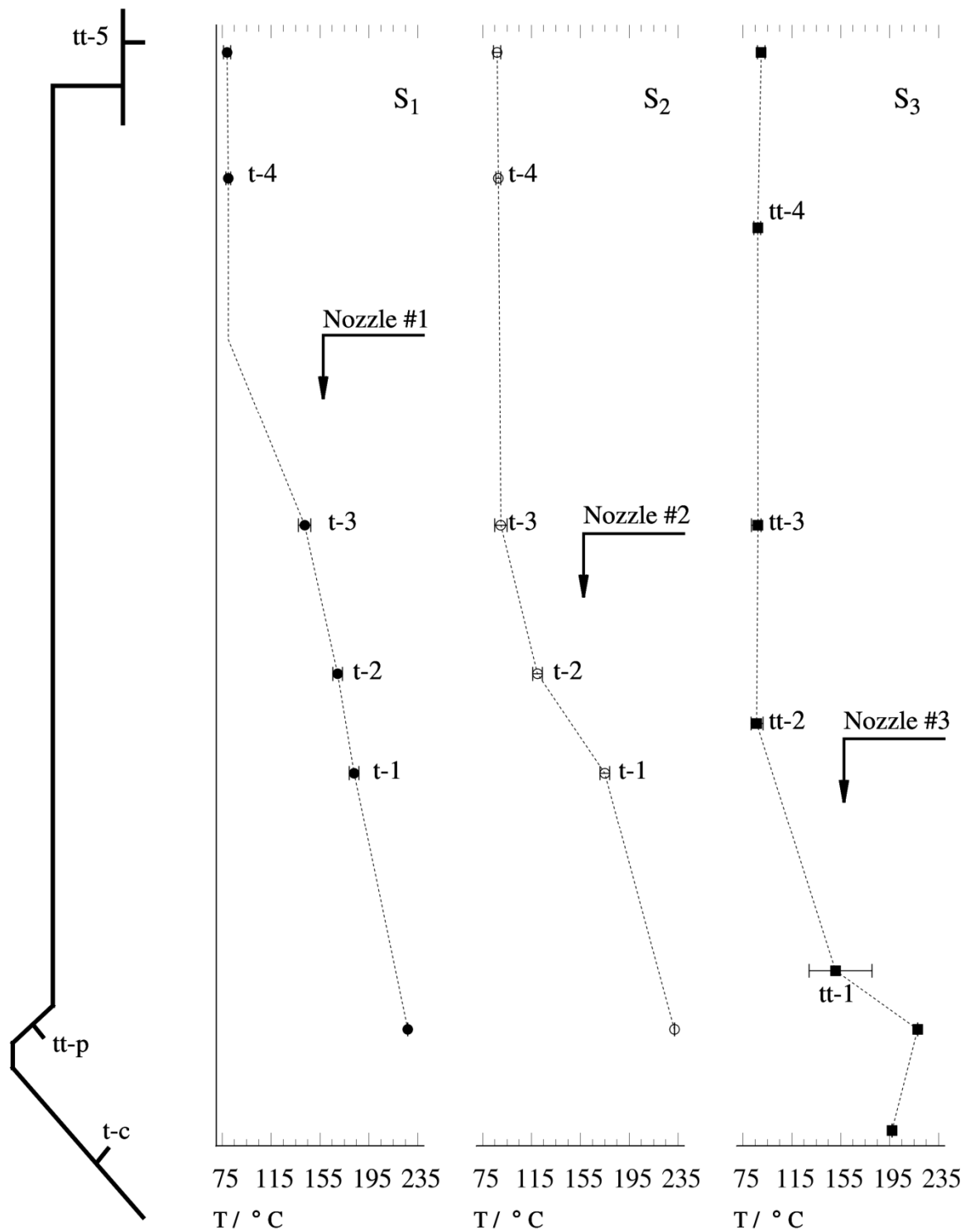


**Figure 2.** Axial distribution of  $\tilde{T}_A$  as a function of nozzle position, including manual punctual measurements ( $t - 1$  to  $t - 4$ ) and the cross-sectional average for  $tt - 1$  to  $tt - 4$ ,  $\tilde{T} = \int \bar{\rho}_A \bar{U}_z \bar{T}_A dA / \int \bar{\rho} \bar{U}_z dA$  where the  $\bar{U}_z$  profiles are assumed from isothermal conditions (Chapter II). Dimensions of the bottom conical region not drawn to scale.

as “puffing”. A more detailed description of drying mechanisms is given in Appendix II.

The point in the dryer at which boiling occurs, if it does, responds to the relative velocity of two transfer rates: the internal water mass transfer controlled by diffusion in the drop and the external heat transfer controlled by the environment (e.g. this can be characterised by the Peclet number  $Pe$ ). Large droplets show a lower surface/volume ratio and thus are more prone to be heated up and boil. But reaching  $T_{Boil}$  depends largely dependent on the drying history. Note that  $T_{Boil}$  rises rapidly as particles dry, particularly when they reach low  $X_w$  values close to exit. Therefore, boiling is expected to occur preferentially when droplets are sprayed near the high  $T_A$  so that the solids face a rapid heat transfer rate while they still contain a large water content. In contrast, when they spend a large residence time  $\tau_p$  in the cylinder they dry progressively, which increases  $T_{Boil}$  and may prevent boiling thereafter.

In all cases shown here there is a large  $\Delta T$  in the air from the plenum  $tt - p$  to the level  $tt - 1$  indicating that a large fraction of the heat is exchanged below the cylinder. As the nozzle is brought down the energy transferred in the cylindrical chamber diminishes but in turn the spray brings the droplets into a region of high  $T_A$  at higher  $X_w$ , which increases the potential for boiling. It is interesting to point to the decrease in the efficiency  $\eta_h$ . One would be inclined to think that spraying from a lower position in  $S_3$  decreases  $\tau_p$ , but in turn promotes the local drying rate by the droplets facing higher  $T_A$  and air velocities  $U_A$ . The fact that  $\eta_h$  reduces significantly can be the consequence of the internal diffusion dominated regime, referred to as “the falling rate drying period” where drying is proportional to the particle residence time  $\tau_p$  in the air or at the deposits, but relatively insensitive to  $T_A$ . To confirm this hypothesis further data including air humidity would be required. The impact of inlet conditions in  $\eta_h$  is discussed further in Appendix III, and the likelihood of boiling in section 1.3.4.2.1.

### 1.3.2. Wall deposits

Table 2 presents the initial net deposition rate,  $r_{d,o}$ , on the inspection hatch areas shown in Figure 3. Most of the unit shows no significant deposition. The highest rates are linked to the projection of the spray,  $6.9 D$  and  $4.5 D$  from nozzles #1 and #2. In these cases, the inspection areas are located within the upper part of the projection area shown in Figure 1. In  $S_3$  no deposition is appreciated at  $2.2 D$  what can be explained by the inspection area lying slightly below the projection from nozzle #3.

The presence of deposits above the nozzle in  $S_2$  and  $S_3$  is an evidence of the migration of fines to

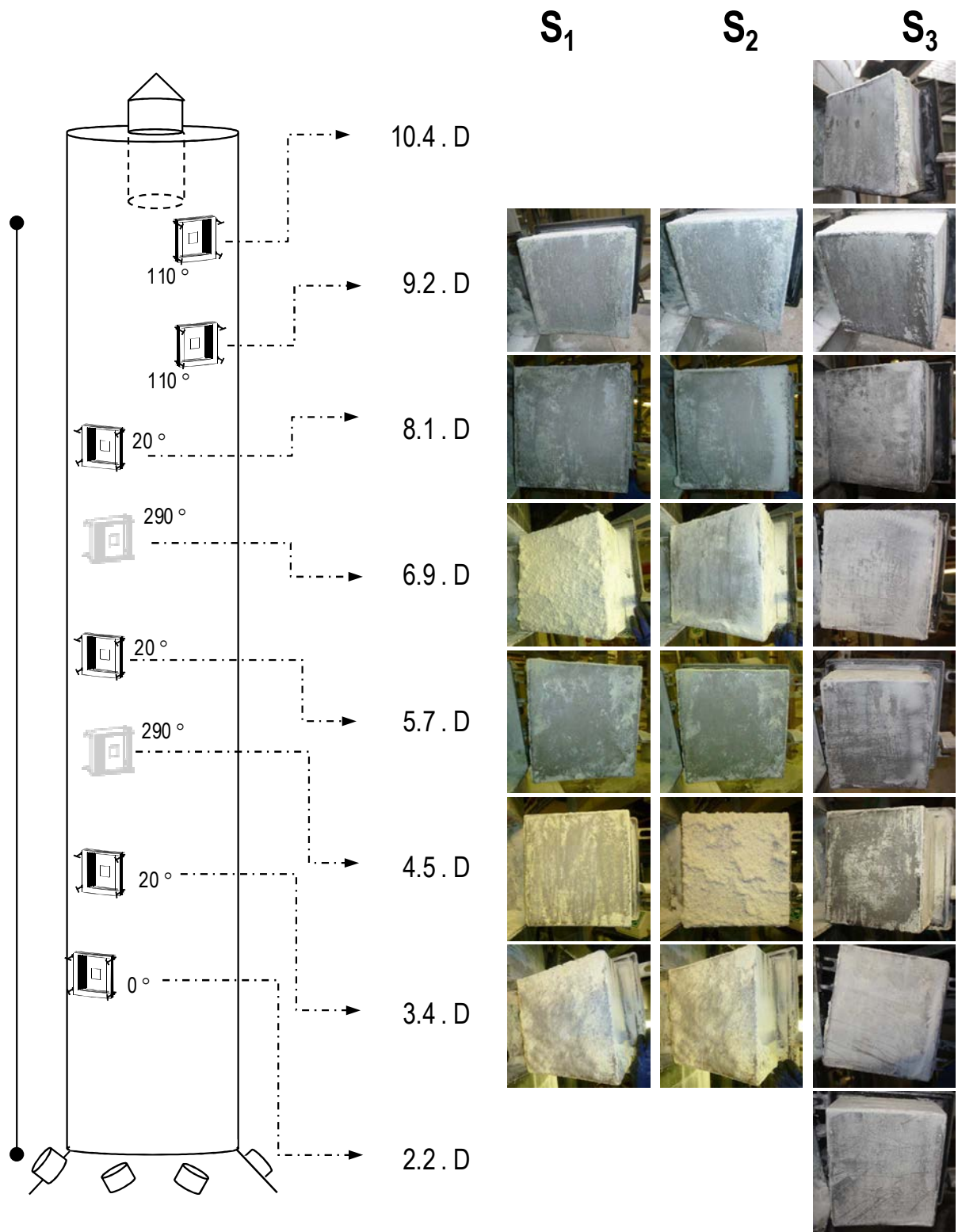


Figure 3. Axial distribution of wall deposits during a period of 10 to 15 min under steady state operation.

**Table 2.** Initial net wall deposition rate,  $r_{d,o}$ , as a function of the nozzle location. Bold denotes the spray projection area.

<i>Level</i>	$S_1$	$S_2$	$S_3$
<i>/D</i>	$g\ m^{-2}\ min^{-1}$		
10.4	-	-	0
9.2	0	0	0
8.1	0	2.1	0
6.9	<b>54.3</b>	1.4	2.3
5.7	0	0	0.2
4.5	0	<b>108.7</b>	0
3.4	0	0	1.1
2.2	-	-	0.6

the wall. The lower  $n$  achieved in the upper part of the dryer (Hassall 2011) explains the reduction in  $r_{d,o}$ . In  $S_1$  the nozzle is much closer to the top exit. This causes the overall elutriation to increase in Table 1 and explains why the fines do not reach the wall and  $r_{d,o}$  drops to zero above nozzle #1.

In the spray region,  $r_{d,o}$  diminishes as the nozzle is brought down from  $S_1$  to  $S_2$ . Both inspection areas are located at a similar distance from the nozzle, and then one expects they are subject to a comparable set of impact velocities. But moving the nozzle down makes droplets to face a higher  $U_A$  and this probably modifies then  $n$  near the wall, affecting the deposits. The replication of  $S_2$  described in Chapter V results in very similar values,  $r_{d,o} = 111\ g\ m^{-2}\ min^{-1}$  at  $4.5\ D$ , which provides confidence in the method's reproducibility. The relative deposition flux, (i.e. normalised versus the solid flow) is around 10 – 20 times higher than the values reported in co-current units (Ozmen and Langrish, 2003 or Kota and Langrish 2006). In a similar way, the data given here serves for the validation of the initial rate of wall impacts retrieved from numerical models.

### 1.3.3. Atomization, aging and solid-liquid separation.

Detergents slurries are non-Newtonian fluids that exhibit a strongly shear thinning behaviour, which facilitates atomization. In this case, shear viscosity follows the power law  $\mu = 85.96 \cdot \dot{\gamma}^{-0.5634}$  and a stress sweep in oscillatory test shows a linear viscoelastic region  $< 10\ Pa$ .

The initial droplet population used in all experiments in Part B of this thesis is compared to one example of the product size distribution in Figure 4a. It presents a single mode between  $390 - 425\ \mu m$  with a wide spread from  $20 - 1000\ \mu m$  and a negative skew. The median volume size,  $x_{p,50}$ , ranges between  $275 - 310\ \mu m$  and  $x_{p,10}$  and  $x_{p,90}$  between  $77 - 98\ \mu m$  and  $521 - 549\ \mu m$

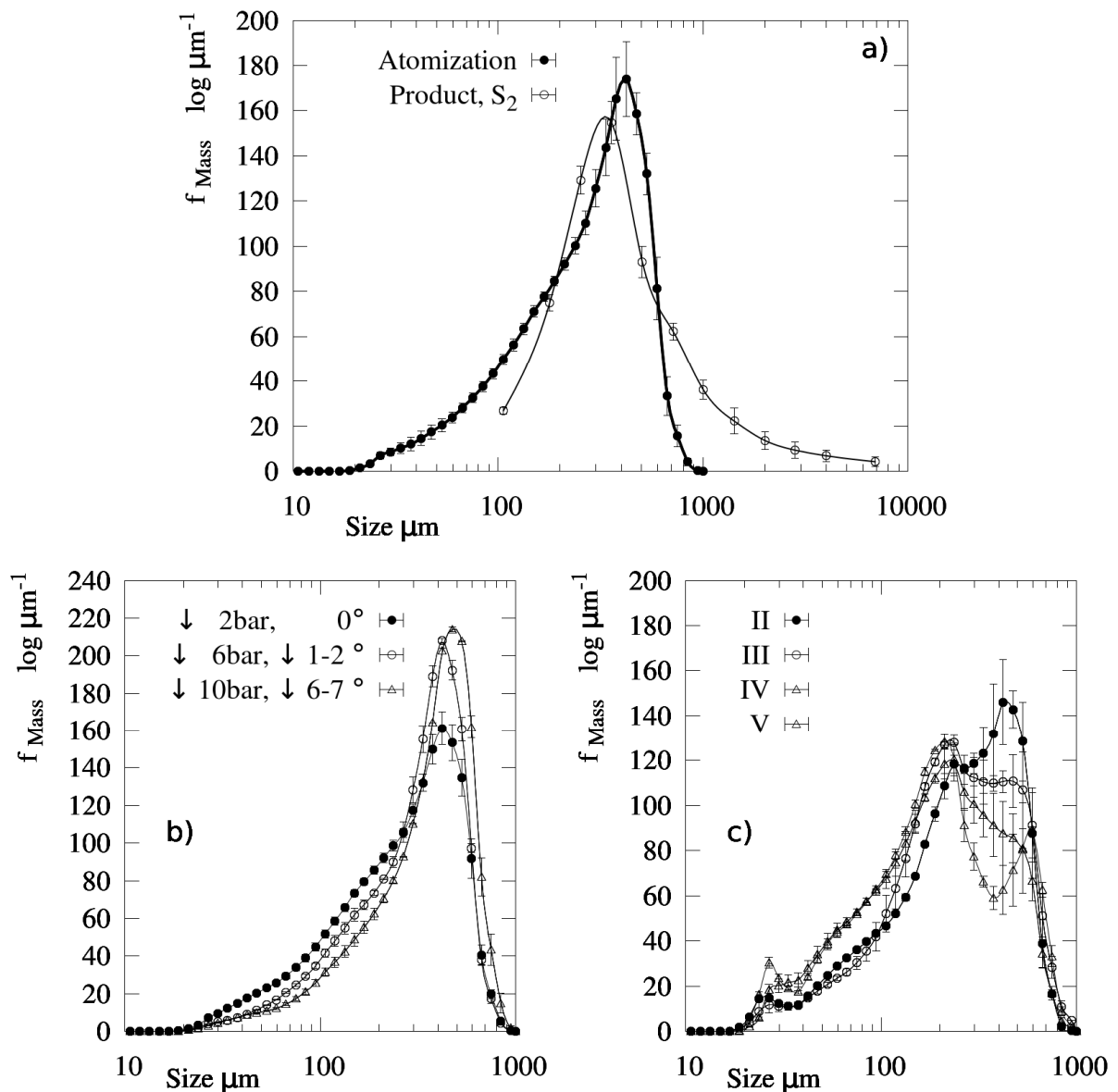


**Figure 4.** a) Comparison of the initial droplet size distribution and the product in  $S_2$  in Figure 5. b) Variation in the atomization associated to increasing  $\mu$  and decreasing pressure. c) Generation of bi-modal droplet size distributions for the same nozzle, rate and  $T$  for comparable detergent slurries to the one used here, denoted II, III, IV and V of decreasing  $\mu$ .

respectively. The spray itself produces a full average angle of  $39 \pm 1^\circ$  and a hollow cone pattern.

Detergents are also susceptible to aging. Water activity results from chemical and physical interactions driven by the phase equilibrium of inorganic salts, polymeric interactions and the surfactant microstructure. Addition of stabilizing and thickening agents, such as solids, and the optimization of the shear history serve to control the microstructure of the slurry during preparation. However, the rheology of the final mix varies if stored for long periods. This has been taken into account in the study of atomization. Figure 4b illustrates the effect of aging in increasing the  $\mu$  of the slurry after large storage times. The discharge coefficient of swirl pressure nozzles is inversely proportional to  $Re$ . An increase in

$\mu$  diminishes the pressure for the same slurry flow rate, forming a smaller air core at the nozzle exit. This generates a narrower spray and a thicker slurry sheet, which result in breakage into larger droplets (Masters 1972). Measurements were taken at decreasing storage times until no differences could be appreciated. The variations seen in the experiments,  $< 2 \text{ bar}$ , produced no measurable differences.

The slurry is comprised of aqueous and organic liquid phases, and a solid phase that contains inorganic salts and their hydrates. The high content in solids has the potential to disrupt the disintegration mechanisms in the atomization causing the separation of solid and liquid phases. Consider the limiting case of mono-sized solids. If the droplets generated are smaller than the solids in the slurry, they will be necessarily comprised only of liquid phases, and if they are comparable in size, they may contain either a single solid particle or none. Homogeneous composition can only be achieved when the droplets are much larger than un-dissolved particles so that they can contain a sufficient number of them. Such a high segregation level is of course unrealistic in real processes where solids are polydispersed.

Solid-liquid separation is a complex issue. It depends not only upon solids size or nozzle design but on the balance between the atomization energy input and the inter-phase forces that dominate the formation of the sheet, its break up into ligaments and the subsequent contraction into drops. All these are believed to be governed by the relative effect of viscosity to surface tension forces (i.e. Ohnesorge number). Authors working with dual nozzles have reported solids  $> 50 \mu\text{m}$  governing the formation of droplet size in scenarios of a low energy input, and causing bi-modal size distributions (Mulhem *et al.* 2006). In the case treated here atomization involves a swirl pressure nozzle and large un-dissolved solids ( $50 < x_p < 200 \mu\text{m}$ ) that exceed the size of many of the droplets generated. As expected solid-liquid separation has been observed comparable to the phenomenon described by Mulhem *et al.* (2004). Figure 4c illustrates the evolution of droplet size as  $\mu$  decreases using the same nozzle and rates in comparable detergent slurries. Bi-modal distributions begin occur at a certain point, which then blend in as  $\mu$  and the energy input increases. A clear transition appears from the data in Figure 4c towards the droplet population used in this work in Figure 4a. Here, a second mode is no longer visible but separation still occurs as will be demonstrated later (see composition in sections 1.3.4.2 and 2.4.3.2)

### **1.3.4. Product Analysis.**

#### **1.3.4.1. Aggregation patterns in the use of single nozzle.**

The size distributions of the exit powder are compared in Figure 5. All show a common single mode

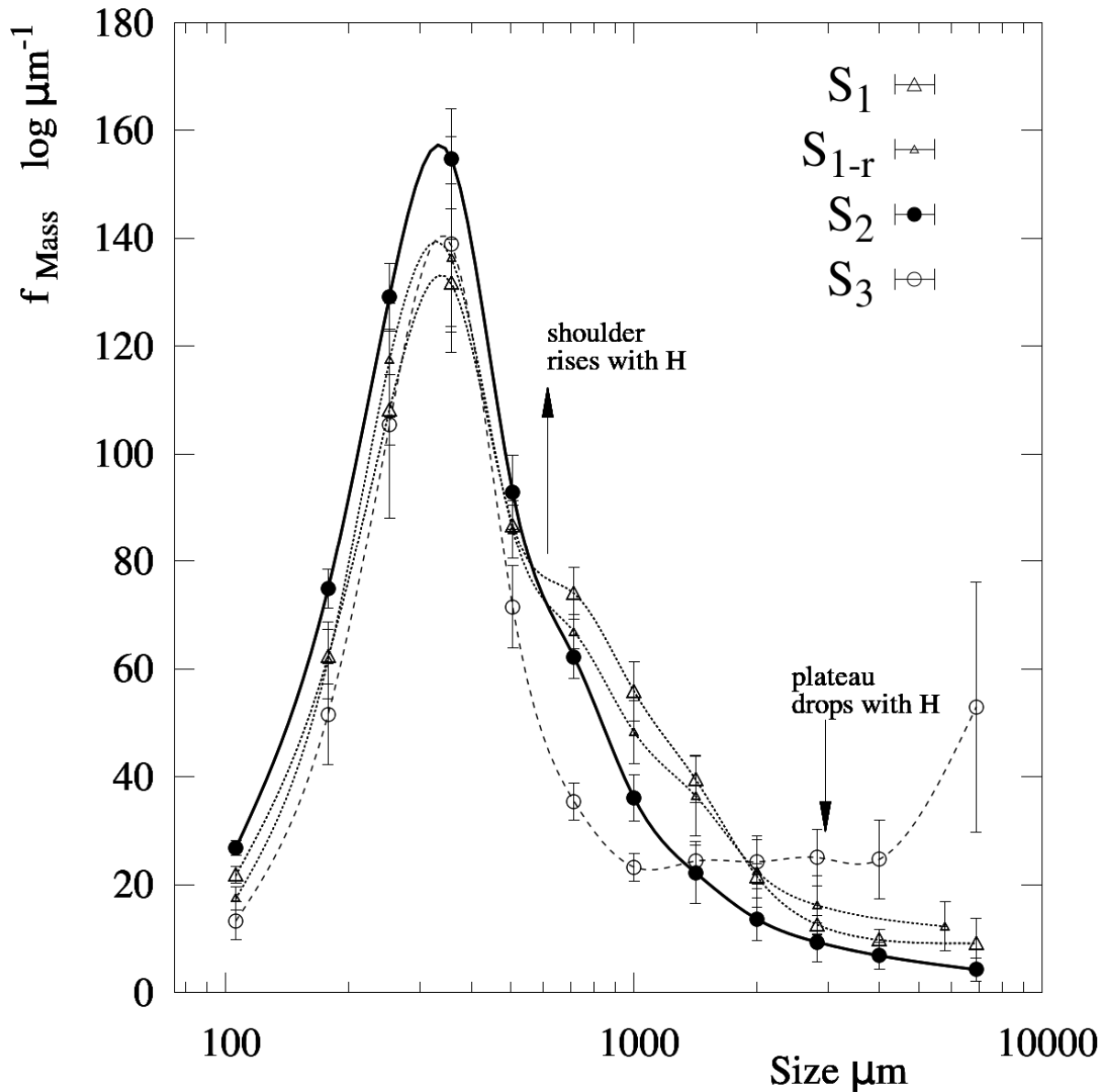


**Figure 5.** Mass base product size distributions as a function of the axial location of the nozzle and different wall conditions.

between 300 – 425  $\mu\text{m}$ , in a comparable range to the droplets in Figure 4a. This might lead one to think both modes are associated, but this is unlikely because the particle morphology indicates that all these fractions are in fact aggregates (see Appendix II). This is not surprising: drops of that size are likely to impact the wall at high  $U_p$  and deposit. Product median mass particle size  $x_{p,50}$  varies from  $413 \pm 15 \mu\text{m}$  to  $360 \pm 10 \mu\text{m}$  and  $456 \pm 98 \mu\text{m}$  as the nozzle moves down from  $S_1$  to  $S_2$  and  $S_3$ , shifting  $x_{p,10}$  and  $x_{p,75}$  respectively from  $173 \pm 4 \mu\text{m}$  to  $161 \pm 3 \mu\text{m}$  and  $195 \pm 12 \mu\text{m}$ , and from  $824 \pm 64 \mu\text{m}$  to  $597 \pm 53 \mu\text{m}$  and  $2224 \pm 1335 \mu\text{m}$ .

The variation in mean values does not reflect the large changes in the tails and the shape of the

distributions, which do not fit any standard function. The tails are in fact very important to the overall process efficiency. The largest percentiles are used to define both production capacity and quality. In detergent manufacture, quality criteria include size thresholds, and excessive generation of large granules in essence causes a high recirculation ratio. Furthermore, the width of the distribution affects the maximum packing factor and the bulk density,  $\rho_{bulk}$ , which in addition to porosity,  $\varepsilon$ , are critical in performance, consumer acceptability and the packing operations.

Several features require comment in Figure 5. A shoulder appears between  $600 - 850 \mu m$  when the nozzle operates from a high location in  $S_1$ . As it is lowered the aggregation is inhibited and the shoulder diminishes in  $S_2$  narrowing the distribution over the mode. This might be related to a fact the nozzle faces a higher  $T_A$ : the outer crust is produced earlier and therefore the surface properties of the granule are less prone to aggregation when particles concentrate near the wall. One would expect a similar effect in the transition towards  $S_3$ . This is indeed the case in the sense that the shoulder vanishes and the primary mode narrows. However, in turn a plateau now develops for sizes  $x_p > 850 \mu m$ . The root of this behaviour could be linked to either the interaction at the walls or the stagnation of particles having located the nozzle in areas of higher  $U_A$  (i.e. see the nozzle region in Chapter IV). Re-entrainment however is the most likely according to the surfactant/s compositions given in later and the conclusions from the operation under different air velocity and temperatures (see Appendix III). It demonstrates that growth is not promoted at higher velocities and concentrations. On the contrary this promotes impacts to the wall and re-entrainment, which appears to reduce the formation of the plateau in Figure 5.

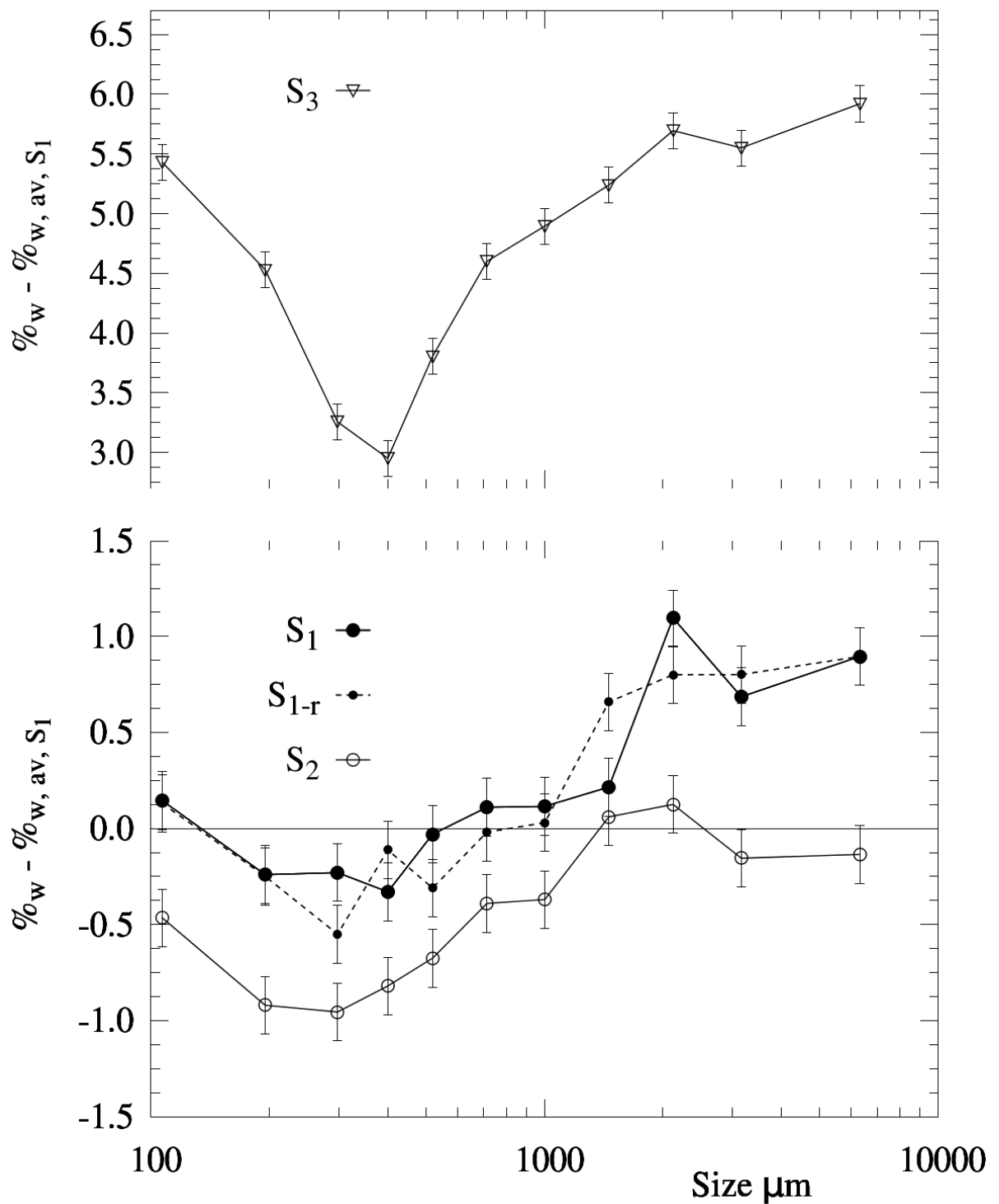
Interestingly, no differences are observed between the product obtained with initial cleaned walls or heavily built up, in  $S_1$  and  $S_{1-r}$  respectively. It would appear that the deposits lead always to a large decay in the swirl once they achieve a steady state thickness, independently from the initial conditions.

### 1.3.4.2. Composition heterogeneity in the use of single nozzles.

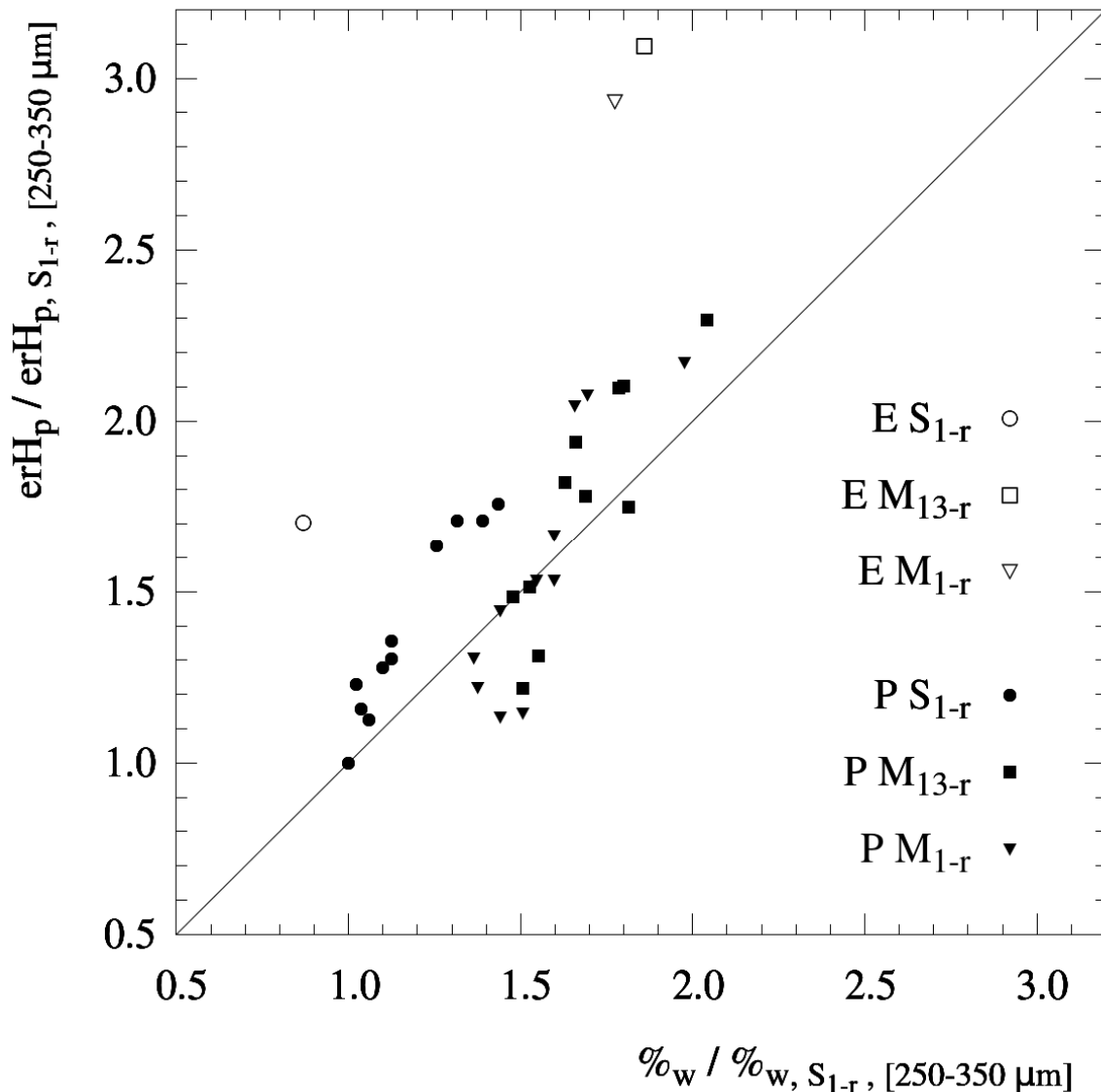
#### 1.3.4.2.1. Water content, $X_w$ .

Figure 6 reports the exit water content,  $X_w$ , of the product as a function of size. All cases show comparable distributions. The mode size class shows the minimum value and fractions  $> 600 \mu m$  show an increasing  $X_w$ , up to 60 – 70 % higher than the mode in  $x_p > 1180 \mu m$ .

Interestingly, particles  $< 355 \mu m$  also show a higher  $X_w$ . This cannot be attributed to fines having a



**Figure 6.** Product water content,  $X_w$ . Variation across the exit size fraction for all cases. Data is given as the difference in % in mass to the average value observed in  $S_1$ .



**Figure 7.** Comparison of product water content,  $X_w$ , and the powder equilibrium relative humidity,  $erH$ , measured at 20 – 25 °C for all the product size. The product  $< 150 \mu\text{m}$  is denoted P and the elutriation, E. Data is given as the % or the % in mass normalised to the value of the mode size fraction.

lower  $\tau_p$  in the chamber nor to a significant variation in their structure: all fractions show a similar relation between  $X_w$  and their equilibrium relative humidity,  $erH$ , see Figure 7. The exception is the elutriated fines, which can be explained by a higher content in surfactant,  $X_s$  (section 1.3.4.2.2) and a different distribution of particle porosity (see Appendix II) because they do not undergo fast drying rates.

The fines may pick up moisture from the environment during the transport in the tower belt in Figure 1 but this cannot justify the rise in  $X_w$  for fractions  $< 300 \mu\text{m}$  because it would require an absolute humidity in the air that is simply not available. However, despite the samples being sealed a certain

re-equilibration could also occur during sieving the bulk powder sample (spanning over  $1 - 4h$ ).

It is also important to recognise the role of re-entrainment. Both fractions, granules  $> 850 \mu m$  and fine particles  $< 212 \mu m$ , contain larger proportions of material coming from the deposits (Chapter V). The deposits show a high  $X_w$ , which in part can explain why the large fractions in the product do also. They detach from the wall and flow down quickly with insufficient  $\tau_p$  at the bottom to dry. The same argument could be applied for the small particles. However, should they be produced at upper levels, they would dry at the bottom of the chamber due to their small size. This suggests that product  $< 300 \mu m$  is not comprised only of particles produced at the deposits, nor from the atomization but it must contain fragments that were produced very close to the exit by the breakage of larger pieces.

Figure 6 shows that  $S_3$  renders higher  $X_w$  values. As explained in section 1.3.1 this causes a lower drying efficiency and may be related to a lower  $\tau_p$  and perhaps the limits owed to the internal diffusion dominated regime. Heating and the evolution of the drop morphology depends largely on the diffusion coefficient in the crust when the droplets enter a high  $T_A$  region (see Appendix II). This has been measured experimentally decreasing from  $2.5 \cdot 10^{-10} - 5.5 \cdot 10^{-10} m^2 s^{-1}$  at the atomization conditions down to  $< 10^{-10} m^2 s^{-1}$  as drying progresses. These values suggest that the drying rate in a mean sized droplet surely becomes dominated by internal diffusion, but it is difficult to assess whether particles heat sufficiently to boil. This depends largely on history and their residence time in the cone. Nonetheless, if boiling was dominant for all cases, one would expect a correlation between the exit product temperature  $T_p$ , similar in Table 1 and the values of  $X_w$  in Figure 6. This is not the case.

#### 1.3.4.2.2. Activity, $X_s$

The analysis of the elutriated powder serves as an indication of the characteristic of the primary droplets. Elutriates are found to be heterogeneous and contain ligaments (see Appendix II). In addition, they show a higher content of surfactant/s,  $X_s$ , which is indicative of the solid-liquid separation during the atomization. In cases  $S_1$  and  $S_2$  they contain 33 – 34% more surfactant/s than the product mode size class in  $S_2$ , rising to as much as 68 % higher  $X_s$  values in  $S_3$ . Such differences are likely to have an effect in the particle drying kinetics and the mechanical properties of the shell formed during drying. It remains unclear how the surface viscosity of particles evolves during drying of detergents, which is the behaviour of the polymers and how the crystallization of salts impact water mobility. These are particularly relevant in a system such as this where the droplet composition varies significantly.

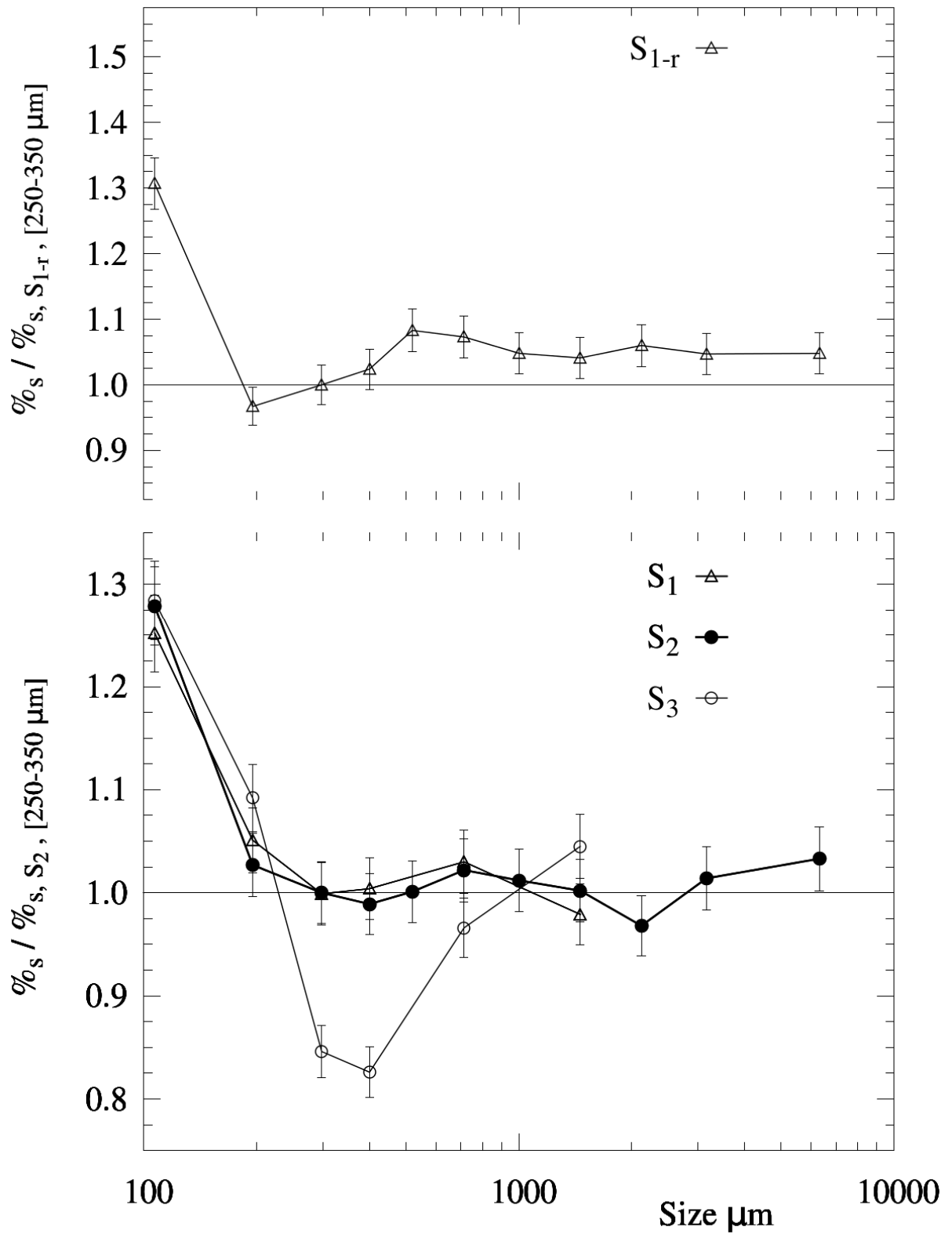


**Figure 8.** Product surfactant/s content,  $X_s$ . Variation across the exit size fraction for all cases. Data is given as the % in mass in dry bases, normalised by the value of the mode size fraction.

These differences are brought into the composition of the product given in Figure 8. The finest fraction in all experiments  $X_S$  shows a higher surfactant/s content, 28 – 31% higher values than the mode in  $S_2$ . This can be explained because it comprises of the droplets smaller than the solids in the slurry, and thus particularly rich in the liquid phases.  $X_S$  is however lower than the values of the elutriates because in the product the finest powder also contain re-entrained material and fragments that come from breakage.  $X_S$  then decreases for larger aggregates as they start to comprise of droplets of a comparable size to the solids in the slurry, thus particularly poor in the liquid phases (see the clear minimum observed in Figure 8 for  $S_3$  and  $S_{1-r}$ ). Ultimately, as the particle size increases further, the aggregates show the average  $X_S$  because they are large enough to contain many primary droplets.

The effect of segregation becomes clearer as the nozzle is brought down. The mode size in  $S_3$  shows 17% less surfactant/s than in  $S_1$  or  $S_2$ . This can be explained by the aggregation being inhibited in this range and the product containing more primary particles, particularly rich in solids. In contrast, as soon as the plateau forms in Figure 5,  $X_S$  shows a sharp increase. This agrees with the observations made earlier for  $S_3$ : it appears that lowering the nozzle position causes simultaneously the inhibition of growth into the mode size and the promotion of it into the final plateau. Both are believed to have a different origin because otherwise one would expect a more progressive increase of  $X_S$  in Figure 8 (see also the same behaviour under different air conditions in section 2.4.3.2.2,  $M_3$  Figure 24).

The replicate in  $S_{1-r}$  shows a similar behaviour, now the segregation is increased. This has been attributed to the use of a different supplier of inorganic salts that may have modified the size of un-dissolved solids, although no experimental data could be made available.

## **2. Investigation of the interaction between multiple sprays.**

### **2.1. Agglomeration sources in a multi-level system.**

Full scale dryers normally use more than one single nozzle in order to maximise production. In P&G spray drying units, several nozzles are fitted in a ring at two or three different axial levels in the dryer (Davies *et al.* 1971). The interaction between neighbouring sprays may become important if they are too close to each other (Huntington 2004), but this effect is not considered in the scope of this work: this section focuses only on the transition from one to two levels of nozzles. This modifies substantially the dispersion of particles in the unit and their drying history. Figure 9 illustrates the spray dispersion and provides a similar subdivision of the unit as first given in Figure 4 in Chapter IV for a single nozzle case.

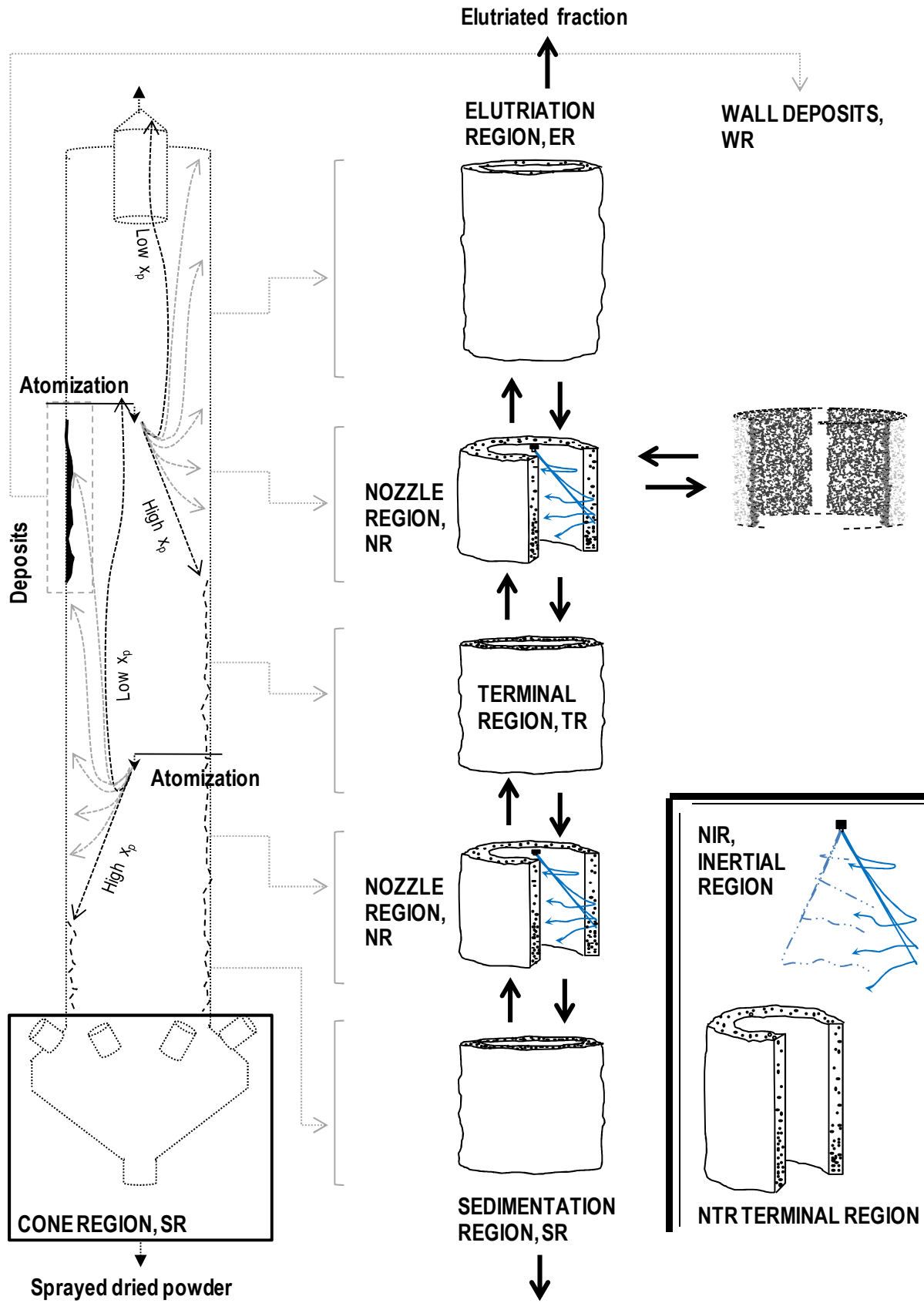


**Figure 9.** Subdivision of a swirl counter-current drying tower and depiction of the agglomeration sources derived from the particle recirculation in systems using various spraying levels.

The transition from a single level to twin levels enhances aggregation in the following ways:

- **Particle collision rate or frequency:** The rate of particle-particle and wall-particle contacts in the dryer increases with higher production rates because the concentration,  $n$ , rises. As the rate of the solids becomes higher it is also necessary to convey a higher overall heat transfer in the dryer. This can be done by increasing the inlet air temperature and mass rate,  $T_{A,IN}$  and  $M_A$ , but leads to higher air velocities,  $U_A$ , in the unit. As a result, the residence time of the solids,  $\tau_p$ , increases and the drag to the air causes more elutriation.
- **Particle collision efficiency:** When the slurry is injected at various levels, it changes the air temperature and velocity field. The droplets sprayed at each nozzle have very different histories. The largest driving force to dry the product is generated at the bottom, where the air temperature  $T_A$  and velocity  $U_A$  are the highest. Particles sprayed here are expected to experience faster drying rates reducing the likelihood of aggregation and deposition. In contrast, those sprayed at the top face cooler and damper air close to the exit, and would thus be more prone to aggregate and deposit.
- **Recirculation and contacts mechanics:** A feature of spraying at various nozzle levels is the fluxes established between each spray region. In a multi-level system, the exit powder can be thought to be comprised of three different populations: i and ii –particles that come from each nozzle without having aggregated or having done so with other particles from the same nozzle (e.g. coalescence near the nozzle,  $NIR$ , in Figure 9) but also iii- a different population of granules that are produced when droplets/particles injected at different nozzles aggregate. The contacts between different levels are likely to occur in the spray regions, see Figure 10:
  - **Top:** Most of the particles flowing up from the bottom spray approach the top near the wall in the annular section denoted  $NTR$  in Figure 9. The finest drops cannot migrate outwards and reach the top at centre,  $NIR$  see Figure 10a, where they face high velocity droplets coming from the top nozzle. These can act as a scrubber and capture the particles flowing up.
  - **Bottom:** The product coming the top flows down close to the wall and crosses the bottom spray,  $NIR$  in Figure 10b. These contacts occur in the same concentrated annulus denoted  $NTR$  in Figure 9. Here particles stagnate, collide one to another and interact with the high velocity drops from the bottom nozzle. The contacts to the particles from the top are no different, simply include particles that have a longer residence time and are probably bigger.

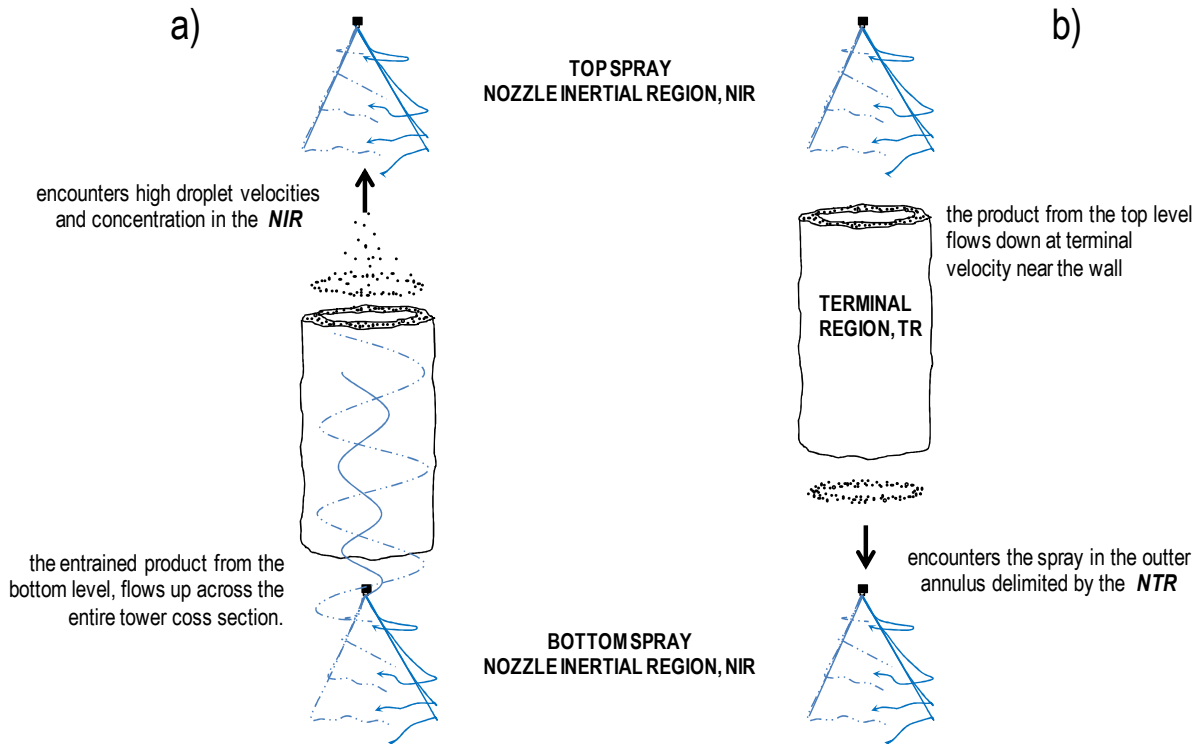


**Figure 10.** Interaction fluxes between the sprays a) flux from the bottom into the top spray across the full cross-section and b) flux from the top into the bottom spray through the outer concentrates annulus.

The purpose of this work is to quantify the growth that occurs in each nozzle region in Figure 9, and due to the recirculation fluxes, illustrated in Figure 10. The next section describes the design and execution of a series of experiments that do so by studying the effect of each of the nozzles independently.

## 2.2. Unit design and operation.

The unit design, operation and all measurements are described in Chapter IV. Figures 11 and 12 are repeated in this section for the benefit of the reader, including the modifications made to the slurry line. Atomization was conducted from twin swirl hollow cone pressure nozzles, #1 and #3, aligned with the cylinder centreline and facing downwards. In this work water dual nozzles (SU82, Fluid Cap 251376; Air Cap 4691312) denoted  $W_1$ ,  $W_2$  and  $W_3$ , were placed at the positions shown in Figure 3, and fed from an storage tank at 60 °C.

In all cases, the walls were cleaned. Different initial conditions were tested by repeating the cases  $M_{13}$  and  $M_1$  described later under heavily built up walls in  $M_{13-r}$  and  $M_{1-r}$  (i.e. Case C in Chapter III).

## 2.3. Experimental design and operation conditions.

When one places a second nozzle in the tower, it is complicated to distinguish between the effects in growth owed to an increase in  $n$  or the different drying kinetics in each nozzle. The experiments

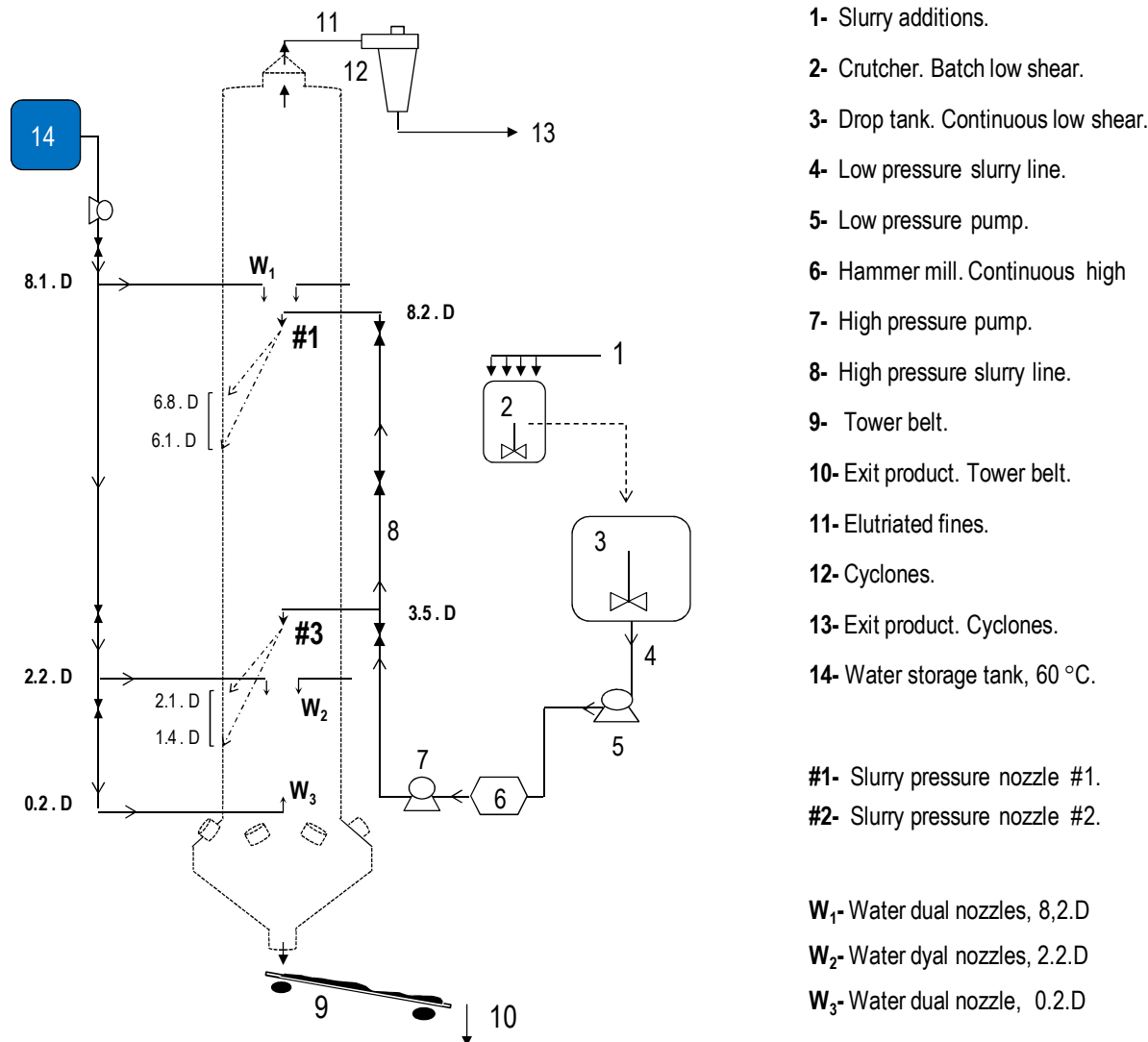


**Figure 11.** Description of product and slurry lines in the dryer, including the nozzles used in the work described in section 2, their projection area, and the accessory water dual nozzles placed across the cylindrical chamber.

outlined in Figure 13 do so by studying what occurs at each spray region. Three stages are followed:

- **Reference.** The case denoted  $M_{13}$  used both nozzles simultaneously. The product is characterized and taken as a reference.
- **Isolation of each spray.** The top in case  $M_1$  and the bottom in cases  $M_3$ ,  $M_{3-ii}$  and  $M_{3-iii}$ .
- **Sensitivity.** The effect of reducing  $T_A$  and  $U_A$  in the spray region is studied in  $M_{3-i}$ .

The isolation experiments are designed to identify which part of the product in  $M_{13}$  comes from nozzle #1, from #3, or is the result of their interaction (i.e. the populations i, ii and iii described in section 2.1)

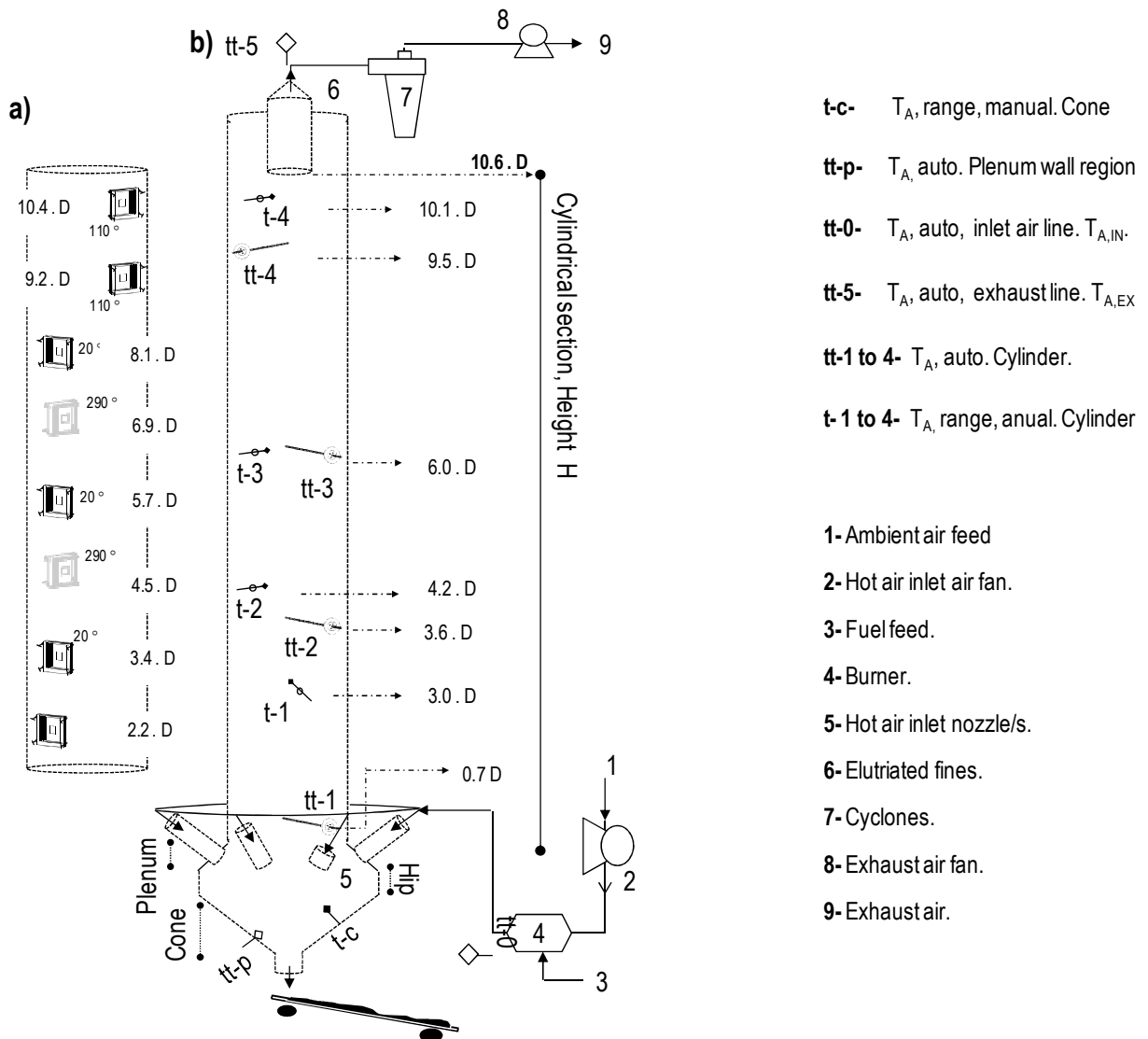
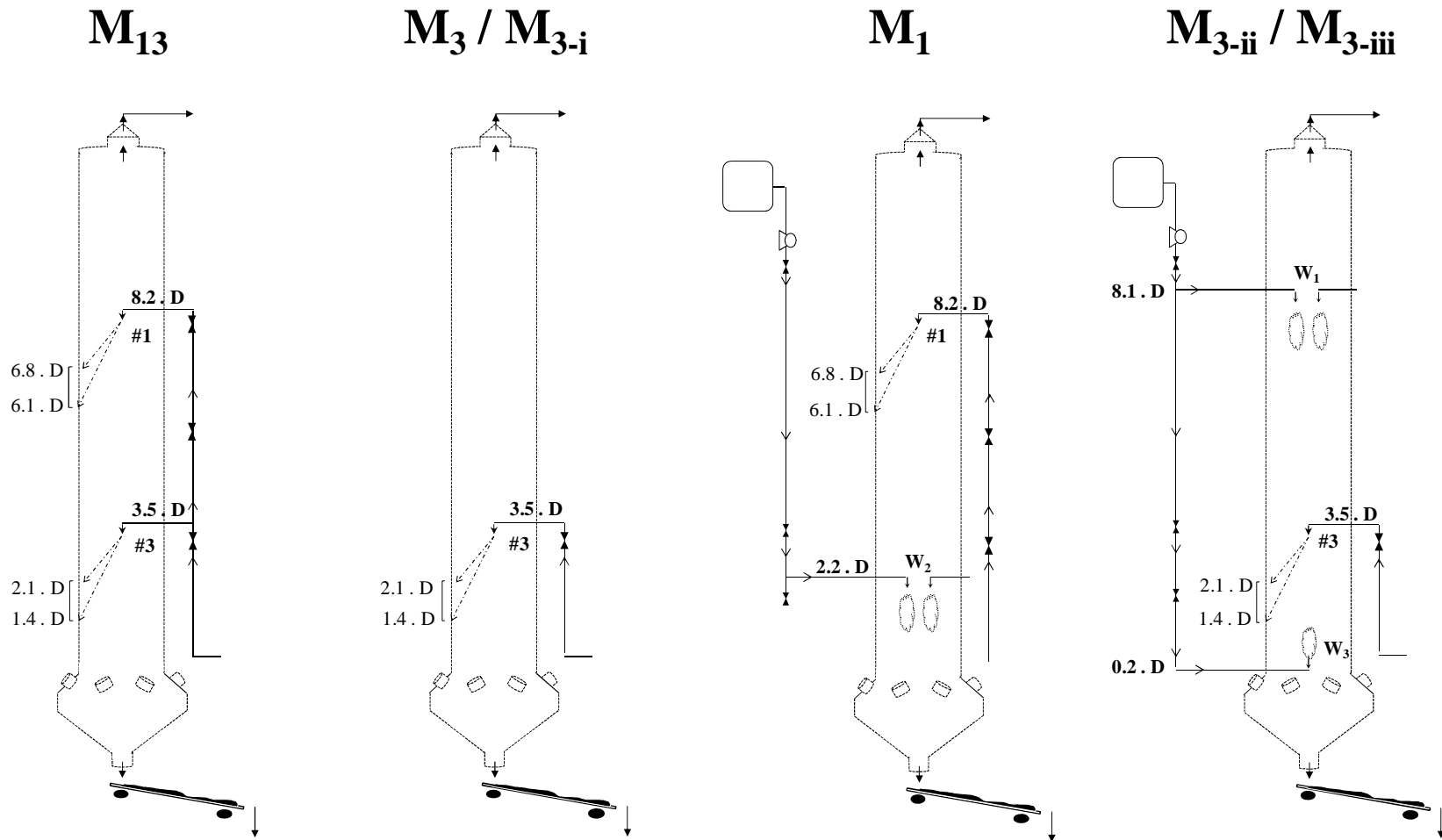


**Figure 12.** (a) location of the wall inspection areas (b) description of the air line and location and nomenclature of the temperature sensors used in the work described section 2.

In order to determine the particles that are originated only by one of the sprays, one needs to operate this nozzle alone but under the same air flow field seen when both are together in the reference,  $M_{13}$ . The air must show a similar  $T_A$ , air relative humidity,  $rH_A$ , and velocity,  $U_A$ , so that the contacts and collisions established are similar. This is particularly important in the spray region where aggregation is most likely. Table 3 summarizes the process conditions for the different cases. Atomization conditions are constant. The changes introduced for each experiment are explained below.

Experiments  $M_1$ ,  $M_{3-ii}$  and  $M_{3-iii}$  manage to replicate the air flow field in the chamber using only one slurry nozzle but matching the overall evaporation rate to the reference. They replace the water that was removed from the slurry with an equivalent amount provided by two sets of air/water dual nozzles:

**Figure 13.** Description of the multi-nozzle system,  $M_{13}$  and the isolation of each of the nozzles, by the ramp of  $T_{A,IN}$  in the cases  $M_3$  and  $M_{3-i}$ , and the use of comparable air temperature and velocity fields by usage of water dual nozzles in  $M_{3-ii}$  and  $M_{3-iii}$ .



- **$M_1$** : During  $M_{13}$  the slurry flow to nozzle #3 is disconnected and the water rate previously evaporated from the slurry is injected as a fine water mist by  $W_2$ , placed at the centre and facing up (Figure 5). As discussed later this permits retaining a comparable  $\bar{T}_A$  field and heat transfer rates,  $r$ , in the top spray region. The product that exits the tower under these conditions represents what would have been generated by nozzle #1 in  $M_{13}$  if the nozzle #3 was absent.
- **$M_{3-ii}$  ,  $M_{3-iii}$**  : In a similar way, they disconnect the slurry flow to nozzle #1 and operate only nozzle #3 using the water sprays  $W_1$  and  $W_3$  to maintain the same evaporation rate. Different injection ratios between  $W_1$  and  $W_3$  were tested. Two considerations must be made:
  - Water dries faster than slurry. This means that the evaporation of droplets from  $W_1$  and  $W_3$  does not extend as far into the bottom of the dryer compared with the behaviour of slurry droplets in  $M_{13}$ . As a result, the air is likely to reach higher  $\bar{T}_A$  at the bottom end and this may enhance drying. Indeed, Table 1 and section 2.4.3.2.1 show that the product in  $M_{3-ii}$  and  $M_{3-iii}$  exhibits at a high exit temperature  $\bar{T}_p$  and a low  $X_w$ . This is not considered an issue to study growth because the contacts causing aggregation occur above, in the cylinder.
  - Re-wetting. There is a risk that particles are re-wet by the water drops, making the surface more sticky. The nozzles used provided fine water drops ( $< 100 \mu m$ ) which are expected to dry rapidly after atomization. However, wall deposits do appear near the sprays (section 2.4.2)

During  $M_{13}$  the air temperature  $T_A$  varies from  $\bar{T}_{A,IN} \sim 300^\circ C$  at the inlet to  $\sim 100^\circ C$  above the nozzle #3 (section 2.4.1). This value can be controlled by modifying the inlet air conditions:

- **$M_3$**  uses the same inlet air mass rate  $M_A$  but reduces the inlet temperature  $T_{A,IN}$  until the  $\bar{T}_A$  above nozzle #3 reaches  $\sim 100^\circ C$ . The product is dried to the same final water content  $X_w$  but now the upper part of the chamber shows high temperatures and velocities.
- **$M_{3-i}$**  keeps on reducing  $T_{A,IN}$  further until the exhaust conditions match those seen in the reference  $M_{13}$ . Of course this reduces the overall drying rate versus the one obtained in  $M_3$  and thus product shows a higher  $X_w$ .

Let us analyse the elutriation from the dryer.  $M_1$ ,  $M_{3-i}$  and  $M_{13}$  show comparable exhaust conditions in Table 3 (velocities are given in section 2.4.1, Table 6). The rate of elutriates,  $\bar{M}_E$

decreases when the nozzle is brought down from  $\bar{M}_E = 8.0\%$  of the full production rate in  $M_1$  to  $6.8\%$  in  $M_{3-i}$ . This is in agreement with the trend observed in for a single nozzle, but shows higher values because the unit operates at higher air velocities (i.e.  $\bar{M}_E$  ranges from  $2.0 - 4.0\%$  in Table 1 for the use of a single nozzle). When using the water sprays in  $M_{3-ii}$  and  $M_{3-iii}$  the elutriation falls further, perhaps as the consequence of a certain interaction with the water drops.

When both nozzles are used together in  $M_{13}$ , the elutriates are  $3.1\%$  of the product but when both operate individually in  $M_{3-i}$  and  $M_1$  the elutriation from both represents  $7.4\%$ . This is a very relevant fact: a quite substantial part of the production,  $4.3\%$ , flows up when both nozzles are operated independently but does not longer exit through the top if they are together, it exits with the product at the bottom. Clearly, this points to the capture of part of the fines at the top spray, so that they grow and flow down. This will be confirmed by the analysis of size and composition.

## 2.4. Results and Discussion.

### 2.4.1. Mass and energy balances across the chamber.

As expected, the thermal efficiency  $\eta_t$  and the overall heat transfer efficiency  $\eta_h$  both increase in the operation of two nozzles in  $M_{13}$ , see Table 3, versus the values for a single nozzle operation in Table 1. This is explained by the increase in  $T_A$  and a substantially higher particle loading.

The time averaged  $\bar{T}_A$  field is presented in Figure 14.

$M_{13}$  and  $M_1$  show comparable profiles below the top nozzle (see  $tt - 3$ ). They show a constant small bias,  $\sim 10\text{ }^\circ\text{C}$  and an increase at the centre of the cylinder, more accentuated in  $M_{13}$ .

$tt - 1$  shows the region immediately below the projection of the bottom spray. Here,  $M_{3-ii}$  and  $M_{3-iii}$  show slightly lower temperatures than the reference,  $M_{13}$ . In the outer part,  $T_A$  varies from  $175 - 180\text{ }^\circ\text{C}$  to  $150 - 175\text{ }^\circ\text{C}$  and  $160 - 180\text{ }^\circ\text{C}$  from  $M_{13}$  to  $M_{3-ii}$  and  $M_{3-iii}$  respectively. In these cases, the central region of high  $T_A$  is lost above the nozzle, but it appears at the top end of the chamber. The reason for this remains unclear. It may be related to the recirculation owed to the contraction identified at isothermal conditions (Chapters II and III).

$M_3$  and  $M_{3-i}$  show different profiles because they do not inject neither slurry nor water at the upper part of the dryer. Here, the entire chamber above the nozzle shows homogeneous  $T_A$ , and thus the elutriates must dry near the nozzles. In  $M_{13}$  and  $M_3$ ,  $tt - 1$  shows similar values, decreasing

**Table 3.** Summary of operation conditions. Both levels in  $M_{13}$ ; isolation of each by: a ramp in  $T_{A,IN}$  ( $M_3$ ,  $M_{3-i}$ ) and the use of water sprays ( $M_1$ ,  $M_{3-ii}$ ,  $M_{3-iii}$ ). The equivalent water rate  $\Delta M_{W,eq}$  is estimated from the  $\Delta M_S$  moving from the single nozzle case to  $M_{13}$  or  $M_{13-r}$ . The actual evaporation rate is given as  $M_{eva}$ . The thermal efficiency is given as  $\eta_t = (T_{A,IN} - T_{A,EX}) / (T_{A,IN} - T_{amb})$  and the overall heat transfer efficiency as  $\eta_h = Q_s / H_{A,IN}$  where  $H_{A,IN}$  is the inlet air enthalpy with ambient air as the reference.

CASE	$M_{13}$	$M_{13-r}$	$M_1$	$M_{1-r}$	$M_3$	$M_{3-i}$	$M_{3-ii}$	$M_{3-iii}$
Slurry line, S, Water lines, W, Product in the tower belt, P, elutriated fines, E, and full exiting power, EP,								
Nozzle/s	#1, #3	#1, #3	#1, $W_2$	#1, $W_2$	#3	#3	#1, $W_1, W_3$	#1, $W_1, W_3$
$\bar{M}_{S,\#1} / \bar{M}_{S,M_{13}}$	0.47 ± 0.02	0.45 ± 0.02	0.52 ± 0.02	0.54 ± 0.04	-	-	-	-
$\bar{M}_{S,\#3} / \bar{M}_{S,M_{13}}$	0.53 ± 0.02	0.54 ± 0.02	-	-	0.52 ± 0.02	0.52 ± 0.02	0.53 ± 0.02	0.56 ± 0.02
$\bar{M}_{W_1} / \Delta \bar{M}_{W,Eq}$	-	-	-	-	-	-	0.36	0.58
$\bar{M}_{W_2} / \Delta \bar{M}_{E,q}$	-	-	0.98	1.00	-	-	-	-
$\bar{M}_{W_3} / \Delta \bar{M}_{E,q}$	-	-	-	-	-	-	0.72	0.58
$\bar{M}_E$ (% $\bar{M}_{EP}$ )	3.1	3.1	8.0	8.3	9.0	6.8	5.2	1.8
$X_w - X_{w,M_{13}}$ (%)	0.00	-0.1	-0.5	0.3	-0.6	4.2	-2.0	-1.6
$\bar{T}_P - \bar{T}_S$ (°C)	2.8 ± 3.7	-3.9 ± 3.7	1.6 ± 5.2	2.4 ± 3.9	46.7 ± 8.1	-14.1 ± 2.2	47.0 ± 14.1	57.6 ± 9.4
Air line, A, inlet, IN, and exhaust, EX, conditions.								
$\bar{M}_A / M_{A,M_{13}}$	1.00 ± 0.06	0.94 ± 0.04	0.98 ± 0.06	0.90 ± 0.06	1.00 ± 0.02	1.00 ± 0.02	1.00 ± 0.02	0.99 ± 0.04
$tt - 0, \bar{T}_{A,IN}$ (°C)	300.1 ± 7.0	300.5 ± 7.2	300.7 ± 5.2	299.8 ± 8.6	238.9 ± 2.6	169.8 ± 1.8	299.8 ± 3.2	301.5 ± 1.2
$tt - 5, \bar{T}_{A,EX}$ (°C)	78.2 ± 2.2	74.0 ± 1.2	82.8 ± 1.6	82.0 ± 1.4	104.8 ± 2.2	82.5 ± 1.0	75.5 ± 4.2	68.7 ± 10.4
$\bar{M}_{eva} / \bar{M}_{eva,M_{13}}$	1.00	0.99	1.00	0.99	0.52	0.46	1.06	1.09
$rH_E$ (%)	29	36	24	27	6	12	35	48
Overall Energy Balance								
$Q_{Loss}$ (% $Q_{EX}$ )	30.2 ± 1.8	28.9 ± 2.2	28.0 ± 0.5	21.2 ± 0.5	36.4 ± 0.9	19.6 ± 1.9	24.9 ± 0.7	24.5 ± 0.7
$\Delta H_{p,Sn}$ (% $Q_{EX}$ )	2.2 ± 2.7	1.3 ± 3.2	2.2 ± 0.7	2.2 ± 0.7	6.0 ± 1.5	-1.9 ± 2.3	4.1 ± 1.0	5.0 ± 1.0
$\eta_t$	0.79 ± 0.02	0.81 ± 0.02	0.78 ± 0.01	0.78 ± 0.02	0.61 ± 0.01	0.58 ± 0.01	0.80 ± 0.01	0.83 ± 0.02
$\eta_h$	0.57 ± 0.02	0.58 ± 0.02	0.57 ± 0.01	0.62 ± 0.01	0.41 ± 0.01	0.47 ± 0.02	0.62 ± 0.01	0.64 ± 0.01

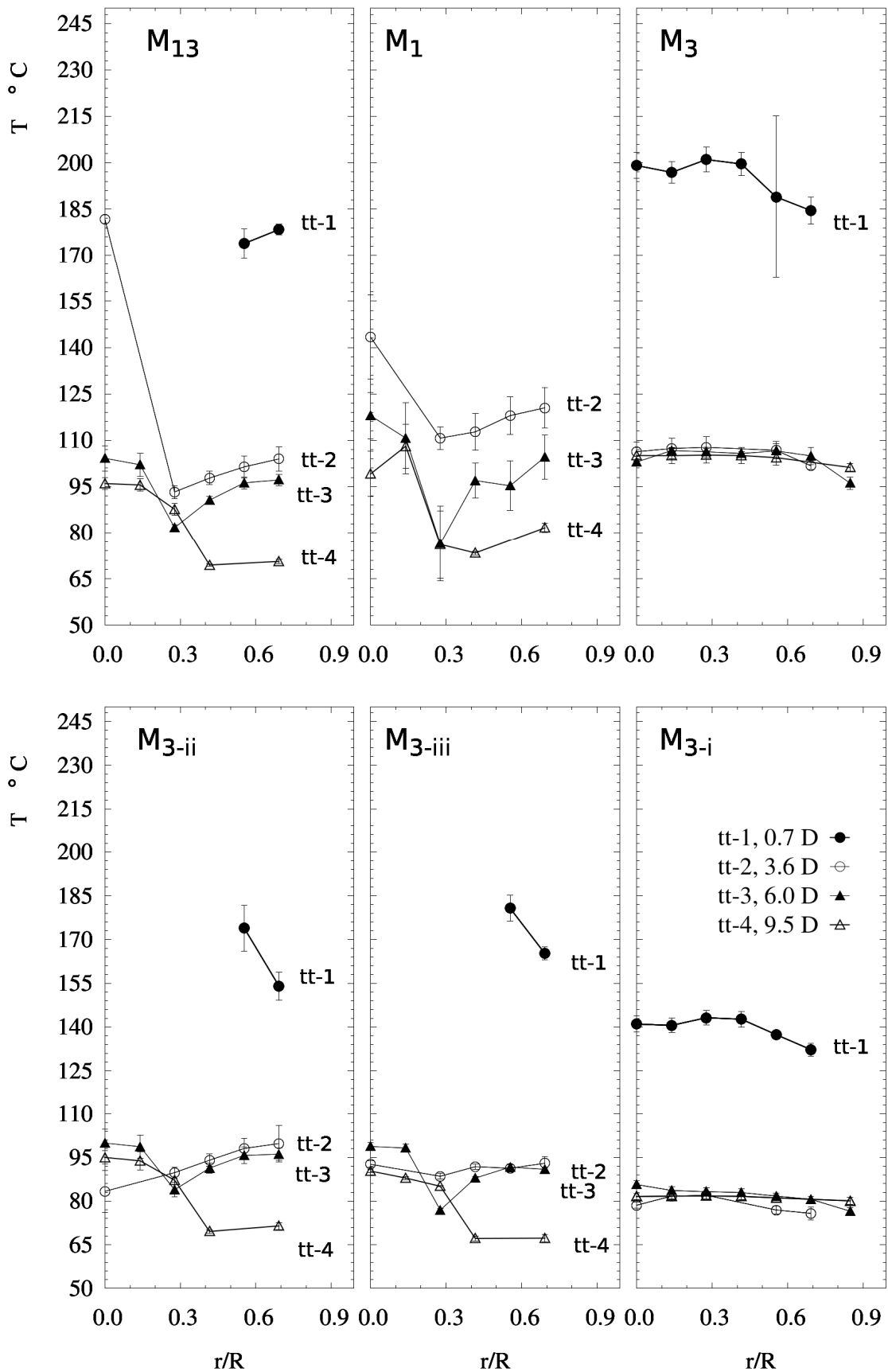


Figure 14.  $\bar{T}_A$  time averaged field from sensors  $tt - 1$  ( $0.7 D$ ),  $tt - 2$  ( $3.6 D$ ),  $tt - 3$  ( $6.0 D$ ) and  $tt - 4$  ( $9.5 D$ ).

towards the wall in an indication of a higher  $n$ , and with a span from  $200 - 185$  °C. Obviously, when the inlet air temperature drops in  $M_{3-i}$  the values decrease,  $145 - 135$  °C in Figure 14.

Figure 15 presents a cross-sectional averaged temperature  $\tilde{T}_A$  and measurements at the plenum  $tt - p$  and cone  $t - c$ . They allow an energy balance to be conducted in the sections shown in Figure 5a, summarised in Tables 4 and 5. The overall evaporation and heat loss,  $Q_{loss}$ , rates are obtained from general mass and energy balances. Equation (1) defines the heat exchanged  $Q_{Ex}$  from the variation of the sensible enthalpy of the dry air  $\Delta H_{DA,Sn}$ , and the product,  $\Delta H_{P,Sn}$  (i.e. inlet slurry, outlet powder and elutriates and outlet water vapour), utilised in evaporation,  $\Delta H_{A,Lat}$ , and in the heat lost to the environment,  $Q_{loss}$

$$Q_{Ex} = \Delta H_{A,Lat} + Q_{loss} = -(\Delta H_{DA,Sn} + \Delta H_{P,Sn}) \quad (1)$$

In order to study how the solids dry at different sections, it is useful to group those terms differently in equation (2) and compute the heat transferred to the solid phase in a section  $i$ ,  $Q_{S,i}$ . This requires one to estimate how the heat is lost in each section. This is largely localised in Section I ( $Q_{loss,I} > 0.84 - 91 Q_{loss}$ ) and particularly due to the  $\Delta T$  between  $tt - 0$  and  $tt - p$  (i.e. the losses in the distributor account for  $0.72 - 87 Q_{loss}$ ). The remaining losses reduce drastically in the cylinder. They can be distributed according to the contact area and the air-wall temperature difference, in the assumption that all sections show comparable heat transfer resistances.

$$Q_{S,i} = -(\Delta H_{DA,Sn,i} + Q_{loss,i}) = \Delta H_{A,Lat,i} + \Delta H_{P,Sn,i} \quad (2)$$

In all cases, heating the solids has a very limited effect (i.e.  $\Delta H_{P,Sn} < 0.10 Q_{Ex}$ ) so that the heat transfer rate calculated from  $Q_S$  is a good indication of the drying rate experienced by the solids.

Table 4 summarizes the axial distribution of  $Q_S$  in the reference,  $M_{13}$ . Notably, a high proportion of heat is transferred below the cylinder,  $> 44$  %, and a low proportion between the nozzles, Section III. There is also a large difference between both spray regions, Sections II and IV. Clearly, most of the particles sprayed at the top, in fact dry below the bottom nozzle in the Sections I and II.

To illustrate the differences between regions, Table 4 includes a specific drying rate,  $r$  (i.e.  $J/s$  per  $m$  of height tower and per  $g$  of slurry). Normalization by the either total rate and that of each nozzle permits the comparison of the heat transferred to each spray in the rest of experiments given in Table 5.

**Figure 15.** Cross sectional average temperature  $\bar{T}_A$  in  $tt - 1$  to  $tt - 4$ ; time averaged  $T_A$  in  $tt - c$  and punctual  $T_A$  measurement in  $t - p$ . a) Location of temperature sensors and definition of sections. b)  $M_{13}$ : nozzle #1 and #3 at 8.2 D and 3.5 D b)  $M_1$ : nozzle #1 and water nozzle  $W_2$  c)  $M_3$  and  $M_{3-i}$ : nozzle #3 at 3.5 D, e)  $M_{3-ii}$  and  $M_{3-iii}$ : nozzle #3 and water nozzles  $W_1$  and  $W_3$ .

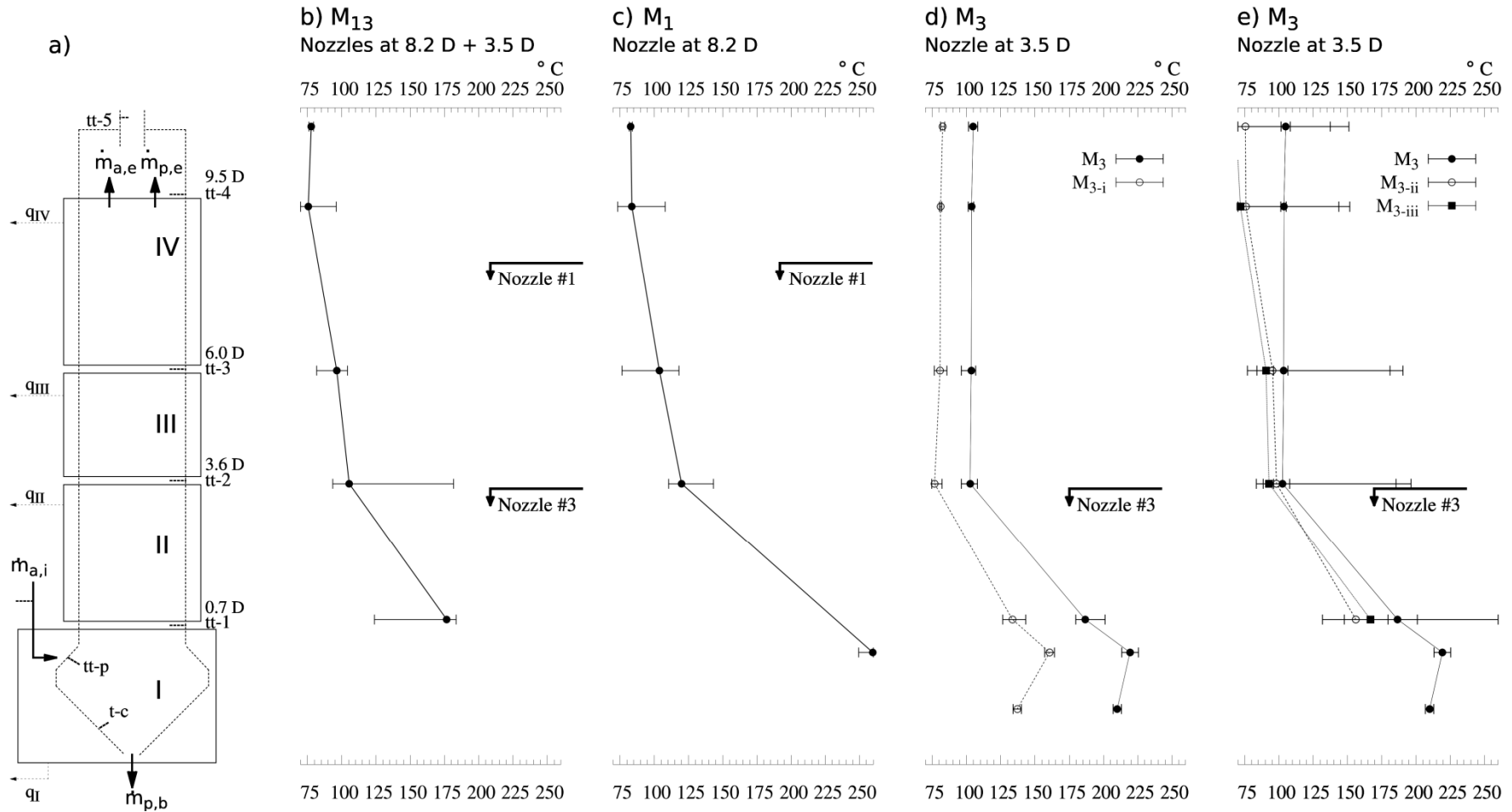


**Table 4.** Energy balance to the multi-level system,  $M_{13}$ . Distribution of the heat transferred to the solids,  $Q_S$ , and specific heat transfer rate,  $r$ , for Section I defined from  $tt - 0$  to  $tt - 1$ , and the Sections II, III and IV in the intervals between  $tt - 1$ ,  $tt - 2$ ,  $tt - 3$  and  $tt - 4$ . Bold denotes the spray regions.

Scenario	$M_{13}$			
	$Q_{S,i}$ %	$^* r$ J/sgm		
Drying load		13	1	3
I < 0.7D	44.7 ± 1.4		-	
II 0.7D-3.6D	40.1 ± 1.1	<b>70.6 ± 0.6</b>	150.3 ± 6.5	<b>133.3 ± 5.8</b> ***
III 3.6D-6.0D	4.0 ± 0.1	8.8 ± 0.3	18.8 ± 1.0	16.7 ± 0.9
IV 6.0D - 9.5D	11.2 ± 0.3	<b>16.5 ± 0.2</b>	<b>35.1 ± 1.5</b> **	31.1 ± 1.4

\*  $r = Q_{S,i} / (\Delta z \cdot M_s \cdot (1 - X_{w,s}))$ , 13, 1 or 3 denote the normalization to  $M_s$ ,  $M_{s,\#1}$  or  $M_{s,\#3}$  respectively

\*\* In this case most the heat exchanged in this section corresponds to the product sprayed from nozzle #1.

\*\*\* In this case, part of the heat is used to dry the product coming from nozzle #1. The minimum rate used to dry to the product from nozzle #3 can be estimated as  $97.0 \pm 4.5$  J/sgm for a direct comparison to  $M_3$ ,  $M_{3-i}$  in Table 5.

**Table 5.** Energy balance. Isolation experiments. Distribution of the rate of heat transferred to the solids,  $Q_S$ , and specific heat transfer rate,  $r$ , for Section I defined from  $tt - 0$  to  $tt - 1$ , and the Sections II, III and IV in the intervals between  $tt - 1$ ,  $tt - 2$ ,  $tt - 3$  and  $tt - 4$ . Bold denote the spray region.

Scenario	$M_1$		$M_3$			
	$Q_{S,i}$ %	$^* r$ J/sgm	$Q_{S,i}$ %	$^* r$ J/sgm		
Drying load						
I < 0.7D	81.0 ± 0.1	-	13.9 ± 1.6	-		
II 0.7D-3.6D			<b>86.1 ± 1.6</b>	<b>161.9 ± 0.4</b>		
III 3.6D-6.0D	8.3 ± 0.1	34.3 ± 0.2	0.0	0.0		
IV 6.0D-9.5D	<b>10.7 ± 0.1</b>	<b>29.3 ± 0.1</b>	0.0	0.0		
Scenario	$M_{3-i}$		$M_{3-ii}$		$M_{3-iii}$	
	$Q_{S,i}$ %	$^* r$ J/sgm	$Q_{S,i}$ %	$^* r$ J/sgm	$Q_{S,i}$ %	$^* r$ J/sgm
Drying Load						
I < 0.7D	29.7 ± 1.8	-	57.4 ± 0.4	0-	50.2 ± 1.4	-
II 0.7D-3.6D	<b>70.3 ± 1.8</b>	<b>102.9 ± 0.5</b>	<b>31.5 ± 0.3</b>	<b>111.7 ± 0.2</b>	<b>39.5 ± 0.4</b>	<b>135.6 ± 0.2</b>
III 3.6D-6.0D	0.0	0.0	0.9 ± 0.1	4.0 ± 0.1	0.6 ± 0.1	2.6 ± 0.1
IV 6.0D-9.5D	0.0	0.0	10.3 ± 0.1	30.4 ± 0.1	9.7 ± 0.1	27.6 ± 0.1

\*  $r = Q_{S,i} / (\Delta z \cdot M_s \cdot (1 - X_{w,s}))$

$r$  is indicative of the efficiency of the heat transfer and particle concentration. For instance, in  $M_{13}$  much lower values are obtained at the top spray region ( $16.5 \text{ J s}^{-1}\text{m}^{-1}\text{g}^{-1}$ ) than at the bottom spray region ( $70.6 \text{ J s}^{-1}\text{m}^{-1}\text{g}^{-1}$ ). This is explained by the lower air temperatures and velocities leading to a lower heat transfer rate to each droplet, and the lower  $n$  of them expected at the top of the chamber.

All experiments aim at reproducing similar particle properties in the spray regions, and thus they need to show a comparable  $T_A$  field in Figure 14, and comparable heat transfer rates in Tables 4 and 5.

$M_1$  shows similar heat transfer rates, yet a slightly lower value at the top nozzle, Section IV, comparing  $r = 34.2$  in Table 4 (1) to  $29.3 \text{ J s}^{-1}\text{m}^{-1}\text{g}^{-1}$  in Tables 5.

At the bottom spray region, Section II,  $M_3$  shows a higher heat transfer rate ( $r = 161.2 \text{ J s}^{-1}\text{m}^{-1}\text{g}^{-1}$ ) versus the values of the reference in Table 4 (3), between  $r = 97.0 - 133.3 \text{ J s}^{-1}\text{m}^{-1}\text{g}^{-1}$ .  $M_{3-i}$  better replicates this range yielding  $r = 102.9 \text{ J s}^{-1}\text{m}^{-1}\text{g}^{-1}$  in Section II. In the cases  $M_{3-ii}$  and  $M_{3-iii}$  comparable rates are observed in the entire dryer thanks to the use of the water sprays, see Table 4 (13) and Table 5. Accordingly, one expects the properties of the particles in Section II in  $M_{13}$  to be somewhere in between the ones obtained in the cases  $M_3$ ,  $M_{3-i}$ ,  $M_{3-ii}$  and  $M_{3-iii}$ . The first two cover the range of  $r$  observed in Table 4 and the last two show similar rates but re-wet the surface of the particles. Interestingly, all result in a very similar product (section 2.4.3.1).

Table 6 illustrates the axial decrease in air velocity  $U_A$  in the chamber by the estimation of the air superficial velocity  $\bar{U}_{av}$ . It enables comparison of the exhaust velocities and explains how the different velocities causes higher concentration of particles at the bottom, and reduce them at the top.

**Table 6.** Axial variation of the air superficial velocity  $\bar{U}_{A,av}$ , estimated as  $U_{A,av} = \bar{M}_{DA}/\bar{\rho}_{DA}\pi R^2$ .

$U = \frac{\bar{U}_{av}}{\bar{U}_{av,M_{13},tt=0}}$	$M_{13}$	$M_1$	$M_3$	$M_{3-i}$	$M_{3-ii}$	$M_{3-iii}$
$tt = 0, \quad 0.0 D$	1.00	0.98	0.89	0.77	1.00	0.99
$tt = 1, \quad 0.7 D$	0.78	0.77	0.80	0.71	0.75	0.76
$tt = 2, \quad 3.6 D$	0.66	0.67	0.66	0.62	0.65	0.63
$tt = 3, \quad 6.0 D$	0.64	0.65	0.66	0.62	0.64	0.63
$tt = 4, \quad 9.5 D$	0.61	0.61	0.66	0.61	0.61	0.60

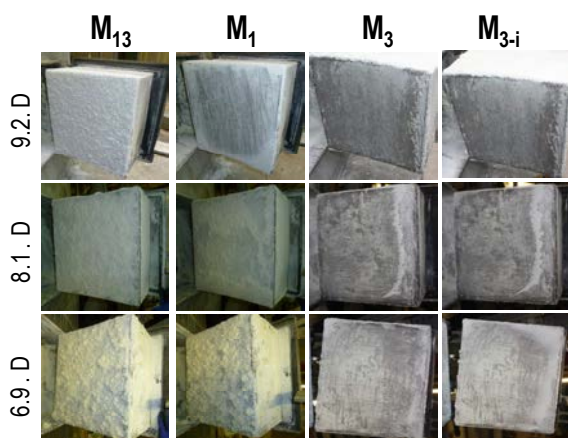
### 2.4.2. Wall deposits.

Table 7 summarises the initial net wall deposition rate,  $r_{d,o}$ . Figures 16 and 17 show a selection of photographs of the walls and their deposits near the sprays. During  $M_{13}$  deposits occur only in the area of projection of the top nozzle at  $6.9 D$ . Deposition above responds to the accumulation of fines and barely no deposition is observed either between the sprays or at the area in  $2.2 D$ , slightly above the projection of the bottom nozzle (see Figures 3 and 4).

The capture of the fines explains why deposits are reduced at the top of the chamber, see level  $9.2 D$  in table 7, from  $M_{13}$  to  $M_1$ . Comparison of  $M_1$  to the operation of the same nozzle alone in Table 2 shows a much higher  $r_{d,o}$  from  $54.3$  to  $112.1 \text{ g min}^{-1} \text{ m}^2$  at the spray projection in  $6.9 D$ . This is a clear indication of the effects of using two levels: a stronger recirculation, higher  $n$  and lower heat transfer rates at the top. This makes particles to impact the wall more frequently and sufficiently wet to cause deposition.

**Table 7.** Summary of the initial deposition rates,  $r_{d,o}$ , at the inspection areas depicted in Figure 2.

Level	$M_{13}$	$M_1$	$M_3$	$M_{3-i}$	$M_{3-ii}$	$M_{3-iii}$
/ D	$\text{g m}^{-2} \text{min}^{-1}$					
10.4	-	-	0.5	0.85	-	-
9.2	30.1	1.7	0	0	0	0
8.1	14.5	32.1	0.1	0.5	0	0
6.9	82.1	112.0	0	0.4	99.5	30.9
5.7	0	0	0	0	0	0
4.5	0	0	0	0	0	0
3.4	0	0	0	0.4	0	0
2.2	3.6	-	0	40.8	89.2	135.0



**Figure 16.** Wall deposits at the top sections, and within the area of the spray projection of the nozzle #1 at  $8.2 D$

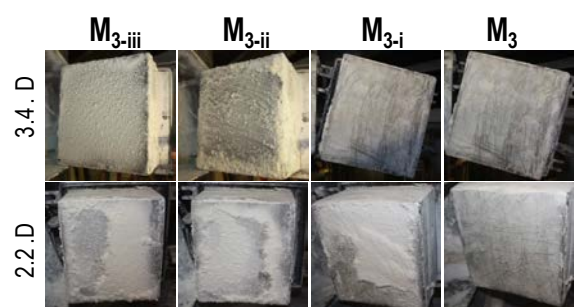


**Figure 17.** Wall deposits immediately above the spray projection from nozzle #3.  $M_3, M_{3-i}, M_{3-ii}$  and  $M_{3-iii}$

No deposits are observed at  $2.2 D$  in either  $M_{13}$  or  $M_3$ . Particles are sufficiently dry when they reach the wall. When drying is reduced in  $M_{3-i}$  particles are wetter and deposits appear in Figure 17.

In  $M_{3-ii}$  and  $M_{3-iii}$  deposits also appear near the water nozzles at  $2.2 D$  and  $6.9 D$ , see Figures 5 and 9. This suggests that the surface of the particles or the wall is re-wet and thus the product may contain more aggregates that would have been produced if the water drops were “invisible” to the particles. As detailed in the next section this poses no restrictions to the conclusions of this work.

### 2.4.3. Product Analysis.

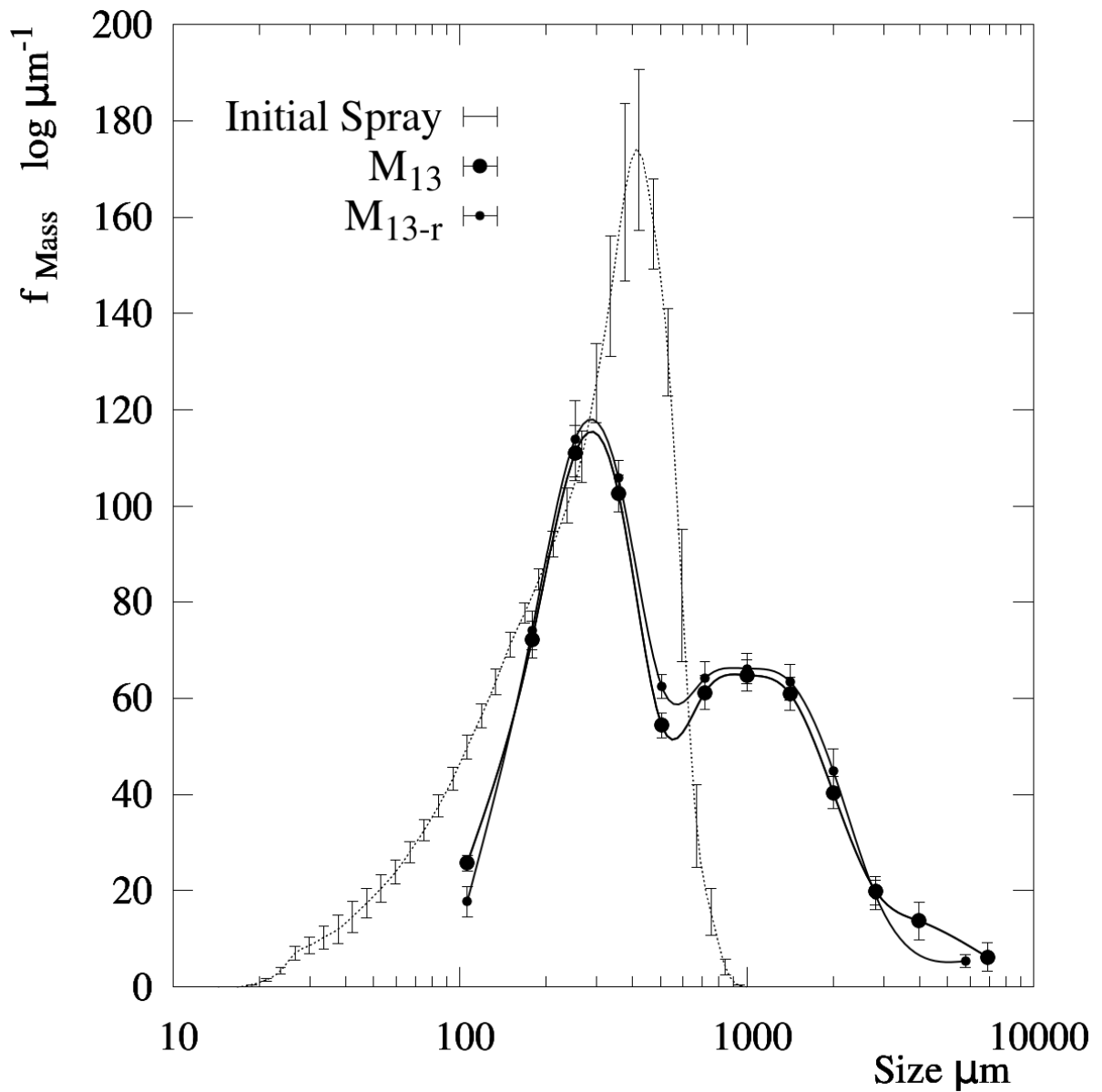
#### 2.4.3.1. Aggregation patterns in multi-level systems.

Figure 18 compares the size distribution of the droplets and the product obtained in  $M_{13}$  and  $M_{13-r}$ . Interestingly no significant changes are observed between  $M_{13}$  and  $M_{13-r}$ , nor between  $M_1$  to  $M_{1-r}$  in Figure 19. This suggests the impact of deposits in the air flow remains comparable in all cases.

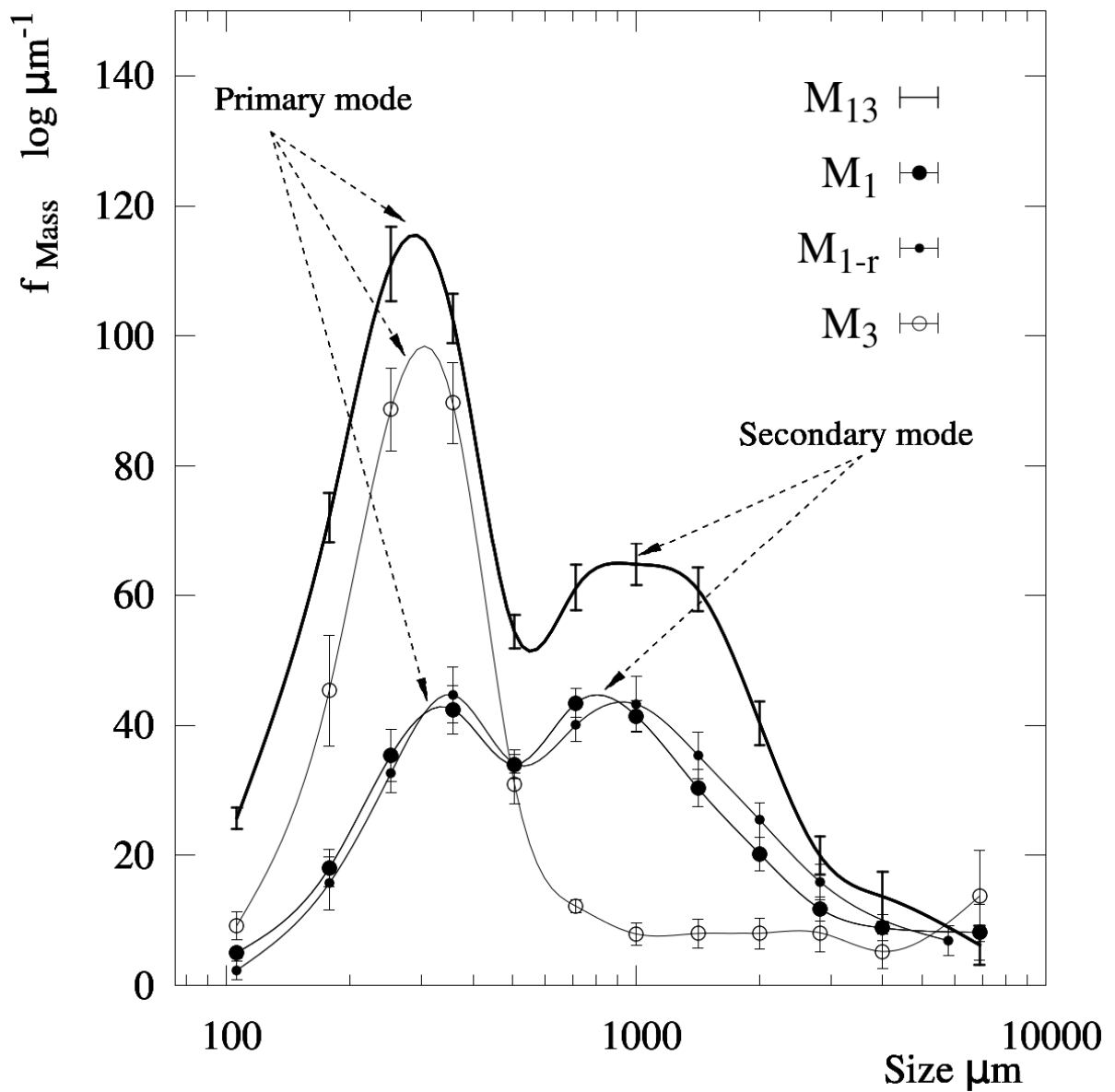
The operation of nozzle #1 and nozzle #3 renders a product size distribution with a single mode between  $300 - 425 \mu m$  (Figure 5, section 1.3.4.1). However, using two nozzles produces a clearly different size distribution shown in Figure 18: it shows a primary mode in the same range but also the formation of a second between  $850 - 1180 \mu m$ . The statistics for all size distributions are summarised in Table 8. It is very interesting to notice how the mass median size  $x_{p,50}$  remains similar between the multi-level case,  $M_{13}$  and the operation of single nozzles  $S_1$  or  $S_3$ . Furthermore,  $x_{p,10}$  and  $x_{p,90}$  are even reduced versus  $S_3$ . This occurs because the formation of secondary mode prevents the final plateau in observed in  $S_3$  in Figure 5 (section 1.3.4.1). It is worth noticing that the two modes observed cannot be reproduced by summation of two log-normal distributions.

Figure 19 compares the reference size distribution in  $M_{13}$  with the contribution expected from each nozzle, top and bottom nozzles given by  $M_1$  and  $M_3$ . All show the same primary mode, but it becomes immediately clear that the production of the secondary mode owes to the product coming from the top nozzle,  $M_1$ . The product coming from the bottom nozzle,  $M_3$ , shows a single and narrow mode.

Figure 20 compares the multi-level conditions in  $M_1$  and  $M_3$  to the single level ones,  $S_1$  and  $S_3$ . It is immediately clear the effect of a higher  $n$  and the different drying kinetics. It promotes growth in the top nozzle, see Figure 20a, where the shoulder in  $S_1$  develops into a large mode in  $M_1$  and reduces in the bottom, see Figure 20b, where the mode in  $S_3$  narrows substantially and the plateau



**Figure 18.** Comparison of the mass based size distribution associated to the atomization to that of the product under the simultaneous operation of both nozzles in  $M_{13}$ .



**Figure 19.** Comparison of the mass based product size distribution in either the simultaneous,  $M_{13}$ , or independent,  $M_1$  &  $M_3$ , operation of nozzles #1 and #3. The density functions are normalised by the production rate of each nozzle/s.

**Table 8.** Statistics of the mass based product size distributions. The confidence intervals provide one standard deviation.

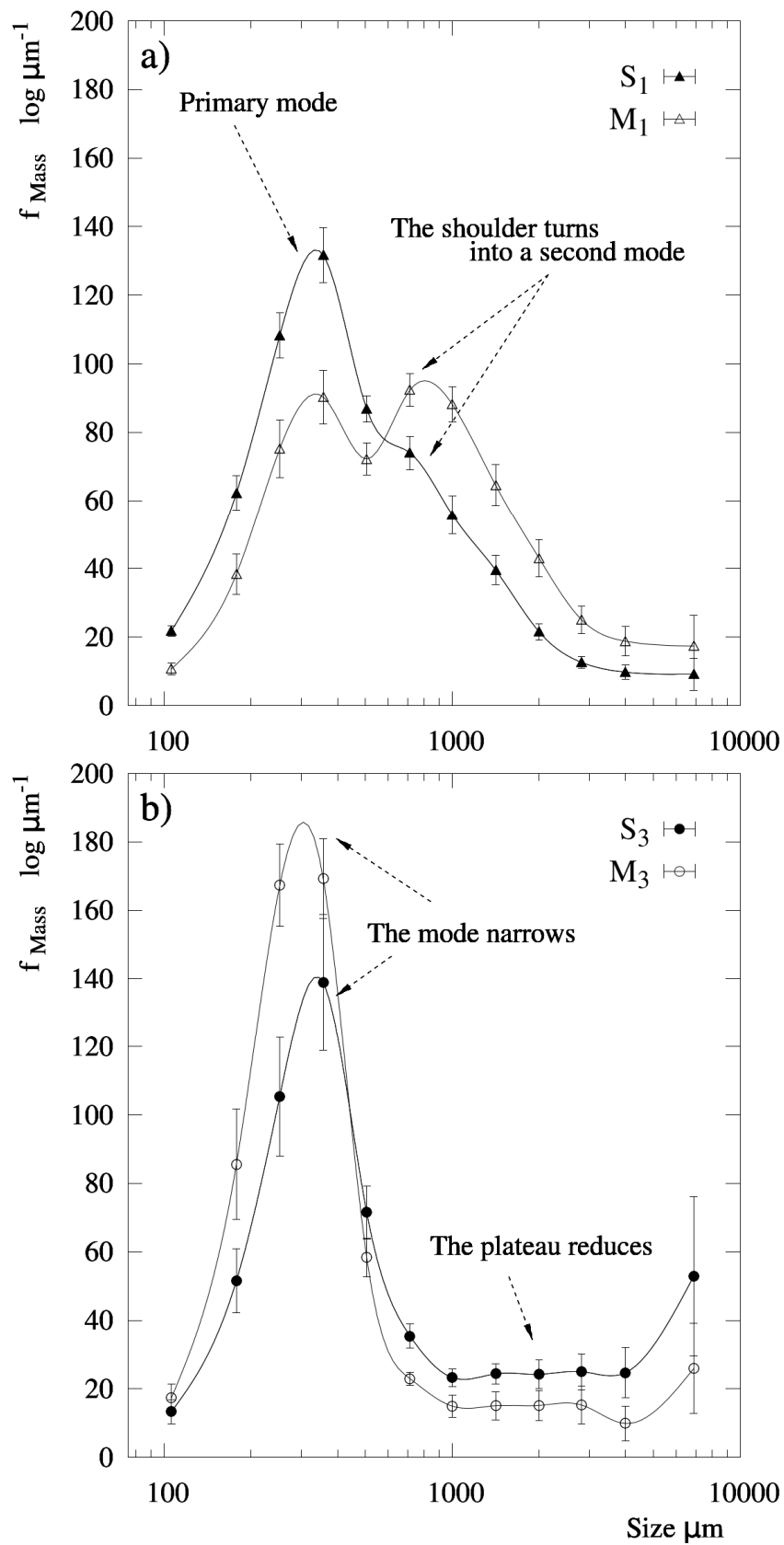
<b>Case</b>	$x_{p,10}, \mu m$	$x_{p,25}, \mu m$	$x_{p,50}, \mu m$	$x_{p,75}, \mu m$	$x_{p,90}, \mu m$
$M_{13}$	<b>163</b> ± 3	<b>246</b> ± 6	<b>423</b> ± 22	<b>1093</b> ± 61	<b>2023</b> ± 186
$M_1$	<b>220</b> ± 11	<b>220</b> ± 11	<b>696</b> ± 76	<b>696</b> ± 76	<b>3115</b> ± 1059
$M_{1-r}$	242 ± 10	242 ± 10	751 ± 55	751 ± 55	2803 ± 572
$M_3$	<b>175</b> ± 13	<b>237</b> ± 13	<b>334</b> ± 25	<b>697</b> ± 392	<b>3482</b> ± 2167
$M_{3-i}$	186 ± 10	261 ± 15	388 ± 30	1070 ± 500	4447 ± (>1100)
$M_{3-ii}$	175 ± 9	236 ± 13	335 ± 29	601 ± 123	2424 ± 1001
$M_{3-iii}$	179 ± 16	240 ± 17	335 ± 28	529 ± 96	1471 ± 833
$S_1$ (section 1)	<b>173</b> ± 4	<b>261</b> ± 7	<b>413</b> ± 15	<b>824</b> ± 64	<b>1724</b> ± 286
$S_3$ (section 1)	<b>195</b> ± 12	<b>282</b> ± 20	<b>456</b> ± 98	<b>2224</b> ± 1575	( $x_{83} = 4760 \mu m$ )

disappears in  $M_3$ .

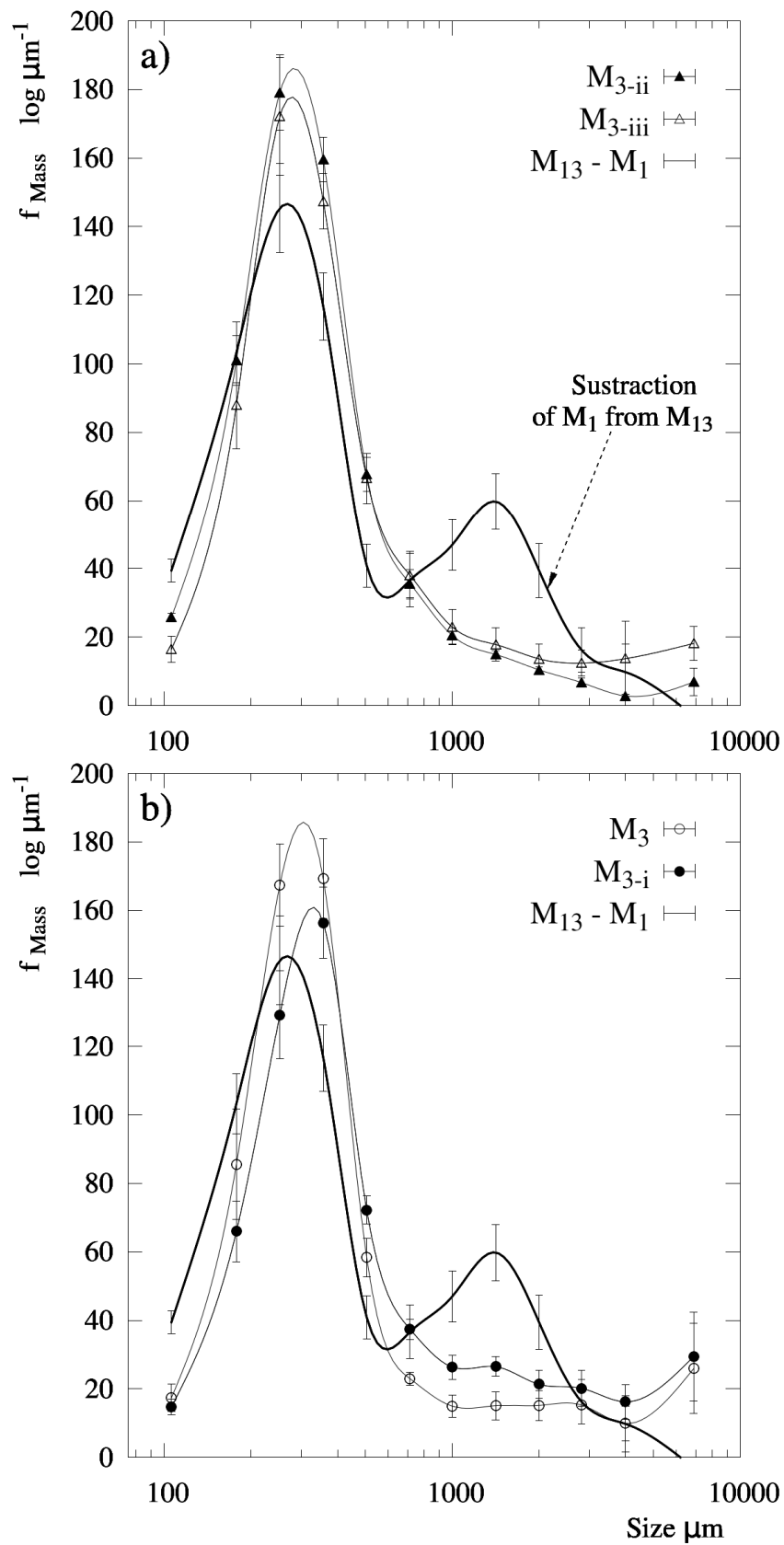
A relevant question remains on whether  $M_{13}$  can be represented by the simple summation of the product from both sprays, or if it involves significant interaction. If the contacts due to the recirculation were negligible, the summation of  $M_1$  and  $M_3$  should result in that of  $M_{13}$  (or at least the minimum particle growth expected given they are over predictions). A simple mass balance demonstrates this is not the case. The secondary size mode in  $M_1$  does not suffice to justify the one observed in  $M_{13}$ . As a maximum it is accountable for 63 % of the product  $> 600 \mu m$ .

Figure 21 helps to illustrate this effect by comparison of a) the product expected from nozzle #3 if there was no recirculation (i.e. subtraction of  $M_1$  from  $M_{13}$ ) and b) all the experiments that study the nozzle #3 alone. The powder obtained from nozzle #3 shows always the same size distribution: a single mode aligned with the primary mode in  $M_{13}$ . Cases  $M_3$  and  $M_{3-i}$  generate a narrower mode and a final plateau, instead of the long tails seen when water is used in  $M_{3-ii}$  and  $M_{3-iii}$ . The lower drying rate in  $M_{3-i}$  causes the plateau to rises and similarly, a wider tail appears in  $M_{3-iii}$ , but in all cases the overall shape and statistics are very similar (see Table 8).

The expectation from the mass balance in Figure 21 however is very different. The product cannot be reproduced by a simple summation of  $M_1$  and  $M_3$  and one must then reject the hypothesis of interactions being negligible. Furthermore, the secondary mode of  $M_{13}-M_1$  in Figure 21 is indicative of



**Figure 20.** Comparison of the production from each spray in a multi-level system to the conditions reported in section 1 for a single level operation ( $S_1$  and  $S_3$ ). a) from nozzle #1,  $M_1$  and  $S_1$  b) from nozzle #3,  $M_3$  and  $S_3$ .



**Figure 21.** Comparison of the expectation from nozzle #3 assuming there are no inter-nozzle interactions (i.e. subtraction of  $M_1$  from  $M_{13}$ ) to a)  $M_{3\text{-ii}}$  and  $M_{3\text{-iii}}$  and b)  $M_3$  and  $M_{3\text{-i}}$

the growth due to recirculation. This can be estimated as the difference between the mass rate with  $x_p > 600 \mu m$  in  $M_{13}$  and that coming from  $M_1+M_3$ . In this way one can argue that, as a minimum, 6 – 11 % of the mass within the secondary mode was in fact generated by inter-level contacts. This represents 3.7 % of the production. Notice this is in a very similar range to the reduction of elutriates observed of 4.3 % (section 2.3). This confirms they have been captured and exit as larger granules.

#### **2.4.3.2. Composition heterogeneity in multi-level systems.**

##### **2.4.3.2.1. Water content, $X_w$**

Figure 22 shows the variation of  $X_w$  with particle size in the product obtained from nozzle #3. All show the same general distribution observed in single nozzles (Section 1.3.4.2.1): a minimum within 350 – 450  $\mu m$  and a substantial rise for both, the fractions below and above 600  $\mu m$ . This is associated to breakage of large granules and the high  $X_w$  of the material worn off the deposits.

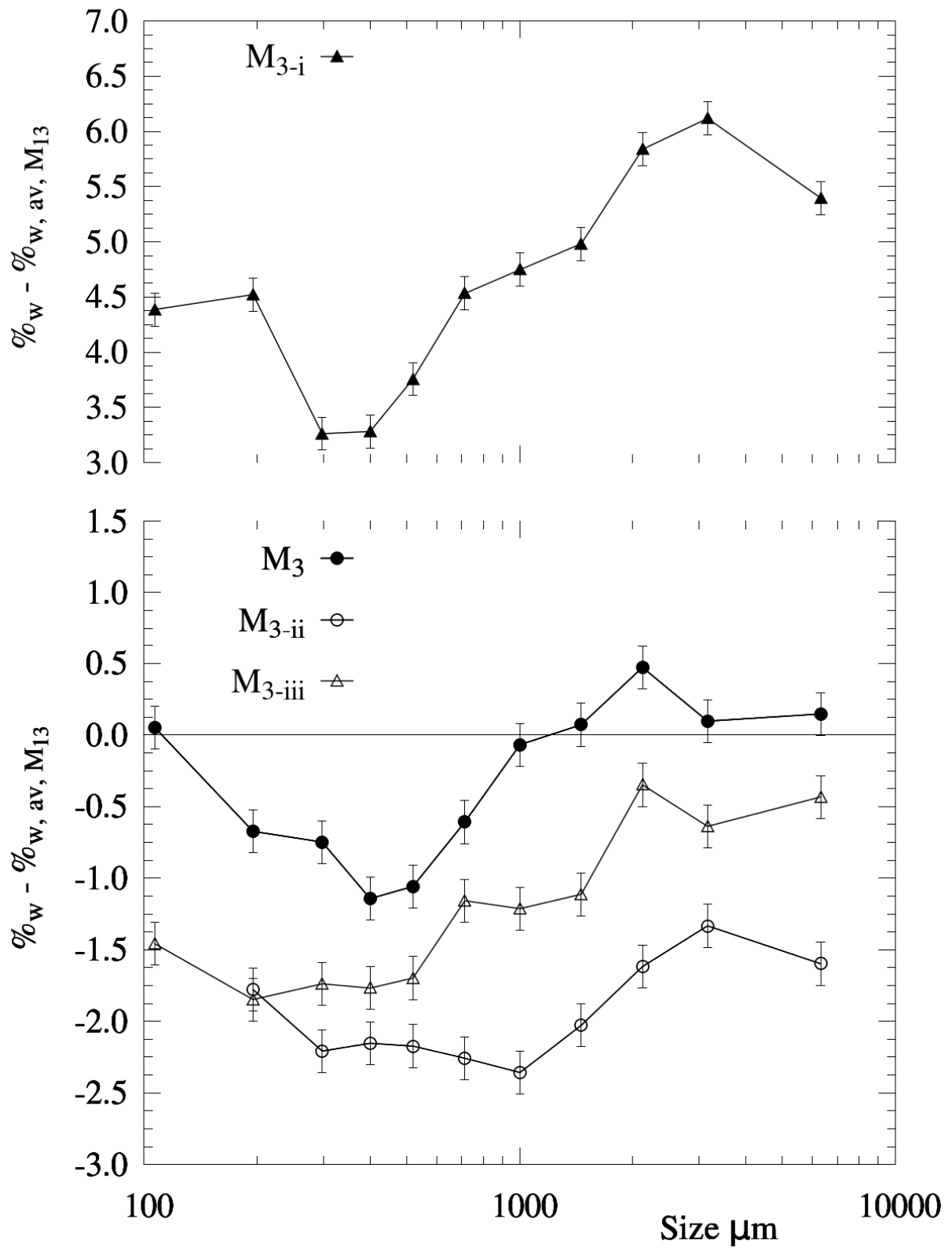
It is particularly interesting noticing the small sensitivity of the size distributions in Figure 21 to the bulk  $X_w$ , reducing from  $M_{3-i}$  to  $M_3$ , to  $M_{3-iii}$  and  $M_{3-ii}$ . This behaviour can be explained by the reports in Chapter V that suggest a large proportion of drying occurs when particles are resident at walls. It also agrees with the study of the sensitivity of the size distributions to air temperatures and velocities given in Appendix III. It concludes that the product size is in fact likely controlled by the breakage of the clusters occurring at the wall or close to it. This means that  $X_w$  is probably more related to the water content in the deposits and explains why size is less sensitive to dispersion or drying kinetics in the air.

Figure 23 includes a comparison of  $M_{13}$  and  $M_1$  to their replicates  $M_{13-r}$  and  $M_{1-r}$ , showing the same general profile. The minimum displaces to lower sizes in the replicates and also in the distribution of surfactant given below, perhaps due the use of a different solids supplier.

##### **2.4.3.2.2. Activity, $X_s$**

The distribution of the surfactant/s content,  $X_s$ , is presented in Figure 24 comparing each size class to primary mode. All show the same general trend of the single nozzle case, given in section 1.3.4.2.2 : the surfactant/s concentrates into the smallest fractions, the ones comparable to the un-dissolved solids show a minimum content, and the growth into large aggregates render homogeneous values.

In the multi-level case the heterogeneity is emphasized.  $M_{13}$  shows far larger differences between the minimum  $X_s$  shown within 350 – 450  $\mu m$  in Figure 24 and the secondary size mode  $> 600 \mu m$ .



**Figure 22.** Variation of the product water content  $X_w$  for the independent, operation of nozzle #3. Difference in % in mass vs that of the primary mode fraction in  $M_{13}$ .

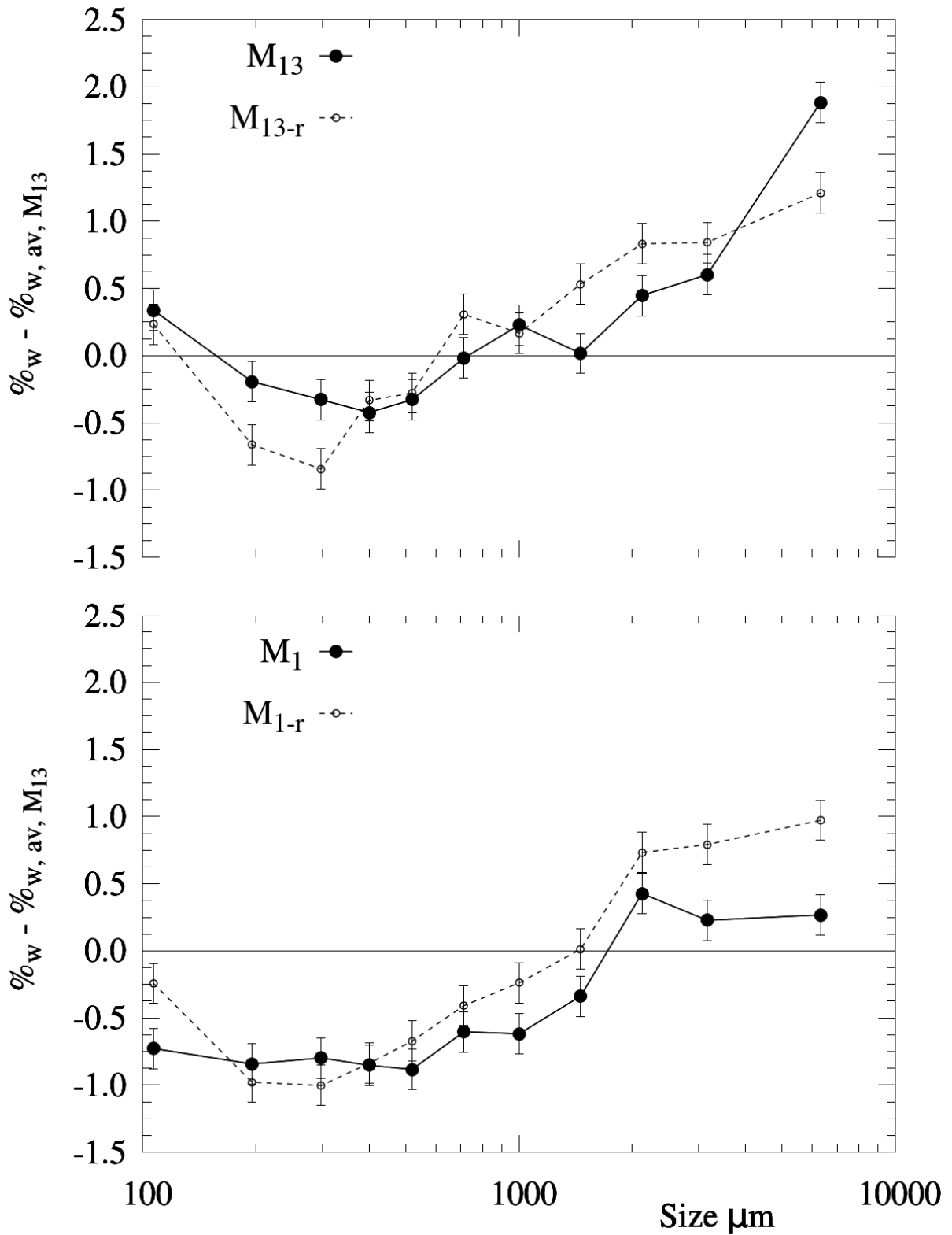


**Figure 23.** Variation of the product water content  $X_w$  for  $M_{13}$  (top) and  $M_1$  (bottom) and the replicates under heavily build up walls. Difference in % in mass versus that of the primary mode fraction in  $M_{13}$ .

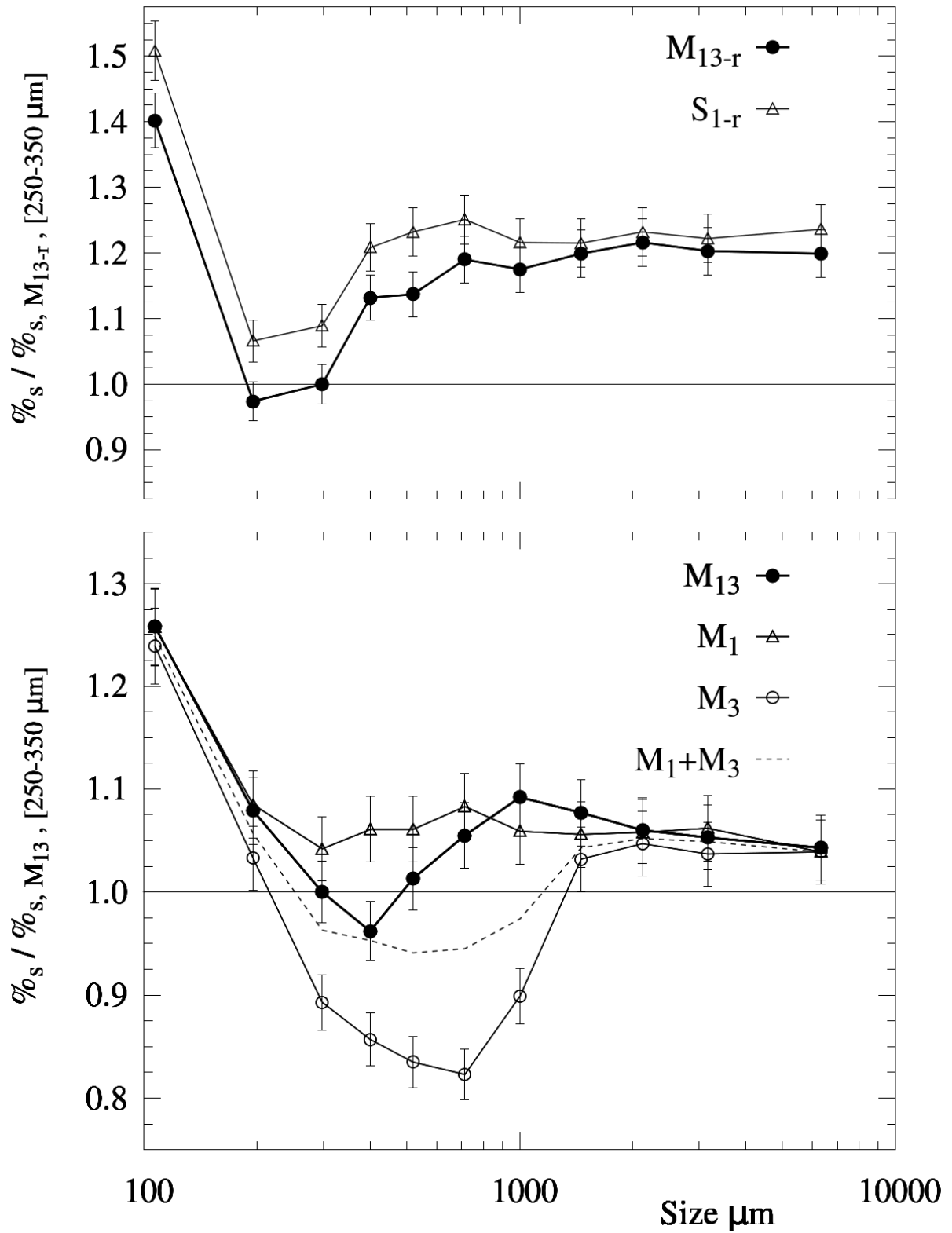


**Figure 24.** Variation of the product surfactant/s content  $X_s$  (top) replicates under heavily build up walls  $M_{13-r}$  and  $M_1$  (bottom) Simultaneous,  $M_{13}$  or independent,  $M_1$  and  $M_3$ , operation of nozzles #1 & #3, and their summation. Ratio of the % in mass versus that of the primary mode fraction in  $M_{13}$  or  $M_{13-r}$ .

This is explained by the lack of aggregation into the primary mode, which now contains more primary particles rich in solids. This becomes clearer in the distribution of  $M_3$ , which shows large differences. In this case, the elutriation shows the same  $X_s$  than in a single nozzle  $S_3$ , but the primary size mode generated shows instead far lower values. There is a clear correlation between the increase of  $X_s$  for the largest sizes and the formation of the plateau in the size distribution in Figures 19 and 20. In contrast, the product obtained in  $M_1$  contains more aggregates and this homogenises the composition. Figure 15 includes a comparison between the surfactant/s observed in  $M_{13}$  and the expectation from the summation of both nozzles  $M_1$  and  $M_3$ . Clearly, in the multi-level system the granules between  $450 - 600 \mu m$  contain higher surfactant/s levels. This confirms the scrubbing effect associated to the top spray. Elutriates are rich in surfactant/s, and as they are captured they increase the  $X_s$  of the granules produced between  $450 - 600 \mu m$ .

## Conclusions

Production of a standard detergent has been characterised using different nozzle locations, configurations and rates, maintaining a common initial median droplet size, between  $275 - 310 \mu m$ .

**a) Operation of single nozzles:** Independent on its location, a single nozzle leads to a product size distribution with a single mode, similar to that in the droplet population, between  $300 - 425 \mu m$ , but comprised largely of aggregates (particle morphology is given in Appendix II). Upper nozzle positions lead to wider distributions and long tails, so  $x_{90}$  range from  $1000 - 7000 \mu m$ . When the nozzle is brought down to regions of high  $T_A$  and  $U_A$  growth diminishes into the mode size range, but in turn a plateau forms  $> 850 \mu m$ . The last is believed to be linked to the re-entrainment from the wall according to the investigation reported in Appendix III. The product is very heterogeneous in respect to its composition. Large granules show a higher  $X_W$  due a lower  $\tau_p$  in the chamber and the contribution of re-entrainment. Small fractions also present a higher content in both water and surfactant/s. This can be explained by the breakage of large particles at the end of bottom end of the unit and by the effect of solid-liquid separation observed during atomization. Heterogeneity increases significantly with decreasing nozzle position and this leads to differences  $> 100\%$  between the surfactant/s content of the mode size fraction and that of elutriates.

A large part of the heat ex-change occurs below the cylindrical region, with a negligible contribution of the levels above the nozzle level and very large heat losses owe to primarily to the air distributor. At the

walls, large initial deposition rates occur only in the projection of the nozzle, decreasing in regions above, where the finest powder migrates to the wall and initiate a downwards flow. This recirculation explains why the rate of elutriation increases as the nozzle is brought up: elutriates are not allowed to pick up the swirl and become captured by the influence of the contraction.

**b) Operation of multiple nozzle levels:** The different drying history experienced by the top and bottom levels in a multi-level system has been linked to the deposition rates in the chamber and the features of the product size distributions. The product shows an extensive particle growth and the generation of two size modes. Despite a very different size distribution, mean sizes remain comparable to a single nozzle operation. However, the powder is more heterogeneous and shows large differences in both the content of water and surfactant/s. Appendix II describes which effect this has in the distribution of porosity.

The contribution of the aggregation occurring at the top and bottom spray regions and through their interaction has been quantified. Growth is inhibited at the bottom and promoted at the top. In twin levels, the generation of the secondary mode owes exclusively to the top spray and accounts for no more than  $\sim 63\%$   $\mu m$  of the mass  $> 600 \mu m$  in the standard conditions described here. Analysis of the elutriation rate, the surfactant/s content and the aggregation patterns demonstrates that the interaction between both sprays is not negligible. It is responsible of at least 6 – 11 % of the mass  $> 600 \mu m$ .

**c) Implications in process operation and unit design:** This is the first report of this sort of data in literature, and has a great relevance in the manufacture of powders in swirl counter-current dryers, which often make use of multiple sprays. In the case of detergents, the unit may now be subdivided in various nozzle regions. This work allows correlation of the aggregation rates to the local heat transfer in each, and quantifies the growth due to their interaction by the capture of elutriated powder. In this way, the data provides here enable validation of numerical models and advancing in the compartmentalization of these towers under some experimental grounds.

It is also important noticing the issues derived from heterogeneous composition observed in product. This affects stability and the product flow ability. It enhances caking, accelerates the degradation of the product and the higher  $X_s$  of the fines increases cohesiveness, impeding the powder to flow easily, which complicates transport and packing operations. Utilising the scrubbing effect of the top sprays in a multi-level system aids to a better homogenisation versus using the bottom nozzles only.



---

## Final Summary, Next Steps

Engineers introduce swirl and counter-current flows in a dryer in order to maximise residence time and the heat and mass transfer. This is beneficial, but requires a large investment in experimentation and eventually the units show very little flexibility because the process is not well understood. The swirl is unstable and it is unclear how it drives particle growth or interactions with the walls. In essence, the design and control must rely on experience. This thesis addresses some of these issues and provides the first comprehensive experimental study on the subject. Numerical models will not be defined at least in the middle and short term, strictly on first principles. One must expect certain experimentation to be carried out at pilot scale, for instance to determine an adjustable parameter in an aggregation kernel (e.g. a Stokes or Tack number characteristic of each formula). However, this work enables engineers to move into a fundamental description of the system and towards models based on a theoretical basis. This will reduce drastically the experiments, permit manufactures to optimise the dryer capacity, energy efficiency and waste production, and facilitate the introduction of new formulas and designs.

This thesis outlines a general numerical frame and the route to be followed to improve models and provide a rigorous experimental validation (Introduction). The current limitations are identified and addressed, namely a) the influence of deposits and friction (Part A), b) the governing role of fouling (Part B1), c) access to experimental correlations of growth to operation conditions, identification of the aggregation sources and the capture of elutriates, and the compartmentalization of the unit (Part B2). Future work must explore the interaction between sprays located in the same level and how their configuration may be optimised. The following sections highlight the main technical recommendations:

### 1. Swirling flows in a confinement with rough walls:

This thesis demonstrates that roughness and the deposits at the walls have a large effect on the fluid dynamics in a swirl dryer. This explains the errors in past models, and the substantial discrepancy between velocity data in laboratories and full scale dryers. Clearly, computational fluid dynamics CFD models must account for the friction. At a first stage, measurements of roughness should be included in the available wall functions. Ali (2014) makes use of the data reported here and argues they can reproduce the flow structure when roughness is low and homogeneous, but fail to predict recirculation, instabilities or turbulence production when deposits are present. Wall functions have serious limitations.

First, they are derived for unidirectional flows, and further research must establish the numerical treatments of the boundary layer in a swirling flow over rough walls. Secondly, wall functions cannot account for steps or bands, which are in essence obstructions comparable to the mesh size. This is inconvenient, but should it be neglected, errors in air velocities or turbulent kinetic energy will be as high as 186 % or 85 % and it will be impossible to predict the vortex breakdown, turbulence production or recirculation. At the moment, it is not feasible to predict simultaneously the flow and how the deposits evolve (i.e. a dynamic coupling between a fouling and a CFD model). Nonetheless deposits are localised in the spray/s regions, and one can make a good guess on thickness based on cleaning procedures, previous production schedules and the location of nozzle/s. Engineers could easily develop a library of wall topologies and perform a list of flow simulations with predefined sets of deposits. This shall provide initial conditions for all remaining models (e.g. dispersion, drying, growth and fouling) in the overall frame (Introduction). Re-computation of the air flow should only be considered if needed. It is important to stress that the particle dynamics is extremely sensitive to the centrifugal inertia of the solids. It determines the concentration close to the wall, elutriation, deposition and re-entrainment of material at the walls and growth. Any model ignoring the friction will be simply unreliable: it will make use of a much stronger swirl than actual, neglect how turbulence is produced and disregard the recirculation of solids.

## **2. Dynamic fouling, clustering and breakage at the walls:**

The most relevant scientific contribution in this thesis is the identification of the dynamics established at the walls. It is at the core of this process. Part of the product results directly from breakage of deposits or through the aggregation of clusters at the wall with material in the air. It was indistinguishable from the rest of the powder because it presented the same size and structure, but it undergoes much higher residence times and dries at the walls for ten to a hundred times longer than expected. These results contradict the assumptions in previous studies which are simply not valid, i.e. solids rebound at the wall, and to a large extent explain why models were not able to explain how the solids dry in the air.

The description of the wall is also vital to understand growth. It is incontrovertible that most of the large particles  $> 850 \mu m$  are generated at the walls, but the observations in Chapter VI and Appendix III suggest similar processes are behind the formation of most aggregates. Despite many particles do not become permanently fixed at the walls, they are still produced from clustering at the walls. The size of the product responds to a balance between the cohesive forces that bind the clusters, which evolve in

time, and the stresses that break them up i.e. aerodynamic forces, gravity, and the impact of other particles. It is essential to understand how this structure forms and breaks. To that effect, this thesis identifies various re-entrainment mechanisms, and correlates them with characteristic time scales and granule sizes. Accordingly, it proposes a complete mechanistic description for a fouling model and provides a sound validation data set. Being able to describe the microstructure at the walls, and how the re-entrainment size responds to the process operation must be the key area of work in the future.

### **3. Standardization, design, control and scale-up criteria:**

The structure of the swirl in full scale dryers is very complex. This work demonstrates that the vortex is easily distorted, oscillates and breaks down depending on the swirl strength. Three possible flow regimes have been identified. A new geometrical design parameter is proposed and used to set new scale-up and standardization criteria that include the prediction of the swirl decay due to friction in any geometry,  $Re$  and wall conditions. Furthermore, engineering modifications are also proposed to manipulate the flow and enhance or suppress the jet and the recirculation zones in any existing tower. This can prove very useful to control residence time, growth or elutriation in different scenarios (e.g. formula, rate, cleaning conditions). These recommendations are very valuable for optimization because they acknowledge for the first time the presence of recirculation and instabilities in these dryers.

Part B and Appendix III clarify how nozzle location and air inlet conditions impact particle growth. Growth can be manipulated by modifying the drying rate in the spray region (Chapter VI) or the concentration and velocity of the solids (Appendix III). In essence, the size appears rather governed by the breakage of clusters at the wall than by aggregation in the air. Operation with high air velocities at low temperature increases concentration, the impacts to the wall and their energy, which reduces the lifetime of clusters and the size they are broken into (Appendix III). In that case more of the heat is lost in the enthalpy exiting within the exhaust air, as opposed to higher temperatures where more heat is lost through the dryer walls. Interestingly, both options are equally efficient. New plants should ensure that the towers can operate at higher air volume rates. This may require new fan designs but would render significant benefits in: a) the ability to control growth by manipulating fouling, b) the potential to increase the energy efficiency if one recovers the enthalpy of the exhaust air, and c) broadening the use of these dryers to other products, perhaps thermal-sensitive powders as the air temperature can get much lower.

#### **4. Applicability into other disciplines of research:**

The method developed to study large vortex flows (Appendix I) and the study in confinements with rough walls (i.e. how the swirl decay transfers energy into the turbulence) is applicable to other devices prone to deposition (e.g. cyclones) or benefiting from a strong turbulence (e.g. combustors). In addition, the study of dynamic fouling and the methods described here are directly relevant for other dryers and many devices in the particle technology industry, in addition to fields subject to significant fouling, such as membranes, burners, heat exchangers or oil transport facilities, where there is a long standing debate on whether wall deposition is suppressed in time or balanced by the re-entrainment of material.





# APPENDIXES

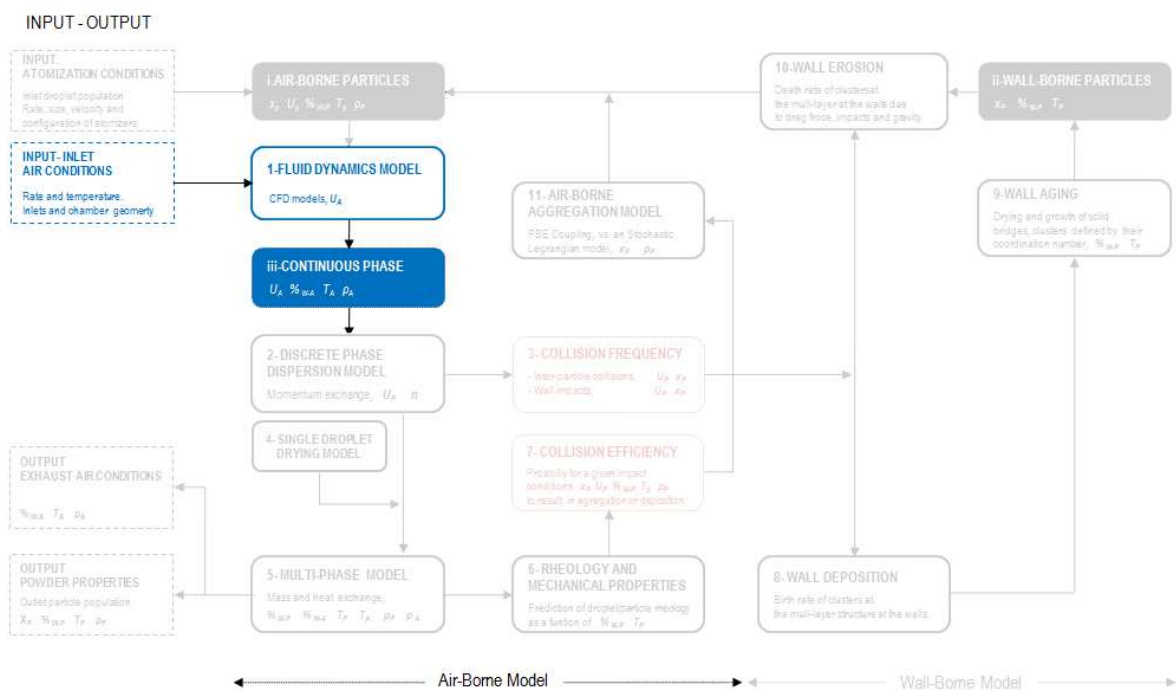
Víctor Francia García

A thesis submitted to the University of Birmingham  
for the degree of Doctor of Engineering, EngD

School of Chemical Engineering  
College of Engineering and Physical Sciences  
University of Birmingham, Birmingham, UK  
September 2014

# APPENDIX I

## THE USE OF SONIC ANEMOMETRY TO STUDY LARGE CONFINED TURBULENT SWIRLING FLOWS.



## Summary

In the particle technology units such as cyclones or spray dryers rely upon complex air swirling fluid dynamics. Laser optics can characterise in detail the flow in confined units at a laboratory or pilot scale facilities but fail to be economical in industry. Data on actual production dryers are scarce, and often fragmented or limited to a qualitative analysis. This work addresses these limitations by introducing sonic anemometry to study confined swirling flows in large industrial units ( $> 100 - 1000 m^3$ ).

A general method is outlined for the application of 3D sonic anemometers to the cylindrical chamber of dryers or cyclones. It includes the appropriate corrections to the signal and a detailed report of the uncertainty. The method developed retains enough detail to facilitate validation for numerical models whilst it is flexible and economical to apply in industry. Compromises need to be made in such context and accuracy in the data is slightly lower than in the conventional uses of anemometry or in laser diagnostics methods. However, they constitute a great advancement versus the usual alternatives in industry, as visualization techniques, cup-and-bowl or hot-wires anemometers or Pitot tubes.

The sources of uncertainty are quantified in relation to 1- time averaging and the presence of large time scale oscillation in the flow, 2- the local aerodynamic disruption and the impact of turbulence and shortcomings in the definition of attack angles, 3- the disruption to the overall vortex development, 4- the use of calibration functions and 5- the potential shift of the sonic pulse. Air velocity fields and turbulence statistics are gathered within reasonable error limits for an engineering application ( $< 1 - 4 \%$  in the velocity magnitude,  $\pm 3^\circ$  in direction and  $\pm 7 - 31 \%$  in turbulent kinetic energy).

The data provided in the Part A of this thesis shows the potential of this technique to be applied in a range of industries and scales. Benefiting from accessing full scale data is the only way to reveal some of the features linked to production. As discussed in Chapters II and III in the research of counter-current spray dryers they include a pronounced decay of the swirling motion due to friction at the walls, a large increase in the turbulent kinetic energy and aerodynamic instabilities.

## 1. Introduction

Strong air swirling flows are complex to scale. This is particularly the case of tall-form dryers, which lack dynamic similarity and show strong dependency between particle density and temperature history (Kemp and Oakley 2002). This makes them one of the most complex unit operations to scale-up (Oakley 1994 or Masters 1995). Their design relies heavily on the experience of manufacturers and the use of numerical fluid dynamics models, which often lack validation at full scale. This is not surprising when one considers that many of the characteristics inherent to production are hard to replicate in a prototype facility: amongst others (a) the range of designs seen in industry, particularly inlet air nozzles and exhaust lines, (b) the range of  $Re$  and thus comparable aerodynamic instabilities at a strong swirl, and (d) comparable wall deposits, and thus friction. To address these issues, it is fundamental to be able to obtain comprehensive and reliable air velocity data at production scales.

This work proposes to apply sonic anemometry to study large industrial confinements in an accurate but simple manner. It targets a high enough level of detail for design purposes and to conduct full scale validations of numerical models, whilst still being affordable. Section 2 details the instrumentation, the methodology and the transformations required in a large swirl counter-current spray drying tower. Section 3 quantifies the sources of error. This work facilitates the studies to reach a large scope (see Part A), far beyond the possibilities of any optical technique in dryers where the unit diameter and height measure in meters and tens of meters (i.e. total volume  $100 - 1000 m^3$  depending on scale). The data are gathered with far simpler experimental arrangement and requires low shut-down times (i.e.  $\sim 5 min$  per location) and simple engineering modifications to both, the unit and the instrumentation. The following sections 1.1 and 1.2 discuss briefly the limitations of laser-based techniques in this context and advantages of anemometry given by the review of the more common applications.

### 1.1. Applicability of laser-based techniques

Laser Doppler Anemometry,  $LDA$ , or Particle Image Velocimetry,  $PIV$ , are examples of laser techniques used for the characterization of air swirling turbulent flows. They function by measuring the velocity of inertia-less particles under an optical arrangement. Unfortunately, their high accuracy affords a delicate set up and application to confined spaces needs to focus primarily in scaled down equipments designed *ad hoc*. These ensure an easy manipulation of the optics and pose no restriction to the experimentation time (e.g. Sommerfeld and Qui, 1991). A similar arrangement in full scale is far more

challenging, even in the absence of particles and with ambient air. It is often impossible due to the dimensions, or simply too expensive. It carries three main issues: 1- costs derived from engineering modifications to provide clear paths into the unit and ensure the equipment withstand the production conditions, 2- the disruption caused by complex optical arrangements whenever it cannot be avoided to place components inside (Hassall 2011), and most importantly 3- opportunity costs associated to shut down production units: these become unaffordable to accommodate the use of laser arrangements for they require a more time consuming set up and safety protocols.

As a result, available air velocity data in large swirling flows is very restricted. In large tall-form spray dryers it is reduced to small sections (Hassall, 2011), unidirectional measurements with mechanical or hot-wire anemometers (e.g. Fieg *et al.* 1994) or a qualitative description (Sharma 1990 or Wawrzyniak *et al.* 2012). It is when moving into smaller research of pilot scale facilities that a more controlled environment allows one to apply laser based devices (Bayly *et al.* 2004), but even then a reasonably large scope only rarely become available (e.g. Zbicinski and Piatkowski 2009). Under these restrictions it is not possible to conduct a reliable full scale validation or study effects linked to production designs.

## **1.2. Use of sonic anemometry**

Sonic anemometers rely upon measuring the shift in the velocity of a sound wave when it propagates through a moving medium. A measurement of the time-of-flight between two transducers suffices to derive the velocity of the medium (Probst and Cardenas 2010), independently on the sound velocity itself (hence the medium temperature or composition). On this basis, many commercially available instruments gather air velocity magnitude and direction making use of two or three independent pairs of transducers, which act alternatively as emitters and receivers of a sonic pulse. This allows the estimation of the air velocity component along each of the anemometer axis (Gill Instruments 2004). Sonic anemometry is long established, in particular in relation to the measurement wind patterns (e.g. Kaimal 1990). It has been used for decades in meteorology providing a robust and reliable method to map large scale wind fields. It is common in many applications ranging from the validation of fluid dynamics geomorphologic models (e.g. Mestayer *et al.* 2005 or Jackson *et al.* 2011) to the characterization of meteorological phenomena (e.g. Cao *et al.* 2009), and widely used for the study of the atmospheric turbulence (Druilhet and Durand 1997; Andreas *et al.* 1998 or Katurji *et al.* 2011), in particular the turbulent boundary layer and the issue of the closure of the energy balance (Oncley *et al.* 2007; Mauder *et al.* 2007).

In these fields, wind speed, direction and fluctuations, are measured simultaneously at fixed locations, for instance over a given terrain. One or two dimensional instruments often suffice for the study of speed if they are properly aligned; however, 3D anemometers are also available for a full resolution (e.g. Walker *et al.* 2009). In this context, three different pairs of transducers are fixed to a mounting device, which is usually placed in an open field and aligned according to the wind direction. The instrument then measures directly in the so called natural coordinates: longitudinal (along the wind streamline) and transversal and vertical directions (i.e. orthogonal with reference to the mean direction). In this situation the velocity fluctuations may be measured directly without the need of axes transformations.

Compared to cup-and-bowl or vane instruments, sonic anemometers have many advantages as the absence of moving parts and high measurement frequencies or simple arrangements. They permit the resolution of turbulence at reasonable time scales and are common for the conduction of eddy covariance analysis in the atmospheric boundary layer where measurements are taken over days, weeks or months at frequencies up to 50 Hz. In conjunction with species concentration, detailed analysis of turbulence allows estimation of fluxes of gasses to the atmosphere. It is in this context and the application to aeronautics where they have gained relevance, for instance in setting standards for the estimation of axial fluxes of greenhouse effect gases (Goulde *et al.* 1996; Aubinet *et al.* 2000; Berger *et al.* 2001 or Hendriks *et al.* 2008). Their implementation in an industrial environment takes advantage of robust instruments, designed to withstand harsh conditions in meteorological and/or marine outdoors facilities. It provides accurate measurements of air velocity magnitude, (also denoted as speed), and direction at frequencies that, although below the capabilities of laser-based optical diagnostic methods, still render a satisfactory resolution of turbulence in most engineering applications.

## **2. Application to a large confined vortex.**

### **2.1. Operation of the units.**

Three industrial counter-current spray drying towers property of Procter & Gamble have been studied (Part A, Chapter I). The overall design and location of the accesses in Scale I are included in Figure 1 for the benefit of the reader. At all times the air is operated at ambient conditions and in the absence of particles. In all cases, the velocity of inlet and exhaust air fans is set making use of *PID* control systems to obtain a target air mass rate and exit pressure. After this, *PID* loops are disconnected and all systems are handled manually to avoid variations in the rate. The effect of time averaging is

discussed in Section 3.2 and the local disruption of the instrument in Section 3.3.1. Both discuss a series of measurements conducted at three fixed radial locations in the cylindrical chamber of Scale I (2.2 D in Figure 1) at a Reynolds number  $Re \sim 1.5 \cdot 10^5$ . The remaining sections compare a selection of the data obtained in Scales I and II at various axial levels.

## 2.2. Instrumentation and Methodology

### 2.2.1 Sonic anemometer.

A commercial research instrument, H50 (Horizontal Symmetry 50 Sonic Solent Anemometer, Gill Instruments Ltd) was used for all measurements. It is comprised of a single metal frame axis and three independent pairs of ultrasonic transducers. These are mounted in a single fork-like head frame, depicted in Figure 2. This particular design minimizes the disruption caused by the head when the flow is orientated axially (up/down in Figures 2a and 2c). The orientation of the mean air flow to the instrument is known as the attack angle. It determines the local disruption that the transducers and the head cause upon the flow field. It is usually defined by the attack angles to the instrument horizontal plane,  $\delta$ , and to the frame axis,  $\lambda$ , shown in Figure 2a and defined below (Gill Instruments 2004).

$$\delta = \cos^{-1} \left( \frac{\sqrt{\bar{U}_{a_2}^2 + \bar{U}_{a_3}^2}}{\sqrt{\bar{U}_{a_1}^2 + \bar{U}_{a_2}^2 + \bar{U}_{a_3}^2}} \right) \quad (1)$$

$$\lambda = \cos^{-1} \left( \frac{\bar{U}_{a_2}}{\sqrt{\bar{U}_{a_2}^2 + \bar{U}_{a_3}^2}} \right) \quad (2)$$

Each anemometer is designed and calibrated to provide accurate measurements within a given range of  $\delta$  and  $\lambda$ . Manufacturers establish the accuracy in a wind tunnel calibration; in this case it is reported as 1% *RMS* in the velocity magnitude and 1° in direction as long as the attack angles are maintained within: a)  $\lambda > 30^\circ$ : this ensures the flow does not attack the instrument from the back, otherwise the frame and the head block the flow into the measurement region (the paths between the sonic transducers), and b)  $\delta < 50^\circ$ , what avoids that the transducers themselves aligning against the flow. A more detailed analysis of the disruption owed to the transducers is given in Section 3.3.1, suggests the definition of  $\delta$  is incomplete and only valid to set maximum limits.

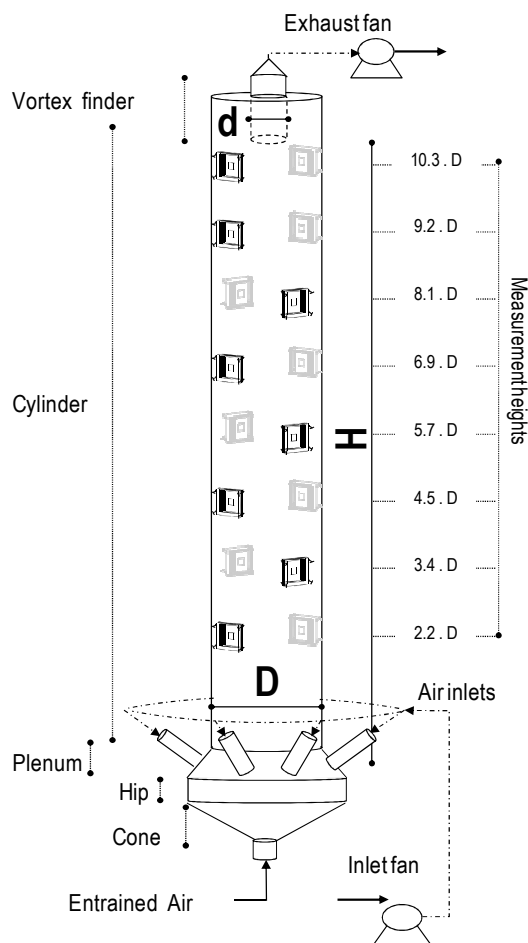


**Figure 1.** General outline of the air system in a tall-form swirl dryer. The illustration corresponds to Scale I, for further details on the coordinates of the inspection doors and the characteristics of Scale II see Chapter I.

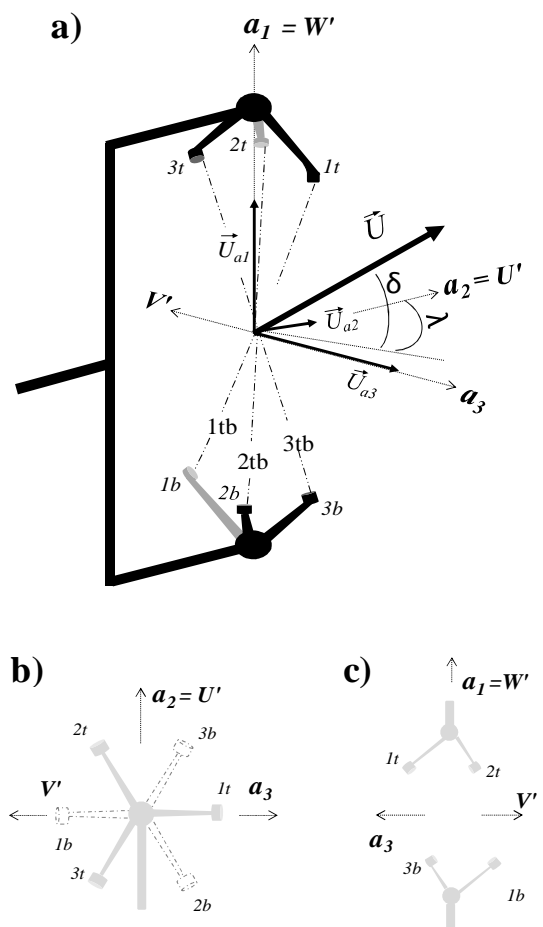


**Figure 2.** Anemometer nomenclature. Spar measurement axis,  $W', U', V'$ , and the frame of reference  $a_1, a_2, a_3$  for an anticlockwise air vortex. Attack angles,  $\delta, \lambda$ . a) provides a perspective view (transducers and frames not to scale). a) and b) provide views to scale from top and front (Gill Instruments, 2004).

### 2.2.2. Location and orientation of the sonic path.

The fork-like head has been placed at various radial, axial and tangential coordinates in the cylindrical chamber of the dryers. To do this, the anemometer was fixed to a unit door engineered *ad hoc* to be re-assembled around its frame. Figure 3a depicts the ensemble and defines the frames of reference taken for the anemometer and the cylinder, and the various alignments. At the back end of the frame a connexion unit connects the anemometer to an electronics unit, *EU*, and from there to the Power and Communications Interface, *PCI*, which is connected to a computer laptop by an *R – 232* data cable. The standard software *Wind-Com* provided by the manufacturer (Gill Instruments Ltd) was used to synchronise the instrument and report the velocity measurements. The default spar measurement axes defined ( $W', U', V'$ ) shown in figure 2a were selected (Gill Instruments 2004). An equivalent frame of

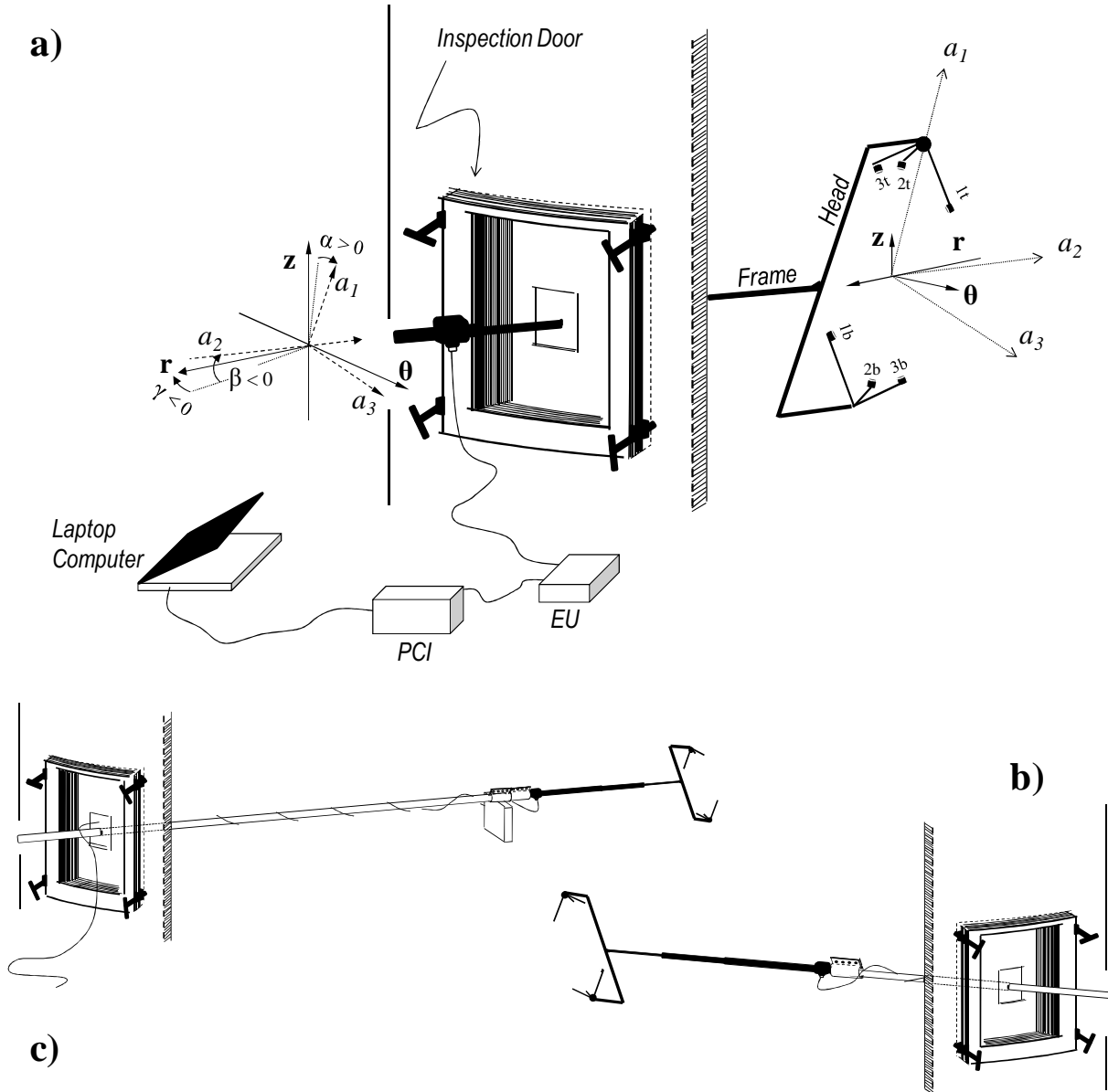


**Figure 3.** a) Depiction of the ensemble and connexions, and definition of the frame of reference of the cylinder,  $(rz\theta)$ , the anemometer measurement axes,  $(a_1a_2a_3)$ , and the alignments,  $\alpha, \beta, \gamma$ . (b) and (c) Illustration of the use of a back extension (b) and (c). Drawings not to scale.

reference has been defined in Figure 2a by  $a_1, a_2, a_3$  changing the positive sense of  $V'$  to the sense of rotation of the flow in the cylinder. Figure 2a depicts both frames of reference when the vortex in the tower rotates in anticlockwise direction and Figure 3a shows the comparison to the polar coordinates of the unit. In the standard method, all measurements were taken with the use of the calibration and at measurement frequency of  $50\text{ Hz}$  (with the exception of Case C, Chapter III,  $20\text{ Hz}$ ).

The mounting door aligns the frame, axis  $a_2$ , with the perpendicular to the door. The head is positioned at the target distance from the wall,  $x$ , by sliding the frame inside while twisting its orientation to align

the axis  $a_1$  to the cylinder vertical axis  $z$ . The orientation of the instrument was measured by an in-built inclinometer and recorded manually. Figure 3a shows the alignment left / right, denoted  $\alpha$ , (i.e. the rotation of the plane  $a_1 - a_3$  over the frame  $a_2$ ) and up / down, denoted  $\beta$  (i.e. the angle between the frame and the horizontal plane). In the standard method both are kept below  $\pm 2^\circ$ .

The alignment of the ensemble in figure 3a needs consideration. In a large scale it is important to account for building tolerances, the orientation of the entry point and the adjustment of the mechanical fittings. It is common that the door is misaligned with the inner wall, which translates into a deviation between  $a_2$  and the true radial direction,  $r$ , denoted  $\gamma$ . Failing to account for it leads to an error in the radial position, wider as measurements are taken closer to the centre. It has no impact in the measurement of the velocity magnitude but it affects the direction, causing an artificial transfer between the tangential and radial components and errors as high as 100 % for locations close to the centre. This artefact has been addressed by applying a correction based on the actual  $\gamma$ .

Measurements have been taken during 60 s. The ensemble in Figure 3 was dismantled and moved from one to another axial location, while the air flow targets were readjusted. In Scales II and III, (Chapter III) all measurements could be covered from 1 – 2 days. But in Scale I (Chapter II) measurements covered periods expanding from days to several weeks to adapt to the availability of the unit. As a result, certain variability in the fan settings was observed and attributed to a different pressure drops in the air ducts due powder deposits in chutes, fans, cyclones and critically, the tower exit conduit (i.e. not at the walls for these are kept constant, Chapter III). The variations in the velocity of the air fans appeared normally distributed and uncorrelated to any process variable or to the errors observed.

An extension bar may be fitted to the back end in order to access distances inside the tower larger than the anemometer frame (Figure 3b; in few cases for the largest scales the *EU* is placed inside, aligned with the swirl to minimise drag, Figure 3c). Measurements are always taken with and without the extension to ensure no differences appear in the profiles. Section 3.3.2 assess the impact in the vortex structure by the comparison of selected data in Scale I and II when the anemometer was inserted up to the centre of the cylinder and beyond (i.e. to the opposite side of the wall).

### 2.2.3. Corrections and transformations.

Transformations are needed to express the position of the sonic path centre and the velocity components in the polar coordinates of the cylinder. The position of the measurement is related in (6) to

the position and alignment of the ensemble. The latter is estimated by measuring manually the offset between the radial direction  $r$  and the projection of the orthogonal to the door in the plane  $r - \theta$ , denoted  $\Delta_y$ , and depicted in Figure 4. Subsequent offsets can be defined in  $x$  and  $\theta$ , denoted  $\Delta_x$  and  $\Delta_\theta$  and given in (3) and (4).

$$\Delta_x = \sqrt{R^2 - \Delta_y^2} - x^* \cdot \cos \beta \quad (3) \quad \Delta_\theta = \sin^{-1} \left( \frac{\Delta_y}{r} \right) \quad (4)$$

Whenever  $\Delta_y \neq 0$ , a gyration angle, denoted  $\gamma$ , is required to align the axis 2 and 3 in Figure 4 with the true  $r$  and  $\theta$ . Depending upon the position of the centre,  $\gamma$  reads

$$\gamma = \begin{cases} \Delta_\theta & \text{for } \Delta_x > 0 \\ \pi - \Delta_\theta & \text{for } \Delta_x < 0 \end{cases} \quad (5)$$

The position in cylindrical coordinates  $r, z, \theta$  is expressed in (6) as function of the position of the door  $\theta^*$  and  $z^*$  and the distance of the head into the cylinder  $x^*$ .

$$\begin{bmatrix} r \\ z \\ \theta \end{bmatrix} = \begin{bmatrix} \sqrt{\Delta_x^2 + \Delta_y^2} \\ z^* + x^* \cdot \sin \beta \\ \theta^* + \gamma \end{bmatrix} \quad (6)$$

The following transformations are used to express the velocity data measured along the spar axes  $W', U', V'$  and the reference axes  $a_1, a_2, a_3$  into the polar frame of the cylinder, denoted  $r, z, \theta$ .

$$\begin{bmatrix} u_{a_1} \\ u_{a_2} \\ u_{a_3} \end{bmatrix} = [W' \quad U' \quad V'] \cdot G_0 \quad (7) \quad \begin{bmatrix} u_z \\ u_r \\ u_\theta \end{bmatrix} = [u_{a_1} \quad u_{a_2} \quad u_{a_3}] \cdot G_1 \cdot G_2 \cdot G_3 \quad (8)$$

where  $G_i$  are functions of the instrument alignment:

$$G_0 = \begin{bmatrix} 1 & 0 & 0 \\ 0 & 1 & 0 \\ 0 & 0 & S \end{bmatrix} \quad (9) \quad G_1 = \begin{bmatrix} \cos \alpha & 0 & \sin \alpha \\ 0 & 1 & 0 \\ -\sin \alpha & 0 & \cos \alpha \end{bmatrix} \quad (10)$$

$$G_2 = \begin{bmatrix} \cos \beta & -\sin \beta & 0 \\ \sin \beta & \cos \beta & 0 \\ 0 & 0 & 1 \end{bmatrix} \quad (11) \quad G_3 = \begin{bmatrix} 1 & 0 & 0 \\ 0 & -\cos \gamma & \sin \gamma \\ 0 & \sin \gamma & \cos \gamma \end{bmatrix} \quad (12)$$

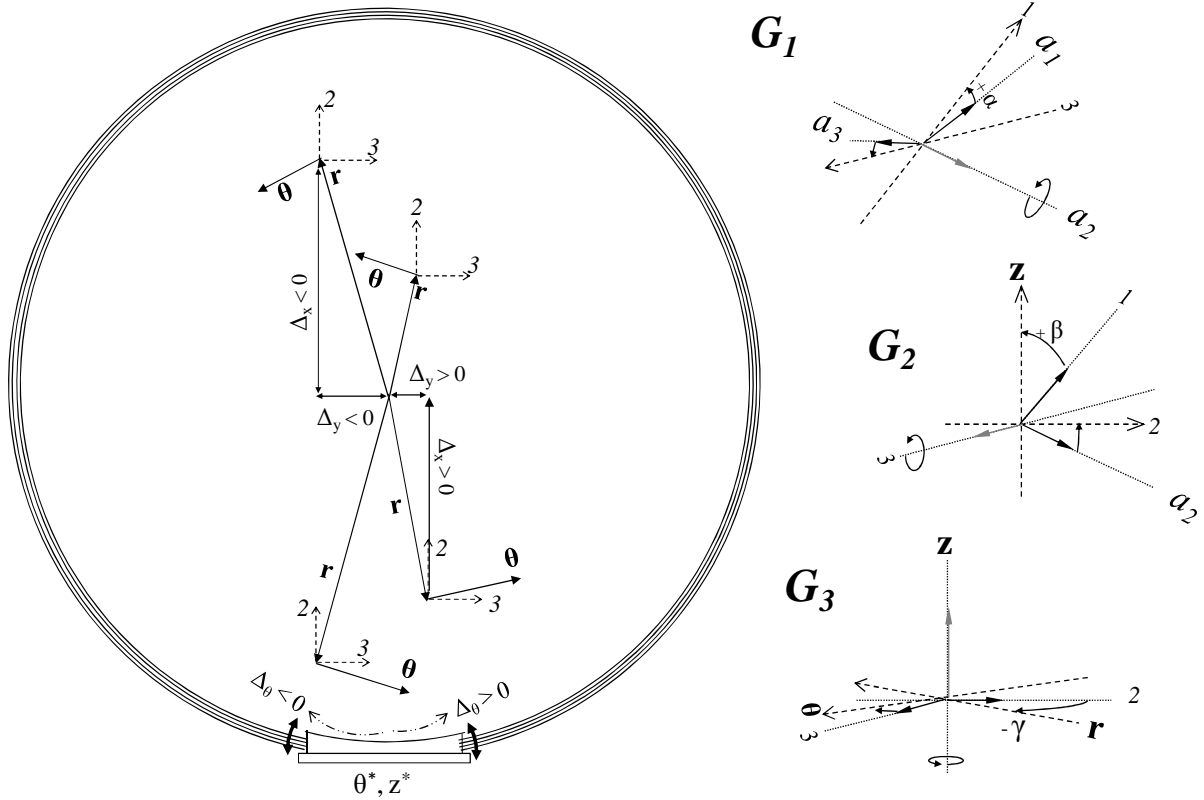


**Figure 4.** Description of the position and misalignment of the ensemble in the horizontal plane. Transformations between the anemometer reference frame to the true polar coordinates.

$G_0$  sets the reference axes in (7) by setting the positive direction of  $a_3$  with the sense of rotation of the flow, where  $S$  reads -1 or 1 for an anticlockwise or clockwise vortex. The first and second terms in (8) correct the alignment of the head with a first gyration over the frame axis  $a_2$  in  $G_1$ , and a second in  $G_2$  over the perpendicular to the anemometer plane (axis 3 in Figure 4). In this manner, one axis aligns with  $z$  while the remaining (2 and 3) are contained in the horizontal plane  $r - \theta$ . The third term  $G_3$  accounts for the actual orientation of the ensemble. A gyration over  $z$  aligns both axes in the horizontal plane to the polar axes  $r$  and  $\theta$ , setting the positive sense of the radial direction outwards.

### 3. Error analysis.

#### 3.1. Sources of uncertainty.

Sonic techniques benefit from decades of research and the sources of error associated to the anemometry have been studied in detail (e.g. Cuerva and Sanchez-Andres 2000, Probst and Cardenas 2010). Some are directly related to the specific design of the head (e.g. Wieser *et al.* 2001 or Cuerva *et al.* 2003), the operation methodology or the analysis and correction procedures applied to the signal (e.g. Wilczaki *et al.* 2001). In general terms, they can be minimized by an adequate selection of the

instrumentation (e.g. Kaimal *et al.* 1990), the experimental set up (e.g. Walker 2005) and the use of post processing algorithms (e.g. Van der Molen *et al.* 2004 or Nakai *et al.* 2006). Others respond to short-coming assumptions in the working principle of commercial instruments. Velocity gradients and the curvature in three dimensional velocity fields cause the trajectory of the sonic pulse to deviate from a linear path, what introduces errors itself dependent on the characteristics of the velocity field to be measured (Franchini *et al.* 2007a). This requires quantification.

The method described deviates significantly from the traditional uses and thus it renders higher errors when compared to similar studies in terms of the technique (e.g. in situ calibrations by Hogstrom and Smedman 2004) or the unit (e.g. *LDA* in laboratory dryers by Bayly *et al.* 2004), but still represents a large improvement versus the available alternatives to measure air velocity at full scale industrial units.

### **3.2. Large time scale variability.**

Averaged over a sufficiently long time, one sees no variations in the statistics of a turbulent flow. However, when dealing with a production unit it is not always practical to take measurements at each position for a long period. That can make the measurements unaffordable because it incurs in high costs derive of shutting down industrial units. In practise, measurement time has been limited to 60 s to preserve flexibility. This allowed covering many positions in a large geometry, but in turn it makes the mean air velocity to include fluctuations at a larger scale than the averaging time. The contribution of large time scale oscillations is taken as an uncertainty in this measurement. It has been characterised by the comparison of series of 30 consecutive measurements of 60 s. Table 1 includes the statistics observed at two positions where the low attack angles warranties a minimum disruption to the flow. They cover the range of interest of the turbulent kinetic energy,  $\kappa$ . The uncertainty in velocity magnitude and direction complies with the report by the manufacturer for lowest  $\kappa$  (Table 1, left), however, at the high end it rises to  $\pm 3 \% U$  (Table 1, right). In  $\kappa$  the uncertainty in lays within  $\pm 7 - 12$ .

### **3.3. Aerodynamic disruption.**

#### **3.3.1. Local aerodynamic disruption.**

The instrumentation parts, transducers and frames in Figures 2 and 3 constitute an obstruction and disrupt the flow. The limits set for the mean attack angles  $\delta$  and  $\lambda$  and the use of the calibration aim at minimising this effect. Several considerations should be made in relation to the how the turbulence, and high attack angles but within the limits, can affect the measurement.

**Table 1.** Uncertainty in steady state at a fixed location under calibrated mode.  $\Delta = X_{60s} - X_{30min}$  shows the error between time averages in 60s and 30min.  $\Delta_{Range}$ ,  $\Delta_{Max}$ ,  $\Delta_{Min}$  and  $\sigma_{\Delta}$  denote the range, and maximum, minimum and standard deviation. Left:  $\kappa = 0.092 \bar{U}_{av}^2$ ; Right:  $\kappa = 0.144 \bar{U}_{av}^2$ .

Variable $X$	$X_{30min}$	$\sigma_{\Delta}$	$\Delta_{Range}$	$\Delta_{Max}$	$\Delta_{Min}$	$X_{30min}$	$\sigma_{\Delta}$	$\Delta_{Range}$	$\Delta_{Max}$	$\Delta_{Min}$
° $\delta$	13.1	0.3	0.9	0.5	-0.4	6.1	0.3	1.2	0.5	-0.8
° $\lambda$	94.6	0.2	1.1	0.6	-0.5	92.2	0.3	1.4	0.7	-0.7
$10^2 \cdot \bar{U} / \bar{U}_E$	100.0	0.4	1.7	0.6	-1.1	100.0	1.2	5.9	3.3	-2.6
$10^2 \cdot \bar{U}_z / \bar{U}_E$	22.7	0.4	1.5	0.8	-0.7	10.6	0.5	2.2	0.9	-1.3
$10^2 \cdot \bar{U}_{\theta} / \bar{U}_E$	97.1	0.4	1.8	0.6	-1.2	99.4	1.2	5.9	3.2	-2.6
$10^2 \cdot \bar{U}_r / \bar{U}_E$	7.8	0.4	1.9	1.0	-0.9	3.9	0.6	2.4	1.2	-1.2
$10^2 \cdot \kappa / \bar{U}_{av}^2$	9.2	0.5	1.9	1.1	-0.7	14.4	0.5	2.0	1.0	-1.0
$10^2 \cdot \overline{u_z u_z} / \bar{U}_{av}^2$	7.3	0.6	2.4	1.5	-0.9	10.1	0.5	1.9	0.8	-1.1
$10^2 \cdot \overline{u_{\theta} u_{\theta}} / \bar{U}_{av}^2$	4.8	0.3	1.1	0.7	-0.4	9.5	0.5	2.4	1.3	-1.1
$10^2 \cdot \overline{u_r u_r} / \bar{U}_{av}^2$	6.4	0.4	1.4	1.0	-0.4	9.3	0.4	1.6	0.7	-0.9
$10^2 \cdot \overline{u_r u_{\theta}} / \bar{U}_{av}^2$	-0.1	0.2	0.6	0.3	-0.3	-0.7	0.3	1.1	0.5	-0.6
$10^2 \cdot \overline{u_r u_z} / \bar{U}_{av}^2$	-1.8	0.2	1.1	0.5	-0.5	-1.4	0.3	1.3	0.6	-0.7
$10^2 \cdot \overline{u_z u_{\theta}} / \bar{U}_{av}^2$	2.1	0.1	0.6	0.3	-0.3	-0.8	0.3	1.4	0.6	-0.8

A mean attack angle does not account for the effect of the variability owed to turbulence (Nakai and Shimoyama 2011). As fluctuations increase, the flow attacks the instrument at a wider range of directions and thus it seems reasonable to try relating the disruption to the statistics of the attack angles (e.g. Gash and Dolman 2003). In the traditional applications this effect is less important because the instrument is re-aligned according to the mean flow (i.e. natural wind coordinates). In this way, the mean  $\delta$  is low and the deviations owing to turbulence can be absorbed without falling beyond the limit angles.

The use of these anemometers in a confined unit is a totally different case. It is not practical to realign the anemometer at all times to work in the least disruptive position. In this method, the anemometer is set at a fixed orientation versus the cylindrical chamber ( $a_1$  is aligned with  $z$ ). This means that when it is moved from one to another location, the change in air field translates in a change in the attack angles  $\delta$  and  $\lambda$ . These are in general far from the optimum ( $\delta = 0^\circ$  and  $\lambda = 90^\circ$ ). They show a mean value due to the mean air direction and a variance due to its turbulence. In zones of the dryer where the axial velocity ( $U_{a_1} = U_z$ ) is comparable to the swirl ( $U_{a_3} = U_{\theta}$ ) the angle  $\delta$  becomes close to the limit,  $50^\circ$ . The limits for  $\lambda$  are much less restrictive. For the most part, the vortex show low radial velocities and  $\lambda \sim 90^\circ$ . Only in regions close to the top contraction or at the core  $\lambda$  falls  $< 30^\circ$ .

In this ranges, a wind tunnel calibration cannot be considered *a priori* an adequate estimate of the error. The effect due to allowing large mean attack angles and large turbulence levels has been quantified independently. The estimation of the error ranges is given in section 3.3.1.1 and a critical analysis of the current definition of  $\delta$  is given in section 3.3.1.2.

### 3.3.1.1. Revolution of the anemometer head.

This section studies how the error evolves when one moves the anemometer in the cylinder, but performing measurements in a fix point. The instrument has been placed at a location in the dryer where the flow is mainly tangential, and then the alignment of the head  $\alpha$  has been modified to cause a rise in  $\delta$ . The air velocity is measured at the best conditions ( $a_1$  aligned with  $z$ ) and then one observes how it varies when the head revolves. Figure 5 illustrates this case. Twisting the anemometer frame aligns the transducers against the mean flow, which increases  $U_{a_1}$  and  $\delta$ . In this position, drag starts to disrupt the measurement region, which now lies behind the transducers. This section reports the measurement during the revolution and correlates the errors to the usual definition of the attack angles. Section 3.3.1.2 then discusses the effect of the transducers position and reports the uncertainty limits. The relevant range of turbulence is considered by conducting the revolution at three different locations. Figures 6 show an illustration of the full revolution. The head frame  $a_1$  is initially aligned with the tower vertical axis,  $z$ , so that the velocity components in polar coordinates ( $U_r U_z U_\theta$ ) are equivalent to

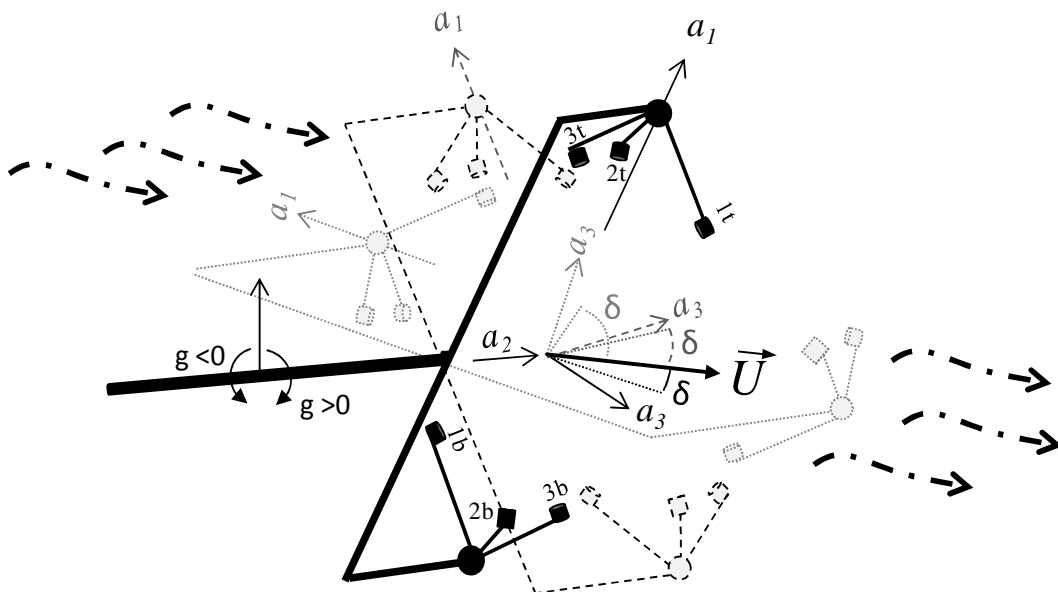


**Figure 5.** Illustration of the anemometer rotation twisting the frame in a tangential flow (left to right). Increment of the attack angle to the horizontal plane,  $\delta$ , as the transducers are aligned against the mean flow. Transducers and frames not to scale.

those in the anemometer frame of reference ( $U_{a_1} U_{a_2} U_{a_3}$ ). The head then rotates over  $a_2$  and measurements are taken in calibrated and un-calibrated mode at 50 rotation angles, denoted  $g$ . This notation is used to distinguish  $g$  from the general method, but note that  $g$  is equal to  $\alpha$  in Figure 3.

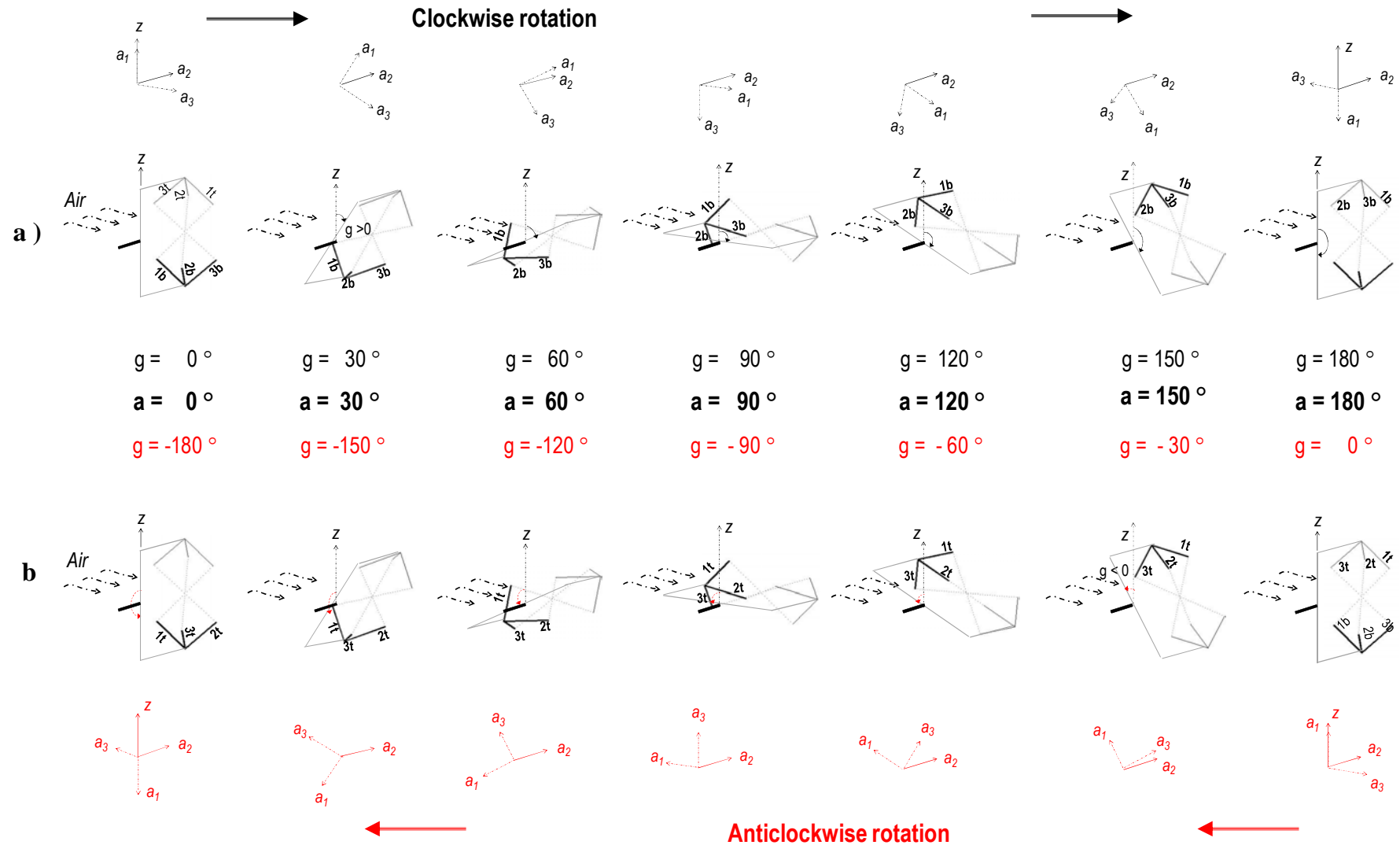
An entire revolution is covered by performing two separate half revolutions in clockwise ( $g > 0^\circ$ ) and anticlockwise ( $g < 0^\circ$ ) directions, illustrated in Figures 6a and 6b. As the head revolves  $a_2$  remains aligned with the radial direction  $r$  and only  $a_1$  and  $a_3$  change. It is important noticing how due the transducers disposition, the position obtained for the same  $g$  in clockwise or anticlockwise sense differs (e.g. compare  $g = 60^\circ$  and  $g = -60^\circ$  in figure 6). The same position is obtained when one rotates the head a given angle  $g$  in anticlockwise direction or an angle  $a = g + 180^\circ$  clockwise, with the only difference of top and bottom transducers being interchanged and pair 2 taking position of pair 3 (e.g. see how the same position is reached moving from left to the right in Figure 6a up to  $g = 150^\circ$ , or from the right to the left in 6b up to  $g = -30^\circ$ ). In this way, two sets of equivalent positions are defined in each half revolution: one corresponds to  $g > 0^\circ$ ,  $a = g$  and the bottom transducers are upstream (Figure 6a), and another corresponds to  $g < 0^\circ$ ,  $a = g + 180^\circ$  and the top transducers are upstream (Figure 6b).

Figure 7 shows the projection of the transducers along the mean air direction, for different positions and attack angles  $\delta$  and  $\lambda$ . It shows how the area exposed to drag differs for the same  $\delta$  and  $\lambda$  in each case, depending on whether the top or the bottom sets are upstream. This leads to three dimensional effects in the error, which is discussed further in the section 3.3.1.2.

The best estimate of velocity, direction and all turbulence statistics is obtained from an average of the measurements that minimize all error sources (i.e.  $\delta < 5^\circ$   $g \sim 0^\circ$ ). Figures 8 to 13 presents how these values, denoted by an  $E$  subscript, are expected to evolve during the revolution for the three different positions considered, where  $\kappa/\bar{U}_{av}^2$  varies from 0.061 to 0.090 and 0.333. Figures 8, 9 and 10 show the evolution of the measurement of  $U$ ,  $\delta$ ,  $\lambda$  and the velocity components, including the raw measurements and those under the use of the calibration (denoted respectively with  $O$  and  $C$ ).

All positions show the same general trend. The revolution commences at  $g = 0^\circ$  showing a low  $\delta$  ( $\delta_{90h}$  denotes the 90<sup>th</sup> percentile of  $\delta$  attack angle). As the head revolves (anticlockwise for  $g < 0^\circ$  or clockwise for  $g > 0^\circ$ ) the transducers start to disrupt the flow and large errors appear. The measurement shows a clear deficit in the velocity magnitude,  $\bar{U}_C - \bar{U}_E$  (see Figure 8a) and as

**Figure 6.** Head revolution in a tangential flow. Position and anemometer frame of reference for rotation angles,  $g$ , in clockwise direction in (a) moving from left to right, and anticlockwise direction, in (b) moving from right to left. Both half revolutions show the same position for angles  $\alpha$  where top and bottom transducers are interchanged and 2 takes the position of 3.



**Figure 7.** Depiction of the drag area and the volume disrupted during the revolution described in Figure 6 for a purely tangential flow (flow moves into the page). The images are drawn to scale and show the projection of the head and the transducers along the direction of the air streamline (the flow moves into the page). Both half revolutions are shown (anticlockwise in the left and clockwise in the right) as a function of the rotation angle,  $g$ , the equivalent sets of positions given by  $\alpha$  and the resulting  $\delta$ . The series of figures in a) shows a radial attack angle  $\lambda = 90^\circ$  and (b)  $\lambda = 105^\circ$ . The grey areas delimit the disruption volume as the shadow projected by surface comprised by union of all the transducers upstream.

**T- Top set of transducers is responsible of the shadow**



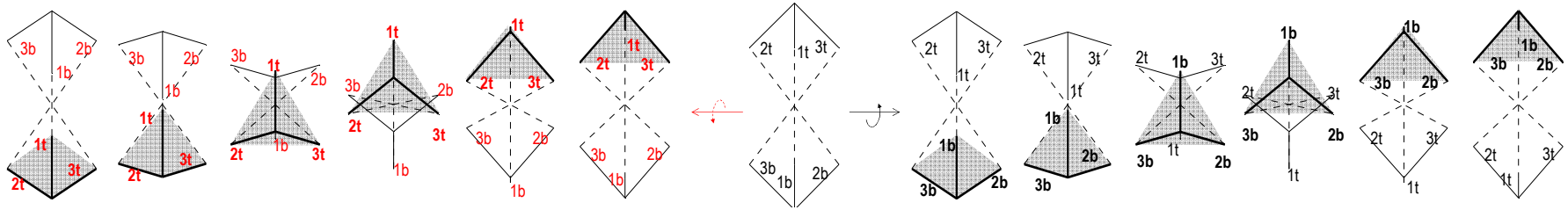
**B- Bottom set of transducers is responsible of the shadow**

$a = 25^\circ$   $a = 45^\circ$   $a = 75^\circ$   $a = 105^\circ$   $a = 135^\circ$   $a = 155^\circ$

$a = 0^\circ$

$a = 25^\circ$   $a = 45^\circ$   $a = 75^\circ$   $a = 105^\circ$   $a = 135^\circ$   $a = 155^\circ$

**a)**

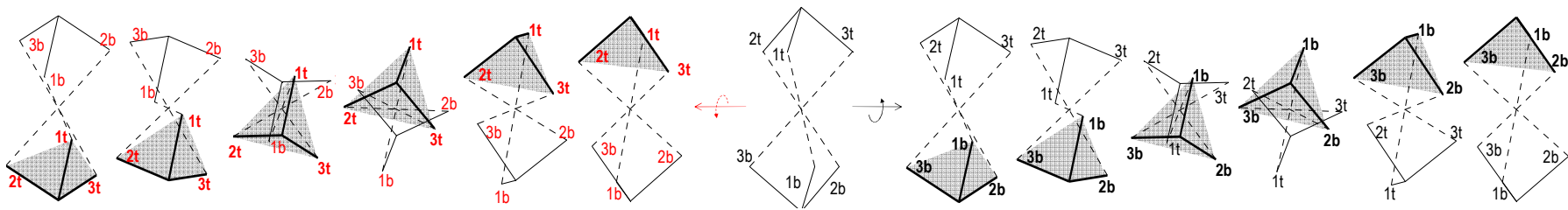


$g = -155^\circ$   $g = -135^\circ$   $g = -105^\circ$   $g = -75^\circ$   $g = -45^\circ$   $g = -25^\circ$   
 $\delta = 25^\circ$   $\delta = 45^\circ$   $\delta = 75^\circ$   $\delta = 75^\circ$   $\delta = 45^\circ$   $\delta = 25^\circ$

$g = 0^\circ$   
 $\delta = 0^\circ$

$g = 25^\circ$   $g = 45^\circ$   $g = 75^\circ$   $g = 105^\circ$   $g = 135^\circ$   $g = 155^\circ$   
 $\delta = 25^\circ$   $\delta = 45^\circ$   $\delta = 75^\circ$   $\delta = 75^\circ$   $\delta = 45^\circ$   $\delta = 25^\circ$

**b)**



the head revolves the velocity from  $\bar{U}_{\alpha_1}$  and  $\bar{U}_{\alpha_3}$  is transferred to one another (see Figures 8e and 8f).  $\bar{U}_{\alpha_1}$  is the most exposed to drag in these instruments and thus it shows a bias up to  $-20\%$ . In addition to the deficit originated in  $\bar{U}$ , the perturbation in direction becomes significant for  $\delta_{90h} > 45^\circ$ . This is particularly visible in the distortion of the radial flow,  $\bar{U}_{\alpha_2,C} - \bar{U}_{\alpha_2,E}$  (see Figure 7d) to the point of changing the sense of the flow and causing a large deviation in  $\lambda$ ,  $\lambda_C - \lambda_E$  (see Figure 8b).

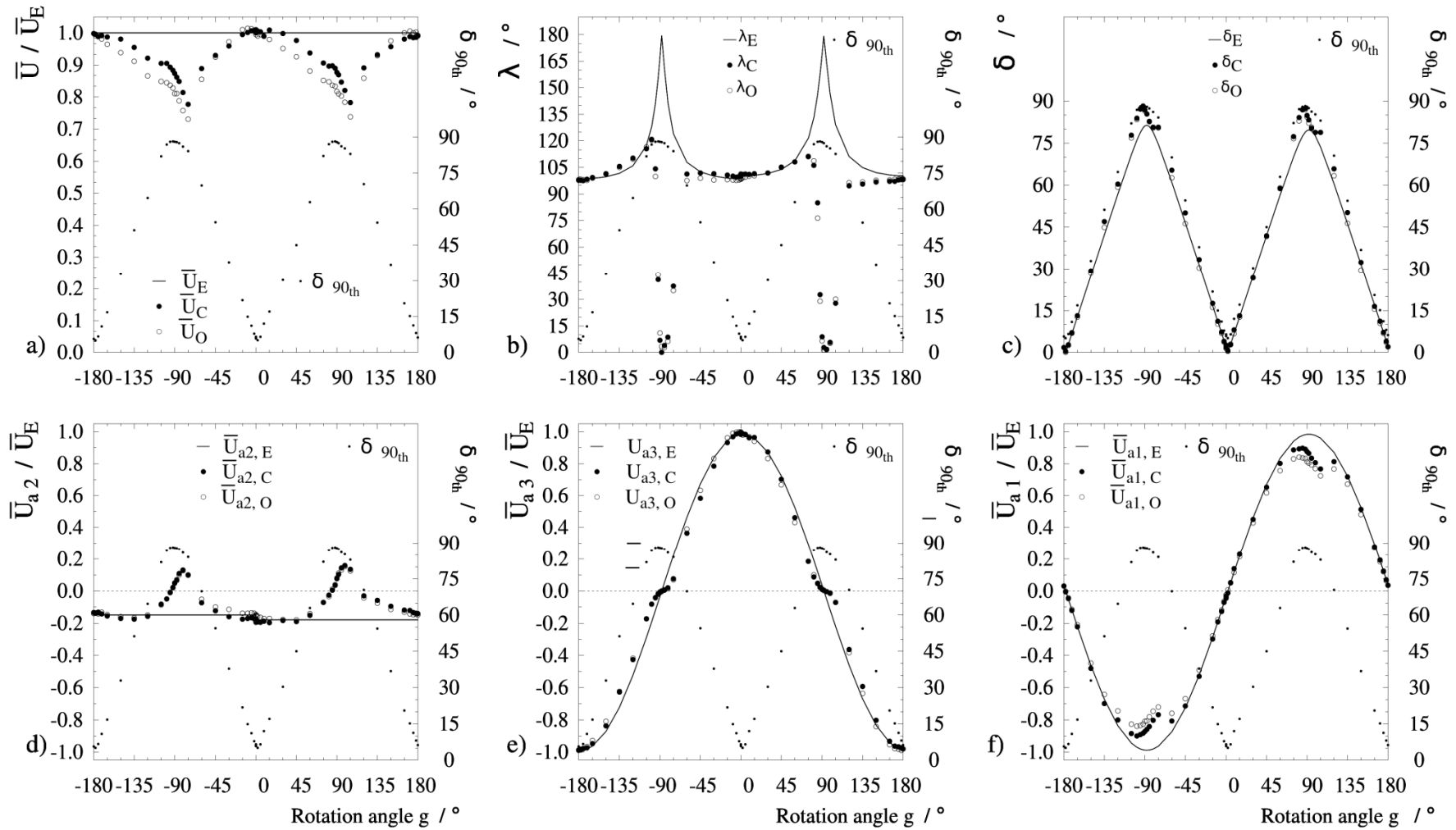
Comparing the Figures 8, 9 and 10, shows that a change in the mean value of  $\delta$  at  $g = 0^\circ$  shifts all the profiles from left to the right. The difference in the radial flow modifies  $\lambda$  and this results in a different pattern for the errors, which will be related later to the design of the head. Clearly, changes in the turbulence level have a very relevant effect in the magnitude of the error. The perturbation in the radial flow widens as  $\kappa/\bar{U}_{av}^2$  increases from Figures 8 to 9 and 10.

Similarly, figures 11 to 13 show the evolution of the turbulence statistics during the revolution in the frame of reference of the anemometer, and Figures 14 to 16 present them in the polar coordinates. The perturbation observed in the radial flow  $\bar{U}_{\alpha_2}$  translates here into the introduction of turbulence within the same region, see Figures 14 to 16. This is unrelated to a change in coordinates and must respond to a local disruption of the flow. The magnitude of the error is particularly relevant in the radial fluctuation. The normal stress  $\sigma_{r,r}$  undergoes two consecutive changes of one order of magnitude in the transition across the maximum large  $\delta_{90h}$  (nearby  $g \sim -90^\circ$  and  $g \sim 90^\circ$ ). This perturbation is responsible of errors in  $\kappa$  changing from negative to positive in the same range (e.g. Figures 16c and 16a).

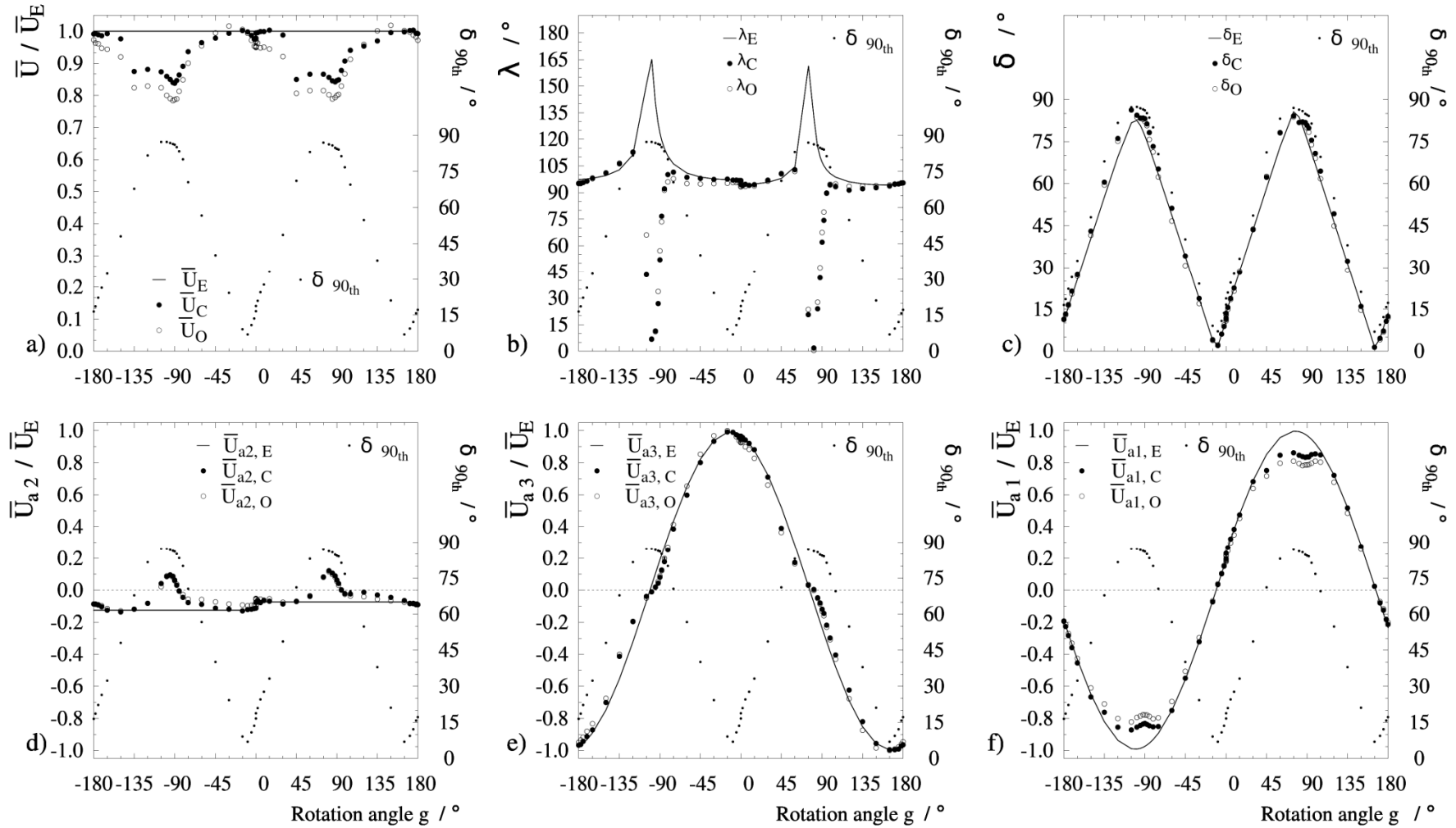
### 3.3.1.2. Correlation to the shadow of the transducers.

In Figures 8 to 16, with the exception of  $\delta$  none of the profiles are symmetric over  $g = 0^\circ$ . The maximum errors are registered at  $g = -75^\circ$  and  $g = 105^\circ$ . This means that positions with the same  $\delta$  have different errors. This is a 3-D effect that cannot be described with the definition of  $\delta$  in (1) but can be explained by considering the projected shadow formed by the transducers. Each set of transducers disrupts the field downstream by generating a local pressure drop. It is the orientation what determines whether the perturbation affects the volume where the measurement takes place. The disrupted volume is defined in Figure 7 as the projection along the streamline of the surface comprised of all the transducers upstream. Notice how the positions with the same rotation angle  $g$  in Figure 6 show a different disposition to a tangential flow. For illustration, see how while  $g = 60^\circ$  presents two

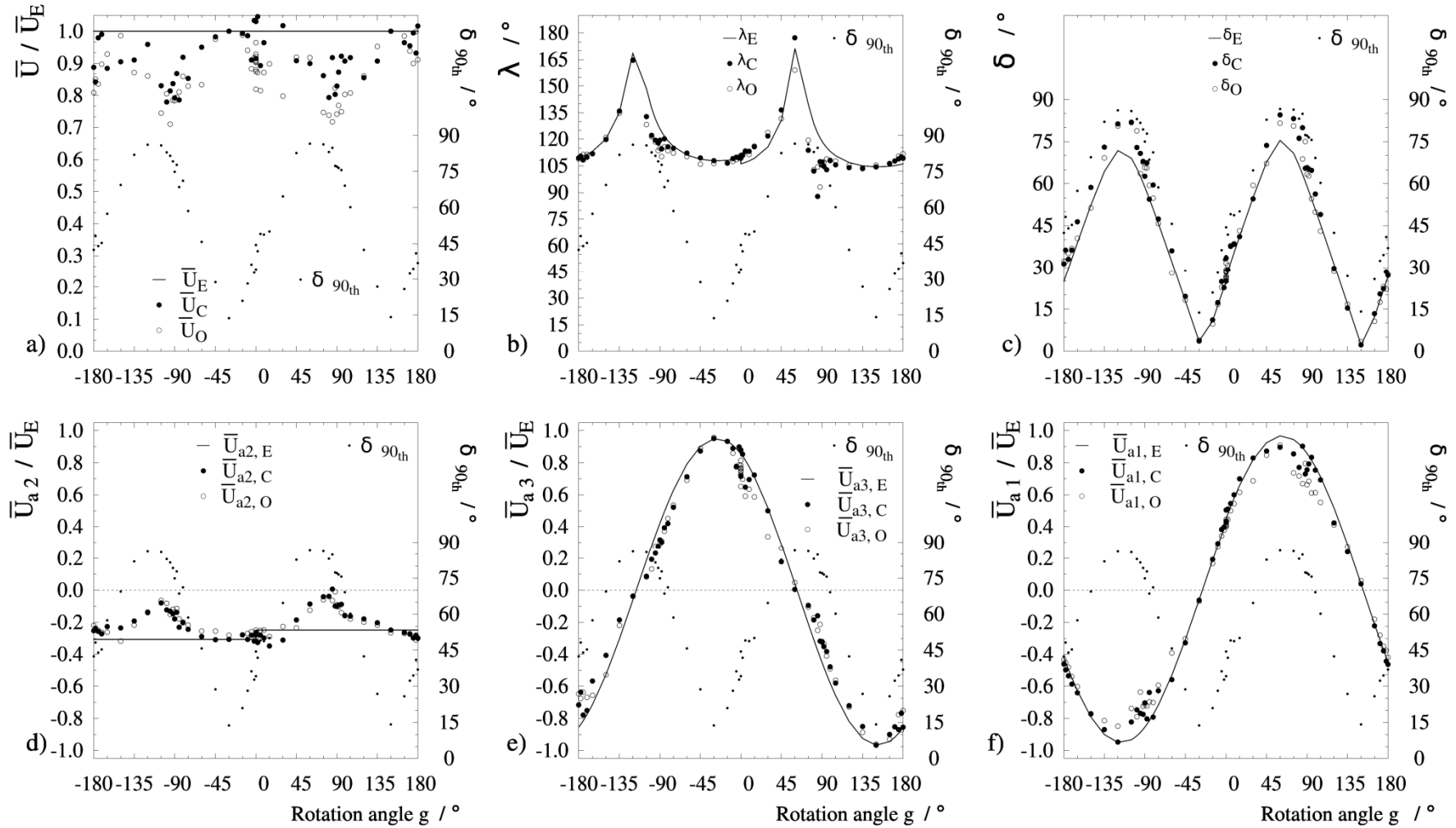
**Figure 8.** Evolution of measurement of velocity in the anemometer frame of reference during the revolution (rotation over axis  $\alpha_2$ ). E, C and O denote estimate and calibrated and raw measurements respectively. Normalised values of a) Velocity magnitude,  $\bar{U}$  b) Attack angle  $\delta$ , c) Attack angle  $\lambda$ , d)  $\bar{U}_{\alpha_2}$  e)  $\bar{U}_{\alpha_3}$  f)  $\bar{U}_{\alpha_1}$ . Position  $r = 0.35 R$ ,  $\kappa/\bar{U}_{av}^2 = 0.061$ .



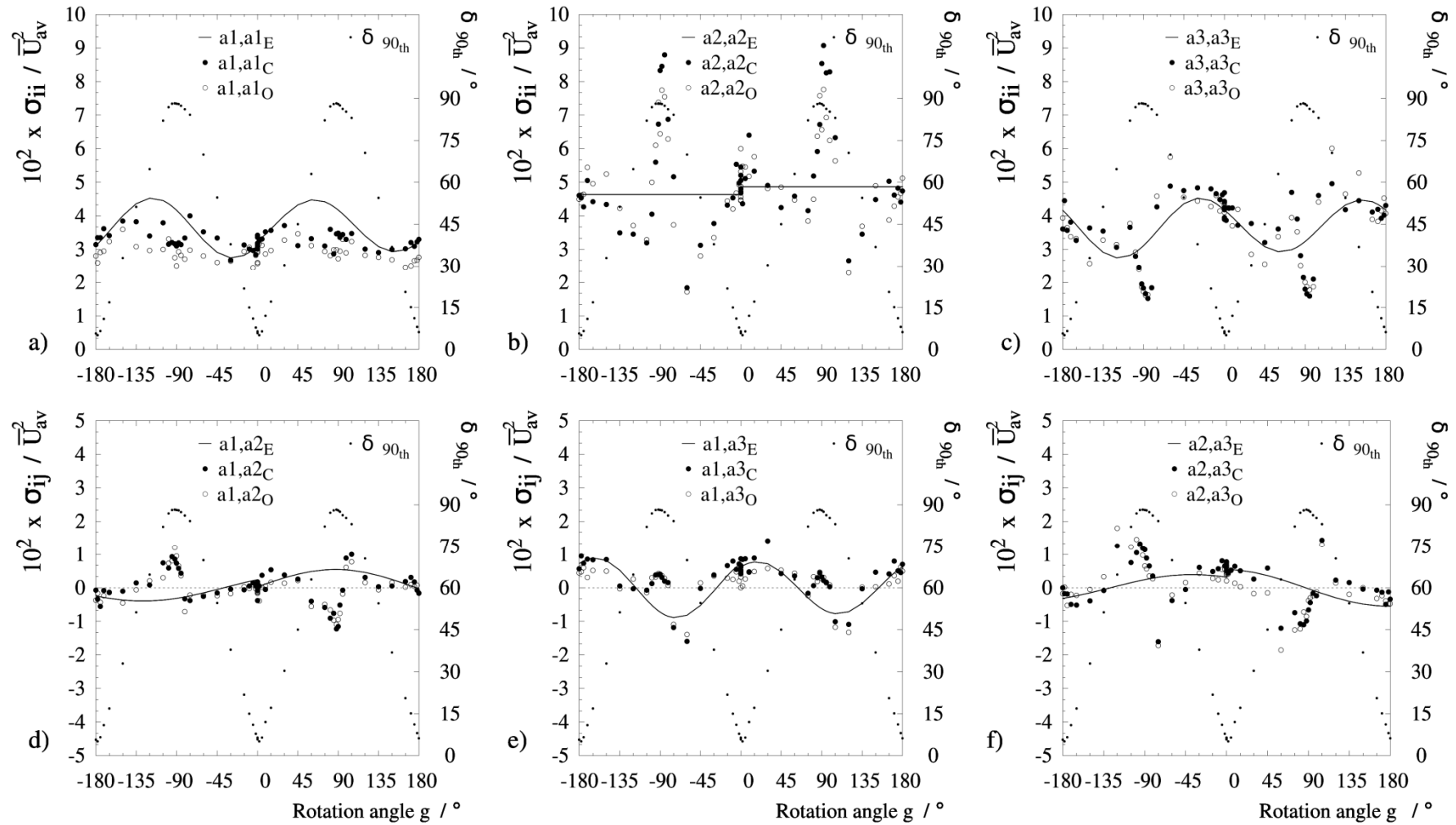
**Figure 9.** Evolution of measurement of velocity in the anemometer frame of reference during the revolution (rotation over axis  $\alpha_2$ ). E, C and O denote estimate and calibrated and raw measurements respectively. Normalised values of a) Velocity magnitude,  $\bar{U}$  b) Attack angle  $\delta$ , c) Attack angle  $\lambda$ , d)  $\bar{U}_{\alpha_2}$  e)  $\bar{U}_{\alpha_3}$  f)  $\bar{U}_{\alpha_1}$ . Position  $r = 0.60 R$ ,  $\kappa/\bar{U}_{av}^2 = 0.090$ .



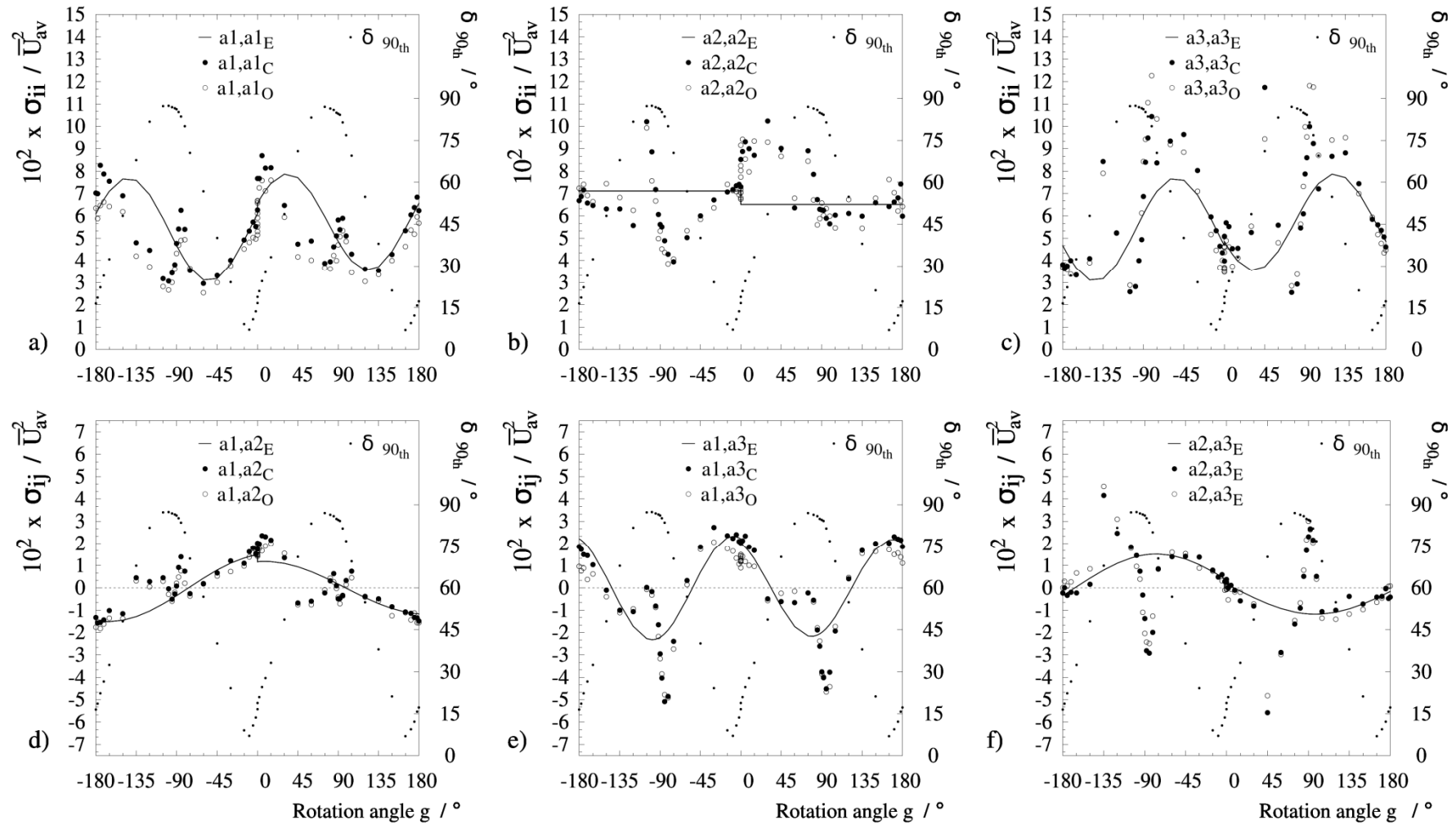
**Figure 10.** Evolution of measurement of velocity in the anemometer frame of reference during the revolution (rotation over axis  $a_2$ ). E, C and O denote estimate and calibrated and raw measurements respectively. Normalised values of a) Velocity magnitude,  $\bar{U}$  b) Attack angle  $\delta$ , c) Attack angle  $\lambda$ , d)  $\bar{U}_{a_2}$  e)  $\bar{U}_{a_3}$  f)  $\bar{U}_{a_1}$ . Position  $r = 0.10 R$ ,  $\kappa/\bar{U}_{av}^2 = 0.333$ .



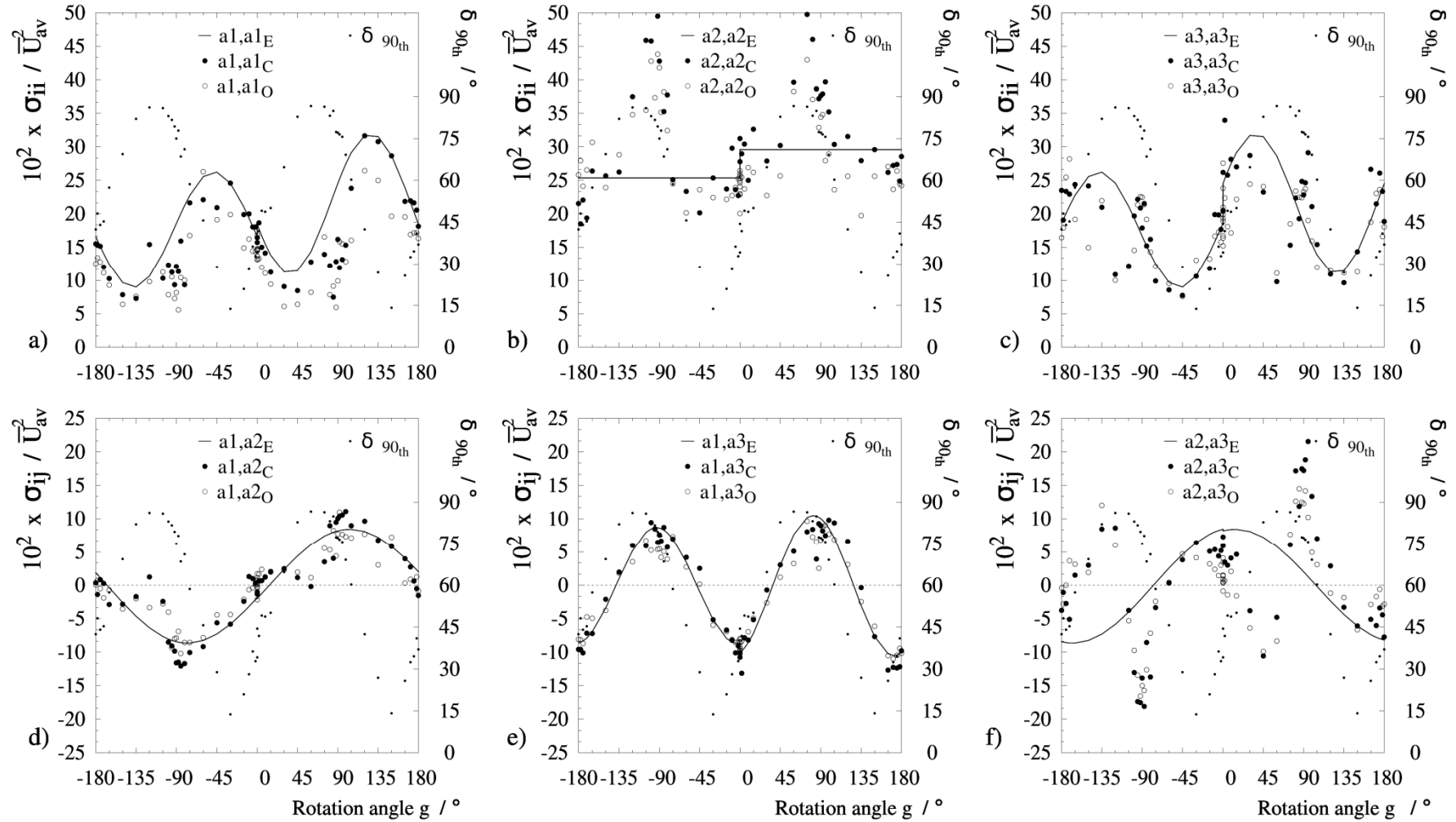
**Figure 11.** Evolution of the measurement of turbulence in the anemometer frame of reference during the revolution (rotation over  $a_2$ ). E, C and O denote estimate and calibrated and raw measurements. Normalised values of a)  $\sigma_{a_1 a_1}$ , b)  $\sigma_{a_2 a_2}$ , c)  $\sigma_{a_3 a_3}$ , d)  $\sigma_{a_1 a_2}$ , e)  $\sigma_{a_1 a_3}$ , f)  $\sigma_{a_2 a_3}$ . Position  $r = 0.35 R$ ,  $\kappa/\bar{U}_{av}^2 = 0.061$ .



**Figure 12.** Evolution of the measurement of turbulence in the anemometer frame of reference during the revolution (rotation over  $\alpha_2$ ). E, C and O denote estimate and calibrated and raw measurements. Normalised values of. a)  $\sigma_{\alpha_1\alpha_1}$ , b)  $\sigma_{\alpha_2\alpha_2}$ , c)  $\sigma_{\alpha_3\alpha_3}$ , d)  $\sigma_{\alpha_1\alpha_2}$ , e)  $\sigma_{\alpha_1\alpha_3}$ , f)  $\sigma_{\alpha_2\alpha_3}$ . Position  $r = 0.60 R$ ,  $\kappa/\bar{U}_{av}^2 = 0.090$ .



**Figure 13.** Evolution of the measurement of turbulence in the anemometer frame of reference during the revolution (rotation over  $\alpha_2$ ). E, C and O denote estimate and calibrated and raw measurements. Normalised values of. a)  $\sigma_{\alpha_1\alpha_1}$ , b)  $\sigma_{\alpha_2\alpha_2}$ , c)  $\sigma_{\alpha_3\alpha_3}$ , d)  $\sigma_{\alpha_1\alpha_2}$ , e)  $\sigma_{\alpha_1\alpha_3}$ , f)  $\sigma_{\alpha_2\alpha_3}$ . Position  $r = 0.10 R$ ,  $\kappa/\bar{U}_{av}^2 = 0.333$ .



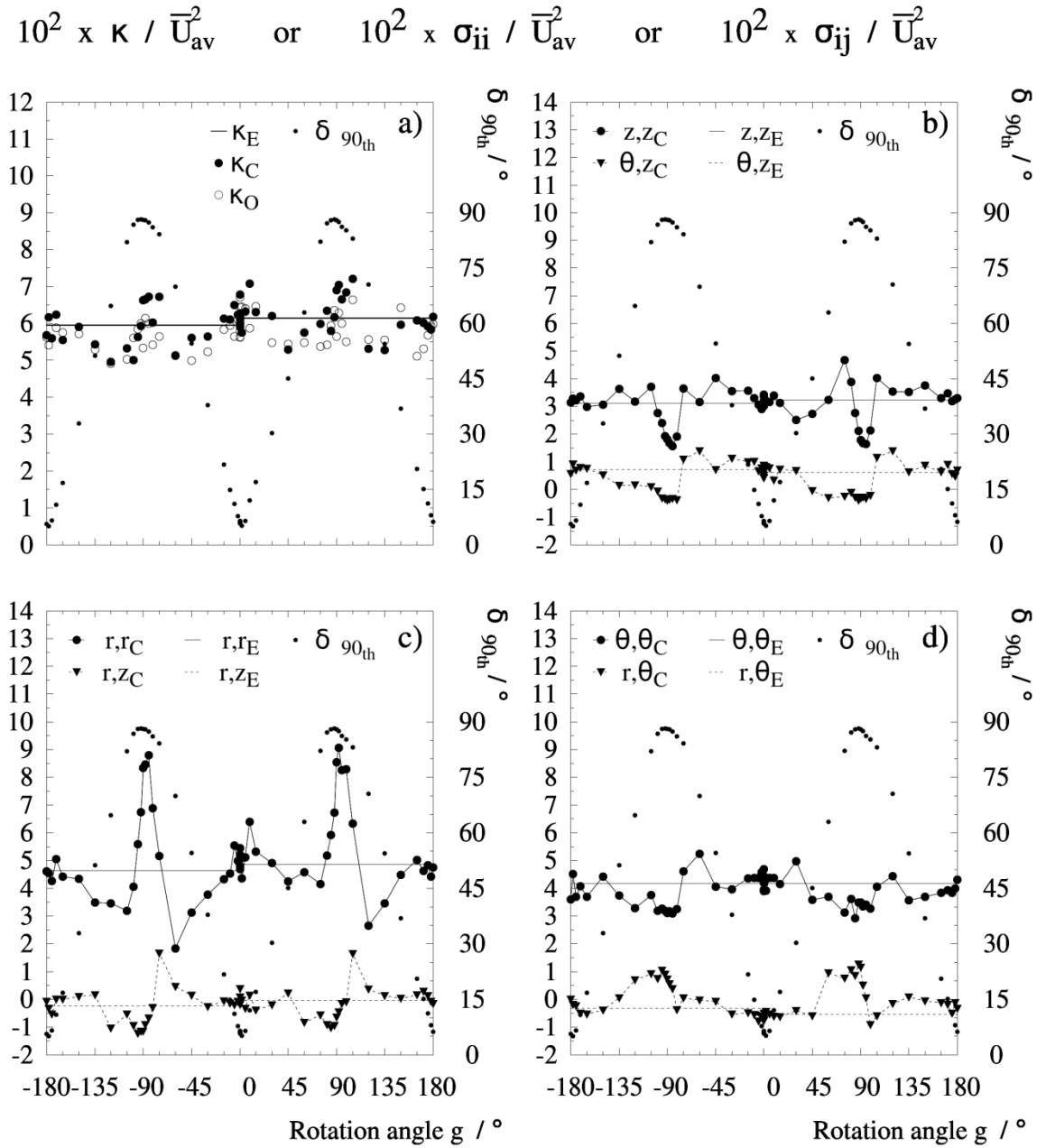


**Figure 14.** Evolution of the measurement of turbulence in the polar frame of reference of the cylinder, during the revolution.. E and C denote the best estimate and calibrated measurements. Normalised values of a)  $\kappa$  , b)  $\sigma_{z,z}$  ,  $\sigma_{\theta,z}$  , c)  $\sigma_{r,r}$  ,  $\sigma_{r,z}$  , d)  $\sigma_{\theta,\theta}$  ,  $\sigma_{r,\theta}$  . Position  $r = 0.35 R$  ,  $\kappa / \bar{U}_{av}^2 = 0.061$ .

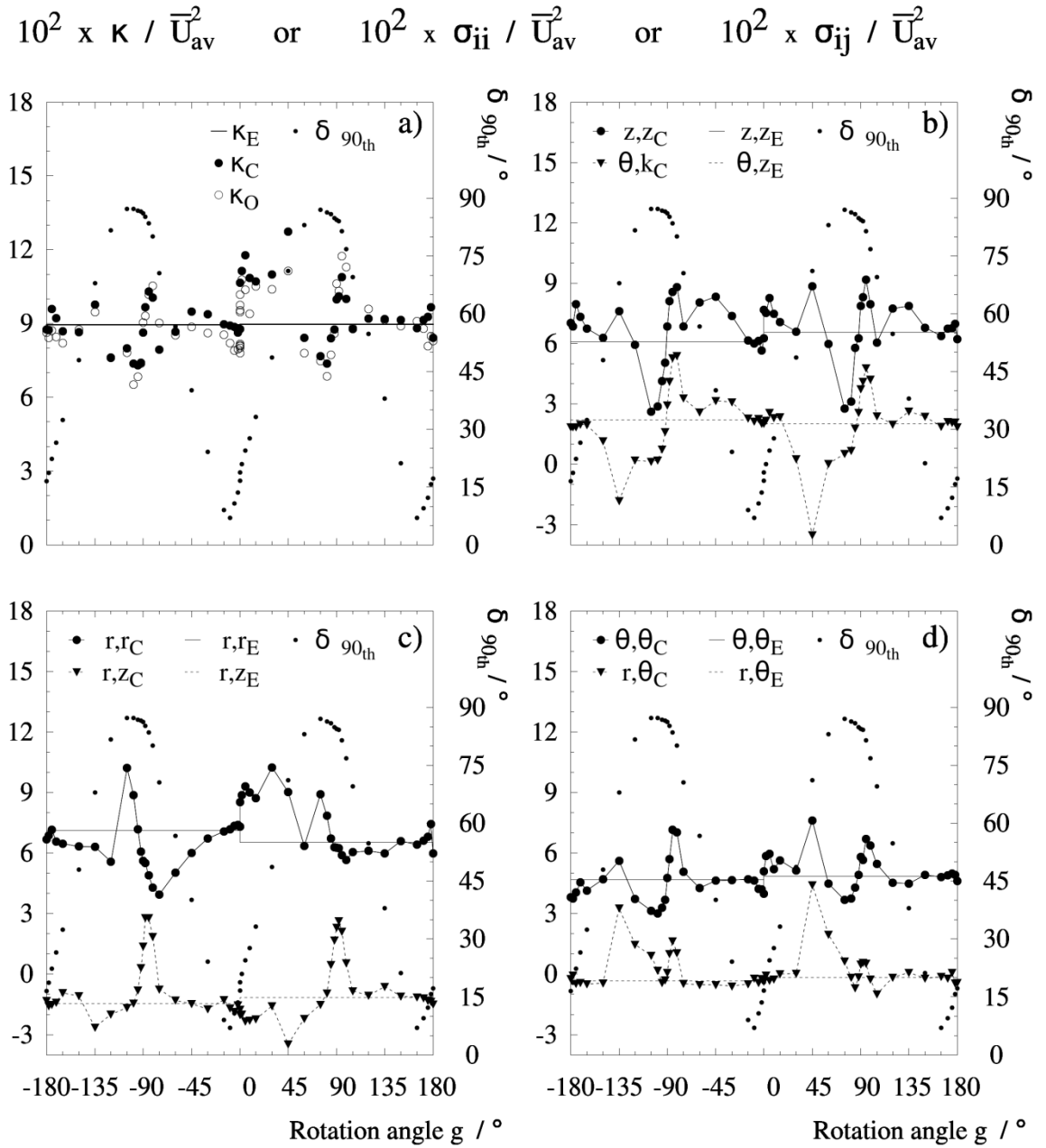


**Figure 15.** Evolution of the measurement of turbulence in the polar frame of reference of the cylinder, during the revolution. E and C denote the best estimate and calibrated measurements. Normalised values of a)  $\kappa$  , b)  $\sigma_{z,z}$  ,  $\sigma_{\theta,\theta}$  , c)  $\sigma_{r,r}$  ,  $\sigma_{r,z}$  , d)  $\sigma_{\theta,\theta}$  ,  $\sigma_{r,\theta}$  . Position  $r = 0.60 R$  ,  $\kappa / \bar{U}_{av}^2 = 0.090$ .

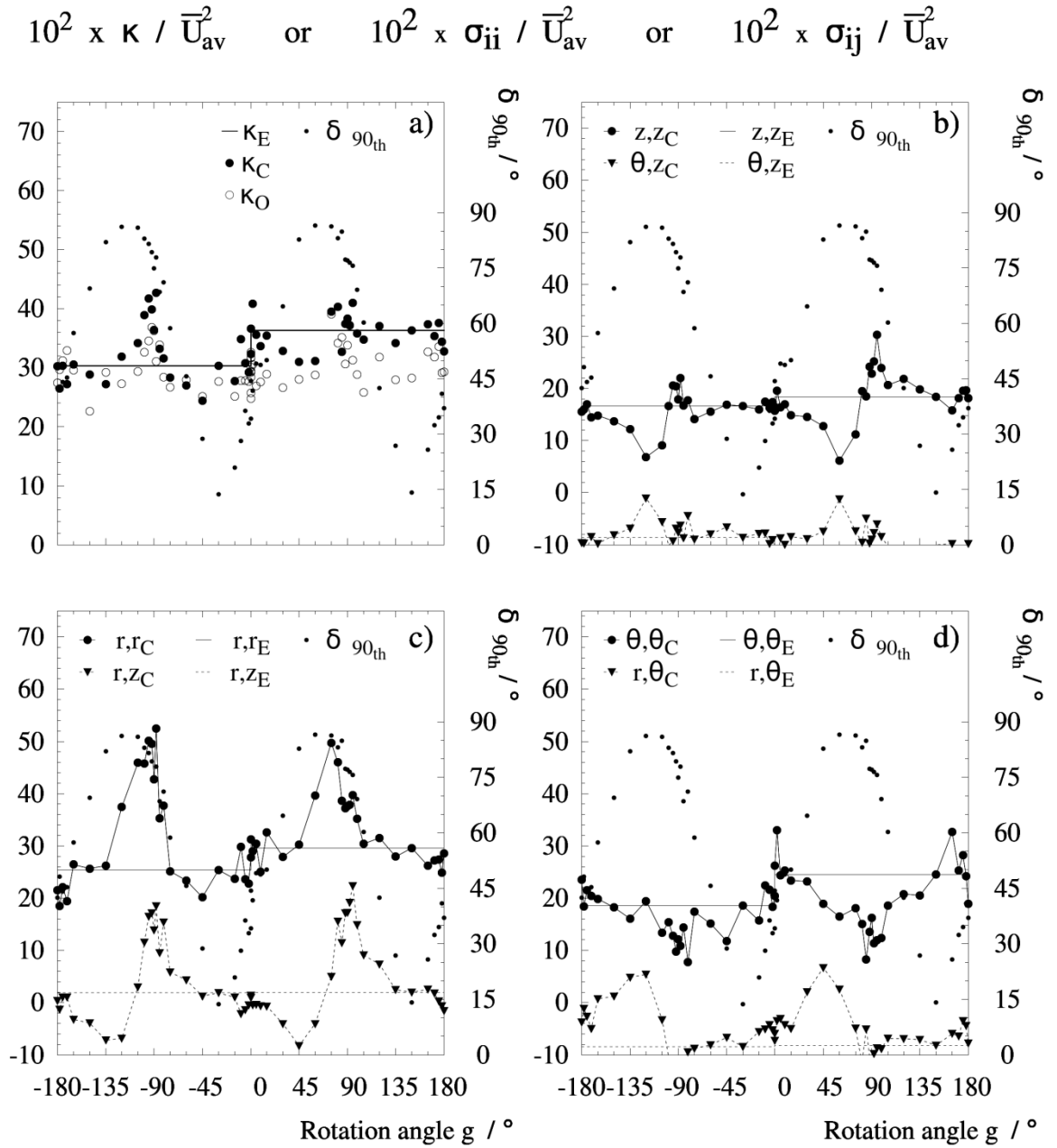


**Figure 16.** Evolution of the measurement of turbulence in the polar frame of reference of the cylinder, during the revolution. E and C denote the best estimate and calibrated measurements. Normalised values of a)  $\kappa$  , b)  $\sigma_{z,z}$  ,  $\sigma_{\theta,z}$  , c)  $\sigma_{r,r}$  ,  $\sigma_{r,z}$  , d)  $\sigma_{\theta,\theta}$  ,  $\sigma_{r,\theta}$  . Position  $r = 0.10 R$  ,  $\kappa/\bar{U}_{av}^2 = 0.333$ .

transducers aligned with the flow and one against it,  $g = -60^\circ$  presents the opposite. This makes positions with the same  $\delta$  in Figure 7 to present a different drag area, see for instance how  $\delta = 75^\circ$  can result in two different dispositions where either one transducer (1) or two (2 and 3) block the sonic paths behind them. The individual path shadows have been calculated as the ratio of each sonic path that is included in the affected volume. Figures 17 to 22 show the shadows associated to all three revolutions. These are purely dependant on geometry and the best estimate of direction and variability. Two numbers are given, the shadow caused by the mean direction  $Ps_U$  and the average shadow caused by all instantaneous orientations, denoted  $\langle Ps \rangle$ . Accounting for variability has a clear impact in the regions close to the limits, where disruption owes precisely to the presence of fluctuations (see how for  $\delta = 45^\circ$  in Figure 7 transducers are on the edge of blocking the paths behind them).

All the error profiles now follow a clear correlation to the shadows. Figure 17 to 19 show the evolution of velocity and direction for all three positions and Figures 20 to 22 include the turbulence statistics. Both half revolutions are presented, not versus  $g$  but comparing the sets of locations that share exactly the same geometry (i.e. given in Figure 6 as the set  $a = g$  and set  $a = g + 180^\circ$  for clockwise and anticlockwise rotation). It is clear that the transition to high errors correlates to positions when the shadow of the transducers starts blocking the sonic paths. All the profiles now overlap. The measurements with the same shadow share the same evolution independently of inter-changing top and transducers. They all show a clear transition on  $a \sim 90^\circ$  and an asymmetric recovery at either side. Comparison of the profiles for  $a < 90^\circ$  or  $a > 90^\circ$  to the path shadows reveals the link to the disposition of transducers. The individual shadows in Figure 20 correlate to the production of turbulence. Regions at either side of  $90^\circ$  correspond to positions where the transducer 1 blocks the sonic path  $1tb$  or the transducers 2 – 3 block the paths  $2tb$  and  $3tb$  (see both positions for  $\delta = 75^\circ$  in Figure 7). A clearly different distortion at either side gives rise to a the mentioned perturbation in the radial flow (see Figure 17c) and a higher variability (see Figures 20a and 20c).

The fact that these asymmetries exist and can be explained by the geometry is very relevant. In the one hand it confirms the aerodynamic origin of the errors and in the other it indicates that the disruption is not purely determined by  $\delta$  and  $\lambda$  in their usual definition, but also by the sense of  $U_{a_3}$ . In essence, the uncertainty varies should the anemometer be subject to an upwards or downwards flow, which indicates that  $\delta$  should be defined from  $0 - 180^\circ$ . In a vortex the axial flow can have either direction, so that the range  $\delta < 50^\circ$  in the full revolution has been used to compute the maximum error limits.

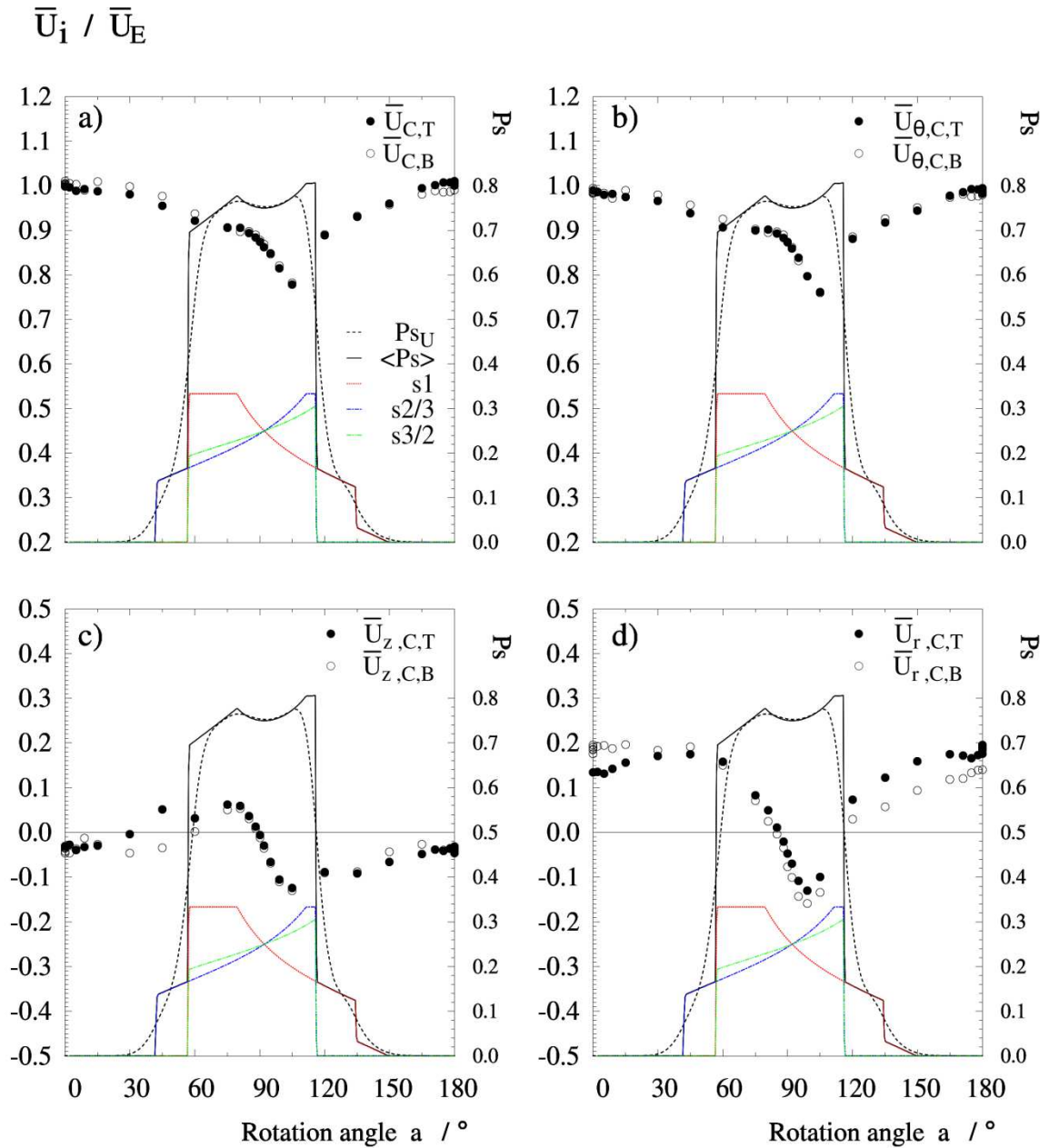


**Figure 17.** Correlation of errors in velocity magnitude and direction with the path shadow in both independent half revolutions. C indicates calibrated mode. T and B indicate that the top or bottom set of transducers is upstream (i.e.  $g < 0^\circ$  or  $g > 0^\circ$ ). The path shadow projected by the mean air direction is given by  $s_1$ ,  $s_2$  and  $s_3$  (1/3 of the shadow between each pairs 1, 2 and 3) and  $Ps_U$  shows the summation.  $\langle Ps \rangle$  shows the combined mean path shadow projected by of all instantaneous directions. Normalised values of. a)  $\bar{U}$  b)  $\bar{U}_\theta$  c)  $\bar{U}_z$  d)  $\bar{U}_r$ . Position  $r = 0.35 R$ ,  $\kappa/\bar{U}_{av}^2 = 0.061$ .

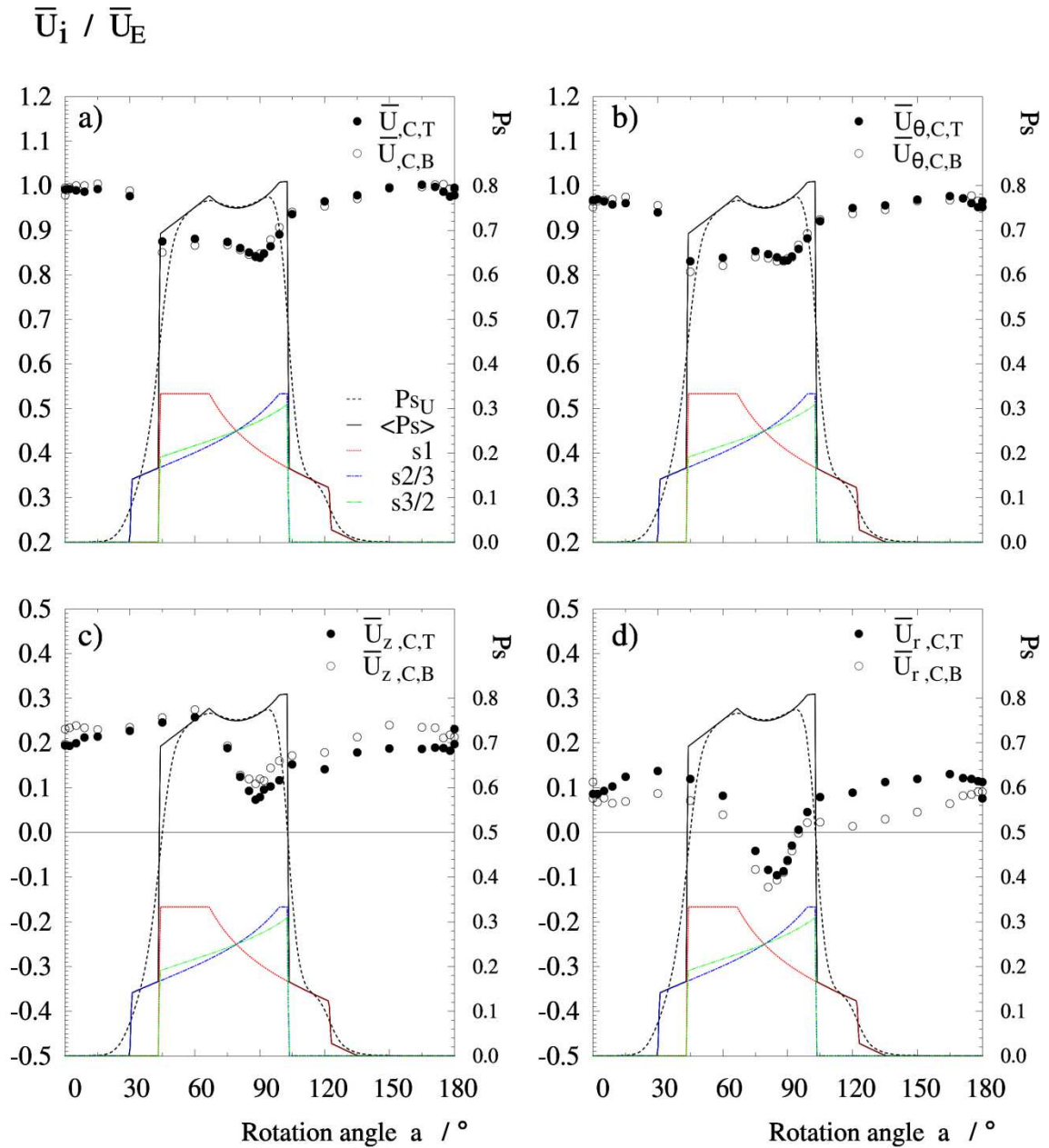


**Figure 18.** Correlation of errors in velocity magnitude and direction with the path shadow in both independent half revolutions. C indicates calibrated mode. T and B indicate that the top or bottom set of transducers is upstream (i.e.  $g < 0^\circ$  or  $g > 0^\circ$ ). The path shadow projected by the mean air direction is given by  $s_1$ ,  $s_2$  and  $s_3$  (1/3 of the shadow between each pair, 1, 2 and 3) and  $Ps_U$  shows the summation.  $\langle Ps \rangle$  shows the combined mean path shadow projected by of all instantaneous directions. Normalised values of. a)  $\bar{U}$  b)  $\bar{U}_\theta$  c)  $\bar{U}_z$  d)  $\bar{U}_r$ . Position  $r = 0.60 R$ ,  $\kappa / \bar{U}_{av}^2 = 0.090$ .

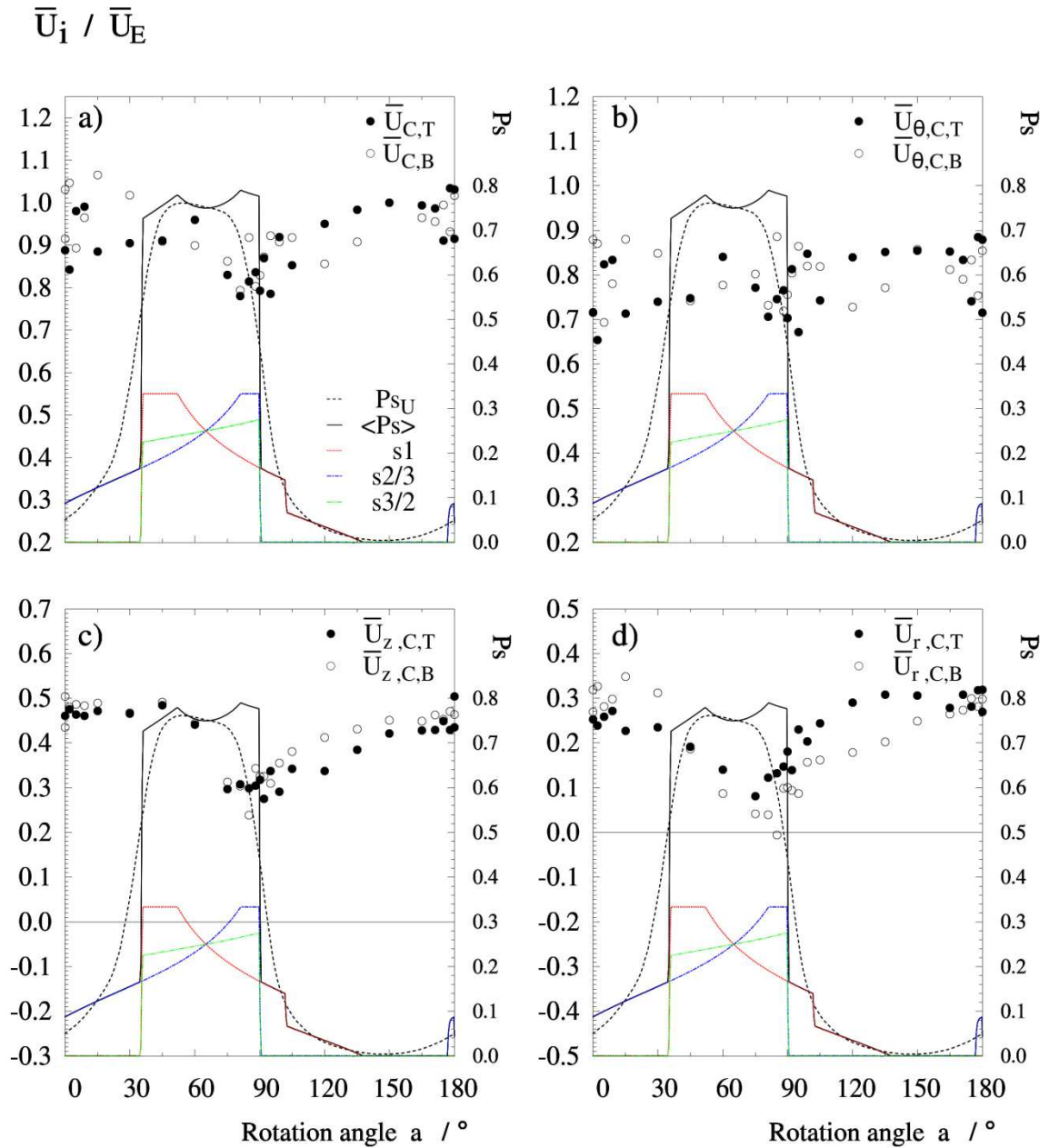


**Figure 19.** Correlation of errors in velocity magnitude and direction with the path shadow in both independent half revolutions. C indicates calibrated mode. T and B indicate that the top or bottom set of transducers is upstream (i.e.  $g < 0^\circ$  or  $g > 0^\circ$ ). The path shadow projected by the mean air direction is given by s1, s2 and s3 (1/3 of the shadow between each pairs 1, 2 and 3) and  $Ps_U$  shows the summation.  $\langle Ps \rangle$  shows the combined mean path shadow projected by of all instantaneous directions. Normalised values of. a)  $\bar{U}$  b)  $\bar{U}_\theta$  c)  $\bar{U}_z$  d)  $\bar{U}_r$ . Position  $r = 0.10 R$ ,  $\kappa / \bar{U}_{av}^2 = 0.333$ .

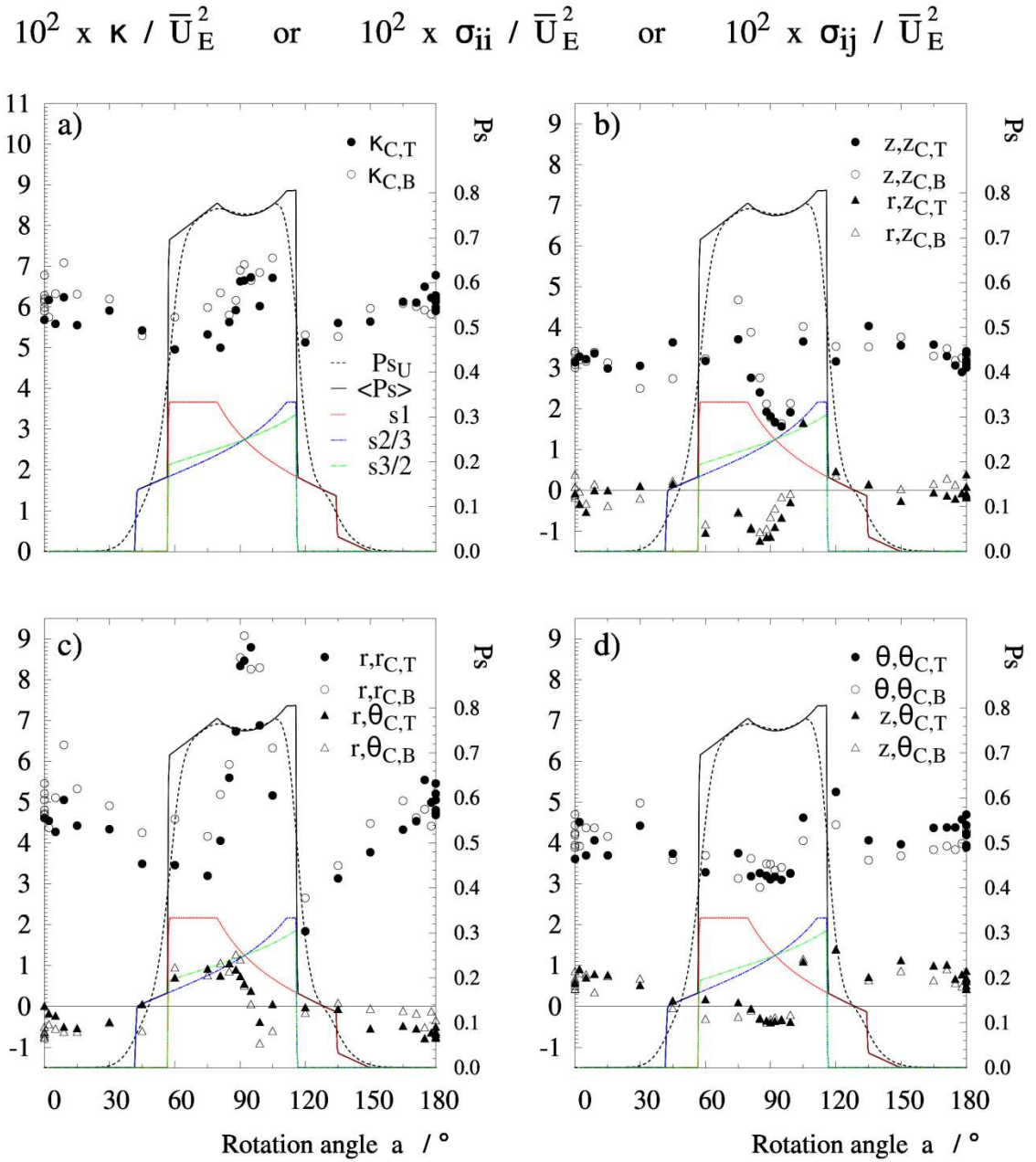


**Figure 20.** Correlation of the errors in variability with the path shadow for both independent half revolutions. C indicates calibrated mode. T and B indicate that the top or bottom set of transducers is upstream (i.e.  $g < 0^\circ$  or  $g > 0^\circ$ ). The path shadow projected by the mean air direction is given by  $s_1$ ,  $s_2$  and  $s_3$  (1/3 of the shadow between each pairs 1, 2 and 3) and  $Ps_U$  shows the summation.  $\langle Ps \rangle$  is the mean path shadow projected by of all instantaneous directions. Normalised values of a)  $\kappa$ , b)  $\sigma_{z,z}$ ,  $\sigma_{r,z}$  c)  $\sigma_{r,r}$ ,  $\sigma_{r,\theta}$  d)  $\sigma_{\theta,\theta}$ ,  $\sigma_{z,\theta}$ . Position  $r = 0.35 R$ ,  $\kappa / \bar{U}_{av}^2 = 0.061$ .

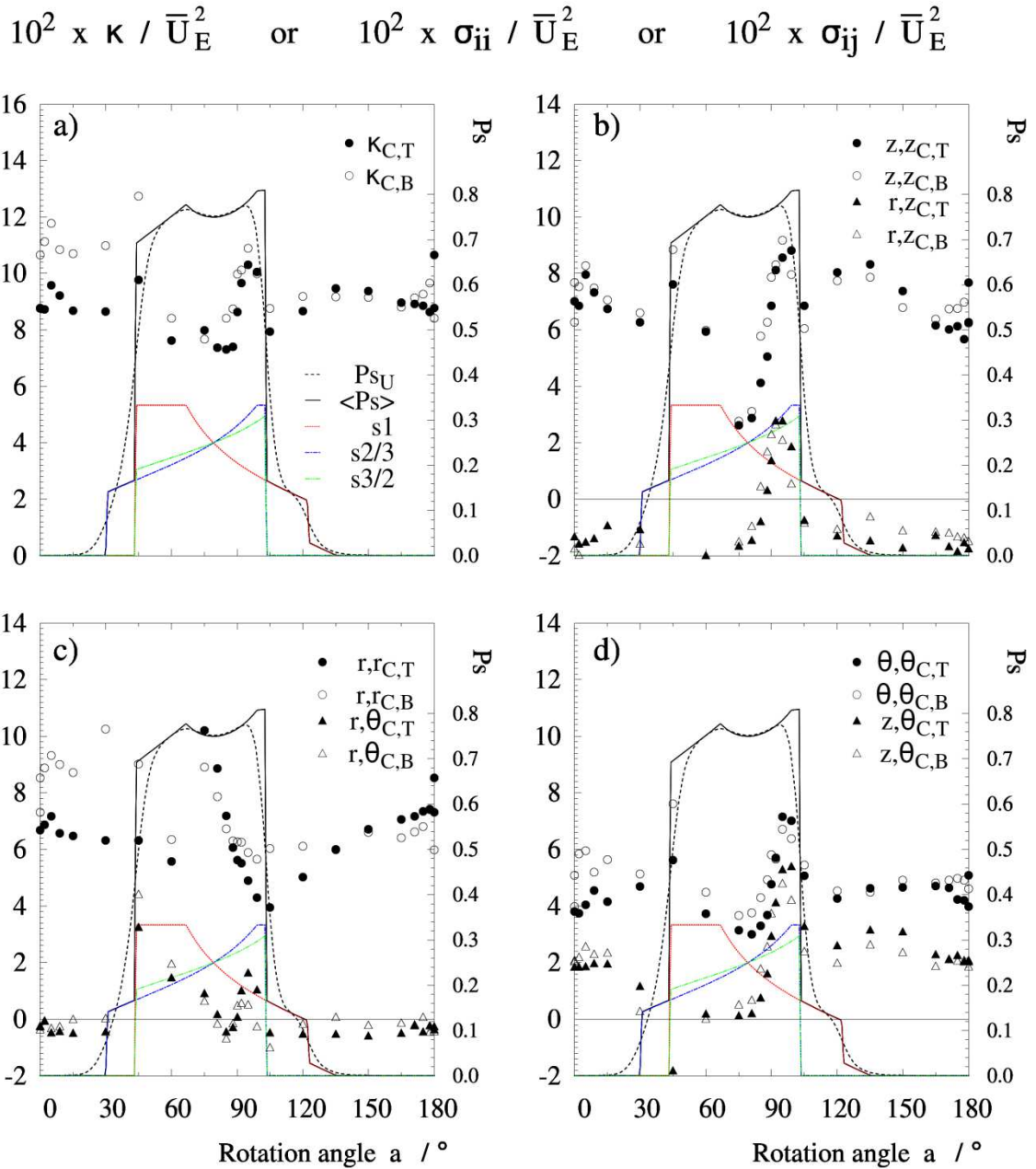


**Figure 21.** Correlation of the errors in variability with the path shadow for both independent half revolutions. C indicates calibrated mode. T and B indicate that the top or bottom set of transducers is upstream (i.e.  $g < 0^\circ$  or  $g > 0^\circ$ ). The path shadow projected by the mean air direction is given by  $s_1$ ,  $s_2$  and  $s_3$  (1/3 of the shadow between each pairs 1, 2 and 3) and  $Ps_U$  shows the summation.  $\langle Ps \rangle$  is the mean path shadow projected by of all instantaneous directions. Normalised values of a)  $\kappa$ , b)  $\sigma_{z,z}$ ,  $\sigma_{r,z}$  c)  $\sigma_{r,r}$ ,  $\sigma_{r,\theta}$  d)  $\sigma_{\theta,\theta}$ ,  $\sigma_{z,\theta}$ . Position  $r = 0.60 R$ ,  $\kappa / \bar{U}_{av}^2 = 0.090$ .

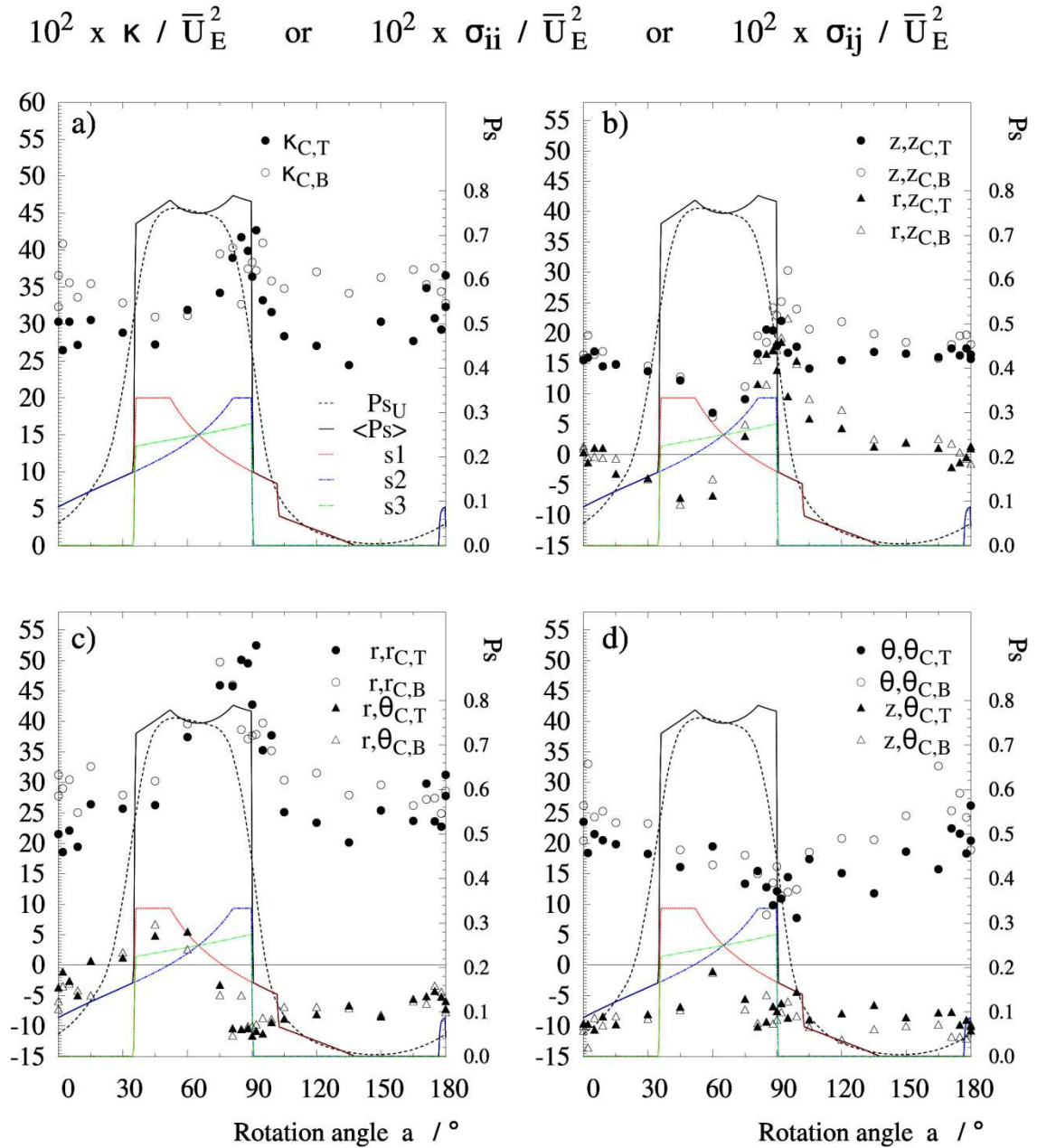


**Figure 22.** Correlation of the errors in variability with the path shadow for both independent half revolutions. C indicates calibrated mode. T and B indicate that the top or bottom set of transducers is upstream (i.e.  $g < 0^\circ$  or  $g > 0^\circ$ ). The path shadow projected by the mean air direction is given by s1, s2 and s3 (1/3 of the shadow between each pairs 1, 2 and 3) and  $Ps_U$  shows the summation.  $\langle Ps \rangle$  is the mean path shadow projected by of all instantaneous directions. Normalised values of a)  $\kappa$ , b)  $\sigma_{z,z}$ ,  $\sigma_{r,z}$  c)  $\sigma_{r,r}$ ,  $\sigma_{r,\theta}$  d)  $\sigma_{\theta,\theta}$ ,  $\sigma_{z,\theta}$ . Position  $r = 0.10 R$ ,  $\kappa / \bar{U}_{av}^2 = 0.333$ .

Figure 23 to 25 show the distribution of the errors in the velocity magnitude and direction and Figures 26 to 28 include those associated to the turbulence. Tables 2 and 3 summarize the statistics of all the measurements that comply with the limits  $\delta_{90th} < 45^\circ$  and  $\lambda_{90th} > 30^\circ$ . The uncertainty increases from that given for an optimum orientation in Table 1, because higher and wider ranges of attack angles are allowed in tables 2 and 3. These values can be considered valid measuring at any position in the vortex that complies with these limits and represent a largely conservative estimate of the uncertainty. This can be used in the characterization of similar confined swirling flows with the *H50*.

The following section 3.3.2 describes limitations in the use of an extension and sections 3.4 and 3.5 restrict the measurements in certain areas of the vortex where the data is unreliable.

### 3.3.2. Disruption of the vortex development.

Independently from the measurement region one must ensure that the instrument does not affect the overall flow structure. This is obvious in meteorological applications but not in a confinement, particularly in a strong swirling flow. The centrifugal force term in the momentum equation leads to a delicate pressure balance and often gives rise to instabilities and periodic oscillations, discussed in detail in the Part A of this thesis (Chapter II). Figure 29 describes the impact of using long arrangements. It provides a comparison between two sets of measurements in Scale I and II (Chapters II and III). The data for Scale II are shown in Figures 29a and 29b, using the extension shown in Figure 3b to penetrate a length  $x < R$  in the cylinder. The data for Scale I are shown in Figures 29c and 29d. In this case, measurements are comprised of two sections measured from opposite sides of the cylinder: in the one the anemometer penetrates a length  $x < R$  at a given  $\theta$  and in the other the same position is reached from the opposite wall, i.e. the arrangement penetrates a length  $D - x > R$  at the position  $\theta + 180^\circ$ , which requires using the same extension, depicted in Figure 3b.

Clear profiles in the velocity and turbulence statistics are observed when the instrument does not cross over the centre in Figures 29a and 29b. When measurements are taken from either side in Figure 29c no significant variations appear in velocity magnitude or direction. The average errors are maintained across the cylinder for the entire *Re* range studied in Chapter II, and certainly within the uncertainty limits given in Table 2. Differences in  $\bar{U}$  close to the exit duct however can rise up to  $\pm 5 - 10\%$ .

The impact upon turbulence is more relevant. Normal and Reynolds stresses show a clear profile in Figure 29b, but a clear bias appears in Figure 29d according to whether the anemometer crosses or

**Table 2.** Uncertainty for  $\delta_{90th} < 45^\circ$   $\lambda_{90th} > 30^\circ$  under calibrated mode. Annular region of the vortex  $r > 0.30 R$ .  $\Delta = X_C - X_E$  shows the average error.  $\Delta_{Range}$ ,  $\Delta_{Max}$ ,  $\Delta_{Min}$  and  $\sigma_\Delta$  denote the range, and maximum, minimum and standard deviation. Left:  $r = 0.35 R$ ,  $\kappa = 0.061 U_{av}^2$ ; Right:  $r = 0.60 R$   $\kappa = 0.090 \bar{U}_{av}^2$ .

Variable $X$	$X_E$	$\sigma_\Delta$	$\Delta_{Range}$	$\Delta_{Max}$	$\Delta_{Min}$	$X_E$	$\sigma_\Delta$	$\Delta_{Range}$	$\Delta_{Max}$	$\Delta_{Min}$
$^\circ \delta$	2.4	0.6	2.4	1.8	-0.6	12.3	0.7	3.0	1.6	-1.4
$^\circ \lambda$	99.5	1.8	7.2	1.8	-5.4	95.8	1.0	3.9	1.1	-2.8
$10^2 \cdot \bar{U}/\bar{U}_E$	100.0	1.3	5.3	1.0	-4.3	100.0	0.9	3.3	0.4	-3.0
$10^2 \cdot \bar{U}_z/\bar{U}_E$	-3.6	1.1	6.2	3.2	-3.0	21.1	1.2	4.9	2.6	-2.3
$10^2 \cdot \bar{U}_\theta/\bar{U}_E$	98.5	1.1	5.0	0.6	-4.4	97.2	0.9	3.1	0.8	-2.3
$10^2 \cdot \bar{U}_r/\bar{U}_E$	16.5	3.0	11.0	2.6	-8.4	9.9	1.8	6.1	1.8	-4.3
$10^2 \cdot \kappa/\bar{U}_{av}^2$	6.1	0.3	1.4	0.9	-0.4	9.0	0.9	3.4	2.8	-0.6
$10^2 \cdot \overline{u_z u_z}/\bar{U}_{av}^2$	4.8	0.5	2.4	1.5	-0.9	6.8	1.1	3.9	2.8	-1.1
$10^2 \cdot \overline{u_\theta u_\theta}/\bar{U}_{av}^2$	4.2	0.3	1.4	0.8	-0.6	4.8	0.5	2.0	1.1	-0.9
$10^2 \cdot \overline{u_r u_r}/\bar{U}_{av}^2$	3.2	0.2	1.3	0.5	-0.7	6.3	0.7	2.7	2.2	-0.4
$10^2 \cdot \overline{u_r u_\theta}/\bar{U}_{av}^2$	-0.4	0.2	1.0	0.5	-0.5	-0.3	0.2	0.6	0.3	-0.3
$10^2 \cdot \overline{u_r u_z}/\bar{U}_{av}^2$	-0.1	0.2	0.8	0.4	-0.4	-1.3	0.5	1.7	0.6	-1.2
$10^2 \cdot \overline{u_z u_\theta}/\bar{U}_{av}^2$	0.7	0.2	0.7	0.4	-0.3	2.1	0.4	1.3	1.0	-0.4

**Table 3.** Uncertainty for  $\delta_{90th} < 45^\circ$   $\lambda_{90th} > 30^\circ$  under calibrated mode. Central jet-like region of the vortex  $r < 0.30 R$ .  $\Delta = X_C - X_E$  shows the average error in the calibrated mode.  $\Delta_{Range}$ ,  $\Delta_{Max}$ ,  $\Delta_{Min}$  and  $\sigma_\Delta$  denote the range, and maximum, minimum and standard deviation.  $r = 0.10 R$ ,  $\kappa = 0.333 \bar{U}_{av}^2$ .

Variable $X$	$X_E$	$\sigma_\Delta$	$\Delta_{Range}$	$\Delta_{Max}$	$\Delta_{Min}$
$^\circ \delta$	25.9	2.4	8.1	6.6	-1.5
$^\circ \lambda$	108.0	2.3	7.5	4.5	-3.0
$10^2 \cdot \bar{U}/\bar{U}_E$	100.0	5.3	19.1	4.6	-14.5
$10^2 \cdot \bar{U}_z/\bar{U}_E$	43.6	2.4	9.1	5.3	-3.8
$10^2 \cdot \bar{U}_\theta/\bar{U}_E$	85.6	5.8	17.3	3.1	-14.2
$10^2 \cdot \bar{U}_r/\bar{U}_E$	27.8	3.9	14.8	7.8	-7.0
$10^2 \cdot \kappa/\bar{U}_{av}^2$	33.3	2.5	10.4	4.5	-5.9
$10^2 \cdot \overline{u_z u_z}/\bar{U}_{av}^2$	27.5	2.5	9.6	4.4	-5.2
$10^2 \cdot \overline{u_\theta u_\theta}/\bar{U}_{av}^2$	21.6	4.2	15.3	8.5	-6.8
$10^2 \cdot \overline{u_r u_r}/\bar{U}_{av}^2$	17.6	1.4	6.1	3.4	-2.7
$10^2 \cdot \overline{u_r u_\theta}/\bar{U}_{av}^2$	-8.3	1.7	5.8	5.8	0.0
$10^2 \cdot \overline{u_r u_z}/\bar{U}_{av}^2$	1.9	2.0	9.3	5.3	-4.0
$10^2 \cdot \overline{u_z u_\theta}/\bar{U}_{av}^2$	-9.3	1.3	5.6	2.0	-3.6

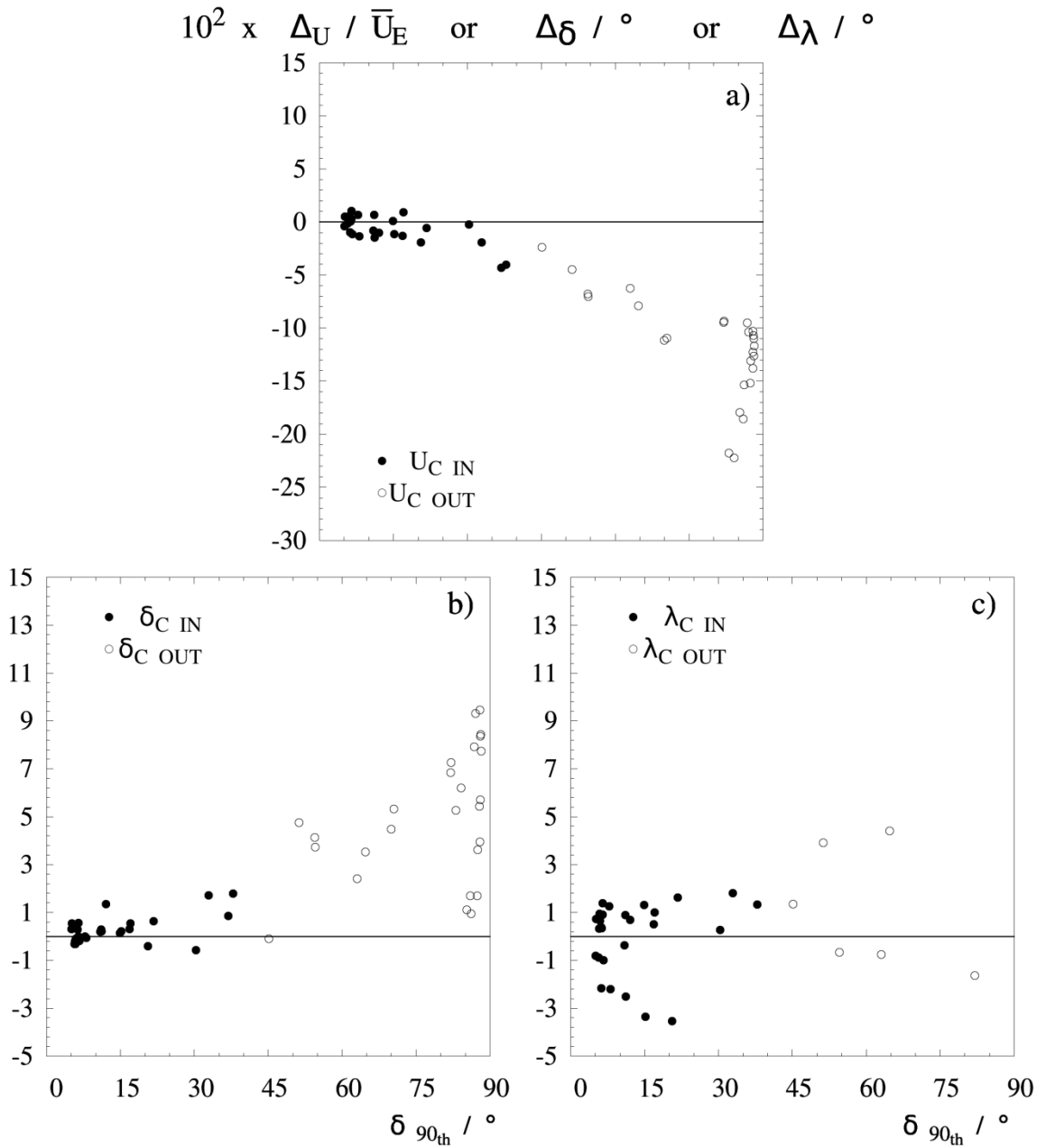


**Figure 23.** Correlation between errors in the velocity magnitude and direction and the attack angle,  $\delta_{90th}$ . C indicates calibrated mode. Filled symbols indicates data within recommended limits (i.e.  $\lambda_{90th} > 30^\circ$ ,  $\delta_{90th} < 50^\circ$ ). Normalised errors in Table 2 for a)  $\bar{U}$  b)  $\delta$  c)  $\lambda$ . Position  $r = 0.30 R$ ,  $\kappa / \bar{U}_{av}^2 = 0.061$ .

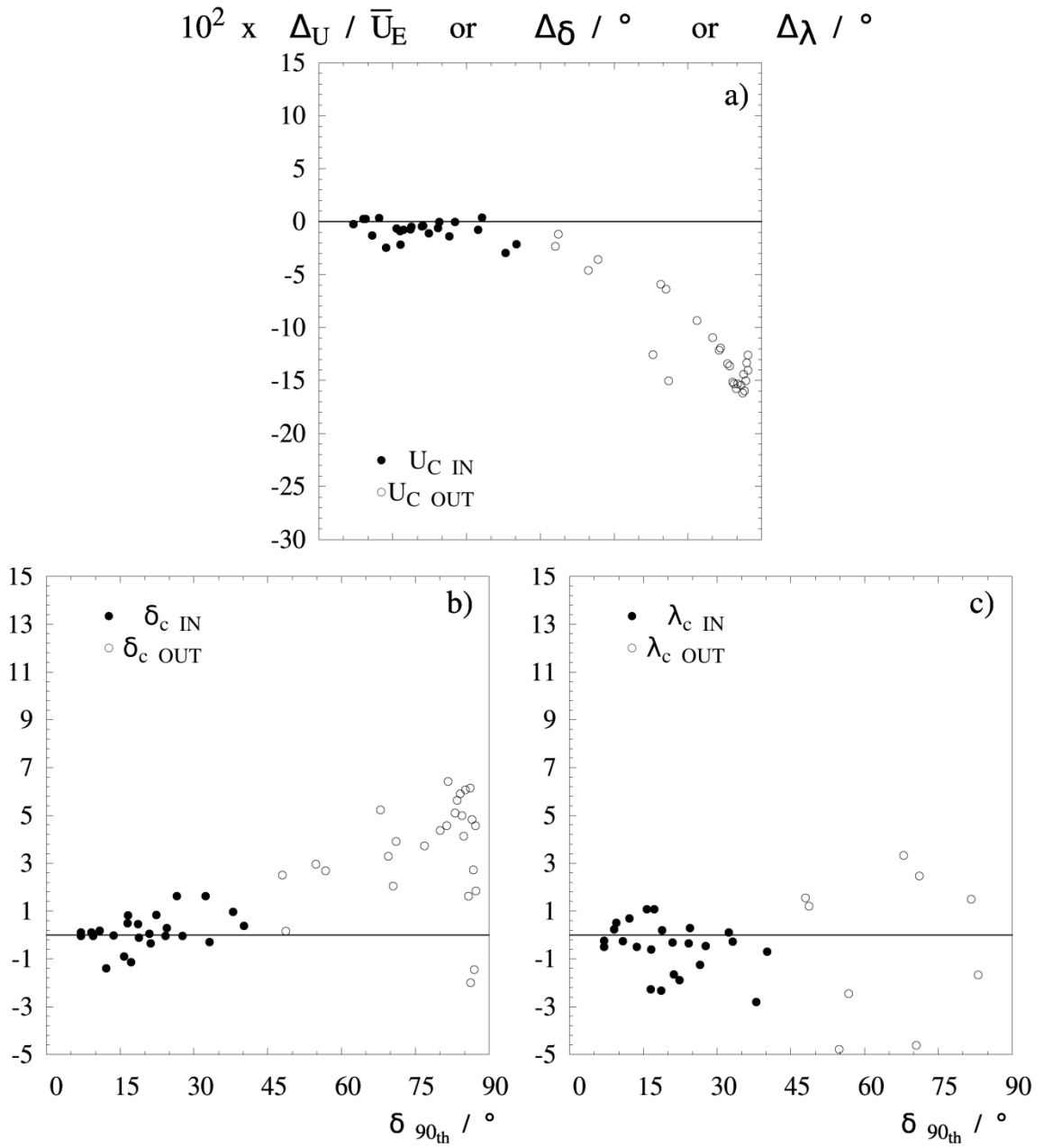


**Figure 24.** Correlation between errors in the velocity magnitude and direction and the attack angle,  $\delta_{90th}$ . C indicates calibrated mode. Filled symbols indicates data within recommended limits (i.e.  $\lambda_{90th} > 30^\circ$ ,  $\delta_{90th} < 50^\circ$ ). Normalised errors in Table 2 for a)  $\bar{U}$  b)  $\delta$  c)  $\lambda$ . Position  $r = 0.60 R$ ,  $\kappa / \bar{U}_{av}^2 = 0.090$ .

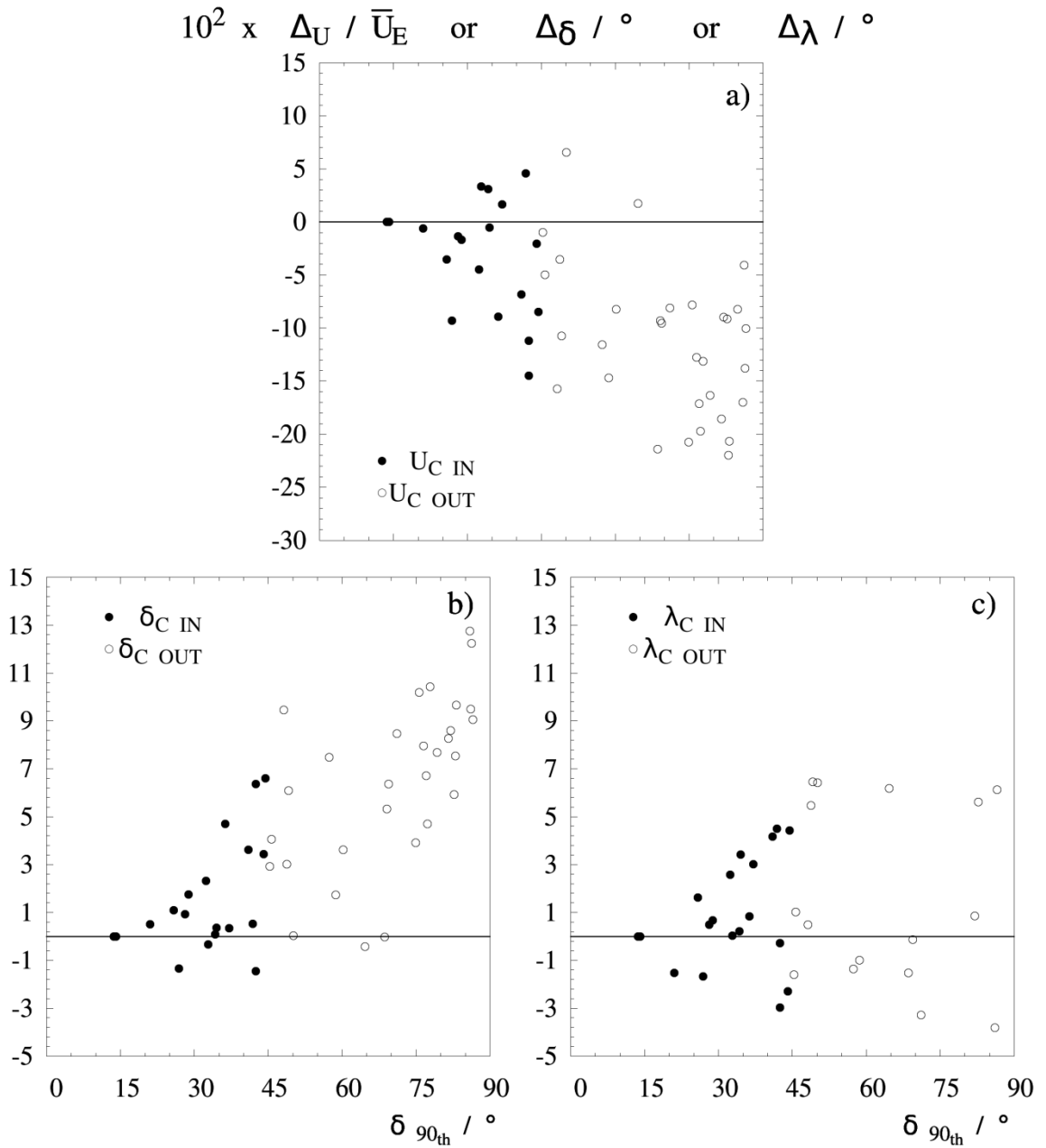


**Figure 25.** Correlation between errors in the velocity magnitude and direction and the attack angle,  $\delta_{90th}$ . C indicates calibrated mode. Filled symbols indicates data within recommended limits (i.e.  $\lambda_{90th} > 30^\circ$ ,  $\delta_{90th} < 50^\circ$ ). Normalised errors in Table 3 for a)  $\bar{U}$  b)  $\delta$  c)  $\lambda$ . Position  $r = 0.10 R$ ,  $\kappa / \bar{U}_{av}^2 = 0.333$ .

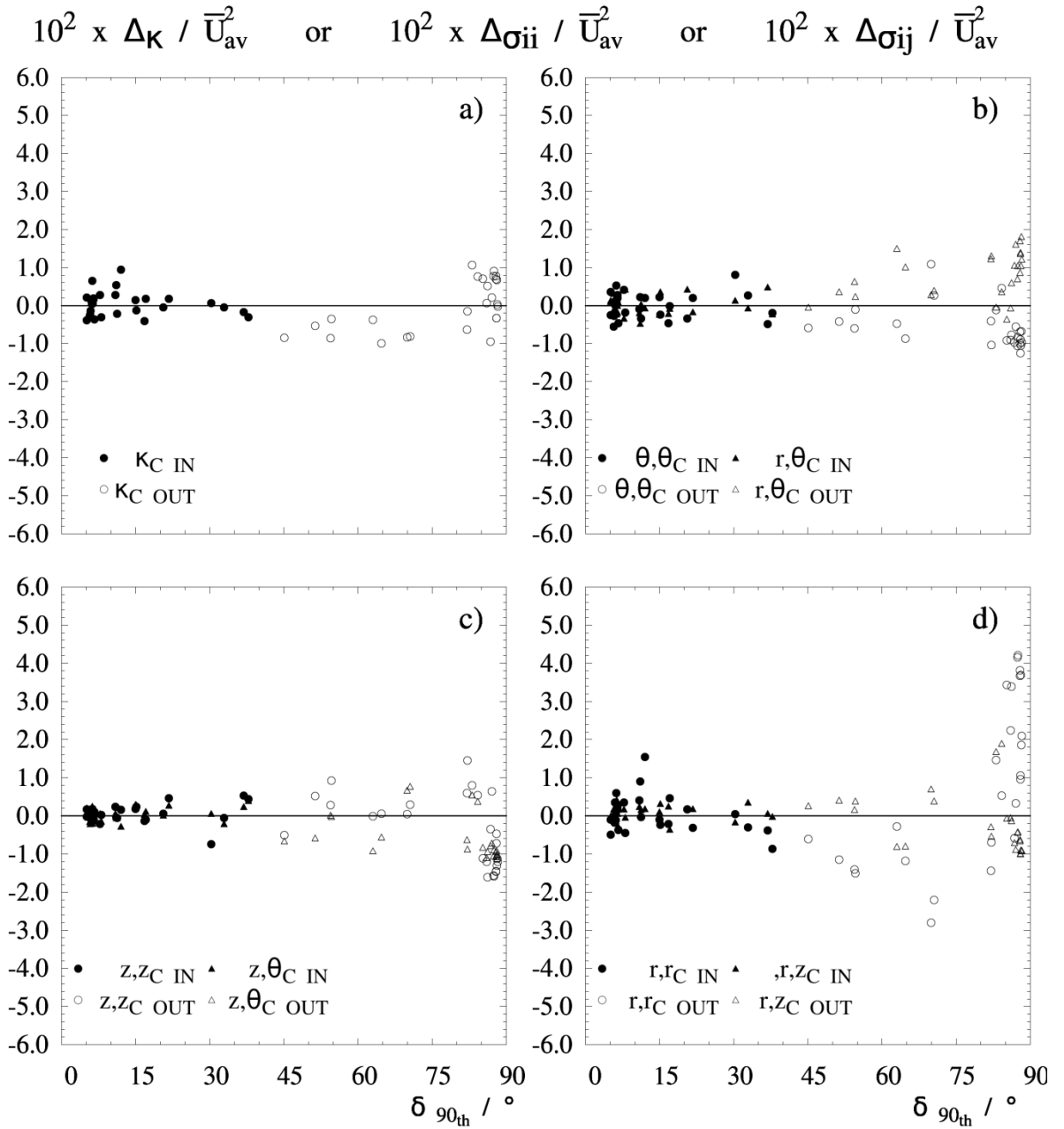


**Figure 26.** Correlation between errors in variability and the attack angle,  $\delta_{90th}$ . C indicates calibrated mode. Filled symbols indicates data within recommended limits (i.e.  $\lambda_{90th} > 30^\circ$ ,  $\delta_{90th} < 50^\circ$ ). Normalised errors in Table 2 for a)  $\kappa$ , b)  $\sigma_{\theta, \theta}$ ,  $\sigma_{r, \theta}$  c)  $\sigma_{z, z}$ ,  $\sigma_{z, \theta}$  d)  $\sigma_{r, r}$ ,  $\sigma_{r, z}$ . Position  $r = 0.35 R$ ,  $\kappa / \bar{U}_{av}^2 = 0.061$ .

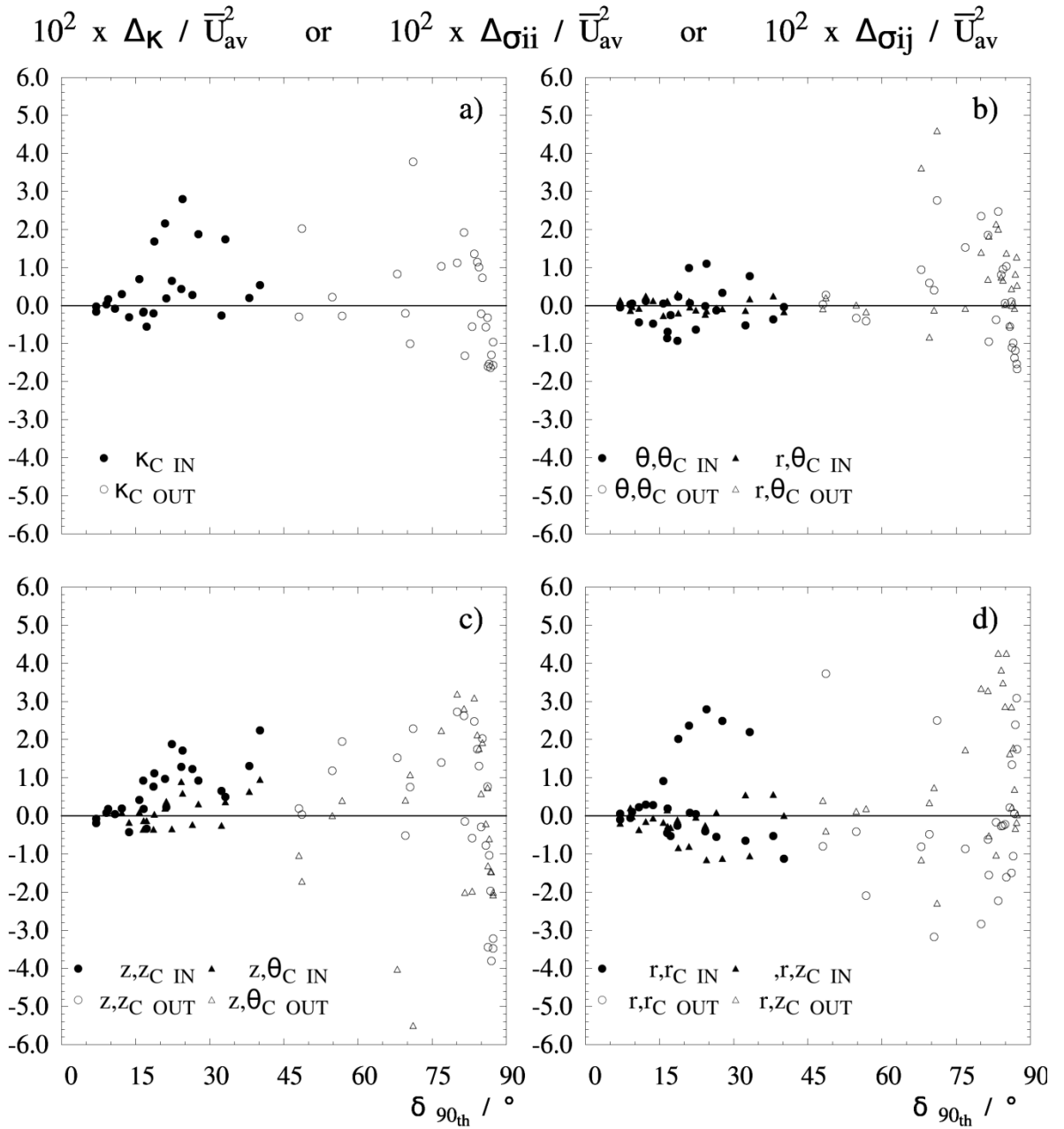


**Figure 27.** Correlation between errors in variability and the attack angle,  $\delta_{90th}$ . C indicates calibrated mode. Filled symbols indicates data within recommended limits (i.e.  $\lambda_{90th} > 30^\circ$ ,  $\delta_{90th} < 50^\circ$ ). Normalised errors in Table 2 for a)  $\kappa$ , b)  $\sigma_{\theta, \theta}$ ,  $\sigma_{r, \theta}$  c)  $\sigma_{z, z}$ ,  $\sigma_{z, \theta}$  d)  $\sigma_{r, r}$ ,  $\sigma_{r, z}$ . Position  $r = 0.60 R$ ,  $\kappa / \bar{U}_{av}^2 = 0.090$ .

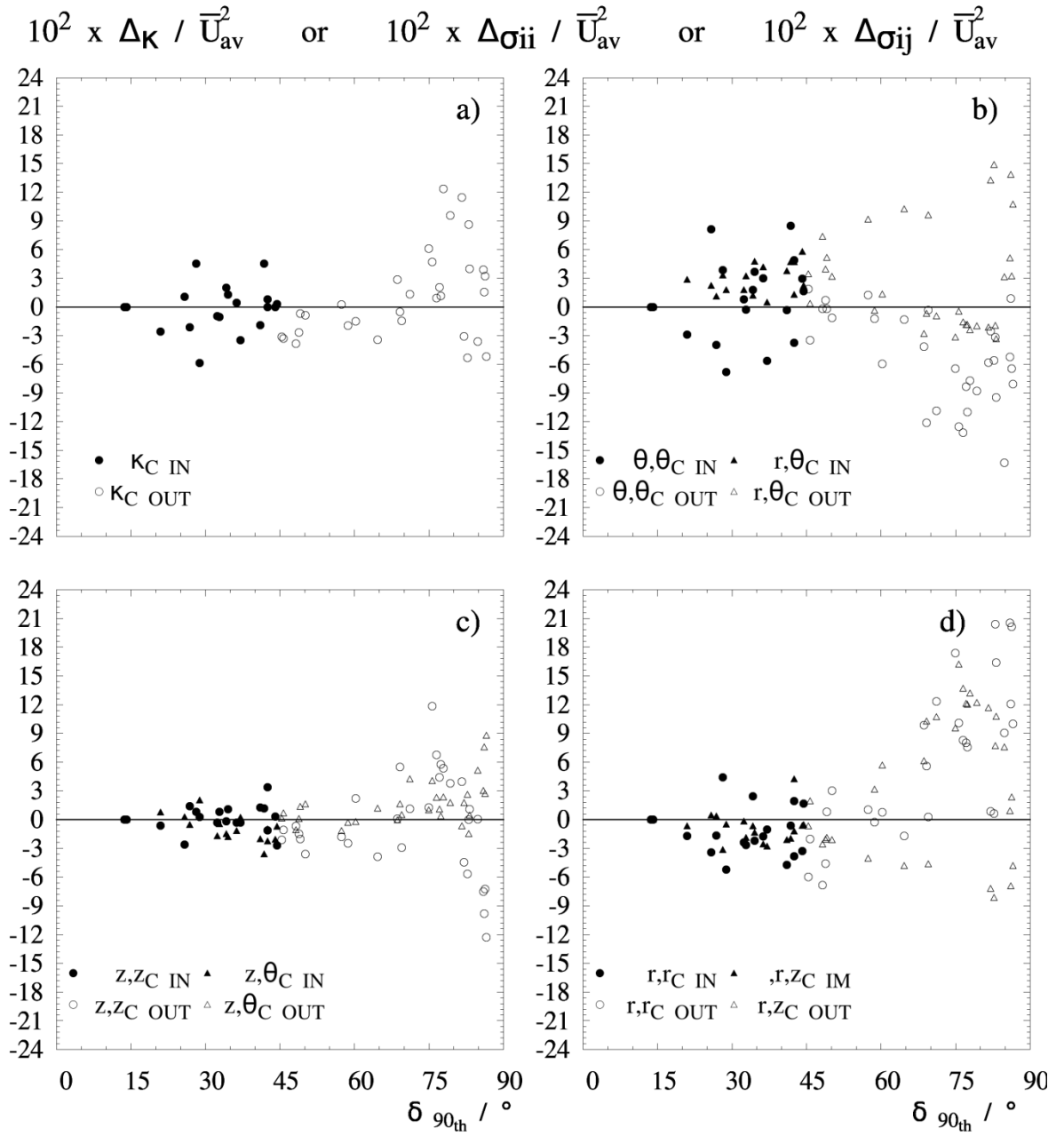


**Figure 28.** Correlation between errors in variability and the attack angle,  $\delta_{90_{th}}$ . C indicates calibrated mode. Filled symbols indicates data within recommended limits (i.e.  $\lambda_{90_{th}} > 30^\circ$ ,  $\delta_{90_{th}} < 50^\circ$ ). Normalised errors in Table 3 for a)  $\kappa$ , b)  $\sigma_{\theta,\theta}$ ,  $\sigma_{r,\theta}$  c)  $\sigma_{z,z}$ ,  $\sigma_{z,\theta}$  d)  $\sigma_{r,r}$ ,  $\sigma_{r,z}$ . Position  $r = 0.10 R$ ,  $\kappa/\bar{U}_{av}^2 = 0.33$ .

not the central region. This may be related to impact of the precession of the vortex core, *PVC*, described in many strong swirling flows and discussed in detail in Chapter II. It seems reasonable to believe that when the frame crosses the core and breaks this oscillation it shall disrupt the transport of turbulence in the plane  $r\theta$ . Measurements taken from the opposite side of the wall may be adequate to obtain a rough indication of the velocity, but do not provide a reliable report of the variability.

### 3.4. Use of internal correction functions.

Figures 8 to 13 include examples of the effect of the use of the in-built calibration. It reduces the error in the velocity magnitude for moderate angles of attack, increasing  $U_{a_3}$  as a function of the values of  $\delta$  and  $\lambda$ . In this particular case, it is not seen to reduce the error in turbulence statistics.

Cuerva *et al.* (2004) describes that in a head design with narrow angles between the transducers, the functions used in wind tunnel calibrations carry implicit certain mathematical singularities. Specific combinations of velocity gradients and orientations reduce the determinant of the Jacobian used in the correction to a null value. In such cases, the measurement is distorted because after applying the correction, it is not possible to recover certain wind directions that have simply become undefined.

A similar phenomenon associated to the use of the calibration has been observed here. It occurs rarely and in locations where the direction of the tangential velocity changes sign (i.e. towers with a different swirl sense or crossing over the tower centreline). It is illustrated in Figure 30 by the comparison of the population of  $\delta$  in cases close the limits, for raw and calibrated measurements. Undefined directions occur in proximity to the limit angles, and thus the restrictions already given ensure no further errors.

### 3.5. Shift in the sonic pulse.

The working principle of commercial anemometers is strictly applicable only when the velocity of the medium across the sonic path is constant. Otherwise, the pulse is shifted and the derivation of the time-of-flight requires from the integration of the propagation velocity. This can be done if the field is known *a priori*. Franchini *et al.* (2007a, 2007b) quantify which is the error in ideal cases from assuming a negligible velocity gradient. It depends on the extent of the gradients and the symmetry and curvature of the velocity field. In general terms, it may be estimated in the order of the second power of the Mach number and for a low curvature, poses no major concerns for an industrial application such as this one.

In the analysis described in section 3.3.1, as the head revolves the linear paths start describing an arc across the cylinder circumference. When this occurs, the velocity gradient across the path increases by

$\bar{U} / \bar{U}_{av}$  or  $10 \times \kappa / \bar{U}_{av}^2$  or  $10 \times \sigma_{ii} / \bar{U}_{av}^2$  or  $10 \times \sigma_{ij} / \bar{U}_{av}^2$

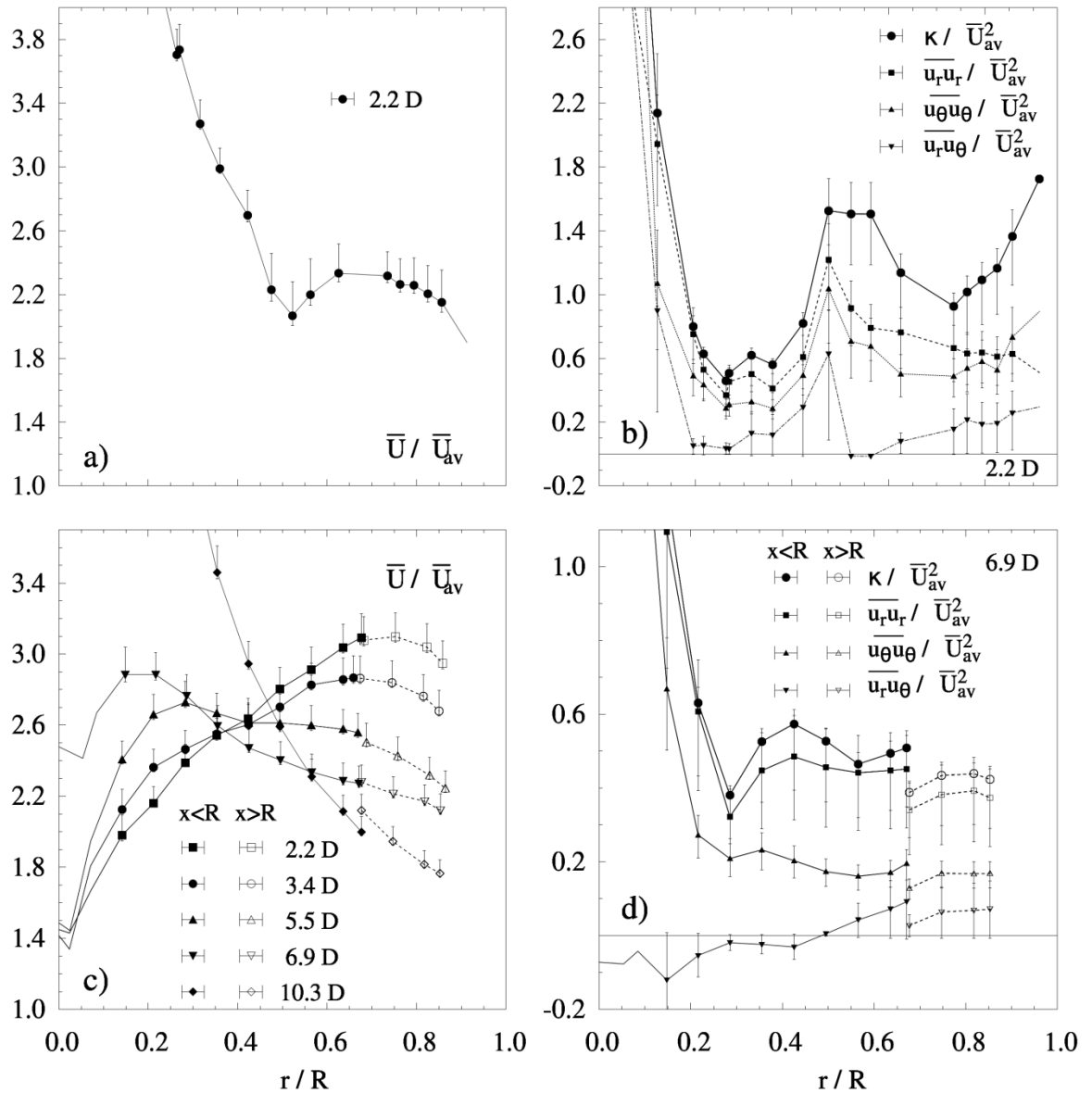


**Figure 29.** Illustration of the disruption to the transport of turbulence.  $x > R$  indicates the positions where the arrangement crosses the centre. Examples of the velocity and turbulence profiles for two different towers a-b) Scale I (Chapters I and II) and 4. c-d). Scale II (Chapters I and III). Normalised values of a-c)  $\bar{U}$ , in c-d)  $\kappa$ ,  $\sigma_{r\theta}$ ,  $\sigma_{rr}$  and  $\sigma_{r\theta}$ .

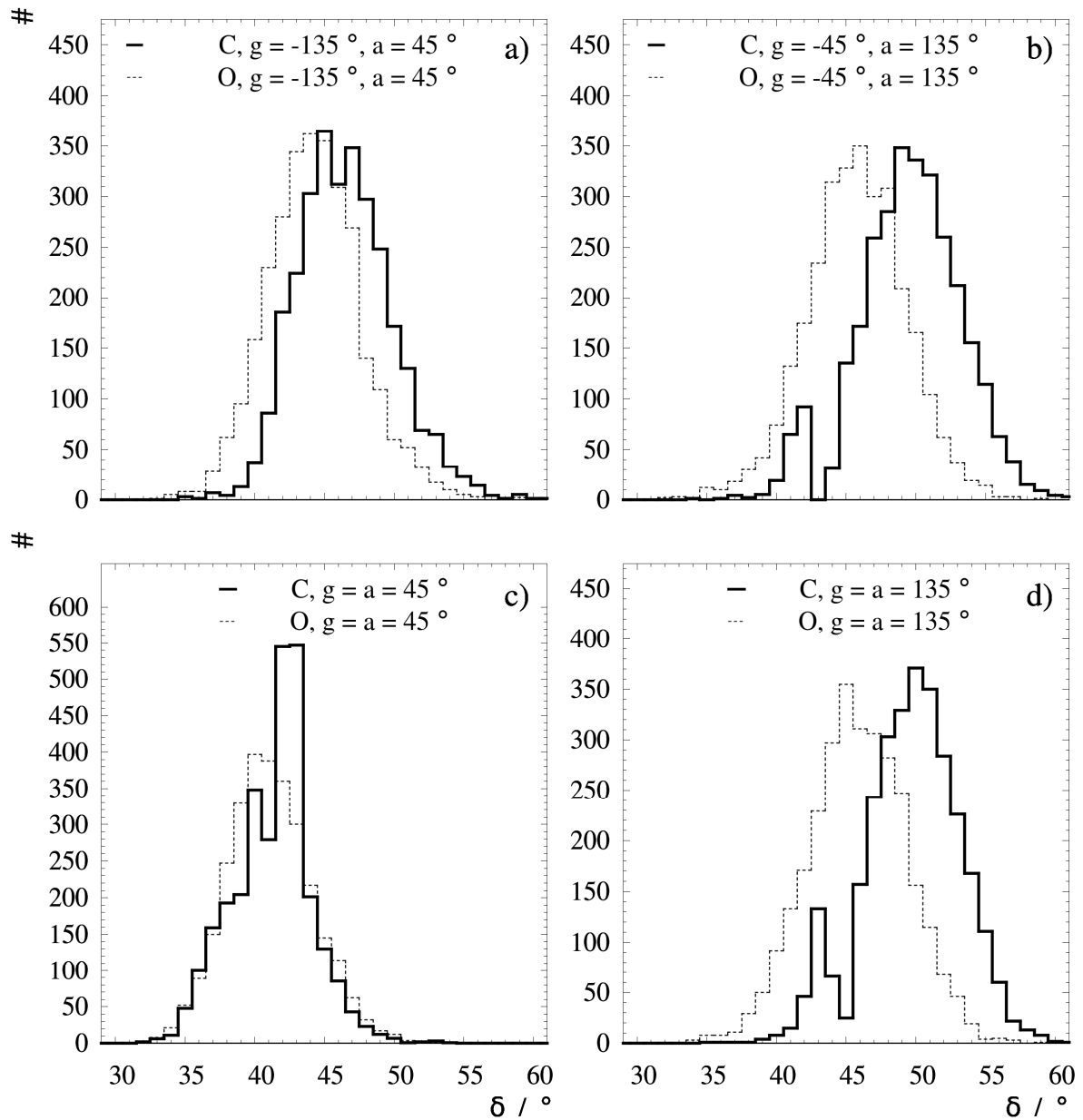


**Figure 30.** Example of the population of instantaneous attack angles  $\delta$ , obtained with and without the use of the calibration function. C and O denote calibrated and raw measurements. The pairs in a-c) and b-d) compare identical positions.

a factor of ten, because they are far larger in the radial than axial direction. The error owed to shift in the pulse is then blended within the aerodynamic disruption, and limited to the range given in Tables 2 and 3

The actual effect of a shift in the best estimates (i.e.  $g = 0^\circ$  where gradients are minimum) could only be quantified in a known flow field. However, a significant contribution can be discarded in this case, based on the following: 1-  $U_\theta$  is in good agreement with previous laser based reports in the same unit and conditions (Hassall, 2011), 2- the integration of  $U_z$  complies with the measurement of the volume rate, and 3- increasing gradients by a factor of ten during the revolution would lead to far larger errors if curvature was significant (Franchini *et al.* 2007a); in contrast it leads here to errors that are correlated to the transducers shadow in Section 3.3.1, and thus have an aerodynamic origin.

Nevertheless, the head,  $\alpha_1$  is aligned with the cylinder axis  $z$  to ensure gradients are minimised. In a long vortex as the one treated, axial gradients are  $< 0.1 s^{-1}$  while radial ones are  $< 10 s^{-1}$ . The exceptions are the core,  $r < 0.10 R$ , the boundary layer (estimated by Hassall 2011 as  $r < 0.98 R$ ) and the vicinity of the exit contraction,  $z > 0.95 H$ . In these areas the gradients are substantially higher and the measurement may carry a higher error.

## Conclusions

This work introduces sonic anemometry to characterization of industrial swirling flows. It describes the application to a large confinement, the adequate transformations and provides a conservative error analysis. Maximum levels of uncertainty are reported as a function of the turbulence level for the annular section of a vortex with the a “concentrated” shape described in Chapters II and III. Certain regions are excluded where gradients and curvature may have an impact upon sonic pulse: the inner force vortex,  $r < 0.10 R$ , the boundary layer,  $r < 0.98 R$  and regions nearby the contraction,  $z > 0.95 H$ .

The uncertainty limits in the annular and outer regions are  $< 1 - 4 \%$  in  $\bar{U}$ ,  $\pm 3^\circ$  in direction and  $\pm 7 - 31 \%$  in  $\kappa$ , considered sufficient for design and engineering applications. Errors arise from the intrusive nature of the technique and are correlated to the disposition of the transducers. The local disruption has been linked to the geometry and orientation of the instrument. Interestingly the errors depend on the sense of the axial flow against the anemometer, indicating that a definition of  $\delta$  from  $0 - 180^\circ$  would be more appropriate. The maximum uncertainty ranges however cover this effect and can be reported on the basis of the usual definitions of  $\delta$  and  $\lambda$ , given by manufactures. In this case, the limits are restricted to  $\delta_{90th} < 45^\circ$  and  $\lambda_{90th} > 30^\circ$ . Other sources of error studied include the

---

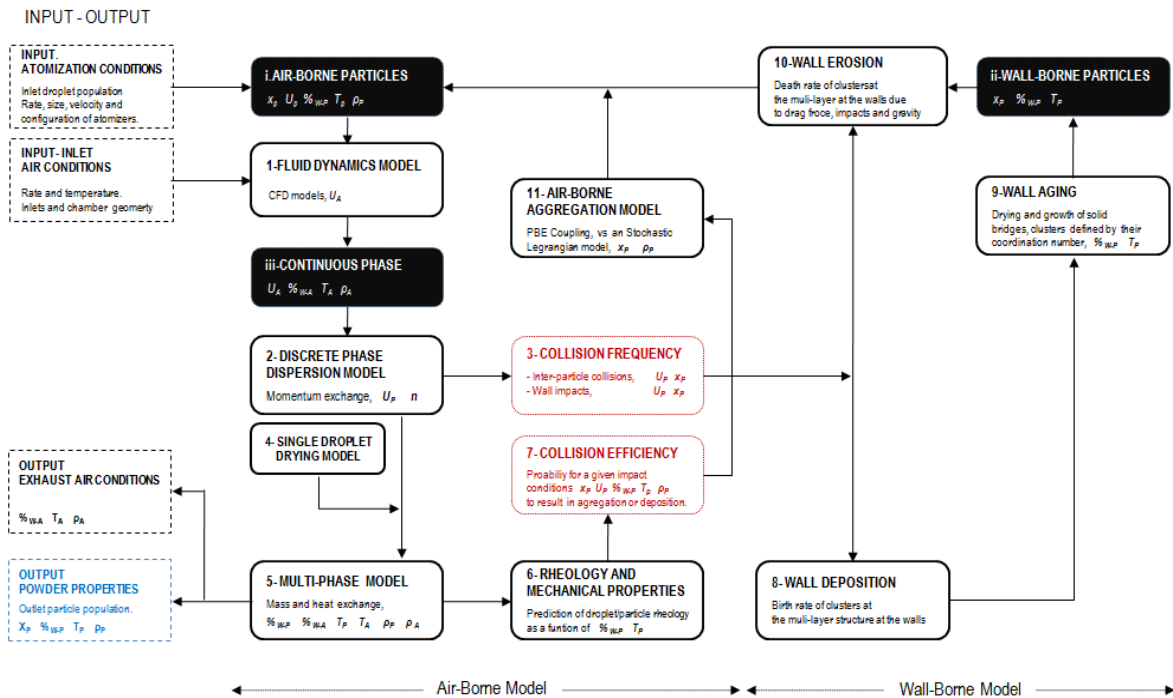
effect of large oscillations in the flow field due to time averaging and the presence of singularities in the use of the calibration function.

The data given in the Part A underscore the ability of this method to identify not only the main features of a large turbulent vortex, but specific phenomena such as asymmetries, the decay of the swirl or aerodynamic instabilities. This level of detail can be obtained in a much simpler fashion and far lower costs than with any laser based technique. To illustrate the context: in a full scale production dryer one may consider the use of dozens of Pitot tubes or a vane or cup-and-bowl anemometer during several hours or a period of days. Such data, along with flow visualization methods are still the most commonly used in scale up, evaluation of new designs or validation of large numerical models. In some cases, alternatives may include hot wire anemometry but seldom engineer new transparent accesses, cleaning devices or mounting rails to support laser measurements over weeks or months. In this context, the method described here represents a major improvement.

This work provides an opportunity to improve the frequency and quality of full scale validation of complex industrial air flow fields. It is worth pointing out once more to the conclusions of the Part A of this thesis. The conduction of *PIV* experiments conducted in the same unit observed an abnormally weak swirl versus the data of Bayly *et al.* (2004) in laboratory units or the numerical models based on smooth walls (Hassall, 2011). However, the complexity of the optics, cost and time restrictions constituted serious challenges for *PIV* to provide a full picture of the flow structure and thus be conclusive. This example may highlight the relevance of obtaining data at production units and the need of adapting the techniques available to deal with a large scale as a whole, retaining sufficient accuracy for the issues at hand, rather than implementing a restricted use of a more complex arrangement. It is only then that actual scale up issues such as those described in Part A may come to light.

# APPENDIX II:

## ANALYSIS OF THE PARTICLE STRUCTURE AND THE GENERATION OF POROSITY.



## Summary

Understanding how the porosity is generated in spray dried detergent granules is an extremely relevant matter for manufactures. This appendix provides supporting data in particle density and morphology for selected cases: the operation of a single nozzle ( $S_2$  in Chapters V and VI) or a multi-level system ( $M_{13}$  in Chapter VI).

At the end of this appendix Figures 6 to 25 provide micrographs of the different size classes in the powder. The heterogeneity of the primary droplets is discussed and it is linked to the different shapes and type of contacts observed in the aggregates. They show complex non-spherical structures and large cavities owe to aggregation. In fact, two sources of porosity have been identified, associated to drying and the formation of low density structures during agglomeration.

The intra-particle porosity  $\varepsilon$  contained in pores  $< 9\mu m$  is found  $\sim 23 - 27\%$  and attributed to drying, whilst the total averaged values rise to  $\sim 37\%$ . The product in a multi-level system  $M_{13}$  shows a higher  $\varepsilon$  for the fractions  $> 350\mu m$ , and presents a different pore size distribution. It is clear from the data that at least for the particles  $> 600\mu m$  aggregation is large contributor to the production of high porosities. Furthermore, the values of  $\varepsilon$  are no higher than the volume of water removed from the droplets, which provides no evidence to support that droplet inflation occurs during boiling.

## 1. Analysis of particle morphology.

Chapter IV lists the techniques used to study the structure, including the measurement of particle density and observation of granules under microscopy. At the end of this appendix, Figures 6 to 25 provide a series of micrographs for each size class analysed, comparing one single nozzle production,  $S_2$  (Chapter VI and Appendix III) to one multi-level production  $M_{13}$  (Chapter VI).

The same general trends can be observed. Most of the powder is clearly a product of agglomeration, including the primary size more (between  $300 < x_p < 425 \mu m$ , Chapter VI). In general no primary droplets / particles can be seen in the product for size fractions  $> 450 \mu m$ , see Figures 17 to 25.

### 1.1 Shape

One can have an idea on how the primary droplets are by looking at the morphology of the elutriated powder in Figures 7 and 8. It is clear these are very heterogeneous. They contain ligaments, see Figures 7-11, 7-13, 8-9 or 8-12, amorphous structures, see Figures 7-14, 7-15 or 8-14, and spherical small drops, see Figures 7-10 or 7-15 or Figure 8. In some cases, one can also see hollow spherical particles with a clearly different composition. This is attributed to the drops that contain only the aqueous phase of the slurry, see Figures 7-18 or 8-16. Such heterogeneous set of droplets agrees well with the solid-liquid separation identified in Chapter VI. The effects are particularly clear in  $M_{13}$ , Figure 8: here one can distinguish many spherical drops and how they form grape-like aggregates, see Figure 8-17.

The ligaments also appear in the product, but they are much less frequent, see Figures 9 and 11. They now have turned into coiled structures, see for instance in 11-14 or in many cases have become part of larger particles, see for instance Figures 12-13, 13-16 or 13-17 and 10-16.

One can also identify primary particles in the fine powder fractions, given in Figures 9 to 14, and many of the small aggregates that are formed only by a few of them, see for instance Figures 15 or 16. However, in most of the cases the aggregates in the product contain many primary particles, particularly when one moves into the larger granules in Figure 17 and above. The grape-like structures observed in the elutriates are very rare and appear only in the smallest size fractions of the product, see Figure 11-15. In general the morphology of agglomerates is far more complex, in part because the droplets are non-spherical and deformable, and also because the ligaments coil around the particle. The Figures 11-13, 11-14, 12-6, 13-9 or those showing the larger granules, Figures 16-10, 16-13, 16-6 or Figures 17-13 to 17-16, provide good examples of the typical morphologies.

In the coarsest fractions, primary particles are themselves larger and in many cases the agglomerates formed show high aspect ratios, see Figures 21-9 or 21-10. In this case this is not related to any ligament as it happens in the fine powder. It is perhaps a consequence of the way the material is worn off the walls.

### **1.2 Contacts and aggregates**

The aggregates contain cavities formed in between the primary particles, see for instance Figures 6-10 to 6-12, 18-13 or 18-14, or the larger sizes Figures 19 or 21. This contributes significantly to reducing their density and it is an important characteristic of the product. It is interesting to note that the cavities are in many cases larger than the primary particles themselves, see for instance voids between 100 – 200  $\mu m$  in granules between 850 – 1180  $\mu m$  in Figure 21-15 or between 100 – 300  $\mu m$  in granules between 1180 – 1800  $\mu m$  in Figures 24-10, 25-8, 25-9 or 25-12. It has been pointed throughout this thesis that this can easily make particles inter-lock in flight or at the walls.

The primary particles are bound together by solid bridges and in many cases they show large contact areas and evidence of diffusion. Figure 13-10 or 13-18, 14-15, 19-17 or 19-18, show good examples of the contacts and explain how large granules such as those in Figures 21 or 22 can be formed. This sort of structures agrees well with the description that Palzer (2011) gives about particle deformation and fast sintering during spray drying. The solid bridges must have been formed either by a long contact time, which allows diffusion to occur (perhaps at the wall), or after drying of the viscous bridges established in a fast sintering process or due a large deformation at the contact.

### **1.3 Drying and breakage**

Two sources of porosity can be distinguished: that associated to drying in the primary particles and that associated by the cavities owed to aggregation.

Primary droplets transform in a porous matrix as drying removes the water. It is widely accepted that they follow an initial shrinkage period, named “constant rate period”, followed by a later “falling rate period” where the evaporation reduces due the formation of a hard outer crust (Kadja and Bergeles 2003, Dalmaz *et al.*, 2007, Mezhericher *et al.*, 2007, Handscomb *et al.*, 2009). This happens at a given content in solids characteristic of the formula, and according to Walton and Mumford (1999) it arrests the shrinkage in particles that form crystalline structures as they dry. Different authors have proposed different mechanisms after the crust is formed. Mezhericher *et al.* (2010) review the more common

approaches for a numerical description. Earlier models considered either diffusion of water to the crust and the formation of concentration gradient (e.g. Meerdink and Riet 1995) or a receding inner interface that thickens the crust (e.g. Nesci and Vodnik 1991 or Farid 2003). More recently, authors such as Mezhericher *et al.* (2008) have included both mechanisms by considering the formation of pores in the shell from which vapour diffuses out, or how the migration of the solids to the surface can also be responsible of the crust formation (Handscorn and Kraft 2010).

In any case, as drying progresses, the droplet porosity increases and therefore the maximum porosity that can be achieved is the volume of water displaced. However, if heat transfer is rapid enough a droplet may be heated to its boiling temperature  $T_{Boil}$  causing the formation of vapour. The increase in pressure can be relieved by bubbles bursting out, what leaves behind cavities but produces no further porosity, or it can inflate the droplet if the crust is elastic (e.g. Hecht and King 2000). Indeed, the evolution thereafter depends greatly on the properties of this shell. Most authors determine them a priori, but Handscomb *et al.* (2009) and Handscomb and Kraft (2010) provide a model based on their evolution. When the droplet dries further the crust may lose elasticity. In this case when the particle cools down and the pressure drops, it remains inflated and shows higher porosities. Different evolutions are also possible. Let us point to two of the limiting cases described by Handscomb *et al.* (2009): 1- a crust that remains inelastic: here a bubble forms at the core and the solids migrate to the surface, leading to a hollow particle that may or not burst, but remains un-inflated, or 2- a crust that remains elastic: here, the particle inflates when it boils but after cooling it collapses.

The product presents many of the structures described above. Typical collapsed drops can be identified in Figures 9-18 or 11-18, note the folded spheres. Hollow particles are also particularly visible in the fine powder, see Figures 9-16, 12-14 or 12-15. However, in reality, most of the product is simply not primary particles. It is then unclear how the evolution of aggregates responds to boiling. They all show a porous interior and hollow sections but it is difficult to establish whether inflation has had any effect. However, it is clear that in addition to this contribution owed to drying, the aggregates also show porosity contained in cavities between the primary particles. Both sources are analysed in sections 2 and 3.

## 2. Particle density

Table 1 summarizes particle density and the porosity between different pore size ranges. Figures 1 and 2 include a comparison to the bulk,  $\rho_{bulk}$ , and skeletal,  $\rho_{ske}$ , particle densities. These are computed

by Hg Porosimetry and correspond to the initial and the highest pressures in the intrusion cycle (i.e. corresponding to a pore diameter of  $353 \mu m$  and  $6 nm$  respectively). It is interesting to note in Figures 1 and 2 that  $\rho_{bulk}$  increases for particles  $> 850 \mu m$ . This is not the result of these having a different composition nor is related to packing. It is explained by the fact that such large granules start to contain a certain porosity in very large cavities  $> 353 \mu m$ , which cannot be accounted by  $\rho_{bulk}$ .

It is also worth noticing that there is a range of porosity only accessible by He pycnometry. The  $\rho_{abs}$  obtained by the compaction of the powder led to lower values than the skeletal density  $\rho_{ske}$  obtained in Hg porosimetry. Both were in general lower than that the values observed in He pycnometry.

Table 1 shows this general tendency. However, some of the samples showed large  $\rho_{ske}$  values, attributed to reproducibility issues due the heterogeneity of the powder. This has also been observed in the analysis of similar detergent granules and requires from a more detailed study. Nevertheless, the averaged  $\varepsilon$  values given in Table 1 can be considered as the expected range in the product. In general,  $M_{13}$  presents a higher porosity. The values reported at the large fractions suggest that the presence of cavities owing to agglomeration is a major contributor to the  $\varepsilon$ . Consider that in  $M_{13}$  a large part of the product in fact owes to the secondary size mode  $> 600 \mu m$  (see Chapter VI).

In all cases, the values of  $\varepsilon$  are lower than the volume of water displaced from the droplets. In this way it cannot be confirmed that the inflation of the droplets in fact occurs in this case, or whether it has any significant impact in the formation of porosity in the fine powder. It could be originated simply after the formation of the outer shell. In the coarser fraction, aggregation has clearly a more significant impact.

### 3. Pore size distributions

The pore size distribution are presented in Figures 3 and 4 for the cases  $S_2$  and  $M_{13}$ . The plots include the entire intrusion cycle to explain the criteria to compute particle densities. It is important to stress the difficulty in the calculation of the envelope density  $\rho_{env}$  and the intra-particle porosity  $\varepsilon$ . A threshold must separate the size of the pores from the size of voids between the particles. Sieved powder was used to cause a poor packing and make voids between particles much larger. In this way they are filled first when the Hg is pressurised and one can distinguish the first pick (i.e. the right hand side in the plots in Figures 3 to 5) from the rest of the volume, which is intruded into the pores. This is clear in the small particles see for instance Figure 3b and 3d or Figures 4b and 4d. It becomes more difficult in larger sizes because a part of the cavities become comparable in size to inter-particle voids

**Table 1.** Variation of particle density and porosity. Bulk, envelope and skeletal densities,  $\rho_{bulk}$ ,  $\rho_{env}$  and  $\rho_{ske}$ , obtained from Hg porosimetry, and absolute density,  $\rho_{abs}$  from He piconmetry. The particle porosity from the envelope to the absolute density is denoted,  $\varepsilon_{abs}$  and the range between the thresholds for envelope and skeletal density is denoted,  $\varepsilon_{ske}$ .

Mm	Single nozzle operation $S_2$ , Chapter V and VI						Multi-level operation $M_{13}$ , Chapter VI					
	kg/m <sup>3</sup>				%		kg/m <sup>3</sup>				%	
Top size	$\rho_{bulk}$	$\rho_{env}$	$\rho_{ske}$	$\rho_{abs}$	$\varepsilon_{ske}$	$\varepsilon_{abs}$	$\rho_{bulk}$	$\rho_{env}$	$\rho_{ske}$	$\rho_{abs}$	$\varepsilon_{ske}$	$\varepsilon_{abs}$
Elutriated	0.67	0.97 <sup>1</sup>	1.79	1.76	45	45	0.74	1.05 <sup>1</sup>	1.90	1.78	45	41
< 152	0.67	0.92 <sup>2</sup>	1.55	1.78	41	48	0.65	0.94 <sup>2</sup>	1.90	1.79	51	48
152- 250	0.68	1.33 <sup>2</sup>	1.79	1.89	26	30	*	*	*	1.87	*	*
250- 355	0.61	1.26 <sup>3</sup>	1.68	1.92	25	35	*	*	*	1.93	*	*
355- 450	*	*	*	1.93	*	*	0.58	1.15 <sup>3</sup>	1.91	1.96	40	41
450- 600	0.56	1.20 <sup>4</sup>	1.77	1.93	32	38	0.57	1.15 <sup>4</sup>	1.86	1.94	38	41
600-850	0.61	1.18 <sup>4</sup>	1.69	1.91	30	38	0.62	1.00 <sup>4</sup>	1.85	1.92	46	48
850-1180	0.69	1.11 <sup>4</sup>	1.56	1.92	29	42	0.76	1.14 <sup>4</sup>	1.81	1.91	37	40
1180-1800	0.88	1.17 <sup>4</sup>	1.69	1.93	31	39	0.94	1.07 <sup>4</sup>	1.78	1.91	40	44
1800-2500	0.81	1.14 <sup>4</sup>	1.62	1.91	30	40	0.86	1.07 <sup>4</sup>	1.65	1.91	35	44
2500-4000	1.15	1.31 <sup>4</sup>	2.01	1.91	35	31	1.19	1.27 <sup>4</sup>	2.07	1.93	38	34
> 4000	1.04	1.11 <sup>4</sup>	1.94	1.89	43	41	1.07	1.10 <sup>4</sup>	1.67	1.91	35	43
Average	0.67	1.19	1.71	1.90	30	37	-	1.19	2.10	1.90	43	-

<sup>1,2,3,4</sup> refer respectively to a pore threshold size to inter-particle cavities of 30.2, 33.0, 60.5, 90.7  $\mu m$ .

\* Samples showing reproducibility issues.

see Figure 3c or 4c. In the coarsest granules (Figures 3a or 4a) this is not an issue because the inter-particle voids are filled at the initial pressure, and the entire volume shown enters cavities and pores.

A threshold has been set in all cases according to the size of the pores observed under microscopy and in a conservative manner, i.e. trying to ensure  $\varepsilon$  is under-predicted. The values of  $\varepsilon_{abs}$  represent the volume contained in pores or cavities smaller than the thresholds given in Table 1. One should stress that in the case of the largest fractions this does not include a part of the cavities, too large to be measured. To keep values comparable, the maximum threshold was kept as 90  $\mu m$  cavities.

The coarsest product in  $S_2$  shows two clear maxima in its pore size distribution, see Figure 3a. One owes to large cavities due to aggregation, 60.5 – 90.7  $\mu m$ , and another in a micron range around 0.8  $\mu m$  owing to drying. In most of the product, the porosity attributable to the micron pores < 9  $\mu m$  ranges between  $\varepsilon_{abs} = 23 - 27\%$ , and decreases only for granules > 2500  $\mu m$  to  $\varepsilon_{abs} = 15\%$  for pores < 20  $\mu m$ . The micron range porosity appears at the same pore sizes in the finest powder, compare Figures 3a and 3b. This agrees well with the presence of fragments in the small fractions described in Chapter VI. Both maxima are distinguishable in Figure 3a because the large

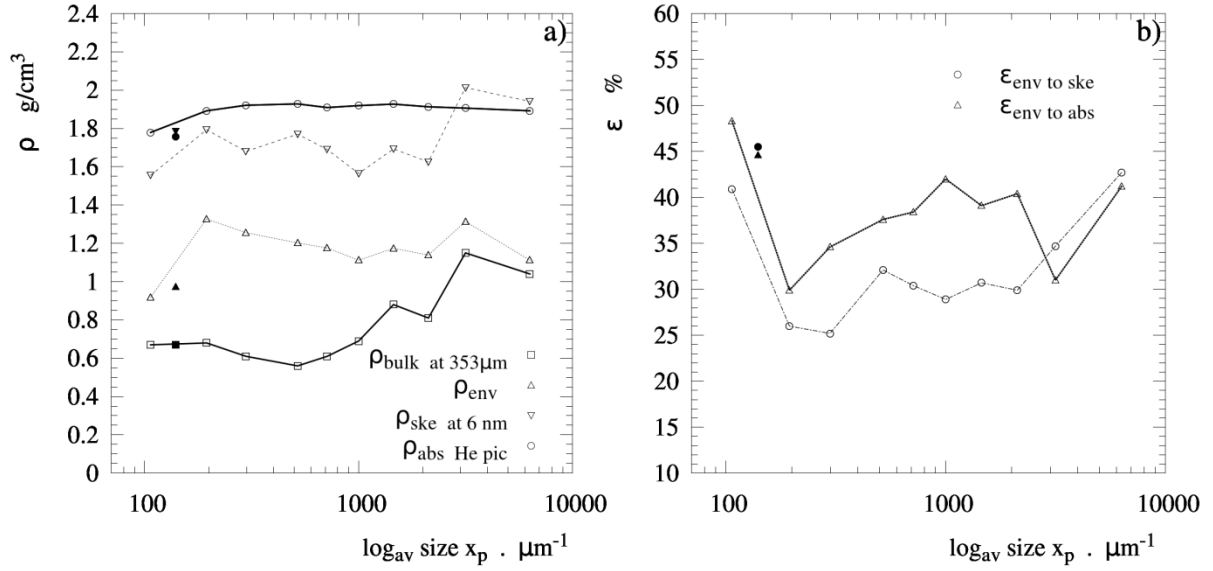


Figure 1.  $S_2$ . Variation across as a function of size of particle a)  $\rho$  b)  $\epsilon$ . For definitions see the nomenclature.

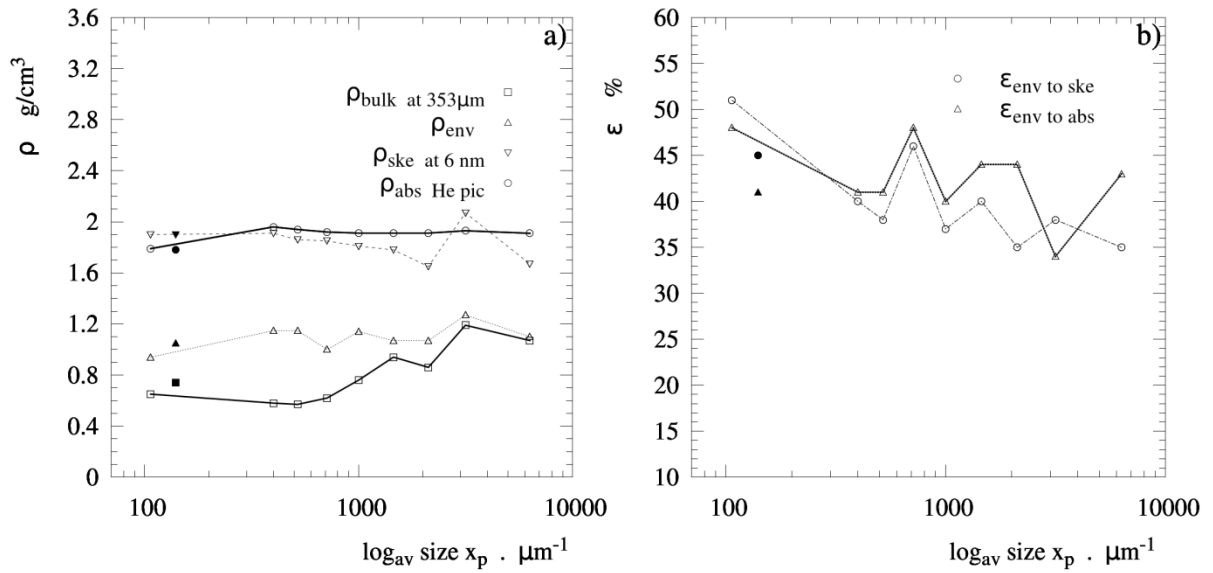
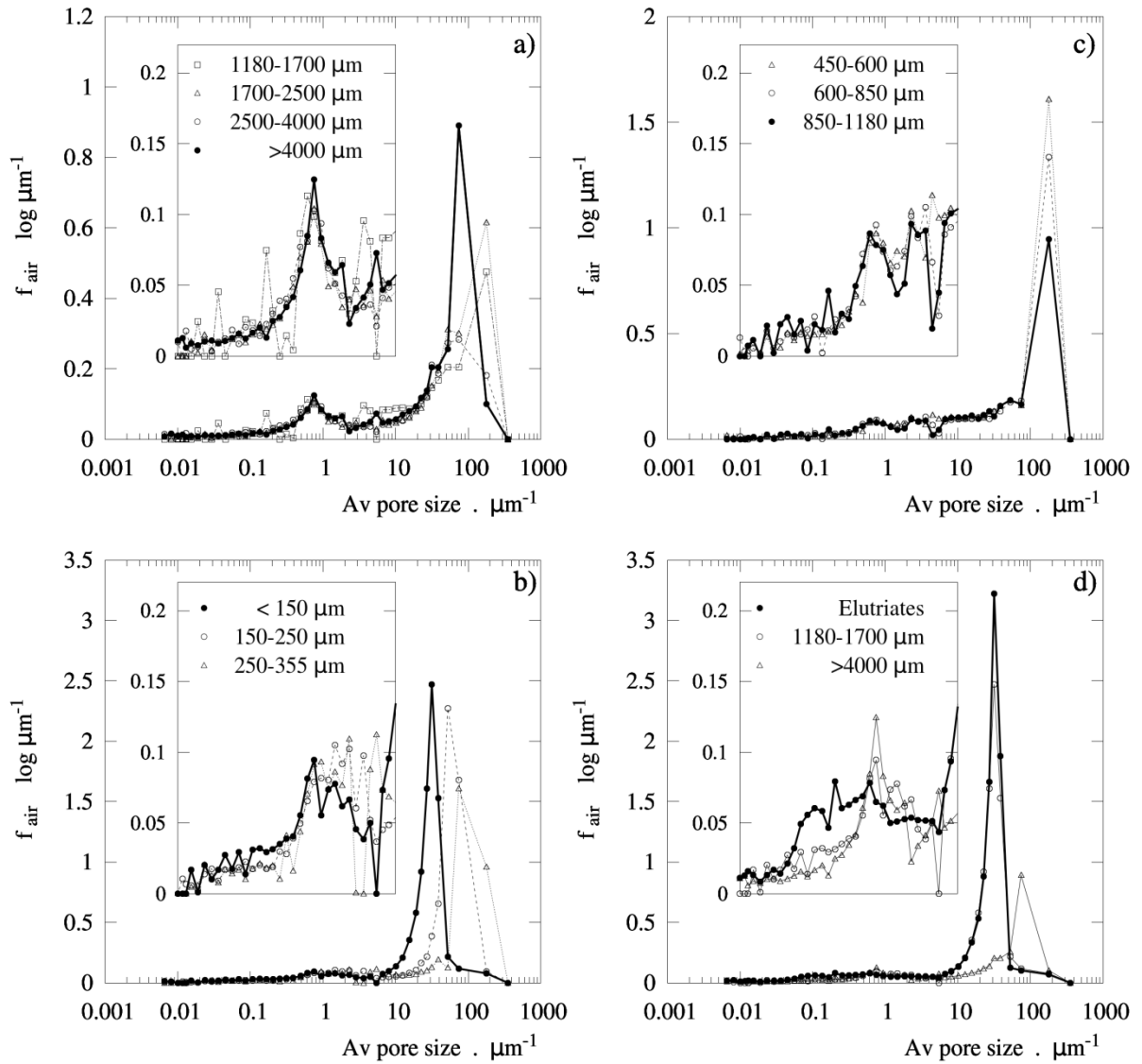
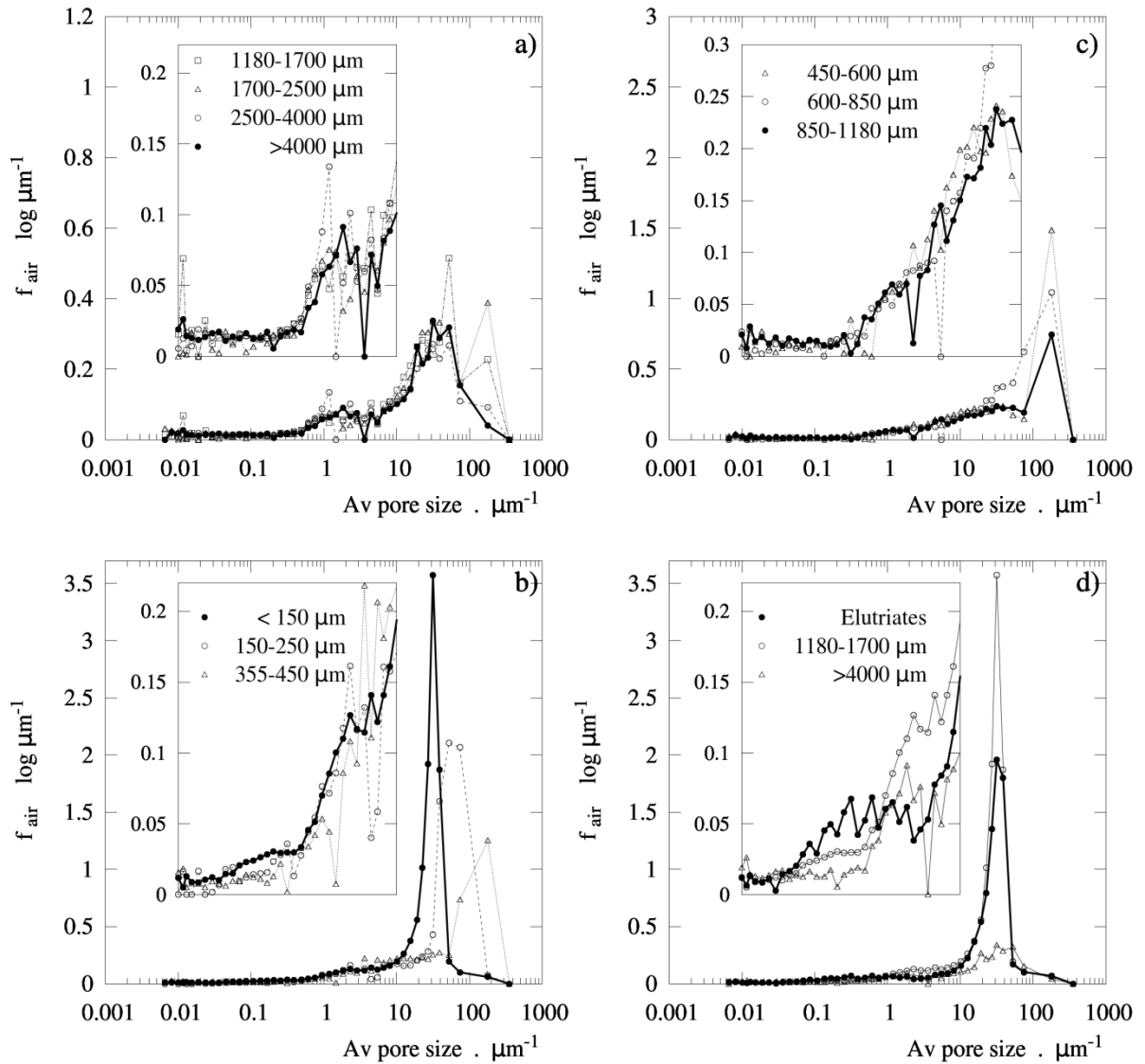


Figure 2.  $M_{13}$ . Variation across particle size fractions of particle a)  $\rho$  b)  $\epsilon$ . For definitions see Table 1.



**Figure 3.** Intrusion curves of Hg for the product in a single nozzle operation  $S_2$  a) large size fractions b) small size fractions c) average size fraction and d) comparison to the elutriates.



**Figure 4.** Intrusion curves of Hg for the product in a multi-level nozzle operation  $M_{13}$  a) large size fractions b) small size fractions c) average size fraction and d) comparison to the elutriates.

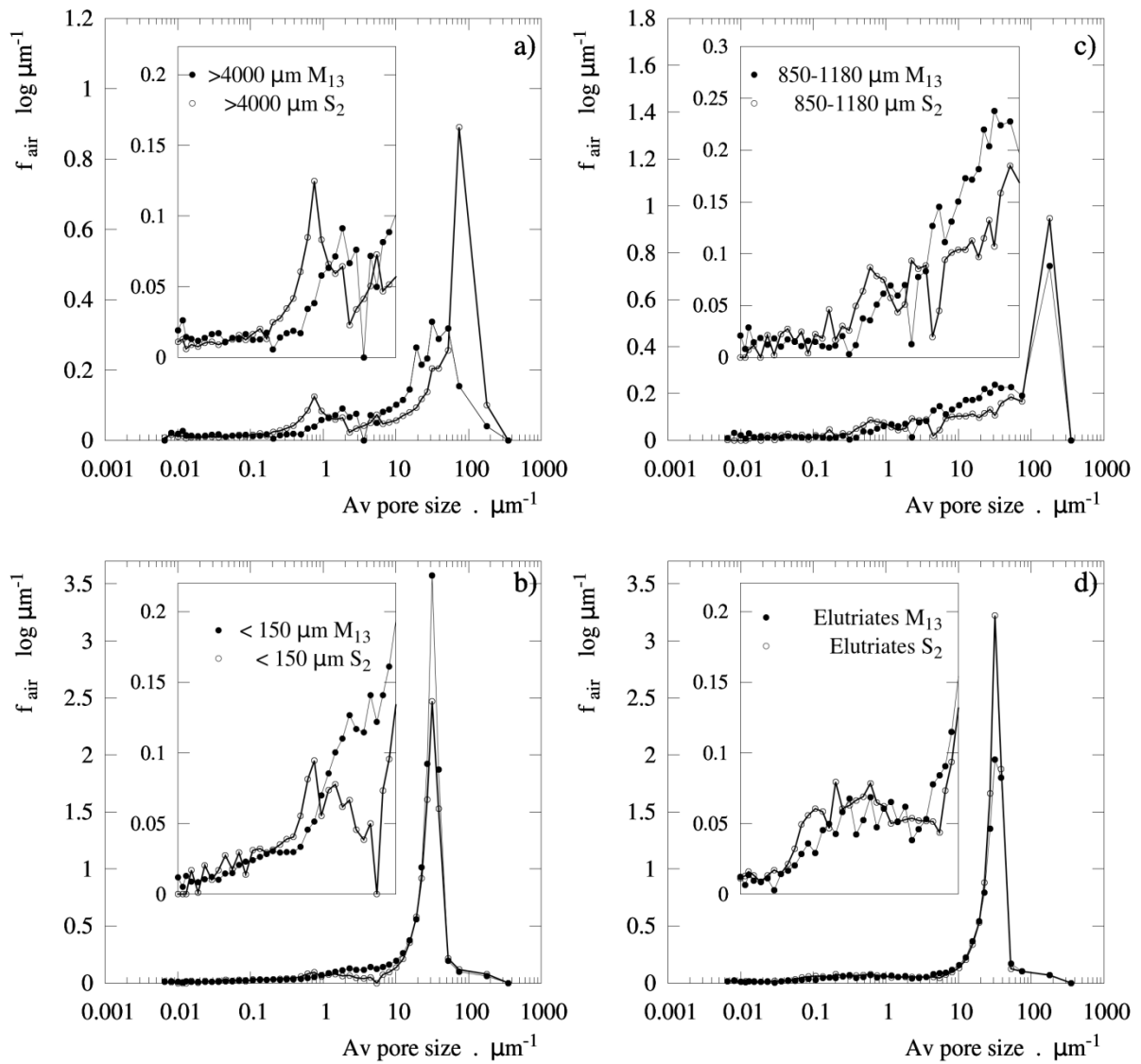


**Figure 5.** Comparison of the intrusion curves of Hg for the product in  $S_2$  and  $M_{13}$  a) the largest fraction b) the secondary size mode in  $M_{13}$  c) the smallest fraction and d) the elutriates.

difference to the size of the cavities, or in Figure 3b, due to the lack of them. However, as the cavities start to be comparable in Figure 3c and both maxima become indistinguishable. The elutriated powder in Figure 3d shows no similar pores due to its different drying history.

The multi-level system  $M_{13}$  is presented in Figure 4. It shows a similar general trend. The coarse granules reveal the same two regimes in Figure 4a but now the ranges differ. Figure 5 compares both cases. In  $M_{13}$  the cavities are shifted to lower values up to  $30 - 40 \mu m$ , see Figure 5a. The micron porosity now moves to larger sizes in both the fine and coarse product in Figures 5b and 5c. But the porosity of elutriates, indicative of the primary droplets, remains comparable in Figure 5d.

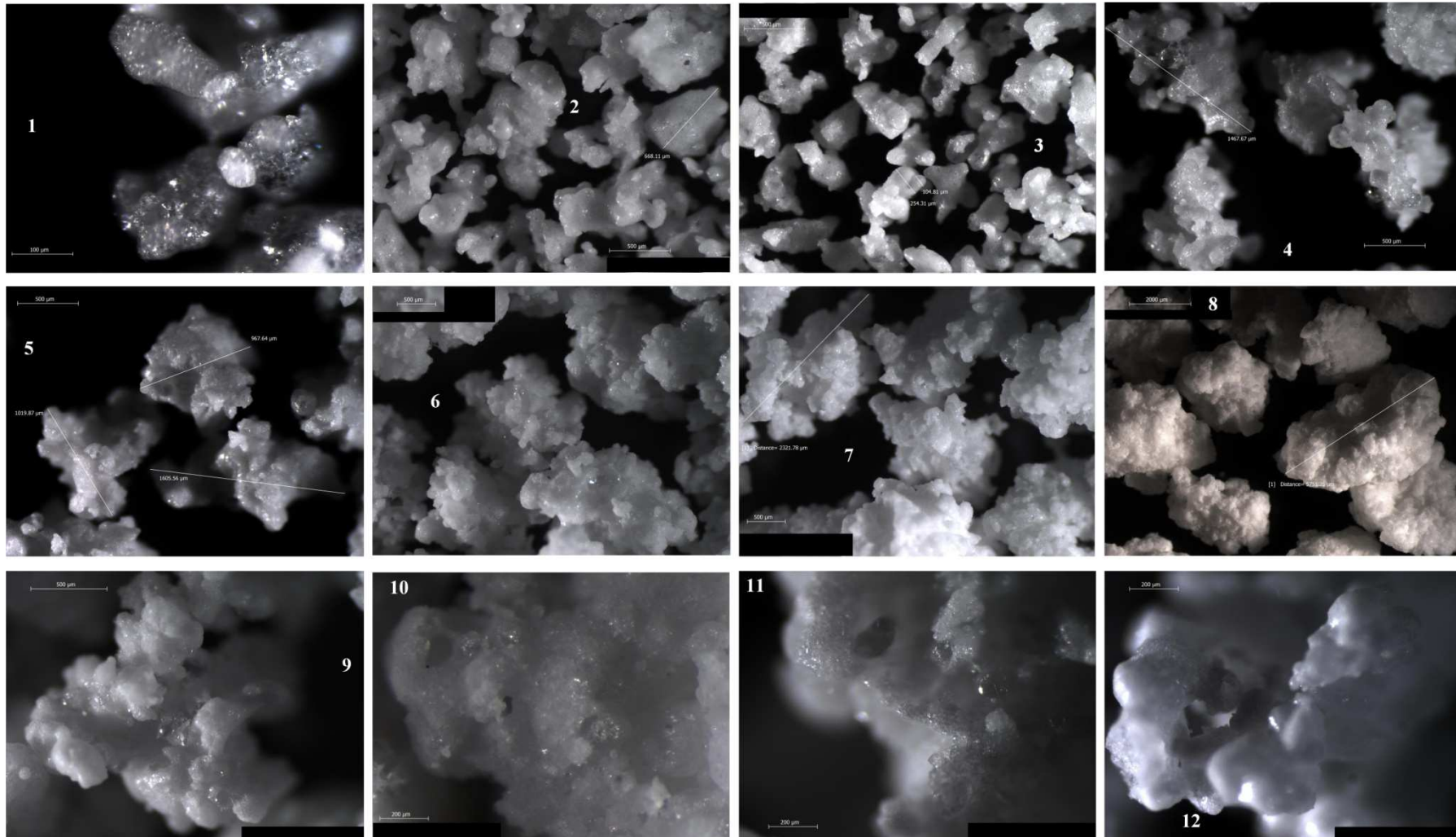
## Conclusions

In vast majority, the product is comprised of aggregates. The heterogeneity of the droplet composition and shape is responsible for very heterogeneous aggregates showing non-spherical shapes, ligaments and collided structures in the product. The primary particles in the granules present large contact areas and are bounded by solid bridges. This leads to an open morphology and the formation of large cavities that are superimposed to micron pores in the primary particles.

The intra-particle porosity,  $\varepsilon$  is originated by 1- surface features in the range of tens to hundreds of  $\mu m$  owing to aggregation and 2- smaller pores in the nm and  $\mu m$  range, owing to the diffusion of water and the bursts of vapour out of primary particles. In the case of a single nozzle, the product shows an intra-particle porosity of at least  $\varepsilon \sim 37\%$ . The part owed to micro size pores can be accounted as  $< 27\%$  while cavities can be responsible for values  $> 25\%$  in the largest granules. Despite the porosity due to cavities in the largest sizes could not be quantified in detail, it is clear from the data that it has a very relevant contribution to the density of the product.

A multi-level operation results in higher values for the product  $> 355 \mu m$ , what can be explained by a different drying and aggregation history. This also affects the pore size distribution where cavities are displaced to lower pore size. The fact that high levels of porosity are maintained for the coarse product is an important observation. It is often believed that one would find an improvement in  $\varepsilon$  by promoting drying at higher temperatures so that droplets are more prone to boil and inflate, reducing also the formation of aggregates. This is not the case here. It is found that  $\varepsilon$  owes to a large extent to the formation of cavities during growth, and thus it is important not to suppress aggregation but to be able to control it in order to meet both quality criteria: sufficiently small aggregates but with a sufficiently high  $\varepsilon$ .

**Figure 6.** Typical morphology of detergent granules under optical microscopy (1)  $150 < x_p < 250 \mu m$ . (2)  $250 < x_p < 450 \mu m$ ; (3)  $450 < x_p < 705 \mu m$ ; (4-5)  $705 < x_p < 1800 \mu m$ ; (6 to 8)  $x_p > 1800 \mu m$ ; (9 to 12) Detail of the granule surface and the solid bridges for  $x_p > 1800 \mu m$ .



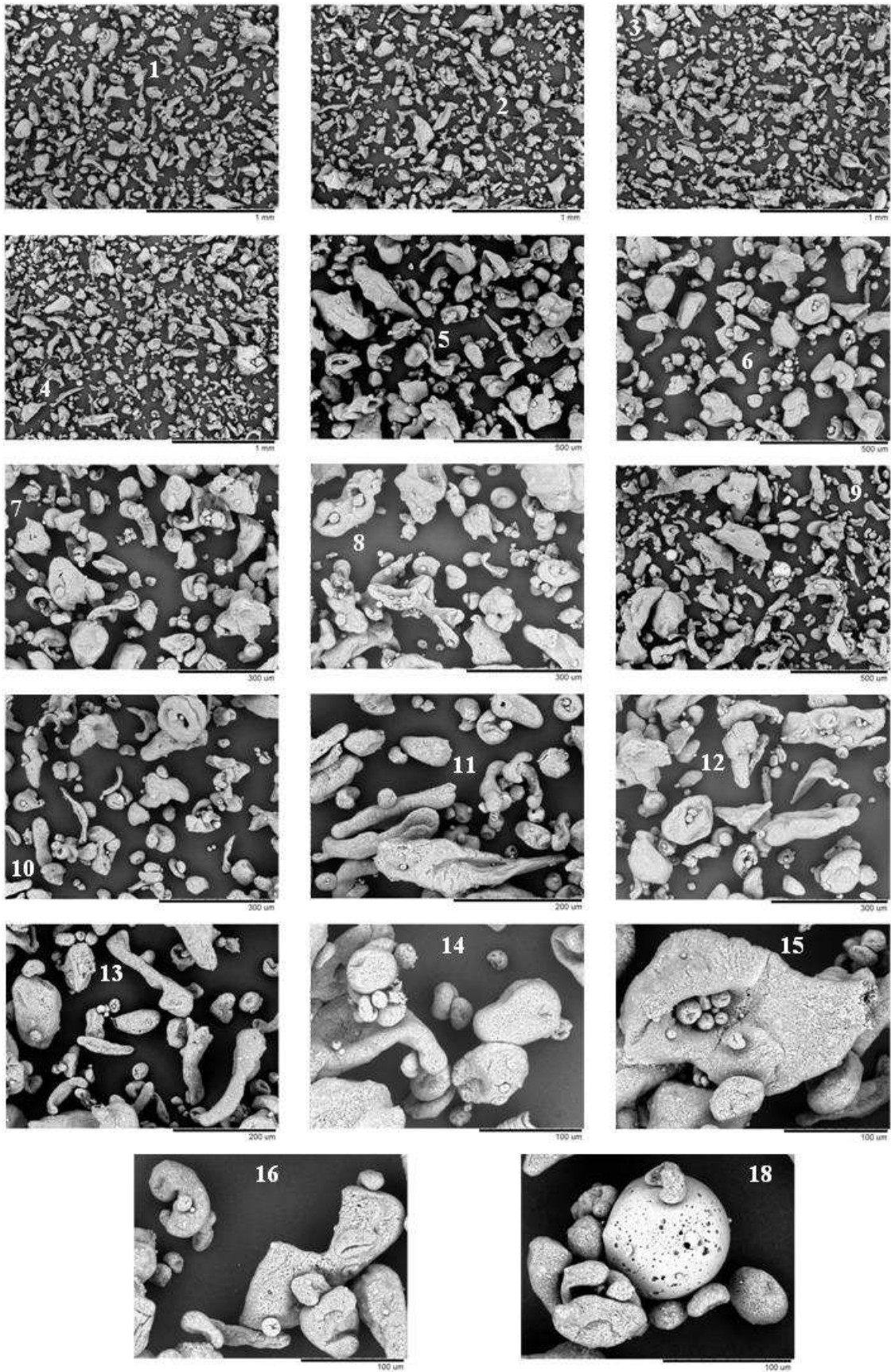


**Figure 7.** Examples of morphology.  $S_2$ . Top to bottom, left to right in decreasing magnification. Elutriates.

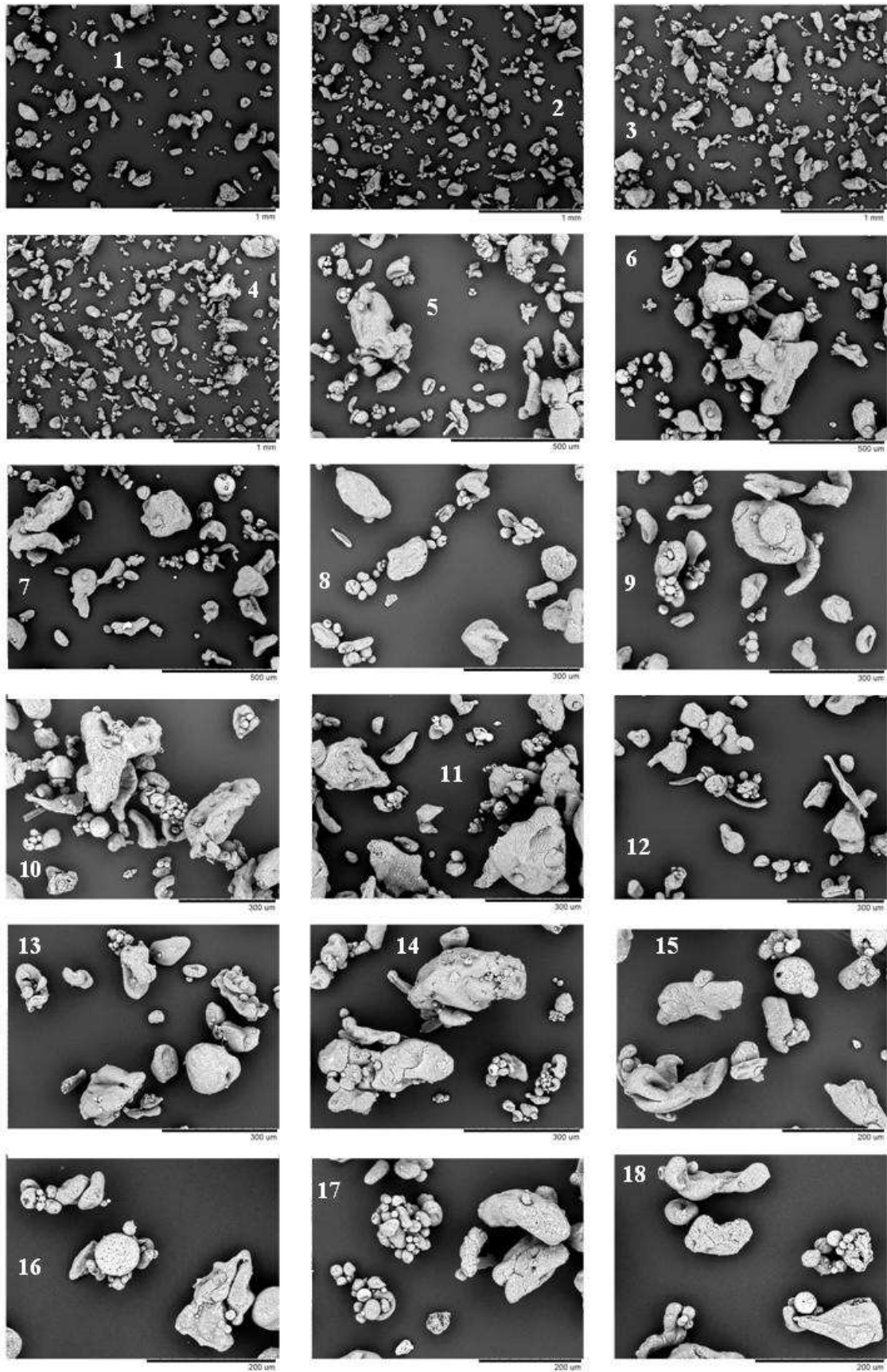


**Figure 8.** Examples of morphology.  $M_{13}$ . Top to bottom, left to right in decreasing magnification. Elutriates.

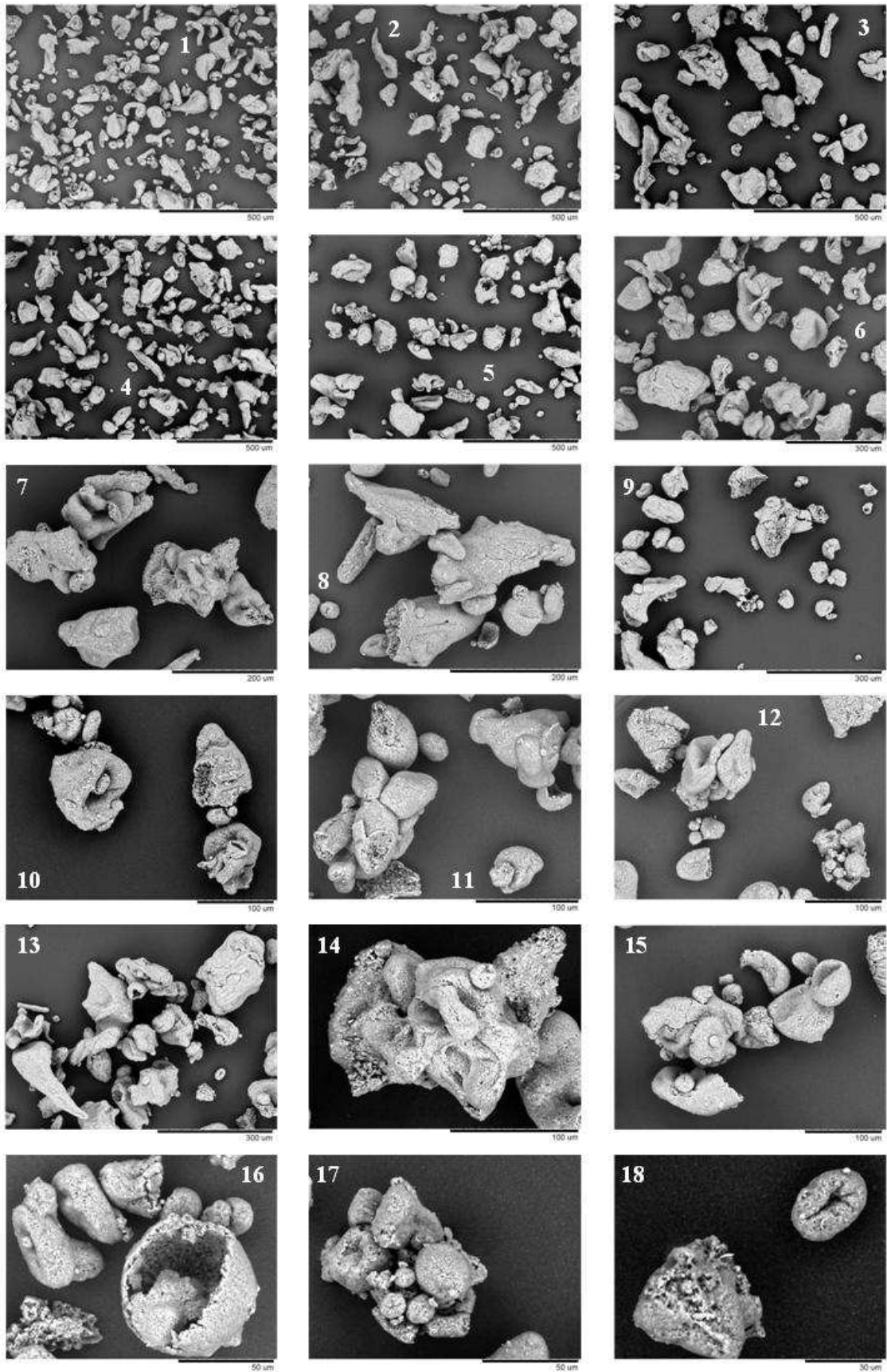


**Figure 9.** Examples of morphology.  $S_2$ . Top to bottom, left to right in decreasing magnification.  $x_p < 150 \mu\text{m}$ .

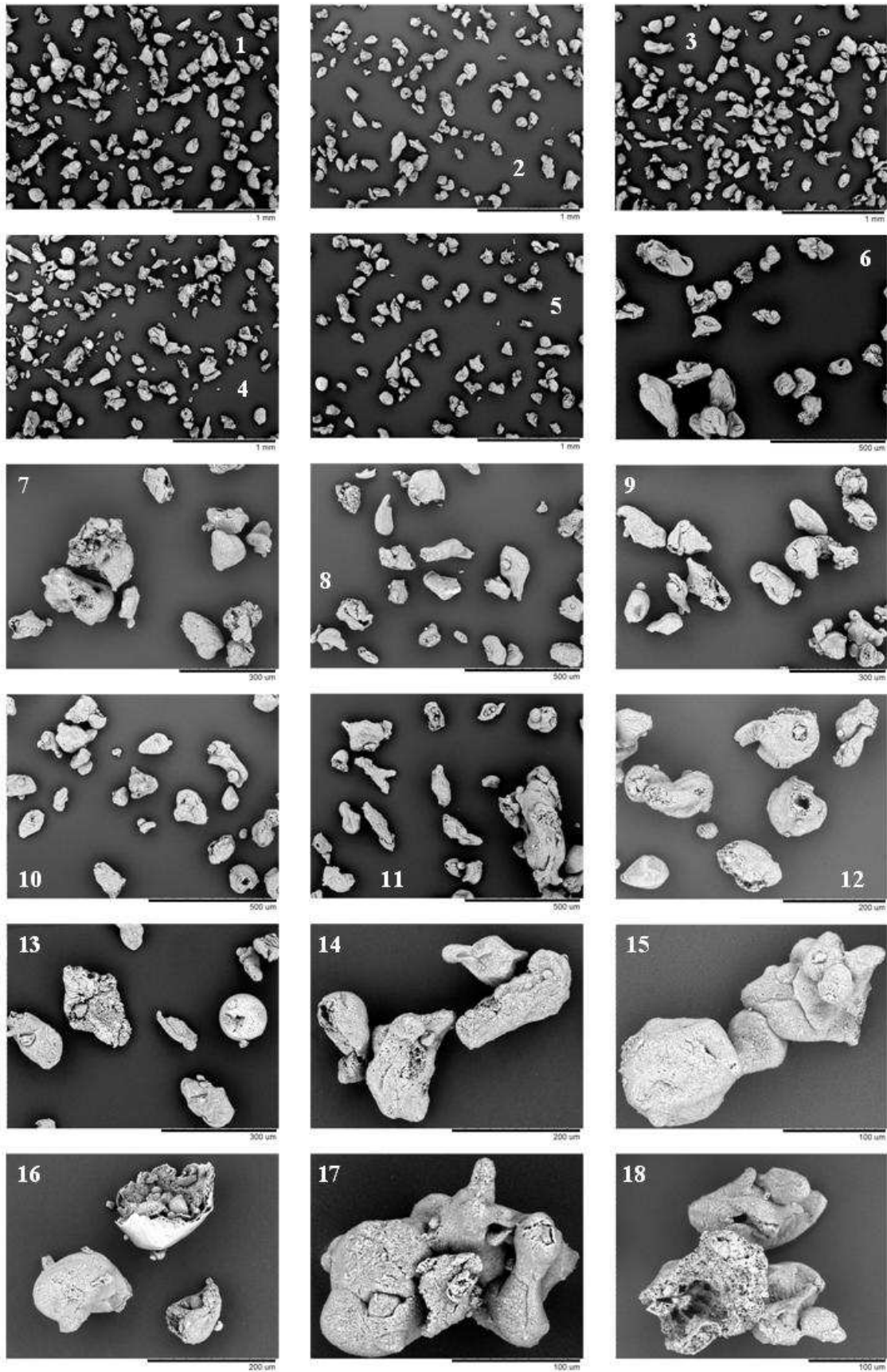


**Figure 10.** Examples of morphology.  $M_{13}$ . Top to bottom, left to right in decreasing magnification.  $x_p < 150 \mu\text{m}$ .

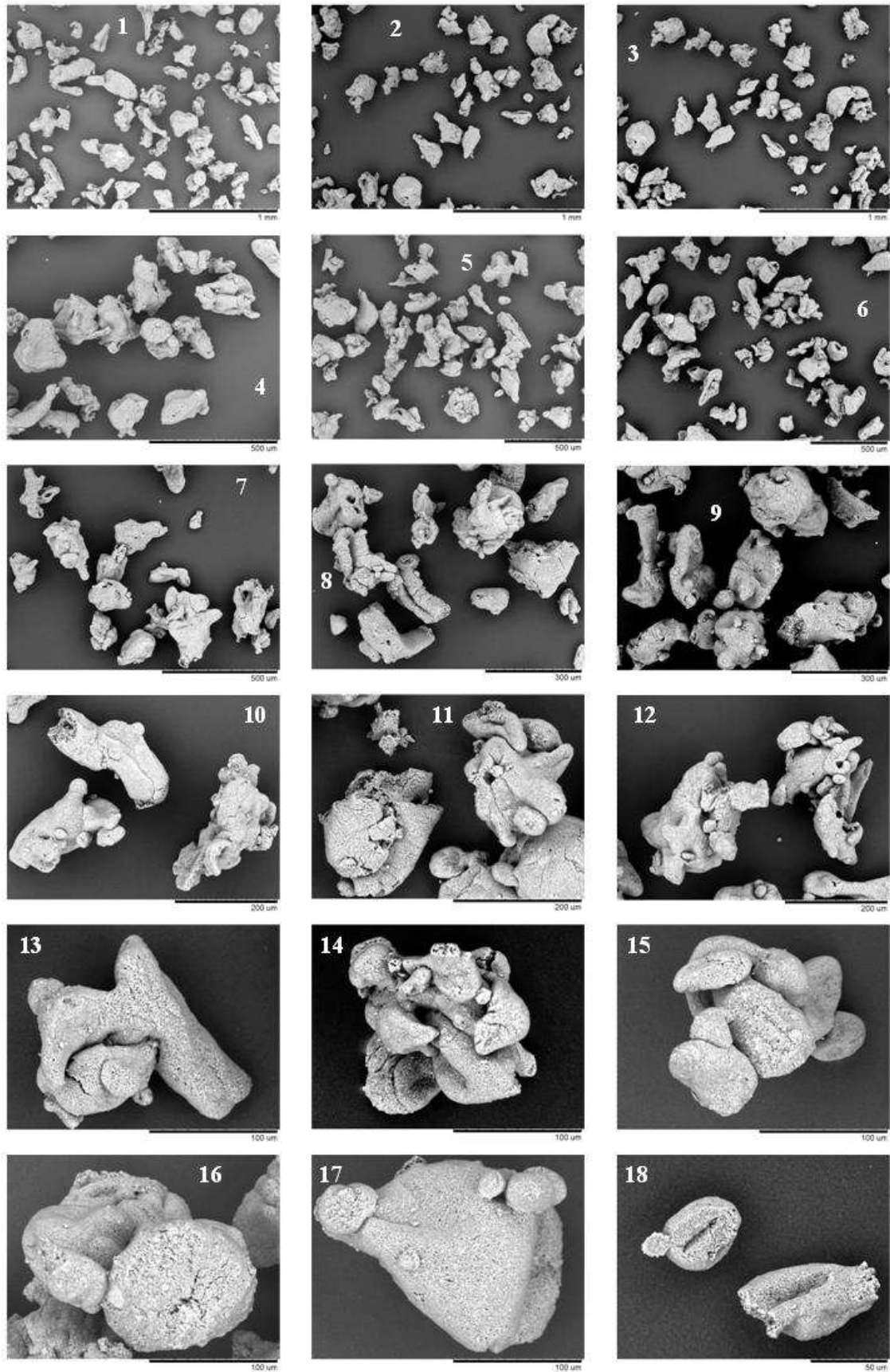


**Figure 11.** Examples of morphology.  $S_2$ . Top to bottom, left to right in decreasing magnification.  $150 < x_p < 250 \mu\text{m}$ .

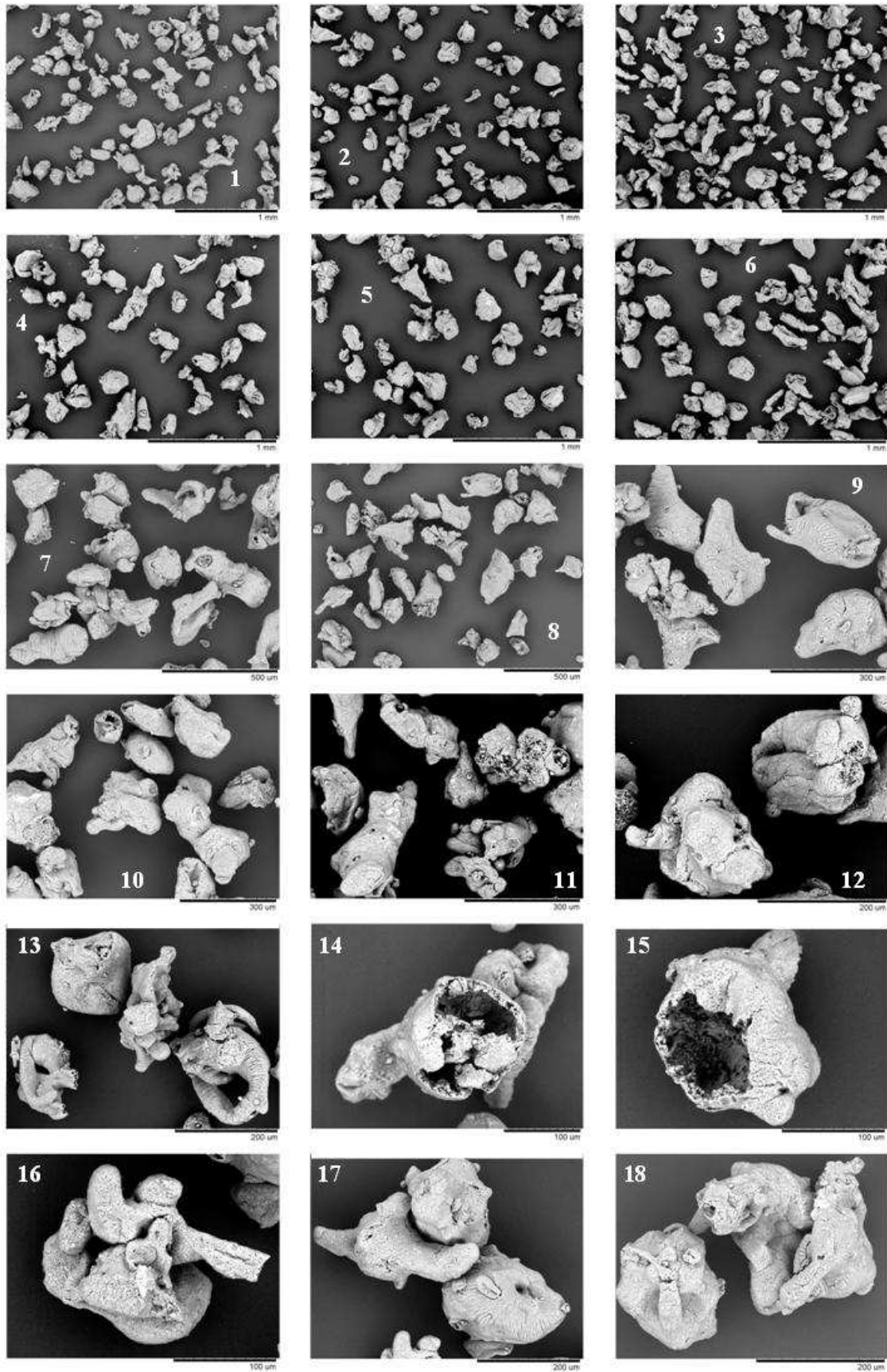


**Figure 12.** Examples of morphology.  $M_{13}$ . Top to bottom, left to right in decreasing magnification.  $150 < x_p < 250 \mu\text{m}$ .

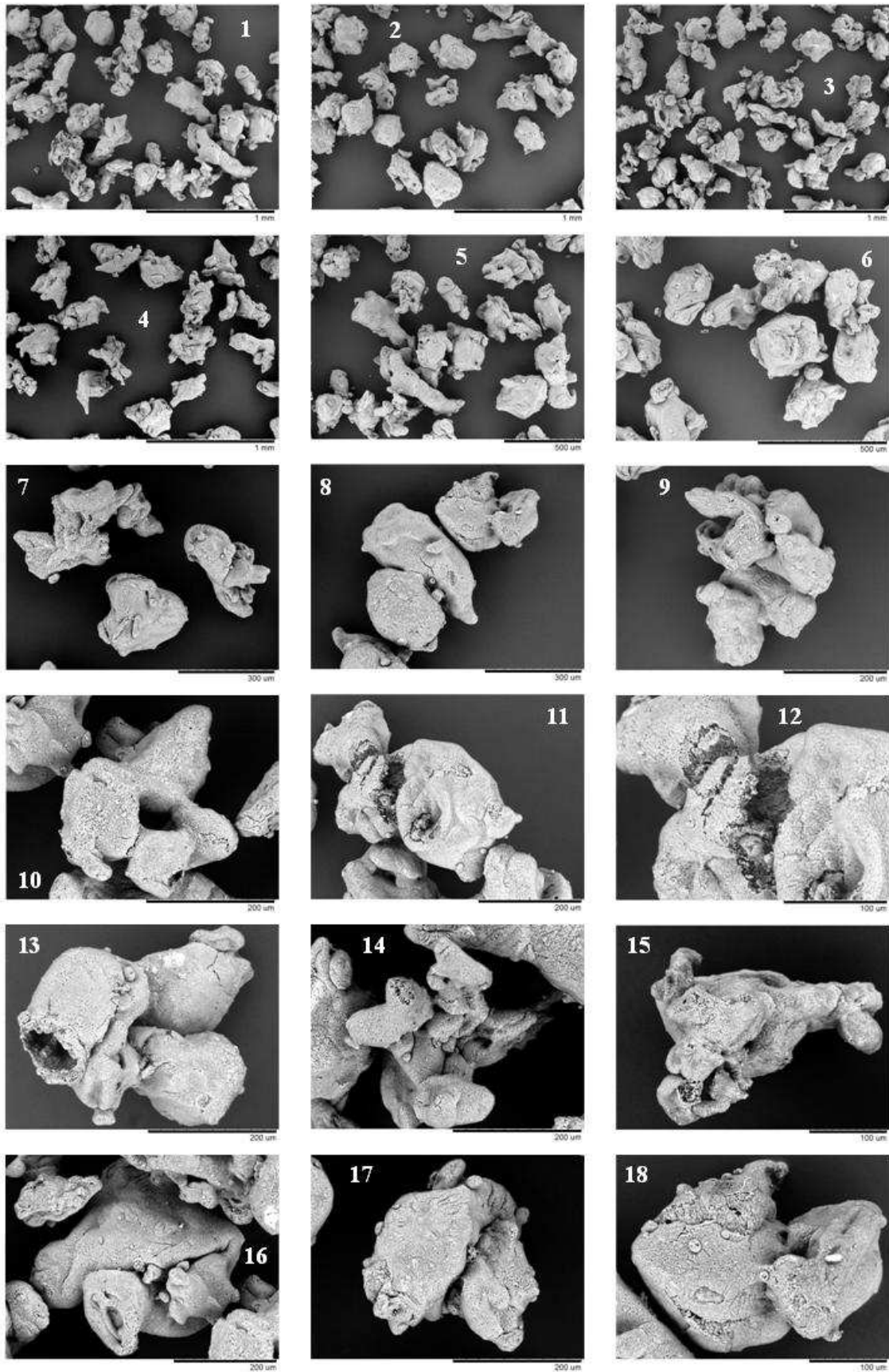


**Figure 13.** Examples of morphology.  $S_2$ . Top to bottom, left to right in decreasing magnification.  $250 < x_p < 355 \mu\text{m}$ .

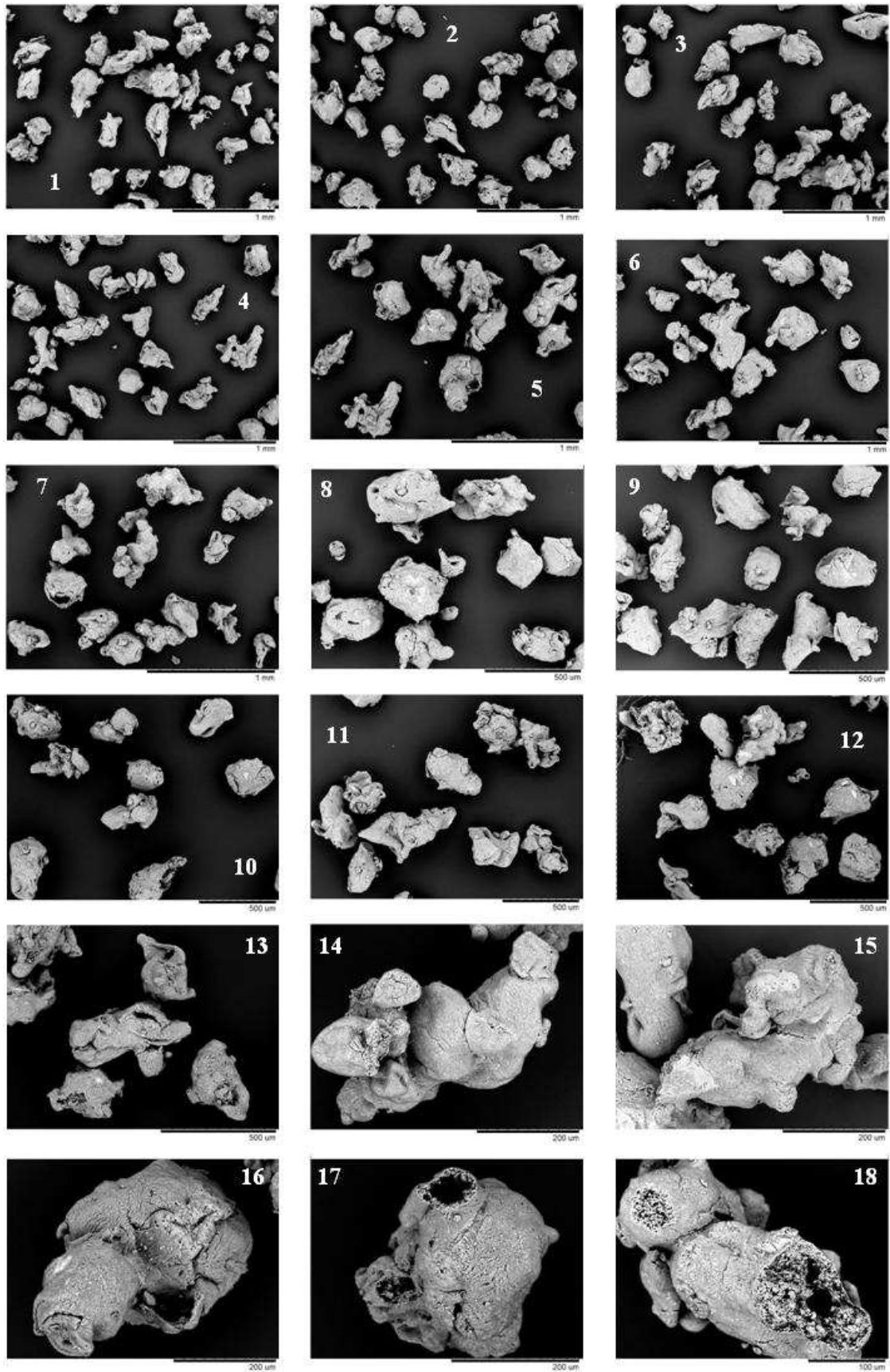


**Figure 14.** Examples of morphology.  $M_{13}$ . Top to bottom, left to right in decreasing magnification.  $250 < x_p < 355 \mu\text{m}$ .

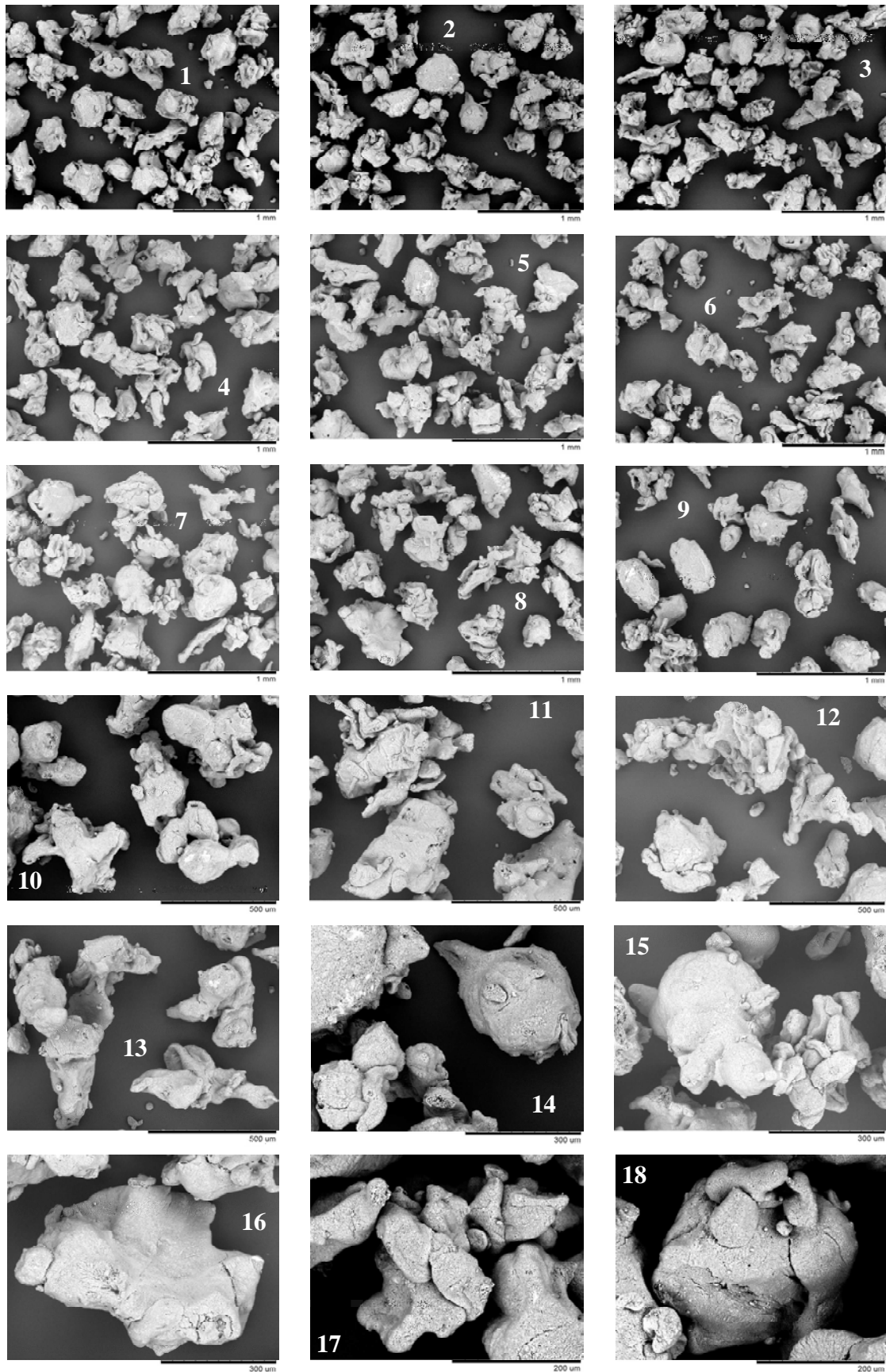


**Figure 15.** Examples of morphology.  $S_2$ . Top to bottom, left to right in decreasing magnification.  $355 < x_p < 450 \mu\text{m}$ .

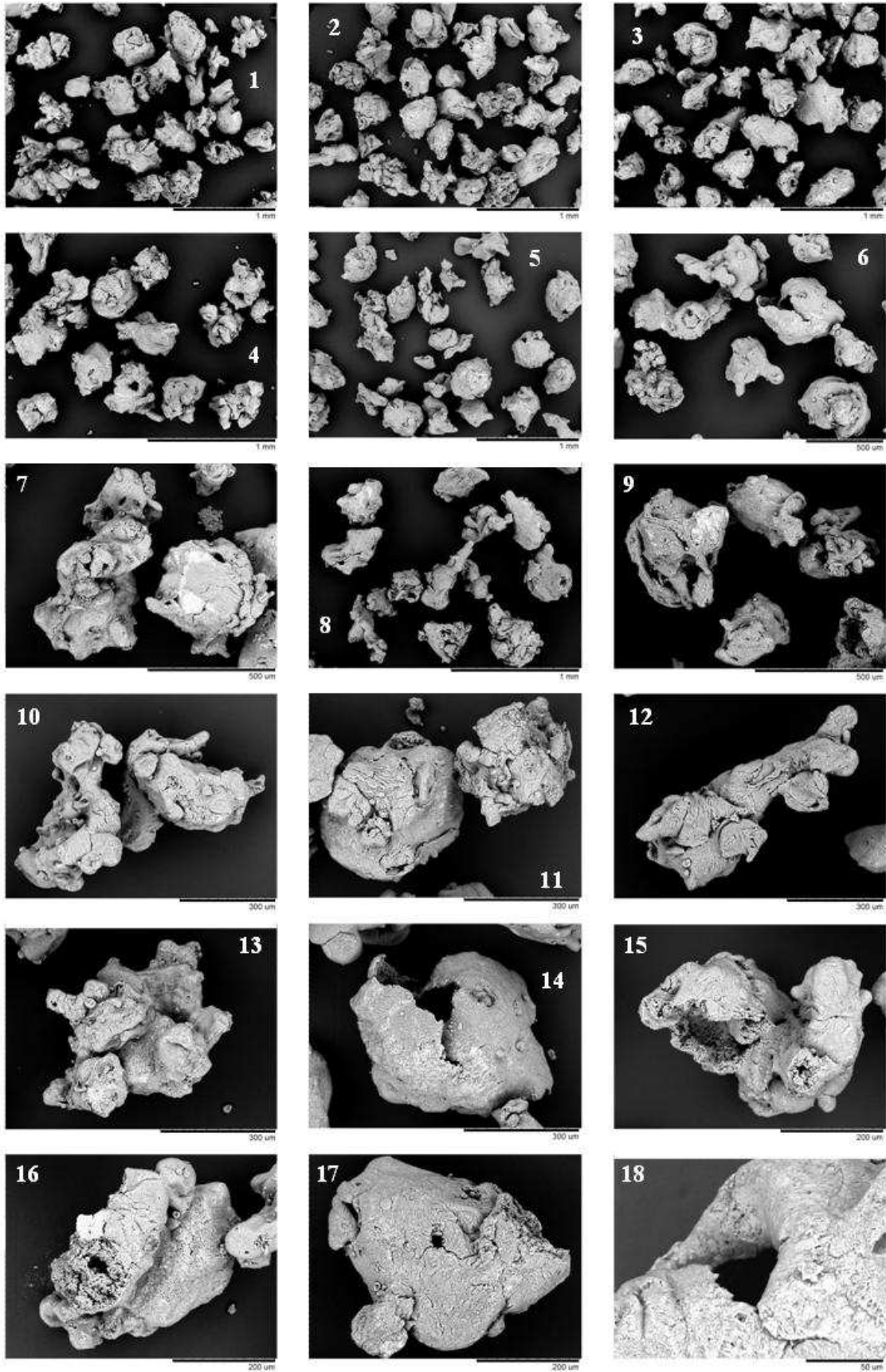


**Figure 16.** Examples of morphology.  $M_{13}$ . Top to bottom, left to right in decreasing magnification  $.355 < x_p < 450 \mu\text{m}$ .

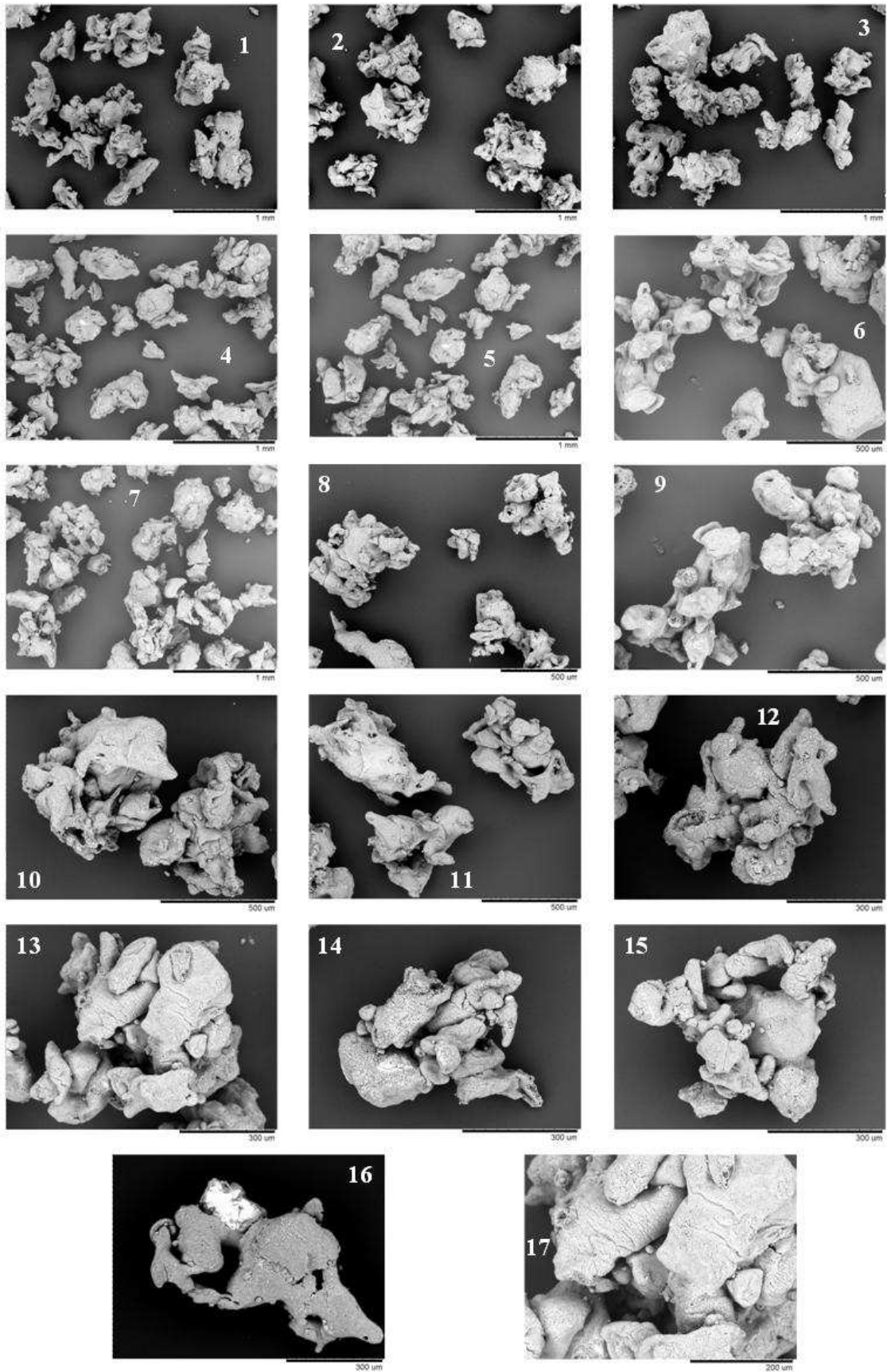


**Figure 17.** Examples of morphology.  $S_2$ . Top to bottom, left to right in decreasing magnification.  $450 < x_p < 600 \mu m$ .

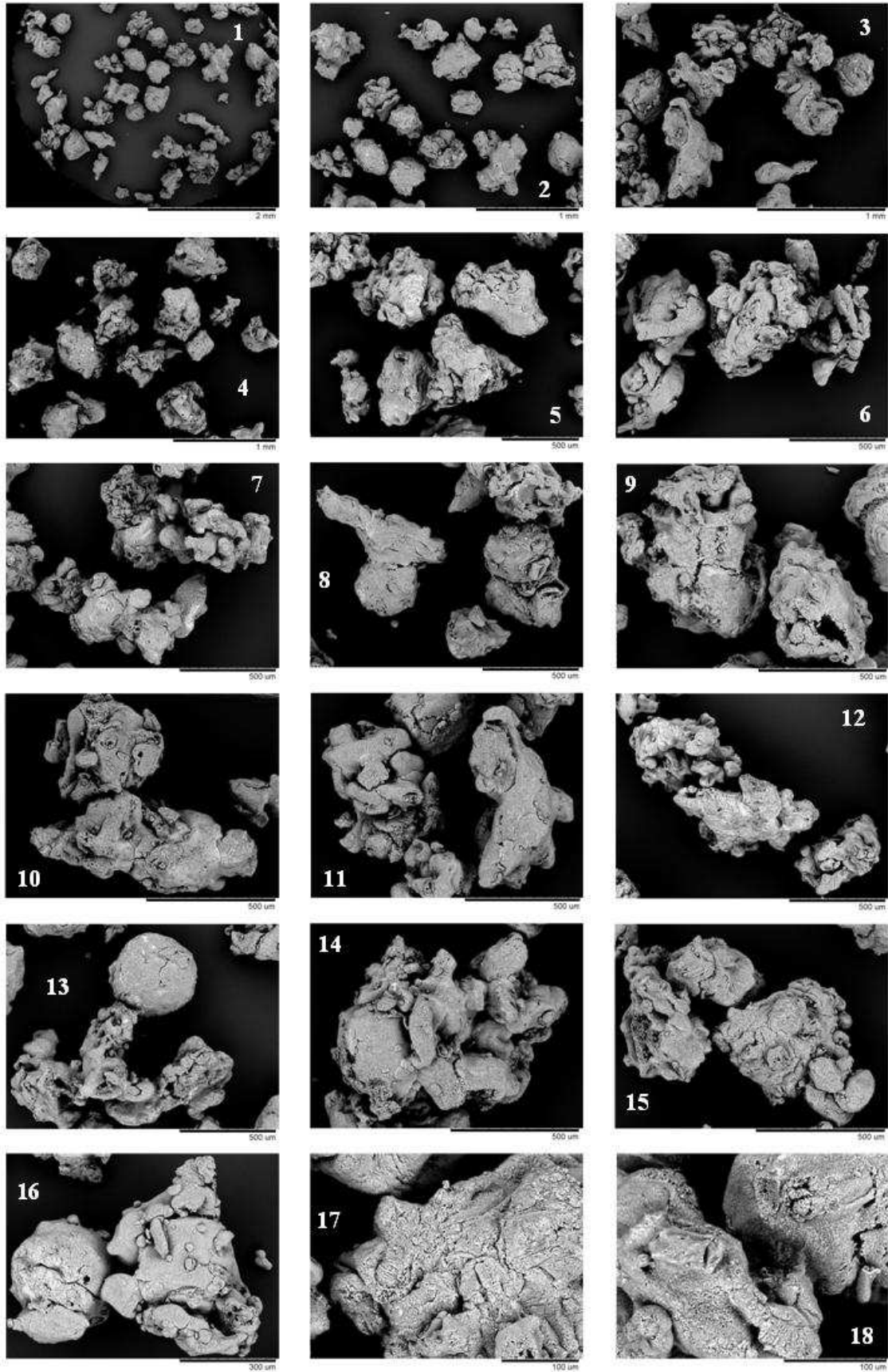


**Figure 18.** Examples of morphology.  $M_{13}$ . Top to bottom, left to right in decreasing magnification.  $450 < x_p < 600 \mu\text{m}$ .

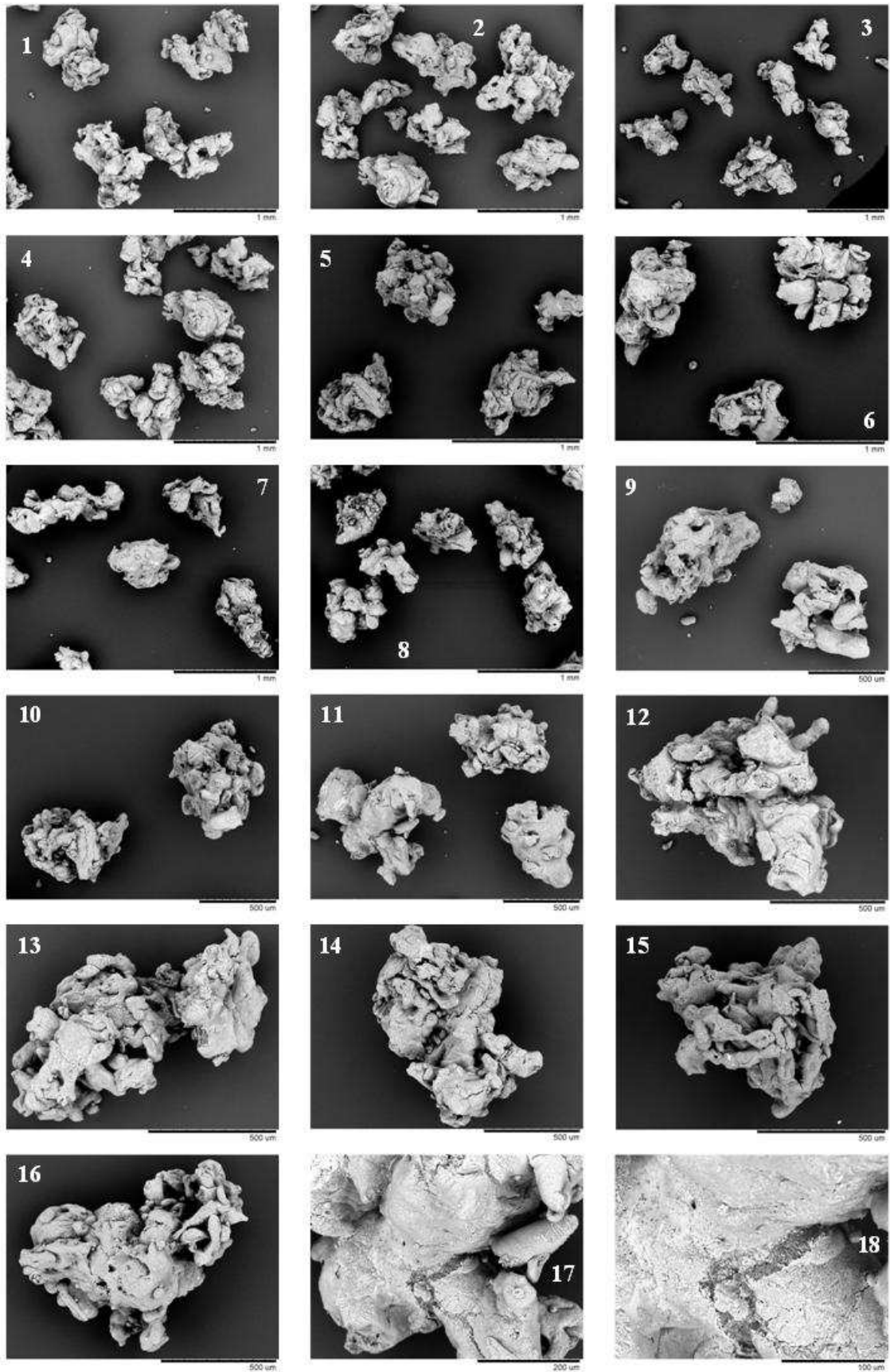


**Figure 19.** Examples of morphology.  $S_2$ . Top to bottom, left to right in decreasing magnification.  $600 < x_p < 850 \mu m$ .

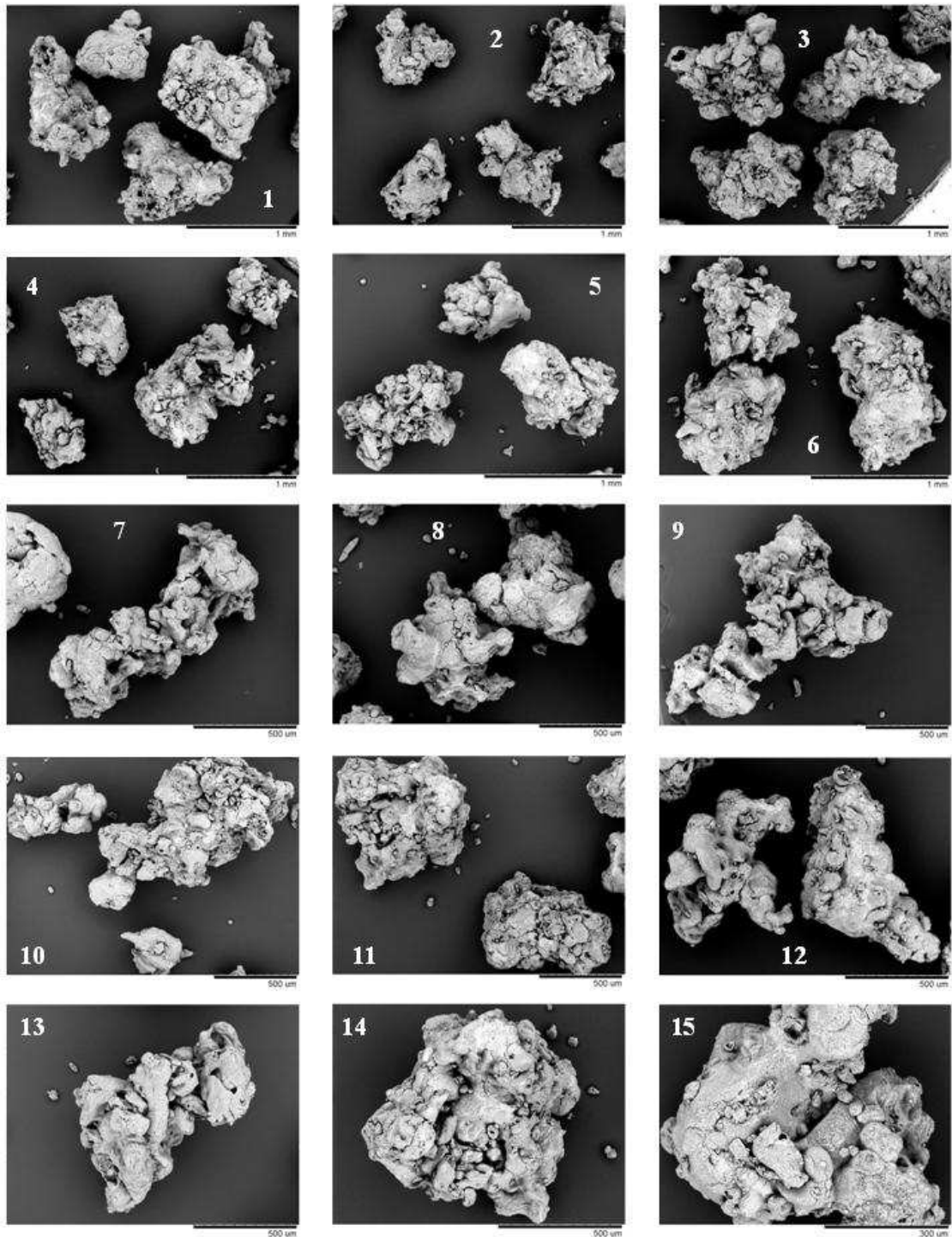


**Figure 20.** Examples of morphology.  $M_{13}$ . Top to bottom, left to right in decreasing magnification.  $600 < x_p < 850 \mu\text{m}$ .

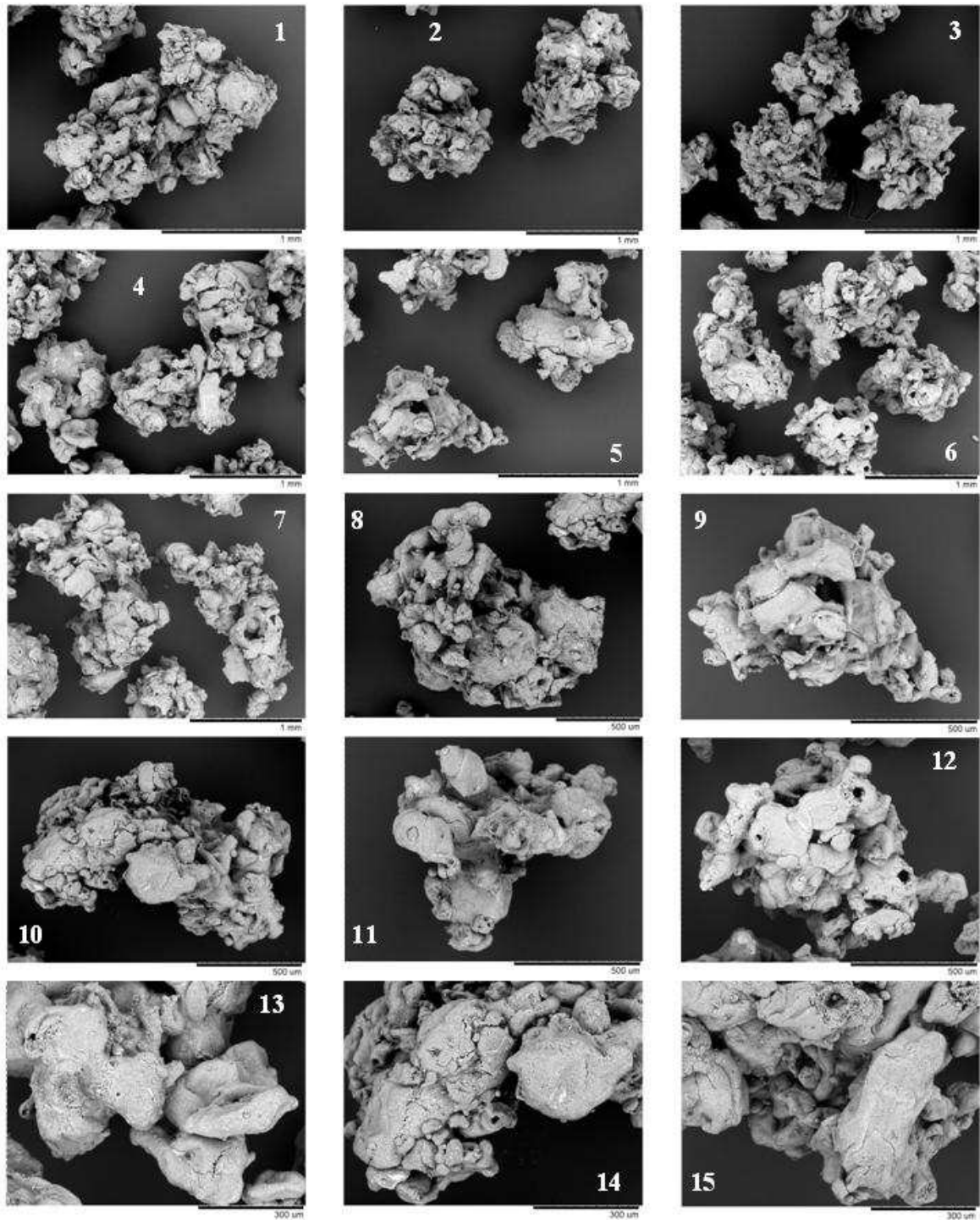


**Figure 21.** Examples of morphology.  $S_2$ . Top to bottom, left to right in decreasing magnification.  $850 < x_p < 1180 \mu\text{m}$ .

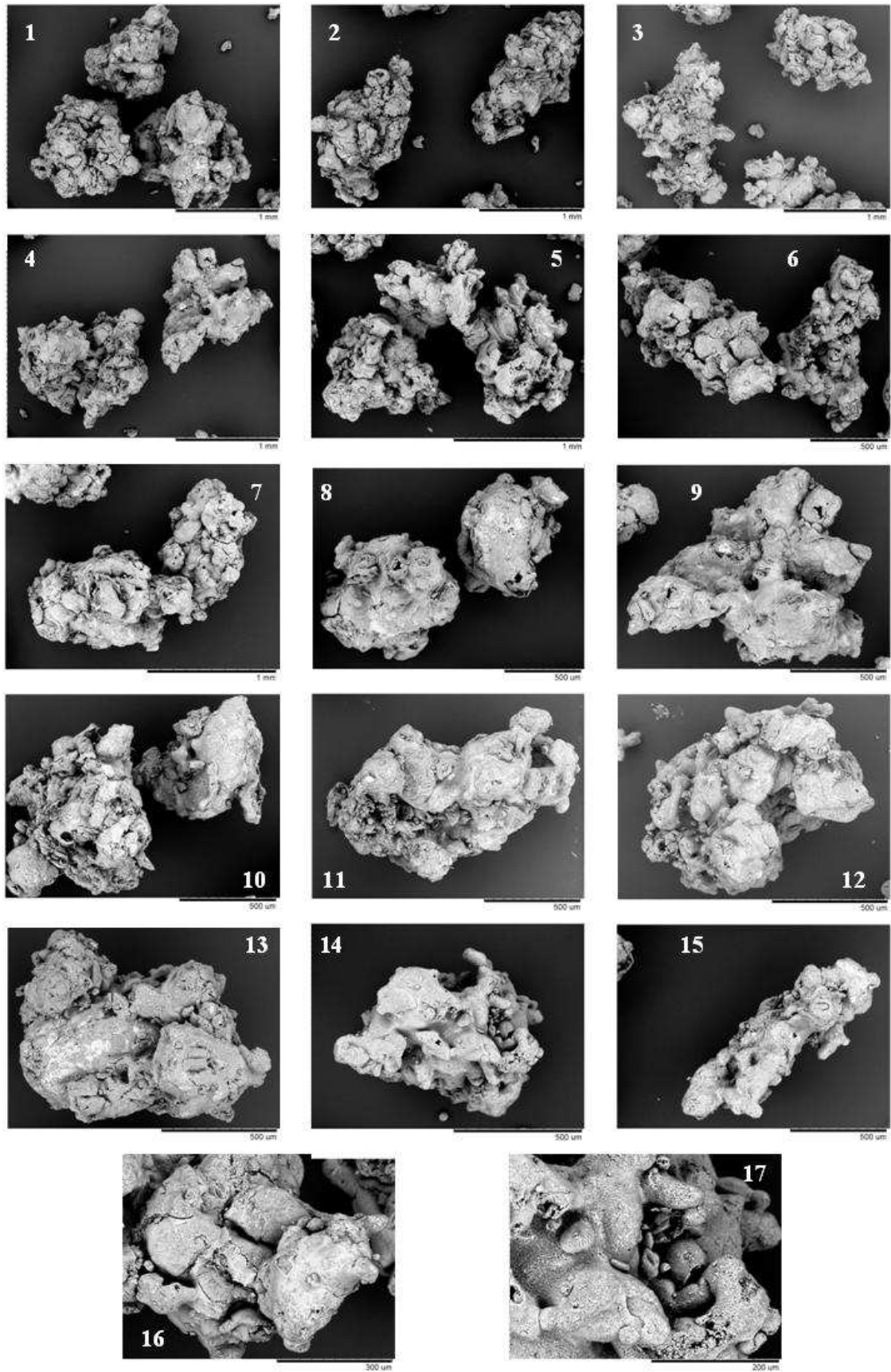


**Figure 22.** Examples of morphology.  $M_{13}$ . Top to bottom, left to right in decreasing magnification.  $850 < x_p < 1180 \mu\text{m}$ .

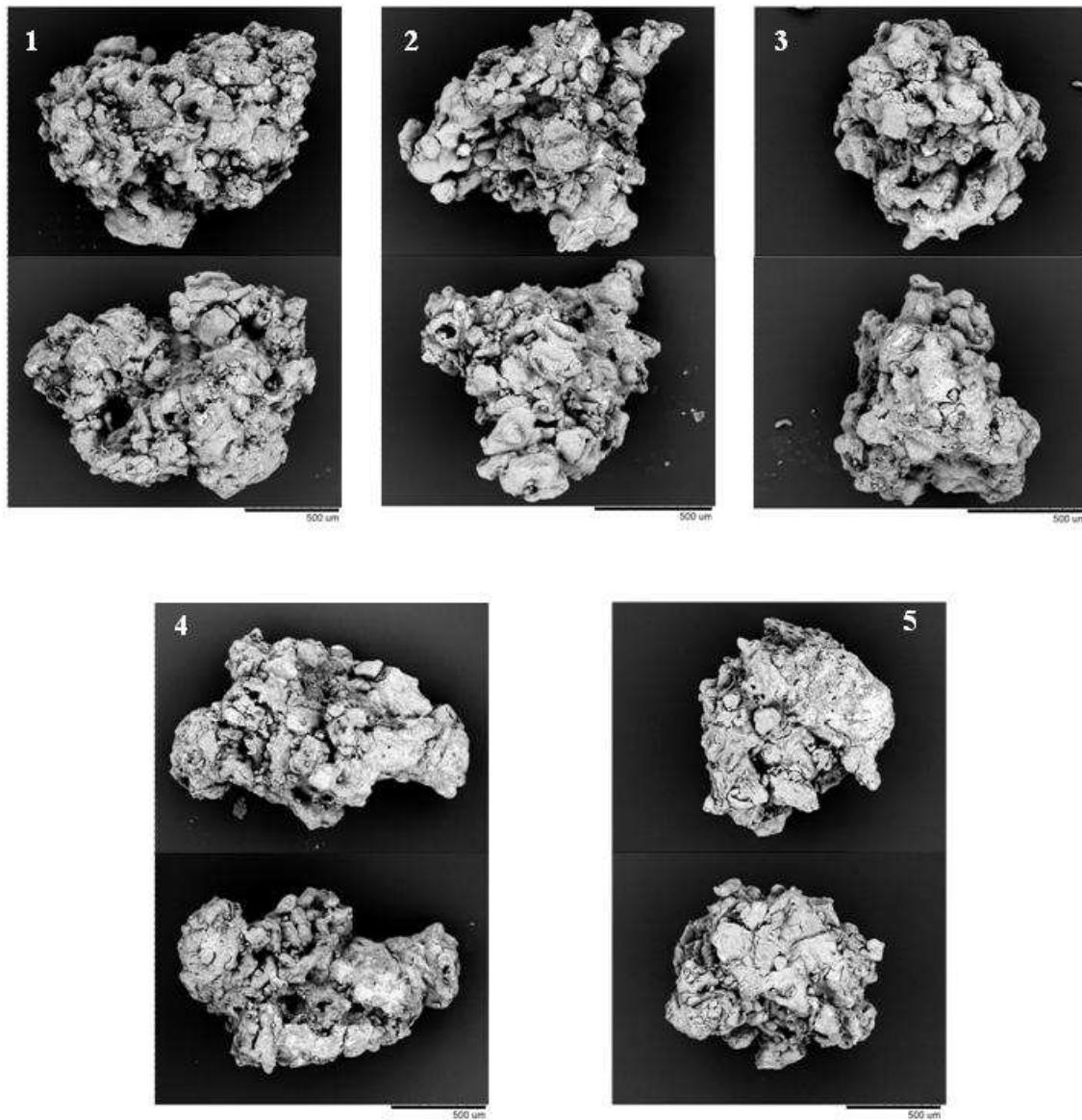


**Figure 23.** Examples of morphology.  $M_{13}$ . Top and bottom in each pair show the front and the back.  $850 < x_p < 1180 \mu\text{m}.$

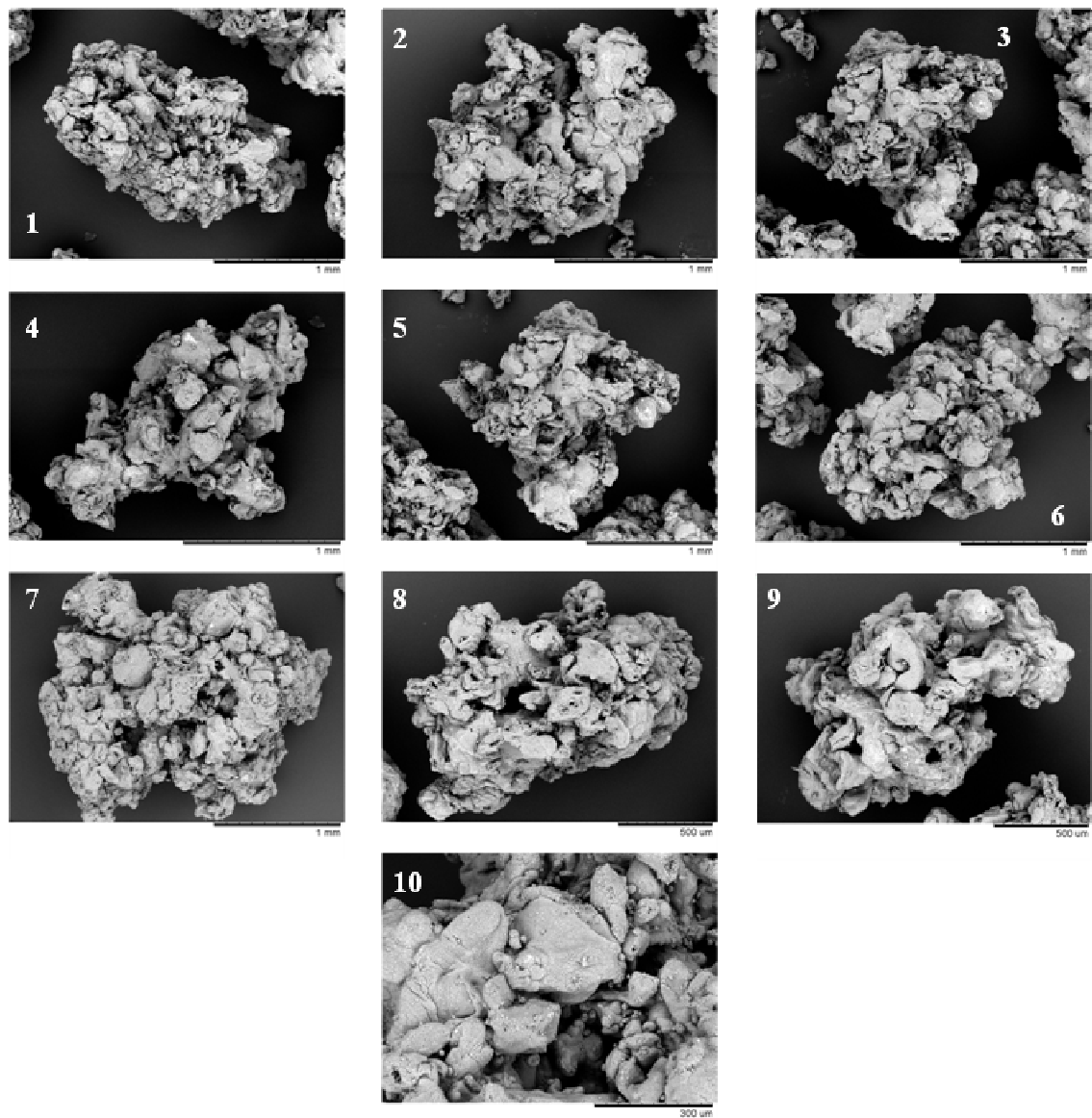


**Figure 24.** Examples of morphology.  $S_2$ . Top to bottom, left to right in decreasing magnification.  $1180 < x_p < 1800 \mu\text{m}$ .

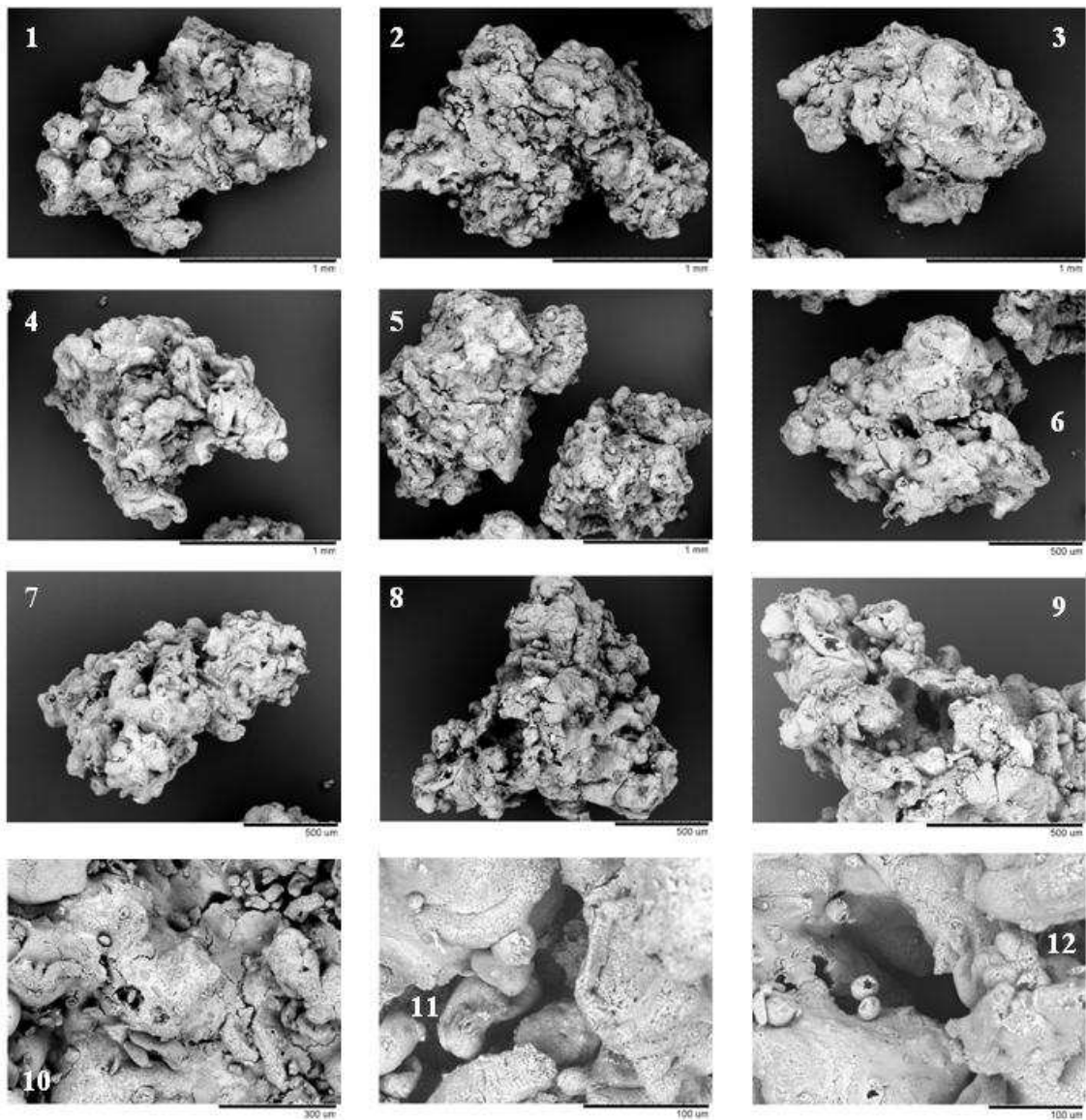
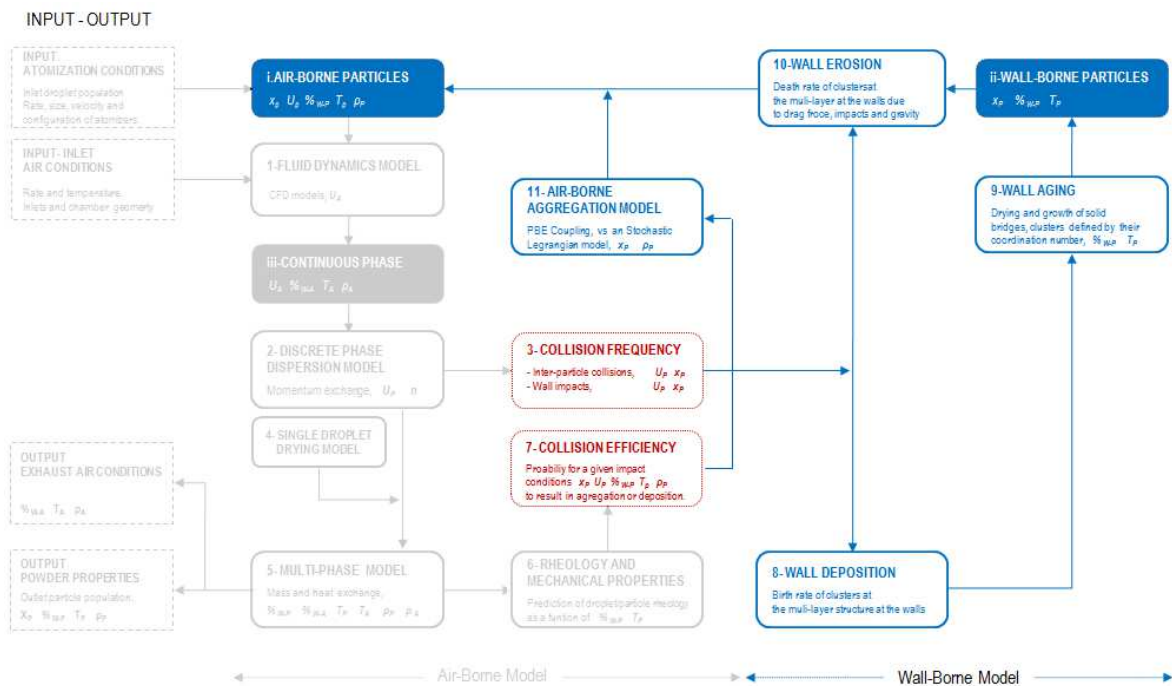


**Figure 25.** Examples of morphology  $M_{13}$ . Top to bottom, left to right in decreasing magnification.  $1180 < x_p < 1800 \mu\text{m}$ .

# APPENDIX III

## CONTROL OF THE GROWTH AND WEAR MECHANISMS.



## Summary

This work extends the investigation given in Chapter VI to the analysis of the system under different air inlet conditions. The focus is placed in describing how one may operate the dryer at different ranges of air temperature and velocity by modifying the air inlet temperature,  $T_{A,IN}$ , and adjusting the mass rate,  $M_A$ . When one opts to use low air temperatures,  $T_A$ , and high velocities,  $U_A$ , the size of the product is reduced. The opposite leads to the formation of coarser particles, particularly granules  $> 850 \mu m$ . This trend points to a more complex relation between growth and the fluid dynamics than anticipated by the contact of particles in the air. It can be explained by the rate and the energy of the impacts to the wall. It appears that one can tailor product properties by the promotion or suppression of the re-entrainment from the deposits, modifying the kinetic energy that the air transfers to the solid phase and utilised later in breaking up the clustered structure that forms at the walls.

It is important to pay more attention to the microstructure of the deposits. The data given here and in Chapter V make clear that the manufacturers would benefit from understanding how the size of the material that is worn off the walls can be related to process conditions such as the inlet air properties. In essence the size at which a cluster is re-entrained responds to a balance between the cohesive forces in the deposits and the stresses exerted by a) gravity as the deposits thickness increases, b) drag and lift forces and c) wall impacts.

## 1. Introduction.

The Chapter VI associates growth patterns to different rates, nozzle configurations, and heat transfer rates in the spray regions. It is interesting to note that product size distributions were found fairly insensitive to the final water content in the product,  $X_w$ . In some ways this contradicts what one expects from the contacts of air-borne particles. As the product dries particles become less sticky and one expects them to be less prone to aggregate. Chapter VI shows several examples (e.g. see  $M_3$  and  $M_{3-i}$ ) where this was not the case: the size distribution in the product remains constant despite substantial differences in  $X_w$ . Perhaps, it is not surprising when one considers that the deposits are involved in the formation of the coarse fractions (Chapter V). But then, this questions whether the description of the particle contacts in the air is the most indicated to understand how the growth occurs.

The analysis given in Chapters V and VI helps in understanding the process but provides no quantifiable means of control. The optimization requires studying how the size distributions respond to changes in the inlet operation conditions. This is the purpose of this appendix. It studies the air operation and pays special attention to the balance between the use of high air temperatures or high air velocities.

## 2. Experimental methodology.

### 2.1. Unit design and operation.

The unit operation and all measurements have been described in Chapter IV. Figures 1 and 2 are given here for support, including the location of nozzles, wall inspection areas and temperature sensors.

### 2.2. Air operation. Temperature vs Momentum.

In a given swirl counter current tower one can opt to modify either the properties of the inlet slurry:

- Changing the slurry rate,  $M_s$  (i.e. atomization pressure, nozzle type and/or number).
- Using a different injection configuration (i.e. number and location of nozzles).
- Modifying the droplet size (i.e. nozzle type, atomization pressure and temperature).

or alternatively, one can change the properties of inlet air

- Inlet air rate,  $M_A$ .
- Inlet air temperature,  $T_{A,IN}$ .

The manufacturers usually try to maximise  $M_s$  under fix nozzle configurations. The effect of modifying the nozzle location, the rate and using nozzles at different levels has been described in Chapter VI. In practise, once the atomization configuration has been selected, the only way to control the process is to find an optimum balance between the air mass rate  $M_A$  and the inlet temperature,  $T_{A,IN}$ .

Put simply, one can modify  $T_{A,IN}$  and change  $M_A$  accordingly to drive the same overall mass transfer. If one drops the air temperature  $T_{A,IN}$  it is necessary to increase the rate  $M_A$  to dry the product to the same level, and vice versa. These changes lead to 1- different flow patterns in the dryer: the use of a higher  $M_A$  originates higher air velocities,  $U_A$ , which increase the residence time of the particles, and 2- different heat and mass transfer kinetics: Section 3.1 shows how the usage of lower temperatures  $T_A$  leads to a lower  $\Delta T$  between the air and the solids at the bottom of the dryer, which reduces the heat

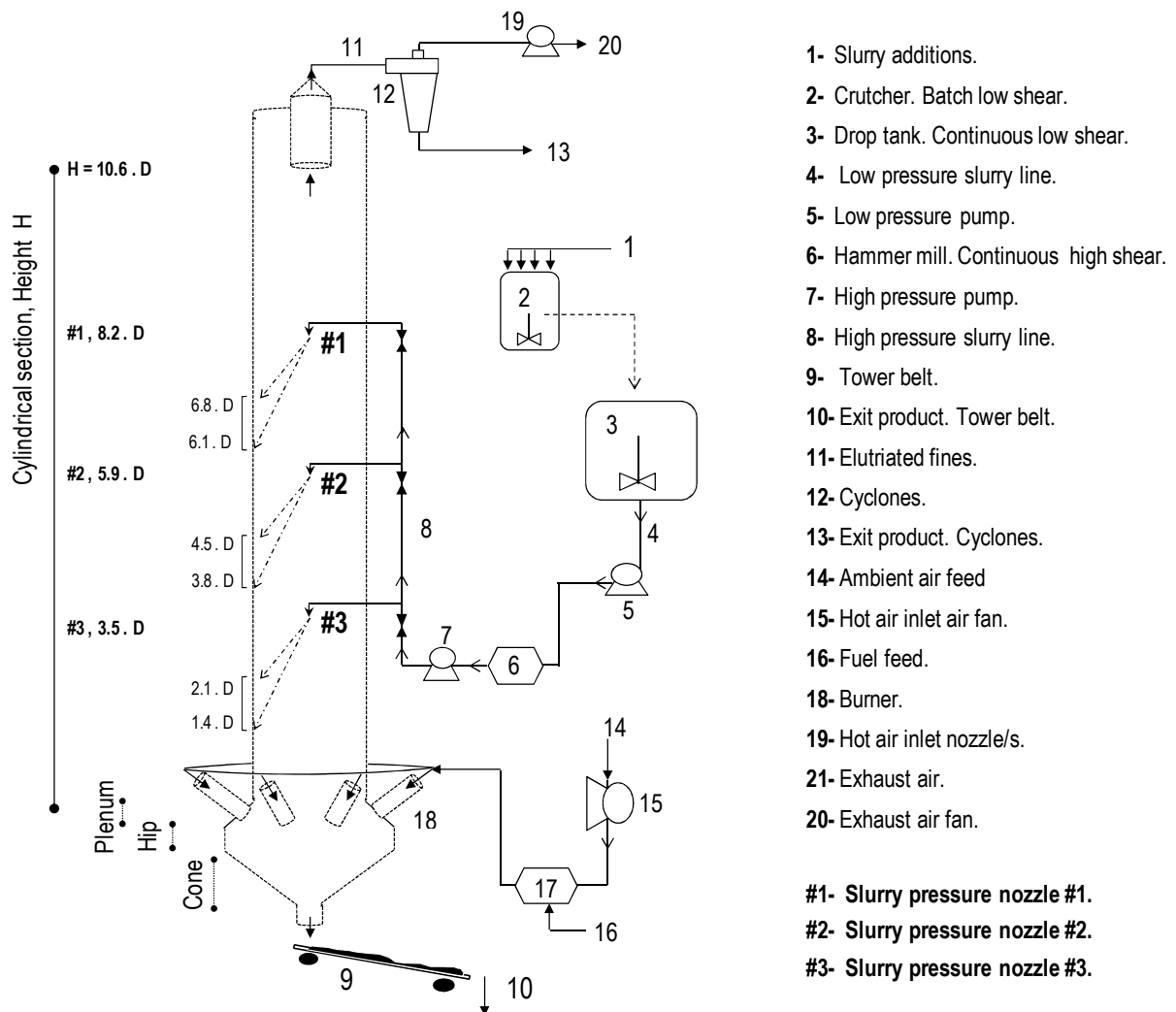
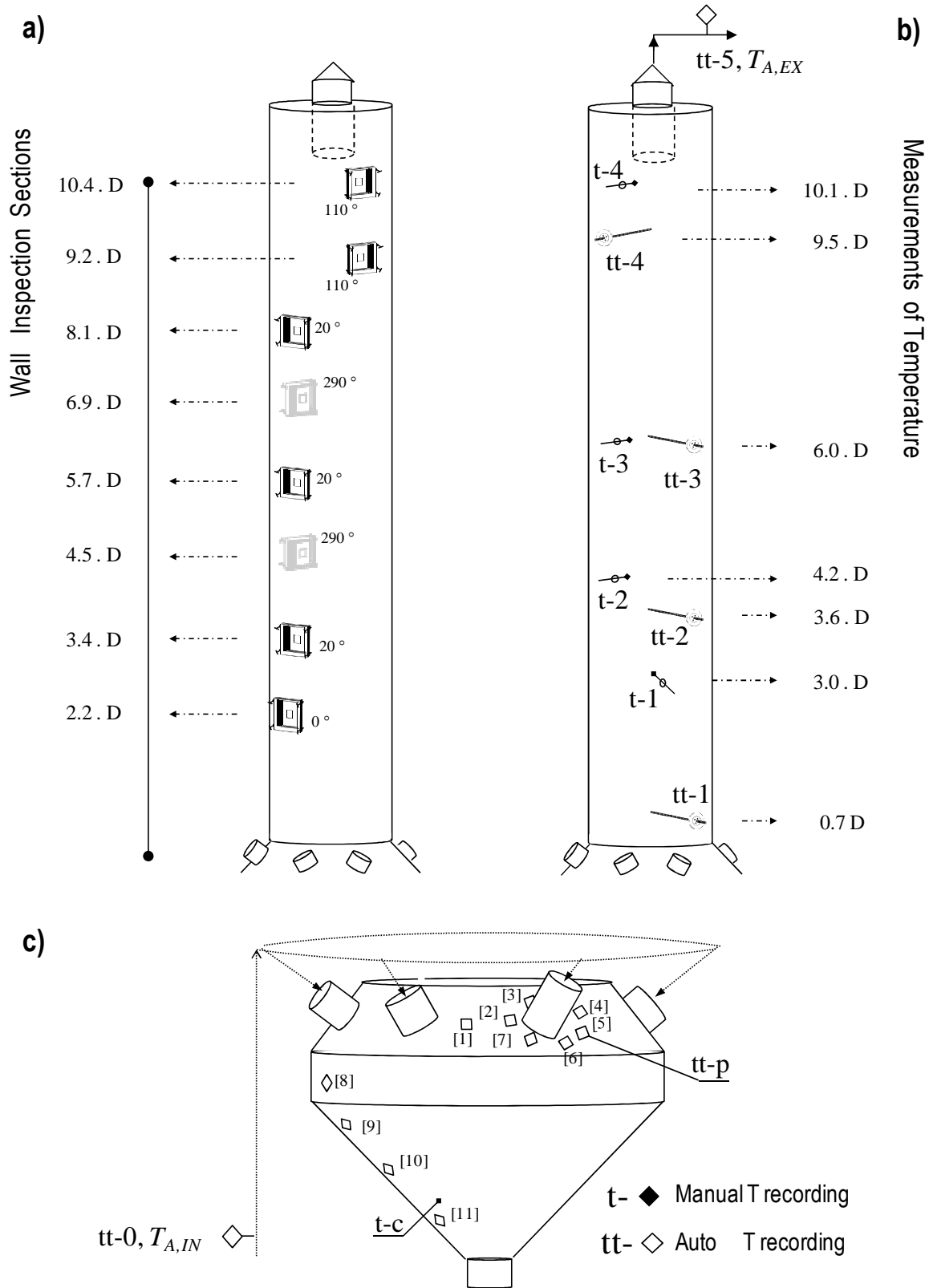


**Figure 1.** General outline of operation of a counter-current spray drying tower. Nomenclature, hot air generation, slurry preparation and atomization lines, including the location of nozzles and the projection area of the sprays at the walls.



[1]-to[7] measure  $T_w$  and  $T_A$  near inlet, averaged as tt-p.

[8] to [11] measure  $T_w$  only.

**Figure 2.** Measurements in the dryer: location of a) Inspection areas of the walls, and b) Air temperature,  $T_A$  sensors in the cylinder and exhaust line, and c)  $T_A$  sensors at the inlet line and the bottom section, and sensors at the dryer walls,  $T_w$ .

exchanged in that section. In addition, it causes a higher particle concentration,  $n$ , in the unit because of the higher drag forces, and enhances the convective heat transfer particularly at the top of the unit.

This work compares both limiting cases. It reproduces the exact same experiments that are presented in Chapter VI but under modified air inlet conditions, increasing or decreasing  $\bar{T}_{A,IN}$  by 40 °C and adjusting  $\bar{M}_A$ . The operating conditions are summarized in Tables 1 and 2, where +, ~ and – denote the operation at a high, reference or low  $\bar{T}_{A,IN}$ . The cases  $S_1$ ,  $S_2$  and  $S_3$  operate a single nozzle from the positions named #1, #2 or #3 in Figure 1 and the multi-level case,  $M_{13}$ , doubles the production rate by using simultaneously the nozzles in positions #1 and #3. In most cases, the product shows a similar  $X_w$ , see section 3.4.

Some experiments in Table 1 show differences between the product exit temperature  $\bar{T}_P$  observed at the reference and the cases + and –. They respond to a seasonal variation owing to the cooling that the product experiences from the tower exit to the sampling point after the belt in Figure 1. This is a common observation in this unit and has been confirmed by the replication of  $M_{\sim 13}$  in the same ambient conditions, obtaining the same similar  $\bar{T}_P$  than  $M_{+13}$  and  $M_{-13}$ . The impact of the seasonal  $\Delta T$  in the overall energy balance is  $< 0.05 Q_{Ex}$ , and has been reflected in the errors given for the energy balance in the next section. The product size distributions reported later are not affected.

In Table 1 the elutriation rate  $M_E$  clearly increases as  $\bar{T}_{A,IN}$  is reduced from the case + to ~ and – because the air velocity becomes higher and the solids are dragged to the top.

### 3. Results and Discussion.

#### 3.1. Axial distribution of the heat exchanged.

This section describes the changes in the air temperature field and how the heat is utilised in different sections of the dryer. The air temperature field for the cases is presented in Figure 3 and the axial decay of the cross-sectional average,  $\bar{T}_A$ , is given in Figure 4.

In  $S_1$  the air temperature  $\bar{T}_A$  is fairly homogeneous, see Figure 3a. The bottom of the chamber shows a high radial span  $\Delta T > 30^\circ\text{C}$  and region of low  $\bar{T}_A$  near the wall region. This is an indication of the high  $n$  and local drying rate. Moving from the cold to the hot cases from  $S_{-1}$  to  $S_{+1}$ , the inlet temperature  $\bar{T}_{A,IN}$  goes up by 80°C but this translates only in an increment of  $\Delta\bar{T}_A \approx 40^\circ\text{C}$  at the bottom of the unit, see  $tt - 1$  in Figure 3a, and of  $\Delta\bar{T}_A \approx 20^\circ\text{C}$  below the spray, see  $tt - 3$ . This

**Table 1.** Time averaged process conditions for the operation of nozzle #1 and #2 in  $S_1$  and  $S_2$ . Comparison of the reference case denoted,  $\sim$ , with the cold scenario, denoted  $-$  ( $\downarrow T_{A,IN}$   $\uparrow M_A$ ), or the hot scenario denoted  $+$  ( $\uparrow T_{A,IN}$   $\downarrow M_A$ ).

Scenario	$S_{-1}$	$S_{\sim 1}$	$S_{+1}$	$S_{-2}$	$S_{\sim 2}$	$S_{+2}$
Slurry line, S, Water lines, W, Product in the tower belt, P, elutriated fines, E, and full exiting power, EP,						
Nozzle/s	#1	#1	#1	#2	#2	#2
$\bar{M}_S / \bar{M}_{S_{\sim 1}}$	$1.04 \pm 0.02$	$1.00 \pm 0.04$	$1.0 \pm 0.04$	$0.93 \pm 0.04$	$1.00 \pm 0.06$	$0.93 \pm 0.02$
$\bar{M}_E$ (% $\bar{M}_{EP}$ )	5.5	4.1	2.7	3.5	2.7	1.8
$\bar{T}_P - \bar{T}_S$ (°C)	$15.0 \pm 7.0$	$-5.1 \pm 6.8$	$27.0 \pm 8.2$	$17.3 \pm 9.8$	$-1.4 \pm 9.2$	$21.3 \pm 12.8$
$X_W - X_{W,S_{\sim 1}}$ (%)	0.7	0.0	1.4	0.6	-0.7	0.6
Air line, A, inlet, IN, and exhaust, EX, conditions.						
$\bar{M}_A / \bar{M}_{A,S_{\sim 1}}$	$1.28 \pm 0.04$	$1.00 \pm 0.02$	$0.86 \pm 0.06$	$1.16 \pm 0.08$	$1.00 \pm 0.02$	$0.84 \pm 0.10$
$tt - 0, \bar{T}_{A,IN}$ , (°C)	$229.5 \pm 2.4$	$272.9 \pm 4.2$	$311.4 \pm 3.2$	$230.1 \pm 6.2$	$273.0 \pm 3.4$	$310.7 \pm 11.2$
$tt - 5, \bar{T}_{A,EX}$ , (°C)	$79.0 \pm 1.6$	$81.7 \pm 1.0$	$85.0 \pm 1.2$	$78.6 \pm 2.0$	$86.8 \pm 1.0$	$85.7 \pm 1.6$
$rH_{EX}$ (%)	19	21	21	19	17	19

**Table 2.** Time averaged process conditions for operation of nozzle #3 or the multi-level operation of #1 and #3 in  $S_3$  and  $M_{13}$ . Comparison of the reference case denoted  $\sim$ , with the cold scenario, denoted  $- (\downarrow T_{A,IN} \uparrow M_A)$ , or the hot scenario denoted  $+ (\uparrow T_{A,IN} \downarrow M_A)$ .

Scenario	$S_{-3}$	$S_{\sim 3}$	$S_{+3}$	$M_{-13}$	$M_{\sim 13}$	$M_{+13}$
Slurry line, S, Water lines, W, Product in the tower belt, P, elutriated fines, E, and full exiting power, EP,						
Nozzle/s	#3	#3	#3	#1, #3	#1, #3	#1, #3
$\bar{M}_{S,\#1} / \bar{M}_{S\sim 1}$	-	-	-	$0.99 \pm 0.02$	$0.91 \pm 0.04$	$0.99 \pm 0.02$
$\bar{M}_{S,\#3} / \bar{M}_{S\sim 1}$	$1.00 \pm 0.04$	$0.99 \pm 0.02$	$0.99 \pm 0.02$	$0.96 \pm 0.02$	$1.01 \pm 0.02$	$0.99 \pm 0.02$
$\bar{M}_E$ (% $\bar{M}_{EP}$ )	4.1	2.0	2.3	5.1	3.1	1.5
$\bar{T}_P - \bar{T}_S$ (°C)	$0.9 \pm 9.4$	$-2.5 \pm 8.6$	$7.5 \pm 14.8$	$34.0 \pm 13.6$	$2.8 \pm 7.4$	$32.7 \pm 10.6$
$X_W - X_{W,S\sim 1}$ (%)	2.9	4.5	2.9	-0.1	0.7	2.0
Air line, A, inlet, IN, and exhaust, EX, conditions.						
$\bar{M}_A / \bar{M}_{A,S\sim 1}$	$1.28 \pm 0.04$	$0.99 \pm 0.02$	$0.87 \pm 0.04$	$1.94 \pm 0.06$	$1.53 \pm 0.06$	$1.30 \pm 0.06$
$tt - 0, \bar{T}_{A,IN}$ , (°C)	$230.3 \pm 2.8$	$269.3 \pm 4.6$	$310.4 \pm 5.2$	$260.0 \pm 4.8$	$300.1 \pm 7.0$	$339.5 \pm 6.6$
$tt - 5, \bar{T}_{A,EX}$ , (°C)	$91.2 \pm 0.8$	$89.8 \pm 1.4$	$95.6 \pm 1.0$	$77.0 \pm 1.8$	$78.2 \pm 2.2$	$75.4 \pm 1.2$
$rH_{EX}$ (%)	11	14	13	26	29	37

**Figure 3.** Time averaged air temperature  $\bar{T}_A$  profiles from  $tt-1$  at  $0.7 D$ ,  $tt-2$  at  $3.6 D$ ,  $tt-3$  at  $6.0 D$ ,  $tt-4$  at  $9.5 D$ . a) Operation of nozzle #1 at  $8.2 D$  b) Operation of nozzle #2 at  $5.9 D$  c) Operation of nozzle #3 at  $3.5 D$ , d) Operation from nozzles #1 and #3.

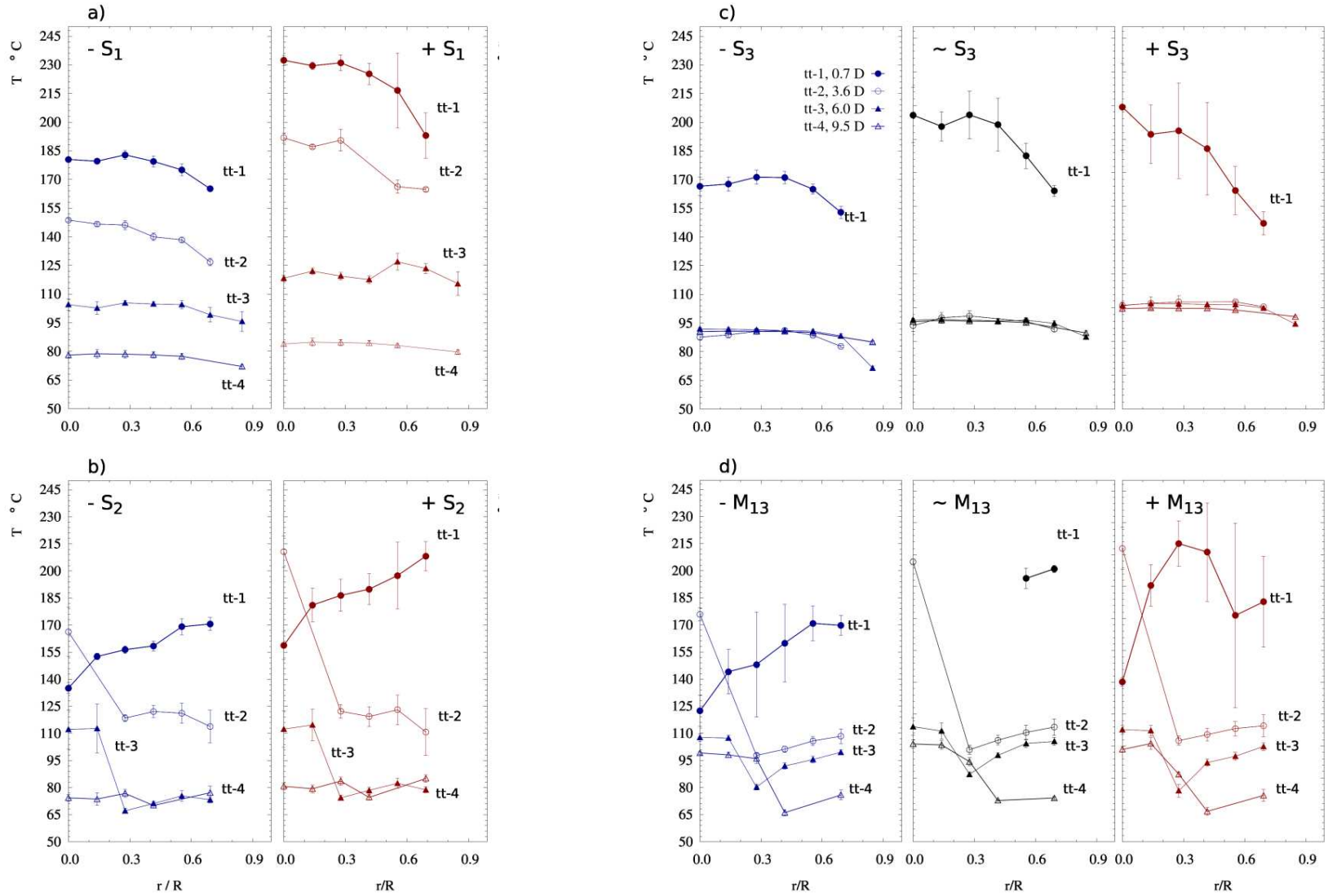
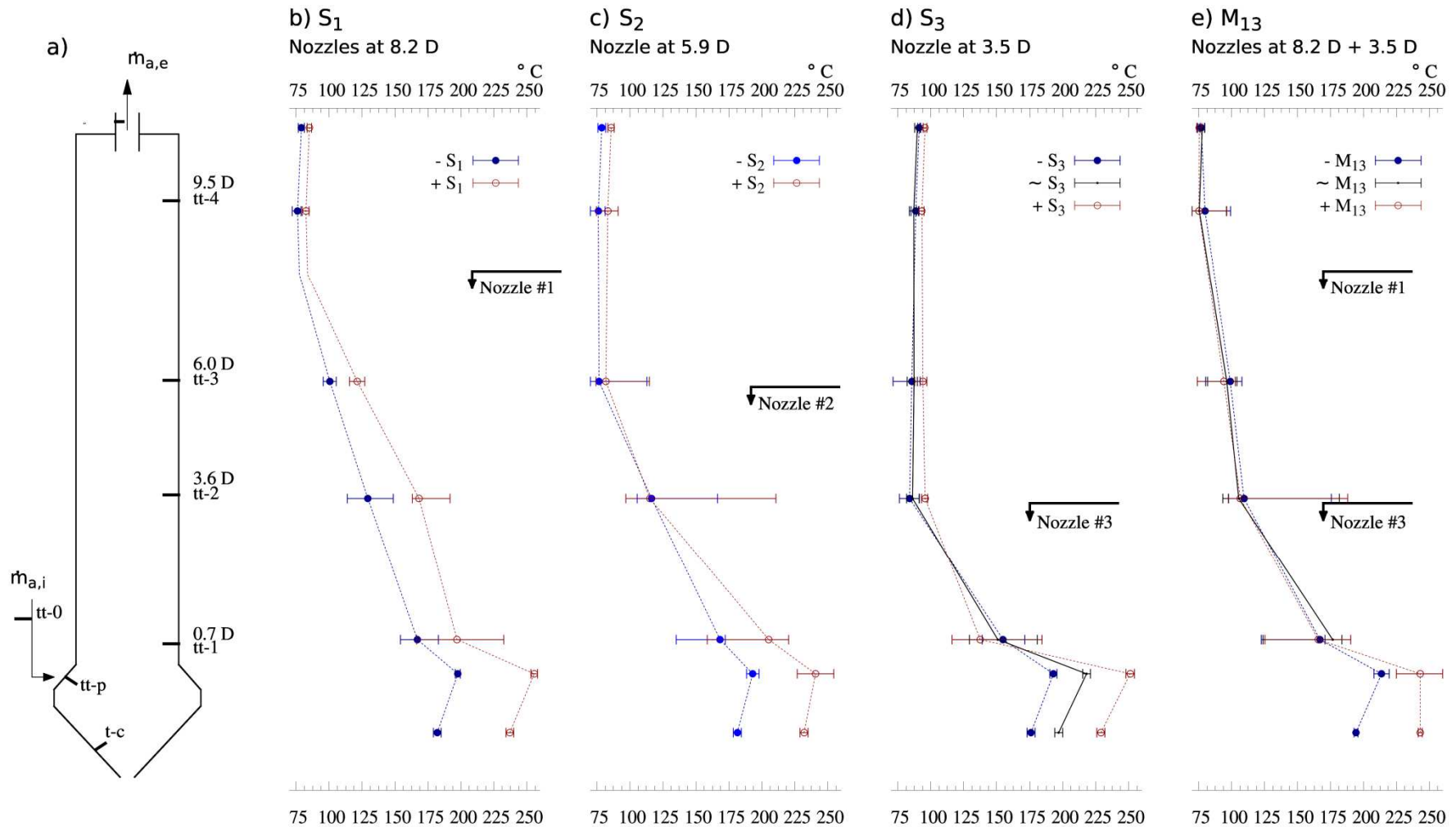


**Figure 4.** Cross-sectional average  $\bar{T}_A$  from  $tt - 1$  to  $tt - 4$ , time averaged  $\bar{T}_A$  measurements in  $tt - p$  and single punctual  $T_A$  measurements in  $t - c$ . a) Location of temperature sensors. b) Operation of nozzle #1 at 8.2 D c) Operation of nozzle #2 at 5.9 D d) Operation of nozzle #3 at 3.5 D, e) Operation from nozzles #1 and #3.



can be explained by the larger heat losses that are driven near the air distributor. Note the large drop between the values of  $\bar{T}_{A,IN}$  at  $tt - 0$  in Table 1 and that at the ports in  $tt - p$  in Figure 4.  $S_2$  originates a different pattern. At the bottom of the dryer,  $\bar{T}_A$  increases towards the wall and shows a large radial span  $\Delta T > 50^\circ\text{C}$ , see  $tt - 1$  in Figure 3b. The increment of  $\Delta\bar{T}_{A,IN} = 80^\circ\text{C}$  from  $S_{-2}$  to  $S_{+2}$  now results in a change of  $\Delta\bar{T}_A \approx 20 - 40^\circ\text{C}$  at  $tt - 1$  but very similar values above. In this case, it can be noticed how a region of high  $\bar{T}_A$  forms at the centre of the tower below the spray projection in the level  $tt - 2$ , which then persists above the nozzle position in  $tt - 3$ .

Placing the nozzle at the bottom end, in  $S_3$ , renders an homogeneous field in all the levels above and a different pattern below the spray projection, see  $tt - 1$  in Figure 3c. In this case,  $\bar{T}_A$  shows a maximum value between  $0.30 < r < 0.50 R$  and then it decreases towards the wall. Interestingly, the temperature increases from  $S_{-3}$  to  $S_{\sim 3}$  but in this case it does not from  $S_{\sim 3}$  to  $S_{+3}$ . Only the radial span becomes affected, increasing when the air carries less velocity in the case  $S_{+3}$ .

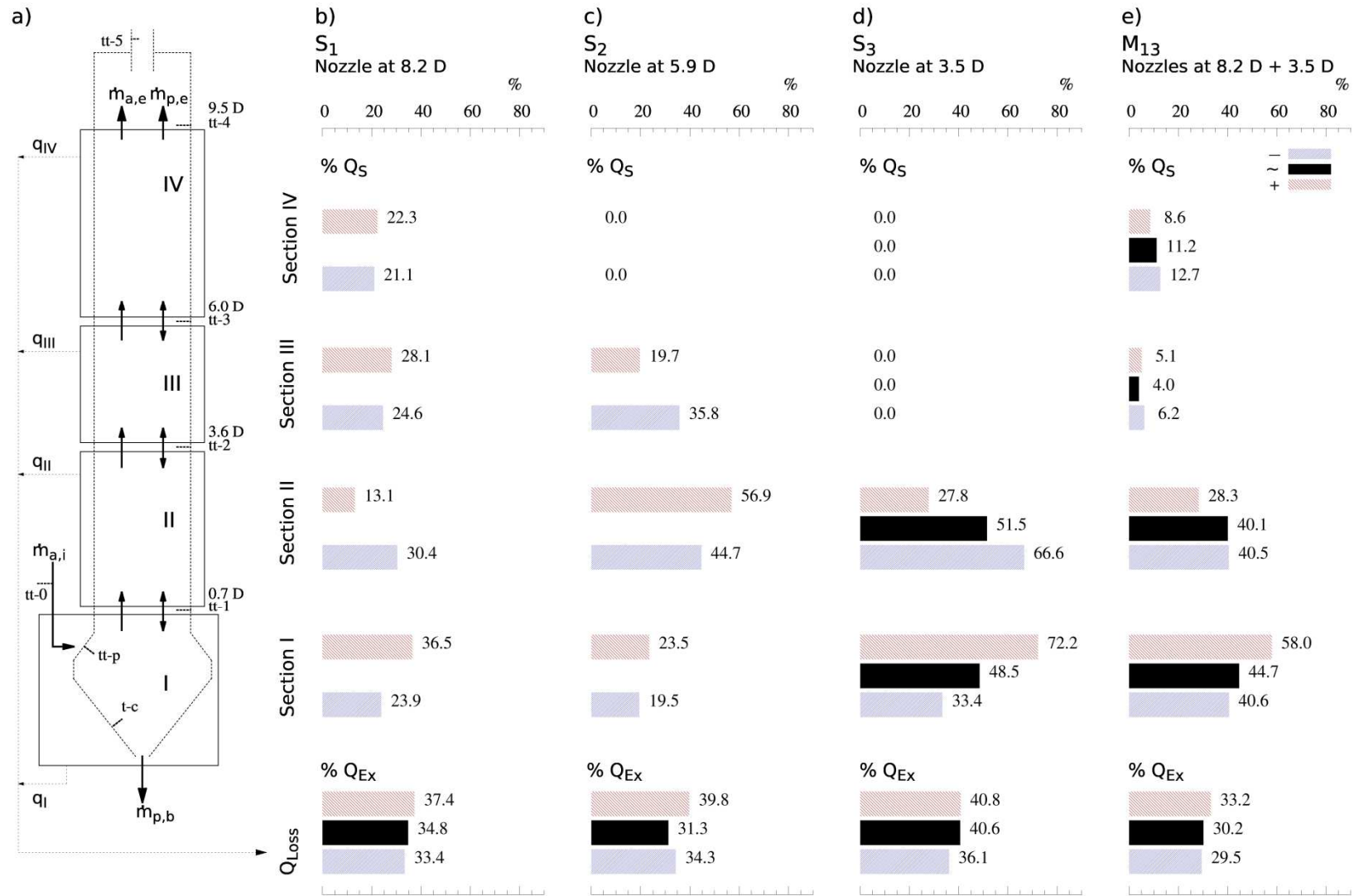
The multi-nozzle system shows some similarities to  $S_2$ . It is characterised by the formation of a region of high  $\bar{T}_A$  at the centre, see Figure 3d. In this case the hot region forms between both nozzles and then extends all the way up to the top. This feature may be linked to similar recirculation and instabilities to those described in Chapters II and III. In production however, the recirculation will be affected also by the disruption of the spray, the density changes and the interaction with the solids. The support of numerical models could prove a very powerful tool to study how these hot spots are produced.

Figure 5 summarizes how the energy input is utilised across different sections of the dryer. It complements the results of the energy balance described also in Chapter VI. The overall evaporation and the heat loss rate are computed from a general mass and energy balance, given in (1).

$$Q_{Ex} = \Delta H_{A,Lat} + Q_{loss} = -(\Delta H_{DA,Sn} + \Delta H_{P,Sn}) \quad (1)$$

where  $Q_{Ex}$  is defined as the heat exchanged. It results from variation in the sensible enthalpy of the dry air,  $\Delta H_{DA,Sn}$  and the product (i.e. the inlet slurry, and the outlet powder, outlet elutriates and outlet water vapour).  $Q_{Ex}$  is utilised in causing the evaporation,  $\Delta H_{A,Lat}$ , and in the heat lost to the environment,  $Q_{loss}$ . It is important noticing that all cases show substantial losses,  $Q_{loss} = 0.29 - 0.41 Q_{Ex}$ . They are negligible above the nozzle and very localised in Section I defined in Figure 5a ( $Q_{loss,I} > 0.77 - 0.93 Q_{loss}$ ). To a large part, they owe to the loss in the air distributor since the

**Figure 5.** a) Definition of Sections I, and Section II (containing nozzle #3), Section III (containing nozzle #2) and Section IV (containing nozzle #1). Losses,  $Q_{Loss}$ , and distribution of the rate of heat transferred to the solids,  $Q_s$ , across the chamber b)  $S_1$ , nozzle at 8.2 D c)  $S_2$ , nozzle at 5.9 D d)  $S_3$ , nozzle at 3.5 D, e)  $M_{13}$ , nozzles at 8.2 D and 3.5 D.



$\Delta\bar{T}_A$  only between  $tt - 0$  and  $tt - p$  is responsible of 63 – 87%  $Q_{loss}$ .

In order to be able to compare how the solids are dried in a given each section  $i$ , it is useful to rearrange the terms in (1) and calculate the heat transferred to the solids,  $Q_S$ , given in (2).

$$Q_{S,i} = -(\Delta H_{DA,Sn,i} + Q_{loss,i}) = \Delta H_{A,lat,i} + \Delta H_{P,Sn,i} \quad (2)$$

$Q_{S,i}$  is utilised in heating and drying the solids. The contribution of heating,  $\Delta H_{P,Sn}$ , is limited so that one can consider  $Q_{S,i}$  an indication of the heat used for the evaporation of water and drying of the solids. To compute these values from (2) one needs to estimate the heat losses in each section. They are very limited in the cylinder, and can be distributed according to the contact area of each section and the temperatures of the air and the wall, assuming all share a comparable heat transfer resistance.

Chapter VI shows how the use of high nozzle positions in  $S_{\sim 1}$  and  $S_{\sim 2}$  results in a similar heat transfer efficiency,  $\eta_h$ . It drops when the residence time is reduced excessively bringing the spray down in  $S_3$ . Increasing the air temperature  $T_A$  and the particle loading in  $M_{\sim 13}$  makes the efficiency rise.

Table 3 shows the impact of the inlet air conditions for each case. The use of higher air temperatures in the cases + causes a large  $\Delta T$  between the air and the solids. In part, this explains why the thermal efficiency  $\eta_t$  rises, that is: more heat is extracted from the air. However, this occurs only because the dryer reaches higher temperatures and  $Q_{loss}$  increases. Notice that the overall heat transfer efficiency  $\eta_h$  (i.e. the heat transferred to the solids) remains constant. This means one requires the same energy input for either type of operation. In cases + more energy is lost to the environment ( $Q_{Loss}$ ). When one reduces  $T_A$  in cases –, the  $Q_{Loss}$  diminishes but more energy leaves the system with the exhaust air (of similar  $T_{A,EX}$  but higher  $M_A$ ). In the end, both approaches are equally efficient, but one may perhaps argue that cases – allow for a potential recovery of heat in the exhaust air.

To account for the size of the sections it is also useful to compare the rate of heat transferred per  $m$  of tower and  $g$  of dry slurry,  $r$ . The overall energy balance and the specific rates are given in Table 3.

It is interesting to notice in Figure 5 that a large proportion of the energy is exchanged within the conical section, Section I, particularly as the nozzle is brought down. The proportion of heat exchanged within the spray region also increases as the nozzle is brought down, from 21.1 – 22.3 % in the cases  $S_1$  (see Section IV in Figure 5) to 19.7 – 35.8 % in  $S_2$  and 27.8 – 66.6 % in  $S_3$ .

**Table 3.** Energy balance. Overall contribution of losses,  $Q_{Loss}$ , and the sensible enthalpy change,  $\Delta H_{p,Sn}$  of the product. Thermal efficiency and the overall heat transfer efficiency in the dryer as defined in Chapter VI and in the nomenclature. Rate of heat transferred to the solids.  $r = Q_s / (\Delta z \cdot M_s (1 - X_{w,s}))$ . Bold indicates the spray region/s.

	$S_{-1}$	$S_{+1}$	$S_{-2}$	$S_{+2}$	$S_{-3}$	$S_{\sim 3}$	$S_{+3}$	$M_{-13}$	$M_{\sim 13}$	$M_{+13}$
Overall Energy Balance										
$Q_{Loss}$ (% $Q_{Ex}$ )	33.4 ± 1.1	37.4 ± 1.7	34.3 ± 0.9	39.8 ± 1.0	36.1 ± 0.7	40.6 ± 0.5	40.8 ± 1.0	29.5 ± 2.1	30.2 ± 1.8	33.2 ± 2.2
$\Delta H_{p,Sn}$ (% $Q_{Ex}$ )	-0.1 ± 1.6	1.3 ± 2.7	0.6 ± 1.4	1.2 ± 1.7	-0.9 ± 1.0	-1.5 ± 0.9	-0.4 ± 1.8	1.6 ± 3.0	-2.2 ± 2.7	1.5 ± 3.3
$\eta_t$ $\left( \frac{T_{A,IN} - T_{A,EX}}{T_{A,IN} - T_{amb}} \right)$	0.72 ± 0.01	0.78 ± 0.01	0.73 ± 0.02	0.77 ± 0.03	0.66 ± 0.01	0.72 ± 0.02	0.74 ± 0.01	0.76 ± 0.02	0.79 ± 0.02	0.83 ± 0.02
$\eta_h$ ( $Q_s / H_{A,IN}$ )	0.49 ± 0.01	0.50 ± 0.02	0.48 ± 0.01	0.47 ± 0.02	0.43 ± 0.01	0.43 ± 0.01	0.44 ± 0.01	0.55 ± 0.02	0.56 ± 0.02	0.57 ± 0.02
Specific drying rate, $r$ $J s^{-1} m^{-1} g^{-1}$										
II 0.7 D - 3.6 D	53.0 ± 0.5	22.3 ± 0.8	77.5 ± 0.4	99.5 ± 0.5	<b>108.3</b> ± 0.3	<b>77.0</b> ± 0.2	<b>43.8</b> ± 0.3	<b>69.5</b> ± 0.7	<b>70.6</b> ± 0.6	<b>46.9</b> ± 0.6
III 3.6 D - 6.0 D	53.6 ± 0.3	59.7 ± 0.6	<b>77.6</b> ± 0.2	<b>43.1</b> ± 0.2	0.0	0.0	0.0	13.3 ± 0.4	8.8 ± 0.3	10.5 ± 0.3
IV 6.0 D - 9.5 D	<b>30.5</b> ± 0.2	<b>31.6</b> ± 0.3	0.0	0.0	0.0	0.0	0.0	<b>18.1</b> ± 0.3	<b>16.5</b> ± 0.2	<b>11.9</b> ± 0.2

Clearly, the droplets are sprayed into regions of higher temperatures and velocities and this increases their residence time. The heat transfer rates  $r$  are quantified in Table 3. They present higher values in the spray region as the nozzle approaches the bottom, moving from  $S_3$  to  $S_2$  and  $S_1$ .

When using low velocities in the cases denoted +, the solids expend a larger part of the residence times in the bottom section of the dryer. As a result, large values of  $r$  appear below the projection of the spray, in Section III for case  $S_{+1}$  or Section II for case  $S_{+2}$  in Table 3. In contrast, increasing the velocities in  $S_{-2}$  and  $S_{-3}$  leads to higher heat transfer rates within the spray region, which are explained by the solids having a higher residence time and a better convection. However, when the nozzle is placed at a higher position in  $S_{-1}$  the air temperature is allowed to decrease further across the cylinder and this causes the heat transfer rate  $r$  to drop near the spray in Section IV. In this case, increasing the inlet air temperature in  $S_{+1}$  is a better way to enhance  $r$  near the spray because it allows maintaining a higher  $\Delta T$  between the phases up to top end of the unit.

It is interesting to notice that in  $S_{-1}$  and  $S_{-2}$  the heat is exchanged more homogeneously at the bottom of the dryer; see  $r$  shows a fairly constant value in Table 3 for Sections II and III. This could be explained by the shrinkage being completed near the spray, and a transition to a diffusion dominated stage below where particle drying responds to changes in concentration but not  $T_A$ . However, to confirm this, further experiments would be required including the measurement of air humidity so that one may compute the evaporation rate from the solids instead of the heat transfer rate  $r$  reported here.

Similar conclusions are drawn in  $M_{13}$ . In all the cases a small fraction of the heat is exchanged above the bottom nozzle, denoted #3. This is an important fact. In contrast to the top nozzle alone in  $S_{+1}$ , it shows that one cannot promote the heat transfer rate nearby the top spray by increasing  $T_{A,IN}$ . In fact, this is detrimental in  $M_{+13}$  because the higher temperatures shift the heat exchanged to the bottom region. In the largest towers, it is common to use multiple nozzles at each level. This serves as a good alternative to control the drying rates: one can modify the slurry rate injected at each level by changing the number of nozzles but maintaining the same droplet size. This has been explored in full scale experiments and constitutes work in progress beyond the scope of this thesis (see Industrial Impact).

### 3.2. Decay of the vortex momentum.

Tables 4 and 5 present an estimation of the air superficial velocity,  $\bar{U}_{av}$ , and the air axial momentum flux,  $\bar{\rho}_A \bar{U}_{av}^2$ , at different levels in the chamber normalised to a reference value. In all the cases using

**Table 4.** Axial variation of the air superficial velocity,  $\bar{U}_{av}$ , estimated with  $\bar{U}_{av} = \bar{M}_A / \bar{\rho}_A \pi R^2$ . Bold denote the limits of the spray region. Red denotes the reference.

$\frac{\bar{U}_{av}}{\bar{U}_{av,s\sim 3,tt=0}}$	$S_{-1}$	$S_{+1}$	$S_{-2}$	$S_{+2}$	$S_{-3}$	$S_{\sim 3}$	$S_{+3}$	$S_{-13}$	$S_{\sim 13}$	$S_{+13}$
$tt - 0, \quad 0.0 D$	1.20	0.94	1.08	0.91	1.20	<b>1.00</b>	0.94	1.92	1.62	1.47
$tt - 1, \quad 0.7 D$	1.05	0.75	0.95	0.75	<b>1.02</b>	<b>0.78</b>	<b>0.66</b>	<b>1.58</b>	<b>1.27</b>	<b>1.06</b>
$tt - 2, \quad 3.6 D$	0.96	0.71	<b>0.84</b>	<b>0.61</b>	<b>0.86</b>	<b>0.67</b>	<b>0.59</b>	<b>1.38</b>	<b>1.07</b>	<b>0.91</b>
$tt - 3, \quad 6.0 D$	<b>0.89</b>	<b>0.63</b>	<b>0.75</b>	<b>0.56</b>	0.86	0.67	0.59	<b>1.34</b>	<b>1.05</b>	<b>0.88</b>
$tt - 4, \quad 9.5 D$	<b>0.83</b>	<b>0.57</b>	0.75	0.56	0.86	0.67	0.59	<b>1.27</b>	<b>0.99</b>	<b>0.84</b>

**Table 5.** Axial variation of the axial momentum flux  $\bar{\rho}_A \bar{U}_{av}^2$  based in the superficial velocity, estimated as  $\bar{U}_{av} = \bar{M}_A / \bar{\rho}_A \pi R^2$ . Bold denote the limits of the spray region. Red denotes the reference.

$\frac{\bar{\rho}_A \bar{U}_{av}^2}{[\bar{\rho}_A \bar{U}_{av}^2]_{s\sim 3,tt=0}}$	$S_{-1}$	$S_{+1}$	$S_{-2}$	$S_{+2}$	$S_{-3}$	$S_{\sim 3}$	$S_{+3}$	$S_{-13}$	$S_{\sim 13}$	$S_{+13}$
$tt - 0, \quad 0.0 D$	1.54	0.81	1.26	0.77	1.54	<b>1.00</b>	0.82	3.75	2.50	1.92
$tt - 1, \quad 0.7 D$	1.35	0.65	1.11	0.63	<b>1.31</b>	<b>0.78</b>	<b>0.58</b>	<b>3.09</b>	<b>1.96</b>	<b>1.38</b>
$tt - 2, \quad 3.6 D$	1.24	0.61	<b>0.98</b>	<b>0.51</b>	<b>1.10</b>	<b>0.67</b>	<b>0.52</b>	<b>2.69</b>	<b>1.65</b>	<b>1.19</b>
$tt - 3, \quad 6.0 D$	<b>1.15</b>	<b>0.55</b>	<b>0.88</b>	<b>0.47</b>	1.10	0.67	0.52	<b>2.61</b>	<b>1.61</b>	<b>1.15</b>
$tt - 4, \quad 9.5 D$	<b>1.08</b>	<b>0.50</b>	0.88	0.47	1.10	0.67	0.52	<b>2.48</b>	<b>1.52</b>	<b>1.09</b>

a low temperature ( $S_{-1}$ ,  $S_{-2}$  and  $S_{-3}$ ) the velocity  $\bar{U}_{av}$  goes up by 8 – 20% and in the cases using high temperatures ( $S_{+1}$ ,  $S_{+2}$  and  $S_{+3}$ ) it is reduced by 6 – 9%. The axial momentum flux is affected by the change in air density. It has been either increased by 26 – 56% or reduced by 19 – 23% for the same cases in Table 5. During the multi-level operation,  $M_{13}$ , the unit works at a higher velocity range. From  $M_{-13}$  to  $M_{+13}$  the air velocity  $\bar{U}_{av}$  and momentum flux  $\bar{\rho}_A \bar{U}_{av}^2$  are increased from 47% to 93% and 192% to 375% higher values respectively.

In a counter-current tower the accumulation of the solids is very sensitive to an increase in the velocity of the air because it determines the size range that tends to stagnation. The differences shown are expected to have an important effect on how particles disperse. This is clear from the increase of the elutriation in Tables 1 and 2 but it also affects how particles concentrate and come into contact.

### 3.2.1. Air-borne contacts.

When one opts to use larger temperatures it enhances the  $\Delta T$  between the phases, particularly at the bottom of the dryer, but instead it reduces convection at the top region (see Table 4). Without the support of numerical models or a measurement of concentration, it is difficult to establish whether the surface of the particles near the spray becomes more or less prone to aggregation. However the growth will be very sensitive to the rate of the collisions, and this increases drastically in the cases denoted –.

Increasing the drag to the air has two differentiated effects. In the axial direction, it opposes the sedimentation of particles and it is likely to cause a higher accumulation of solids. This can be very important if happens close the sprays. In parallel, the tangential component of the drag entrains the solids in a stronger swirl. This means that when using high air velocities, the solids also present a higher terminal velocity because they despite they flow at lower velocity down, they do it faster in the tangential direction. This has a limited effect in the relative velocity between different particles, but it increases their concentration and essentially troughs more solids outwards at higher velocity, as illustrated in Figure 6.

### 3.2.2. Wall contacts.

A large part of the product was at some point part of the deposits. One should ask the question of how these respond to the same changes. It is helpful to describe an overall energy balance to the air. Drag transfers some of the kinetic energy carried by the air into the solids. As explained before, this energy is used to hold the solids and increase their momentum. When they are brought to the wall the kinetic

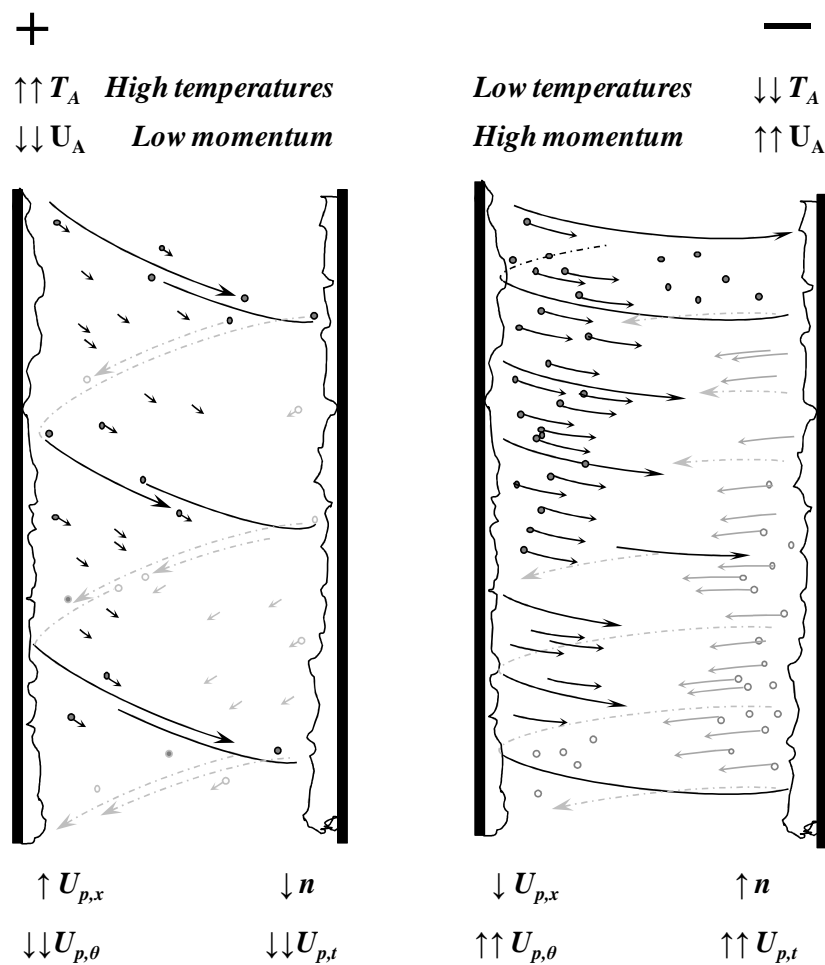


**Figure 6.** Description of concentration, dispersion and the rate of wall impacts associated to the transition of the swirling air flow by increasing the velocities and reducing the drying temperature from cases + to -

energy results in certain stresses upon the deposits. The contact can be simplified by a restitution coefficient, but this fails to acknowledge the microstructure of the clusters at the wall. The way in which they form and how they break respond to this stresses. The size of the material that comes from the wall is then a manifestation of the balance between the cohesive forces that hold the clusters and the stresses responsible of breakage: a) gravity, b) aerodynamic forces and c) the inertia of impacts. In the cases denoted + the wall is subject to low stresses, low adhesion forces may be overcome and the breakage produces a lower number of particles of a large size. This may happen only if they grow sufficiently for gravity to make them detach. But when the air velocity rises the clusters need to sustain larger aerodynamic forces, more particles impacts and of a higher energy, and this makes them to break up into smaller pieces. In this way, increasing or decreasing particle concentration  $n$  in cases - and + can modify the wearing time scale and form either a) a thinner active layer by there-entrainment of small fragments, or b) allow it to grow thicker and cause the detachment of large pieces.

### 3.3. Wall deposits.

Tables 6 and 7 summarize the initial net deposition rate,  $r_{d,o}$ . Selected positions are shown in Figures 7 and 8. The same general trends given in Chapters V and VI are maintained here. Most of the unit shows no deposition, due a low  $n$  in the upper part and the dry state of particles at the bottom.

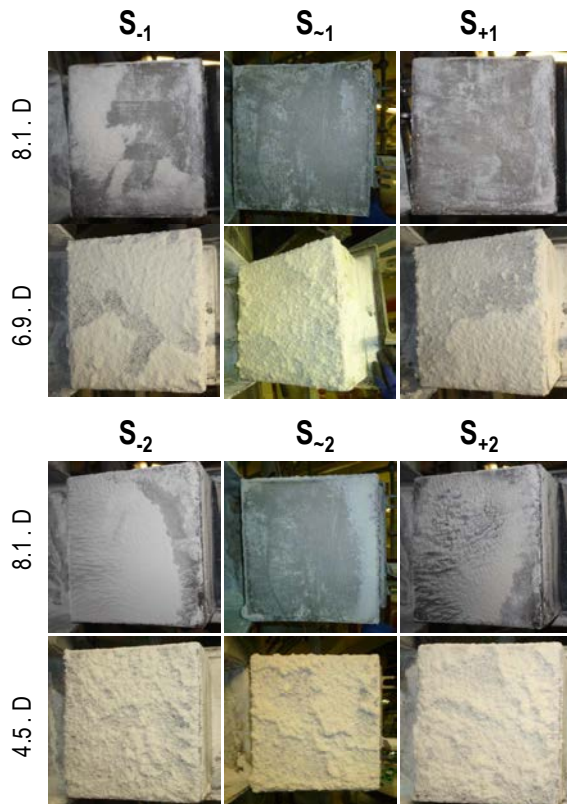


**Figure 7.** Inspection of the wall deposits at the top levels and the spray projection. Top: case  $S_1$ . Bottom: case  $S_2$ .

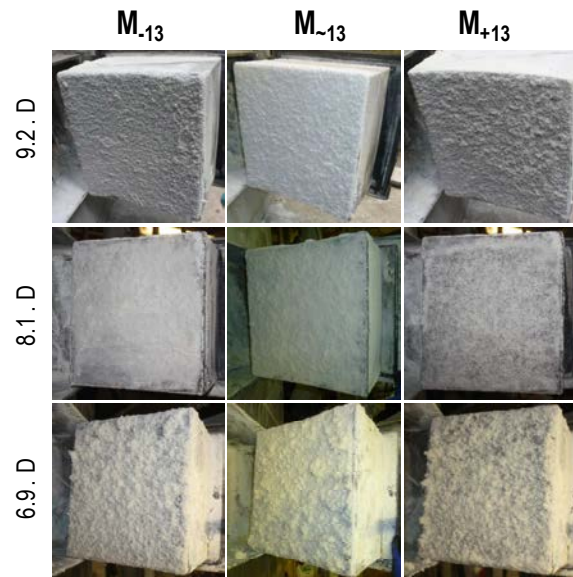


**Figure 8.** Inspection of the wall deposits associated to the levels and the spray projection in  $M_{13}$

**Table 6.** Initial wall net deposition rate,  $r_{d,o}$ , in the areas shown in Figure 2 and 7. Bold indicates the closest to the spray projection, depicted in Figure 1. Cases  $S_1$  and  $S_2$ .

Level	$S_{+1}$	$S_{\sim 1}$	$S_{-1}$	$S_{+2}$	$S_{\sim 2}$	$S_{-2}$
/D	$g\ m^2\ min^{-1}$					
10.4	0.2	-	1.8	-	-	-
9.2	0	0	0	0.4	0.8	0
8.1	17.0	0	0.9	8.2	2.1	5.3
<b>6.9</b>	<b>44.8</b>	<b>54.3</b>	<b>88.7</b>	0	1.4	1.1
5.7	0	0	0	0	0	0
4.5	0	0	0	<b>60.0</b>	<b>108.7</b>	<b>75.4</b>
3.4	0	0	0	0	0	0
2.2	0	-	0	-	-	-

The highest rates correspond to the projection of the sprays. Comparison between the low to high velocity cases in  $S_1$  and  $M_{13}$  (from case + to -) shows how deposition increases at the spray projection. This can be explained by the stronger drag. It shifts up the droplet trajectories from the spray so that when they impact the wall they cover more of the inspection area centred at  $6.9 D$  in Figure 2 (see how in Figure 1 the projection area is defined according to the spray angle between  $6.1 - 6.8 D$ ).

$S_2$  shows the maximum deposition at the reference and a decrease into  $S_{-2}$ . This can be explained by the same effect because now the area of projection starts to fall above the inspection area. This is what happens also in  $S_3$  where the last available inspection area is  $2.2 D$ , above the spray projection.

It is important highlighting these are initial rates, when the walls are cleaned. At this stage, deposition is not balanced by the re-entrainment and the thickness increases, typically at a constant rate  $r_{d,o}$  (see Figure 10 in Chapter V). As this happens, the stresses become stronger and the thickness stabilises. This however can take a long time (i.e.  $> 60 \text{ min}$  during  $S_{-2}$  in Chapter V) and therefore, one should consider the values given for  $r_{d,o}$  as an indication of the rate of impacts to the wall, not to be mistaken with the final thickness of the deposits. While in the cases - one sees a higher rate of impacts, and thus  $r_{d,o}$ , this does not mean that the final deposits are thicker at steady state conditions.

### 3.4. Product Analysis.

#### 3.4.1. Aggregation patterns under different air inlet conditions.

Figure 9 provides a comparison of the initial droplet size distribution to the product in the references given in Chapter VI for a single nozzle case,  $S_{-3}$ , characterised by a mono-modal distribution and a

**Table 7.** Initial wall net deposition rate,  $r_{d,o}$ , in the areas shown in Figure 2 and 8. Bold indicates the closest to the spray projection depicted in Figure 1. Cases  $S_3$  and  $M_{13}$ .

Level	$S_{+3}$	$S_{-3}$	$S_{-3}$	$M_{+13}$	$M_{-13}$	$M_{-13}$
/D	$g \text{ m}^2 \text{ min}^{-1}$					
10.4	0.3	0	1.1	-	-	-
9.2	0	0	0	37.5	30.1	24.4
8.1	0.4	0	0.3	23.3	14.5	35.6
<b>6.9</b>	3.0	2.3	1.4	<b>62.5</b>	<b>82.1</b>	<b>88.4</b>
5.7	0	0.2	3.1	0	0	1.8
4.5	1.4	0	0	0	0	0
3.4	0	1.1	0	0	0	0
2.2	0	0.6	0	-	3.6	-

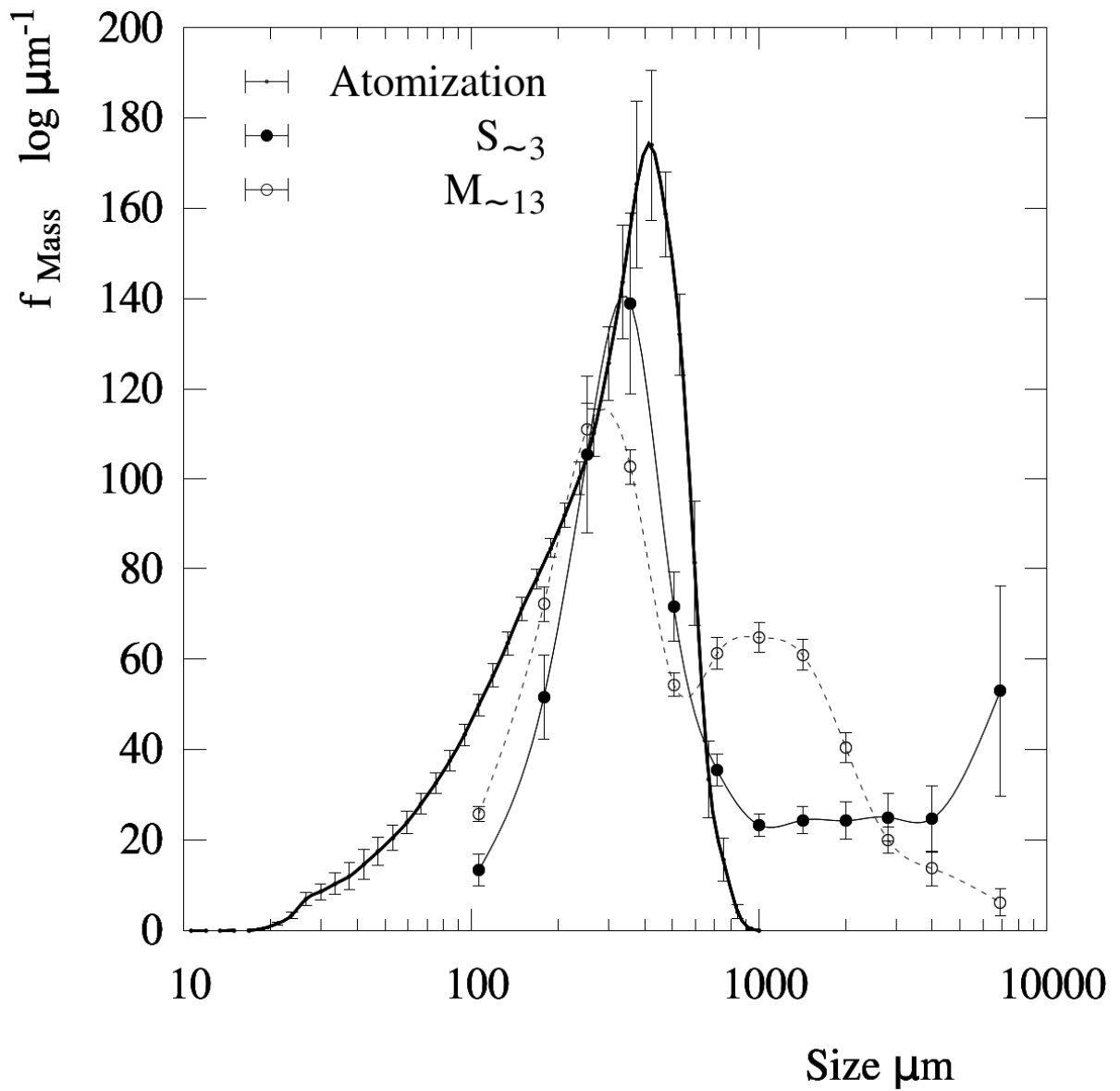


Figure 9. Standard growth patterns from Chapter VI. Comparison of the droplet size to  $S_{\sim 3}$  and  $M_{\sim 13}$ .

final plateau, and a multi-level system,  $M_{\sim 13}$ , resulting in a bi-modal size distribution. Table 8 compares the statistics of the size distributions for the cases described.

Figures 10, 11 and 12 show the evolution of a single nozzle comparing the reference to the operation at low or high temperatures. The same trend appears in all. The reduction of air velocity from the case  $-$  to  $\sim$  and  $+$  causes the formation of coarse granules  $> 850 \mu m$ , increasing  $x_{p,50}$  and  $x_{p,90}$  in Table 8. In Figure 10, the transition from  $S_{+1}$  to  $S_{-1}$  inhibits the growth into such large fractions. Instead the growth shifts into lower size ranges, turning the tail into a shoulder between  $600 - 1180 \mu m$  in  $S_{\sim 1}$  or into a secondary mode in  $S_{-1}$ . A similar trend is observed in Figures 11 and 12: moving from high to low air velocities reduces the mass within of the final tail in  $S_{-2}$  or the final plateau in  $S_{-3}$ . The reduction in size happens despite temperatures are lower and the particle concentration is likely higher. This is considered a clear indication of the promotion of the breakage at the walls.

One must also refer to the possibility of a better convective heat transfer being the responsible of the air-borne particles becoming drier and less prone to stick. Surely this is the case and could be used explain the effects in the mean product size if there was a congruent evolution of the size distributions. This is not the case, because it cannot explain why the production of granules  $> 850 \mu m$  is reduced. One expects that if the particles in the air were less prone to stick, the size of their aggregates should

**Table 8.** Statistics of the exit product size distribution, for all cases. Confidence intervals give one standard deviation.

Case	$x_{10}, \mu m$	$x_{25}, \mu m$	$x_{50}, \mu m$	$x_{75}, \mu m$	$x_{90}, \mu m$
<b>Droplet size</b>	85 $\pm$ 7	157 $\pm$ 10	292 $\pm$ 11	427 $\pm$ 9	530 $\pm$ 14
$S_{+1}$	185 $\pm$ 7	290 $\pm$ 12	546 $\pm$ 47	1352 $\pm$ 153	4463 $\pm$ (>560)
$S_{\sim 1}$	173 $\pm$ 4	261 $\pm$ 7	413 $\pm$ 15	824 $\pm$ 64	1724 $\pm$ 286
$S_{-1}$	183 $\pm$ 7	278 $\pm$ 8	458 $\pm$ 28	862 $\pm$ 50	1438 $\pm$ 123
$S_{+2}$	158 $\pm$ 3	239 $\pm$ 5	371 $\pm$ 14	684 $\pm$ 66	1443 $\pm$ 214
$S_{\sim 2}$	161 $\pm$ 3	238 $\pm$ 5	360 $\pm$ 10	597 $\pm$ 53	1168 $\pm$ 232
$S_{-2}$	166 $\pm$ 6	239 $\pm$ 14	359 $\pm$ 33	565 $\pm$ 93	901 $\pm$ 180
$S_{+3}$	198 $\pm$ 16	283 $\pm$ 26	508 $\pm$ 157	2145 $\pm$ 1128	( $x_{86} = 4760 \mu m$ )
$S_{\sim 3}$	195 $\pm$ 12	282 $\pm$ 20	456 $\pm$ 98	2224 $\pm$ 1575	( $x_{83} = 4760 \mu m$ )
$S_{-3}$	187 $\pm$ 14	258 $\pm$ 16	388 $\pm$ 39	1670 $\pm$ 1062	( $x_{84} = 4760 \mu m$ )
$M_{+13}$	166 $\pm$ 3	254 $\pm$ 8	541 $\pm$ 63	1464 $\pm$ 146	2761 $\pm$ 216
$M_{\sim 13}$	163 $\pm$ 3	246 $\pm$ 6	423 $\pm$ 22	1093 $\pm$ 61	2023 $\pm$ 186
$M_{-13}$	162 $\pm$ 3	240 $\pm$ 4	383 $\pm$ 13	858 $\pm$ 76	1606 $\pm$ 160

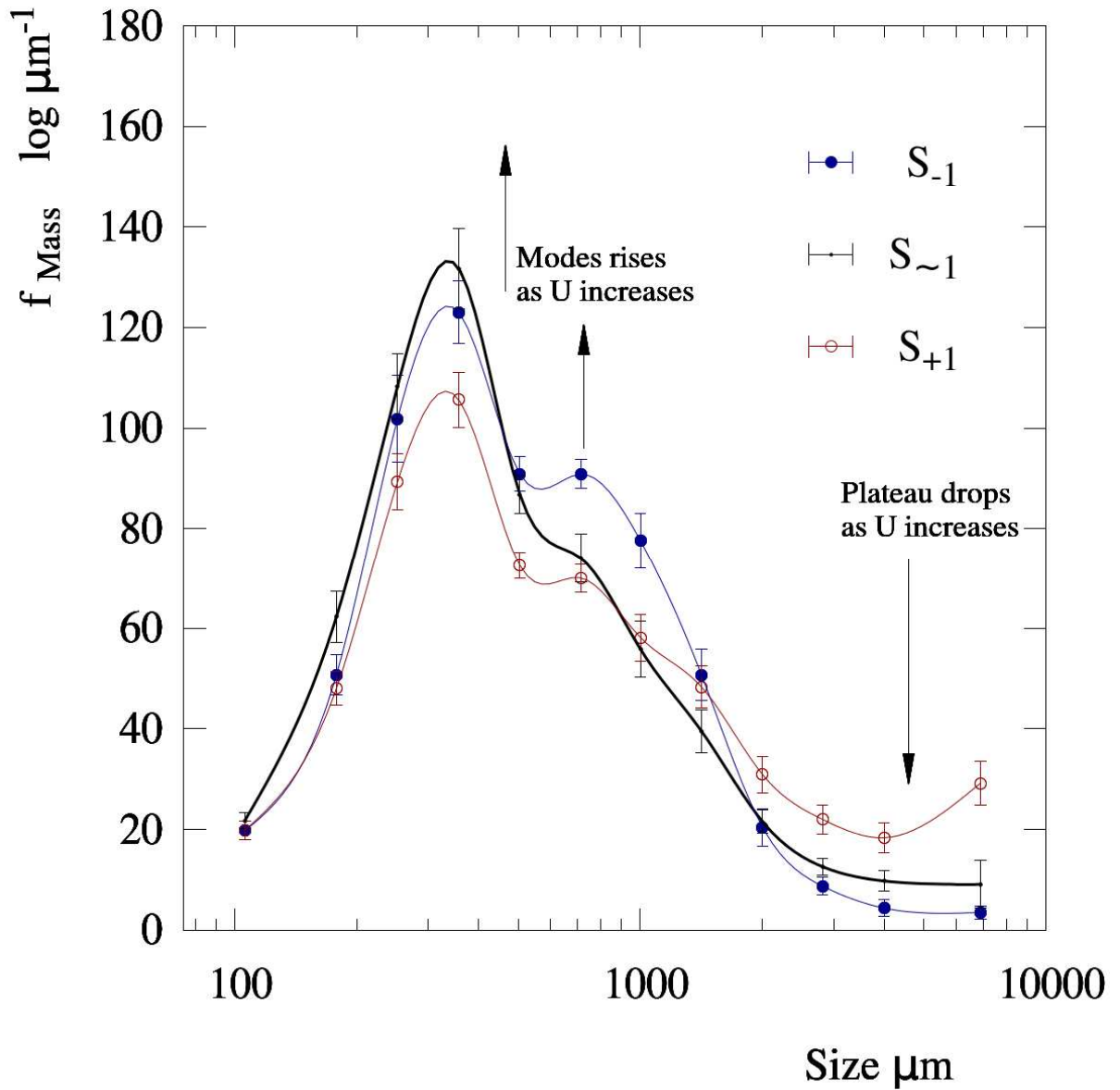


**Figure 10.** Variation of the product size distribution. Top nozzle #1.  $S_1$ . Reference conditions  $S_{\sim 1}$  (black) to high inlet temperature  $\uparrow T_A \downarrow U_A^2$  in  $S_{+1}$  (red) and low inlet temperatures  $\downarrow T_A \uparrow U_A^2$  in  $S_{-1}$  (blue).

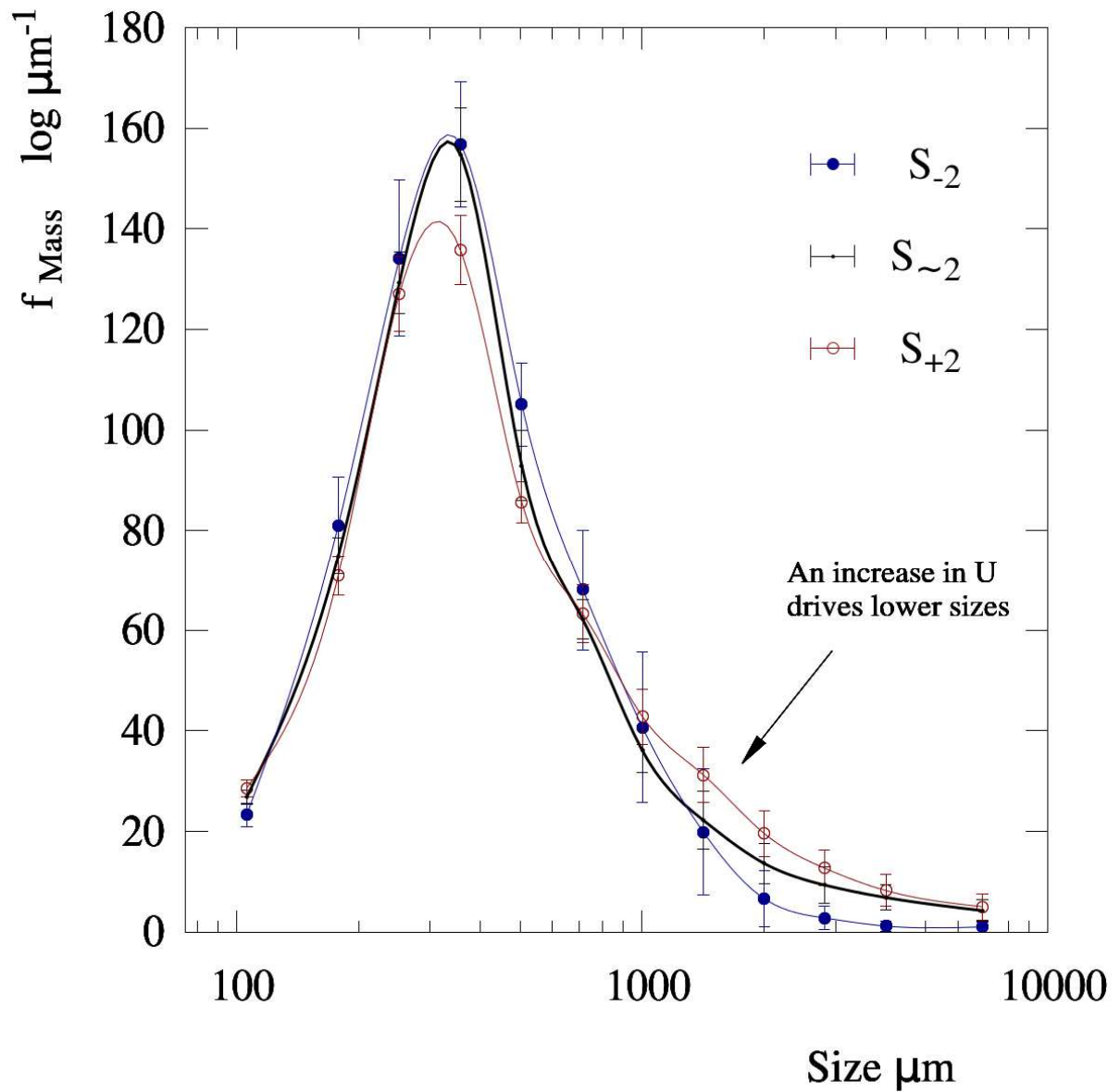


**Figure 11.** Variation of the product size distribution. Middle nozzle #2.  $S_2$ . Reference conditions  $S_{\sim 2}$  (black) to high inlet temperature  $\uparrow T_A \downarrow U_A^2$  in  $S_{+2}$  (red) and low inlet temperatures  $\downarrow T_A \uparrow U_A^2$  in  $S_{-1}$  (blue).

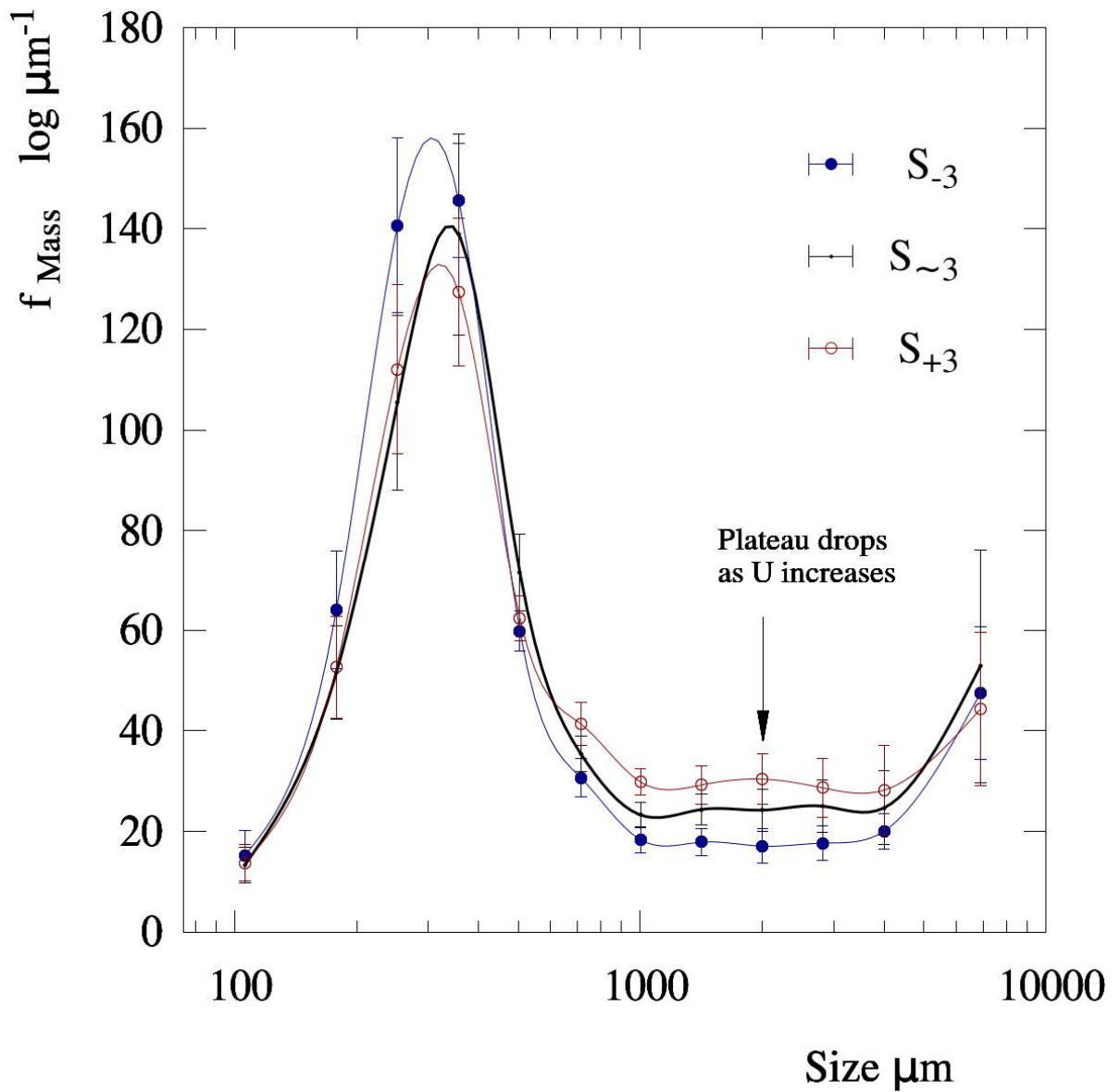


**Figure 12.** Variation of the product size distribution. Bottom nozzle #3.  $S_3$ . Reference conditions  $S_{\sim 3}$  (black) to high inlet temperature  $\uparrow T_A \downarrow U_A^2$  in  $S_{+3}$  (red) and low inlet temperatures  $\downarrow T_A \uparrow U_A^2$  in  $S_{-1}$  (blue).

have been shifted to the left in the size distribution separating them from the granules formed at from the wall  $> 850 \mu m$  which appear as mixtures of deposits and droplets in Chapter V. Potentially one would have expected that the size of primary mode to be reduced, since Chapter V shows it contains particles free from any deposits or tracer. This does not occur. Instead one sees a reduction precisely in the granules that are formed at the walls. Figure 11 is clear: the reduction observed in the tail involves the exact same particles that in Chapter V are shown as mixtures of atomized and re-entrained material. This can only be explained by a change in the type of interaction with the wall.

A similar transition appears in a multi-level case, Figure 14. Here the secondary mode represents the product originated at the top nozzle (see Chapter VI). It moves to lower sizes when high velocities are used what means that it must also be related to deposits formed near the top spray and discards a significant effect of the stagnation close to the spray, which would be the highest in  $M_{-13}$ .

At this point, it is important to notice that when one looks at the concentrated area near the wall in Figure 13, all particle contacts present a similar mechanics. It is a matter of the contact time scale that one considers a particle fixed at the deposits or in the air. Most are either in contact to a particle at the wall or very near it, so that all form a sort of clustered structure. Most of them are highly non-spherical and this makes them interlock (see Appendix II). What the data in this appendix reveals is that the larger the air velocity, the higher is the number and velocity of particles in regions such as those in Figure 13b, and therefore the stronger the disruption is and the smaller the fragments generated. In contrast, if one lets the particles in Figure 13b to move towards the wall at low velocities they would spend a long time in contact, cluster and sinter so that they are detached only when they grow sufficiently. One can think

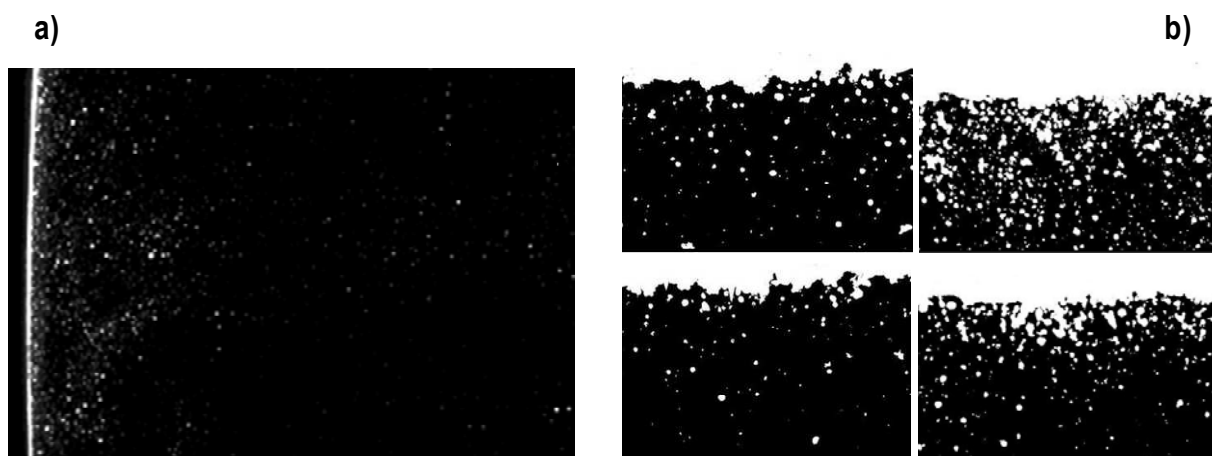


**Figure 13.** Visualization of the near wall region through Particle Image Velocimetry , PIV, experiments, reported by Hassall (2011) a) near wall particle concentration, and b) wall multi-layered deposits. Reproduction with permission from the authors.

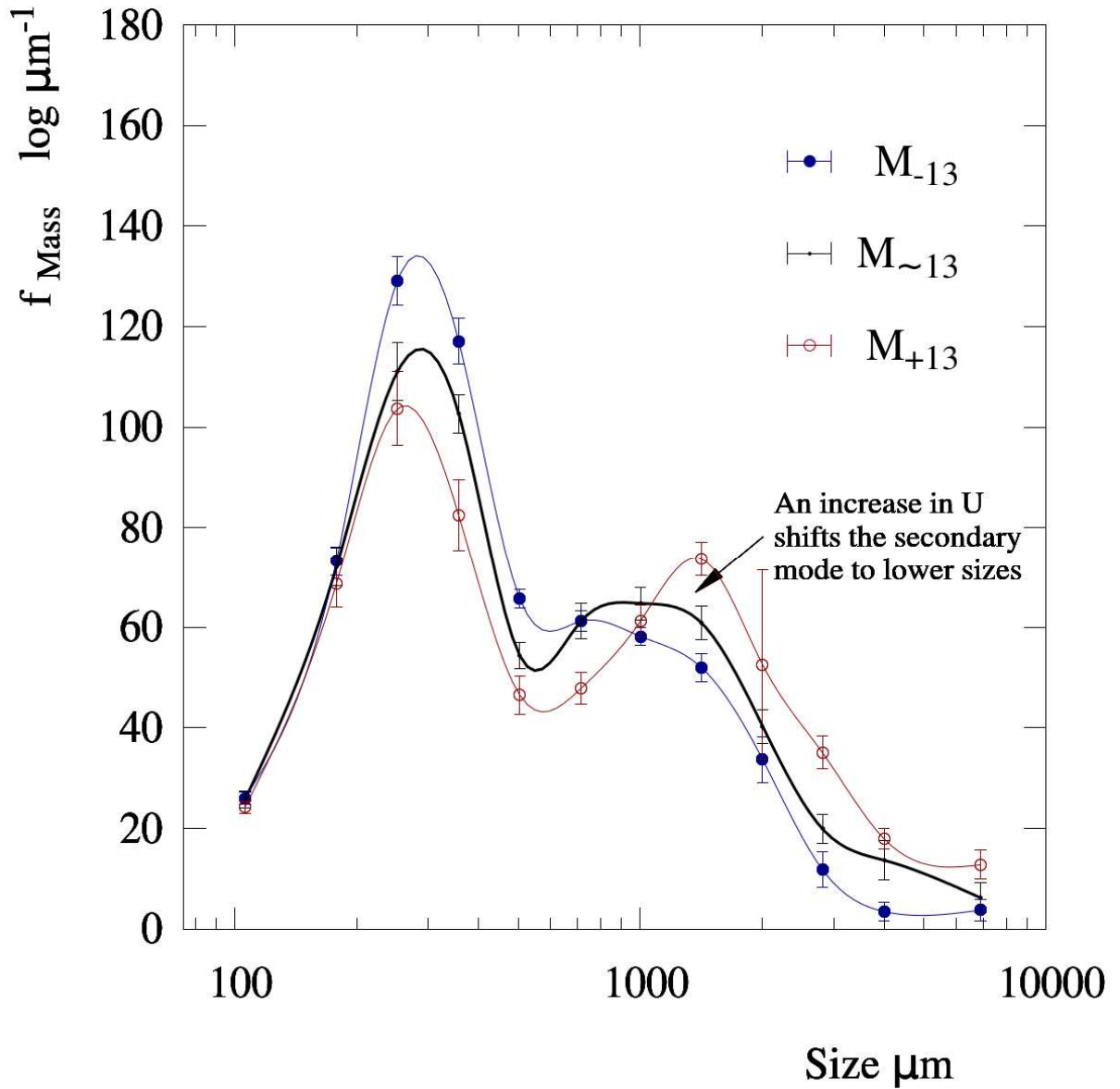


**Figure 14.** Variation of the product mass based particle size distribution. Two nozzle levels,  $M_{13}$ . Reference conditions  $M_{\sim 13}$  (black) to high inlet temperature  $\uparrow T_A \downarrow U_A^2$  in  $M_{+13}$  (red) and low inlet temperatures  $\downarrow T_A \uparrow U_A^2$  in  $M_{-13}$  (blue).

---

on this behaviour in a similar way to the reduction in a cluster lifetime for increasing levels of turbulence. To sum up, the trends reported here suggest that the product size is likely related to the enhancement or suppression of the breakage of deposits. Using lower temperatures to reduce particle size is counter-intuitive and constitutes a relevant guide for the manufactures. One should highlight here the importance of the reduction in  $x_{50}$  and  $x_{90}$  reported in Table 8. This allows decreasing the amount of material discarded after production and is extremely relevant for the efficiency of the process.

### **3.4.2. Composition heterogeneity under different air inlet conditions.**

Chapter VI explains how the final water content  $X_w$  is a strong function of size in a spray dried powder. In the reference productions, the fine and coarse fractions of the product showed larger water contents, which were explained by the lower residence time of the large granules, and in the case of the fractions  $< 212 \mu m$  to the potential contribution of breakage and the re-entrained material. Figures 15 and 16 present the deviations of  $X_w$  for the rest of the cases. Interestingly, the changes in the air flow field do not introduce a significant variation in the distribution across particle size, which shows the same maxima. The higher overall values seen in case  $S_3$  versus the other configurations are associated in Chapter VI to effect of the internal diffusion drying stage and the lower residence time of the solids.

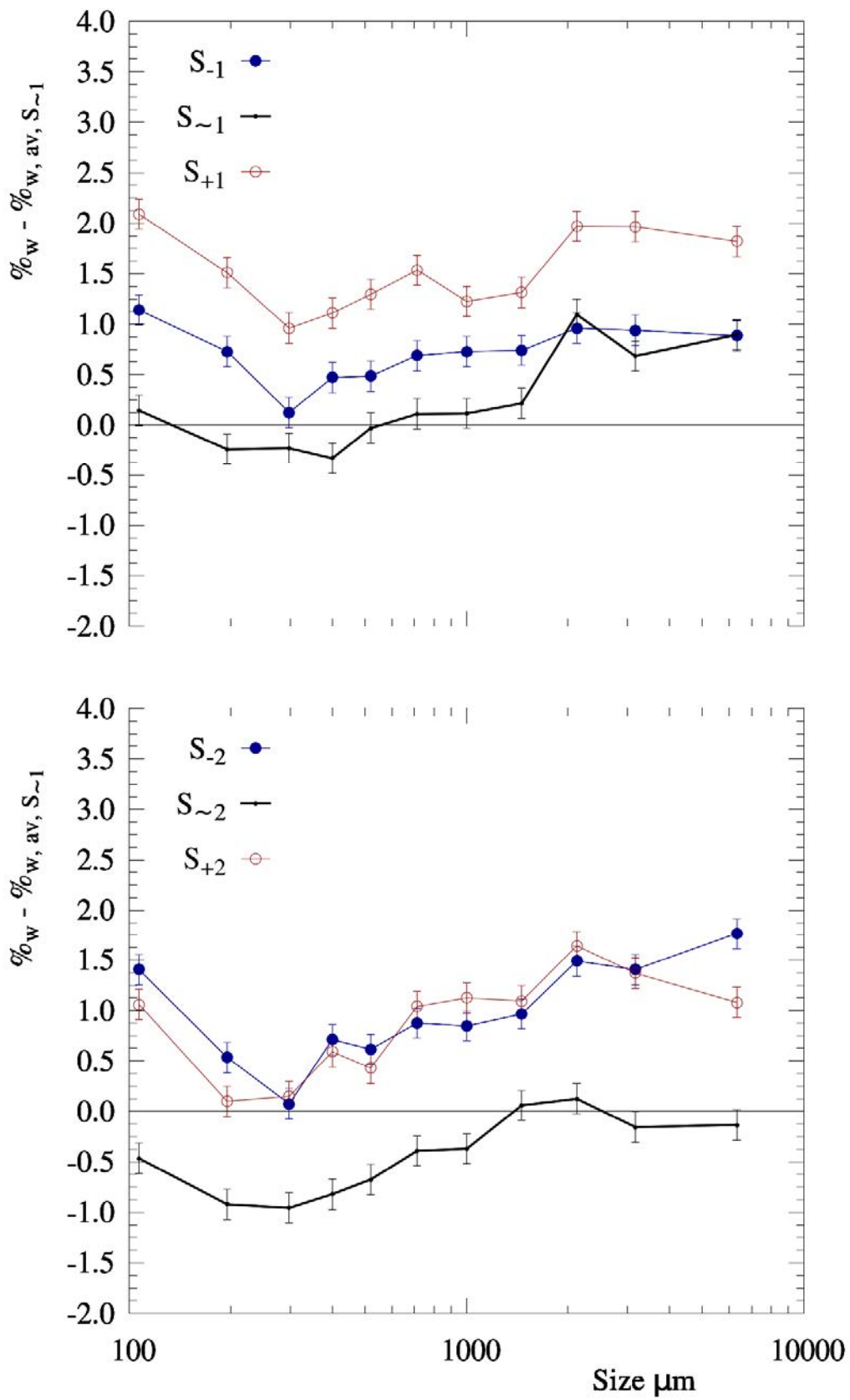


**Figure 15.** Size dependency of  $X_w$ . a)  $S_1$  b)  $S_2$ . Reference conditions ( $\sim$ , black) to high inlet temperature  $\uparrow T_A \downarrow U_A^2$  ( $+$ , red) and low inlet temperatures  $\downarrow T_A \uparrow U_A^2$  ( $-$ , blue).

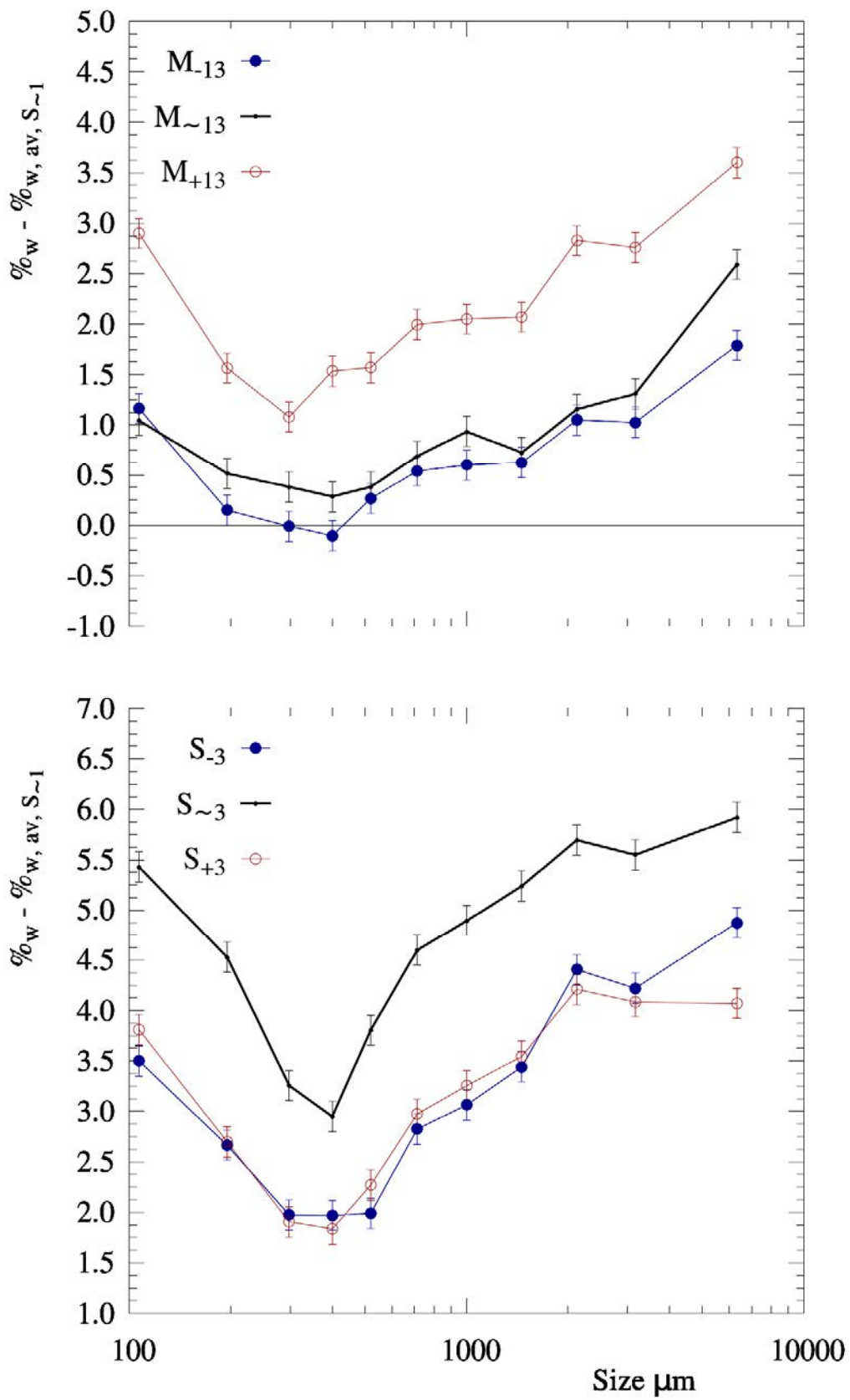


Figure 16. Size dependency of  $X_w$ . a)  $S_3$  b)  $M_{13}$ . Reference conditions ( $\sim$ , black) to high inlet temperature  $\uparrow T_A \downarrow U_A^2$  (+, red) and low inlet temperatures  $\downarrow T_A \uparrow U_A^2$  (-, blue).

## Conclusions

This work studies the impact of either high air temperatures or high velocity ranges in the properties of the product of a detergent swirl spray dryer:

**a) Recirculation:** The temperature field suggests that the usage of high inlet air temperatures results in an enhancement of the heat transfer near the spray only when it is located sufficiently far in the cylinder. When the sprays are brought down, the effect of the air velocity becomes dominant and using high air velocities better the heat transfer near the nozzle by increasing the residence time of the solids and allowing for a better convection. This is also the case when using twin nozzle levels.

**b) Particle growth:** In all cases, increasing the air momentum inhibits the generation of aggregates  $> 850 \mu m$ . This trend is independent on rate, nozzle location or the operation of single or multi-level systems. This is a very relevant fact. It points to the product size being dominated by breakage at the walls and how the changes in process conditions modify the stresses sustained by the deposits.

The correlation between the rate of impacts to the wall and particle size, along the observations of Hassall (2011) and the tracer experiments given in Chapter V demonstrate the wall is intimately involved in the formation of most of the product. In fact, it appears that a swirl counter-current detergent spray dryer works by bringing most of the powder in contact close to the wall and then breaking up the clusters formed by the momentum obtained from the swirl. Indeed, this represents a significant change to the description of growth given by Huntington (2004), but one must also consider that Huntington (2004) focuses in all types of past formulations and especially in the context of the larger towers where many more nozzles are used and their interaction also become important.

In any case, it is clear that optimization must start focusing in the description of the microstructure of deposits and how breakage is driven. The reduction in size reported here shows that controlling this dynamics has the potential to improve the efficiency and the production capacity of this industry.



## References

- Adhikar, B. Howes, T. Bhandar, B.R. and Troung, V. (2003). In situ characterization of stickiness of sugar-rich foods using a linear actuator driven stickiness testing device. *Journal of Food Engineering*, 58, 11–22.
- Adhikar, B. Howes, T. Bhandar, B.R. and Troung, V. (2004). Effect of addition of maltodextrin on drying kinetics and stickiness of sugar and acid-rich foods during convective drying: experiments and modelling. *Journal of Food Engineering*, 62, 53–68.
- Andreas. E.L , Hill, R.J , Gosz, J.R. , Moore, D.I., Otto, W.D, and Sarma, A.D (1998). Statistics of surface layer turbulence over terrain with metrescale heterogeneity. *Boundary-layer meteorology*, 86, 379–408.
- Ali M. (2014). Numerical modelling of a counter-current spray drying tower. PhD thesis. University of Leeds. Leeds. United Kingdom.
- Ali M., Mahmud T., Heggs P.J., Ghadiri M., Francia V., Bayly A.E., Djurdjevic D., Ahmadian H. and Martin L. (2013). CFD modeling of a counter-current spray drying tower. International conference in multiphase flow. Jeju, South Korea.
- Appel. P.W. (2000). Modern methods of detergent manufacture. *Journal of surfactants and detergents*, 3, 3.
- Aubinet, M., Grelle, A., Ibrom, A., Rannik, U., Moncrieff, J., Foken, T., Kowalski, AS., Martin, PH., Berbigier, P., Bernhofer, C., Clement, R., Elbers, J. , Granier, A., Grunwald, T., Morgenstern, K., Pilegaard, K., Rebmann, C., Snijders, W., Valentini, R. and Vesala, T. (2000) Estimates of the annual net carbon and water exchange of forests: The EUROFLUX methodology . *Advances in ecological research*, 30, 113 – 175.
- Bhandar B., Datta N. and Howes T. (1997) Problems associated with spray drying of sugar rich foods, *Drying Technology* 15 , 2 , 671–684.
- Bashir M.S, Jensen P.A., Frandsen F., Wedel S., Johansen KD., Wadenbäck, J. and Pedersen S.T. (2012). Ash transformation and deposit build-up during biomass suspension and grate firing: Full-scale experimental studies. *Fuel processing technology*, 97, 93-106.
- Bayly, A. E., Jukes, P., Groombridge, M and McNally, C. (2004). Airflow Patterns in a Counter-Current Spray Drying Tower - Simulation and Measurement. International drying symposium, Sao Paulo, Part B, 22-25, 775-781.
- Berger, B.W., Davis, K.J. and Yi. C. (2001). Long-Term Carbon Dioxide Fluxes from a Very Tall Tower in a Northern Forest: Flux Measurement Methodology. *Journal of atmospheric and oceanic technology*. 18, 529-542.
- Bikaa D., Tardos G.I., Panmaia S., Farbera L. and Michaela J. (2005). Strength and morphology of solid bridges in dry granules of pharmaceutical powders. *Powder Technology*. 150, 104-116
- Boonyai P., Bhandaria B. and Howes T. (2004). Stickiness measurement techniques for food powders: a review. *Powder Technology* 145, 34–46.
- Cao S., Tamura T., Kikuchi N., Saito M., Nakayama I. and Matsuzaki Y. (2009). Wind characteristics of

- a strong typhoon. *Journal of wind engineering and industrial aerodynamics*, 97, 11-21.
- Chan, C.W., Seville, J.P.K., Fan, X. and Baeyens, J. (2009). Particle motion in CFB cyclones as observed by positron emission particle tracking. *Ind. Eng. Chem. Res.*, 48, 253–261
- Chang, F and Dhir, V. K. (1994). Turbulent flow field in tangentially injected swirl flows in tubes. *International journal of heat and fluid flow*, 15, 5, 346-356.
- Chang, F and Dhir, V. K. (1995). Mechanisms of heat transfer enhancement and slow decay of swirl in tubes using tangential injection. *International journal of heat and fluid flow*, 16, 2, 78-87.
- Chao, Y.C., Leu, J.H., Hung, Y.E. and Lin, C.K. (1991). Downstream boundary effects on the spectral characteristics of a swirling flowfield. *Experiments in Fluids* 10, 341-348.
- Chen, X.D. and Lin, S.X.Q. (2005) Air Drying of Milk Droplet under Constant and Time-Dependent Conditions. *AIChE Journal*, 51, 6, 1791-1799.
- Cortes, C. and Gil, A. (2007). Modeling the gas and particle flow inside cyclone separators. *Progress in Energy and Combustion Science*, 33, 409–452.
- Crowe, C. T. (1980). Modeling spray-air contact in spray-drying systems. *Advances in drying*, 63-99.
- Crowe, C. T. (1983). Droplet-gas interaction in counter-current spray dryers, *Drying Technology*, 35-56.
- Cuerva, A. and Sanchez-Andres, A. (2000). On sonic anemometer measurement theory. *Journal of wind engineering and industrial aerodynamics*, 88, 25-55.
- Cuerva, A., Sanchez-Andres, and Navarro, J. (2003). On multiple-path sonic anemometer measurement theory. *Experiments in fluids*, 34, 345–357.
- Cuerva, A., Sanchez-Andres, A., and Lopez, O. (2004). Singularities and undefinities in the calibration functions of sonic anemometers. *Journal of atmospheric and oceanic technology*, 21, 1868-1875.
- Dalmaz, N., Ozbelge, H.O., Eraslan, A.N. and Uludag, Y. (2007). Heat and mass transfer mechanisms in drying of a suspension droplet: A new computational model. *Drying technology*, 25, 1-3, 391-400.
- Davis, R.P.; Haines, M.S. and Sagel, J.A. (1971). Multilevel Spray-Drying Apparatus. US Patent 3, December 28 1971, 629, 955, The Procter & Gamble Company. Cincinnati, Ohio.
- Derksen, J.J. (2005). Simulations of confined turbulent vortex flow. *Computers & Fluids*, 34, 301–318.
- Derksen, J.J. and Van den Akker, H.E.A. (2000). Simulation of vortex core precession in a reverse-flow cyclone. *AIChE Journal*, 46, 7, 1317-1331.
- Druilhet, A. and Durand, P. (1997). Experimental investigation of atmospheric boundary layer turbulence. *Atmospheric Research*, 43, 345-388.
- Dubrovsky V.V., Podvysotsky A.M. and Shraiber A.A. (1992). Particle interaction in three-phase polydisperse flows. *International journal of multiphase flow*, 18, 3, 337-352.
- Epstein, N. (1983). Thinking about heat transfer fouling: A 5x5 matrix. *Heat transfer engineering*, 4, 1, 43-56.
- Erdal, F. (2001). Local measurements and computational fluid dynamics simulations in a gas-liquid cylindrical cyclone separator. Ph.D. thesis, The University of Tulsa. USA.
- Escudier, M.P., Bornstein, J. and Zehnder, N. (1980). Observations and LDA measurements of confined turbulent vortex flow. *Journal of Fluid Mechanics*, 98, 1, 49-63.

- Escudier, M.P. and Keller, J.J. (1985) Recirculation in Swirling Flow: A Manifestation of Vortex Breakdown. *AIAA Journal*, 23, 1, 111-116.
- Fieg, G., Wozny, G., Buick, K. and Jeromin, L. (1994). Estimation of the drying rate and moisture profiles in an industrial spray dryer by means of experimental investigations and a simulation study. *Chem. Eng. Technol.*, 17, 235-241.
- Farid, M., (2003). A new approach to modelling of single droplet drying. *Chemical Engineering Science*, 58, 13, 2985–2993.
- Fletcher, D. F., Guo, B., Harvie D.J.E., Nijdam, J.J. and Williams, J. (2006). What is important in the simulation of spray dryer performance and how do current CFD models perform?. *Applied Mathematical Modelling*, 30, 1281 – 1292.
- Focke C., Kuschel M., Sommerfeld M. and Bothe D. (2013). Collision between high and low viscosity droplets: Direct Numerical Simulations and experiments. *International journal of multiphase flow*, 56, 81-92.
- Franchini, S., Sanchez-Andres, A. and Cuerva, A. (2007a). Effect of the pulse trajectory on ultrasonic fluid velocity measurement. *Experiments in fluids*, 43, 969–978.
- Franchini, S., Sanchez-Andres, A and Cuerva, A. (2007b). Measurement of velocity in rotational flows using ultrasonic anemometry: the flowmeter. *Experiments in fluids*, 42, 903- 911.
- Gash J.H.C. and Dolman, A.J. (2003). Sonic anemometer (co)sine response and flux measurement I. The potential for (co)sine error to affect sonic anemometer-based flux measurements. *Agricultural and Forest Meteorology*, 119, 195–207.
- Gianfrancesco, A., Turchiuli, C., Dumoulin, E. and Palzer, S. (2009). Prediction of powder stickiness along spray drying process in relation to agglomeration, *Particulate Science and Technology*, 27, 5, 415–427.
- Gill Instruments Ltd. (2004). HS-50 Horizontally Symmetrical ultrasonic research anemometer. User manual, 1199, 02.
- Gomez, L., Mohan, R. and Shoham, O. (2004). Swirling Gas–Liquid Two-Phase Flow. *Experiment and Modeling Part II: Turbulent Quantities and Core Stability. Journal of Fluids Engineering*, 126, 943-959.
- Goulden, M.L., Munger, J.W., Fan, S.M., Daube, B.C. and Wofsy, S.C. (1996). Measurements of carbon sequestration by long-term eddy covariance: Methods and a critical evaluation of accuracy. *Global change biology* 2, 3, 169-182.
- Guingo M. and Minier J.P. (2008). A new model for the simulation of particle resuspension by turbulent flows based on a stochastic description of wall roughness and adhesion forces. *Aerosol Science*, 39, 957-973.
- Guo, B., Fletcher, D. F. and Langrish, T. A. (2004). Simulation of the agglomeration in a spray using Lagrangian particle tracking. *Applied Mathematical Modelling*, 28, 273–290.
- Gupta, A.K., Lilley, D.G. and Syred, N. (1984). *Swirl flows*. Tunbridge Wells, Abacus Press, UK.
- Handscomb C.S., Kraft M. and Bayly. A.E. (2009). A new model for the drying of droplets containing suspended solids. *Chemical engineering science*, 64, 628-637.
- Handscomb C.S. and Kraft M. (2010). Simulating the structural evolution of droplets following shell

- formation. *Chemical Engineering Science*, 65, 713–725.
- Hapgood K.P., Litster J.D. and Smith R. (2003). Nucleation regime map for liquid bound granules. *AIChE Journal*, 49, 2, 350-361.
- Hassall G. (2011). Wall build up in spray driers. EngD thesis. Chemical Engineering. University of Birmingham. Birmingham. United Kingdom.
- Harvie, D.J.E, Langrish, T.A.G and Fletcher, D.F. (2001). Numerical simulations of the gas flow patterns within a tall form spray dryer. *Trans IChemE*, 79, 235-248.
- Harvie D.J.E., Langrish T.A.G. and Fletcher D.F. (2002). A computational fluid dynamics study of a tall-form spray dryer. *Trans IChemE*, 80, Part C, 163-175.
- Hanus M.J. and Langrish T.A.G. (2007a). Re-entrainment of wall deposits from a laboratory-scale spray dryer. *Asia-Pac. Journal of chemical engineering*, 2, 90-107.
- Hanus M.J. and Langrish T.A.G. (2007b). Resuspension of wall deposits in spray dryers. *J. Zhejiang University Science A.*, 8, 11, 1762-1774.
- Hecht, J.P. and King, C.J. (2000). Spray drying: influence of developing drop morphology on drying rates and retention of volatile substances. 1. Single drop experiments. *I & E Chemical Research*, 39 , 6, 1756–1765.
- Hendriks, D.M.D., Dolman, J., Van der Molen, M. K. and Van Huissteden, J. (2008). A compact and stable eddy covariance set-up for methane measurements using off-axis integrated cavity output spectroscopy. *Atmos. Chem. Phys.*, 8, 431–443.
- Henry C., Minier J.P. and Lefevre G. (2012). Towards a description of particulate fouling: From single particle deposition to clogging. *Advances in colloid and interface science*, 185-186, 34-76.
- Hoekstra, A.J., Derksen, J.J. and Van Den Akker, H.D.A. (1999). An experimental and numerical study of turbulent swirling flow in gas cyclones. *Chemical Engineering Science*, 54, 2055-2065.
- Hoeven M.J. (2008). Particle - Droplet collisions in spray drying. Ph.D. thesis. School of Engineering. University of Queensland. Brisbane. Australia.
- Hogstrom, U. and Smedman, A.S. (2004). Accuracy of sonic anemometers: Laminar wind-tunnel calibrations compared to atmospheric in situ calibrations against a reference instrument. *Boundary-Layer Meteorology*, 111, 33–54.
- Hreiz, R., Gentric, C. and Midoux, N. (2011). Numerical investigation of swirling flow in cylindrical cyclones. *Chemical engineering research and design*, 89, 2521–2539.
- Huntington D. H. (2004). The influence of the spray drying process on product properties. *Drying technology*, 22, 6, 1261-1287.
- Huang, L. X., Kumar, K. and Mujumdar, A. S. (2006). A comparative study of a spray dryer with rotary disc atomizer and pressure nozzle using computational fluid dynamic simulations. *Chem. Eng. Proc.*, 45 , 461-470.
- Iveson S.M., Litster J.D., Hapgood K.P. and Ennis B.J. (2001). Nucleation, growth and breakage phenomena in agitated wet granulation processes: a review. *Powder technology*, 117, 3-39.
- Jackson D. W. T., Beyers J. H. M., Lynch, K., Cooper, J.A.G., Baas, A.C.W. and Delgado-Fernandez, I. (2011). Investigation of three-dimensional wind flow behaviour over coastal dune morphology under

- offshore winds using computational fluid dynamics (CFD) and ultrasonic anemometry. *Earth Surf. Process. Landforms* 36, 1113–1124.
- Jakirlic, S., Hanjalic, K and Tropea, C. (2002). Modelling rotating and swirling turbulent flows: A perpetual challenge. *AIAA Journal*, 40, 1984-1996.
- Jimenez, J. Turbulent flow over rough walls. (2004) *Annual Reviews in fluid mechanics*, 36, 173-96.
- Kadja, M. and Bergeles, G. (2003). Modelling of slurry droplet drying. *Applied thermal engineering*, 23, 7, 829 -844.
- Kaimal, J.C, Gaynor J.E., Zimmerman H.A. and Zimmerman G.A. (1990). Minimizing flow distortion errors in a sonic anemometer. *Boundary-layer meteorology*, 53, 1-2, 103-115 .
- Kaya, F., Karagoz, I and Avci, A. (2011). Effects of surface roughness on the performance of tangential inlet cyclone separators. *Aerosol Science and Technology*, 45, 988-995.
- Kariuki W.I.J., Freireich B., Smith R.M., Rhodes M. and Hapgood K.P. (2013). Distribution nucleation: Quantifying liquid distribution on the particle surface using the dimensionless particle coating number. *Chemical engineering science*, 92, 134-145.
- Katurji, M., Sturman, A. and Zawar-Reza, P. (2011). An Investigation into ridge-top turbulence characteristics during neutral and weakly stable conditions: Velocity spectra and isotropy. *Boundary-layer meteorology*, 139, 143-160.
- Keey, R.B. and Pham, Q.T. (1997). Residence time distribution in a tall-form spray chamber. *Chemical Engineering Science*, 32, 1219-1226.
- Kemp, I.C. and Oakley, D.E (2002). Modeling of particulate drying in theory and practice. *Drying Technology*, 20, 9, 1699–1750.
- Kieviet, F.G., Van Raaij, J., De Moor, P.P.E.A and Kerkhof, P.J.A.M. (1997). Measurement and modelling of the air flow pattern in a pilot-plant spray dryer. *Trans IChemE*, 75, A, 312-328.
- Kim, C.H. and Lee, J.W. (2001). A new collection efficiency model for small cyclones considering the boundary-layer effect. *Aerosol Science*, 32, 251-269.
- Kitoh, O. (1991). Experimental study of turbulent swirling flow in a straight pipe. *Journal of fluid mechanics*, 225, 445-479.
- Kota K. and Langrish T. A. G. (2006). Fluxes and patterns of wall deposits for skim milk in a pilot-scale spray dryer. *Drying technology*, 24, 8, 993-1001.
- Kota K., and Langrish T.A.G. (2007). Prediction of wall deposition behaviour in a pilot-scale spray dryer using deposition correlations for pipe flows. *Journal of Zhejiang University Science A*, 8, 301–312.
- Kuriakose, R. and Anandharamakrishnan, C. (2010). Computational fluid dynamics (CFD) applications in spray drying of food products. *Trends in Food Science & Technology*, 21, 383-398.
- Kuschel M. and Sommerfeld M. (2013). Investigation of droplet collisions for solutions with different solids content. *Experiments in Fluids*, 54, 1440.
- Langrish, T. A. (2009). Multi-scale mathematical modelling of spray dryers. *Journal of Food Engineering*, 93, 218–228.
- Langrish, T. A. and Fletcher, D. F. (2003). Prospects for the Modelling and Design of Spray Dryers in the 21st Century. *Drying Technology*, 21, 2, 197-215.

- Langrish T.A.G. and Kocke T.K. (2001). The assessment of a characteristic drying curve for milk powder for use in computational fluid dynamics modelling. *Chemical engineering journal*, 84, 1, 69-74.
- Langrish T.A.G. and Zbiciński I. (1994). The effects of air inlet geometry and spray cone angle on the wall deposition rate in spray dryers. *Chemical engineering research and design*. 72, A3, 420-430
- Langrish, T.A.G., Williams, J. and Fletcher, D.F. (2004). Simulation of the effects of the inlet swirl on gas flow patterns in a pilot-scale spray drier. *Chemical Engineering Research and Design*, 82, A7, 821–833.
- Langrish, T.A.G., Oakely, D.E., Keey, R.B., Bahu, R.E. and Hutchinson, C.A. (1993). Time dependent flow patterns in spray dryers. *Trans IChemE*, 71, A, 355-360.
- Levelspiel O. (2004). *Ingeniería de las reacciones químicas*. Limusa Wiley. 3<sup>rd</sup> Ed, 12, 284 - 285. ISBN 968-18-5860-3.
- Liao, Y. and Lucas, D. (2010). A literature review on mechanisms and models for the coalescence process of fluid particles. *Chemical Engineering Science*, 65, 2851–2864
- Litvinov, I.V., Shtork, S.I., Kuibin, P.A., Alekseenko, S.V. and Hanjalic, K. (2013). Experimental study and analytical reconstruction of precessing vortex in a tangential swirler. *International Journal of Heat and Fluid Flow*, 42, 251–264.
- Liu L.X., Iveson S.M., Litster J.D. and Ennis. B.J. (2000). Coalescence of deformable granules in wet granulation processes. *AIChE*, 46, 529-539.
- Liu, Z., Jiao, J., Zheng, Y., Zhang, Q. and Jia, L. (2006). Investigation of Turbulence Characteristics in a Gas Cyclone by Stereoscopic PIV. *AIChE Journal*, 52, 12, 4150-4160.
- Luca-Negro, O and O'Doherty, T. (2001). Vortex breakdown: a review. *Progress in energy and combustion science*, 27, 431-481.
- Maddahian, R., Kebriaee, A., Farhanieh, B and Firoozabadi, B. (2011). Analytical investigation of boundary layer growth and swirl intensity decay rate in a pipe. *Archives of applied mechanics*, 81, 489-501.
- Marshall J.S. (2007). Particle aggregation and capture by walls in a particulate aerosol channel flow. *Journal of aerosol science*, 38, 333–351.
- Mauder, M., Oncley, S.P., Vogt, R., Weidinger, T., Ribeiro, L., Bernhofer, C., Foken, T., Kohsiek, W., De-Bruin, H.A.R and Liu, H. (2007). The energy balance experiment EBEX-2000. Part II: Intercomparison of eddy-covariance sensors and post-field data processing methods. *Boundary-layer meteorology*, 123, 29–54.
- Masters, K. (1972). *Spray Drying: An introduction to Principles, Operational Practice and Applications*. London: Leonard Hill Books.
- Masters, K. (1995). Scale-up of spray dryers. *Drying Technology*, 12, 1-2, 235-257.
- Meerdink G. and Riet, K. (1995). Prediction of product quality during spray drying. *Trans Institution of Chemical Engineers*, 73, C, 165-170.
- Mestayay, P.G., Durand, P., Augustin, P., Bastin, S., Bonnefond, JM., Benech, B., Campistron, B., Coppalle, A., Delbarre, H., Dousset, B., Drobinski, P., Druilhet, A., Frejafon, E., Grimmond, CSB., Groleau, D., Irvine, M., Kergomard, C., Kermadi, S., Lagouarde, JP., Lemonsu, A., Lohou, F., Long, N., Masson, V., Moppert, C., Noilhan, J., Offerle, B., Oke, TR., Pigeon, G., Puygrenier, V., Roberts, S., Rosant, JM., Said, F., Salmond, J., Talbaut, M., and Voogt, J. (2005) The urban boundary-layer

- field campaign in Marseille (UBL/CLU-ESCOMPTE): Set-up and first results. *Boundary-Layer Meteorology* 114, 315-365.
- Mezhericher, M., Levy, A. and Borde, I. (2007). Theoretical drying model of single droplets containing insoluble or dissolved solids. *Drying technology*, 25, 4-6, 1025-1032.
- Mezhericher, M., Levy, A. and Borde, I. (2008). Heat and mass transfer of single droplet/wet particle drying. *Chemical Engineering Science*, 63, 1, 12-23.
- Mezhericher, M., Levy, A. and Borde, I. (2010a). Spray drying modelling based on advanced droplet drying kinetics. *Chem. Eng. Proc.*, 49, 1205–1213.
- Mezhericher, M., Levy, A. and Borde, I. (2010b). Theoretical Models of Single Droplet Drying Kinetics: A Review. *Drying technology*, 28, 2, 278 -293.
- Mezhericher, M., Levy, A. and Borde, I. (2012). Probabilistic hard-sphere model of binary particle–particle interactions in multiphase flow of spray dryers. *International Journal of Multiphase Flow*, 43, 22–38.
- Moody, L.F. (1944). Friction factors for pipe flow. *Transactions of the ASME*, 66, 8, 671-684.
- Moshkin, V., Desyatov, A.V. and Kakurkin, N.P. (2007). Hydrodynamic stability of the two-phase nonisothermal flow in a countercurrent spray dryer. *Theoretical foundations of chemical engineering*, 41, 6, 816 -821.
- Mulhem B., Schulte G. and Fritsching U. (2006). Solid–liquid separation in suspension atomization. *Chemical engineering science*, 61, 2582 – 2589.
- Najafi, A.F., Mousavian, S.M. and Amini, K. (2011). Numerical investigations on swirl intensity decay rate for turbulent swirling flow in a fixed pipe. *International Journal of Mechanical Sciences* 53, 801-811.
- Nakai, T and Shimoyama, K. (2011). Ultrasonic anemometer angle of attack errors under turbulent conditions. *Agricultural and forest meteorology*, 162-163, 14-26.
- Nakai, T., Van der Molen, M.K., Gash, J.H.C. and Kodama, Y. (2006). Correction of sonic anemometer angle of attack errors. *Agricultural and Forest Meteorology* 136, 19–30.
- Nesci, S. and Vodnik, J. (1991). Kinetics of droplet evaporation. *Chemical Engineering Science*, 46, 2, 527–537.
- Nijdam, J.J., Guo, B., Fletcher, D.F. and Langrish, T. A. (2006). Lagrangian and Eulerian models for simulating turbulent dispersion and coalescence of droplets within a spray. *Applied Mathematical Modelling*, 30, 1196–1211.
- O'Doherty, T., Griffiths, A.J., Syred, N., Bowen, P.J. and Fick, W. (1999). Experimental analysis of rotating instabilities in swirling and cyclonic flows. *Dev. Chem. Eng. Mineral Process.*, 7, 3/4, 245-267.
- Oakley, D.E. (1994). Scale-up of spray dryers with the aid of computational fluid dynamics. *Drying Technology: An International Journal*, 12, 1-2, 217-233.
- Oakley, D.E. (2004). Spray Dryer Modeling in Theory and Practice. *Drying Technology: An International Journal*, 22, 6, 1371-1402.
- Oncley, S.P., Foken, T., Vogt, R., Kohsiek, W., DeBruin, H.A.R., Christian Bernhofer, C., Christen, A., Van Gorsel, E., Grantz, D., Feigenwinter, C., Lehner, I., Liebethal, C., Liu, H., Mauder, M., Pitacco, A.,

- Ribeiro, L. and Weidinger, T. (2007). The Energy Balance Experiment EBEX-2000. Part I: overview and energy balance. *Boundary-layer meteorology* 123, 1 - 28.
- Ozmen L. and Langrish T.A.G. (2003). An experimental investigation of the wall deposition of milk powder in a pilot-scale spray dryer. *Drying technology*, 21, 7, 1235–1252.
- Palzer, S. (2005). The effect of glass transition on the desired and undesired agglomeration of amorphous food powders. *Chemical Engineering Science*, 60, 3959 – 3968.
- Palzer, S. (2009). Influence of material properties on the agglomeration of water-soluble amorphous particles. *PowderTechnology*, 189, 318–326.
- Palzer S. (2011). Agglomeration of pharmaceutical, detergent, chemical and food powders. Similarities and differences of materials and processes. *Powder technology*, 206, 2–17.
- Palzer, S. Dubois, C. and Gianfrancesco, A. (2012). Generation of Product Structures During drying of food products. *Drying Technology: An international journal*, 30, 1, 97-105.
- Papavergos P.G. and Hedley, A.B. (1984). Particle deposition behaviour from turbulent flows. *Chemical Engineering Research and Design*, 62, 5, 275–295.
- Paris, J.R., Ross, P.N., Dastur, S.P. and Morris, R.L. (1971). Modeling of the Air Flow Pattern in a Counter current Spray-Drying Tower. *Ind. Eng. Chem. Process Des. Develop.*, 10, 2, 157-164.
- Podvysotsky A.M. and Shraiber A.A. (1984). Coalescence and break-up of drops in two-phase flows. *International journal multiphase flow*, 10, 195-209.
- Post, S.L., Abraham, J. (2002). Modeling the outcome of drop–drop collisions in Diesel sprays. *International Journal of Multiphase Flow*, 28, 997–1019
- Probst, O and Cardenas, D. (2010). Review state of the art and trends in wind resource assessment. *Energies*, 3, 1087-1141.
- Qian J. and Law C.K. (1997). Regimes of coalescence and separation. *Journal of fluid mechanics*, 331, 59-80.
- Reeks M.W. and Hall D. (2001). Kinetic models for particle resuspension in turbulent flows: theory and measurement. *Aerosol science*, 32, 1, 31.
- Reeks, M.W., Reed, J. and Hall, D. (1988). The resuspension of small particles by a turbulent flow. *Journal of physics D*, 21, 574-589.
- Rüger, M. Hohmann, S. Sommerfeld, M. and Kohnen, G. (2000). Euler/Lagrange calculations of turbulent sprays: the effect of droplet collisions and coalescence. *At. Sprays* 10, 47–81.
- Senoo Y. and Nagata T. (1972). Swirl flow in long pipes with different roughness. *Bulletin of the JSME*, 5, 90, 1514.
- Seville, J.P.K. Silomon-Ptflug, H and Knight, P.C. (1998). Modelling of sintering in high temperature gas fluidisation *Powder Technology* 97, 160-169.
- Silva L.F.L.R., Damian R.B. and Lage, P.L.C. (2008). Implementation and analysis of numerical solution of the population balance equation in CFD packages. *Computers and Chemical Engineering*, 32, 2933–2945
- Simons, S.J.R., Seville, J.P.K. and Adams, M.J. (1994). An analysis of the rupture energy of pendular liquid bridges. *Chemical Engineering Science* 94, 14, 2331-2339.

- Sharma, S. (1990). Spray dryer simulation and air flow pattern studies, Ph.D thesis. The University of Aston. Birmingham. United Kingdom.
- Sloan, D.G., Smisth, P.J. and Smooth, L.D (1986). Modeling of swirl in turbulent flow systems. *Progress in Energy and Combustion Science*, 12, 163-250.
- Soldati A. and Marchioli C. (2009). Physics and modeling of turbulent particle deposition and entrainment: Review of a systematic study. *International journal of multiphase Flow*, 35, 827-839.
- Sommerfeld M. (1992). Modeling of particle-wall collisions in confined gas-particle flows. *International journal of multiphase flow*, 18, 6, 905-926.
- Sommerfeld M..(2001). Validation of a stochastic Lagrangian modeling approach for inter-particle collisions in homogeneous isotropic turbulence. *International Journal of Multiphase Flow*, 27, 1829-1858.
- Sommerfeld M. and Qui H. (1993). Characterization of particle-laden, confined swirling flows by phase-doppler anemometry and numerical calculation. *International journal of multiphase flow*, 19, 6, 1093-1127.
- Southwell, D.B and Langrish, T.A.G. (2001). The effect of the swirl on the stability of spray dryers. *Trans IChemE*, 79, A, 222-234.
- Steenbergen, W and Voskamp, J. (1998). The rate of decay of swirl in turbulent pipe flow. *Flow Measurement and Instrumentation*, 9, 67–78.
- Subramaniam, S. (2013). Lagrangian Eulerian methods for multiphase flows. *Progress in Energy and Combustion Science* 39, 215-245
- Syred. N. (2006). A review of oscillation mechanisms and the role of the precessing vortex core (PVC) in swirl combustion systems. *Progress in Energy and Combustion Science*, 32, 93–161.
- Tan, H.S. (2004). Kinetics of fluidised bed melt granulation. Ph.D thesis. Department of chemical and process engineering. University of Sheffield, Sheffield, UK.
- Tan, H.S., Goldschmidt, M.J.V., Boerefijn, R., Hounslow, M.J., Salman, A.D. and Kuipers, J.A.M. (2004). Building population balance for fluidized bed granulation: lessons from kinetic theory of granular flow. *PowderTechnology*, 142, 103–109.
- Tan, H.S. , Salman, A.D. and Hounslow M.J. (2006). Kinetics of fluidized bed melt granulation—II: Modelling the net rate of growth. *Chemical Engineering Science*, 61, 3930 – 3941.
- Tardos G.I. and Gupta R. (1996). Forces generated in solidifying liquid bridges between two small particles. *Powder Technology*, 87, 2, 175-180.
- Usui, H., Sano, Y., Yanagimoto, Y. and Yamasaki, Y. (1985) Turbulent flow in a spray drying chamber. *Journal of chemical engineering of Japan*, 18, 3, 243-247.
- Van der Molen, M.K., J.H.C. Gash and Elbers, J.A. (2004). Sonic anemometer (co)sine response and flux measurement II. The effect of introducing an angle of attack dependent calibration. *Agricultural and Forest Meteorology* 122, 95–109.
- Vatistas N.T. (1992). Effect of adhesion time on particle deposition: re-entrainment and rolling. *Industrial engineering and chemistry research*, 31, 6, 1554-1559.
- Vehring, R., Foss, W.R. and Lechuga-Ballesteros, D. (2007). Particle formation in spray drying. *Aerosol Science* 38, 728–746

- Verdurmen R.E.M., Menn P., Ritzert J., Blei S., Nhumaio G.C.S., Sørensen T.S., Gunsing M., Straatsma J., Verschueren M., Sibeijn M., Schulte G., Fritsching U., Bauckhage K., Tropea C., Sommerfeld M., Watkins, A.P., Yule A.J. and Schønfeldt H. (2004). Simulation of agglomeration in spray drying installations: The EDECAD project. *Drying technology*, 22, 6, 1403-1461.
- Volino. R.J., Schultz. M.P. and Flack. K.A. (2007). Turbulence structure in rough- and smooth-wall boundary layers. *Journal in Fluid Mechanics*, 592, 263–293.
- Walker, I. J. (2005). Physical and logistical considerations of using ultrasonic anemometers in aeolian sediment transport research. *Geomorphology*, 68, 57–76.
- Walton, D.E., and Mumford, C.J. (1999). Spray dried products - Characterization of particle morphology. *Chemical engineering research and design*, 77, A1, 21 -38.
- Wang H. and Harb J.N. (1997). Modeling of ash deposition in large-scale combustion facilities burning pulverized coal. *Progress in energy and combustion science*, 23, 267-282.
- Walker, I. J., Hesp, P.A., Davidson-Arnott R.G.D, Bauer, B.O, Steven L. Namikas, S.L. and Ollerhead. J. (2009). Responses of three-dimensional flow to variations in the angle of incident wind and profile form of dunes: Greenwich Dunes, Prince Edward Island, Canada. *Geomorphology*, 105, 127–138.
- Wawrzyniak, P., Podyma, M., Zbicinski, I., Bartczak, Z and Rabaeva, J. (2012). Modeling of air flow in an industrial counter-current spray drying tower. *Drying Technology*, 30, 217-224.
- Weber, R. and Dugué, J. (1992). Combustion accelerated swirling flows in high confinements. *Progress in Energy and Combustion Science*, 18, 349-367.
- Werner, S.R.L., Jones, J.R. and Paterson, A.H.J. (2007). Stickiness of maltodextrins using probe tack test during in situ drying. *Journal of Food Engineering* 80, 859-868.
- Wieser, A., Fiedler, F. and Corsmeier, U. (2001). The Influence of the sensor design on wind measurements with sonic anemometer systems. *Journal of atmospheric and oceanic technology*. 18, 1585-1608.
- Wilczak J.M., Oncley, S.P., and Stage, S.A. (2001) Sonic anemometer tilt correction algorithms. *Boundary-layer meteorology*, 99, 127–150.
- Williams, A.M. Jones, J.R. Paterson, A.H.J. and Pearce D.L. (2009). Effect of Fines on Agglomeration in Spray Dryers: An Experimental Study. *International Journal of Food Engineering* 5, 2, 7. 1-36.
- Woo M.W., Daud W.R.W., Mujumdar A.S., Tasirin S.M. and Talib M.Z.M. (2010). Role of rheological characteristics in amorphous food particle-wall collisions in spray drying. *Powder technology*, 198, 252-257.
- Yajnik, K.S and Aubbaiah, V. (1973) *Journal of fluid mechanics*. Experiments on swirling turbulent flows. Part 1. Similarity in swirling flows, 60, 665-687.
- Zbicinski, I. (1995). Development and experimental verification of momentum, heat and mass transfer model in spray drying. *The Chemical Engineering Journal*, 58, 123-133.
- Zbicinski, I. and Piatkowski, M. (2007). Analysis of the mechanism of counter-current spray drying *Transp Porous Media* 66, 89–101 .
- Zbicinski, I. and Piatkowski, M. (2009). Continuous and discrete phase behavior in counter current spray drying. *Drying Technology*, 27, 12, 1353–1362.
- Zbiciński, I. and Xuanyou, L. (2006). Conditions for Accurate CFD Modeling of Spray-Drying.

DryingTechnology, 24, 9, 1109–1114.

Zbicinski, I. and Zietara, R. (2004).CFD model of counter-current spray drying process. Drying, São Paulo, Brazil, A, 169-176.

Zbicinski, I., Strumillo, C., and Delag, A. (2002a). Drying kinetics and particle residence time in spray drying. Drying Technology, 20, 9, 1751-1768.

Zbicinski, I. Delag, A. , Strumillo, C. and Adamiec, J. (2002b). Advanced experimental analysis of drying kinetics in spray drying. Chemical Engineering Journal, 86, 207–216.

Zbogar A., Frandsen F., Jensen P.A. and Glarborg P. (2009). Shedding of ash deposits. Progress in energy and combustion science, 35, 31-56.

Zhang F., Reeks M. W. and Kissane M. (2013). Resuspension of small particles from multilayer deposits in turbulent boundary layers. International conference in multiphase flow. Jeju, South Korea.

Ziskind G., Fichman M. and Gutfinger C. (1995). Resuspension of particulates from surfaces to turbulent flows.Review and analysis. Journal of aerosol science, 26, 4, 613-644.

Zonta F., Marchioli C. and Soldati A. (2013). Particle and droplet deposition in turbulent swirled pipe flow. International journal of multiphase flow, 56, 172-183.

